Remote
of Sea Ic
Northern S
Studies and A

Remote Sensing of Sea Ice in the Northern Sea Route

Studies and Applications

Ola M. Johannessen, Vitaly Yu. Alexandrov,
Ivan Ye. Frolov, Stein Sandven, Lasse H. Pettersson,
Leonid P. Bobylev, Kjell Kloster, Vladimir G. Smirnov,
Yevgeny U. Mironov and Nikolay G. Babich

Remote Sensing of Sea Ice in the Northern Sea Route

Studies and Applications

Springer

Published in association with
Praxis Publishing
Chichester, UK

PRAXIS

Professor Ola M. Johannessen
Founding Director
Nansen Environmental and Remote Sensing Center
Mohn-Sverdrup Center for Global Ocean Studies
and Operational Oceanography
Geophysical Institute, University of Bergen,
Bergen, Norway

Professor Stein Sandven
Nansen Environmental and Remote Sensing Center
Bergen, Norway
University Courses on Svalbard—UNIS,
Longyearbyen, Norway

Mr. Lasse H. Pettersson
Mr. Kjell Kloster
Nansen Environmental and Remote Sensing Center
Bergen, Norway

Dr. Vitaly Yu. Alexandrov
Nansen International Environmental and Remote
Sensing Center
St. Petersburg, Russia

Dr. Leonid P. Bobylev
Nansen International Environmental and Remote
Sensing Center
St. Petersburg, Russia
Nansen Environmental and Remote Sensing Center
Bergen, Norway

Professor Ivan Ye. Frolov
Dr. Vladimir G. Smirnov
Dr. Yevgeny U. Mironov
Arctic and Antarctic Research Institute (AARI)
St. Petersburg, Russia

Mr. Nikolay G. Babich
Murmansk Shipping Company
Murmansk, Russia

SPRINGER–PRAXIS BOOKS IN GEOPHYSICAL SCIENCES
SUBJECT *ADVISORY EDITOR*: Dr Philippe Blondel, C.Geol., F.G.S., Ph.D., M.Sc., Senior Scientist, Department of Physics, University of Bath, Bath, UK
Published in association with the Nansen Centers in Bergen and St. Petersburg
Nansen Center's Polar Series No. 4

ISBN 10: 3-540-24448-4 Springer-Verlag Berlin Heidelberg New York

Springer is part of Springer-Science + Business Media (springer.com)

Bibliographic information published by Die Deutsche Bibliothek

Die Deutsche Bibliothek lists this publication in the Deutsche Nationalbibliografie;
detailed bibliographic data are available from the Internet at http://dnb.ddb.de

Library of Congress Control Number: 2006924127

Printed in Germany

Cover design: Jim Wilkie
Project management: Originator Publishing Services, Gt. Yarmouth, Norfolk, UK

Printed on acid-free paper

Contents

Preface

The Northern Sea Route (NSR) consists of the sailing routes in the Russian Arctic between the Barents Sea in the west and the Bering Strait in the east (Figure 1). It is the shortest sailing route linking northwestern Europe and northeastern Asia. The distance between Yokohama and Hamburg is almost half of that through the Suez Canal and 10–14 days in sailing time can be saved using the northern route. However, the presence of sea ice significantly hampers navigation. In winter the sailing routes are covered with ice, and even in summer some parts are ice-covered, especially in the Laptev and East Siberian Seas. Therefore, a fleet of conventional and nuclear Russian icebreakers supports safe and cost-effective ship transportation during the different seasons.

Hydrometeorological information, including sea ice data, is accordingly an essential and integral part of navigation safety. Therefore, the Northern Sea Route Administration, founded in 1932, established a service of hydrometeorological support for the region.

From the start of this service, polar aviation began ice reconnaissance to support all shipping transport in the Arctic. By 1935, all foreign aircraft—except *Dornier Wal* seaplanes which were used for ice reconnaissance until 1945—were replaced by aircraft manufactured in Russia. In the 1950s, visual airborne ice reconnaissance continued to be the main tool for sea ice monitoring and hydrometeorological services for Arctic navigation. Annually, 30–40 Russian aircraft carried out 500–700 ice reconnaissance flights. In 1964, the scientific and manufacturing association NPO Leninets began developing SLAR specifically for ice reconnaissance. In summer of 1966 AARI obtained the first TV images from *ESSA-2* and *Meteor-1*. In 1975 the first satellite of the Russian *Meteor-2* series was launched and used for sea ice monitoring. In September of 1983 the first satellite of the Russian *Okean-01* series with SLR (side-looking radar) was launched and, as a result, almost immediately shipping support became more efficient.

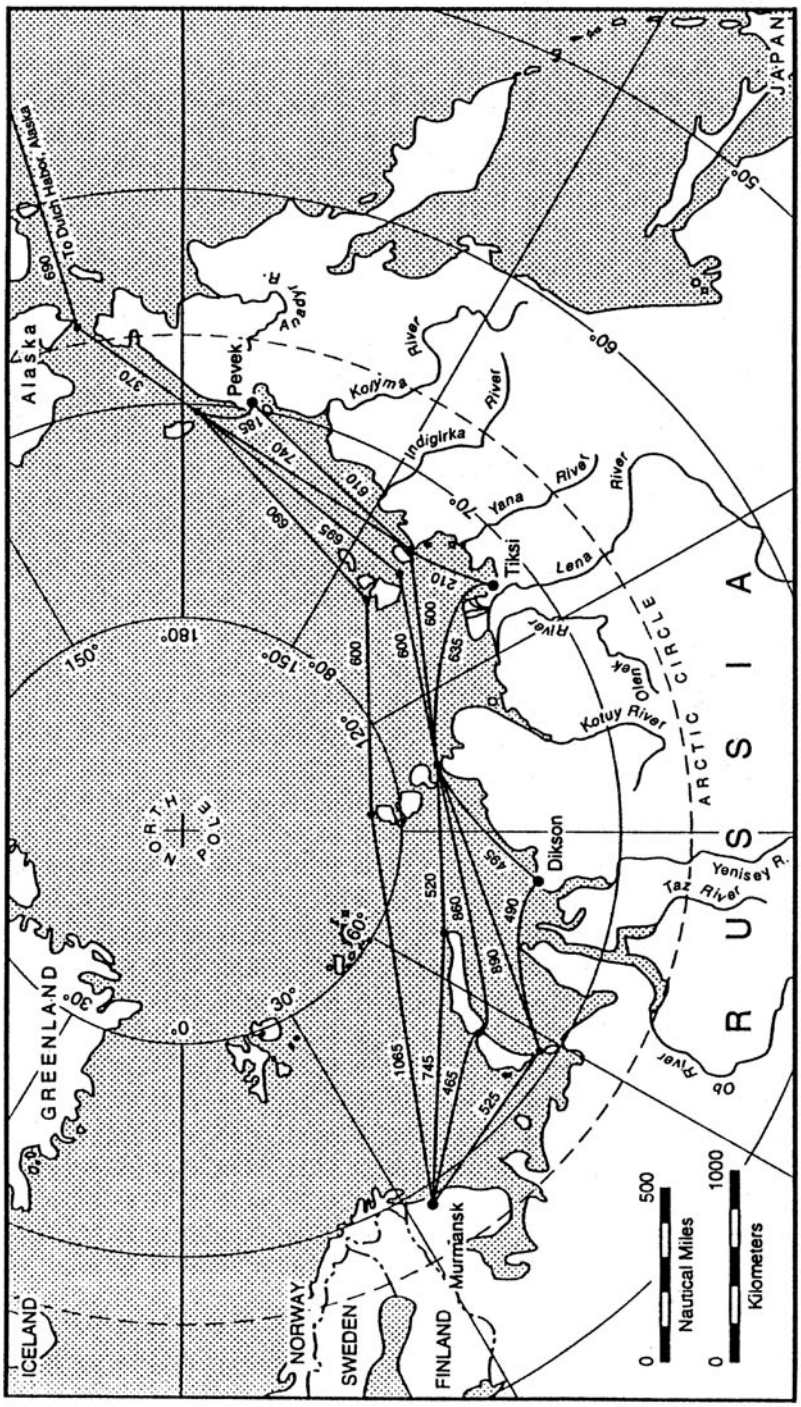

Figure 1. The major sailing routes along the NSR and distances between different sections in nautical miles.

Routine sea ice monitoring today is primarily based on satellite remote-sensing data in the optical and infrared range. However, weather- and light-independent satellite remote-sensing data in the microwave range significantly improved the availability of sea ice information. This began in the NSR in August 1991, just 2 weeks after the launch of the European Space Agency (ESA) *ERS-1* satellite, when real time synthetic aperture radar (SAR) images were transmitted to the French vessel *L'Astrolabe* to assist her navigation through the NSR from Europe to Japan. The *L'Astrolabe* expedition, headed by Pierre Sauvadet, included an *ERS-1* SAR project between ESA, with Guy Duchossois as *ERS-1* mission manager and the Nansen Environmental and Remote Sensing Center (NERSC) in Bergen, Norway, with Ola M. Johannessen as the project leader.

After the success of using SAR to route *L'Astrolabe* through the ice, the Nansen Centers in Bergen and St. Petersburg, and the Murmansk Shipping Company (MSC), conducted a number of campaigns to demonstrate the use of SAR for supporting the operations of the nuclear icebreakers of the MSC and their convoys. The principal project demonstrating the use of SAR in the NSR was "Icewatch" or, to give it its full title, "Real-Time Sea Ice Monitoring of the Northern Sea Route Using Satellite Radar Technology" that ran from 1994 to 1996. This was the first joint earth observation project between ESA and the Russian Space Agency (RKA). Partners in the "Icewatch Project"—in addition to ESA and RKA—were the Nansen Center in Bergen, the scientific and manufacturing association NPO Planeta and, later, the Scientific Research Centre for Exploration of Natural Resources (NITs IPR) in Moscow, the Arctic and Antarctic Research Institute (AARI) of Rosshydromet in St. Petersburg, the Scientific Foundation Nansen International Environmental and Remote Sensing Center in St. Petersburg and the Murmansk Shipping Company (MSC). Project leaders were Ola M. Johannessen of the Nansen Center and Alexey M. Volkov of the Scientific Research Center for Exploration of Natural Resources (NITs IPR) under RKA, with Guy Duchossois and Günther Kohlhammer of ESA and Georgy M. Polishuck of RKA as space agency representatives.[1] Based on the "Icewatch Project" two *ERS-1* and *-2* SAR receiving stations were installed in the Russian Federation—one in Moscow and the other in Khantymansiisk in western Siberia.

Following on from the "Icewatch Project", SAR data from *ERS-1* and *-2*, the Canadian *Radarsat* and the ESA *Envisat* started to be used semi-operationally in the NSR jointly with ice monitoring from AARI. This is the basis for this book, which is jointly written by authors from NERSC, AARI, NIERSC and MSC. Half of the writing of this book was funded by ESA through José Achache when he was Director of Earth Observation in ESA and Joseph Aschbacher, Programme Coordinator at ESA, while the remaining half was financed by institutional funding.

This book was also a component of the EU/INTAS Climate and Environmental Change in the Arctic (CECA) project, which was led by Prof. Ola M. Johannessen,

---

[1] Mr. Alain Fournier-Sicre, Head of the ESA Permanent Mission in the Russian Federation, Moscow, was instrumental in facilitating the cooperation between the two space agencies.

NERSC, with Dr. Leonid Bobylev, NIERSC, and Prof. Lennart Bengtsson, Max-Planck Institute for Meteorology, as partners. The CECA Project was awarded the Laureate of the EU transnational research Descartes Prize in Earth Science for 2005.

Ola M. Johannessen Director NERSC	*Leonid Bobylev* Director NIERSC	*Ivan Frolov* Director AARI
Nina Novikova NTsOMZ	*Volker Liebig* Director of EO, ESA	*Anatoly Eu. Shilov* Head of Department, RKA

Acknowledgments

This book is based primarily on the joint research and demonstration projects carried out between 1991 and 2005. The first was the European Space Agency's (ESA) project "*ERS-1* SAR Ice Routing of the *L'Astrolabe*" which supported the French vessel in her voyage through the Northern Sea Route in 1991. Subsequent projects were: the ESA–Norwegian Space Center's "*ERS-1* Pilot Demonstration Project—Real-time Sea Ice Monitoring of the Northern Sea Route Using *ERS-1* Satellite Radar Images" (1992–1995); the Nansen Center in Bergen's "SAR Strategy Program" (1994–1996) funded by the Research Council of Norway; ice routing of the Japanese project "*Kandalaksha '95* Voyage" through the Northern Sea Route; the ESA–Russian Space Agency's (RKA) "Real-time Sea Ice Monitoring of the Northern Sea Route Using Satellite Radar Technology—Icewatch Project" (1994–1996); the three EU projects "Ice Routes" (1997–1998), "Arctic Demonstration and Exploratory Voyage—ARCDEV" (1998–1999) and the "Integrated Use of New Microwave Satellite Data for Improved Sea Ice Observations—IMSI" project (1997–1999); as well as the ESA GMES project "SAR Ice Monitoring for Climate Research—ICEMON" (2003–2005).

The authors acknowledge financial support of these projects given by these agencies and contributions from the many personnel who took part in these projects. We are especially grateful to the Murmansk Shipping Company (MSC), which has been, and still is, a close partner throughout these years. Of particular importance has been the support from Mr. Yu.F. Glushko and Mr. A.G. Gorshkovsky, Chiefs of MSC's nuclear icebreaker fleet. We appreciate cooperation in the field of the captains, ice pilots and crew of the MSC icebreakers *Sovetsky Soyuz*, *Yamal*, *Taymyr*, *Vaygach* and *Kapitan Dranitsyn*. We are also thankful to the Russian Ice Monitoring Service: in particular, hydrologist V.E. Pashchenko, Captain A.V. Smirnov, hydrologist A.Ya. Winter; Chief of the Marine Operational Headquarters (MOH) Mr. B. Berdnikov and Chief of the Science Operational Group (SOG) Dr. N. Adamovich, both located in Dikson.

Studies with objectives of determining ice conditions in Arctic seas and developing methods for satellite information processing and analysis were carried out within the framework of these projects with the financial support of the Federal Service for Hydrometeorology and Environmental Monitoring and the Ministry of Education and Science of the Russian Federation. The authors are especially thankful to Professor A.V. Bushuyev, lead scientist in methods of sea ice remote sensing and Professor Z.M. Gudkovich, lead scientist in ice regime research at the Arctic and Antarctic Research Institute.

The Authors

Figures

Tables

Abbreviations

AARI	Arctic and Antarctic Research Institute
ACIA	Arctic Climate Impact Assessment
AFC	Aerial photo camera
AIISA	Automated Ice Information System for the Arctic
AIJEX	Arctic Ice Joint Experiment Study
AIRP	Automated Information Receiving Point
AMSR	Advanced Microwave Scanning Radiometer
ANSR	Administration of the Northern Sea Route
AO	Arctic Oscillation
AP	Alternating Polarization
APT	Automatic Picture Transmission
ARCDEV	ARCtic Demonstration and Exploratory Voyage
ARGOS	Satellite-based location and environmental data collection system
ARI	Arctic Research Institute
ARKTOS	Advanced system for classification of sea ice types in satellite radar images
ARO	Arctic Research Observatory
ASAR	Advanced SAR
ASF	Alaska SAR Facility
AVHRR	129, 149–150
BMP	Windows BitMaM
CCG	Canadian Coast Guard
CIHMI	Center for Ice and Hydrometeorological Information
CIM	Composite Ice Map
CIS	Canadian Ice Service
CNSR	Committee of the Northern Sea Route
DARMS	Drifting Automatic Radio Meteorological Stations

DMI	Danish Meteorological Institute
DMSP	Defense Meteorological Satellite Program
DN	Digital Number
ECDIS	Electronic Chart Display and Information System
ECHAM-4	Max-Planck Institute for Meteorology in Hamburg, Germany
ECNIS	Electronic Cartographic Navigation Information System
EEA	Exclusive Economic Area
EM	ElectroMagnetic
EO	Earth Observation
EOS	Earth Observation System
ERS	European Remote Sensing satellite
ESA	European Space Agency
ESMR	Electrically Scanning Microwave Radiometer
ESTEC	European Space Research and TEChnology Centre of ESA
ETSI	Expert Team on Sea Ice
EU	European Union
EUMETSAT	EUropean organization for the exploration of METeorological SATellites
FNMOC	Fleet Numerical Meteorological and Oceanographic Center
FRI	Full-Resolution Image
FTP	File Transfer Protocol
FYI	First-Year Ice
GHG	GreenHouse Gas
GIF	Graphic Interchange Format
GIS	Geographical Information System
GLCM	Gray Level Co-occurrence Matrix
GLONAS	A global positioning system
GMES	Global Monitoring for Environment and Security
GMT	Greenwich Mean Time
GPR	Ground Penetrating Radar
GPS	Global Positioning System
HadCM3	Hadley Centre at the UK Met Office
HDF	Hierarchical Data Format
HF	High Frequency (radar)
HH	Horizontal polarization
HMS	HydroMeteorological Service
HRPT	High-Resolution Picture Transmission
HV	Transmission is made in one polarization and receiving in another
IABP	International Arctic Buoy Program
ICG	Icelandic Coast Guard
ID	IDentifier
IFREMER	French Research Institute for Exploitation of the Sea
IICWG	International Ice Charting Working Group

IIP	International Ice Patrol
IMO	Icelandic Meteorological Office
IPCC	Intergovernmental Panel on Climate Change
IR imager	InfraRed radiometer
IR	InfraRed
JPEG	Joint Photographic Expert Group (file format)
KSAT	Kongsberg SATellite Services, Tromsø, Norway
LDA	Linear Discriminant Analysis
LFO	Low-Frequency Oscillation
LKF	Linear Kinematic Feature
LNG	Liquefied Natural Gas
LRI	Low-Resolution Image
MANSR	Main Administration of the Northern Sea Route
MCC	Multiple Cross Correlation
met.no	Norwegian Meteorological Institute
MIZ	Marginal Ice Zone
MLP	Multi-Layer Perceptron
MMF	Ministry of Marine Fleet
MODIS	MODerate-resolution Imaging Spectroradiometer
MOH	Marine Operations Headquarters
MOS	Japanese Marine Observation Satellite
MSC	Meteorological Service of Canada
MSC	Murmansk Shipping Company
MYI	Multi-Year Ice
NAO	North Atlantic Oscillation
NASA	National Aeronautical and Space Administration
NAVICECEN	Naval Ice Center
NAVOCEANO	Naval Oceanographic Office
NCEP	National Center for Environmental Prediction
NERSC	Nansen Environmental and Remote Sensing Center
NESDIS	National Environmental Satellite Data Information Service
NIB	Nuclear IceBreaker
NIC	National Ice Center
NIERSC	Nansen International Environmental and Remote Sensing Centre
NOAA	National Oceanographic and Atmospheric Administration
NORSEX	NOrwegian Remote Sensing EXperiment
NPI	Norwegian Polar Institute
NRT	Near-Real Time
NSIDC	National Snow and Ice Data Center
NSRA	NSR Administration
NZN	Novozemelsky northern ice massif
NZS	Novozemelsky southern ice massif
OY	Ob'–Yenisey
PAF	Processing and Archiving Facility (ESA)

PALSAR	Phased Array L-band Synthetic Aperture Radar
PDF	Probability Density Function
RAR	Real Aperture Radar
RGPS	*Radarsat* Geophysical Processor System
RICAE	Riga Institute of Civil Aviation Engineers
RKA	Russian Space Agency
RMS	Root Mean Square
RRMC	Regional Radio-Meteorological Center
RT	Real Time
SAR	Synthetic Aperture Radar
SAT	Surface Atmospheric Temperature
SLAR	Side-Looking Airborne Radar
SLP	Sea Level Pressure
SLR	Side-Looking Radar
SMMR	Scanning Multi-channel Microwave Radiometer
SRES	Special Report on Emission Scenarios
SSM/I	Special Sensor Microwave/Imager
SST	Sea Surface Temperature
SWK	SouthWestern Kara Sea (SWK)
SZE	Severozemelsky eastern ice massif
SZW	Severozemelsky western ice massif
TIFF	Tagged Image File Format
TM	Thematic Mapper
TSS	Tromsø Satellite Station (now KSAT)
UGMS	Yakutian Administration of the Hydrometeorological Service
UL, ULA	Classes of ice-strengthened ships
ULS	Upward-Looking Sonar
URL	Uniform Resource Locator
VH	Transmission is made in one polarization and receiving in another
VH	Vertical polarization
VPI	Russian system for broadcasting of information
WMF	Windows Meta File
WMO	World Meteorological Organization
WS	Wide-Swath
WSM	Wide-Swath radar Mode on *Envisat*
WWW	World Wide Web
YY	Yamalo–Yugorsky

Authors

Prof. Ola M. Johannessen
Nansen Environmental and Remote Sensing Center,
Mohn-Sverdrup Center for Global Ocean Studies and Operational Oceanography and
Geophysical Institute, University of Bergen, Bergen, Norway
Ola.Johannessen@nersc.no

Dr. Vitaly Yu. Alexandrov
Nansen International Environmental and Remote Sensing Centre, St. Petersburg, Russia
Vitali.Alexandrov@niersc.spb.ru

Prof. Ivan Ye. Frolov
Arctic and Antarctic Research Institute, St. Petersburg, Russia
Frolov@aari.nw.ru

Prof. Stein Sandven
Nansen Environmental and Remote Sensing Center, Bergen, Norway and
University Courses on Svalbard—UNIS, Longyearbyen, Svalbard, Norway
Stein.Sandven@nersc.no

Mr. Lasse H. Pettersson
Nansen Environmental and Remote Sensing Center, Bergen, Norway
lasse.pettersson@nersc.no

Dr. Leonid P. Bobylev
Nansen International Environmental and Remote Sensing Centre, St. Petersburg, Russia and
Nansen Environmental and Remote Sensing Center, Bergen, Norway
Leonid.Bobylev@niersc.spb.ru

Mr. Kjell Kloster
Nansen Environmental and Remote Sensing Center, Bergen, Norway
Kjell.Kloster@nersc.no

Dr. Vladimir G. Smirnov
Arctic and Antarctic Research Institute, St. Petersburg, Russia
Vgs@aari.nw.ru

Dr. Yevgeny U. Mironov
Arctic and Antarctic Research Institute, St. Petersburg, Russia
Mir@aari.nw.ru

Mr. Nikolay G. Babich
Murmansk Shipping Company, Murmansk, Russia
Deyneka@msco.ru

Contributing authors

Alexandrov, Vitaly Yu.
Nansen International Environmental and Remote Sensing Centre, St. Petersburg, Russia
Vitali.Alexandrov@niersc.spb.ru

Babich, Nikolay G.
Murmansk Shipping Company, Murmansk, Russia
Deyneka@msco.ru

Babiker, Mohamed
Nansen Environmental and Remote Sensing Center, Bergen, Norway
Mohamed.Babiker@nersc.no

Bobylev, Leonid P.
Nansen International Environmental and Remote Sensing Centre, St. Petersburg, Russia and
Nansen Environmental and Remote Sensing Center, Bergen, Norway
Leonid.Bobylev@niersc.spb.ru

Bogdanov, Andrey V.
Ruhr-Universitaet, Institut fuer Neuroinformatik, Bochum, Germany
Andrey.Bogdanov@neuroinformatik.ruhr-uni-bochum.de

Borodachev, Viktor Ye.
Arctic and Antarctic Research Institute, St. Petersburg, Russia
Aaricoop@aari.nw.ru

Bushuev, Andrey V.
Arctic and Antarctic Research Institute, St. Petersburg, Russia
Aaricoop@aari.nw.ru

Frolov, Ivan Ye.
Arctic and Antarctic Research Institute, St. Petersburg, Russia
Frolov@aari.nw.ru

Gorbunov, Yury A.
Arctic and Antarctic Research Institute, St. Petersburg, Russia
Gua@aari.nw.ru

Gudkovich, Zalman M.
Arctic and Antarctic Research Institute, St. Petersburg, Russia
Aaricoop@aari.nw.ru

Johannessen, Ola M.
Nansen Environmental and Remote Sensing Center, Mohn-Sverdrup Center for Global Ocean Studies and Operational Oceanography and Geophysical Institute, University of Bergen, Bergen, Norway
Ola.Johannessen@nersc.no

Karelin, Igor D.
Arctic and Antarctic Research Institute, St. Petersburg, Russia
Aaricoop@aari.nw.ru

Karklin, Valery P.
Arctic and Antarctic Research Institute, St. Petersburg, Russia
Karklin@aari.nw.ru

Kloster, Kjell
Nansen Environmental and Remote Sensing Center, Bergen, Norway
Kjell.Kloster@nersc.no

Losev, Stanislav M.
Arctic and Antarctic Research Institute, St. Petersburg, Russia
Aaricoop@aari.nw.ru

Loshchilov, Viktor S.
Arctic and Antarctic Research Institute, St. Petersburg, Russia
Lvs@aari.nw.ru

Lundhaug, Maria
Nansen Environmental and Remote Sensing Center, Bergen, Norway
Maria.Lundhaug@vesta.no (current affiliation)

Melentyev, Vladimir V.
Nansen International Environmental and Remote Sensing Centre, St. Petersburg, Russia
Vladimir.Melentyev@niersc.spb.ru

Miles, Martin
Bjerknes Centre for Climate Research, Bergen, Norway and
University of Bergen, Bergen, Norway
Martin.Miles@geo.uib.no

Mironov, Yevgeny U.
Arctic and Antarctic Research Institute, St. Petersburg, Russia
Mir@aari.nw.ru

Myrmehl, Cathrine
Nansen Environmental and Remote Sensing Center, and
Mohn-Sverdrup Center for Global Ocean Studies and Operational Oceanography, Bergen, Norway
Cathrine.Myrmehl@nersc.no

Paramonov, Alexandr I.
Arctic and Antarctic Research Institute, St. Petersburg, Russia
Paramonov@aari.nw.ru

Pettersson, Lasse H.
Nansen Environmental and Remote Sensing Center, Bergen, Norway
lasse.pettersson@nersc.no

Sandven, Stein
Nansen Environmental and Remote Sensing Center, Bergen, Norway and
University Courses on Svalbard—UNIS, Longyearbyen, Svalbard, Norway
Stein.Sandven@nersc.no

Shcherbakov, Yuriy A.
Arctic and Antarctic Research Institute, St. Petersburg, Russia
Jas@aari.nw.ru

Smirnov, Vladimir G.
Arctic and Antarctic Research Institute, St. Petersburg, Russia
Vgs@aari.nw.ru

Spichkin, Vladimir I.
Arctic and Antarctic Research Institute, St. Petersburg, Russia
Aaricoop@aari.nw.ru

Zaitsev, Lev V.
Nansen International Environmental and Remote Sensing Centre, St. Petersburg, Russia
Lev.Zaitsev@niersc.spb.ru

Introduction

This book covers a range of topics related to the monitoring of sea ice conditions in support of navigation in the Northern Sea Route (NSR). It includes the history of exploration of the Northern Sea Route, organization of sea ice monitoring, analysis of sea ice conditions, methodologies of satellite remote sensing of sea ice for supporting navigation and climatic variability of sea ice conditions in the Arctic Ocean and the Northern Sea Route. Use of the most advanced microwave techniques of sea ice monitoring—such as SAR data provided by the European *ERS-1*, *ERS-2*, *Envisat* and the Canadian *Radarsat* satellites—is specifically addressed.

Chapter 1 presents a brief history of Northern Sea Route exploration, the present period and future prospects for its use. During the 17th century the Russian Pomors and Cossacks sailed along the western and eastern parts of the Northeast Passage and discovered the Bering Strait. In the early 18th century the Great Northern Expedition mapped almost the entire coast of the Arctic Ocean. Many renowned expeditions were accomplished in the 19th century. Thus, Nordenskjöld onboard *Vega* passed for the first time through the entire NSR. De-Long attempted to reach the North Pole onboard *Jeannette*. Fridtjof Nansen's *Fram* sailed eastward through the Kara and Laptev Seas, where her transarctic drift started. Also, from the second half of the 19th century, trade shipping was developed in the Kara Sea for exporting Siberian mineral resources and importing industrial goods. By the beginning of the 20th century the whole Arctic coast had been discovered and studied, and navigation maps of Eurasian Arctic seas produced.

Studies and exploration of the Northern Sea Route continued during the Soviet period using icebreakers, aircraft, research vessels and a network of hydrometeorological stations. In 1932 the Northern Sea Route Administration was given the task of finally laying out the sea route from the White Sea to the Bering Strait, equipping and maintaining it in good state and ensuring safe navigation along it. Accordingly, a service of hydrometeorological support including sea ice monitoring for navigation was organized. In 1933 the *Sibiryakov* completed her voyage all along the NSR during

one navigation summer season. Since 1935, shipping operations—servicing the extensive industrial development in the Eurasian coastal Arctic area—were conducted according to the Soviet plan for cargo operations. Transport of goods in the Northern Sea Route continuously increased and during the late 1980s more than 6 million tons per year were shipped.

From July 1991 the NSR was officially declared open for non-Russian merchant vessels, and the French vessel *L'Astrolabe* was the first to pass through from west to east. However, after the Soviet period, much of the industrial production in the northern regions decreased and cargo turnover through the NSR was only 1.5–2.0 million tons after 1996.

However, the recent increase in oil and gas exploration and production and the associated increase in industrial activities in the areas of the far north of Russia will cause a further increase in transport in the NSR in the years to come, since the shelf area of the Arctic Ocean has 20–25% of the world's remaining oil and gas reserves. Therefore, safe operation in ice-infested waters in the NSR requires real time hydrometeorological and sea ice information of high quality and reliability.

Chapter 2 is devoted to sea ice conditions for the whole Arctic Ocean and in Eurasian Arctic Shelf seas. Significant seasonal changes in ice area in the Arctic Ocean occur in the marginal seas, with the seasonal maximum and minimum of ice extent in March–April and in September, respectively. Two major features of ice drift in the Arctic Ocean are the anticyclonic Beaufort Gyre and the transarctic ice flow between the North Pole and the northern margins of Eurasian Shelf seas, towards the Greenland Sea and Fram Strait.

Knowledge of sea ice conditions in Eurasian Arctic seas is essential for navigation in the Northern Sea Route and the offshore industry. Analysis of 50 years of observations from Russian polar stations and visual ice reconnaissance data allowed studying of ice formation and ice thickness growth, ice exchange between Eurasian Arctic seas and the Arctic Basin, distribution of fast ice, flaw polynyas and drifting ice. First-year ice prevails in Arctic Shelf seas; however, multi-year ice is often observed in the East Siberian Sea and in the northern parts of the Laptev and Kara Seas. On average, before the annual onset of ice formation, 80% of the eastern Laptev Sea and 85% of the southwestern Chukchi Sea are ice-free while the Barents Sea and the southwestern Kara Sea are almost ice-free. The northeastern Kara Sea and the western areas of the Laptev Sea and the East Siberian Sea become approximately 50% ice-free.

Chapter 3 addresses various aspects of sea ice monitoring and services in the NSR and in other Arctic countries. Soviet sea ice reconnaissance flights were made part of the hydrometeorological service for navigation at the beginning of the 1930s, and later on ice reconnaissance flights were made every 10 days more or less regularly during the entire navigation period. In the last decades of the 20th century various airborne remote-sensing techniques—such as side-looking airborne radars, radar video-impulse sea ice thickness meter, optical and radar satellite images—were implemented and widely used for operational support of shipping and compilation of weekly composite ice charts for the entire NSR. The first stage of an automated ice information system for the Arctic was accepted for commercial operation in 1989.

The Center for Ice and Hydrometeorological Information at the Arctic and Antarctic Research Institute (AARI) provides ice information to users in near-real time. They regularly issue ice charts and ice forecasts. With the end of regular airborne ice reconnaissance in the early 1990s, satellites became the main tool for acquisition of sea ice information.

To ensure safe operations in ice-covered seas operational monitoring of sea ice and icebergs has been developed in Arctic countries over several decades. The major ice services in the northern hemisphere are the U.S. National Ice Service, the Canadian Ice Service, the Danish Ice Service for Greenland waters, the Icelandic Ice Service and the Norwegian Ice Service, all of which are briefly described.

A study of users' requirements for sea ice information was done as part of the "Icewatch Project". The major user of sea ice information for navigation in the NSR is the Murmansk Shipping Company, being responsible for provision of icebreaker escort of merchant ice class cargo vessels and tankers. Depending on the purpose, tasks and objectives, ice information is divided into three main categories: strategic, operational and tactical. Analysis of different remote-sensing data concludes that *Envisat* and *Radarsat* SAR radar images, which can cover the entire area of the NSR in a 48-hour period, to a large extent satisfy users' requirements for support of navigation in sea ice, and therefore need to be routinely implemented in AARI's operational systems.

Chapter 4 deals with methodologies of satellite remote sensing of sea ice. Currently, Russian sea ice monitoring of the Northern Sea Route is based primarily on the optical and infrared images from *NOAA* and *Terra* satellites. Classification of sea ice parameters from these images is done, and derivation of ice thickness using IR images is also possible in the absence of clouds and for sea ice up to 120 cm thick.

The major principles of synthetic aperture radar (SAR) are described. Analysis of backscatter (σ^0) from sea ice shows that, at the C-band, surface scattering is predominant for young and first-year ice, as well as summer ice, while volume scattering is typical of old ice in winter conditions. Typical changes in radar backscatter from sea ice during winter are: low backscatter from grease and new ice and nilas; increase for pancake and gray ice; decrease in first-year ice; and, finally, increase for multi-year ice. Significant differences between the backscatter of the same ice types was found between sea ice at the ice edge and within the pack ice, but this was due to different roughness.

Signatures of the principal sea ice types and their expressions in *ERS*, *Radarsat* and *Envisat* SAR images have been specified and verified based on a series of subsatellite field experiments. The main sea ice parameters—including stages of ice development, forms of fast ice and pack ice, ice edge location, polynyas, ice surface features and icebergs—have been derived from radar images. Some ambiguities in their interpretation are caused by the similarity of signatures between different sea ice types and features. Techniques currently used for automatic classification of SAR images are presented. Furthermore, description of the methodology of ice chart compilation from satellite images and principles of sea ice mapping and generation of digital ice chart data are described. Examples of ice charts compiled from

different satellite sensor systems are presented including the use of Geographical Information System (GIS) tools.

Chapter 5 is devoted to studies of sea ice conditions in western and eastern parts of Eurasian Arctic seas. Regular use of satellite images for monitoring the Barents and Kara Seas began in the early 1970s, and after 1991 composite ice charts have been based on the optical and infrared range as well as side-looking radar (SLR) satellite imagery from the Russian *Okean* satellite. In spite of relatively coarse resolution they allow detection of ice edge, boundaries of landfast ice and polynyas and zones of different concentration and age with sufficient accuracy, including seasonal changes.

Satellite SAR data are used semi-operationally for studies of sea ice conditions in the NSR, and some results of these studies are described. The fast ice boundary in the western part of the Eurasian Russian Arctic and around Franz Josef Land was determined from *Radarsat* ScanSAR images for selected years. Furthermore, using *ERS* SAR and *Radarsat* ScanSAR images, the mean and standard deviations of polynya widths have been determined in the western Eurasian Arctic. Short-term, medium-term and long-term ice drift estimates were derived from successive satellite images for the Laptev Sea. The SAR imagery represents a unique capability for mapping ice drift in straits and near the coasts where other data sources provide limited information because of limited spatial resolution and cloudiness.

Chapter 6 deals with semi-operational use of SAR data for supporting ice navigation. Since 1991 the Nansen Centers in Bergen and St. Petersburg together with Murmansk Shipping Company have demonstrated the use of SAR data for planning and selection of the navigation route in sea ice. Ten expeditions are described. In these expeditions *ERS-1/2*, *Radarsat* and *Envisat* SAR images were transmitted to icebreakers in near-real time to help them navigate in sea ice. This experience proves that high-resolution light- and weather-independent SAR images can be effectively used for both strategic and tactical support of icebreaker operations in sea ice. In 2004–2005 *Envisat* ASAR images for the western part of the NSR were routinely transmitted every 3 days to the MOH at the Murmansk Shipping Company, which selected and transmitted sailing routes to the nuclear icebreakers. Even in relatively easy sea ice conditions during winter–spring 2005 the average speed of ships in ice increased by about 30–40% as a result of using SAR data for ice routing.

The methodology of using SAR data onboard icebreakers for their tactical navigation in sea ice was also tested in many of the expeditions. It includes processing SAR raw data to make images, transmission of the images to icebreakers in the Northern Sea Route and their use by captains for ship routing. Experience of using satellite imagery in the optical and infrared band onboard the icebreakers is also described. Here, particular attention is drawn to the present technique of *NOAA* and *Meteor* imagery presentation onboard icebreakers in the Electronic Chart Display and Information System (ECDIS) of ship navigation.

The future of sea ice monitoring in the NSR should combine use of remote-sensing data in different spectral ranges, including routine use of SAR data, implementation of new information products for ice services and efficient distribution to users. Any future system of satellite monitoring for the purpose of ice navigation

should primarily be based on satellite data with a spatial resolution of at least 50–100 m and subject to daily coverage.

Chapter 7 is devoted to the climatic variability of sea ice in the Arctic with the emphasis on the NSR. Long, continuous, observational data sets are necessary in order to investigate the long-term climatic fluctuations of sea ice. AARI data are the most comprehensive record for the Northern Sea Route and the greater Eurasian Arctic.

Overall, the interannual fluctuations of ice area in Eurasian Arctic seas during the 20th century indicate a gradual decrease through the century. However, interannual to multi-decadal variability in the ice cover area of the Arctic Ocean and its seas can also be characterized as having a quasi-periodic behavior on multiple time scales. AARI data analysis found these variations to be characterized by cyclic fluctuations with periods of 2–3, 5–7, 8–12 years and about 20 and 50–60 years, respectively.

Sea ice data sets derived from passive microwave data are among the longest continuous satellite-derived geophysical records, extending over the last quarter century. Analyses of merged SMMR–SSM/I data establish the decrease in Arctic sea ice area and extent (1978–2005) to be about ~3% per decade. Sea ice decrease in recent decades has been larger during summer, and September 2005 was the absolute minimum extent observed. A relatively large (~7% per decade) reduction in the multi-year ice area was found for the same period.

Knowledge of the long-term variability of ice cover in the Arctic Ocean and its marginal seas is of crucial scientific importance for climate study development, but also of strategic importance for planning shipping and other types of economic activities—such as gas and oil production in the Arctic, particularly in the Northern Sea Route.

The AARI authors of this book present sea ice scenarios for the 21st century using statistical models based on observed climatic variability of sea ice cover in the 20th century and predict that the ice extent will vary with a dominant period of 50–60 years reaching maximums around 2030–2040 and 2090–2095, respectively, and minimums in-between.

On the other hand, the Norwegian group of authors (Johannessen *et al.*, 2004) predict—by use of two coupled global climate models—that a reduction in the ice extent of 80% will occur during the summer as a result a doubling of CO_2 in the atmosphere and 20% during wintertime. These predictions are also strongly supported by the ACIA (2004). However, internal variability of the climate system—as observed with the strong warming event that peaked around 1940 and caused a major reduction in sea ice extent—can upset these predictions (Johannessen *et al.*, 2004). Finally, an assessment is made on how future climate will affect ice conditions in the Northern Sea Route.

The **Afterword** discusses present and future situations regarding gas and oil production and reviews other industrial activities, including the future use of the Northern Sea Route.

1

History of the Northern Sea Route

"History is a lantern to the future, which shines to us from the past"
V.O. Klyuchevskiy

1.1 FIRST VOYAGES
(*V.Ye. Borodachev, V.Yu. Alexandrov*)

The history of the exploration of the North is full of heroic spirit and tragedy—the voyages and expeditions that accompanied geographical discoveries—the history of scientific studies—organization of a system of stationary and non-stationary observations—creation of the scientific–technical support service for the Northern Sea Route (NSR)—all in all, the history of a fierce battle against the incredibly severe conditions of the Arctic.

It is challenging to comprehensively reconstruct the background to this history. The famous Norwegian polar explorer and scientist Fridtjof Nansen wrote: "We speak about the first discovery of the North—but how can we know when the first man appeared in the Earth's northern regions? We know nothing except for the very last migration stages of humanity. What occurred during these long centuries is still hidden from us" (Nansen, 1911).

Indeed, we have some evidence on Pytheas, a Greek from Massalia, who between 350 and 310 BC reached England and then a "gloomy land" he called Thule, beyond which "there is no sea or land or air with some mixture of all these elements hanging in space" (Belkin, 1983). Such a perception of the earth's northern regions was preserved for many centuries and only began to change in the 9th to 11th centuries with the appearance of first the Norsemen in the Barents and White Seas. Between 870 and 890 AD, more than a thousand years after the voyage of Pytheas, the Norwegian seafarer Ottar rounded the northern tip of Europe and explored the Barents and White Seas. The Norsemen also sailed to the mouth of Severnaya Dvina after Ottar: Eric Bodek in 920, Harald Grey Cloak in 965, Tore Hund in 1026, Haakon in 1090, and Ivar in 1222 (Henning, 1944).

The camps of Pomors,[1] who actively developed areas of the White and Barents Seas hunting seals and walruses, appeared in the mouths of the Onega, Dvina and Pechora Rivers in the 10th century. In 1032 a team headed by the Novgorodian voevode[2] Uleb made the first known sea voyage eastward of the White Sea and reached Kara Gate and Yugorskiy Shar (Belov, 1977). In the 12th century, Novgorodian merchants, developing the fur trade in Yugorskiy Land,[3] seem to have crossed the Yamal Peninsula getting as far as the lower reaches of the Ob' River. Throughout the 13th to 15th centuries the Pomors sailed into the Kara Sea, reaching it through the sea's southern Novozemelsky Straits and Matochkin Shar Strait.

Among the achievements of the Norsemen and Pomors who sailed in the White and Barents Seas was the discovery of a number of islands including Novaya Zemlya and Spitsbergen. These voyages were highly risky because they were made onboard small wooden boats and without knowledge of climate, ice and navigation conditions. It was seafarers like these who were the first to accumulate knowledge about the nature of sea ice. Investigating winds and currents, tidal and other natural phenomena, they associated them with changes in sea ice state. For example, the appearance of fractures in ice as tidal currents changed from flowing to ebbing was called by the Pomors "ice divergence". This term is still used in modern dictionaries. Seafarers got to know the basic ice-drift pattern in the Barents Sea. They also knew about ice export through the Greenland Sea. As part of their preparation for an expedition to the North Pole from the north shore of Spitsbergen, English explorers collected sea ice data from the Pomors.

1.2 VOYAGES IN THE 16TH–17TH CENTURIES (*I.Y. Frolov, V.Yu. Alexandrov, V.Ye. Borodachev*)

At the beginning of the 16th century, the dominance of Spain and Portugal over all known shipping lanes forced other European countries to search for alternative routes, mainly across the Nordic seas. It was at this time that a proposal to sail to China using the Northern Sea Route was proposed by Sebastian Cabot and a Moscow diplomat Dmitriy Gerasimov (Vize, 1939; Belov, 1970). Geographical knowledge of the Arctic at that time was rather vague, as can be seen from the map of the polar region published by a Dutch cartographer, Mercator (Figure 1.1). The contours of the mainland and archipelagos are significantly different from those of contemporary maps. The central Arctic was completely unknown and speculations about land there were quite common.

In the second half of the 16th century, Dutch and English merchants organized several expeditions to the Arctic with the aim of passing eastward through the polar ice. Ships under the command of Hugh Willoughby and Stephen Burrough reached the eastern Barents Sea. The Dutch merchant Olivier Brunel together with Russian

[1] The Pomors are a native Russian population living along the White Sea coast.
[2] A voevode is a military leader, ruler of Slavic nations.
[3] This corresponds to the present region on the border between the Barents and Kara Seas.

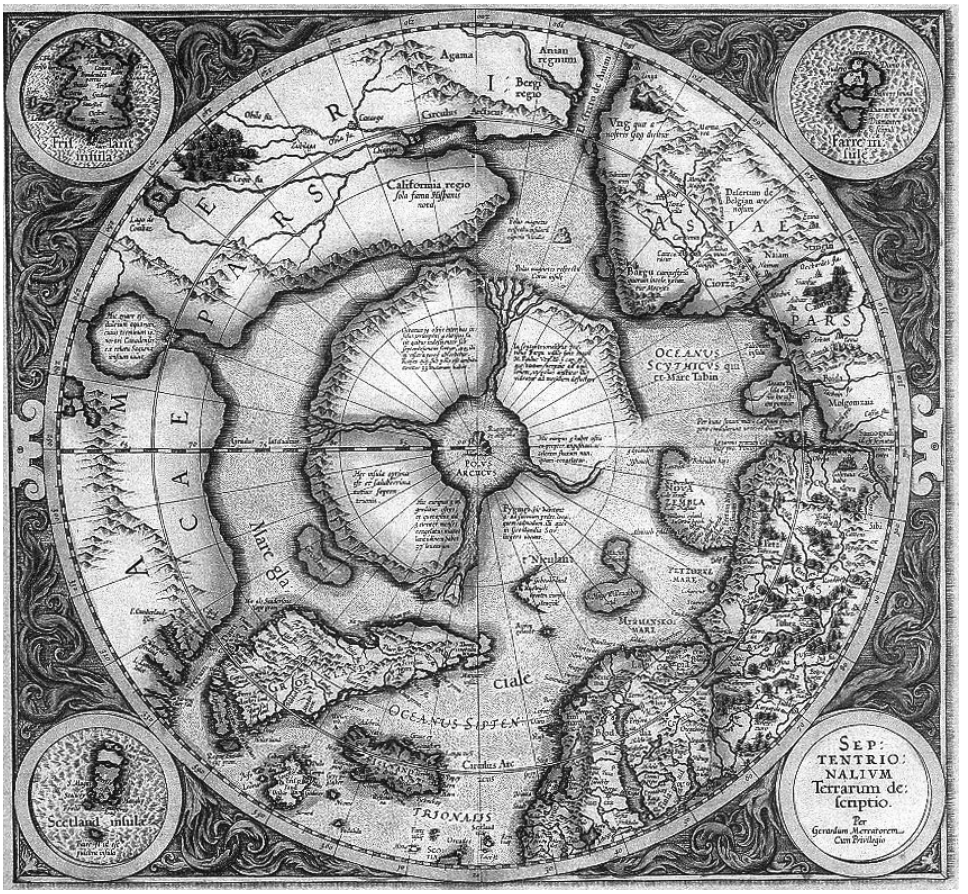

Figure 1.1. Map of the Arctic by Gerhardus Mercator (1512–1594). The map was modified several times and published in 1606 with Spitsbergen drawn on it. From Drivenes and Jølle (2004).

seafarers made a sea voyage from the mouth of the Pechora to the lower Ob', while the expedition commanded by Arthur Pet and Charles Jackman sailed across Yugorskiy Shar Strait to the Kara Sea (Vize, 1939). At the end of the 16th century, three expeditions were organized to the Arctic under the command of Willem Barents. During the last of these, explorers rounded the northern tip of Novaya Zemlya where their ship was trapped in ice and damaged in the bay called *Ledyanaya Gavan'* (Ice Harbor). After a severe winter they continued and eventually reached the Kola Settlement, but at great cost: Willem Barents died on the way and was buried on the northern island of Novaya Zemlya (Vize, 1939).

After Barents's voyages, interest in the Northeast Passage decreased considerably. However, at the end of the 16th century Russia began intense exploration of Siberia and the Far East, and the Asian continent from the Urals to the Pacific Ocean

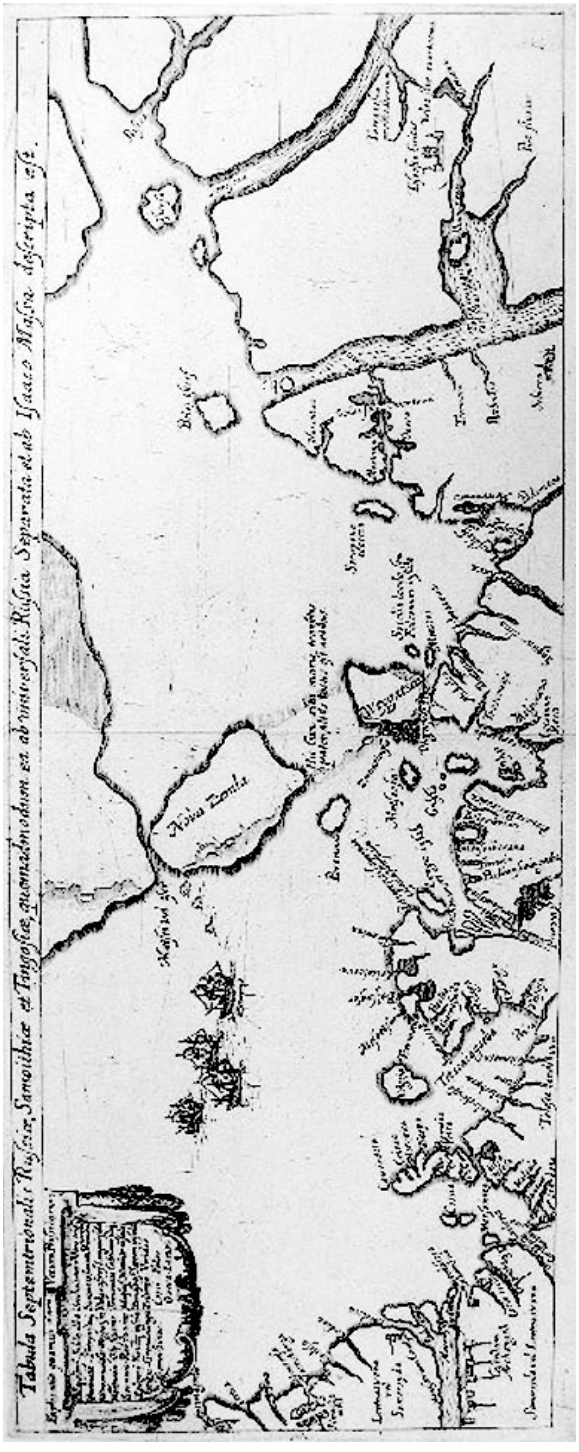

Figure 1.2. Map of the northern coast of Russia made by Isaac Massa in 1611.

was spanned in slightly more than a half-century (1581–1641). The northern lands and seas were claimed by Russia, who took the leading role in the development of Arctic shipping. This contributed to the development of "overseas" trade, concentrated in the 16th and 17th centuries in the only seaport, Arkhangelsk. During this time a continuous flow of cargo was transported along the Severnaya Dvina (Belov, 1956).

At the end of the 16th century, shipping along the coast of the Arctic Ocean became significantly more active. Pomors and manufacturers made voyages from the White Sea to Novaya Zemlya and Spitsbergen. Between 1610 and 1619 no fewer than 16 or 17 ships sailed annually along the Ob' and Taz Rivers to Mangazeya. However, use of this route was banned by the Moscow Government in order to prevent foreign penetration into Siberia, causing a lot of harm to the development of shipping in the north (Rudnev and Kulik, 1915). From data gathered in Russia, Isaac Massa published in 1611 a map of the Arctic coast (Figure 1.2), depicting the Ob' Delta, the Yamal Peninsula, and also the mouths of the Yenisey and Pyasina, where sea mammals were hunted. In the 17th century, Russian seafarers passed through the most difficult part of the Northeast Passage along the Taymyr Peninsula coast and rounded Cape Chelyuskin (Belov, 1977).

In the first half of the 17th century, Cossacks sailed to what they termed the "Icy Cold Sea" along Siberian rivers. The main voyages of Cossack seafarers were made from Yakutsk and Zhigansk along the Lena River to the sea and then to the Kolyma River along the coast (Figure 1.3).

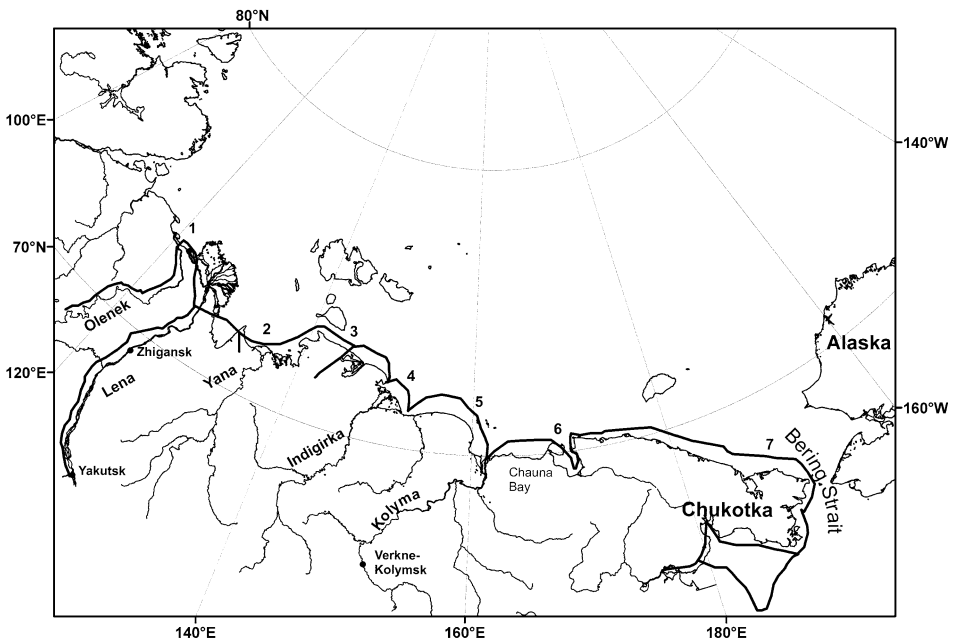

Figure 1.3. Eastward advances of the Russians in Northeast Asia in the 17th century: (1) I. Rebrov (1638), (2) I. Perfilyev (1637), (3) I. Rebrov (1633), (4) D. Zyryan (1642), (5) D. Zyryan and M. Stadukhin (1643), (6) I. Ignatyev (1646) and (7) S. Dezhnev (1648).

Typically, as many as ten ships sailed together in these voyages. In the 15 years following 1633 the Cossacks discovered the mouths of all major rivers flowing to the Laptev and East Siberian Seas. Simultaneously, settlements appeared along the coast between the Lena and Kolyma, which, however, did not exist for long (Khmyznikov, 1937).

In 1646 the first attempts to pass by sea to the east of Kolyma were undertaken by Ivan Ignatyev, who sailed to Chaunskaya Bay along the coastal polynya. The advance of Russian seafarers along the Eurasian Arctic coast ended with the voyage of Simon Dezhnev. In 1648, the Russian ships under his direction sailed from the Kolyma to the Pacific Ocean and discovered the Bering Strait 80 years earlier than the Bering expedition. The northeastern cape of Chukotka discovered by Dezhnev, was named after him in 1898 (Vnukov, 2000).

As a result of expeditions in the 16th and 17th centuries, during which mainland shores, islands and encountered rivers were discovered and described, knowledge of the real length of the Northeast Passage, coastline of the Eurasian Arctic seas and ice conditions was significantly expanded. "All north coast of Eurasia, excluding probably part of Taymyr, was passed by the Russian seamen before 1650 and this achievement really belongs to the Russians" (Armstrong, 1996).

1.3 FROM THE 18TH TO THE EARLY 20TH CENTURY (*V.Y. Alexandrov, V.Y. Borodachev, I.Y. Frolov*)

1.3.1 Expeditions and geographical discoveries

As a result of Peter the Great's reforms, Russia became a powerful sea state, necessary to support and protect regular shipping to its territories in the Far East and necessary for the development of foreign trade. This is the reason much attention in the first half of the 18th century was devoted to exploring the coast of Eurasia from the White Sea to Kamchatka. In 1728 an expedition headed by V. Bering onboard *Svyatoy Gavriil* passed to the north of Kamchatka, discovered the Komandorskiye and Aleutian Islands and found that Asia did not connect with America. The Great Northern Expedition, commanded by V. Bering, obtained the most important geographical discoveries and scientific results in 1733–1743. It surveyed the coast of the Arctic Ocean and divided it from west to east into four sectors: (1) to the west of the Ob', (2) between the Ob' and Yenisey, (3) between the Yenisey and Lena, and (4) east of the Lena, each of which were studied by individual teams

The ships of the two western teams were able to pass from Arkhangelsk to the Yenisey, perform a survey of part of the coastline and conduct observations of tides and currents. Exploration of the most difficult segment of the Northeast Passage between the Yenisey and Lena, around the Taymyr Peninsula, was carried out both from the western and from the eastern sides. In spite of this, attempts to round Taymyr from the sea were unsuccessful and inventory of a significant part of the

peninsula coast was made from land. During this work, S. Chelyuskin in 1742 reached the northern tip of Eurasia later named after him, Cape Chelyuskin. The eastern team passed by sea from the Lena to the Indigirka, then to the Kolyma River, and described the coast. In summer of 1741 in an attempt to pass further eastward, the expedition's ships reached Cape Bolshoy Baranov, where they encountered compact, thick ice.

In general, the Great Northern Expedition is a worthy member of the most effective expeditions in the history of earth's exploration. It described and mapped almost the entire coast of the Arctic Ocean and discovered Alaska. Based on the collected data, M.V. Lomonosov compiled in 1763 a map of the polar regions, which correctly described the coast of the Eurasian Arctic. Using the same data he also determined some regular features that form the natural conditions of the Arctic Ocean (Lomonosov, 1952). Maps, sailing directions, data of depth measurements, and information on ice conditions were widely used by the following generations of seafarers. These voyages also showed that ice conditions along the NSR during the period 1733–1743 were considerably more severe than in the 17th century and at present. All ships were frequently trapped in ice yet they continued to sail to their various destinations for many years. In spite of enormous efforts, they were unable to pass along the coast of the Taymyr Peninsula and exit to the Pacific Ocean. It was obvious that wooden ships could not make such voyages along the NSR.

Nevertheless, attempts to master the Northeast Passage continued. Based on the hypothesis of "open sea" in the northern polar area, M.V. Lomonosov proposed a plan to sail to the Pacific Ocean across the Pole. In 1765–1766 six ships under the command of Admiral V.Ya. Chichagov twice attempted to do so but both times they were stopped by the ice and returned to Arkhangelsk.

Attempts to sail along the NSR from the Pacific Ocean to the west began more than 200 years later than in the European part. In 1778, James Cook's ships *Resolution* and *Discovery* passed through the Bering Strait and sailed westward, but near Cape Schmidt compact sea ice blocked their way. The next year this expedition was headed by Clark, after Cook's death, and made one more attempt, but once again it was unable to pass farther than Cape Schmidt. This was interpreted in England as conclusive proof of the impossibility of using the NSR (Vize, 1939). After that, no further attempts were made until the middle of the 19th century.

In the 18th century, there were several expeditions to the islands and the coast of the Arctic Ocean. In 1741, Savva Loshkin made an outstanding voyage around Novaya Zemlya and proved that the prevailing concept in cartography of the 16th to 18th centuries of a giant Novaya Zemlya was incorrect. A couple of decades afterwards, the expedition of Fedor Rozmyslov made a survey of Matochkin Shar Strait. In 1760–1762 a Yakutian[4] merchant Nikita Shalaurov sailed from the mouth of the Lena to Cape Shelagskiy and tried to round the northeast tip of Asia. Based on conducted measurements he issued a map depicting the shore between the mouth of the Lena and Cape Shelagskiy that was highly accurate for that time (Vize, 1939). In 1764, Shalaurov sailed eastward again, but 53 sailors onboard the *Vera*, *Nadezhda*, and *Lubov'* perished trying to overcome the ice of the Chukchi Sea. In 1787 the

[4] The Yakuts are one of the nations living in the northeastern part of Russia.

Northeastern Expedition, led by Joseph Billings and Gavriil Sarychev, began to explore the coast of the Chukotka Peninsula and land to the north of the mouth of the Kolyma. The explorers onboard the *Pallas* and *Yasashna* attempted three times to pass eastward, but each time ice stopped them in the vicinity of Cape Bolshoy Baranov. Some 4 years later the Northeastern Expedition made a further attempt to sail westwards from the Bering Strait onboard the *Slava Rossii*, which they built in Kamchatka, but again without success. However, a map of the north coast of Chukotka was made by questioning the indigenous people (Pasetsky, 1983).

At the beginning of the 19th century a number of important expeditions were carried out in the northeastern Arctic. Yakov Sannikov investigated Stolbovoy, Faddeyevskiy, and Novaya Sibir' Islands. The expedition of the college registrar, M.M. Gedenstrom, made a transit from Novaya Sibir' Island to the mouth of the Kolyma, reported for the first time the existence of the Siberian Polynya, and made a survey of the coast between the mouths of the Yana and Kolyma Rivers (Vize, 1939). While on Kotel'nyy Island, Gedenstrom saw in the northeast "a dark-blue color quite similar to the one sometimes visible above a distant land." Thus, the legend about the hypothetical "Sannikov Land" was born, one which existed for more than 100 years. During 1820–1823, the expedition headed by a naval officer P.F. Anjou made the first reliable map of the New Siberian Islands. At the same time, a team under naval lieutenant F.P. Wrangel made an instrumental inventory of the coast from Cape Shelagskiy to Kolyuchinskaya Bay and tried to find the land said to be located, from rumors, to the north of Cape Shelagskiy (Tammiksaar, 1998). The existence of this land was confirmed when, in open water some 25 km from its southwestern tip, Wrangel marked it on the map. Later, this island was observed from the *Gerald*, and was completely mapped by T. Long's American expedition onboard the *Rogers* in the second half of the century.

Several important expeditions were made to Novaya Zemlya: by F.P. Litke (1821–1824), P.K. Pakhtusov (1834–1835), and A.K. Tsivol'ka (1837–1839). Under severe conditions, surveys of much of the west and east shores of the southern and northern islands of Novaya Zemlya were made. These expeditions paid a lot of attention to oceanographic, ice, meteorological, and other studies, but were however rather separate regarding synchronous coverage of water areas and time of observations. In 1870 a Norwegian manufacturer E. Johannessen for the first time after Loshkin rounded Novaya Zemlya. On the basis of this voyage the Norwegian meteorologist Henrik Mohn made a map of the northern part of Novaya Zemlya, which differed significantly from previous maps (Vize, 1939).

Although the existence of land to the northeast of Novaya Zemlya had been long advocated, this area in the middle of the 19th century was indicated by a white spot on the map. In 1873 the unknown land was discovered by the Austro-Hungarian expedition under the command of Karl Weyprecht and Julius Payer onboard the *Tegetthoff*, when transported along by drifting ice. The next year, the explorers surveyed and mapped a significant portion of the archipelago which they named after the Austrian Emperor Franz-Josef. After that, the expedition of Leigh Smith onboard the steam yacht *Eira* discovered the islands Nordbruk, Bruce, George Land and Alexandra Land, and the expedition of Frederick Jackson sailed through the

British Channel and mapped a number of new islands to the west and east of this strait (Vize, 1939).

The first voyage to successfully pass through the NSR was conducted by a Swedish scientist A.E. Nordenskjöld, who was supported and financed by the Russian goldmine owner A.M. Sibiryakov, Swedish King Oscar II, and manufacturer O. Dikson. The voyage was made onboard the *Vega*, which on 30 July 1878 departed from the Kara Sea together with Sibiryakov's ship *Lena*. During August both ships under favorable ice conditions passed Dikson, rounded Cape Chelyuskin and—following along the coast of Taymyr, which turned out to be located much more westward than in the data of the Great Northern Expedition—reached the mouth of the Lena (Vize, 1939). From here, the *Vega* continued her voyage alone. East of the Medvezh'i Islands, the ice conditions sharply deteriorated and the ship moved eastward along the flaw polynya. Particularly heavy ice was observed near Cape Schmidt and on 29 September the *Vega* had to overwinter to the east of Kolyuchinskaya Bay. In summer of the next year the ship took just 2 days to reach the east cape of Asia. Thus, the first passage from the Atlantic to the Pacific Ocean along the NSR was made without loss or ship damage. The route of the *Vega* is shown in Figure 1.4. In spite of the successful voyage, Nordenskjöld believed that shipping between Europe and the mouth of the Yenisey in the west and between the Pacific Ocean and the mouth of the Lena in the east had greater importance than through-voyages. "This route as far as the ice regime near the shores of Siberia is known will hardly ever have any actual importance for trade" (Nordenskjöld, 1936).

In 1879–1891 the De-Long expedition onboard *Jeannette*, organized by the owner of the *New York Herald* G. Bennett, attempted to reach the North Pole. After drifting from Gerald Island and discovering the archipelago, named later after De-Long, the ship was crushed by the ice and sank 800 km northeast of the mouth of the Lena. The expedition reached the mainland by sledge and in boats. Some expedition members were able to save themselves; however, De-Long and another group froze to death in the Lena Delta. The drift of the *Jeannette* demonstrated that the "open sea" hypothesis was ungrounded.

During this period some scientists believed that Greenland stretched far to the north to the central Arctic. This is shown in a map from the renowned German geographical publication *Petermans Geographische Mitteilungen* (see Figure 1.5).

On 24 June 1893 the Norwegian Fridtjof Nansen set out on one of the most daring and exciting research expeditions the world had ever seen. Its aim was to drift across the North Pole in a ship frozen in the ice. The expedition of Fridtjof Nansen onboard the *Fram* was scientifically justified and carefully prepared. The rounded shape of the ship hull was specially designed so that at compression by ice the ship was simply lifted upward by the ice, rather than crushed and sunk. Entering the Kara Sea on 4 August 1893, the *Fram* almost immediately encountered drifting ice and it took to the middle of August to pass the northern coast of Yamal. During the course of further navigation in open water, the expedition discovered Sverdrup and Scott-Hansen Islands. To the east of the Nordenskjöld Archipelago the ship sailed into heavy ice; however, it was able to pass Cape Chelyuskin and much of the Laptev Sea, sailing along the shore. In its easternmost reach, the *Fram* headed northward and on 20 September 1893

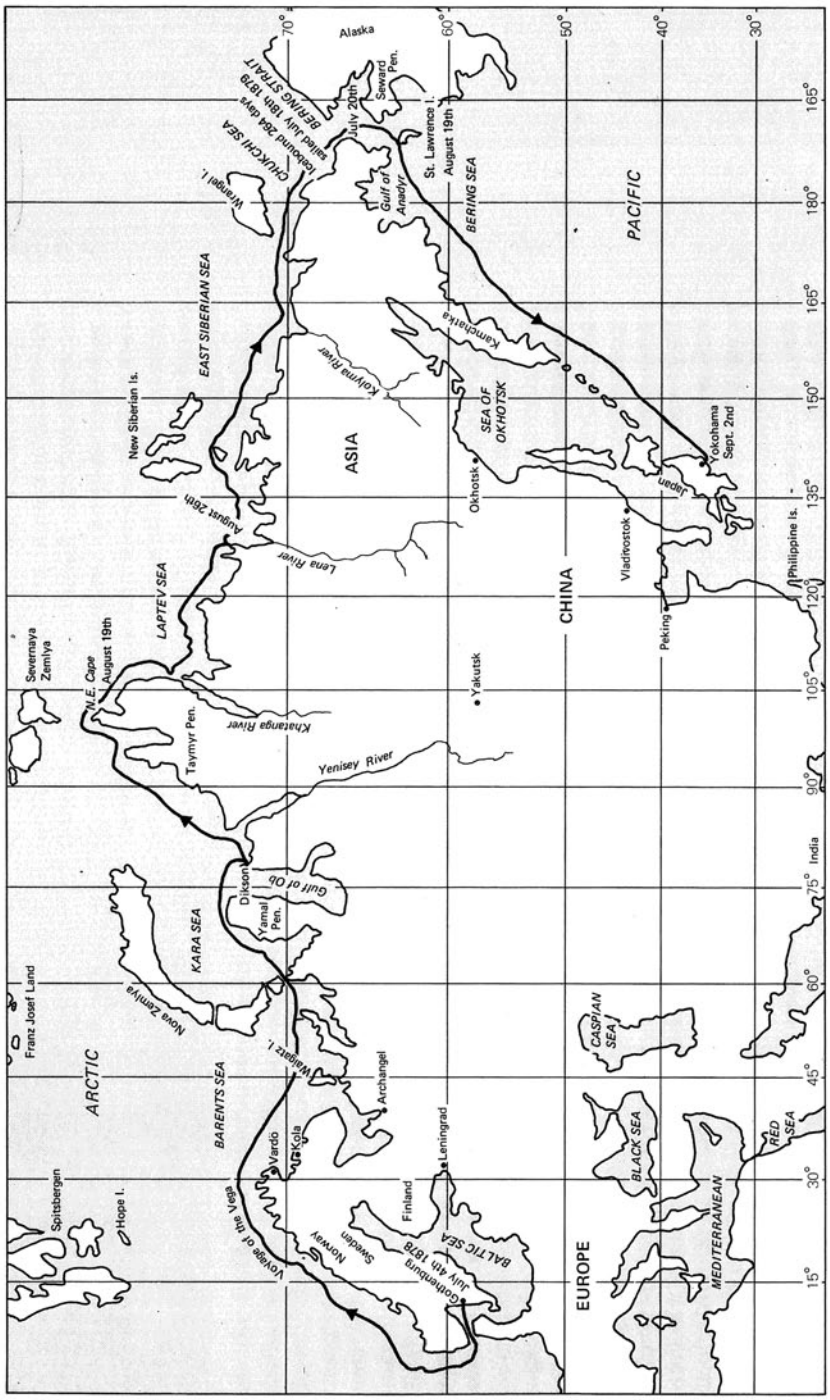

Figure 1.4. The route of the first through-sailing in the Northern Sea Route by Nordenskjöld onboard *Vega*. From Mountfield (1974).

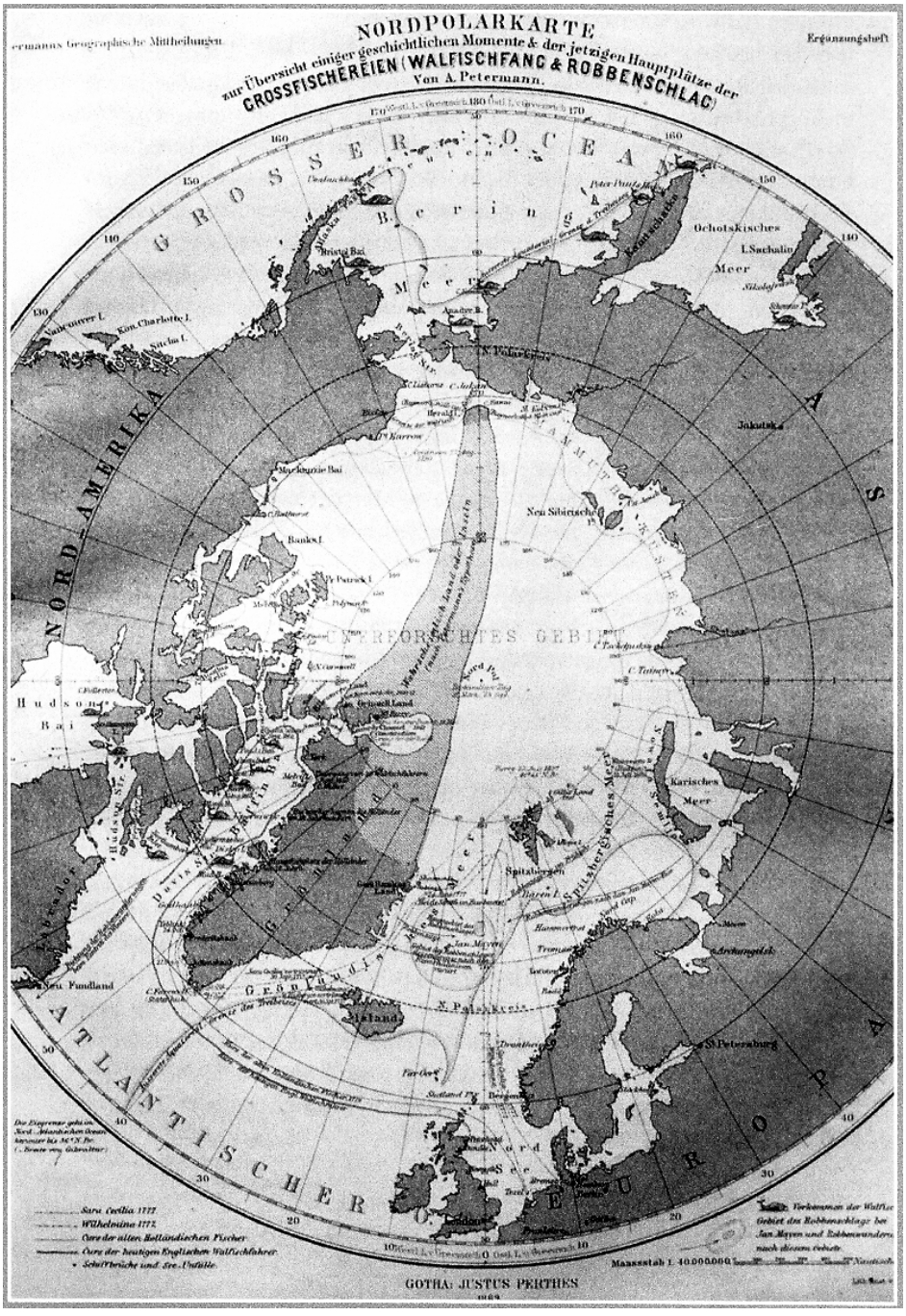

Figure 1.5. The map of the Arctic Ocean published by the *Petermans Geographische Mitteilungen* (Germany) in 1869. From Drivenes and Jølle (2004).

reached the ice edge in the vicinity of 78°N, from where it began its historical drift in which it reached latitude 85°56′N (Nansen, 1898). The most important results of this were the discovery of the deep Polar Basin and that the ice drifted to the right of the wind due to the effect of the Coriolis force. Nansen also found for the first time that water depths between 200 to 600 m had an above-zero temperature and constituted a continuation of the Gulf Stream into the Arctic Ocean.

The end of the 19th and beginning of the 20th centuries are characterized by the renewed interest of the Russian Government in Arctic studies. In 1894–1897 the Hydrographic Expedition headed by A.I. Vilkitskiy made a detailed survey of Ob' Bay and the Yenisey Gulf and charted the first safe courses through their mouths (Vize, 1939). In 1898–1904 the region from the west of Ob' Bay to the Norwegian border was also explored (Barr, 1991). At the turn of the century, the Emperor's Academy of Science organized a polar expedition headed by Edward von Toll onboard the schooner *Zarya*, the purpose of which was to conduct studies in the Laptev Sea and in the New Siberia Islands and to search for the rumored land to the north of this archipelago. It was highly significant in mapping the coast and made a considerable contribution to meteorology, ice research, geology, geophysics, botany, and zoology. Unfortunately, Toll himself perished during the traverse on foot from Bennett Island to the New Siberian Islands.

The strategic importance of the NSR increased after the Russian–Japanese War of 1904, and surveys of the Arctic coast were continued. In 1909 the Lena–Kolyma and Chukotka Expeditions mapped the shoreline between the Lena and Alazeya Rivers and made a survey of the coast between the Kolyma River and Cape Dezhnev. Of large importance to the hydrography, oceanography, meteorology, and navigation of the Arctic was the Hydrographic Expedition to the Arctic Ocean in 1910–1915 onboard the icebreakers *Taymyr* and *Vaygach*, which arguably made the most important geographical discovery of the 20th century—the Severnaya Zemlya Archipelago. In September 1916 the Russian Government officially claimed these lands as part of the territory of Russia (Gramberg and Ushakov, 2000). Arriving in autumn of 1915 to Arkhangelsk, the ships completely traversed the NSR from east to west. Similar to Nordenskjöld, they were unable to complete navigation during one summer, which did not speak well of a possible use of this route for practical shipping. However, the expedition made the first hydrographic description and issued navigation maps for the entire length of the NSR. In 1912, Brusilov onboard the *Svyataya Anna* and Rusanov onboard the *Gerkules* made an attempt to pass along the NSR from west to east, but both voyages ended tragically.

By the beginning of the 20th century the shores of the islands and the mainland had been surveyed and hydrographic work accomplished, all of which resulted in the publication of navigation maps of Russia's Arctic seas. Observations of the ice cover of the seas made by the expeditions were episodic. However, it was proved that the Arctic seas were not 100% covered with sea ice and their ice regime was not the same from year to year. The first books summarizing the results of sea ice studies were published by Kolchak (1909) and Lesgaft (1913). The conditions for provision of accident-free shipping along the NSR were gradually prepared, but these achieve-

ments were not able at the time to solve all the problems facing the development of regular navigation in the ice of the Arctic seas.

1.3.2 Beginning of trade shipping

Beginning in the second half of the 19th century, trade shipping began to develop in the Kara Sea—especially, around the mouths of the Ob' and Yenisey Rivers—exporting Siberian mineral resources and importing industrial goods. Ships of the Swedish polar explorer Nordenskjöld in 1875 and 1876 delivered goods from Tromsø to the mouth of the Yenisey. Without exception all the cruises of the English Captain Viggins (in 1874, 1876, 1878, 1884, 1887, 1888, 1889, 1890, 1893 and 1894) achieved similar results (Vize, 1939). In general, during the period 1876–1900, 60% of the cruises along the Kara Sea Route were successful, and ships transported 21,000 tons of cargo (Arikainen, 1984). During the period 1901–1910, no commercial voyages were made due to the absence of customs facilities and high insurance rates, except for 1905 when the Northern Sea Expedition escorted ships from Europe to the Yenisey. In 1911, voyages were resumed and were carried out until 1919 (see Table 1.1).

From 1911 in the eastern part of the NSR, 2,300 tons of cargo were transported from Vladivostok to the Kolyma River, and an attempt was also made to sail between the mouths of the Lena and Yana Rivers (Arikainen, 1984).

The development of shipping cargo along the Kara Sea Route necessitated the development of technical facilities to support this. In order to explore the Arctic Ocean and bring about cargo ship communication with the Ob' and Yenisey, the Russian Admiral S.O. Makarov proposed using a polar icebreaker approved by the Marine Ministry of Russia. The *Yermak* constructed by A. Vitvort had a deadweight of about 9,000 tons and was equipped with an engine of 10,000 hp. However, after her not quite successful Arctic voyages in 1899 and 1901, confidence in the use of icebreakers to penetrate the central Arctic was undermined and the *Yermak* was relocated

Table 1.1. Number of ships and volume of shipping along the Kara Sea Route in 1901–1919. From Arikainen (1984).

Period (year)	Number of ships			Shipping volume (1,000 tons)		
	Total	Successful	Unsuccessful	Total	Export	Import
1901–1904			No voyages			
1905	16	14	2	11.8	—	11.8
1906–1910			No voyages			
1911–1915	12	11	1	12.5	6.5	6.0
1916–1919	14	12	2	10.0	5.1	4.9
Total	42	37	5	34.4	11.6	22.7
Total for 1876–1919	122	86	36	55.2	18.3	36.9

to the Baltic Sea. The Russian icebreaking fleet was only increased during the First World War. The flotilla formed in Arkhangelsk numbered 24 icebreakers by 1917.

The voyages and expeditions set out the principles for the future organization of Arctic shipping. V. Rusanov in 1911 wrote that this required special organization: much finance, technical capabilities, icebreakers and ice-strengthened ships, and provision along the route of a network of radio- and meteorological stations. The radio stations set up in Arkhangelsk (1911), Yugorskiy Shar (1913), Vaygach Island and Marre-Sale (1914), and on Dikson Island (1915) allowed ships to receive meteorological and ice information, thereby contributing significantly to the study of the ice conditions and exploration of the north. Rusanov also proposed ice reconnaissance using a ship with a balloon, which became possible after 1920.

In general, during the pre-revolution period in Russia, significant progress was achieved in the study and exploration of the NSR; however, the problem of how to use it rationally and economically was not resolved.

1.4 THE SOVIET–RUSSIAN SYSTEM FOR SUPPORTING NAVIGATION (*I.Ye. Frolov, V.Ye. Borodachev, V.Yu. Alexandrov*)

After the October Revolution, the Arctic Ocean was investigated on a large scale in a planned and purposeful way. A systematic study of the Russian Arctic using icebreakers and aircraft and a network of hydrometeorological and research stations under one centralized organization was made. With this aim, special research institutions dealing with the study of the Arctic seas and land were set up in 1920–1921 (Belov, 1959). Foremost among these were the Northern Research Commercial Expedition—later reorganized into the Arctic and Antarctic Research Institute (AARI)—and the Floating Marine Institute—later to become the State Oceanographic Institute.

Soon after the Russian Revolution, Roald Amundsen passed for the third time along the entire NSR. For this expedition, a ship with an even rounder hull than the *Fram*'s was built; this was called the *Maud* after the Norwegian queen. The ship began the voyage in summer of 1918 and in heavy close ice could only reach Cape Chelyuskin, where it stopped for wintering. From here, two expedition participants Knutsen and Tessem headed for Dikson on skis with dogs, but perished during the traverse. (In 1958, at the initiative of Soviet polar explorers, a monument was constructed at the place of Tessem's death—see Belov, 1959.) The following summer, the *Maud* was only able to move eastward again on 12 September, and in 10 days, passing the mouth of the Kolyma, wintered again near the west coast of Ayon Island. The expedition reached Alaska only in the third year of navigation, where Amundsen left the ship and flew to Norway for a subsequent flight to the Pole by airplane (Borodachev and Shilnikov, 2002). Since the main expedition's objective consisted in reaching the North Pole, the *Maud* began its drift in 1921, but advanced very slowly through to the next summer. Finally, in the following year the *Maud* was frozen in ice and began to drift in a general westward direction. An outline of her navigation and drift in the Chukchi and East Siberian Seas is presented in Figure 1.6.

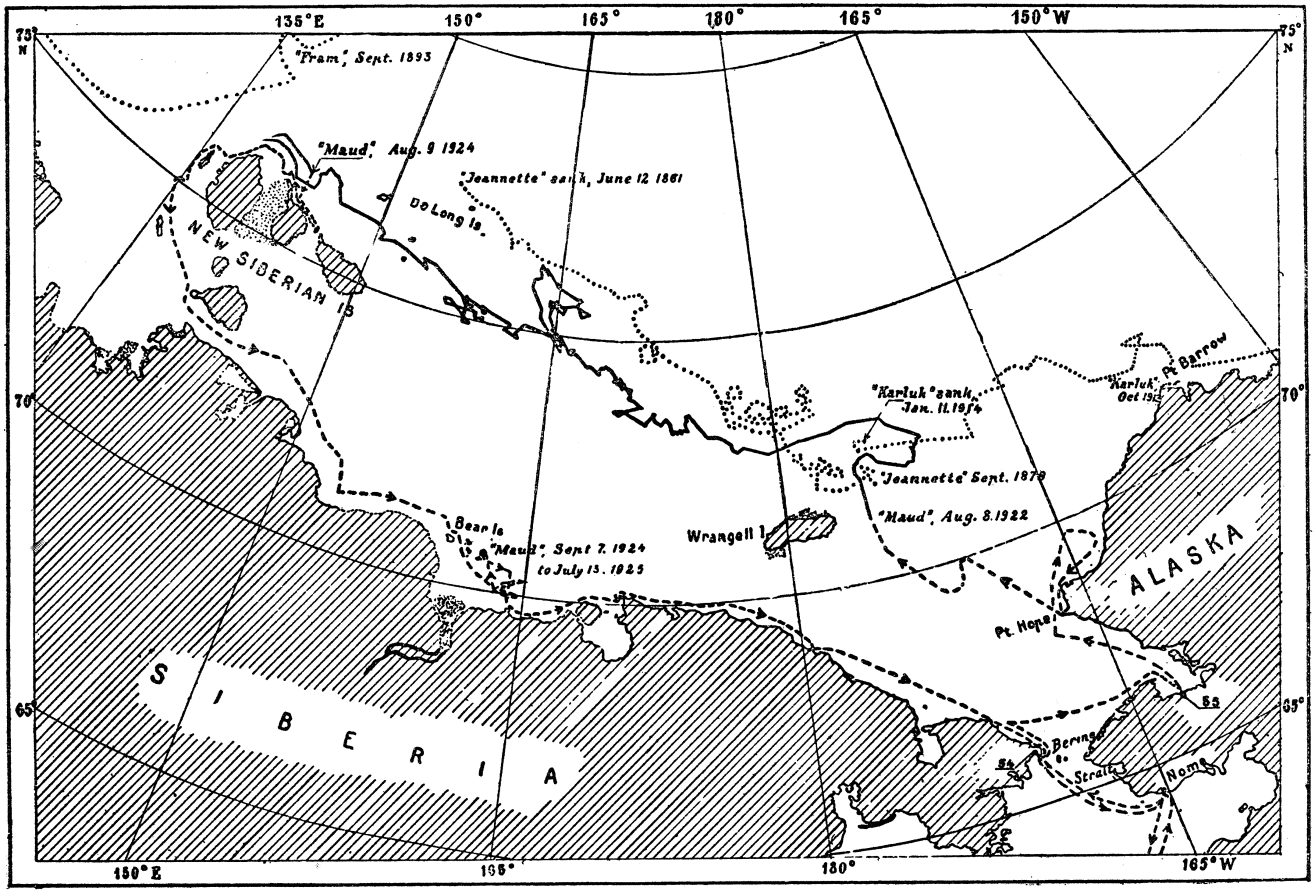

Figure 1.6. The route of *Maud* (1922–25), her route under sail and engine (dashed line) and ice drift (solid line). The drift of *Fram*, *Jannette* and *Karluk* are indicated (dotted lines). From Sverdrup (1928).

The *Maud* voyage was quite successful from a scientific point of view. H.U. Sverdrup obtained valuable results on the water dynamics (Sverdrup, 1936a) and ice drift of the North Siberian Shelf (Sverdrup, 1936b), and F. Malmgren on sea ice properties (Malmgren, 1933).

During the post-revolution period the Soviet Union faced the problem of supplying bread to starving people in the northwest of the country. To resolve this, a "bread" expedition was organized in 1920 onboard the vessel *Ob'* that safely returned after the delivery of 11,000 tons of bread. The following year serious efforts were undertaken to establish a strong basis for Kara Sea operations. Later, during navigation in 1924, the export of Siberian timber began, which was economically beneficial due to a decrease in cargo and insurance rates (Arikainen, 1984). As a result, during the period 1920–1933, the annual volume of shipments increased more than six-fold and towards the end of this period timber exports comprised 82% of the entire cargo flow. From 1929, icebreakers regularly provided support for navigation, which increased in duration from 23–32 to 60–75 days (Arikainen, 1984).

Between 1923 and 1931, ten cruises were made from Vladivostok to deliver cargo to the northeast coast of the Arctic, and four of them ended with forced overwintering. These cruises were made without icebreaking support or airborne ice reconnaissance. Voyages between the Lena and Kolyma were also resumed.

The Kara trade exchange expeditions of 1921–1931 made a significant contribution not only to the economy of the country but also to the formation of a scientific–technical support system for shipping in the ice. First, the Hydrographic Service initiated support for voyages. Second, the weather services necessary for shipping were established: in Murmansk (1921) and in Novyy Port (1923). Third, Russian scientist N.V. Roze developed the first forecast of the ice state in the Kara Sea. Later on, polar researchers B. Multanovsky and V. Vize laid the foundation of ice and meteorological forecasts in the Barents and Kara Seas using a series of systematic ice observations. Daily weather and ice bulletins began: initially only from data of meteorological stations, and from 1926 from data of ice reconnaissance. Since 1926, groups of hydrometeorologists were based onboard the lead icebreakers to observe ice conditions and relay information to captains. The Russian pilot Ya.I. Nagurskiy made the first ice reconnaissance airplane flights as early as 1914 (Borodachev and Shilnikov, 2002). In 1924, the *Ju-20* (a Junkers aircraft) was allocated to the Hydrographic Administration. B.G. Chukhnovskiy made flights that supported the icebreaker *Lenin* and provided hydrographers with sea ice information. From 1929, airborne ice reconnaissance became an integral part of marine transport operations and studies in the Arctic (Belov, 1970). These innovations were dictated by the needs of shipping in the ice and carried the first components of scientific–operational support system for shipping along the NSR.

In June 1928, instead of the NSR Committee (a decision-making authority), a powerful economic organization was set up to develop industry, transport and trade. This was the North Siberian state joint stock company of industry and trade Komseveroput that stepped up activity in the development of the northern Ob'–Yenisey area. Usage of the river fleet was improved and the number of cargo vessels was increased to include large-tonnage seagoing vessels. Mining, commercial fishery and hunting were

developed. Finally the port of Igarka and the Igarka Wood-processing Center were created. However, the means of ship navigation in the Kara Sea did not change significantly.

From 1929 a network of polar stations began to be created. Ten stations were constructed and remained in operation until 1933. General geographical studies were also developed. In 1930 an expedition onboard the icebreaker *Georgiy Sedov* headed by O.Yu. Schmidt surveyed the northern Kara Sea. This expedition discovered Vize, Isachenko and Voronina Islands as well as the Sedov Archipelago. In August the expedition landed four winterers—G.A. Ushakov, N.N. Urvantsev, V.V. Khodov and S.P. Zhuravlev—on Domashniy Island with the aim of exploring the Severnaya Zemlya Archipelago. In October 1930, during the first exploration by sledge, the Oktyabr'skoy Revolyutsii and Pioneer Islands were discovered. In 1932–1934, different expeditions to the Kara Sea discovered several new islands: Izvestiy Ts.I.K., Arkticheskogo Instituta, Kirova and Ushakova. Later, based on the results of the expedition onboard the *G. Sedov*, the chart of the northern Kara Sea was published (Vize, 1939).

In the early 1930s the Kara trade exchange expeditions reached the limit of their development while the ships of Kola voyages struggled to cope with the delivery of goods for the Kolyma–Indigirka territory. The question of organizing voyages of merchant ships from the west to Tiksi and Kolyma and from the east to Tiksi was now on the agenda. In 1930, cargo ships used for the first time the route around Cape Zhelaniya. In 1932, specialists from the Arctic Research Institute (ARI) planned a through-voyage along the NSR that was successfully realized onboard the *Sibiryakov* in one navigation season. Professor O.Yu. Schmidt and Captain V.I. Voronin were its leaders. Similar to many voyages before, this cruise was made without ice reconnaissance. Although the voyage of the *Sibiryakov* dispelled to a certain degree the doubts about suitability of the NSR as a transportation thoroughfare, it became however even more evident that sea operations under the complicated Arctic conditions using low-speed, weak icebreakers and an unreliable cargo fleet could never be completely successful. This was subsequently demonstrated by the voyage of the propeller-driven *Chelyuskin*, which was unsuited for ice navigation and sank as a result of strong ice pressure in February in the Chukchi Sea.

On 17 December 1932, the Main Administration of the Northern Sea Route (MANSR) was organized and entrusted with the objective "to finally lay the sea route from the White Sea to Bering Strait, equip this route, maintain it in a good state and ensure safety of navigation along this route" (Belov, 1959). The MANSR was in addition given control over the icebreaking and transport fleets, polar aviation, polar stations, a hydro-base,[5] industrial facilities and the ARI (Frolov, 2002).

In 1932–1933 the Special North-East Polar Expedition of Narkomvod onboard eight ships with the icebreaker *Fedor Litke* at the head delivered cargo from Vladivostok to Dal'stroy. Provision of ice reconnaissance support was given by aircraft, used for the first time in the east (*R-5*, pilot A.M. Berdnik; *Savoya-62*, pilot Ye.M. Koshelev). Although the ships could not be completely unloaded and

[5] Russian hydro-meteorological station, providing meteorological and oceanographic data.

had to overwinter in Chaunskaya Bay, this expedition signalled a new period in ice voyages from Vladivostok to Kolyma, one that differed in the organization and methods of routing compared with previous voyages.

Thus, by the time of creation of the MANSR, composite parts of the scientific–technical system for providing services to ice shipping in the Arctic had already been tested. Under common leadership and financing, a combination was made of: icebreakers and the cargo fleet, ports, hydrographic and scientific support, aviation and communication. All composite parts of the system influenced the success of sea operations. The MANSR began practical development of the polar route in 1933. In summer of 1934, the icebreaker *Fedor Litke* made the first transit voyage from east to west in one season. The same year, routing of cargo ships from the west to the mouth of the Lena and between the Lena and the Kolyma was performed.

In 1935, under the MANSR, sea operations began to be conducted according to a common plan of cargo operations, necessary as a result of intense industrial construction in the Arctic. For most of the regions of the north coast of Siberia, cargo ships were the only means of transport (Belov, 1969). As a consequence, Kara, Lena and Kolyma cruises were included from that year in the general plan of Arctic navigations. All icebreakers were distributed throughout the separate segments of the NSR for escorting ships along the entire route. This allowed successful traverses of the *Vantsetti* and *Iskra* from Leningrad to Vladivostok and of *Stalingrad* and *Anadyr'* in the reverse direction. In the same year the marine fleet transported through the NSR 246,800 tons of cargo and the river fleet 124,100 tons.

During the subsequent two years, the volume of cargo shipping increased. However, there was a catastrophe during the navigation season of 1937, when several ships including three of the four escorting icebreakers had to overwinter at the end of the season in different parts of the Arctic. In January 1938, as a result of intense ice pressure, the propeller-driven *Rabochiy* sank. The icebreaker *Sedov* had a seriously damaged rudder and could not exit from the ice and drifted across the central Arctic for 812 days. One of the causes of these failures was weak aviation support. Another, according to the government, was "poor organization of the work of the MANSR, complacency and conceit" (*Soviet Arctic*, 1938). From 1939, the Arctic Institute was heavily involved in shipping support in the Arctic.

For the first time since the *Maud*, a foreign ship was permitted to sail along the NSR in 1940, when, before the USSR entered World War II, the German Navy's *Kometa* passed along this route (Belov, 1969). It was escorted through the ice in the Laptev Sea by the icebreakers *Lenin* and *Stalin*, and to the east of Sannikov Strait by the icebreakers *Malygin* and *Kaganovich*. Beyond Pevek, the ship continued navigation without icebreaking support. For 23 days, 2,200 nautical miles were passed, 720 of them through the ice (Ruthe, 1943). After the *Kometa*, no foreign ship voyages were made along the NSR for more than half a century—until 1991, when a French ship *L'Astrolabe* sailed successfully through it.

The development of the NSR during the pre-war period was related to the production needs of the Arctic region and all aspects of Arctic shipping—icebreakers, ice class ships, ports, navigation-hydrographic, scientific and aviation support, and also the communication facilities. In these years, the flow of cargo constantly

increased and the mean duration of the navigable period between 1935 and 1940 increased, compared with 1925–1930, from 45 to 107 days in the western Arctic and from 30 to 79 days in the eastern Arctic. Before the war, 4.3 million tons of cargo were transported through the NSR.

The Arctic did not escape the Great Patriotic War (WWII)[6] of 1941–1945—particularly so in its western region, where German submarines and the battleship *Admiral Scheer* operated. The major part of cargo turnover, which decreased in 1942 to 144,000 tons and then again began to increase, was reoriented to the eastern segment of the route. During the war years, most of the goods and food supplies were transported along the NSR to plants in the north and to people in Yakutiya, Chukotka, Kamchatka and Magadan (Belov, 1969).

How did the various components of the system for servicing the Northern Sea Route develop? Well, before the war, the icebreaking fleet still comprised old icebreakers of the type *Yermak*, *Krasin* and *Lenin* with engines that gave 10,000 horsepower, and the icebreaker *Litke*. In 1944–1945 the icebreakers *Severnyy Veter* and *Severnyy Polyus*, received by lend-lease from the USA, were operating in the NSR. From 1936, ice class timber ships of the *Arktika* type and cargo ships of the *Volga* type supplemented the transport fleet. In 1938, the icebreakers *S. Dezhnev* and *Levanevskiy* were introduced into operation and ships of the type *Anadyr'*, *Igarka* and tankers *Nenets* and *Yukagir* were built. The Hydrographic Administration, which possessed many vessels and icebreakers, was involved in hydrographic work and the production of charts. Since 1936, measurements of sea depth were implemented from the ice during winter.

The scientific support of navigation along the NSR was based on observations from polar stations, ice reconnaissance, ice patrol and ARI expeditions. During ice reconnaissance flights the functions of onboard observers were gradually transferred from polar aviation navigators to specialists from the ARI, resulting in the creation of standardized symbolism for ice charts and expansion of the reconnaissance methods with winter reconnaissance beginning in 1939. Ice reconnaissance was subdivided into strategic reconnaissance, including flights every 10 days, and operational–tactical reconnaissance using aircraft to escort ships across complicated segments. Hydroaviation began to be replaced by land aviation and special airfields were constructed for its use in the vicinity of large ports (Borodachev and Shilnikov, 2002). New instrumentation was developed and was incorporated in ice reconnaissance: from 1945 aerial photography, from 1952 radar stations Kobalt and PSBN-M, from 1964 side-looking radar stations, the first one was Igla and then Toros onboard *AN-24* aircraft. The flights using Toros equipment began on 13 August 1968. From 1973, IR radiometers and a radar video-pulse meter to measure ice thickness were used for ice reconnaissance. In 1978 the Nit' system entered operation, which was installed in an airplane where the ice information was sent down to the icebreaker (Borodachev and Shilnikov, 2002). From the early 1980s, the Nit' system was used onboard *IL-18D* aircraft, later called *IL-24N*. In 1991 a multi-frequency side-looking radar station was tested. These remote-sensing methods are described in Chapter 3.

[6] Soviet term for the latter years of World War 2.

Scientists from the ARI began to make long-range ice forecasts, based on the studies of the ice regime of the seas. From the 1940s, development of meteorological forecasts began on the basis of a synoptic circulation method.

In the post-war years (until 1960), the system operated faultlessly and successfully despite using obsolete icebreakers, which could not escort ships in heavy ice. In these years, research–operational groups—a necessary link for scientific shipping support in ice—began to actively influence managerial decision making of sea operations. It is not by chance that the increase of cargo shipments through the NSR from the 1940s to 1960 corresponded to the increase in the number of ice reconnaissance flights and short-term ice forecasts. From 1954 at Dikson, Tiksi and Pevek, scientific research observatories started their operations and were actively included in scientific–operational activity.

In 1955, the first ice tank was set up at the ARI. As a result of studies, the basic theory of modeling ship motion in ice was developed and the methodology for calculating ice loads exerted on ships' hulls was developed and substantiated theoretically and experimentally. The methodology developed in these years was widely applied in practice. From 1961 a new direction in sea ice research was developed: study of the conditions of ship navigation in ice. This contributed to improvement in the ice navigation tactics of isolated ships and ships in convoy. The influence on navigation conditions of such indicators as composition of the convoy of ships, order of sailing in a convoy and motion speed dependence on conditions of visibility, ice concentration, thickness, stage of melting, hummock and ridge concentration and the degree of ice pressure were investigated. The performance of ships (without and under the escort of icebreakers) in ice was determined, as were the optimal dates for transport in the Arctic.

Studies of the nature of Polar regions expanded. In 1937 the first drifting research North Pole 1 (NP-1) station was set up, and from spring of 1954 one or, simultaneously, two NP stations drifted in the ice of the Arctic Basin (Frolov *et al.*, 2005). Their personnel and payload were usually delivered by aircraft of the High-Latitudinal Airborne Expedition Sever. The Sever Expedition carried out exploration using aircraft. After landing aircraft on the ice at points marked in advance, hydrological stations were set up, ice and meteorological observations were carried out and a number of other objectives connected with the support of ship navigation along the NSR were addressed (Konstantinov and Grachev, 2000). These expeditions discovered the underwater ridges Lomonosov and Mendeleyev. Data from these expeditions were widely used in the development of the *Atlas of the Arctic Ocean* (Gorshkov, 1980) and the *Atlas of the Arctic* (Treshnikov, 1985), and also in operational work for ship navigation support. These data were important in the preparation of long-range meteorological and ice forecasts. Physical–statistical and numerical methods based on hydrodynamic and thermodynamic models of ice process change and ice cover evolution were developed. The scientific basis for a tracing and prognostic automated system was created for the purpose of monitoring the Arctic Ocean and acquisition of information on its actual state (Frolov, 1995). All studies of the Arctic Research Institute were primarily aimed at providing support for shipping in ice along the NSR.

Significant work on navigational development of the NSR was performed by the Hydrographic Enterprise. First, hydro-bases were set up at different points along the Arctic coast. Ice class ships of the type *Meridian* constantly supplemented the hydrographic fleet. For depth measurements, new radio navigation systems were introduced. Radio beacons and the radio-navigation systems RSVT-1S were also introduced.

In 1964 there were changes in the structure of NSR management. The MANSR was reorganized and became the Administration of the NSR (ANSR) under the Ministry of Marine Fleet with responsibility for surveillance. The next year AARI was transferred from the Ministry of Marine Fleet to the Hydrometeorological Service (Frolov, 2002).

From the early 1960s, the icebreaking and transport fleet developed. The diesel–electric icebreakers *Moskva*, *Leningrad* (1961), *Kiev* (1965), *Murmansk* (1968) and *Vladivostok* (1969), whose engines gave about 20,000 horsepower, became operational. Slightly later, the *Yermak*, *Admiral Makarov* and *Krasin* with more than 30,000 horsepower appeared. For work in shallow depths, the icebreakers *Kapitan Sorokin*, *Kapitan Nikolayev*, *Kapitan Dranitsyn* and *Kapitan Khlebnikov* were built. All these icebreakers had helicopters for ice reconnaissance. In 1960 the first nuclear icebreaker *Lenin*, with a capacity of 44,000 horsepower, began operation along the route. The transport fleet of UL and ULA[7] classes was rapidly supplemented. At the start of the 1970s, a new generation of nuclear icebreakers became operational: *Arktika*, *Sibir'*, *Rossiya*, *Sovetsky Soyuz* and *Yamal*. The nuclear icebreakers *Taymyr* and *Vaygach*, with drafts of 9 m, were specially built for navigation support on the Yenisey.

The appearance of these icebreakers drastically changed the tactics of ice navigation and significantly extended navigation duration. From 1970, navigation to Dudinka was made almost on a year-round basis, and was only interrupted by flood periods and spring ice drift. From 1976, winter voyages of ships to the Yamal Peninsula began, whose cargo was unloaded on fast ice and subsequently transported onshore.

During the post-war period, the volume of cargo transportation along the NSR increased (Table 1.2). However, as a result of the economic reforms after the collapse of the Soviet Union, much production in the north was stopped and cargo turnover along the NSR began to decrease, and from 1996 it comprised approximately 1.5–2.0 million tons. In 2000 the export of oil from Ob' Bay, Varandey and Kolguyev to Europe began. Gas is exported from northwest Siberia to Rotterdam in accordance with an agreement between the European Union and Russia, coordinated by the Finnish company Fortum Oil and Gas. From 1 July 1991 the NSR was officially declared open for foreign ships.

Voyages along the NSR are carried out along coastal, marine, high-latitudinal and near-pole routes (Figure 1.7). Coastal routes are the most traditional. The main areas for sea transportation are: the Barents Sea (Murmansk port), Dikson (Dikson port), Cape Chelyuskin (Chelyuskin port), Tiksi (Tiksi port), Kolyma River (Kolyma

[7] Classes of merchant vessels operating in the Arctic according to the category of the strength of the hull.

Table 1.2. Marine cargo transportation along the NSR. From V.Ya. Plaksiy (pers. commun).

Year	Cargo flow (1,000 tons)	Year	Cargo flow (1,000 tons)	Year	Cargo flow (1,000 tons)	Year	Cargo flow (1,000 tons)
1945	441.1	1980	4,983.7	1987	6,578.8	1994	2,300.1
1950	500.0	1981	5,004.8	1988	6,295.2	1995	2,361.3
1955	632.0	1982	5,109.5	1989	5,823.0	1996	1,642.0
1960	962.5	1983	5,443.9	1990	5,510.5	1997	1,945.0
1965	1,455.1	1984	5,834.7	1991	4,804.0	1998	1,458.4
1970	2,947.7	1985	6,181.3	1992	3,909.2	1999	1,580.2
1975	4,065.0	1986	6,454.7	1993	3,015.7	2000	1,587.0

port), Pevek (Pevek port), Cape Schmidt (Cape Schmidt port) and Bering Strait. Routes through the the main Siberian rivers and estuaries have been charted: to Cape Kamennyy in Ob' Bay, to the port of Igarka on the Yenisey and to the port of Cape Zelenyy on the Kolyma. Marine routes include the route from Cape Zhelaniya (northern tip of Novaya Zemlya) to Dikson and from the New Siberian Islands to the port of Pevek. The high-latitudinal route, shorter for crossings, passes to the north of Cape Zhelaniya, Cape Arkticheskiy (northern tip of Severnaya Zemlya) and the New Siberian Islands. The fourth route, which is 700 miles shorter than the coastal

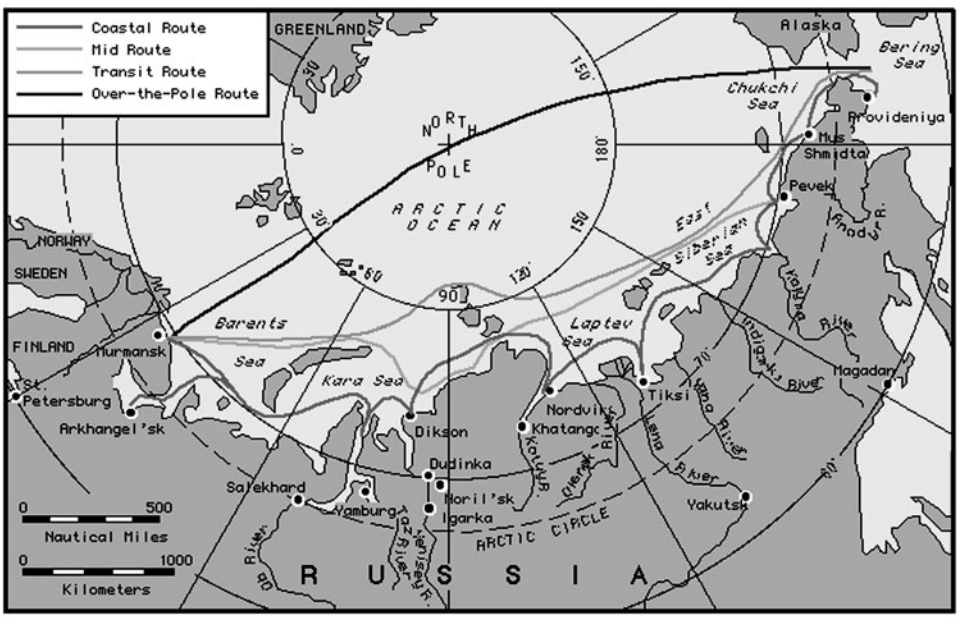

Figure 1.7. Map of the Northern Sea Route with the main transit routes (see also color section). From Mulherin (1996).

route, passes the large circle across the geographical North Pole (Mulherin, 1996). For planning the routes of ships in ice, the most important factor appears to be optimal use of zones with the easiest ice conditions, regardless of whether they are encountered on coastal or high-latitudinal routes.

2

Sea ice conditions in the Arctic and in the Northern Sea Route

2.1 SEA ICE CONDITIONS IN THE ARCTIC OCEAN (*Ye.U. Mironov, Z.M. Gudkovich, V.P. Karklin, C. Myrmehl*)

2.1.1 Seasonal changes

The main mass of Northern Hemisphere sea ice is concentrated in the Arctic Ocean. The ice cover extends southward in the form of three meridional tongues: East Greenland, East Canadian and Pacific. The ice cover area in the ice-covered seas of the Pacific and the Atlantic Oceans and in the semi-enclosed and inland seas—the Baltic Sea, the Black Sea, the Sea of Azov and the Caspian Sea—is typically no greater than 30% of the total ice area in the Arctic Ocean. In the deepwater part of the Arctic Ocean and the Arctic Basin, the ice is predominantly multi-year ice, which is preserved for up to several years, while in the marginal seas, ice is seasonal and melts in summer.

The main features of the geographical distribution in the northern hemisphere are generally consistent with polar and mid-latitude ocean circulation. Zones of the greatest ice advance to the south are located near the east coasts of Greenland, North America and Asia, exactly where the persistent cold currents flow: the East Greenland, Labrador and Oyashio. In the areas subject to the influence of warm currents (the North Atlantic and Kuroshio currents), the ice edge retreats to the north. Thus, these areas represent the major departures from the general latitudinal zonality in sea ice extent in the Northern Hemisphere (Zakharov, 1996).

The seasonal maximum of ice extent is in March–April. Later on with increasing incident solar radiation the ice cover melts and begins shrinking. Ice melting propagates from south to north, reaching the North Pole area usually in June. Ice cover decay occurs during the spring and summer period. The seasonal minimum of ice extent in the Arctic Ocean is in September. An integral characteristic of ice extent is its area. The most reliable estimates of the drifting ice area for large regions have become possible with the appearance of satellite remote sensing of sea ice. Estimates of

Table 2.1. Estimates of the average ice area (million km^2) in different regions of the northern hemisphere during the period of seasonal maximum (March) and minimum (September).

Region	March	September	Seasonal change
Northern hemisphere	15,416	8,020	7,396
Arctic Basin and marginal seas	7,890	6,233	1,657
Nordic seas	1,793	0,630	1,163
Northwest Atlantic	1,519	0,174	1,345
Far Eastern seas	2,080	0	2,080

Note:
1. Marginal seas: Kara, Laptev, East Siberian, Chukchi, Beaufort and Lincoln Seas.
2. Nordic seas or "North European Basin": Norwegian, Greenland, Barents and White Seas.
3. Northwest Atlantic: Baffin Bay, Labrador Sea and Davis Strait.
4. Far Eastern seas: Bering Sea, Sea of Okhotsk and Sea of Japan.
5. Northern Hemisphere: includes regions 1–4, Canadian Archipelago straits and Hudson Bay.

seasonal changes in the ice area in the entire northern hemisphere and specific regions over the last 20–25 years (Table 2.1) were made by Zakharov (1981, 1996).

The estimate of the ice area for the northern hemisphere presented in Table 2.1 is quite consistent with the estimate (15.5 million km^2) obtained by Sanderson (1975) on the basis of data from the British Met. Office for 1966–1974, but is slightly greater than the estimate by Walsh and Johnson (1979) obtained from generalized ice charts for 1953–1971 comprising 14.1 and 7.2 million km^2 for the periods of seasonal maximum and minimum, respectively. However, the calculations of Walsh and Johnson did not take into account the ice area of the Sea of Okhotsk and the Sea of Japan, which significantly underestimates the total area. In addition, due to significant multi-year fluctuations in ice conditions, estimates of the total ice area in the northern hemisphere and its large regions depend on initial data (airborne ice reconnaissance and satellite data of different spectral ranges) and on the period of averaging.

Nevertheless, the data in Table 2.1 suggest that the greatest seasonal changes in the ice area occur in the northwest Atlantic and in Far Eastern seas, where practically all ice cover melts in the summertime. In the Nordic seas including the Barents Sea (termed the "North European Basin" in some translations of Russian studies), about 65% of the ice area melts away, while in the Arctic Basin and in the marginal Arctic seas (i.e., the Siberian Arctic), the ice area decreases by about 20%. However, whereas in the Arctic Basin the ice area decreases insignificantly, in the marginal Arctic seas the ice area decreases by 30 to 85% (Table 2.2) over a short summer period, which lasts for 2–3 months according to data from V.F. Zakharov (1996).

Thus, on average, almost all seasonal ice area changes in the Arctic Ocean occur in the marginal seas. However, the fraction of summer ice reduction relative to the maximum ice extent area differs in each region, with the fraction of ice-free area in the Arctic seas of the Siberian Shelf being two to three times smaller than in the regions with sea boundaries and constant presence of an ice edge. Substantial clearance of the water area during the summer is typical of the seas of the northwest Atlantic and the European Arctic.

Table 2.2. Estimates of the average ice area (million km^2) in the marginal seas of the Arctic Ocean during the period of the seasonal maximum (March) and minimum (September).

Sea	March (million km^2)	September (million km^2)	Seasonal changes (%)
Greenland	0.657	0.346	47
Barents	0.855	0.128	85
Kara	0.830	0.266	68
Laptev	0.536	0.196	63
East Siberian	0.770	0.516	33
Chukchi	0.595	0.196	67
Beaufort	0.481	0.346	28

The partial contribution of interannual variability in the ice area of the regions to the total interannual variability of the ice area of the entire Arctic Ocean can be assessed by the formula:

$$m_i = \frac{\sigma_i r_{io}}{\sigma_o}$$

where σ_i and σ_o are partial and standard ice area deviations, respectively; and σ_{io} is the partial correlation coefficient between the ice area in the ocean and the corresponding ice area in the region.

As a result of the analysis it was determined (Table 2.3) that, in the wintertime, variability in the ice area of the Nordic seas predominated in the total variability of the ice area in the Arctic Ocean.

Most of the Nordic seas are governed by the fact that the area of ice cover in the Arctic Basin and the Arctic seas of the Siberian Shelf does not change significantly every year throughout the seven to eight winter months, whereas interannual changes in the average ice area in the Nordic seas region reach a maximum precisely during the winter–spring period.

The contribution of the interannual variability in ice area of the northwest Atlantic to the total interannual variability in winter is almost three times less than that of the Nordic seas region. This means that the winter ice area in the

Table 2.3. Estimates of the contribution (m_i, %) of interannual ice area variability of individual regions to total interannual ice area variability of the Arctic Ocean.

Region	Spring	Autumn
Seas of the Northwest Atlantic	27	2
Nordic seas or North European Basin	73	26
Arctic seas of the Siberian Shelf	0	72

Note:
The Nordic seas or North European Basin includes the Greenland and Barents Seas, Denmark Strait and the region near the south coast of Greenland.
The Northwest Atlantic includes Baffin Bay, the Labrador Sea and Davis Strait.

east Canada ice belt is not subjected to the changeable impact of warm Atlantic currents and, therefore, varies little from year to year.

In summer, the multi-year variability in the ice cover area in the Arctic Ocean is predominantly due to interannual changes in the average ice area in the Arctic seas of the Siberian Shelf. Interannual changes in the average ice area in the Nordic seas region in summer are minimal, being half as large as those in winter, while in the east Canada ice belt there is practically no ice by August.

In general, this means that the major thermodynamic factor determining the interannual variability of the ice cover area in the Arctic Ocean in the wintertime is warm currents and extensive areas of thin ice typical of the winter period in the European Arctic. However, since the era of satellite-borne passive microwave observations we have observed a negative trend in Arctic sea cover. Johannessen *et al.* (1999a) report a decrease in the total ice cover of 3–4% per decade since 1978. Other studies confirm this trend (Johannessen *et al.*, 1995a; Bjørgo *et al.*, 1997; Gloersen *et al.*, 1999; Parkinson *et al.*, 1999; Comiso, 2002, 2003; Comiso *et al.*, 2003; Johannessen *et al.*, 2004)—see Section 7.2.

The main factors determining the interannual variability of the ice cover area in the Arctic Ocean in summer are the intensity of solar radiation absorption by ice, the ice age composition and the thickness of ice formed in autumn.

The ice volume in the Arctic Ocean, including the Nordic seas, the Arctic Basin and the Arctic seas, was estimated by Mironov (1987, 2004) on the basis of combining observed data and calculation methods and by Hilmer and Lemke (2000) using numerical models. The contribution of ridged ice features to total ice volume by means of calculating the "equivalent" thickness added to level ice thickness was also taken into account. Estimates for the periods of seasonal minimum and maximum are given in Table 2.4.

The contribution of sea ice in the Nordic seas to the total ice volume of the Arctic Ocean in spring comprises 10%, which is quite a significant value. During the summer–autumn period, due to melting of young and first-year ice over an extensive

Table 2.4. Estimates of ice volume in the Arctic Ocean and its large regions for the periods of seasonal maximum and minimum.

Region	Spring		Autumn	
	km^3	%	km^3	%
Nordic seas or North European Basin*	2,673	10	764	5
Arctic seas**	7,125	25	1,805	12
Arctic Basin	17,795	65	13,122	83
Arctic Ocean	27,593	100	15,691	100

Note:
* Greenland and Barents Seas.
** Kara, Laptev, East Siberian, Chukchi and Beaufort Seas.

Table 2.5. Estimates of ice volume (in 1,000 km^3) accounting for ridged ice features in the Arctic Ocean during the periods of maximum and minimum ice cover development based on the data from different authors.

Author (year)	Spring	Autumn
Chizhov, O.P. (1976)	31.1	22.3
Lebedev, A.A. and Uralov, N.S. (1981)	28.0	17.1
Romanov, I.P. (1992)	25.5	—
Mironov, Ye.U. (2004)	27.6	15.7

area, the amount of ice in the Greenland and Barents Seas decreases to 5% of its maximum level.

The greatest seasonal changes of the ice volume occur in the Arctic seas (75% of the maximum ice volume) and in the Nordic seas (71%, comprising only 26% in the Arctic Basin).

The obtained estimate of the ice volume of the Nordic seas ($2.7 \times 10^3\ km^3$) is in good agreement with the estimate obtained by Lebedev and Uralov (1981): $3.0 \times 10^3\ km^3$. Estimates by different authors of the ice volume in the Arctic Ocean taking into account ridged ice features are presented in Table 2.5.

The ice volume derived in Chizhov (1976) appears to be slightly overestimated, because during calculations visual data converted to a percentage of the ice area occupied by ice ridges on the basis of linear dependence were used. However, the dependence of ice hummock and ridge concentration on points and the number of ice ridges per unit length is nonlinear.

The results obtained by Lebedev and Uralov (1981) and the estimates of Mironov (2004) are very close, although different methodologies and data for different time intervals were used for calculations. This increases the reliability of the obtained ice volume estimates in the Arctic Ocean: about $28 \times 10^3\ km^3$ during the seasonal maximum and about $16 \times 10^3\ km^3$ during the seasonal minimum.

The ice thickness distribution and hence the ice cover volume is determined in many respects by the ice drift system in the Arctic Basin, which has interannual, seasonal and synoptic variability (Rothrock *et al.*, 1999, 2003; Tucker *et al.* (2001); Wadhams and Davis, 2000; Winsor, 2001; Laxon *et al.*, 2003; Haas, 2004).

2.1.2 Ice drift and its spatial and temporal variability

Except for the restricted areas of ice-covered seas where landfast ice is established over a more or less prolonged time, the Arctic Ocean including its marginal seas is covered by drifting ice, which is in continuous motion. Ice movement (its drift) is determined by interaction of the ice cover with forcing from the atmosphere and the ocean. The shores and the landfast ice cover areas (landfast ice, stamukhas and shallow water) restrict the ice movement.

Ice drift significantly influences the state of ice cover: thickness distribution, concentration, hummock and ridge concentration, ice floe size distribution and

other characteristics on which navigation conditions and other important aspects of economic activity depend in the ice-covered seas. Since ice cover is one of the climatic system components, its state and hence its drift participate in the formation of climate change.

The significance of ice drift has always attracted many researchers to its study. A review of ice drift observation methods is presented in Gudkovich and Doronin (2001) and Pfirman *et al.* (2004). Extensive data on the ice drift in the Arctic Basin and the adjoining marginal seas accumulated at the present time made it possible to reveal some regularities in the spatio-temporal variability of drift velocity vectors and their dependence on external conditions (wind velocity, sea currents and sea level).

Ice drift observation data indicate that the statistical characteristics (average scalar and resulting drift velocities, corresponding standard deviations, parameters of stability, ellipticity, etc.) depend on the scale of averaging (Volkov and Gudkovich, 1967).

Table 2.6 presents the statistical characteristics of ice drift velocity annually averaged for the main regions of the Arctic Basin, depending on the scale of averaging. In this table: W_s, W_r are, respectively, average magnitude and resultant drift vector velocity (in cm/s); σ_s, σ are corresponding scalar and vector standard deviations (in cm/s); l is the degree of dispersion ellipticity; q, λ are parameters of stability of ice drift; and n is the number of vectors. The corresponding expressions for the normal elliptical distribution, which describes the distribution of ice drift velocities, are established by Gudkovich and Doronin (2001).

As follows from Table 2.6, with an increase in the period of averaging (T) the average ice drift velocity decreases from 7.5 cm/s to 2.2 cm/s for daily and annual periods, respectively (i.e., almost 3.5 times). In contrast, the values of ellipticity (l) and stability (q and λ) parameters significantly increase as the period increases. The dependencies of W_s, σ and σ_s on T are well approximated by power functions derived by the least squares method (with the initial data averaged over the year for the entire basin):

$$W_s = 7.5T^{-0.217} \quad [\text{cm/s}] \tag{2.1}$$

$$\sigma = 8.7T^{-0.333} \quad [\text{cm/s}] \tag{2.2}$$

$$\sigma_s = 4.4T^{-0.290} \quad [\text{cm/s}] \tag{2.3}$$

Table 2.6. Statistical ice drift characteristics averaged over a year for different periods.

Periods	l	q	λ	W_s	σ_s	σ	W_r	n
Day	—	0.30	0.28	6.5/7.5	3.5/4.0	7.0/8.1	—	9,816
10-day period	0.28	0.48	0.47	42/4.9	25/2.9	44/5.1	20/2.3	1,682
Month	0.41	0.65	0.74	90/3.5	50/1.9	84/3.2	59/2.3	582
Season	0.53	0.80	1.11	215/2.8	88/1.1	152/2.0	168/2.2	269
Half-year	0.56	0.88	1.48	388/2.5	151/1.0	232/1.5	345/2.2	159

Expressions (2.1)–(2.3) can be easily transformed to values expressed in km for a period of T days, for which power indicators have to be increased by 1 and the values of empirical coefficients multiplied by 1.1574 (conversion of dimensions from cm/s to km/day). Most of the considered characteristics change considerably in space and depend on the season.

For a number of practical objectives, data on the drift velocity of the prescribed probability are necessary. Formula (2.4) (Anapolskaya and Gandin, 1958; Gudkovich *et al.*, 1989) yields satisfactory results at its estimation:

$$P(W > w) = \exp\left[-\delta\left(\frac{W}{W_s}\right)^{\gamma}\right] \tag{2.4}$$

where γ and δ are the parameters that depend on the variation coefficient, σ_s/W_s. Their values for period T are presented in Table 2.7.

The statistical characteristics of ice drift velocity have annual variations. As seen from Figure 2.1, the average drift velocity modules for daily, 10-day and monthly periods vary within a year concordantly: the smallest mean drift velocities are observed in March and the largest ones at the end of summer–beginning of autumn (August–October). Similar to average velocity, the amplitude of its seasonal changes decreases with increasing scale. However, average velocity modules change little over 3-month periods throughout the year and become practically equal for 6-month periods, since seasonal velocity increase is compensated, by the end of summer, by its decreasing stability.

The above statistical characteristics allow calculation of the dispersion ellipses (value and direction of their main axes) for different time scales, reflecting the variability of drift vectors in specific restricted areas. Depending on the adopted ratio between the sizes of half-axes and the main RMS deviation values, one can determine the probability of a random vector getting to the corresponding ellipse.

Figure 2.2 shows the dissipation ellipses of the resulting monthly drift velocity for two seasons obtained for ten regions in the Arctic Basin. In combination with the mean resulting velocity vector, which characterizes the most probable ice drift during the indicated season over a month, the ellipses presented in the figure allow us to estimate possible dispersion of random vectors at a probability of 80%. As can be seen, the sizes of dispersion ellipses, the degree of ellipticity and the directions of the main axes vary significantly in space and from season to season.

Table 2.7. Values of the distribution function parameters of ice drift velocity modules depending on the period of averaging of the resulting speed.

Parameters	Periods of averaging			
	1–30 days	3 months	6 months	12 months
γ	1.58	1.96	1.85	2.06
δ	0.80	0.85	1.27	1.17

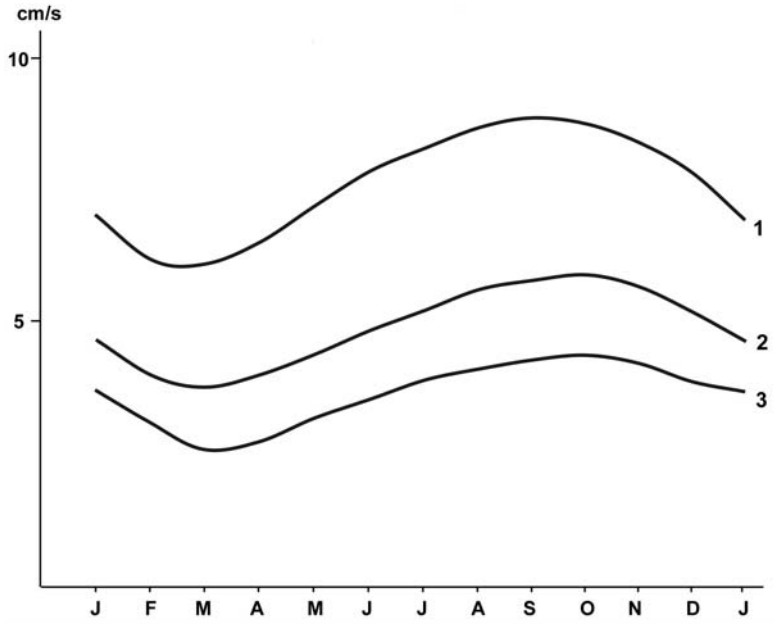

Figure 2.1. Annual variations in the average drift velocity module for daily (1), 10-day (2) and monthly (3) periods.

In addition to the dispersion ellipses, the considered statistical characteristics allow us to calculate simple drift velocity diagrams for the same areas on the basis of the normal elliptic distribution law. They make it possible to estimate the probability of drift direction within the prescribed sector and its average velocity in this direction.

Charts of ice drift roses and dispersion ellipses contain a lot of useful information on spatio-temporal variability in ice drift velocity. However, they do not provide an understanding of the gradual change occuring in the region of such characteristics as the module and the direction of the average resulting drift vector, which express the most probable ice displacement during a given period. The ice drift patterns illustrating such information can be derived by calculation using dynamic models. Unfortunately, systematic errors in the methodologies are accumulated in the calculations for long time intervals reducing the reliability of the results. The quality of drift pattern calculations based on approximating the ice drift velocity change in space is much higher when the large data sets on ice drift, archived at present, are considered.

Figure 2.3 illustrates the patterns of mean ice drift in the Arctic Basin for winter and summer periods calculated by means of the corresponding approximation formulas. These patterns reflect the presence of the Transpolar Drift Stream (often termed the "Transarctic Ice Flow" in Russian studies) that moves toward the Greenland Sea between the near-pole area and the northern margins of Eurasian shelf seas. A large quantity of ice exported from the Russian Arctic seas joins this flow on the left, while the anticyclonic gyre area in the Beaufort Sea, with its center approximately at 78°N, 150°E, adjoins it on the right.

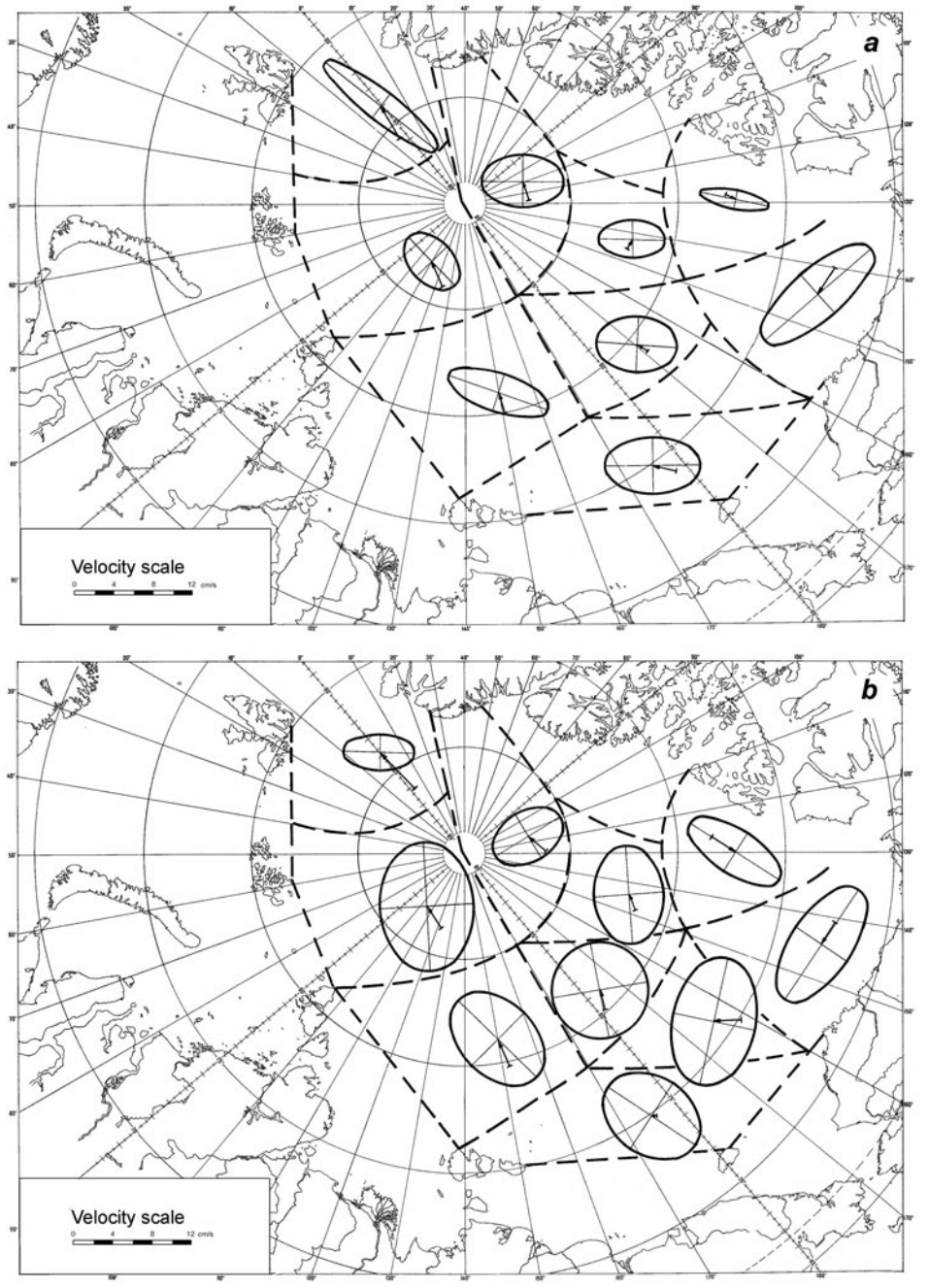

Figure 2.2. Vectors of the average monthly drift velocity and dispersion ellipses ($P = 80\%$) in January–March (a) and July–September (b) by region (limited by dotted lines). Average vectors have arrow heads pointing towards the centre of the ellipse..

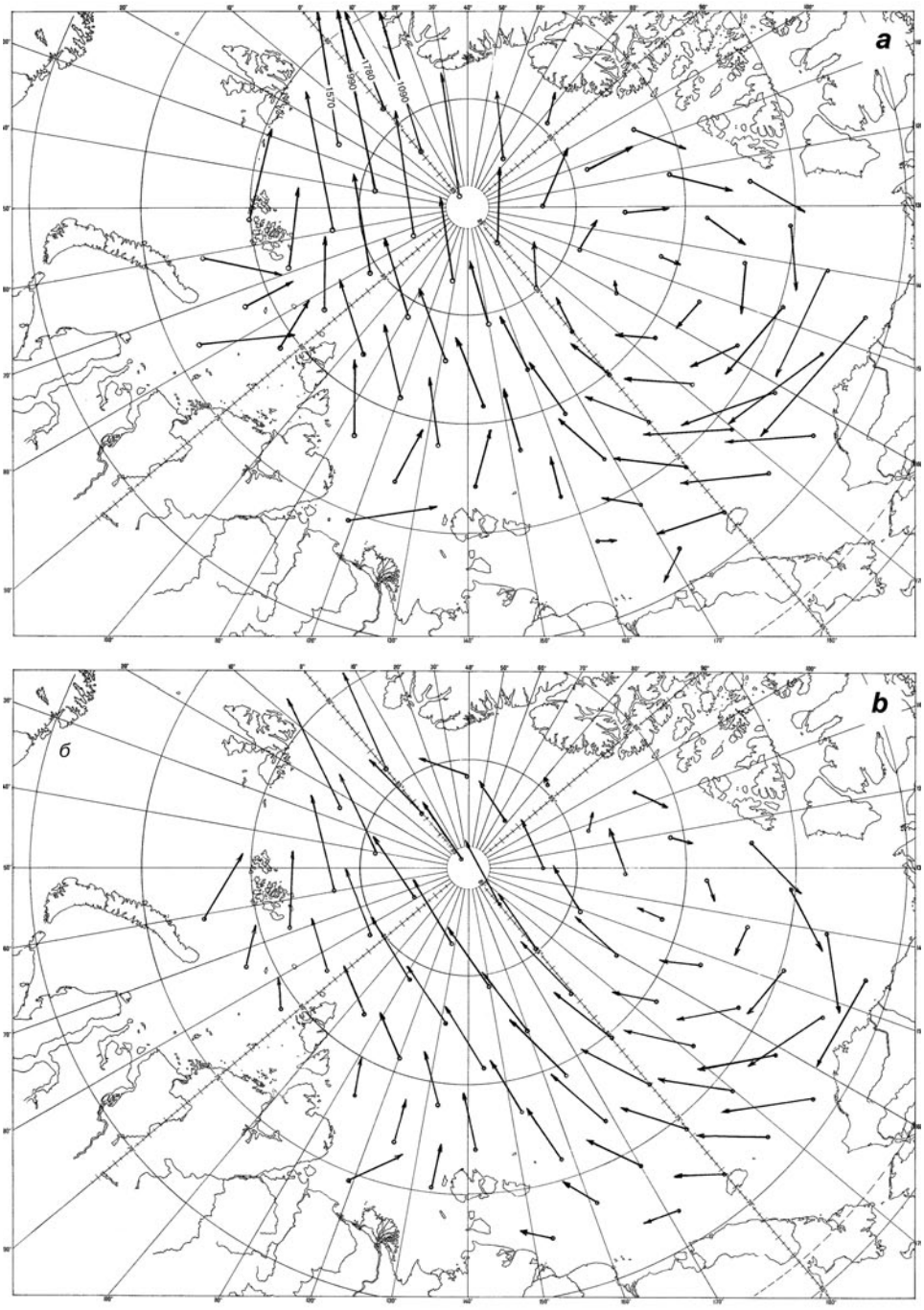

Figure 2.3. Patterns of the mean ice drift for October–March (a) and April–September (b).

Ice entrained by the Transpolar Drift Stream from the Kara Sea is exported to the Greenland Sea in 1–2 years, from the Laptev Sea in 2–3 years, from the East Siberian in 3–4 years and from the Chukchi Sea in 4–5 years. The period of ice circulation within the anticyclonic gyre changes from 4 to 10–12 years. The lower bound refers to the quasi-circular ice drift area in the Beaufort Sea and northward, and the upper to trajectories passing across the stagnant region adjoining the north shores of Greenland and the Canadian Arctic archipelago. In summer, ice from this area is partly transported to the straits of the Canadian Arctic archipelago and further to Baffin Bay.

In connection with changes in circulation modes (''Arctic Oscillation''), the sizes of anticyclonic water and ice gyre change considerably. As a result, the ice area participating in the gyre can change (approximately from 2.5 to 3.5 million km^2). Variability in the general ice drift pattern is also manifested by the significant deviation of some branches of the Transpolar Drift Stream from their usual position. As a result of this, closed cyclonic ice circulations occur in some years or seasons in the Laptev Sea and in the vicinity of Wrangel Island, whereas the normal export flow from the Kara Sea to the Arctic Basin reverses its direction (Gorshkov, 1980). Such changes are most frequent in the summertime when interannual variability in ice drift is most strongly pronounced. These changes have a considerable influence on the ice exchange between the marginal seas and the Arctic Basin (Wang and Ikeda, 2000).

Comparison of the ice drift patterns illustrated in Figure 2.3 for winter and summer periods reveals some specific differences between them. Most noticeable are the differences in ice drift velocities at the approaches to the Fram Strait, where a velocity increase is observed in winter. Another regular feature is a displacement of the Transpolar Drift Stream core from Eurasia to America and the corresponding decrease in anticyclonic gyre area from winter to summer.

Ice exchange through the Fram Strait determines the largest portion of the Arctic Basin ice exchange with the surrounding seas and thus influences the thermal and dynamic processes in the basin and its marginal seas. Observational data from the ''North Pole 1'' station (1937–1938) and the expedition onboard the icebreaker *G. Sedov* (1937–1940), and later data on the drift of automated buoys allowed the development of methods of calculation of ice exchange through this strait (Gordienko and Karelin, 1945; Gudkovich and Nikolayeva, 1963; Vinje and Finnekasa, 1986; Vinje, 2001; Schmith and Hansen, 2003; Kwok *et al.*, 2004). Most methods are based on the empirical dependence of ice drift velocity in the strait on the pressure gradient in the direction approximately perpendicular to the East Greenland Current—this is why data on interannual and multi-year changes in the area and the volume of ice exported through the strait obtained by different methods are in satisfactory correlation.

The estimates of mean annual ice area export through the Fram Strait made by different authors differ significantly: between $600 \times 10^3\,km^2$ and $1{,}508 \times 10^3\,km^2$. Discrepancies in the estimates of ice exchange through the Fram Strait of different authors are mainly attributed to the different observational data used as the basis for methodologies, different approaches to determining the speed of gradient currents,

different ways of taking into account the transverse non-uniformity of ice drift and currents, flow width and ice cover concentration. The most reliable estimate of the mean annual volume of ice export comprises around 5,000 km^3 (standard deviation of 500 km^3) with two-thirds of the ice exchange value falling in the winter period. In the interannual fluctuations of ice export, one identifies cycles that last between 8 and 3–4 years. These fluctuations influence the ice exchange of the marginal seas with the Arctic Basin and ice conditions in these seas (Gudkovich and Nikolayeva, 1963; Alekseev *et al.*, 1997). The intensified ice export to the Greenland Sea is accompanied by deterioration of ice conditions in the western sector of the Arctic and their improvement in the eastern sector.

Ice drift in the Arctic Basin is known to have two main components: a purely wind component closely connected with the local wind, and a "non-wind" component, which does not depend on the local wind at the moment of observation (Nansen, 1902; Buinitsky, 1951; Vorobiev and Gudkovich, 1976; Gudkovich and Doronin, 2001; Pfirman *et al.*, 2004). The first component is caused by stresses at the upper ice cover surface determined by relative air motion (wind) and the second is determined by different interrelated factors, such as gradient currents, sea level tilts and tidal phenomena. Estimates of the role of the "non-wind" component in general ice drift in the Arctic Basin show that it accounts for about 60%, on average. The role the current plays is maximum in mid-summer and minimum during the transient seasons. It increases with increasing time interval (scale of averaging), which is explained by the much greater stability of gradient currents that have a predominantly baroclinic character compared with the wind. The role of the current also increases when the ice approaches the strait between Greenland and Spitsbergen, where it accounts for around 70%, on average, increasing to 90% in the Greenland Sea at latitude 74–78° in the summertime (Gudkovich and Pozdnyshev, 1995; Schmith and Hansen, 2003). Noted regularities lead, on the one hand, to general ice drift being determined to a greater extent by a system of gradient currents and, on the other hand, to drift variability, both over short and long periods, depending primarily on the anomalies in wind flows.

Gorbunov *et al.* (1982, 1985; Losev *et al.*, 1986) considered the non-uniformities (large-scale eddy motions of ice, drift divides and zones of increased and decreased drift velocities) in the ice drift fields using data from automatic buoys for a restricted period (1979) and their characteristics (dimensions, duration of existence, etc.) are determined.

The structure of the ice drift velocity fields in the Arctic Basin over short intervals of averaging is characterized by its significant complexity and variability in time. However, structural-specific features of the ice drift field and their variability are insufficiently studied. Observations of ice motion in the Arctic Basin under the international "Arctic Buoys" program (carried out for more than two decades) allow estimation of seasonal and interannual variability in the short-period structure of the ice drift field on the basis of their subdivision into types. For this purpose, ice drift fields over 5-day time intervals for 22 years (1979–1990, 1993–2002) were used. As a result of their analysis (Losev *et al.*, 2002), six major types of structures in ice drift velocity fields were identified:

(1) large-scale anticyclonic circulation (Figure 2.4a);
(2) large-scale cyclonic circulation (Figure 2.4b);
(3) large-scale anticyclonic and cyclonic circulations;
(4) the prevailing ice drift from the sub-Atlantic part of the basin to its Asian–American area;
(5) the prevailing ice drift from the Asian–American area of the basin to its sub-Atlantic part; and
(6) random ice drift in different directions.

The sizes and location of anticyclonic and cyclonic circulations of the ice drift were not taken into account in further analysis. To investigate variability in the ice drift field structure, 1,425 5-day periods were used. Table 2.8 presents frequency of occurrence of the structural types of the ice drift field for each month and on average for a year. According to all data, type 1 has the largest frequency of occurrence (34.8%) and type 3 the least (3.0%). Seasonal change in the frequency of occurrence is characteristic of most types of structures. Anticyclonic ice circulations are more frequent in April, May, November and December, cyclonic ones occur mostly in June–September and a simultaneous presence of anticyclonic and cyclonic circulations in the ice drift field is observed in June–October. Differences in the frequency of occurrence of the types in the winter (November–May) and summer (June–October) periods are significant. Thus, the average frequency of occurrence of type 1 in November–May and June–October in all years was 40.3% and 26.9%, respectively; type 2, 14.3% and 31.4%; type 3, 0.8% and 6.0%; and type 5, 11.4% and 5.5%. Seasonal changes in the frequency of occurrence of types 4 and 6 are insignificant.

Interannual changes in the frequency of occurrence quite clearly manifest as predominant for types 1 and 2 of the ice drift field structure. Thus, in 1979–1987 the average frequency of occurrence of type 1 was higher than the average multi-year (4.5%) and comprised 5.8% of the number of 5-day periods referring to this type (495). In 1988–1990 and 1993–2000 the average frequency of occurrence of this type decreased to 3.4%, but increased in 2001 and 2002 up to 5.5%. It is reasonable to assume that over the next few years the increased frequency of occurrence of anticyclonic circulation in the ice drift field in the Arctic Basin will be preserved, especially in the winter period.

The average frequency of occurrence of type 2 in 1979–1984 was less than that of an average multi-year one and was equal to 3.2%. In 1985–1990, 1993 and 1994, it was almost twice as high (6.2%), decreasing again in 1995–1999 down to 2.7% and increasing in 2000–2002 up to 5.9%. The increased frequency of occurrence of the cyclonic circulation type in the ice drift field in the Arctic Basin in the summertime will likely persist through the next few years.

2.1.3 Ice cover distribution

The ice cover of the Arctic Basin is essentially a conglomerate of ice of different age composition (different time of formation), and hence different thickness. The main portion is comprised of multi-year ice older than 2 years. Multi-year ice is found

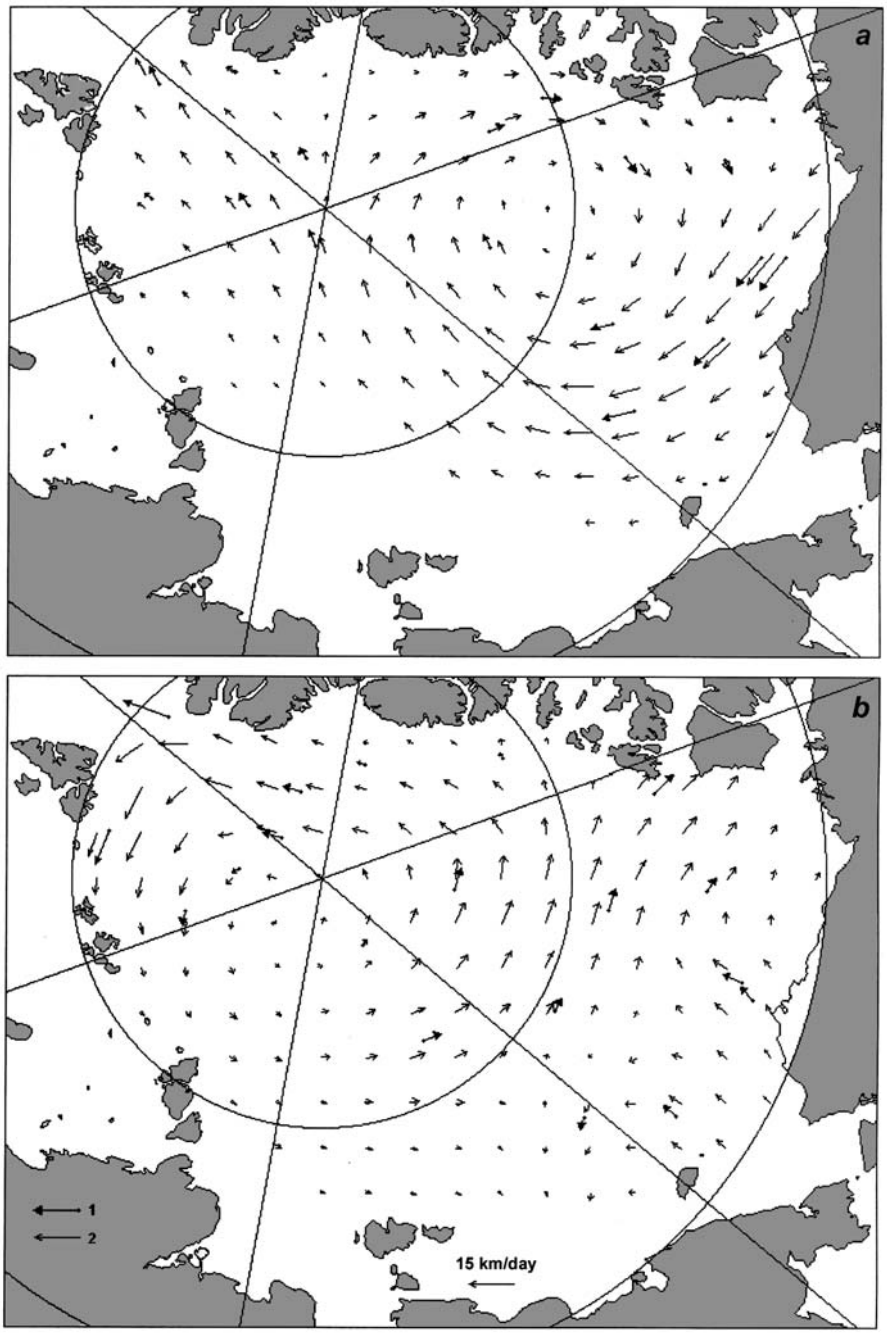

Figure 2.4. Fields of the ice drift velocity in the Arctic Basin, calculated on the basis of the objective data interpolation for 1–5 June 1982 (a) and 21–25 July 1981 (b). 1 = Buoy speed vector. 2 = Drift velocity vector calculated at the grid point.

Table 2.8. Frequency of occurrence of types of structures in the ice drift field in the Arctic Basin, 1979–2002 (%).

Months	Types						Number of periods
	1	2	3	4	5	6	
1	36.8	20.5	1.7	8.5	6.8	25.6	117
2	26.4	13.6	0.0	5.5	11.8	42.7	110
3	28.1	19.0	1.7	3.3	9.9	38.0	121
4	43.0	10.5	0.0	0.0	14.9	31.6	114
5	53.7	9.9	0.8	0.8	15.7	19.0	121
6	28.2	31.6	6.0	1.7	9.4	23.1	117
7	27.9	38.5	5.7	2.5	4.9	20.5	122
8	23.8	38.5	5.7	5.7	1.6	24.6	122
9	28.1	29.8	5.8	1.7	5.0	29.8	121
10	26.3	18.6	6.8	5.1	6.8	36.4	118
11	49.6	15.7	1.7	2.5	10.7	19.8	121
12	44.6	10.7	0.0	8.3	9.9	26.4	121
Year	34.8	21.5	3.0	3.8	8.9	28.0	100
No. of periods	495	307	43	54	127	399	1,425

mostly in the near-polar and Canadian–Greenland regions (Figure 2.5). Its location and age are connected with the anticyclonic ice drift in the Beaufort Sea (Gudkovich and Doronin, 2001). Ice entrained within this gyre is not exported from the Arctic Basin for many years. According to some estimates (Vovinkel and Orvig, 1970; Mironov and Uralov, 1994), about 2% of this ice is comprised of ice as much as 20 years old.

In the Transpolar Drift area, the quantity of multi-year ice varies within 50–80%, decreasing to 10% towards the boundaries of the marginal seas (Mironov, 1986a; Romanov, 1992). On average, multi-year ice occupies around 75% of the entire area of the Arctic Basin. Second-year, first-year and young ice account for the other 25% (Zakharov, 1996).

According to the multi-year observation data by Romanov (1992), the fraction of first-year ice in the multi-year and second-year ice over much of the Arctic Basin is no greater than one-tenth (10%). This fraction, however, increases towards the boundaries with marginal seas, where it comprises 70–100%. Nevertheless, it should be mentioned that these are climatological estimates that may not be representative of the most recent years, when a transformation in the ice cover in terms of multi-year versus first-ice areas (Johannessen *et al.*, 1999a) has been going on, as described in Section 7.2.

In spite of the difficulties connected with direct ice thickness measurements in the Arctic Basin, sufficient data obtained from the "North Pole" drifting stations, from numerous landings of aircraft on sea ice and from submarines, have been archived at

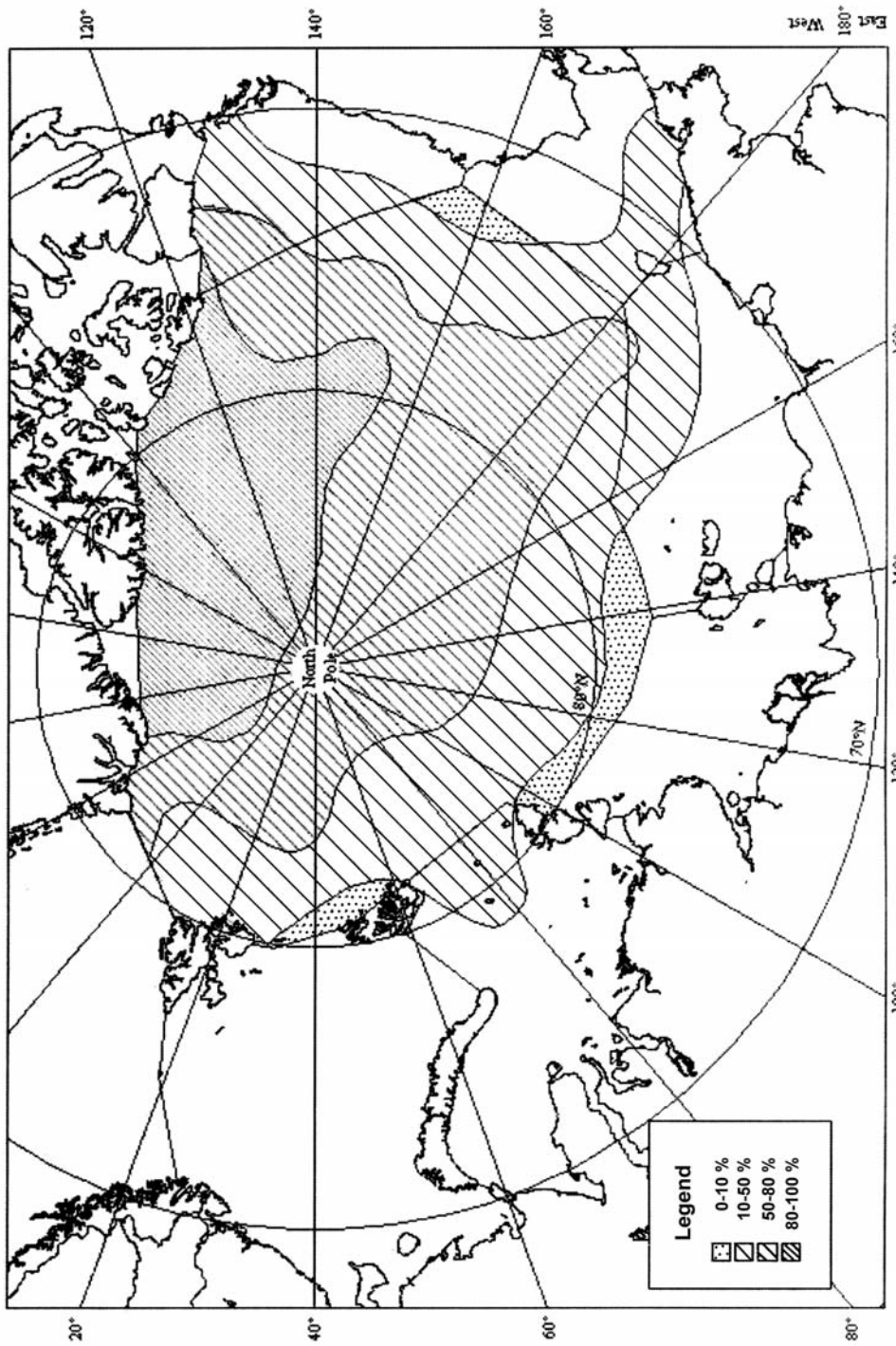

Figure 2.5. Probability of multi-year ice presence in the Arctic Basin (%).

the present time to give a good understanding of the general character of ice thickness distribution and values in the basin.

To investigate large-scale ice thickness variability, two methods are generally used: bottom ice surface relief measurements by sonar from submarines or evaluation of ice thickness by mathematical calculation.

When considering real ice drift and evaluating its thickness for several "growth–melt" cycles, the longest (more than 3 years) trajectories of three Soviet (NP-6, NP-19 and NP-22) and two US (T-3, Arlis-2) drifting stations were chosen by Mironov and Uralov (1994). All these stations were located on ice islands; however, no continuous observations of ice thickness and growth and melting of the ice cover were made. Therefore, a method of ice thickness calculation by the analytical expression proposed by Mironov (1986b) was used for pre-processing the station data (Mironov and Uralov, 1994).

Calculation of winter ice growth values during the prolonged drift period of the stations is made for two variants—ice growth in open water and at an initial ice thickness of 3 m. The results obtained by Mironov and Uralov indicate that in spite of the different drift trajectories and periods, and, correspondingly, different hydrometeorological conditions, the range of ice growth values over a number of "growth–melt" cycles is insignificant (no greater than 11 cm). In the event of drifts exceeding 5 years, the range of growth values is between 30 and 55 cm. Thus, for thick ice (more than 3 m) drifting in the Arctic Basin the growth in ice thickness in winter months depends to a great extent on the initial ice thickness rather than on hydrometeorological conditions.

Analysis of the level ice thickness values calculated along the long-term trajectories of the drifting stations shows maximum thickness values to be within 4.5 and 5.0 m. In actual ice drift in the Arctic Basin, the hydrometeorological conditions of ice cover growth and melting change significantly. Therefore, even after ice drift for 22 years (T-3 station), its ice thickness does not achieve equilibrium.

The presence of ice under constant climatic conditions is possible in the event of landfast ice preservation. According to the observation data, long-term landfast ice preservation (for more than 4 years) is possible only in the straits of the Canadian Arctic archipelago, where extreme values of level ice thickness (i.e., 6–10 m) have been recorded (Walker and Wadhams, 1979; Hibler, 1980).

The empirical coefficients derived on the basis of multi-year full-scale observations at the "North Pole" drifting stations were applied to models (Appel and Gudkovich, 1992; Mironov, 1986b), which allowed the seasonal distribution of ice cover thickness and partial concentration to be obtained; this was found to correspond with modern understanding. Comparison of the distribution of the mean weighted ice thickness calculated taking into account ridged ice features (Mironov, 1986b) and ice draft distribution derived on the basis of several underwater surveys (Bourke and Garrett, 1987) during the maximum ice cover development (Figure 2.6) indicates good agreement for the Arctic Basin and much lower correspondence for the Arctic seas. Maximum ice thickness (7–8 m) is noted in a narrow zone adjoining Greenland and the Canadian Arctic archipelago; ice thickness values in the near-pole area are 3–4 m. On our chart of ice draft distribution (Figure 2.6a) their values are

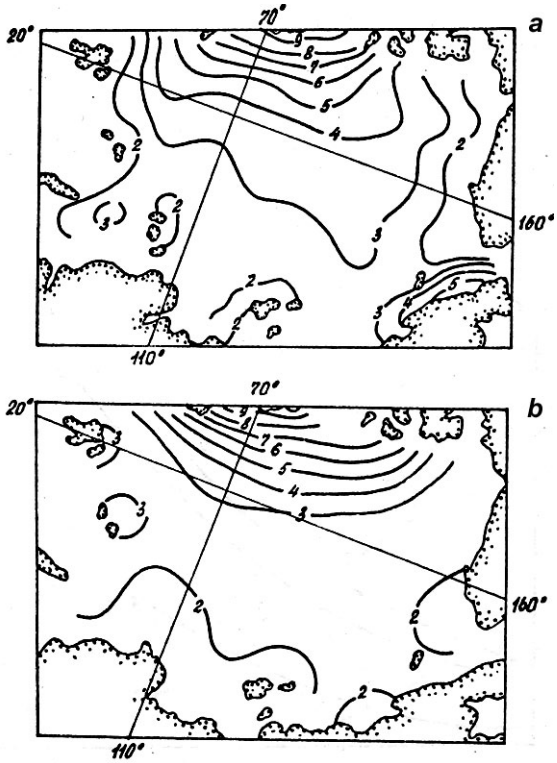

Figure 2.6. Ice thickness distribution taking into account ridged ice features in the Arctic Basin during the spring period according to calculations (Mironov, 1986b) (a) and from underwater sounding data (Bourke and Garrett, 1987) (b).

evidently underestimated in the Arctic Seas, as a result of the absence of underwater sounding data in these regions.

Estimates of mean weighted ice thickness distribution taking into account ridged ice features, derived by means of mathematical modeling and statistical analysis of underwater sounding data (Table 2.9), show similar results.

Given the results of model calculations and underwater sounding data, the following main regularities of large-scale ice thickness variability taking into account ridged features can be formulated:

- the maximum ice thickness zone taking into account ice ridges (7–8 m) is located to the north of Greenland and the Canadian Arctic archipelago;
- the largest spatial ice thickness variability is typical of the most dynamic regions (sub-Atlantic and Canadian regions of the Arctic Basin, the Chukchi Sea), whereas the smallest variability characterizes regions with a small ice hummock and ridge concentration (Asian part of the Arctic Basin, the Laptev Sea);

Table 2.9. Estimates of mean weighted ice thickness distribution taking into account ridged ice features in the Arctic Basin during the spring period from underwater sounding data (Blidberg *et al*., 1979) and calculations (Mironov, 1986b).

Author (year)	Ice thickness (m)	Standard deviation (m)
LeSchack (1983)	4.1	2.5
Blidberg *et al*. (1979)	4.3	2.6
Mironov (1986b)	4.0	1.8
McLaren *et al*. (1984)	4.1	—

- estimates of the average ice thickness taking into account ridged features for the Arctic Basin during the period of the maximum ice cover development indicate that these values are within 4.0 and 4.3 m;
- estimates of the maximum multi-year level ice thickness indicate that it is within 4.5–5.0 m and large values occur only in extreme cases;
- seasonal ice thickness changes in the Arctic seas are greater than those in the Arctic Basin;
- the main regularities in the spatial ice thickness distribution persist from month to month during the annual cycle.

The beginning of ice melting depends both on the latitude of the region in the Arctic Basin, and on the snow cover thickness, which acts as a thermal insulator decreasing the heat flux to the ice surface (Belchansky *et al*., 2004). Ice melting begins at mean daily air temperatures of -0.2 to -0.5. According to multi-year observation data at the "North Pole" drifting stations (Romanov, 1992; Buzuyev *et al*., 1999), ice in the near-pole area begins to melt in early June, and puddles appear by 20–25 June (Table 2.10).

Regular observations at the melting profiles allowed the quantitative ratios of ice melting at different relief features to be obtained (Table 2.11).

Studies of the dynamics and morphometry of the ice cover of the Arctic Ocean are of great significance for improving the mathematical models of ice cover evolution, estimates of climate change and the development of ice forecasting methods.

Table 2.10. Time of onset of main ice melting stages in the Arctic Basin (Romanov, 1992).

Characteristic	Average date	Most probable bounds
Beginning of melting	6 June	± 6 days
Appearance of puddles	23 June	± 6 days
Maximum development of puddles	5 July	± 6 days
Stable freezing of puddles	22 August	± 5 days

Table 2.11. Ice melting value (cm) at different multi-year ice relief features (Buzuyev *et al.*, 1979).

Relief areas	Melting value (cm)	
	Average	Maximum
Tops of hillocks	30.3	50
Slopes of hillocks	30.0	74
Level areas	27.9	87
Troughs without puddles	35.9	87
Puddles	57.6	104

2.2 THE ARCTIC EURASIAN SHELF SEAS (*Ye.U. Mironov, Z.M. Gudkovich, V.P. Karklin*)

Economic activities in the Arctic Shelf seas depend to a great extent on the ice conditions. Seasonal and interannual variations in the sea ice extent restrict navigation routes and create difficulties in conducting surveys and activities on the shelf of the Arctic Seas. The most severe ice conditions are observed in the Arctic seas of the Siberian Shelf through which the Northern Sea Route passes.

In the annual cycle of the ice cover state in the Arctic Shelf seas, the processes of ice formation and growth occur approximately for 7 months (from October to May). During this period all Siberian Shelf seas are completely covered by ice of different age (thickness) at concentrations of 90 to 100%. In the coastal shallow water areas, landfast ice is established. Beginning in late May–early June, the ice cover of the Arctic seas begins to melt and decay under the influence of thermal and dynamic processes. Almost simultaneously with the onset of ice melting, the ice extent decreases and the seas are gradually ice-cleared. However, ice does not disappear completely in the summertime.

The conditions of ice cover formation and decay in the Barents Sea differ significantly from the Arctic seas of the Siberian Shelf. The ice regime of the Barents Sea mainly forms under the influence of advection of warm Atlantic water transported by the North Atlantic Current system. Due to its influence, the Barents Sea is not completely ice-covered even during the most severe winters (Shapiro *et al.*, 2003).

The Arctic seas are subdivided by their typical ice regime features into natural regions identified in the process of multi-year observations and studies. Within the Barents Sea's boundaries, three regions are identified and in the Kara, Laptev and East Siberian Seas, two regions in each of the seas can be identified (Figure 2.7). In the Chukchi Sea, the southwestern part is delineated, its ice regime forming to a great extent by the influence of advection of comparatively warm Bering Sea water. The ice cover characteristics in the autumn–winter and summer periods will be presented for different seas and their regions.

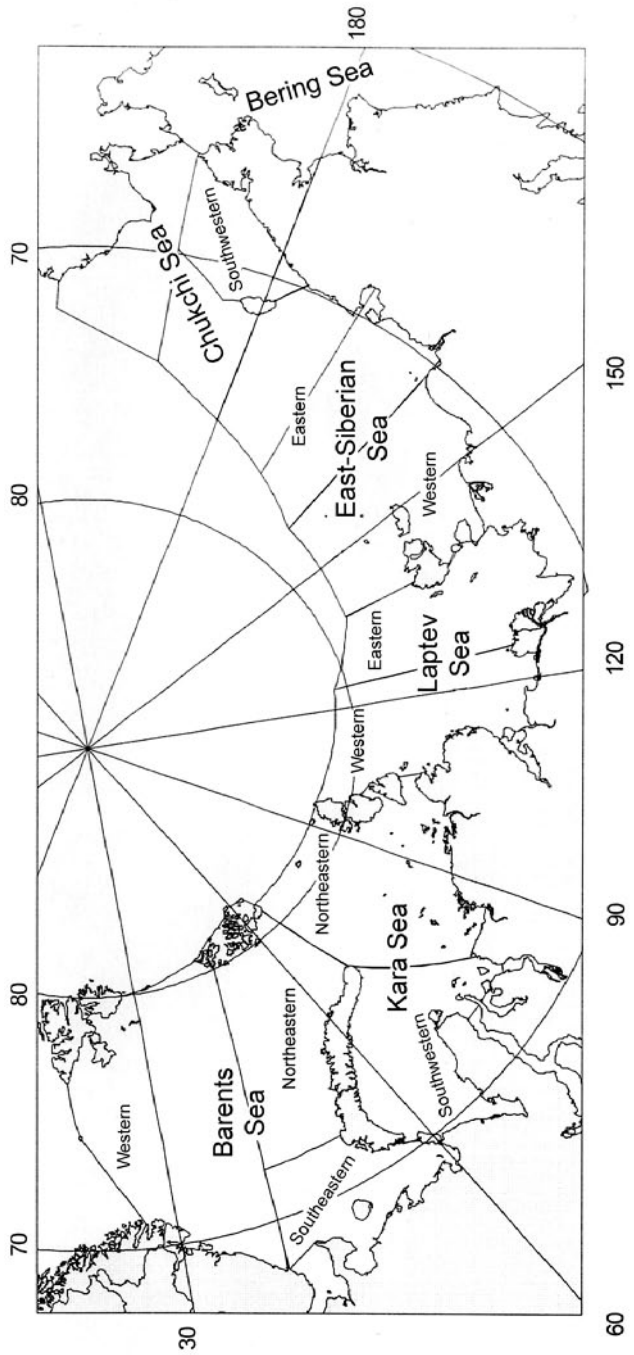

Figure 2.7. The Arctic Eurasian Shelf seas and their regions.

2.2.1 Ice formation and ice thickness growth

The process of ice formation in the Arctic seas is a result of interaction of heat accumulation in the sea during the period of its heating and intensity of heat release during the period of its cooling. The process of sea cooling occurs in late August–early September, ends with the appearance of new ice types in the ice-free areas: frazil ice, grease ice, slush and shuga.

Average dates of ice formation

The large geographical extent of the Arctic seas, from the Siberian Shelf to the Barents Sea, and their corresponding regional differences create variable conditions for ice formation in these seas. The spreading of ice formation is illustrated by our chart of average dates of ice formation in Figure 2.8. The chart is based on a 50-year data series of polar stations and observations in open sea areas carried out during the period of visual airborne ice reconnaissance. Ice formation begins in late August in the northern East Siberian Sea. In the first 10 days of September, young ice appears in the north of the Kara and Laptev Seas and by the end of the second 10-day period of September in the north of the Chukchi and Barents Seas. In the coastal shallow water regions of the Arctic seas, ice formation begins, on average, during the first 10 days of October.

From the onset of ice formation, the Laptev and East Siberian Seas are completely covered by young ice in 35–40 days, on average, and the Kara and Chukchi Seas in 80–85 days.

The large heat supply of Barents Sea water, compared with the Arctic seas of the Siberian Shelf, restrains the processes of ice formation, and it slowly spreads from the straits of Franz Josef Land and the Spitsbergen archipelago to central sea regions at the Barents Sea. According to mean multi-year data, ice formation stops in the middle of April at a region with a high heat content of water—that is, the Polar Ocean Front in the Barents Sea. The entire water column to the west and south of the April isochrone (Figure 2.8) has a sufficiently high temperature, hindering further ice spreading. As a result, about one-third, on average, of the Barents Sea area remains ice-free.

Variability in the dates of ice formation

The meteorological and hydrological conditions of the spring–summer and autumn periods, on which the dates of ice formation depend, experience significant inter-annual variations. Therefore, the dates of ice formation of some years may differ considerably from mean multi-year dates. Depending on regional conditions, the variability of the amplitudes of the dates of ice occurrence in the Arctic seas of the Siberian Shelf vary within 30 to 80 days. In the Barents Sea—within the area with a 100% probability of ice presence in April (Zubakin, 1987)—the multi-year amplitudes of the dates of stable ice formation change between 40 and 120 days.

The spatio-temporal variability in the dates of ice formation is related to both the conditions of water cooling in the Arctic seas that precede ice formation, and the presence or absence of ice that does not melt during summer (Krutskikh, 1970). These

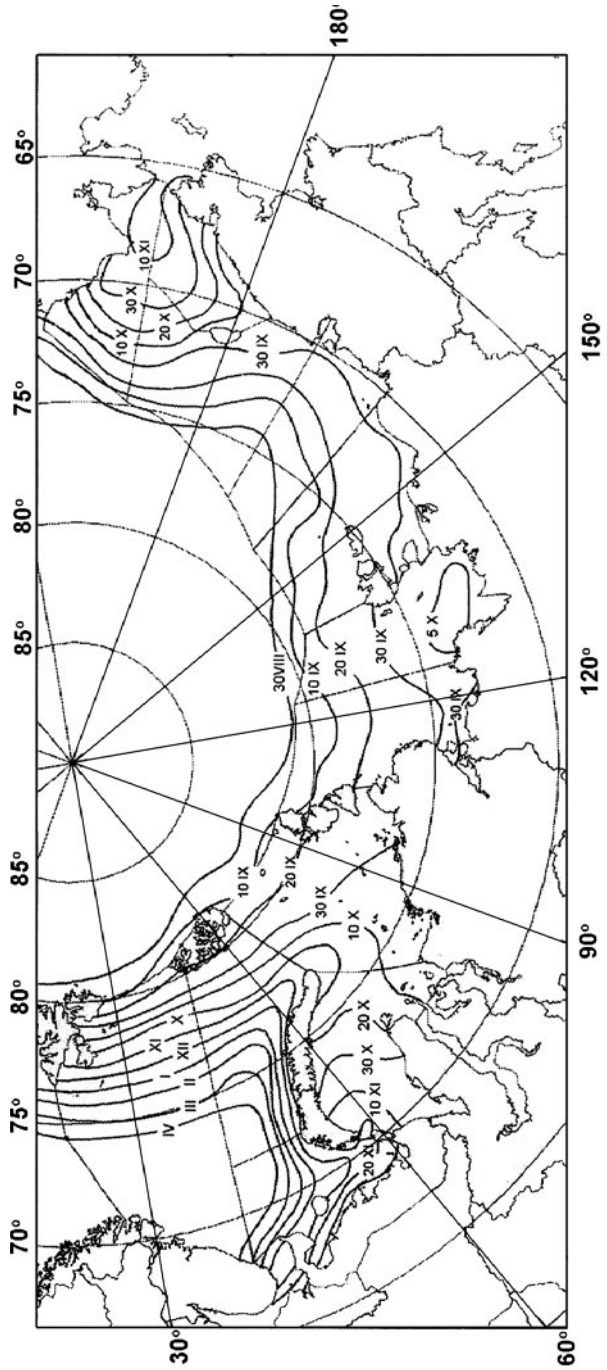

Figure 2.8. Average dates of ice formation in the Arctic seas.

peculiarities are reflected in the distribution of standard deviations of the dates of stable ice formation in the Arctic seas, presented in Figure 2.9 (Karklin, 1987).

The least variable dates of ice formation are in the coastal shallow regions of Arctic seas freshened by river water. In these regions, standard deviations are no greater than 10 days (Figure 2.9). The same value is characteristic of standard deviations in the central Chukchi Sea.

In the northern areas of the Arctic seas and the adjoining water of the Arctic Basin, where ice formation occurs almost always among close ice, standard deviations of the dates of ice formation comprise 10–12 days.

The variability in ice formation dates increases in the regions characterized by a 50% probability of the presence of ice in late September. They include the central areas of the East Siberian and the Kara Seas and the northern areas of the Laptev and the Chukchi Seas. Standard deviations here are 16–18 days (Figure 2.9). Standard deviations in the regions subjected to the influence of heat advection by currents are of the same order. In the Kara Sea, this is a region adjacent to Kara Gate Strait and in the Chukchi Sea to Bering Strait. The most significant variability in the dates of ice formation is observed at the boundary of the Kara and Barents Seas and in the Barents Sea, where they exceed 20 days (Figure 2.9).

Ice thickness growth

After ice formation, the ice cover thickness increases. According to multi-year data from polar stations (Gudkovich *et al.*, 1972), the ice thickness growth rate increases from October to November. In November, ice grows as rapidly as possible (on average, 11 cm over a 10-day period), then with increasing ice thickness the process of ice growth slows and in May ice grows by 2 cm, on average, over a 10-day period (Table 2.12).

The ice thickness growth rate varies in different regions of the Arctic seas. The range can be seen by comparison of the southwestern Kara Sea with the eastern Laptev Sea, distinguished by the least and largest ice growth rates, respectively (Table 2.12).

Spatial change in the ice thickness in the Arctic seas during the period of ice cover growth is related to regional variations. Ice thickness, calculated by its mean growth rate in the regions of the Arctic seas, shows that throughout the entire cold period the ice thickness in the central areas of the Arctic Seas exceeds the thickness in the

Table 2.12. Average ice thickness growth rate in the Arctic seas based on data from polar stations (cm/10-day period).

Region	Months							
	Oct.	Nov.	Dec.	Jan.	Feb.	Mar.	Apr.	May
All seas	9.5	11.0	10.0	9.0	7.0	6.5	4.0	2.0
Southwestern Kara Sea	5.0	9.5	8.5	7.5	5.5	4.0	3.0	2.0
Eastern Laptev Sea	11.5	12.5	11.5	11.0	8.0	7.5	5.0	3.0

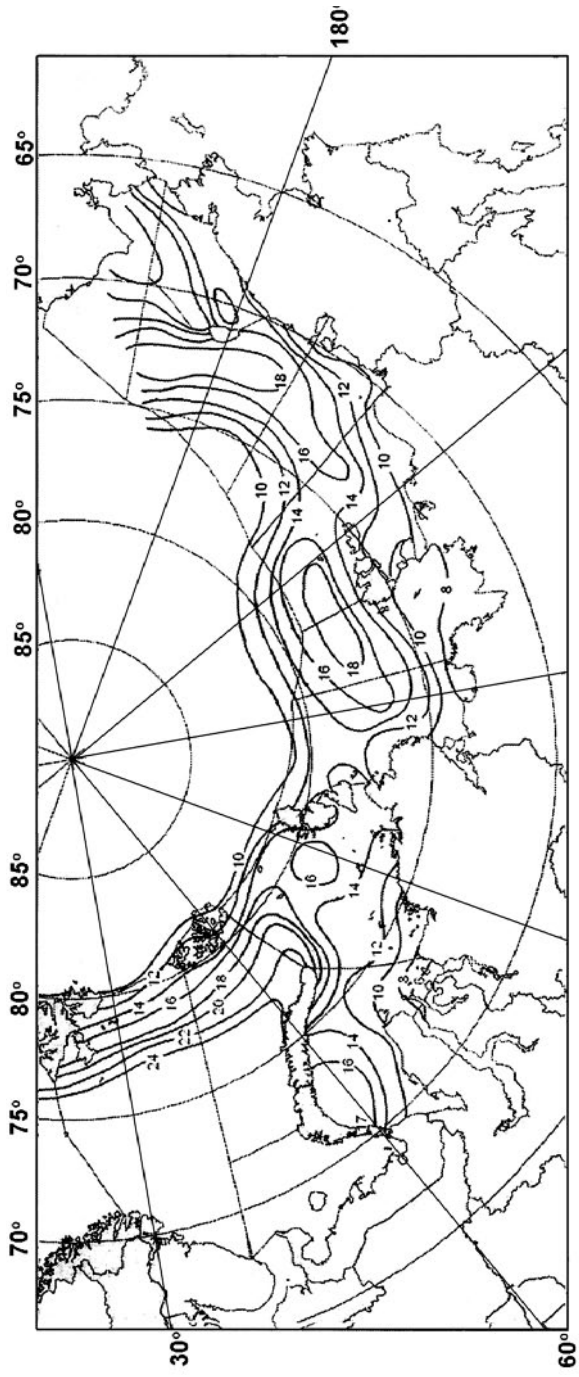

Figure 2.9. Standard deviations of the dates of ice formation in the Arctic seas.

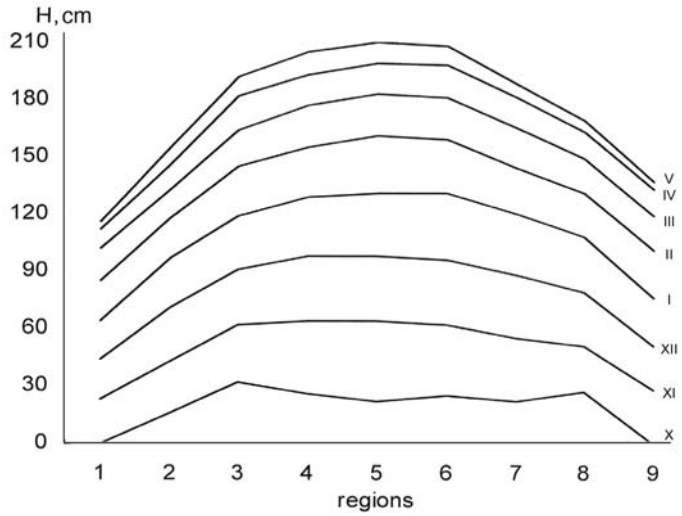

Figure 2.10. Changes in calculated mean multi-year ice thickness in the regions of the Arctic seas from October (X) to May (V). 1 = Southeastern Barents Sea and western straits of the Kara Sea; 2 = southwest and 3 = northeast of the Kara Sea; 4 = west and 5 = east of the Laptev Sea; 6 = west and 7 = east of the East Siberian Sea; 8 = southwestern Chukchi Sea; 9 = Bering Strait.

southern areas of the Kara and the Chukchi Seas subjected to the influence of the Atlantic and Pacific Ocean that mitigate the severity of the Arctic winter (Figure 2.10).

In mid-October in most regions of the Arctic seas, young ice exceeds, on average, 20 cm in thickness. The exception is the southeastern Barents Sea and the southwestern Kara Sea, and also the southern Chukchi Sea near Bering Strait where ice formation begins later than in the other regions. During the second–third 10-day periods of May, ice in all regions of the Arctic seas achieves its maximum thickness (Figure 2.10).

As can be seen from Figure 2.10, the greatest thickness of ice formed in autumn is typical of the regions of the Laptev and East Siberian Seas, where according to calculations, it is 190–210 cm, on average. In the southwestern Kara Sea, ice thickness is 150–160 cm, on average, and in the southern Chukchi Sea it is 170 cm.

Depending on the severity of winter conditions, the ice thickness growth rate experiences interannual fluctuations: being greater in colder winters and less in comparatively mild winters. As follows from the calculations, multi-year changes in ice thickness are on average in the ±30–50-cm interval (Figure 2.11). Ice thickness in the eastern Laptev Sea and in the East Siberian Sea is distinguished by its smaller variability: within ±30–35 cm relative to the average over the region.

Age (thickness) of drifting ice

The aforementioned characteristics (Figure 2.11) of spatial ice thickness change refer to the landfast ice of the Arctic seas. After landfast ice is established, it undergoes

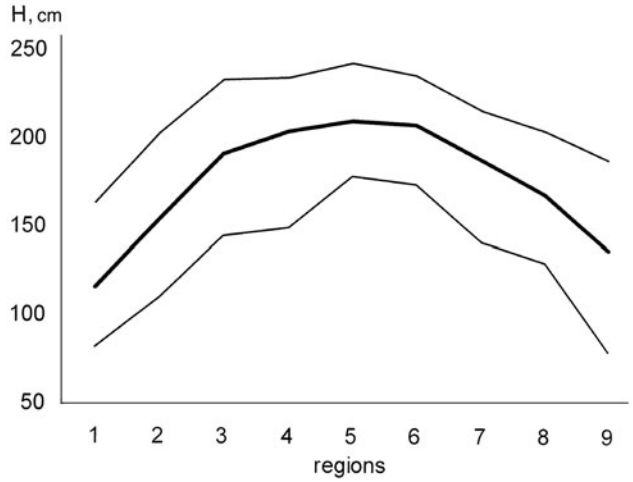

Figure 2.11. Calculated average (bold line) and extreme (thin lines) landfast ice thickness in the regions of the Arctic seas at the end of the growth period (same symbols as in Figure 2.10).

successively the age stages from young to thick first-year ice. In the open regions of the Arctic seas, ice of different age categories is present simultaneously throughout the autumn–winter season. This is due to the non-simultaneous onset of ice formation in different areas. An important mechanism is convergence and divergence of ice fields caused by the drift, which results in the formation of cracks, leads and fractures where young ice forms. Near the landfast ice boundary, polynyas are created with formation of new ice.

It is known that ice age is determined by qualitative airborne visual or instrumental observations or satellite images. In accordance with the Sea Ice Nomenclature (WMO, 1989), WMO stages of development are defined according to thickness intervals: young first-year ice 10–30 cm, thin first-year ice 30–70 cm, medium first-year ice 70–120 cm, thick first-year ice >120 cm and second-year and multi-year ice >250 cm.

First-year ice prevails in the regional seas of the NSR (Table 2.13). Second-year and multi-year ice is more often observed in the East Siberian Sea and in the north of the Laptev and Kara Seas. The areas occupied by this ice change little on average throughout the autumn–winter. Its maximum concentration of about 30% is located in the eastern East Siberian Sea (Table 2.13).

By the end of October, young ice prevails in all regions of the Arctic seas (Table 2.13). The area it occupies varies between 24% (in the southwestern Chukchi Sea) and 74% (in the eastern Laptev Sea). Thin ice is absent in the southwestern Kara Sea, occupying about 10% of the area of the northeastern Kara Sea and the western Laptev Sea. In other regions, the area occupied by this ice is insignificant. In February all ice age types are represented in the Arctic seas. In most regions, thick ice is predominant occupying 50 to 70% of their water areas. The exception is the southwestern Kara and Chukchi Seas, where medium age ice prevails. By the end of the

Table 2.13. Ice age composition in some regions of the Arctic seas in the autumn–winter period (in percentage of the region's area).

Ice age	Month	Regions of the seas						
		SWK	NEK	WL	EL	WES	EES	SWC
No ice	October	60	17	15	12	10	9	63
	February	0	0	0	0	0	0	0
	May	0	0	0	0	0	0	0
Young first-year	October	40	60	60	74	64	47	24
	February	12	2	10	3	5	2	3
	May	15	6	8	7	4	2	2
Thin first-year	October	0	11	10	8	4	8	5
	February	35	10	5	5	3	2	5
	May	3	5	3	3	2	1	1
Medium first-year	October	0	6	5	3	5	6	0
	February	53	20	26	20	17	10	45
	May	20	5	8	4	2	2	8
Thick first-year	October	0	0	0	0	0	0	0
	February	0	65	50	71	60	54	35
	May	62	81	73	86	80	65	73
Second-year, multi-year	October	0	6	10	3	17	30	8
	February	0	3	9	1	15	32	12
	May	0	3	8	0	12	30	16

Note: SWK and NEK = southwestern and northeastern Kara Sea; WL and EL = western and eastern Laptev Sea; WES and EES = western and eastern East Siberian Sea; and SWC = southwestern Chukchi Sea.

period of growth in May, thick first-year ice predominates everywhere in the Arctic seas (Figure 2.12). It occupies 60 to 85% of the total area of the Arctic seas. Note that the thickness of thick ice by the end of winter differs significantly in the regions of the Arctic seas. While in the Laptev and the East Siberian Seas it comprises about 190–210 cm, on average, in the southwestern Kara and Chukchi Seas it is equal to 150 and 170 cm, respectively. Due to the ridging of drifting ice, its thickness increases by 20%, on average (Karelin, 1945).

The drifting ice of the Barents Sea usually forms within the sea itself. But, in some years old ice is transported in winter to the western part of the sea from the Arctic Basin through the strait between Spitsbergen and Franz Josef Land, whereas ice from the northern Kara Sea is exported to the northeastern part of the sea.

The distribution of ice of different ages in the Barents Sea is generally zonal, according to multi-year observations (visual and instrumental airborne and satellite) supplemented by calculations. Near the ice edge, there is a zone of young ice with a thickness of 10–30 cm, with zones of thicker ice to the north and east. During the two months after the beginning of ice formation (November), thin first-year ice and young ice are formed. As ice formation develops through the winter the areas of different ice

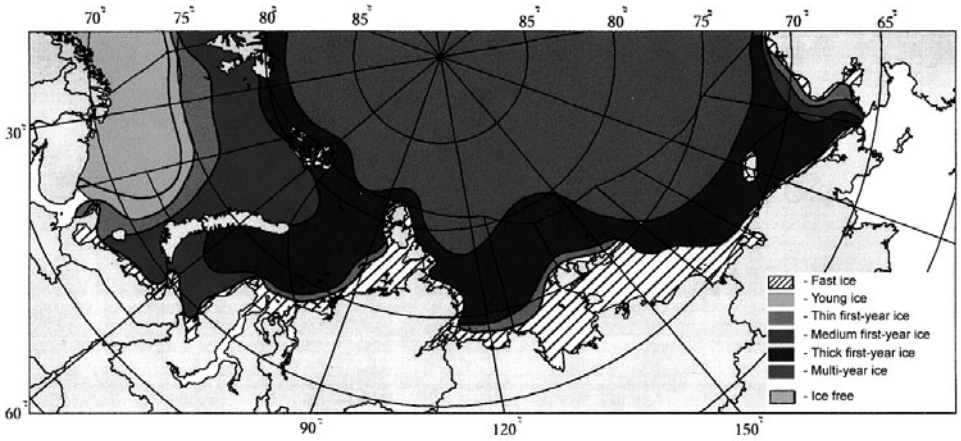

Figure 2.12. Average distribution of ice of different age in the Arctic seas at the end of the ice cover freezing period (see also color section).

thickness categories change. This process continues up to the maximum development of the ice cover, resulting in the areas of ice of different age shown in Table 2.14.

In November, most of the Barents Sea is ice-free, with the remaining part of the sea covered by young and thin ice. In the southeastern part, all ice formed is at the stage of young ice with a thickness of up to 30 cm. In February, three ice age categories—from young to medium ice—are present in the western and northeastern parts of the sea. In the southeastern part, thin first-year ice occupying 52% of its area is predominant. In April, ice in this part of the sea gradates to medium first-year ice, achieving a thickness of 70–80 cm. The same ice (but with a thickness of 90–120 cm) covers much of the northeastern sea region with the area occupied by young and thin ice significantly decreased. In the western part of the sea, thin first-year ice and young ice occupy about one-quarter of its area and the same refers to medium ice. Thick first-year ice with a thickness of 130–150 cm forms only in the north of the western and northeastern parts of the sea, occupying about 7–8% of their areas. Ice thickness in

Table 2.14. Ice age composition in the autumn–winter period in the Barents Sea regions (in percentage of the region's area).

Region	Month														
	Nov.	Feb.	Apr.	Nov.	Feb.	Apr.	Nov.	Feb.	Apr.	Nov.	Feb.	Apr.	Nov.	Feb.	Apr.
	No ice			Young ice			Thin first-year			Medium first-year			Thick first-year		
WB	75	54	47	20	10	8	5	24	15	–	12	24	–	–	7
NEB	59	25	14	14	4	2	27	16	6	–	55	70	–	–	8
SEB	93	39	30	7	9	8	–	52	21	–	–	41	–	–	–

Note: WB, NEB and SEB = western, northeastern and southeastern areas of the Barents Sea.

remote parts of the region is estimated on the basis of numerical calculations and the data from polar stations on the west coast of Novaya Zemlya.

On the basis of the Global Digital Sea Ice Data Bank (a WMO project)[1] over the period 1950–1994, a mean chart of ice distribution by age in the Arctic seas for the end of the winter period was constructed (Figure 2.12). As seen from the figure, most of the areas of the Siberian Shelf seas are covered by thick first-year ice. However, as follows from Figure 2.10, its thickness in sea regions is different. The greatest thickness of thick first-year ice is observed in the eastern Laptev Sea and in the western East Siberian Sea, where it is more than 200 cm. Ice of this age increases to a thickness of 120–140 cm in the southwestern parts of the Kara and Chukchi Seas. Zones occupied by young and thin ice with a thickness of 30–70 cm can be identified. These ice types mainly form in polynyas in the Kara, Laptev and Chukchi Seas behind landfast ice along the Alaskan coast and also in the marginal zone of the Barents Sea.

Second-year and multi-year ice extends further to the northern sea regions as a result of ice exchange with the Arctic Basin.

2.2.2 Ice exchange of the Arctic seas with the Arctic Basin

There is an almost continuous ice exchange between the Arctic marginal seas and the Arctic Basin. The Arctic Basin plays the role of a reservoir capable to receive large ice masses exported from the marginal seas and supply these areas with thicker multi-year ice. The intensity and direction of ice exchange depend to a great extent on wind forcing, particularly in the northern regions of the marginal seas. Ice export from the marginal seas largely depends on ice export from the Arctic Basin to other regions, predominantly to the Greenland Sea. Another factor influencing ice exchange is the water circulation in the Basin, and in the marginal seas (Gudkovich and Nikolayeva, 1963).

Except for the Fram Strait, there are no long observations of ice drift at the boundaries of the marginal seas in the Arctic Basin. A simple method to estimate the ice flux is to use the "isobaric drift" ratios proposed by N.N. Zubov:

$$w = k\frac{\partial P}{\partial x} \tag{2.5}$$

where w is the projection of ice drift velocity to axis y; k is the isobaric coefficient; $\partial P/\partial x$ is the projection of the atmospheric pressure gradient to axis x.

If axis x is directed along the "entry" section with length l, approximately coinciding with the northern sea boundary, then by integrating expression (2.5) along this axis from the western sea boundary to the eastern one, we obtain:

$$S = \oint_l w\,dx = k\oint_l \frac{dP}{dx}dx = k(P_l - P_0) = k\,\Delta P \tag{2.6}$$

[1] More information is available at the following websites *http://nsidc.noaa.org/noaa/gdsidb/* and *http://www.aari.ru/gdsidb/*

where S is the area of the ice cover that passed through section l per unit time, which is expressed by coefficient k and the corresponding scale of averaging of atmospheric pressure. When using mean monthly charts of atmospheric pressure at sea level, the dimension of the isobaric coefficient is in km^2 hPa/month. The values of the latter were obtained from the data of observations of the total ice drift in the Arctic Basin enlarged by 25% (according to the empirical ratio of corresponding mean annual values).

As follows from formula (2.6), the resulting ice exchange area does not explicitly depend on the section length being proportional to the atmospheric pressure difference at its ends. It is assumed that ice cover (regardless of ice concentration) does not disappear over the entire section length. It is natural that, for realistic assessment of the ice exchange volume, information on ice concentration and thickness and their changes in time are required.

Based on mean monthly atmospheric pressure differences in Mendeleyev Strait (between Franz Josef Land and Severnaya Zemlya) and in Makarov Strait (between Novaya Zemlya and Franz Josef Land), and on monthly values of isobaric coefficients published in Gudkovich and Nikolayeva (1963), estimates of the ice exchange area of the Kara Sea with the Arctic Basin were obtained for a number of years (1937–2003). Based on these data, seasonal changes in the corresponding mean multi-year values presented in Figure 2.13(1) were determined. As follows from this figure, ice is transported in summer (May–August) to the Kara Sea from the Arctic Basin, and in winter (September–March) ice is exported to the Arctic Basin. Taking into account the ice exchange with the Barents Sea through Makarov Strait, the period of ice transport to the Kara Sea decreases between June to August. These data indicate that more than 138×10^3 km^2, on average, of the ice cover (standard deviation of 90×10^3 km^2) is exported from the Kara Sea northward for the winter season (from October to March), and 24×10^3 km^2, on average, of ice (standard deviation of 70×10^3 km^2) is transported from the Arctic Basin in the summer period (from April to September). Thus, 115×10^3 km^2 of ice is annually exported from the sea to the north, which comprises about 14% of the area of the entire sea or 23% of its northeastern area. The estimates presented do not explicitly take into account the influence of currents.

A similar methodology was used to calculate ice exchange between the Laptev Sea and the Arctic Basin, where mean monthly atmospheric pressure differences between Cape Arktichesky (Komsomolets Island) and Kotelny Island were used. Figure 2.13(2) shows seasonal changes in mean monthly values of the calculated ice exchange through this transect. Ice export from the Laptev Sea to the Arctic Basin dominates during most of the year except for June and July. The mean annual area of total ice export through the indicated transect is 343×10^3 km^2, with a maximum in winter (from October to March).

To estimate the reliability of the calculated values, the location of the close ice ($\frac{7}{10}$ to $\frac{10}{10}$) boundary in late September was compared with the boundary of dominance of old ice (second-year and multi-year) in March of the next year. The latitudinal difference in location of the indicated boundaries at meridians (in 5° of longitude) was assumed to be a value of ice movement along the corresponding meridians for the six

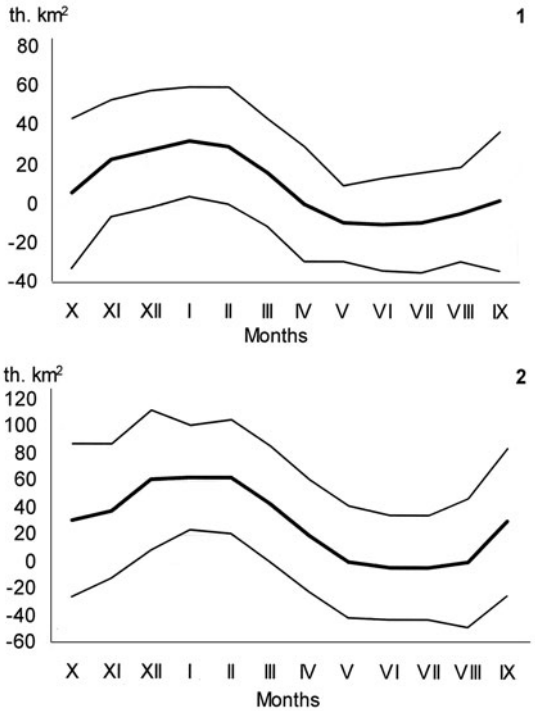

Figure 2.13. Mean multi-year values of seasonal changes in calculated ice exchange of the Kara (1) and Laptev (2) Seas with the Arctic Basin (thin lines characterize data enlarged or reduced by the value of standard deviations).

winter months (October–March). The ice exchange area with the Arctic Basin for the indicated time was determined by the formula:

$$S = 12{,}350 \cdot \Delta\varphi_{cp} \cdot \Delta\lambda \cdot \cos\varphi_{cp} \tag{2.7}$$

where $\Delta\varphi_{cp}$ is the mean difference of latitudes between the location of the aforementioned ice boundaries at meridians (in degrees); $\Delta\lambda$ is the longitudinal difference between the meridians of the eastern and western sea boundaries (in degrees); φ_{cp} is the latitude of both ice boundaries averaged by meridians; coefficient 12,350 converts the degrees of latitude to area dimensions in km^2.

The mean value of ice exchange between the Laptev Sea and the Arctic Basin for the winter season (1954–1991) calculated by formula (2.7) is on average 328×10^3 km^2 (61% of the sea area), which is only 10% greater than the value presented above, calculated from the atmospheric pressure difference. The calculated ice exchange areas for the other seasons are assumed to have similar accuracy.

To estimate ice exchange between the Arctic Basin and the East Siberian and Chukchi Seas is a more difficult problem. In the winter period, these areas frequently have onshore winds, which should lead to a large quantity of ice transported from the Arctic Basin to these seas. The intensity of this process increases from west to east.

However, analysis of the ice cover area change in the eastern East Siberian and Chukchi Seas reveals that during winter, ice export from these seas to the Arctic Basin prevails (Gudkovich and Nikolayeva, 1963).

This conclusion is also confirmed by the data from the present study: the calculated area of ice cover exported to the Arctic Basin over the winter period is only 38×10^3 km^2, whereas its value determined by variation in the location of the close ice ($\frac{7}{10}$ to $\frac{10}{10}$) boundary at the end of September and the boundary of old ice (second-year and multi-year) dominance in March is greater than 440×10^3 km^2. About 100×10^3 km^2 of this value refers to the region located to the north of the New Siberian Islands and mainly characterizes the additional ice export from the Laptev Sea. But, even in this case the ice export from the East Siberian Sea (about 45% of its area) presents a substantial contribution to the supply of ice to the Arctic Basin by the shelf seas.

It should however be considered that a dynamic divergence of the ice cover near the northern boundary of the sea, which is often observed at prevailing cyclonic air pressure fields in summertime, can significantly influence the location of the boundary of prevailing old ice at the end of winter, and hence lead to an overestimation of the value of ice export to the north as obtained by using the considered methodology.

In summer, the frequency of occurrence of offshore winds in this sea significantly increases, allowing us to calculate more reliably the values of the ice exchange of this sea with the Arctic Basin.

Without northward currents in the Bering Strait and shores restricting ice transport from the north, the Chukchi Sea would be jammed with multi-year ice from the Arctic Basin and the Beaufort Sea at the end of winter. The average values of the ice area flux to the Chukchi Sea, calculated by the pressure difference from Wrangel Island to Cape Barrow, is 305×10^3 km^2 in winter and 124×10^3 km^2 in summer. However, calculations based on a comparison of the location of the considered ice cover boundaries at the end of summer and winter show that, on average, more than 222×10^3 km^2 of ice (about 60% of the sea area) is exported from this sea to the Arctic Basin over winter. It is difficult to estimate the ice exchange between this sea and the Arctic Basin in summer due to the intensified Pacific Current in the Bering Strait and heat advection in the atmosphere. In some years, when an atmospheric low-pressure depression persists for a substantial period of time over the neighbouring areas of the Arctic Basin, an "ice avalanche" can occur resulting in a large ice quantity transport to the Chukchi Sea from the northwest and the north.

In the winter months more than 1 million km^2 of the ice cover is transported from the Arctic marginal seas to the Arctic Basin, which is comparable with recent estimates of the ice area exported through the Fram Strait (Koesner, 1973; Mironov and Uralov, 1991; Vinje and Finnekasa, 1986; Houssais and Herbaut, 2003; Koberle and Gerdes, 2003; Schmith and Hansen, 2003). Given the typical ice thickness values, one can obtain an estimate of the ice volume exported to the Arctic Basin over winter, which is about 1,500–2,000 km^3. This is about half as large as the available estimates of ice export to the Greenland Sea over winter (Vinje and Finnekasa, 1986; Alekseev *et al.*, 1997), which can be explained by taking into account the time of ice movement to Fram Strait, ridging processes, etc.

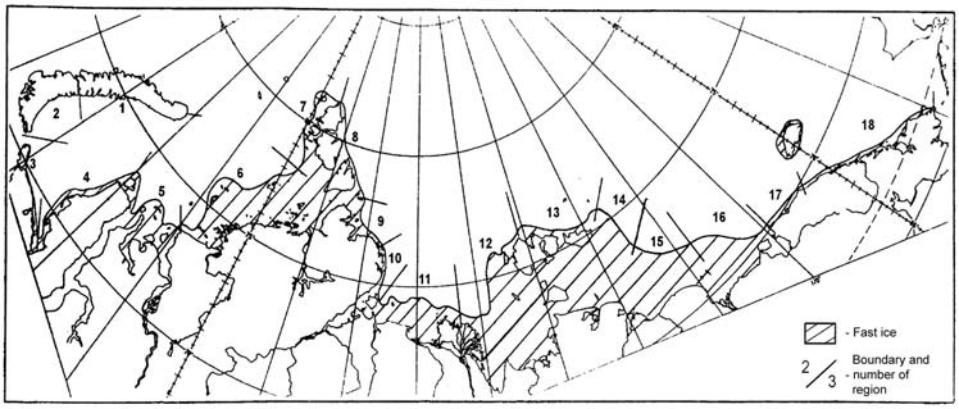

Figure 2.14. Location of landfast ice and flaw polynyas in the Arctic seas of the Siberian Shelf. 1 = Northern Novozemelskaya; 2 = Southern Novozemelskaya; 3 = Amderminskaya; 4 = Yamalskaya; 5 = Ob'–Yeniseyskaya; 6 = Central Kara; 7 = Western Severozemelskaya; 8 = Eastern Severozemelskaya; 9 = Northeastern Taymyrskaya; 10 = Eastern Taymyrskaya; 11 = Anabaro-Lenskaya; 12 = Western Novosibirskaya; 13 = Northern Novosibirskaya; 14 = Eastern Novosibirskaya (west); 15 = Eastern Novosibirskaya (east); 16 = Aionskaya; 17 = Western Chukotskaya; 18 – Eastern Chukotskaya.

Because the thickness of the ice cover involved in ice exchange continuously varies, a most correct approach to estimate the corresponding ice volumes should be based on dynamic–thermodynamic models of ice cover evolution. To solve the indicated problems, it is necessary to perform model calculations over prolonged time intervals (years) (Gudkovich and Doronin, 2001).

2.2.3 Landfast ice and polynyas of the Arctic seas

Landfast ice is a typical ice regime feature in the Arctic seas in wintertime. The main zones of landfast ice formation are connected with shallow water and island regions of the Arctic seas. Along the landfast ice edge over its entire length, flaw polynyas (Figure 2.14). Landfast ice and flaw polynyas significantly influence the dynamics and thermo-dynamics of seawater as well as the temperature and the circulation regime of the atmosphere above the regions of recurring polynyas. The presence of flaw polynyas also helps navigation in the wintertime. Cargo is also transported through landfast ice in the offshore zone of the Arctic seas.

Establishment and development of landfast ice

The formation of landfast ice becomes possible when the young ice achieves a thickness of 10–30 cm. Fast ice appears in different areas of the Arctic seas at different times—from the middle of September to early December. As a rule, the unstable character of landfast ice establishment and development is observed in regions in which the onset of ice formation is late and in regions with active

Table 2.15. Average and maximal areas of landfast ice in regions of the Arctic seas over the period 1949–2002.

Regions of the seas	Minimum area		Average area		Maximum area	
	1,000 km^2	%	1,000 km^2	%	1,000 km^2	%
Southwestern Kara Sea	33.5	10	46.9	14	97.2	26
Northeastern Kara Sea	45.8	9	111.3	26	149.5	33
Western Laptev Sea	27.6	11	43.3	27	64.6	26
Eastern Laptev Sea	137.8	48	147.4	53	160.2	56
Western East Siberian Sea	110.4	30	190.1	51	229.2	63
Eastern East Siberian Sea	48.5	12	73.1	21	156.4	38
Southwestern Chukchi Sea	3.5	2	10.6	6	19.4	11

dynamic processes (ice drift, tidal phenomena). In closed embayments and in shallow areas, landfast ice is rapidly formed—typically, during the first 10 days after the onset of ice formation. The external boundary of established landfast ice, during the first period of stabilization, passes within several kilometers of the shore, approximately along the 5–10-m isobath. The landfast ice edge is often found at islands and shoals, as well as defined by stamukhas (grounded thick ice).

With increasing ice thickness, the landfast ice boundary spreads seaward achieving a stable location along the 20–30-m isobath by the end of January–early February. Near shores with a sharp depth difference, the width of landfast ice can range from 2–4 to 10–30 km. Such landfast ice is formed near the shores of Novaya Zemlya, along the Amderma and Yamal coast, the east shores of the Severnaya Zemlya archipelago and the Taymyr coast in the Laptev Sea, as well as along the Chuckchi Sea coast. Landfast ice occupies about 25%, on average, of the total area of the Arctic seas and up to 35% at its maximum development. In the regions of the Arctic seas, the areas occupied by landfast ice can range from 6 to 53%. Landfast ice develops least of all in the southwestern Chukchi Sea, and the most significant areas of landfast ice are observed in the eastern Laptev Sea and in the western East Siberian Sea.

Depending on hydrometeorological conditions, landfast ice reaches its maximum development in February, March or May. Its area in some regions of the seas can vary significantly from year to year (Table 2.15).

The least significant interannual changes in the area of landfast ice are typical of the eastern Laptev Sea: the magnitude of oscillations is only 8% of the area of the region (Table 2.15). The greatest magnitude of interannual fluctuations in the landfast ice area is observed in the western East Siberian Sea, comprising about 40% of the total area. In other regions of the Arctic seas, the amplitude of changes in the area of landfast ice ranges from 14 to 17% of the areas of the regions and only in the southwestern Chukchi Sea does it reach 9%.

Unlike the Arctic seas of the Siberian Shelf, landfast ice in the Barents Sea is not widespread, covering only about 2% of the sea. Stable landfast ice is annually formed

in the inner parts of the bays and fjords on Spitsbergen, in the straits of Franz Josef Land, in inlets of the west coast of Novaya Zemlya, near the coast of Bely, Viktoria and Kolguyev Islands and also in some bays of the south coast (Pechora Gulf and Khaipudyrskaya Gulf).

Flaw polynyas

The appearance of flaw polynyas and of coastal polynyas, in the absence of landfast ice, depends on the direction and duration of off-ice and offshore (i.e., from the shore) wind, and also on the orientation of the ice boundary relative to the wind direction. Polynyas present extensive areas of tens to hundreds of kilometers of open water or young ice up to 30 cm thick forming between landfast ice and drifting ice. The places where polynyas form in the Arctic seas are given in Figure 2.14.

Flaw polynyas appear from the moment of landfast ice formation during the entire winter period and can exist constantly or episodically. The frequency of occurrence of polynyas serves as the basis for their classification (by stability): at a frequency of occurrence greater than 75%, polynyas are considered recurring; at 50 to 74% they are stable; and less than 50% they are occasional. Following this criterion, most Arctic polynyas are stable. The Amderminskaya and Ob'–Yeniseyskaya polynyas in the Kara Sea, the Anabaro-Lenskaya and Western Novosibirskaya polynyas in the Laptev Sea and Northern Novosibirskaya polynya in the East Siberian Sea belong to the recurring type of polynyas (Table 2.16). Farther eastward, there are no recurring polynyas.

The Western and Eastern Chukotskaya polynyas are the least stable polynyas along the Chukchi Sea coast. The largest polynyas by area are the Western Novosibirskaya, Central Kara and Anabaro-Lenskaya, and the smallest polynyas are the Southern Wrangelevskaya and Western Chukotskaya (Table 2.16). The total mean multi-year area of polynyas in November–May is: $-47 \times 103\,\text{km}^2$ in the Kara Sea, $34 \times 103\,\text{km}^2$ in the Laptev Sea, $7 \times 103\,\text{km}^2$ in the East Siberian Sea and $6 \times 103\,\text{km}^2$ in the southwestern Chukchi Sea.

Flaw polynyas in the Barents Sea form near the south and southwest coast of Franz Josef Land, along the shores of Novaya Zemlya, near Kolguyev and Vaygach Islands. Some characteristics of the flaw polynyas of Franz Josef Land are available from the data of airborne ice observations (Table 2.17). According to the table, the western and northeastern polynyas of Franz Josef Land are stable. The southeastern polynya by its frequency of occurrence is close to occasional. Polynyas occasionally forming along the entire south coast of the Pechora Sea are ephemeral. Their existence varies between 1 and 22 days. Polynyas at different segments of the coast last from 2 to 4 days.

2.2.4 Ice distribution during ice cover decay

Ice cover melting

Melting of the ice cover in the Arctic seas begins in late April in the marginal zone of the Barents Sea. The mean dates for the onset of melting in the region adjoining

Table 2.16. Mean multi-year characteristics of flaw polynyas in the Arctic seas for the period November to June.

Polynyas	Frequency of occurrence (%)	Average width (km)	Average length (km)	Average area (1,000 km^2)
Kara Sea				
Northern Novozemelskaya	65	29	325	9.8
Southern Novozemelskaya	62	41	275	11.6
Amderminskaya	77	33	275	9.5
Yamalskaya	63	27	395	12.0
Ob'–Yeniseyskaya	87	43	275	12.4
Central Kara	71	34	445	15.6
Western Severozemelskaya	52	27	275	7.8
Laptev Sea				
Eastern Severozemelskaya	57	25	300	8.2
Northeastern Taymyrskaya	68	31	175	5.6
Eastern Taymyrskaya	57	23	190	4.6
Anabaro-Lenskaya	79	36	380	13.6
Western Novosibirskaya	81	40	370	15.9
East Siberian Sea				
Northern Novosibirskaya	84	32	460	11.3
Eastern Novosibirskaya	57	25	530	12.8
Aionskaya	43	23	225	5.3
Western Chukotskaya	27	20	185	4.0
Chukchi Sea				
Eastern Chukotskaya	31	18	370	7.2
Southern Wrangelevskaya	33	20	125	2.9
Northern Wrangelevskaya	57	23	150	3.8

Yugorsky Shar Strait falls on the end of the third 10-day period of May, and in the Franz Josef Land straits on 20 June. As a result of the significant length of the Barents Sea, the intensity of ice melting in its various regions considerably differs, decreasing from south to north. Thus, while ice thickness in the vicinity of Vaygach Island

Table 2.17. Mean multi-year characteristics of flaw polynyas of Franz Josef Land in February to May.

Polynyas	Frequency of occurrence (%)	Average width (km)
Northeastern	60	24
Southeastern	50	15
Western	74	60

decreases by 70 cm, on average, by the end of June and near the west coast of Novaya Zemlya by 50 cm at the same time, it is reduced only by 10 cm near Franz Josef Land.

The onset of ice melting in the Arctic seas of the Siberian Shelf falls between the middle of May and the second 10-day period of June. The intensity of melting depends on the dates of the onset of melting. The earlier ice melting begins, the greater the thickness of melt ice and the sooner ice clears from the seas. By the end of summer under average conditions of melting, all age types of ice melt except for thick first-year ice (the thickness of which decreases to 20–40 cm), old and ridged ice (Yanes, 1962).

In the process of ice melting there are various stages, culminating in the breakup of landfast ice and then its final decay. The breakup usually begins at the side of the landfast ice edge and extends for a short period of time (about a day) over a significant distance, spreading sometimes up to the very shore. Drifting ice forms as a result of landfast ice breakup, presenting concentrations of vast ice floes, which due to diverging and melting fracture into smaller features (medium floes, small floes and ice cake). Usually 10–20 days pass between the breakup of landfast ice and its final decay. The breakup of landfast ice occurs, on average, in July. In the southwestern Kara Sea and near the Chukchi Sea coast, the final decay of landfast ice occurs, on average, in the second half of June.

Ice clearance in the Arctic seas

Under average conditions of melting, ice disappearance in the Barents Sea in open parts is more rapid than in the Siberian Shelf seas due not only to the thermal but also to the dynamic impact of currents. The ice edge retreats northward right up to the shores of Novaya Zemlya. By July the west shores of Novaya Zemlya are usually completely ice-free with ice also disappearing in the southeastern part of the sea. In August the ice edge reaches Spitsbergen and Franz Josef Land (Figure 2.17).

With the onset of ice melting and under the influence of the dynamic processes in the Arctic seas, zones of open water, open ice (at concentrations of 40–60%) and very open ice (at concentrations of 10–30%) appear. The area of the Arctic seas occupied by ice of all categories of concentration begins to decrease as the ice melts. However, the beginning of ice disappearance of the seas is not simultaneous and occurs at different intensities, which is related to the regional features of each of the regions of the Arctic seas. Thus, in late June the ice cover largely persists in the East Siberian Sea and the northeastern Kara Sea. At the same time, 10 to 27% of the other areas of the Arctic seas are ice-free (Table 2.18). The most intense disappearance of the Arctic seas is observed during August and terminates in late September, when ice formation begins in the northern sea. On average, before the onset of ice formation, 80% of the eastern Laptev Sea and 85% of the southwestern Chukchi Sea are ice-free and the Barents Sea and the southwestern Kara Sea are almost completely ice-free. The northeastern Kara Sea and the western areas of the Laptev Sea and the East Siberian Sea become approximately 50% ice-free. At the end of the melting period, ice persists longest in the eastern East Siberian Sea: only 27%, on average, of its area becomes ice-free.

Table 2.18. Area of ice-free regions in the Arctic seas during the period of melting (%).

Regions of the seas	Month					
	April	May	June	July	August	September
WB	47	53	61	76	89	93
NEB	14	21	38	64	80	85
AWB	30	45	78	97	100	100
SWK	0	0	17	40	85	95
NEK	0	0	0	18	41	53
WLJI	0	0	10	24	45	51
EL	0	0	10	33	69	80
WES	0	0	0	10	31	49
EES	0	0	0	6	17	27
SWC	0	0	27	57	75	85

Note:
WB = ; NEB = ; AWB = ; SWK = Southwestern Kara; NEK = Northeastern Kara; WLJI = ; EL = Eastern Laptev; WES = western East Siberian; EES = eastern East Siberian; SWC = Southwestern Chukchi.

Ice distribution

The location of zones with different ice concentration during the period of melting and ice clearance in the Arctic seas is illustrated by the charts of median (50%) ice distribution in late June–September (Figures 2.15–2.18) plotted on the basis of 10-day review AARI charts for the period 1933–1992 from the data archive of the Global Digital Sea Ice Data Bank.

As seen in Figures 2.15–2.18, as the area of close ice increases (70–100%), there is an increased amount of very open and open ice (10–60%), which forms as a result of non-uniform melting of close ice due to the presence of ice of different thickness in its composition and the dynamic processes. The area occupied by this ice increases

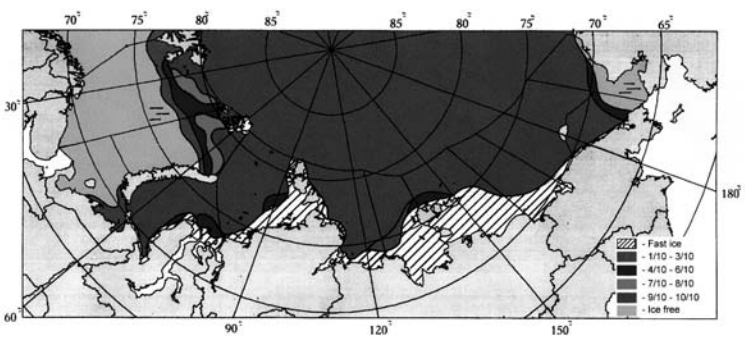

Figure 2.15. Distribution of ice of different concentration in June (with a probability of 50%) (see also color section).

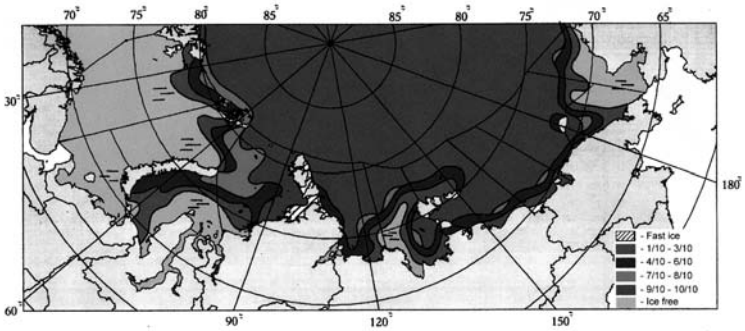

Figure 2.16. Distribution of ice of different concentration in July (with a probability of 50%) (see also color section).

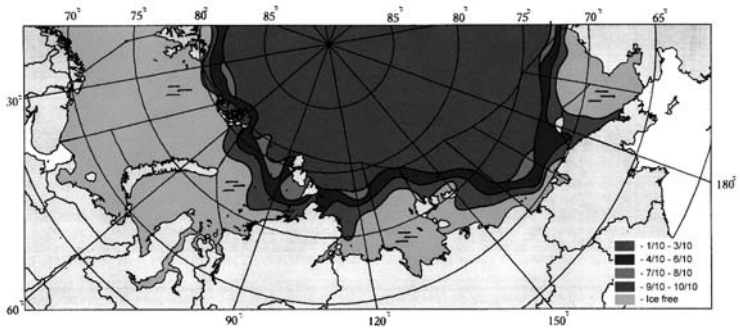

Figure 2.17. Distribution of ice of different concentration in August (with a probability of 50%) (see also color section).

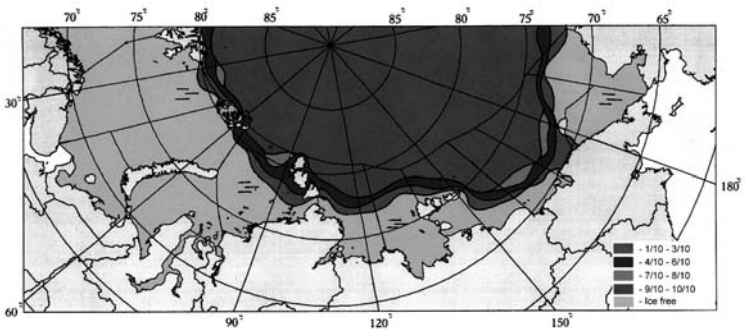

Figure 2.18. Distribution of residual ice of different concentration in September (with a probability of 50%) (see also color section).

sharply in July–August. Whereas in July a substantial portion of the Northern Sea Route is hindered by close ice with a probability of 50%, only very open and open ice is found at the approaches to Vilkitsky and Long Straits from the west and the east, and the remaining part of the route is ice-free.

3

Sea ice monitoring

3.1 HISTORY OF ICE MONITORING IN THE NORTHERN SEA ROUTE (*A.V. Bushuev, V.S. Loshchilov, V.Yu. Alexandrov, S. Sandven, O.M. Johannessen, K. Kloster, L.H. Pettersson*)

During the course of early voyages in the Barents and Kara Seas from the 11th to 17th centuries and the subsequent marine expeditions to the Arctic described in Chapter 1, extensive areas were mapped and described—for example, the northwest coast of North America, the north coast of Siberia, many islands in Arctic seas and discovery of the Bering Strait. These voyages and expeditions also provided scientific data on Arctic seas and experience in navigation under different ice conditions.

However, observations were irregular with interruptions of decades; so, it was not possible to obtain a comprehensive overview of the ice distribution and dynamics in individual marginal seas, and especially so in the central Arctic Ocean. The possibility for Arctic sea ice monitoring—regular observations of ice distribution, characteristics and dynamics of ice and its interannual and seasonal variability—began to be realized with the onset of aircraft studies.

The first visual remote observations of sea ice were made in 1897 by Salomon Andree from an air balloon during his attempt to reach the North Pole. This flight demonstrated the possibility of visual remote observations of sea ice, but simultaneously showed that balloons were not viable for this purpose. On 17 December 1903, the Americans Wilbur and Orville Wright made the first airplane flight. After this, aviation developed rapidly and by 1909 there were already 77 aircraft in different countries. Airplanes in these years were considered as a means of airborne land and sea surveys, rather than for transportation or military purposes.

In 1913, following an expedition onboard the icebreakers *Taymyr* and *Vaygach*, the possibility of using a dedicated airplane for ice reconnaissance was proposed by B.A. Vilkitskiy. The Russian pilot Yan Nagursky onboard the seaplane *Maurice Farman* implemented this idea in 1914 during a search for the lost expedition of

G. Sedov. On 8 August Nagursky made the first flight over Arctic ice and between 9 and 31 August, he made four ice reconnaissance flights to the northwest of Novaya Zemlya in support of the ship *Andromeda*. This represented the birth of airborne ice reconnaissance and marked the beginning of sea ice remote sensing (Borodachev and Shilnikov, 2002).

In subsequent decades, an extensive system of sea ice monitoring in the Northern Sea Route was developed. It has provided a hydrometeorological service (HMS) for shipping and other types of Arctic activity ever since. The current system includes the use of tools and methods of remote sensing in the form of visual observations, aerial photography, side-looking airborne radar (SLAR), satellite radiometers, side-looking radar (SLR) and synthetic aperture radar (SAR). From the start of this system up to the present, the many changes in (1) the structure of shipping and economic activity management bodies, (2) terms, regions and volumes of freight traffic, and (3) the ice strength of ships has resulted in corresponding changes in systems for monitoring and HMS. This includes the infrastructure to establish central and regional data acquisition and processing centers, an observation network, etc.

Many aspects of the current system are of great importance. This includes the technical characteristics of remote sensing airplanes and helicopters, such as operating heights and velocity, flight range and base conditions. Processing technology, tools and methods for information dissemination to users are also important. The introduction of new remote sensing instruments did not result in the exclusion of previous ones from the observation system. Thus, visual observations remained one of the main remote sensing means until the 1990s and ended only recently for economic reasons. The use of aerial photography is still in operation on a restricted basis. In this chapter the history of the development of sea ice monitoring in the NSR is presented in chronological order.

3.1.1 Airborne ice reconnaissance (1924–1932)

After the first ice reconnaissance flights in the Arctic made by Yan Nagursky, there was a break for a decade in the use of aviation for ice observations due to World War I and, then, the Russian Civil War. However, transport operations in the Kara Sea did not stop. As early as 1920, the first Siberian "bread expedition" sailed from Arkhangelsk to the mouths of the Ob' and Yenisey Rivers, and from 1921 to 1928 Kara Sea trade exchange expeditions were made on a regular basis. In order to supervise these expeditions, the Committee of the Northern Sea Route (CNSR) was set up in 1920. Later, in 1921 the Overseas Bureau of the CNSR—the Soviet Joint Stock Company Arkos—was organized in London; the CNSR provided the trade operations for all Kara Sea expeditions. In 1920, the Northern Research Commercial Expedition was established, which was commissioned to conduct not only geographical studies but also investigations on behalf of many branches of the national economy (geological exploration, fishery, hunting, etc.). In 1921, the first forecast of the probable ice state in the Kara Sea was prepared, and the Weather Service, created in Murmansk, issued

information on ice and weather in the Kara Sea using data from polar stations. Note that, by the early 1920s, hydrographic, navigation and hydrometeorological support was practically absent. There were only four broadcasting stations in the Arctic (all in the western Kara Sea), no sailing directions and navigation equipment, and no ice observations were made. Meanwhile, the first Kara Sea expeditions revealed the need to determine not only the optimal dates to begin and cease navigation but also ice conditions vital for navigation.

Beginning in 1924, in connection with the increasing export of Siberian timber, foreign ships began to call at the mouths of the Ob' and Yenisey Rivers in addition to Russian ships. Intensification of shipping in the Kara Sea necessitated the development of hydrographic and scientific–operational support. A special hydrographic expedition was organized with this purpose, and a two-seat Junkers seaplane *JU-20*—giving 185 hp, a flight velocity of 170 km h^{-1} and a flight duration of 4 h—was attached to it. The airplane was transported to Novaya Zemlya in kit form onboard a ship. After its assembly, the pilot Boris G. Chukhnovsky in August 1924 made 12 flights with a total duration of about 13 hours (Borodachev and Shilnikov, 2002).

In 1925 the Northern Research Commercial Expedition was reorganized as the Research Institute on the Study of the North (from 1930, the All-Union Arctic Institute). It was under this institute that oceanographic, meteorological, geophysical and geographic investigations were developed.

In the late 1920s, the volume of cargo and the number of vessels continued to increase. In 1929, 26 transport vessels were running the course. Strict dates were set for arrival at the Siberian ports. Routing of ships was made in groups using the icebreaker *Krasin* which operated during that navigable period. This required regular rather than episodic ice reconnaissance in that route segment. B.G. Chukhnovsky carried this out with a *Dornier Wal* airplane with a crew of four people that included an onboard observer for the first time. The duration of ice reconnaissance flights increased to 5–6 hours. In 1930, ice reconnaissance flights were already being made by three *Dornier Wal* airplanes. Their purpose was to survey separate areas of the Kara Sea rather than to choose the optimum route to be taken by vessels. However, some tactical ice reconnaissance escort flights continued in these and subsequent years, both in the western and eastern Arctic, despite being limited in observation time and area, aiming to provide support for specific vessel transit. Thus, the icebreaker *Krasin* during the expedition of 1928 was sent to rescue the crew of the airship *Italy*. The *Krasin* had onboard an *SH-2* seaplane piloted by B. Chukhnovsky, who also detected Malmgren's group.

In July–September 1932, the expedition of the Arctic Institute headed by O.Yu. Schmidt and V.Yu. Vize onboard the icebreaker *A. Sibiryakov* (captained by V.I. Voronin) sailed for the first time in one navigation season from Arkhangelsk to Bering Strait and further to the Pacific Ocean—that is, along the entire Northern Sea Route. During preparations for this expedition, V.Yu. Vize predicted for the first time the total sea ice extent in all Arctic seas during the navigable season. It was planned to conduct ice reconnaissance from an airplane onboard the *A. Sibiryakov* during the expedition. However, the aircraft had an accident during the flight

from Leningrad to Arkhangelsk. The M/S *Chelyuskin* repeated the voyage of the *A. Sibiryakov* in 1934 and had onboard an *SH-2* seaplane. During the voyage, the pilot M.S. Babushkin made several ice reconnaissance flights in the vicinity of Severnaya Zemlya and the Chukchi Peninsula.

During these escort ice reconnaissance flights, routes were prepared from the ship as radial track lines at distances from 50 to 100 km. To survey certain sea areas, the sketch of the routes presented a combination of parallel and radial track lines. Note that flight charts at that time were not quite accurate because the navigation equipment of airplanes included only a magnetic compass (which operates unreliably under Arctic conditions), a speedometer and a navigation cursor. Pilots or navigators performed ice observations—visual assessment of the ice distribution and characteristics—in addition to their main duties. With no aids and instructions, the pilots themselves developed indicators characterizing ice conditions and methods for compiling the ice charts. The observers determined, assessed and plotted the ice edge position, concentration, shapes of ice floes and characteristics of their surface (level ice, ridged ice, snow puddles) on the charts. For the preparation of ice charts, conventional symbolism as given in ship instructions was used. The development and improvement of the method of visual airborne ice observations also continued in subsequent years and this method was finalized in the late 1940s. The next section presents a more detailed description of this method including its possibilities, restrictions and drawbacks.

3.1.2 Visual observations of sea ice from aircraft (1933–1950)

Ice observations before World War II

In December 1932 the U.S.S.R. Government mandated creation of the Main Administration of the Northern Sea Route (MANSR). This was entrusted with the objective to "finally lay the Northern Sea Route from the White Sea to Bering Strait, equip it, maintain it in the good state and provide safe navigation along it." Ice class ships and icebreakers, polar stations and the Arctic Research Institute (ARI) were attached to MANSR. Polar aviation and the hydrographic administrations were formed within this organization. In addition to marine operations and their hydrometeorological support, MANSR was also responsible for river transport in the north, arrangement of seaports and airports, development of industry, exploration for minerals, trading, etc. (Ruksha, 2002).

All these areas of activity developed rapidly. From 1933, cargo cruises were made regularly along the entire route. In 1936, 160 vessels operated in the Arctic with 14 of them having made a through-voyage. In addition to the three steam icebreakers available in the early 1930s, four new icebreakers (with the lead icebreaker *I. Stalin*) started operation. Before the Great Patriotic War, 80 ships on average operated annually in the NSR under the escort of six icebreakers. The seaports of Dikson,

Tiksi, Igarka and Pevek along with airports and offshore unloading piers in the mouths of the Indigirka, Ob', Khatanga and Yana Rivers were built and started operation.

Simultaneously, the HMS system was developed and improved, its scientific center being the Arctic Research Institute. This system included polar stations, a weather bureau, ice reconnaissance aircraft, marine operations headquarters (MOHs) onboard icebreakers and provision of a service of long-range forecasting and planning of marine operations at ARI. The network of polar stations developed rapidly. During the Second International Polar Year (1932–1933), the number of coastal polar stations doubled from 13 to 26. In 1935–1937, the number of stations increased to 53, and before the war 75 polar stations were in operation and uniformly distributed along the NSR. At polar stations, surface temperature and pressure, cloudiness and precipitation were observed at standard synoptic hours. Ice and snow thickness and fast ice formation and breakup were also regularly recorded. Icebreakers were on duty for routing ships and convoys through those segments with heavy ice conditions. Later, MOHs were transferred from icebreakers to Dikson (1942) and Pevek (1950). The marine expeditions of the Ice Patrol began in 1935–1937. They recorded the ice edge location and carried out *en route* oceanographic observations.

Also, polar aviation began ice reconnaissance and air transport in the Arctic. By 1935, foreign aircraft—except the *Dornier Wal* seaplanes that were used for ice reconnaissance until 1945—were replaced by aircraft manufactured in Russia: two-seat *U-2* (*Po-2*), *R-5*, cargo-passenger (8–10 passengers) *ANT-9*, *K-5* and *Stal'-2*. These aircraft, especially the two-seat *Po-2* and *R-5*, had however a very limited range and were not suitable for conducting ice observations and preparing ice charts onboard. Note that in the first years after the creation of MANSR, its leaders and navigators underestimated the significance of ice reconnaissance for successful accomplishment of sea operations. The number of airplanes allocated was insufficient and the absence of observers onboard as well as the unsatisfactory observation conditions inevitably influenced the quality of service provided. For example, in 1937 only nine aircraft were used for ice reconnaissance. That year, 25 transport vessels and almost the entire icebreaking fleet had to overwinter at different places along the route because of anomalously severe ice conditions.

As a result of this, the scientific–operational support of navigation was significantly improved. In 1938 several of the branches and enterprises that MANSR was involved in that had nothing to do with transport organization (geological prospecting, cattle breeding, fishery, communication, etc.) were transferred to other institutions and the activity of MANSR was focused on shipping along the NSR and its hydrometeorological support. In that year, the Department of Ice Service was created at ARI, which was later called the Department of Ice Forecasting. From that time, ice reconnaissance was conducted first in June, then also in May and April. Based on data from these reconnaissance flights, ARI developed ice forecasts for Arctic navigation and planned sea operations. More aircraft were used for ice reconnaissance (19 to 24 annually from 1938 to 1941). From 1939, onboard observers were assigned to some ice reconnaissance aircraft.

Airborne ice observations in the war years (1941–1945)

During the war, the role of the NSR sharply increased. It was used to evacuate industrial plants to Siberia, delivery of cargos from east to west, transit of allied convoys with military equipment and provisions delivered by lend-lease to Arkhangelsk and Murmansk (Peresypkin, 2002).

Despite the fact that a number of polar pilots were enlisted in the Soviet Air Force, 10–12 airplanes made 100–150 ice reconnaissance flights annually. The conditions for performing ice reconnaissance significantly improved after using twin-engine aircraft—*LI-2* (cruising speed 250 km h^{-1}, range 2,240 km) and *IL-14* (cruising speed 280–350 km h^{-1}, range 2,100 km)—into operation in 1942–1944. Before these aircraft were commissioned for ice reconnaissance, they were generally re-equipped at polar aviation airports (i.e., additional fuel tanks installed in passenger cabins increasing the flight range and duration, and glass blisters were provided for observers, thus considerably improving observation conditions, and a table for plotting the ice charts).

ARI developed a standard scheme of ice reconnaissance routes made during the navigation period. As a result 10-day period ice reconnaissance flights were made more or less regularly, while the dates and navigable regions were determined and corrected depending on ice and navigation conditions.

Several ARI lead specialists, including N.A. Volkov, P.A. Gordienko, D.B. Karelin and M.M. Somov, developed jointly with pilots and navigators of the Polar Aviation, B.G. Chukhnovsky, M.S. Babushkin, I.P. Mazurok, V.V. Mal'kov, V.P. Padalko, P.M. Banyushevich, N.M. Zhukov, V.A. Akkuratov and many others, specified and improved the terminology, scales and composition of observed sea ice parameters. In 1940, navigator A.P. Shtepenko began to delineate zones of ice of different concentration on ice charts, P.A. Gordienko developed a five-point scale of ice hummock and ridge concentration, and M.M. Somov and N.A. Volkov elaborated in 1943 a scale of ice melting stages. The system of conventional ice characteristics was also constantly being improved. Already in 1934 the Interagency Ice Forecasting Bureau, organized under MANSR, had introduced a new table of symbols. This table did not, however, show ice charts of zones of different total and partial ice concentration. Only from 1941 did observers begin to assess total ice concentration in tenths, which was given in a circle. In 1942, navigator N.V. Zubov added color to zones in accordance with concentration gradations and P.A. Gordienko and V.P. Padalko added color by age in the wintertime. In 1944, navigator V.P. Padalko began indicating partial concentrations of different ice types in a circle in addition to total ice concentration. Thus, by the end of the war the terminology, scales used and system of symbols was mainly established, elaborated only by some minor changes and additions introduced later. By the middle of the 1940s, ARI specialists prepared jointly with pilots and navigators of the Polar Aviation, a comparatively complete manual on visual airborne ice reconnaissance that was published in 1946 (Karelin *et al.*, 1946).

Airborne ice observations after the war

The methods and technology of airborne ice reconnaissance continued to be improved in the years to follow (*Classification and Terminology*, 1954; Bushuev and Volkov,

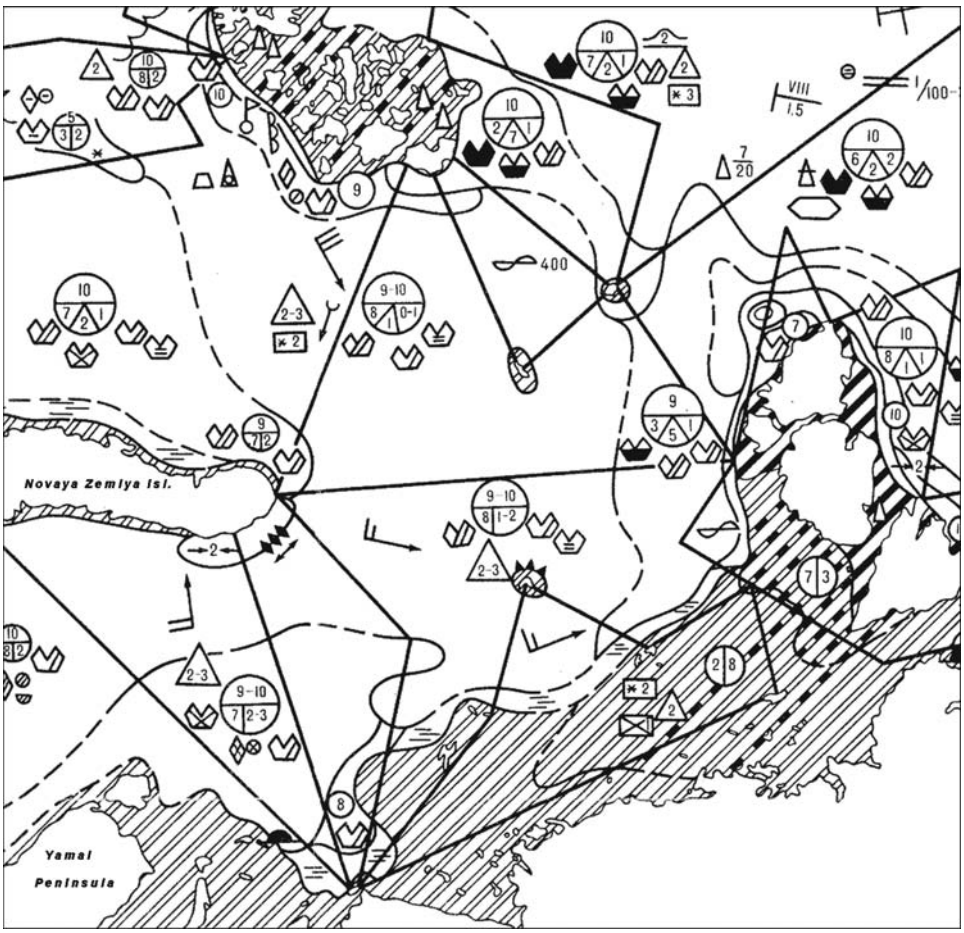

Figure 3.1. An example of the operational ice distribution chart in the wintertime (November–May), using ice chart symbols (see Table G.1, p. 432).

1974; *Handbook*, 1981). In compliance with the *Handbook*, the results of observations during ice reconnaissance flights were entered in the log of airborne ice observations where the flight conditions—altitude, visibility, wind, course, landmarks and turning point coordinates—were recorded. In separate graphs, the times of change in sea ice characteristics and the characteristics themselves were recorded. Then, after flight route correction, a working ice chart was prepared based on these records by means of distributing route segments with the same sea ice characteristics recorded in the log over the route and transferring them to a blank chart. After plotting two or three track lines, the chart was generalized and zones with the same characteristics were identified and depicted using the conventional designations adopted (Figure 3.1).

Visual ice observations were made from airplanes and helicopters of different type from altitudes of 100 to 600 m. At these low altitudes, the human eye's resolution is

equal to 0.1 meters at the surface. Such high resolution allowed observers to determine—by the character of the surface—snow cover state, type of rafting and ridged features, ice floe thickness in the fractures, snow puddle size and shape, color shades of ice floe surface, their fragments, bottom of puddles; that is, predominantly all the main ice cover characteristics. They included location of the drifting and fast ice edge, ice concentration, its age composition, forms, rafting and ridge concentration, stages of melting, open water among ice, snow cover depth and character, ice pressure, contamination and quantity, and forms of ice of land origin. The accuracy and reliability of the assessment of sea ice parameters and characteristics significantly depended on the conditions of illumination, horizontal visibility, meteorological conditions and the correct choice of flight altitude under specific conditions.

The procedure of determining each sea ice characteristic—both during visual and instrumental observations—comprises two stages: (1) identification of ice of the given type or having the given characteristic and (2) quantitative assessment of the area of this ice relative to other ice or to the total sea area surveyed. An ice observer performed the qualitative and approximate quantitative estimate of the ice distribution and state. The observer performed the analysis and generalized heterogeneous indications (rejecting less reliable ones), determined the boundaries of zones, and made the necessary statistical processing. Given a restricted flight time over each segment, it is obvious that an observer could not process all the information. As a result of investigating the accuracy of visual airborne observations by comparing them with data from synchronous aerial photography (Bushuev and Loshchilov, 1967), significant errors in the quantitative estimates were revealed. Even the most experienced observers determined total and partial concentrations with an RMS error of $\pm(1.2 - 2.0/10)$. In addition to accidental errors, there was systematic overestimation of total ice concentration and partial concentration of old ice by as much as two-tenths. Due to a restricted view swath during observations from low altitudes, only 10–20% of the study area was viewed directly, leading to considerable errors in interpolation and extrapolation of boundaries.

Observation data were disseminated to users in several ways. Immediately after landing at the airport, a copy of the working ice chart was transferred to the headquarters. For transferring reconnaissance results to icebreakers and ships, the method of dropping was widespread—a copy of the ice chart was put in a special box with a long red ribbon, which was dropped from a low-level flight onto the icebreaker's or ship's deck. The method of ice observation data transmission from onboard aircraft in the form of radio-telegraph ice reports—a prototype of today's digital ice charts—was also very widespread. An ice report was a summary of the working ice chart content and allowed the addressee to compile an identical chart. Depending on the type of reconnaissance, ice conditions were described either along the flight route or over the area—characteristics of ice zones and turning points of their boundaries were given. It was permissible to combine ice zones according to accepted concentration gradations (1–3/10, 4–6/10, etc.). Ice phenomena (ice pressure and diverging, fast ice breakup, beginning of ice formation) and ice features (icebergs, stamukhas and giant ice floes) and recommended transit routes were also included in the reports.

3.1.3 Development of aircraft and satellite remote sensing (1951–1984)

This was the period of the most intense development of the Northern Sea Route. Re-equipment of the fleet began. In 1954–1956 at shipyards in Finland, three icebreakers of the type *Captain Belousov* with diesel capacity of 10,500 hp were built, and in 1960–1969 five diesel–electric icebreakers of the *Moskva* type that gave 26,000 hp. In 1959, the first nuclear-powered icebreaker in the world *Lenin* (44,000 hp) started operation. Ice-strengthened ships of the Arctic ice class ULA of the *Lena* type and ships of UL class were introduced. In the 1950s, the maximum duration of Arctic navigation was 120 days. More than 100 ships and 10 icebreakers operated along the route. The shipping volume increased ten-fold from 1932.

The HMS developed rapidly. In the 1950s and 1960s, about 100 polar meteorological stations operated along the NSR. Six regional radio-meteorological centers (RRMCs)—Amderma, Dikson, Chelyuskin, Tiksi, Pevek and Schmidt—were operational, their objectives included organizing communication and supporting the operations of polar stations. AARI created four Arctic research observatories (AROs) located in Kheis Island, Dikson, Tiksi and Pevek. These AROs carried out an HMS for local organizations, studied hydrometeorological conditions and implemented regional expeditions.

AARI's program of scientific studies included: oceanographical, hydrometeorological, geophysical and special observations conducted in the high-latitudinal airborne Sever expeditions; two drifting North Pole stations; marine expeditions on ships and icebreakers; and airplane ice flights.

A three-level HMS system was formed:

- a central forecasting service (Moscow);
- a service of long-range navigation forecasting and planning at AARI; and
- scientific–operational groups at three MOHs (Dikson, Tiksi and Pevek) based at AROs for support of ice navigation by means of short-range forecasts and recommendations (Frolov, 2002).

In 1964, MANSR was reorganized as the Administration of the Northern Sea Route (ANSR) of the Ministry of Marine Fleet (MMF) and had surveillance functions. Transport ships and icebreakers were given to MMF shipping companies, the Administration of Polar Aviation to the Ministry of Civil Aviation and the HMS for shipping in the Arctic and Antarctic and its operators (AARI, RRMC, a network of polar stations) were transferred to the U.S.S.R. Hydrometeorological Service. The AROs were reorganized as Hydrometeorological Service (HMS) departments of RRMCs.

In the 1950s, visual airborne ice reconnaissance continued to be the main tool for sea ice monitoring and HMS of Arctic navigation. Annually, 30–40 aircraft carried out 500–700 ice reconnaissance flights. However, the accuracy of visual observations was not good enough for navigators and scientists. Based on visual observation data, it is impossible to make a detailed, large-scale chart or, to be exact, an ice plan from which navigators could choose the optimum sailing route. Therefore, for routing ships and convoys under especially severe ice conditions, patrolling was applied—this

involved routing ships across the ice zone with the help of aircraft that were constantly searching for a route through the ice and supervised ship transit via radio communication. These circumstances determined the need for transition to instrumental ice observations, especially for direct navigation support.

Application of aerial photography of sea ice

In the 1940s, aerial photography was the only airborne remote sensing tool. From 1946 to 1948, AARI made the first experimental aerial photography of sea ice under the direction of V.I. Avgevich. With the purpose of covering a larger area with each survey, the nadir-oblique aerial photography proposed by V.I. Avgevich was applied similar to the Canadian method of mapping undeveloped territories at small scales (Avgevich, 1951). Survey was carried out as a series of three photographs with deviation of the optical axis of the aerial photo camera from the vertical to the left and right from the flight direction. However, as a result of the large number of photos obtained and the complexity of photogrammetric processing this method was not used for ice mapping; moreover, standard methods of laboratory processing of photographs did not ensure the timeliness necessary for ship routing. Thus, the introduction of aerial photography into practice of ice observations was not as simple as was first believed.

In 1951 a small (six to eight people) aerial photography group was formed at the scientific–operational sector of the Department of Ice Forecasting. In 1967 the Laboratory of Instrumental Ice Reconnaissance was created on the basis of this group at the same department and in 1984 an independent department for improvement of the system and methods of ice observations was established. The group continued work on the use of aerial photography for direct routing of ships until the mid-1960s. To fulfil this objective, it was necessary to develop a method of rapid photochemical processing onboard aircraft and provide the survey swath (no less than 8–10 km) necessary for choosing the route in ice.

The first problem was comparatively successfully solved by the staff of the Vavilov State Optical Institute, who developed under the direction of V.A. Veidenbakh the so-called "self-developing process" (Veidenbakh, 1958). The onboard model of the photographic developing machine was manufactured at the AARI by the team under V.I. Suvorov. In this photographic developing machine, fixer was put between the emulsion layer of the taken film and the paper roll and a gelatin layer applied from a draw plate. After 1–2 min of contact between the aerofilm and the paper tape, ions of fixed silver were diffusely transferred onto the gelatin layer, producing a negative, and a positive brownish-black copy of which could be dropped to the icebreaker. For prolonged film storage, additional fixing under laboratory conditions was required. A.I. Gaudis supervised the overall work. He also took the largest part in the flight tests of different modifications of the self-developing process and the photographic developing machines. On 10 August 1959, A.I. Gaudis and V.I. Suvorov perished in an aircrash at Cape Shelagskiy while testing the equipment. After this accident, work on accelerated processing was temporarily stopped. However, the

experience gained was fully used to resolve a similar problem for the SLAR Toros station.

In the process of solving the second problem AARI tested all aerial photo cameras (AFCs) existing at that time (topographic, frame perspective, slot and panoramic). It was found that some AFCs could be successfully applied in scientific studies and for solving some operational tasks, but none met the requirements formulated above. In 1960, A.V. Bushuev developed in principle a scheme for a circular plan-perspective aerial photo camera, each photo of which covered the entire visible area (Bushuev, 1961), and in 1963 AARI produced an onboard model according to the author's drawings, which allowed photos to be obtained in the shape of a circle 220 mm in diameter with high resolution and uniform illumination over the entire photo area. The onboard model of the circular AFC was successfully applied in several AARI expeditions, being especially efficient for ice survey in river mouths in April–May (Figure 3.2). During this spring flood period, ice frozen to the bottom in shallows is covered by a water layer and starts to float in areas with large depths, which made it possible to determine way point location from photos without depth measurements (Antonov *et al.*, 1970).

However, the photographs could not be used on an operational basis due to the impossibility of accelerated processing of separate frames and the absence of facilities for the comparatively complicated photogrammetric processing of plan-perspective photographs onboard aircraft. Therefore, after a more promising instrument appeared—the side-looking airborne radar (SLAR) station—work on putting the circular AFC in practice for scientific–operational navigation support was stopped. The use of aerial photography for research purposes was more successful. During observations for this purpose, the disadvantages of the aerial photography method, almost excluding its operational use, such as dependence on meteorological conditions and illumination, large number of photos and complexity of their photochemical and photogrammetric processing and restricted areas of the survey from low altitudes were of minor significance, while its advantages outweighed the disadvantages: high resolution, geometric distinctness of photos, allowing simulation of a spatial model of the locality and determining the coordinates of the imaged points with high accuracy, objectivity and unambiguity of the derived data.

Aerial photographs of sea ice are close to how the human eye perceives them, both in tonal structure and resolution. This means that practically all sea ice characteristics can be determined from aerial photographs similar to visual observations. The possibility of analyzing fixed images, their comparison with benchmarks, and photometric, linear and areal measurements make aerial photography one of the most informative tools. From the early 1950s, *en route* aerial photography surveys were made annually during the Arctic ice reconnaissance surveys in April. During the navigable period in summer regular surveys were made in Arctic seas.

It was at this time that the polygon method of sea ice studies was used for the first time. This consists in comprehensive remote sensing, visual and *in situ* observations (regular, area and *en route* aerial photography, astronomical determination of coordinates, surface relief survey, snow line measurement surveys, measurements of freeze-up and melting at typical points, etc.) in one and the same area (polygon) during a long

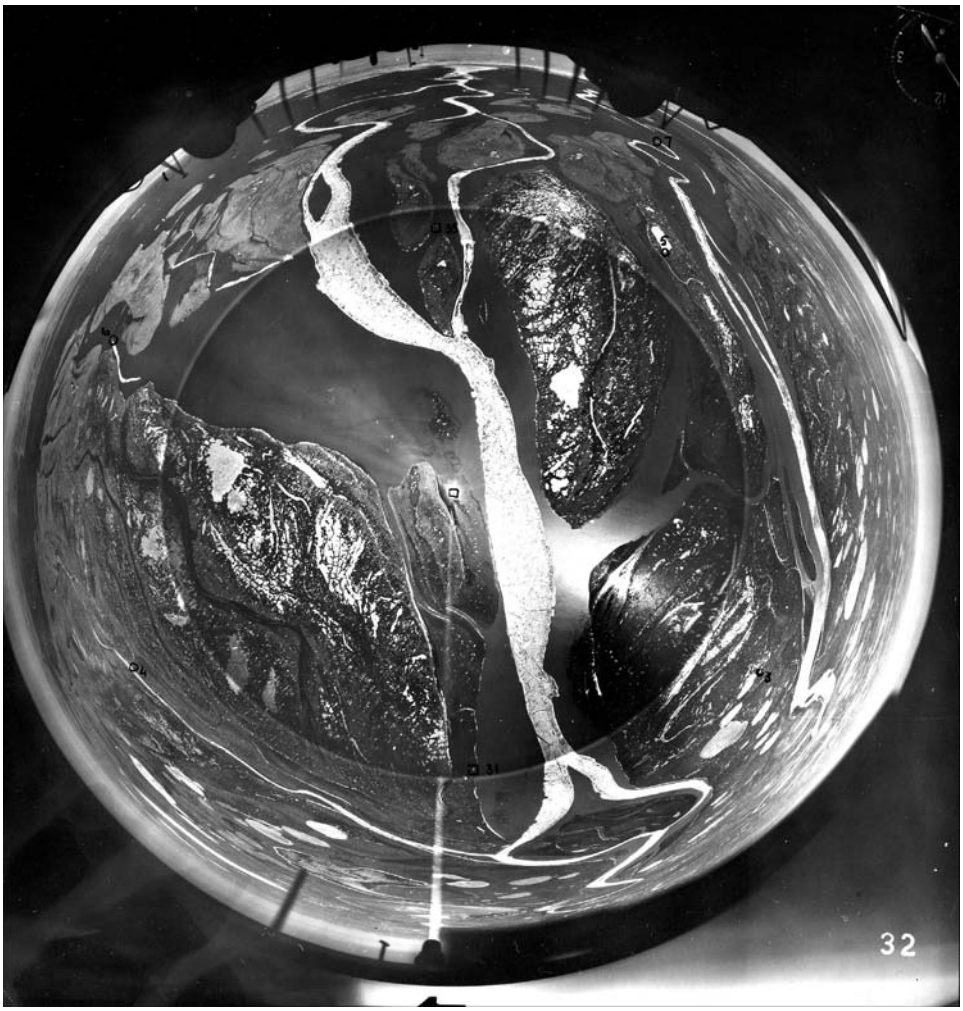

Figure 3.2. Aerial photo made by a circular plan-perspective AFC in the Lena River delta during the spring flood period (May 1968).

period of time. Such observations were made at polygons of the high-latitudinal Sever expeditions in 1952, 1961 and 1962 and at drifting stations NP-4 (1956–1957), NP-6 (1956), NP-8 (1959–1960) and NP-13-f (1965–1966). Note, especially, the comprehensive character and large volume of observations during the Sever-13 expedition (March–May 1961). The permanent base for *LI-2* aircraft and three remote points at the corners of a quadrangle with 70–90-km sides were established where synchronous astronomical determinations of coordinates and oceanographic, meteorological and

ice observations were carried out. From *LI-2* aircraft periodical small-scale aerial photography surveys of the entire polygon and regular *en route* aerial photography along its edges were performed (Bushuev and Loshchilov, 1967).

Unlike previous years when aerial photographs were used only as illustrative material, thematic processing (i.e., sea ice measurements) began. The first such work, performed already in 1952–1953, was measurement of a relative area of ice ridges and stereo-photogrammetric measurement of ice ridge heights. According to data from this study, the actual hummock and ridge concentration of first-year ice is no greater than 15% with the most probable values of 3–8% and of multi-year ice 20% with the most probable values of 1–6%. Thus, it was determined that the area of ice ridges according to the adopted five-point scale—with each point equal to 20% of the relative area—was overestimated approximately 10 times. This drastically changed the earlier existing understanding of the role of hummocking in sea ice formation. However, during visual observations, ice hummock and ridge concentration continued to be assessed by the previous five-point scale. This is explained by the fact that during these observations, a qualitative assessment rather than a quantitative one was made, which was given in the last *Handbook* along with relative areas in percentages (0 = level ice; 1 = rare ridges on level ice, etc.). Thus, the scale points had no specific values for ice hummock or ridge areas.

In the following years the character of ice distribution, periodicity of cracks and leads, and the properties of ice dynamics and deformation were revealed. Work of the aerial photography group on this is most fully reflected in the monograph *Physical–geographical Characteristics of the Ice Cover of the Arctic Basin and the Marginal Seas* published in three volumes in 1964.

The use of aerial photography for validation, verification and estimation of the accuracy of all other instruments for sea ice remote sensing is an equally important area. As noted in the previous section, study of the accuracy of visual ice observations was the first such work. Aerial photography continued to be efficiently used for trials, exploitation and introduction of new remote sensing tools (IR and microwave radiometers, radar thickness meter, SLAR, etc.) until the early 1990s when airborne ice observations essentially ceased in Russia. As an example, one can present the study of laser aero-profiler accuracy made in 1979 at NP-22 (Figure 3.3).

In the 1950s and 1960s, new remote sensing instruments began to appear in addition to aerial photography. From 1953, ice reconnaissance aircraft were equipped with panoramic radar stations. Given their operation under all weather conditions, they were tested by the AARI as an ice observation tool. A methodological aid was prepared and published in 1958 (Demin *et al.*, 1958). However, due to their low-resolution, non-uniform image contrast and large radio shadows from ice ridges at flights in low altitudes, they were not put into practice for ice observation. In 1964 one of the first national airborne infrared radiometers (IR imager) was tested. Flight experiments showed the possibility of differentiating the ice age by thermal contrasts up to an ice thickness of 100–120 cm. However, due to the need of cooling by liquid nitrogen, and the dependence on meteorological conditions, these instruments were not used for ice observation.

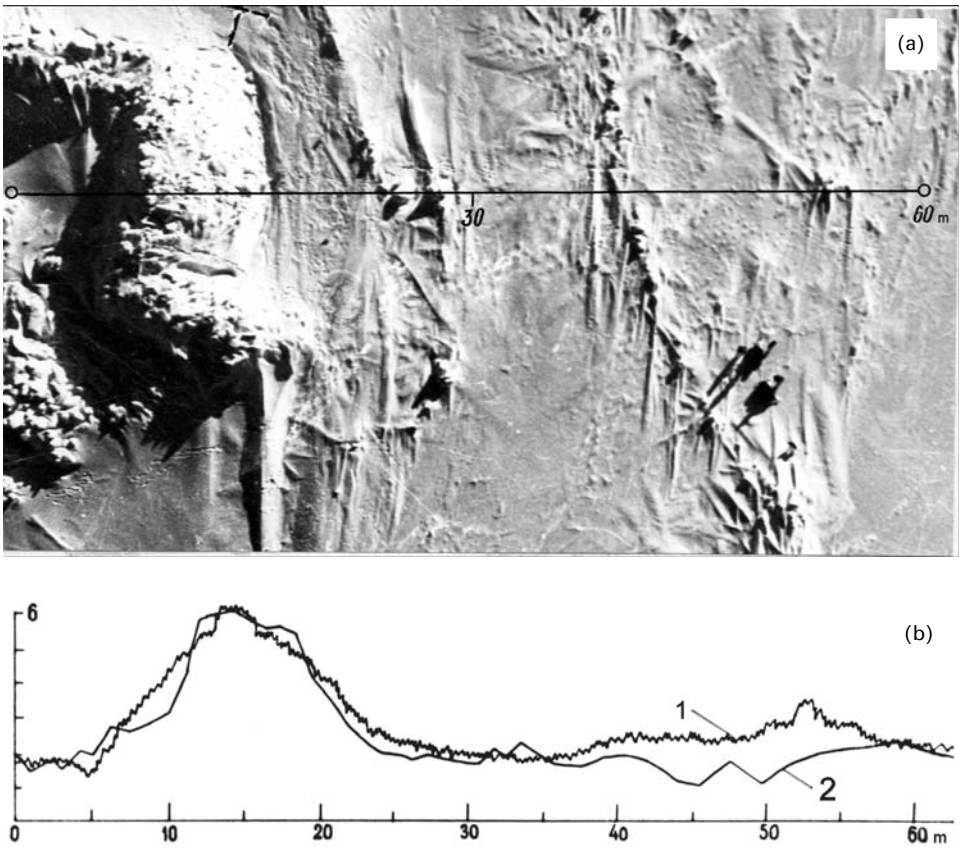

Figure 3.3. Study of the accuracy of laser aero-profilograms: (a) fragment of aerial photograph at the 1:2,000 scale with plotted measurement route; (b) profiles: 1 = data of aero-profiler, 2 = data of stereo-photogrammetric measurements (vertical axis in meters).

Radar measurement of sea ice thickness

Between 1958 and1972, a method for sea ice thickness measurement using a succession of video impulses was developed at the Riga Institute of Civil Aviation Engineers (RICAE) under the supervision of M.I. Finkelshtein. An onboard model of the radar video-impulse sea ice thickness meter was created. The principle behind the method consists in sea ice illumination by special, sounding radio impulses and measurement of the time interval between the separately observed signals reflected from the upper and lower ice surfaces. To increase the accuracy of measurements, it is necessary to increase the radio-signal frequency and decrease the number of periods in each impulse. However, with increasing frequency of oscillations, the damping coefficient in sea ice increases, preventing separation of signals from the upper and lower surfaces. In the developed instrument this contradiction was solved by using a wide-band radar

signal and its subsequent processing by separating the high-frequency components (Finkelshtein and Glushnev, 1972).

From 1973, RICAE and AARI annually tested different modifications of onboard radar meter models. Taking into account the results of these tests, the Ural Production Design Bureau Detal' developed an off-the-shelf instrument Akvamarin, which began to be used as a standard tool for ice observation.

Radio-echo sounding allowed sea ice thickness measurements with an accuracy of 10% in the 45–250-cm thickness range, qualitative assessment of the character of ice surface (ridge concentration), identification of old and river ice, and also determination of approximate ice thickness in the range from 0 to 45 cm (Finkelshtein and Lazarev, 1977; Bushuev *et al.*, 1977a). Unfortunately, the instrument was restricted in its operating height (from 200 to 2,000 m) and could not be used onboard high-altitude airplanes with Toros and Nit' SLAR stations. However, onboard the visual ice reconnaissance *IL-14* and *AN-2* aircraft, the Akvamarin was used for observation of polygons until the complete stop of airborne observation in the early 1990s.

Side-looking airborne radar (SLAR)

In 1964 the scientific production association NPO Leninets began developing SLAR specifically for ice reconnaissance. AARI participated in preparation of the technical design, trials of the model, laboratory and pilot requirements, and the state trials. The first ice reconnaissance flights using the experimental SLAR Igla were made in summer and autumn of 1965. The flight program envisaged a need for two stages—the first in August when sea ice was undergoing intense melting and maximum thermal decay and the second in late October when there is intense formation and growth of young ice. At approximately the same time, the U.S.A. also began using airborne SLAR for sea ice observations (Anderson, 1966).

In September 1967 the NPO Leninets completed work on creating another airborne SLAR called "Toros", with which two airplanes—*AN-24* (cruising speed 450–475 km h^{-1}, range 2,700 km, operating altitude 5,000–6,000 m)—were equipped. In the tail compartment, a topographic aerial photo camera and a device for dropping the box containing the ice chart onto the decks of icebreakers and ships from a low altitude were also installed (Figure 3.4).

Toros included two independent SLARs (left and right sides), combined by a common operating and control panel, and surveyed the underlying surface with bandwidths of 15 or 30 km on the left and right from the aircraft route line. The width of the non-surveyed swath under the aircraft was equal to 1.5–2.0 times the flight altitude (Glushkov *et al.*, 1970). Toros radar images were formed in slant range with approximate slant-to-ground range transformation. The angle of drift was not taken into account. Radar images were displayed on a screen and were simultaneously registered on film. The photo films were developed by liquid photo reagents by means of a special processing device onboard, providing the possibility of their operational use.

For the successful use of SLAR survey data it was necessary to reveal the decoding indicators of different sea ice types on radar images and develop methods

Figure 3.4. Ice reconnaissance aircraft *AN-24T* equipped with SLAR Toros.

for their coordination. By 1970, a methodological instruction manual *Airborne Observations of the Ice Cover Using SLAR Toros* (Loshchilov, 1970) had already been prepared. By making synchronous radar and aerial photography surveys at the polygons and along the ice reconnaissance routes, updating and revealing new decoding indications was also made in the subsequent years (Figures 3.5 and 3.6). Generalized data on SLAR information properties (capability, accuracy and limitations in determining sea ice parameters and characteristics) as a tool of sea ice remote sensing are presented in a special section of the *Handbook* (Bushuev, 1997).

Characteristics of radar reflection of sea ice

Sea ice remote sensing using radar involves measuring and registering the energy of the received radar signal, which is determined by the reflectivity of the radar target—that is, the capability to re-emit a larger or smaller portion of the electromagnetic energy received. The backscatter coefficient σ^0 (or reflectivity) is determined by the physical properties of the surface—mainly, the roughness and complex dielectric permittivity. These depend on the surface relief, its physical properties and the moisture content. The radar wavelength and polarization of the transmitting and receiving antennas are also important. If surface irregularities are less than the radar wavelength (e.g., level first-year fast ice or quiet sea surface), a mirror reflection occurs and the signal strength in the direction of the receiving antenna is close to 0. For irregularities comparable or greater than the radar wavelength, diffuse scattering occurs in all directions including that towards the radar. Rough ice targets include

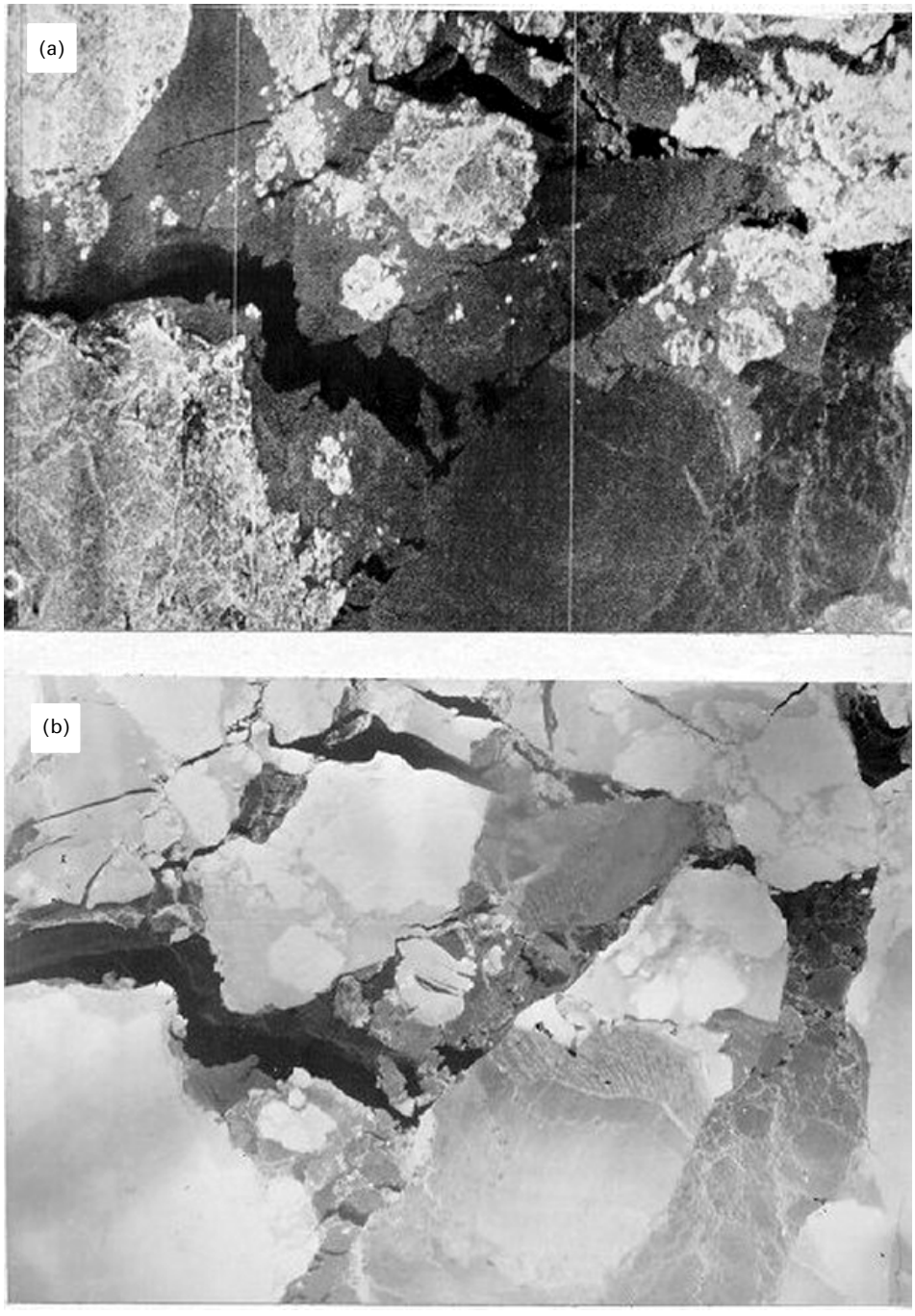

Figure 3.5. Radar image (a) and a photograph (b) of one and the same sea ice area in autumn: large floes of old (residual) ice among grey, grey-white and nilas ice (October, Laptev Sea).

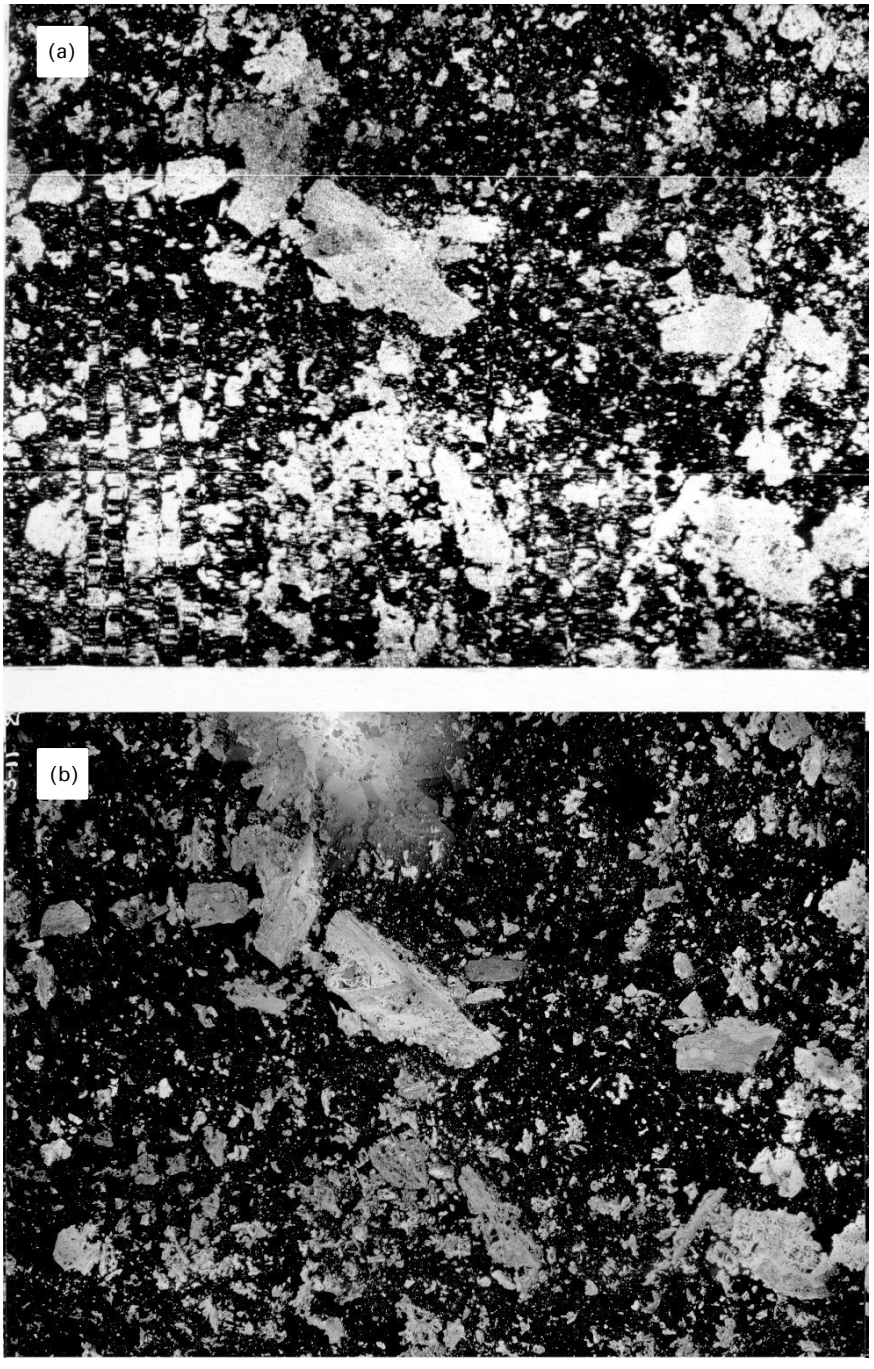

Figure 3.6. Radar image (a) and a photograph (b) of one and the same sea ice area in summer: open first-year small ice floe (August, Chukchi Sea).

nilas and young ice formed of shuga and slush, pancake ice, level grey–white ice with salt crystals at the surface formed as a result of freezing, small ice cake, etc.

In addition to surface reflection and scattering there is always volume scattering due to penetration of radio waves into the surface layer. The penetration depth depends primarily on the complex dielectric permittivity of this layer. Waves with a length of 2–3 cm penetrate into sea ice to a depth of 0.1 m, into freshwater ice to a depth up to 10 m and into freshwater to a depth of only 1–2 mm (Ramseier *et al.*, 1977). This effect explains the strong, reflected signals from multi-year, rough and level river ice. However, the strongest signal occurs when the energy is reflected from sites giving a mirror reflection in the radar direction by forming a dihedral angle acting as a corner reflector. Ice ridges, icebreakers and ships, glacier barriers and steep shores may present such targets. The numerical values of σ^0 of different ice features must always be given together with radar frequency, polarization of the transmitting and receiving antennas and incidence angle. Modern radar may transmit and receive the same horizontal or vertical polarization (HH, VV) but may also work in cross-polarization mode, when transmission is made in one polarization and receiving in another (HV, VH).

Studies of the influence of different combinations of polarizations and observation angle values on σ^0 were carried out in the framework of the 1970s' Arctic Ice Joint Experiment Study (AIJEX). Analysis of σ^0 measurements was made by an instrument with an operating frequency of 13.3 GHz (wavelength of 2.25 cm), using all possible polarization combinations for transmitting and receiving, and within the observation angles of 5° to 60°. These measurements indicate good correlation between σ^0 and all the main ice types. For all polarization types, the σ^0 value of multi-year ice is greater than the σ^0 of first-year and young ice. Measured differences were 8–10 dB and 15–18 dB for equally polarized and cross-polarized signals, respectively.

The σ^0 of grey ice at incidence angles greater than 20° is slightly higher than first-year ice. However, at small observation angles, an inverse dependence takes place. The σ^0 of all ice types decreases with increasing incidence angle at all polarizations. This effect is less for HV polarization (Ramseier *et al.*, 1977). However, long-term experience of using aircraft and satellite radar for ice observation indicates that the experimental σ^0 values presented above are difficult to apply under real conditions. The σ^0 under real conditions depends not only on the ice type, but also on its surface relief, its stage of melting and other factors.

For radar wavelengths of 2–3 cm the dependence of σ^0 on ice thickness can be described in the following way: the signal from calm open water is completely absent as a result of mirror reflection. Grease ice slightly increases the reflectivity of the sea surface, and therefore this ice is shown as dark spots, almost equal to that of calm open water. The σ^0 increases with ice growth and achieves at maximum the development stage called "grey ice". If salt crystals are formed on the grey ice surface, which usually occurs in the Arctic under low air temperature conditions, σ^0 increases and becomes approximately equal to the σ^0 of old ice. To distinguish grey from multi-year ice in this case, useful indicators are shape (round for multi-year ice fields and elongated or rhomb-like for leads and fractures covered by grey ice) and the matt texture of grey ice in images.

With further ice thickness increase, σ^0 decreases relatively quickly, attaining a minimum value for thin first-year ice. With further ice thickness increase and its transition to medium and then to thick first-year ice, there is a very small σ^0 increase.

The σ^0 of multi-year ice is appreciably higher than other sea ice types (stages). A high σ^0 is also observed for river ice, both exported during the period of ice formation and during its drift from the mouths of Arctic rivers to the sea. The contribution of volume scattering for river ice is significant, as is the case for multi-year ice. Fresh ice in glaciers and icebergs also has a very high σ^0.

However, the described variations in σ^0 with increasing ice thickness are valid only for quiet growth under ideal conditions. In reality, very large variations in σ^0 and corresponding brightness in the radar image can be observed, depending on sea ice formation and development conditions.

A very high backscatter coefficient is typical of first-year rough ice. Its surface roughness can be due to ice breakup and ridging at the young ice stage, or due to freezing together of pancakes or ridge fragments, or collapsing of fractures between converging and diverging processes. Irregularities in the ice cover are significant in converging ice. During the summer melting period, all minor irregularities on the surface of ice floes are smoothed, and therefore this relief type is typical only for first-year ice. As noted above, multi-year ice usually has the highest σ^0 value of sea ice. However, due to (a) the varying age of multi-year ice floes, (b) different hillock concentration, (c) different melting conditions in the previous summer seasons, and (d) other causes, the radar signals from multi-year ice can vary over a significant range.

Drastic changes in the character of radar images occur during the summer melting period. Sometimes during the initial period of melting, the image tone and character may depend on the azimuth direction of the radar. This phenomenon can be explained by the change in micro-relief of ice in floes under the action of solar radiation (mainly from the south) and the predominant wind direction. However, many peculiarities of radar images of first-year ice in summer are difficult to explain (Bushuev *et al.*, 1983).

In late June–early July, when the melt pond coverage of the sea ice is at maximum and whole floes can be flooded, a relatively high backscatter from this ice is observed. Following the melting process, a freshwater ice layer is formed at the surface of first-year and multiyear ice. As a result, backscatter from multi-year and first-year ice is identical. and it is impossible to separate them in radar images.

At the beginning of the freezing season, all ice that has survived the summer is defined as multi-year ice (old ice). This ice can easily be distinguished from newly formed young ice. However, the finer subdivision of this ice—into (a) residual first-year, (b) second-year and (c) multi-year—by radar images is practically impossible.

Based on radar data, it is possible to map the ice types, and thus to determine their partial concentration as well. Among the many types are young ice, first-year ice and old ice. It is very difficult to determine the stages of development of first-year ice (thin, medium and thick)—which is unfortunate—due to their large navigation significance. To determine residual first-year ice among old ice is also difficult. Therefore, there is a need for combined use of remote sensing tools operating in different spectral ranges

(microwave, visible and IR), further combined with ship and icebreaker data, and the calculation of first-year ice thickness using physical models.

SLAR Nit'

It was noted that Toros radar images were formed by means of the slanted distance, in which the scale along the track line was calculated but the angle of drift was not taken into account. For compiling *en route* ice charts, the observer—after correction of track lines by shore marks—effected their graphical transformation. However, this method did not allow compilation of the radar photographic charts of a polygon. In 1975, A. Bushuev developed and AARI produced a slit photo-transformer for reducing SLAR Toros images to plan form. Until the development of the second generation of the airborne SLAR Nit', in which the noted drawbacks of image formation were eliminated, it was used for processing polygon area surveys. Development of the Nit', in which the AARI Laboratory of Instrumental Ice Reconnaissance also directly participated, was carried out in 1974–1978. In 1978–1979 a method of analytical geolocation was devised and a program for analytical processing of radar surveys was elaborated (Bushuev *et al.*, 1983).

In the late 1970s, when aircraft equipped with SLAR were widely used for operational purposes, the most important objective was delivering the entire volume of information collected onboard aircraft to the captain on an icebreaker's bridge. Note that this objective has still not been completely reached today, when radar satellites and powerful satellite communication systems exist. In the early 1970s, fragments of the paper ice charts made onboard the aircraft in near-real time were transmitted to the icebreakers by facsimile radio-communication. This method provided for timely delivery but the level of detail did not always satisfy the captains. In addition, there were justified hopes of improving the information quality of radar images due to using modifications to the different polarizations of emitted and reflected signals and their combination in the new SLAR.

The first example of the new, improved SLAR developed by NPO Leninets called the "Nit' radar ice reconnaissance system" was installed onboard an *AN-24N* aircraft in 1978. This system used the same wavelength range (2.2 cm), resolution parameters and two-board viewing as Toros, but many significant and new (at that time) theoretical developments and ideas in the field of radio-electronics were realized.

Nit' included an airborne complex Nit'-C and the icebreaker's data receiving and processing system Nit'-L. Receiving systems were installed onboard the nuclear icebreakers *Rossiya* and *Sibir'*. Nit'-C provided the possibility of real time translation of radar images via a special radio line to an icebreaker or any other ground-based receiving point at a distance up to 350 km. Such a system arrangement was needed for providing routing of transport vessel convoys under heavy ice conditions in any weather and during the polar night. In addition, Nit'-C SLAR had six different operation modes including the horizontal and vertical polarization of emitted and reflected signals and the possibility of combining signals with different polarizations or cross-polarization. The use of different polarizations allowed improvement in radar image interpretation, more reliable identification of the sea ice development stage and

choosing the easiest ship routes through the ice. Radar swath widths on the left and right of the flight line could be selected that were equal either to 37.5 or 15 km (i.e., the total swath width comprised 75 or 30 km). A radar image onboard an aircraft (and in translation mode onboard an icebreaker) simultaneously appeared on operational indicator screens and on the wide photo film of recording devices. Diffusive photochemical processing of photo films took place onboard and provided continuous supply of photo documents ready for use in 4–8 min after the survey.

The Nit'-C complex was connected to the automated aero-navigation system that put aircraft geographical coordinates, operational mode and other auxiliary information on the radar image. The icebreaker's Nit'-L system, which was in fact identical to the receiving system of the airplane, allowed the reception of the translated radar image and all auxiliary information in real time.

The tactic of using aircraft *AN-24N* with Nit' and Toros SLAR systems for sea ice monitoring and support of ship routing was determined by the flight characteristics of aircraft that had a relatively small flight range. Some base airports were located at a great distance from the route, leading to significant flight time losses and restricting operational use of aircraft. Problems were especially numerous in the summertime when airports on the Arctic coast were often closed due to weather conditions, while landing at a reserve airport meant reducing the amount of time for ice observations.

During that period, traffic in the NSR constantly increased and new users of ice and radar information appeared—in particular, the geological services that used radar survey data for geological mapping and prospecting of natural resources in difficult-to-access areas. Therefore, the Nit' radar system was installed onboard an aircraft with a large flight range, and several state organizations of different agencies were among its clients. A turbo-prop passenger airplane *IL-18D* was selected for this purpose, which after re-equipment was called the "*IL-24N* airplane-laboratory of remote ice reconnaissance and geophysical studies with the radar Nit'-C system."

At the end of 1984, two *IL-24N* airplanes were equipped with Nit'-C, and from 1986 they were constantly used for ice reconnaissance in the Arctic (Figure 3.7a). The *IL-24N* had four turbo-prop engines (cruising speed 650 km h^{-1} at a flight altitude of 6–7 km, range up to 6,500 km). During ice reconnaissance, this aircraft could be based at any of the main Arctic civil aviation airports and during cold periods at reserve airfields. In non-flying weather, even in several coastal airports, this aircraft was capable of flying to the nearest reserve airport in the central part of Russia.

IL-24N airplanes were also equipped with aerial photography instrumentation for control of photographic surveys, facsimile instruments for transmission of ice maps and the most advanced (at that time) navigation system connected to the aircraft onboard control system and Nit'-C (Figure 3.7b). The system of navigation and pilot equipment of the airplane allowed conducting a radar ice survey in the Arctic at any time of the day and any time of the year on flights above the clouds. In addition, the airplane could carry out tactical ice reconnaissance under heavy ice conditions and pass on translated radar images to icebreakers to oversee ship routing.

In addition to the NSR, the aircraft were capable of making ice observations throughout practically the entire Arctic Basin (Figure 3.8). During the navigable period, the route and area surveys at the NSR were made constantly in accordance

Figure 3.7. (a) Aircraft of remote ice reconnaissance *IL-24N* (base aircraft *IL-18D*) equipped with the radar system Nit'-C; (b) Panel of on-line depiction of radar images and control of the Nit'-C system onboard *IL-24N*.

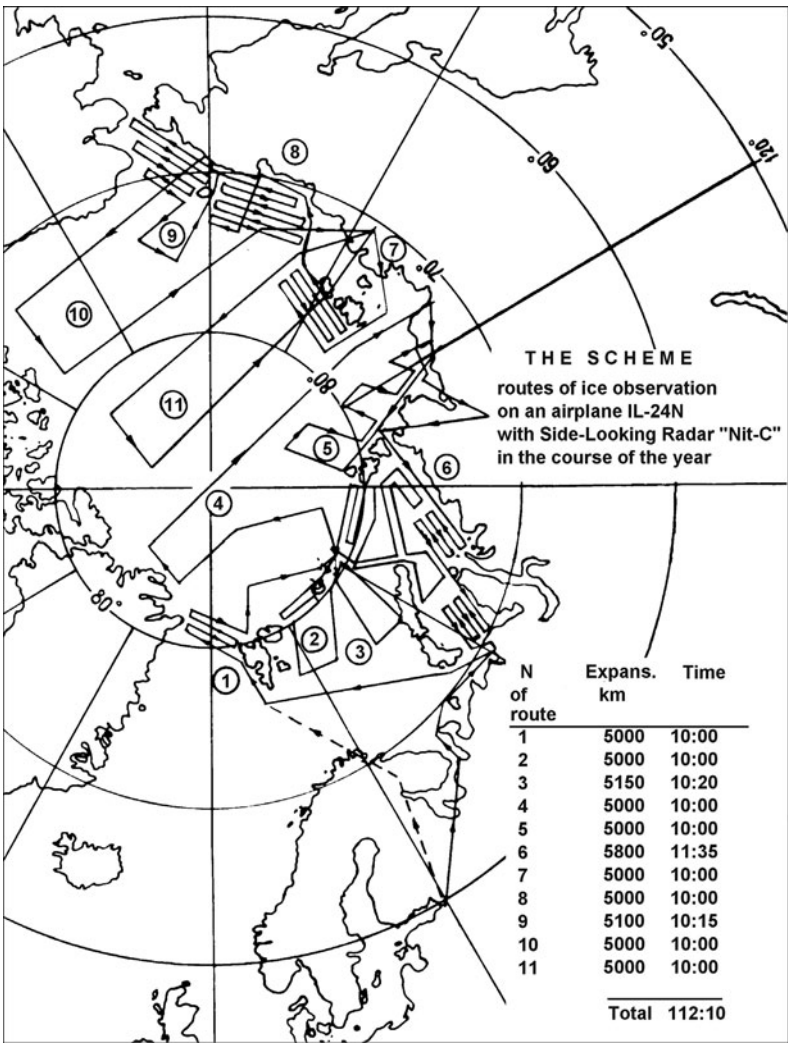

Figure 3.8. Standard layout of flown ice observation routes, onboard an *IL-24N* using the SLAR Nit', made periodically during the year. Time given in flight hours.

with the operational situation. To investigate ice distribution and dynamics, area surveys of entire seas and polygons at higher latitudes were occasionally carried out. Strategic (review) ice reconnaissance flights also began to be made during the polar night in December and February.

Observation results were operationally used as an aid to navigation and research studies. The aircraft were included in the ice information acquisition subsystem of the Automated Ice Information System for the Arctic (AIISA) that was created at that time. The experience gained of ice reconnaissance in Arctic seas revealed that the use

of *IL-24N*-type airplanes with a large range is more economically and operationally efficient than *AN-24N* airplanes. Thus, the airborne Toros and then Nit' SLAR stations from the time of their creation have become one of the main tools of ice observations for operational navigation support and sea ice studies.

Note that launching the first *Okean* radar satellites in the early 1980s did not exclude the need of airborne SLAR for sea ice monitoring, operational navigation support in Arctic seas and sea ice studies. Satellite and airborne methods of remote sensing of sea ice had their niches and supplemented each other. Airborne SLAR can also be successfully and efficiently used at present for addressing a wide range of operational and research problems in the Arctic region. However, the economic transformations and reforms that began in the 1990s in Russia resulted in a sharp decrease in budget funds for airborne ice observations, and then financing stopped entirely.

Use of satellite images

The *Tiros-1* satellite launched in the U.S.A. in 1960 had onboard instrumentation that included TV cameras, predominantly for cloud observations. The first publications advocating the possible use of satellite images for sea ice observations appeared in 1961. In 1966 the U.S.A. launched *Essa-2* with a scanning radiometer, which had a swath width of about 1,000 km and resolutions of 2.5 km and about 8 km in nadir and at the image edge, respectively. In the same year, a Russian satellite of the *Meteor-1* series made frame-by-frame imaging using two TV cameras with optical axes that deviated from the vertical. The swath width from altitudes of 600–700 km was about 1,000 km and resolution from 1.5–2 km. Information was only received by main, ground-stations (Moscow, Novosibirsk and Khabarovsk).

In the summer of 1966, AARI obtained TV images from *Essa-2* and *Meteor-1* for the first time. The images were sent by mail which excluded their operational use. However, they began to be used immediately for supplementing and updating ice charts compiled on the basis of airborne visual and instrumental observations—in particular, data in regions where observations were absent. These images were used for production of about 20 charts and, as a result of their processing, the first experience of sea ice interpretation and ice chart preparation from TV satellite images was gained.

A graphical method similar to Canadian perspective grids was developed for geolocation and transformation of these images. A measurement transparency (coordinate grid) was superimposed on the image. Then, the reference points (coastline, rivers and lakes) and boundaries of ice zones were put on the transformation grid, which presented a picture of the image coordinate grid on the chart at the prescribed projection and scale. After matching the reference points on transformation and ice charts, the ice edges and boundaries of zones with different ice characteristics were transferred to the ice chart.

In 1975, the first satellite of the *Meteor-2* series was launched. Satellites of this series, which orbited at an average altitude of about 900 km and an inclination to the

equatorial plane of 81.3°, had visible range (0.5–0.7 μm) scanning radiometers with a swath width of about 2,000 km. Scanning was performed in the plane perpendicular to the orbit plane within ±45° from nadir. Scanning was uniform over the spherical Earth, and the resolution of images was 3.2 km by frame and about 2 km by scanning line. Information in analog format was transmitted not only to the main receiving centers, but also in on-line transmission mode to automated information receiving points (AIRPs), including AARI. Constant operation in on-line mode allowed using received information to address operational tasks while simultaneous work in storage mode made it possible to make ice observations on a global scale.

As a result of sub-satellite experiments (synchronous surveys by airborne SLAR and aerial photography and *in situ* observations), which were made annually over a special AIRP polygon based on Zhokhov Island, a system of direct, indirect and logical decoding indications both for some ice targets (floes, fractures and leads) and uniform ice zones was developed.

For operational production of ice charts, an optical–mechanical method of geolocation was developed. For image receiving an upgraded photo-telegraph system Neva was used with a changed lead-screw pitch, which provided approximate equality of scales by line and frame. Then, the image was placed into a modernized photo transformer and projected onto a paper blank chart on which ice conditions were drawn. However, in spite of the good operational capability of this method the potentially possible accuracy was not provided.

In the same year, 1975, an algorithm and software for analytical geolocation using a somewhat imperfect computer system called "Iskra-1250" were elaborated. This computer with operational memory of only 30 cells did not have a display. Determination of coefficients in correction equations was carried out by means of measuring the coordinates of image points and the corresponding chart slide at a stereo-comparator. Restriction in memory was compensated by constant data release to magnetic tape and receiving necessary data from the tape for successful problem solution. The software was successfully brought into operation during the POLEX-Sever Expedition onboard the R/V *M. Somov* in 1976. The accuracy of geolocation increased four- to five-fold, enabling one to compile not only ice charts but also to determine ice drift. The developed methods of interpretation, geolocation and ice chart production were presented by Bushuev and Bychenkov (1978).

The possibility of satellite ice observations in the optical range is limited by meteorological conditions and illumination, and therefore the regularity and timeliness of observations required for sea ice monitoring were not provided. In 1979 the Design Bureau Yuzhnoye (Dnepropetrovsk) began development of an oceanographic satellite (*Okean*) with side-looking radar (SLR). The instrumentation onboard this spacecraft in addition to SLR included scanning sensors in the optical range, a passive microwave radiometer RM-08 and a system for data collection and transmission from automatic buoys. Satellite data in on-line transmission and storage-replay modes were transmitted both to the main receiving stations and to AIRPs. Unlike many other developments, the work program included not only spacecraft creation but also the development of methods of processing and using the received information. The main purpose of *Okean* was observation of ice conditions in the seas and oceans. AARI

from the very beginning was among the the first to develop methods of data processing and use, as well as development of automatic ice stations.

During the period of satellite construction, a preliminary, methodological handbook was prepared. The main problem in its preparation was a description of the interpretation indications of sea ice on future images. This was done by analysis of the images, resampled from airborne SLAR images with a similar radar wavelength. As a result, immediately after launching this spacecraft in September 1983, shipping support became more efficient. In October–November 1983, very difficult ice conditions formed in the eastern sector of the Arctic and several ships were beset in ice in Long Strait. Staff of the AARI scientific–operational group in the Marine Operations Headquarters constantly carried out ice reconnaissance flights on an *AN-24* equipped with a SLAR station Toros, while information from *Okean* was received at the AIRP of the Pevek Regional Center. Such combined satellite and airborne information provided a means for all ships to avoid being beset in ice and was held in high esteem by sailors. The advantages of all-weather radar satellite survey were clearly illustrated (*Methodological Instructions*, 1985). A more detailed description of *Okean* is presented in Section 3.1.4.

3.1.4 The *Okean* radar satellite

The first satellite of the *Okean* series was launched on 28 September 1983. In February 2000 the last satellite of this series (*Okean-01*, No. 7) ended active operation. The main orbit parameters were: average altitude 650 km, inclination 82.5° and period 98 min. The satellite orbit parameters gave a 3-day repetition cycle (44 revolutions).

Instrumentation onboard Okean-01

The main characteristics of the onboard instrumentation of *Okean-01* used for sea ice monitoring are presented in Table 3.1. A diagram of the swath bands of *Okean-01*'s sensors is presented in Figure 3.9.

Okean operation and data receiving modes

The onboard instrumentation could operate in different modes in more than 20 combinations as controlled by the ground-station. They provided generation of multichannel images, which contained information simultaneously from SLR, scanning radiometer RM-08 and one of the MSU-M channels, all at the same scale. During the polar night SLR + RM-08 mode was usually used. In the summertime, SLR + RM-08 + channel 4 of radiometer MSU-M combined operation mode was used (Figure 3.10). In addition, each sensor could operate in its own mode with data transmission to the receiving station via a decimeter or meter wavelength radio link. The MSU-S could operate in its own mode only via the decimeter wavelength radio link.

Information was transmitted from satellite by means of three modes (in accordance with inbuilt control software):

Table 3.1. Main characteristics of onboard instrumentation of satellite *Okean-O1*.

Instrument	Channels and spectral bands	Scanning frequency	Incidence angle from nadir (°)	Swath width (km)	Resolution range × azimuth (km)
Side-looking radar (SLR)	9,519 MHz (X-band, VV)	(APT 4 Hz)	20–45.3, left	460, left only	0.85–1.3 × 2.4/2.8 × 2.4 (APT)
Passive microwave radiometer (RM-0.8)	36.62 GHz (Ka-band, H)	(APT 4 Hz)	20–49.7, left	587, left only	25 × 25 (APT)
Multi-channel scanning radiometer (MSU-M)	1: 0.5–0.6 μ 2: 0.6–0.7 μ 3: 0.7–0.8 μ 4: 0.8–1.1 μ	(APT 4 Hz) linear scanning by sphere	104.9 full/ 0–52.44 left only	1,875 full/ 937.5 left only	1.0 × 1.7/ 1.5 × 1.7 (APT)
Multi-channel scanning radiometer of medium resolution (MSU-S)	2: 0.57–0.72 μ 4: 0.70–1.00 μ	50 Hz linear scanning by angle	90 full	1,380	0.345 × 0.345 in nadir
Instrument for collection and transmission of information from drift buoys (“Kondor-2”)				1,600	3.5 × 2.5 error in location of buoys

(1) In direct transmission mode via the meter wavelength radio link (137.4 MHz frequency). Information was transmitted at the international APT standard and could be received at basic ground-stations by any user (including icebreakers and separate vessels having receiving stations onboard) within the radio-visibility zone.
(2) In direct transmission mode via the analog radio link of the meter wavelength range (466.5 MHz frequency). Information could be received only by the main ground-stations of Roshydromet in Moscow, Novosibirsk and Khabarovsk.
(3) In memory mode onboard a satellite with transmission of information in any subsequent orbit to the ground-station, when passing its radio-visibility zone. This mode allowed receiving information at one ground-station—for example, Sever Center (AARI, St. Petersburg)—along the entire NSR and in any other area (excluding areas with latitudes greater than 80°S around the South Pole) with a minimum time delay equal to the sum of satellite revolutions in intermediate orbits (Figure 3.11).

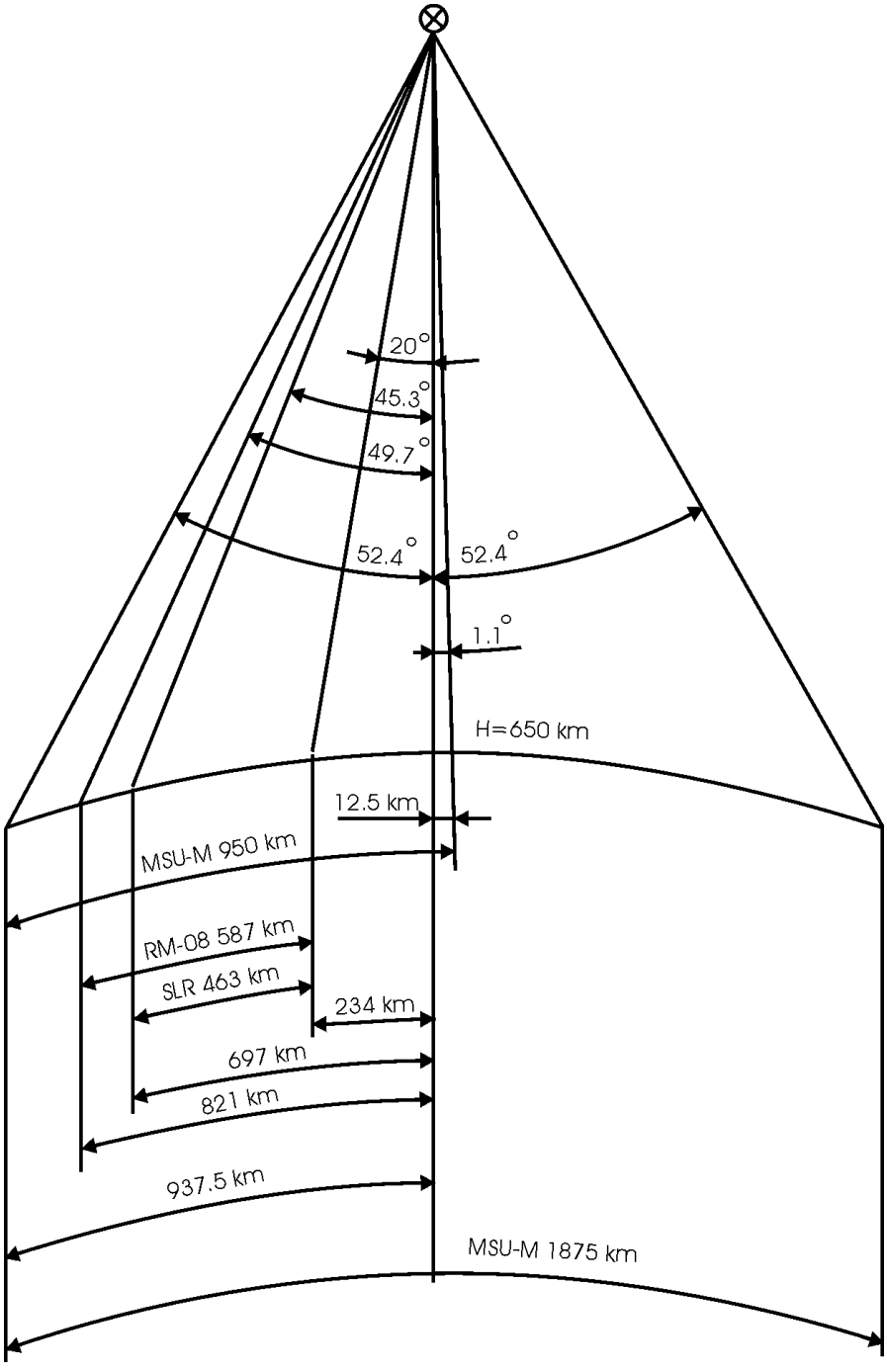

Figure 3.9. Diagram of earth surface coverage by *Okean* sensors.

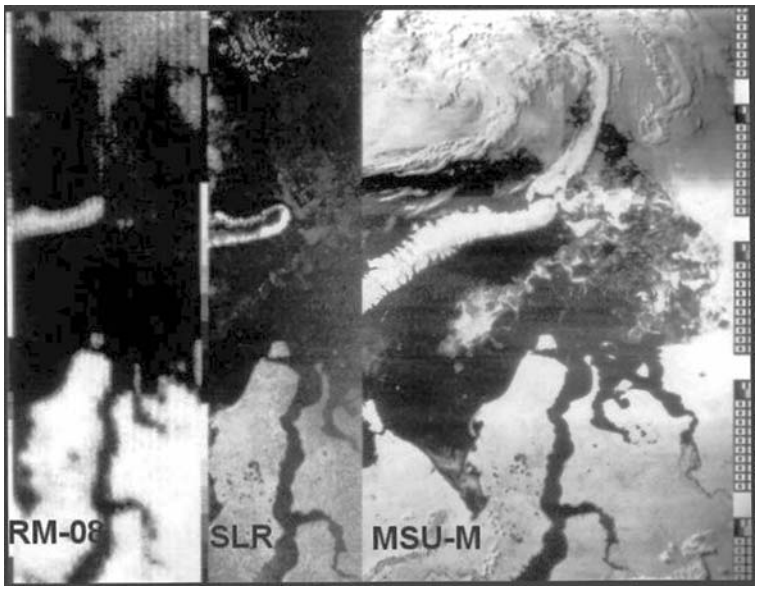

Figure 3.10. Example for the Kara Sea of superimposed images (RM-08, SLR, MSU-M sensors) of *Okean* for 14 August 2000 (calibration levels are at the left of RM-08 and SLR images, and support information is at the right of the MSU-M image).

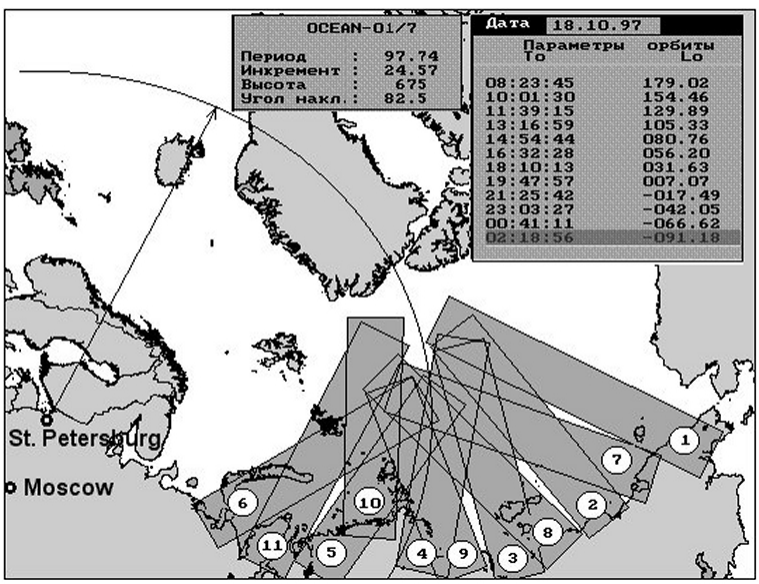

Figure 3.11. Coverage of the NSR by *Okean-O1* SLR images after 11 successive orbits. The radius of the zone receiving data in real time in St. Petersburg is shown. Period, increment, altitude and inclination of the satellite, as well as parameters of forecast orbits are shown in the pop-up menus.

Each of the aforementioned operation modes of the satellite sensors was used for sea ice monitoring along the NSR. The satellite control software for sensor turn-on was devised in such a way as to obtain maximum image coverage of Arctic seas within a minimum period of time and provide for data receiving in direct transmission mode and memory mode by selected ground-stations. Continuous SLR operation in direct transmission mode was allowed for no more than 12 min and in memory mode for 6 min. These restrictions did not however influence the quality of sea ice monitoring along the NSR.

Information properties of SLR and RM-08 images

The SLR noise floor (signal : noise) corresponds to a backscattering coefficient of -20 dB. Signal amplification is linearly increased along the scanning line and so compensates signal attenuation caused both by increased distance to the surface and angular dependence of the backscattering coefficient. Other radiometric corrections of SLR images were not usually applied.

Extensive fractures and leads in the ice can be detected if contrast in their backscattering is sufficiently large. The minimum width of leads in old ice in winter that can be identified on images with a contrast of 3 dB is 500 m. Areas of close old ice surrounded by young and first-year ice in the wintertime are identified on the images with a contrast of 3 to 9 dB (Figure 3.12).

The contrast depends to a great extent on the degree of first-year ice roughness and partial concentration of old ice. A high level of backscattering by old ice is explained by strong volume scattering in the upper porous and freshened ice layer. One often observes fresh fractures, flaw polynyas and leads covered with young ice with a very high backscattering coefficient on SLR images in the cold season (a similar effect is also observed on *ERS-1/2* SAR images). This ice is sometimes erroneously interpreted as open water surface and strong wind. As a result of the analysis of such images, it was found that young ice with high backscatter forms in fractures and polynyas at air temperatures below -20°C and a wind speed of more than $5\,\mathrm{m\,s^{-1}}$. Later, the backscatter of this ice decreases, and contrast with surrounding young and first-year ice disappears almost completely.

The spatial resolution of the microwave radiometer RM-08 was by an order of magnitude less than SLR; however, its images presented important information in addition to radar data. This is connected with a negative correlation between the intensity of emitting and scattering of electromagnetic waves by ice of the same type. On SLR images, old (second-year and multi-year) ice gives a strong scattered signal which on RM-08 images appears faint. Young and first-year ice gives on the contrary a weak scattered signal and appears bright (Asmus *et al.*, 2002). This possibility of simultaneous images enables differentiation between first-year ice, multi-year ice and open water in large fractures and polynyas. During the period of intense summer melting, backscattering of old ice decreases. However, in most cases it is still possible to identify the location of the boundary between multi-year and first-year ice, as well as between the ice edge and a rough, open water surface using both SLR and RM-08 images (Figure 3.13).

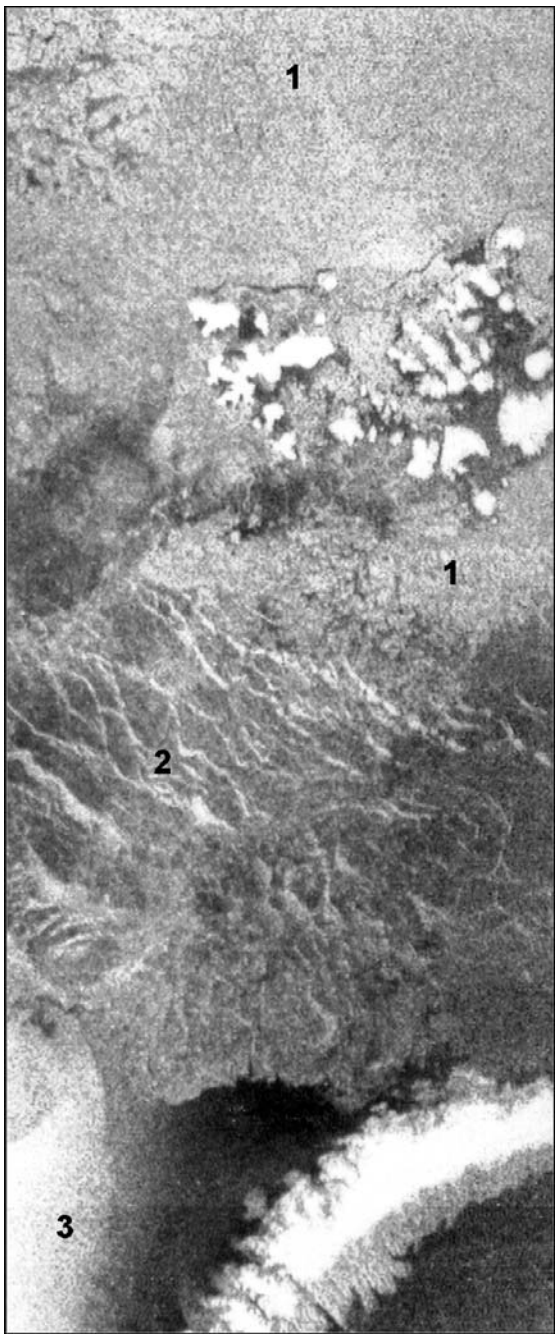

Figure 3.12. *Okean* radar image (November 1988) of: (1) old ice to the north and around the Franz Josef Land archipelago, (2) thin first-year ice with young ice in fractures to the north of Novaya Zemlya and (3) open water westward of Novaya Zemlya.

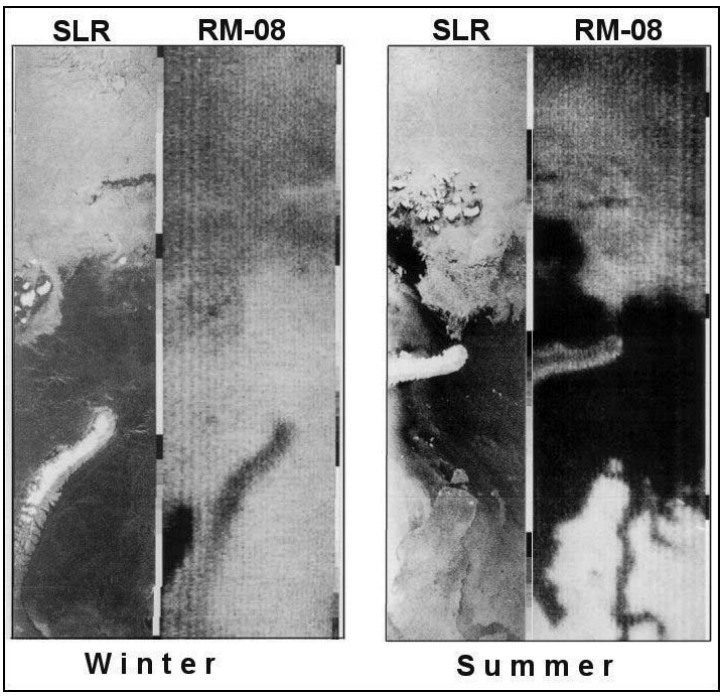

Figure 3.13. Example of simultaneous (SLR and RM-08) sea ice images during the winter (January 1988) and summer (August 1988) (calibration greytones are at the right edge of each image).

Sea ice monitoring and mapping

Monitoring of sea ice for navigation support along the NSR can be most reliably provided by satellite microwave data, which are not dependent on daylight illumination and cloud cover conditions. Therefore, the Sever Center widely used *Okean* data both for mapping ice conditions for operational shipping support (Figure 3.14a, see also color section) and compilation of weekly composite ice charts for the entire NSR (Figure 3.14b). Special technology and the necessary software for its application were developed for mapping. The methods of manual analysis and interpretation of images that were used in the mapping procedure included quantitative assessment of total and partial ice concentration, and interactive delineation of boundaries of ice zones (Alexandrov and Loshchilov, 1985; Alexandrov *et al.*, 1989; Alexandrov and Loshchilov, 1993). Combined analysis of simultaneous images of SLR and RM-08 significantly facilitated the identification of old ice among first-year ice and determination of its boundaries.

For production of ice charts for a large part of the NSR area, the most rational way was to make a mosaic from several images made at different times. Mosaics were generated from SLR images that were normalized by brightness and transformed to a stereographic cartographic projection (Asmus *et al.*, 2002). Use of such mosaics

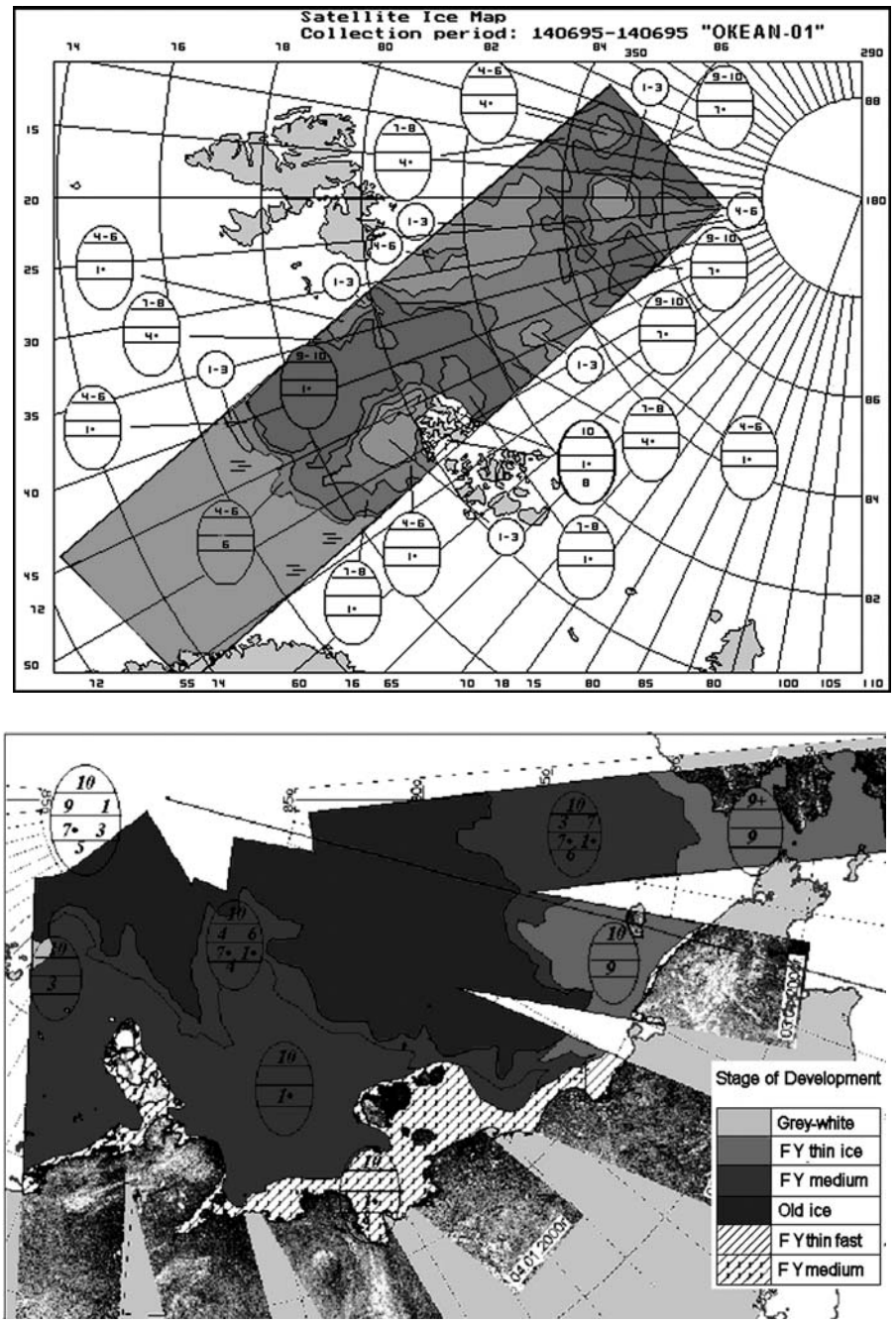

Figure 3.14. Examples of operational ice charts based on: (a) one SLR image, and (b) weekly composite ice chart from a mosaic of *Okean* radar images from seven successive orbits on 1–7 January 2000 (see also color section).

significantly facilitated the analysis and interpretation of radar images for large sea ice areas.

After the end of airborne ice observations in 1990, practically the entire volume of information on ice conditions along the NSR was received from meteorological satellites. The most valuable information for operational navigation support was received from *Okean*, as before *Radarsat* it was the only satellite equipped with wide-swath side-looking radar.

3.1.5 Creation and development of an automated ice information system for the Arctic (1975–1991)

In the 1980s, 16 icebreakers (7 of which were nuclear) and 200–300 transport vessels with a maximum cargo turnover of 6.6 million tons *per annum* operated along the NSR. The navigation period increased during this period and on some Kara Sea segments navigation was year-round. Development of satellite and airborne remote sensing tools significantly increased the flow of primary hydrometeorological information with a simultaneous increase in technical capabilities with respect to the rate and volume of information transmission.

Earlier, the use of a large number of ground-stations and remote sensors was necessary for full characterization of the ice cover. Information was supplemented by *in situ* measurement data, including forecasts. It was later necessary to combine all observation tools and different level processing centers in one common system. By the mid-1970s, it became obvious that operational users of ice and hydrometeorological information for the entire Arctic Ocean, combination and use of advanced technologies for automatic processing and analysis, taking into account constantly expanding and changing requirements of different users, was feasible only on the basis of a systematic approach to effecting these tasks. In 1975–1976, AARI developed the concept of an automated ice information system for the Arctic (AIISA). It integrated all main subsystems such as:

- information acquisition and collection;
- processing, analysis, calculations and forecasts; and
- transmission and dissemination.

Characterized by its structure, functions, technical facilities, character of the operation area and the information process, AIISA belongs to a class of sophisticated, open, spatially distributed automated measurement information systems (Bushuev *et al.*, 1977b). In accordance with the work program for AIISA creation, the individual components of this system were first developed. During this period (1976–1980), based on theoretical studies and calibration observations, methodological manuals on interpretation, geolocation and use of all main remote sensing instruments were prepared. The digital format of ice chart coding and regular chart production allowed solution of operational and research objectives by means of numerical methods using computers (Bushuev, 1991).

An AIISA prototype was used in May 1978 for the scientific–operational support of the early experimental voyage along the entire NSR of the diesel/electric ship *Kapitan Myshevsky* under the escort of the nuclear icebreaker *Sibir'*. As a result of this experiment, the system structure was specified and the possibility of transition from visual to instrumental observations combining airborne and satellite means was demonstrated. Extensive ice information, which was received during the voyage, was held in high esteem by navigators who noted that, exclusively due to high ice information quality, it was possible to reduce voyage duration by 7–10 days.

In 1983 the Commission of the Presidium of the U.S.S.R. Council of Ministers adopted Directive No. 304 "On the development and creation of the automated ice-information system for the Arctic (AIISA)." In 1981–1985, the technical requirements and design of AIISA were developed. In March–August 1985, test operation of some AIISA components was carried out during scientific–operational support for releasing the R/V *Mikhail Somov* from its enforced drift in the Weddell Sea. Based on the *Okean* and *Meteor-2* images received onboard the icebreaker *Vladivostok*, ice charts were produced and the images themselves were used to choose the optimum route through the ice. Simultaneously, photo montages of the drift area and the ice charts were prepared on a daily basis at AARI using *Okean* radar images received from the Main Center for Data Receiving and Processing through the Main Radio-Meteorological Center, and transmitted in digital format to the R/V *M. Somov*. This experiment confirmed the accuracy of the design of the system decisions.

In 1986, by a mandate from the Interagency Commission, AIISA was introduced to test operation; and by mandate from Goskomhydromet, the Center of Ice and Hydrometeorological Information (CIHMI) was organized at AARI. In 1989, AIISA was accepted for commercial operation, which is still ongoing today.

Prior to the early 1990s, remote observations (satellite and aircraft) comprised the basis of the measurement part of the system. It was also planned to use data obtained at the polar stations, the North Pole drifting stations, automated ice stations, and observations conducted onboard icebreakers and ships. Analysis of the technical capabilities of these ice observation tools showed that their use in a system provides a means of obtaining all important ice cover parameters with sufficient accuracy and temporal and spatial sampling for navigation.

In accordance with AIISA's hierarchical structure, processing of ice and hydrometeorological information should be performed at centers at different levels. Based on satellite data, airborne reconnaissance flights, polar stations and other sources, the regional centers (Arctic centers for hydrometeorology and environmental monitoring) regularly issued ice charts for their areas of responsibility and transmitted them operationally to the AIISA Center, Marine Operation Headquarters, icebreakers, ships and other users. In addition, short-range (1–3 days) meteorological and ice forecasts and specialized forecasts for shipping support were issued.

The main AIRP at the AIISA Center and a remote AIRP that was created and functioned on one of the drifting stations from 1980 received information on the entire Arctic Ocean in direct transmission mode from *Okean*, *Meteor* and *NOAA* satellites. Information in memory mode received by the main centers (Moscow, Khabarovsk) was also operationally retranslated to the Center. Strategic winter and summer

overview ice reconnaissance flights were made by aircraft equipped with Toros and Nit' SLARs.

Dissemination of operational ice information to users

The AIISA Center (CIHMI, AARI) processed all reported primary satellite and airborne information, together with generalized information from the various Arctic administrations of hydrometeorology and environmental monitoring. From this was prepared a composite ice chart of all seas in the Arctic Ocean, which was disseminated to users in the ministries and agencies and in the Arctic hydrometeorological services (Bushuev *et al.*, 1995). Based on the information on current ice and hydrometeorological conditions, the Center prepared medium-range (7–8 days) meteorological and ice forecasts on a permanent basis and operationally disseminated them to users.

The AIISA Center regularly transmitted overview, regional and local ice charts compiled from *Okean* images to users. Ice charts in contour format, given as a digital file, were generated automatically in the process of interpretation and interactive chart making of satellite images by means of the original Videobox software. This format used WMO international symbols for sea ice charts and a conventional palette providing easy perception of the color chart on the computer display. The AIISA Center transmitted ice charts in contour format to icebreakers, ships and the regional Arctic centers via *Inmarsat* system communication channels. Users without a computer or the corresponding software received ice charts in facsimile mode or as text cables in contour format allowing reproduction of the ice chart content manually on any cartographic basis or on the sea chart of the route itself.

AIISA was created on the basis of the existing technical equipment for information receiving, collection and dissemination to users. Therefore, it was only possible at the first stage to make some technological processes automatic. The most labor-intensive processes of geolocation and interpretation of satellite and airborne video-information were not automated. However, the system at the time of its introduction surpassed the similar ice information systems of other countries with respect to organization and tactical–technical characteristics.

3.1.6 Satellite synthetic aperture radar

Synthetic aperture radar (SAR) imagery from satellites as well as aircraft combines high spatial resolution and independence of natural light and clouds. The principal disadvantage of SLAR is that the antenna length limits its along-track resolution. The development of SAR overcame this disadvantage, and consequently has proved to be the most useful instrument for regular and detailed mapping of sea ice on regional and local scales. The first series of SAR images from satellites was obtained by *Seasat* during its 3-month operation period in 1978. This L-band horizontally polarized radar operated at a wavelength of 23 cm at an incidence angle of 20° (see Table 3.2).

Although this SAR was intended primarily for ocean wave imaging, some of the radar images were also acquired over Arctic sea ice. More than 100 passes over the Beaufort Sea were recorded on nearly a daily basis for analysis of sea ice motion and

Table 3.2. The parameters of SAR systems mounted onboard *Seasat* and *Space Shuttles*.

Parameter	Synthetic aperture radar				
	Seasat	SIR-A	SIR-B	SIR-C/X	X-SAR
Orbit inclination (deg)	108	38	57	57	57
Altitude (km)	800	260	225	225	225
Angles of incidence (deg)	20–26	47–53	15-60	20–55	20–55
Frequency (GHz)	1.28	1.28	1.28	1.25 and 5.3	9.6
Polarization	HH	HH	HH	HH, VV, VH, HV	VV
Swath width (km)	100	50	30–60	15–90	15–45
Pixel size for four looks (m)	25×25	40×40	25	25	$30 \times (10–20)$

changes in sea ice distribution. These data have shown the potential of using satellite radar data both for scientific and operative applications in sea ice covered regions, but the relatively short lifetime of the satellite precluded acquisition of significant data sets. During several years various SAR instruments, operating at different wavelengths, polarizations and incidence angles were also mounted onboard several *Space Shuttles*: SIR-A (1981), SIR-B (1989) and SIR-C/X (1994).

The first U.S.S.R. SAR mission started in July 1987 with the launch of *Cosmos-1870* which was equipped with S-band SAR. Its operation ended in July 1989. This was followed by *Almaz-1* with similar SAR parameters, which operated from May 1991 until October 1992. Its technical parameters are presented in Table 3.3 (Kramer, 1996). The raw data of up to 300 km long strips could be stored onboard these satellites and transmitted to a receiving ground-station near Moscow, where SAR images were presented as photographs.

Applications of SAR data included studies of various ocean phenomena and sea ice. Although the orbits of these satellites precluded their use in high northern and southern latitudes, several SAR surveys were conducted both in the Antarctic and Arctic. *Almaz-1* SAR data were used to support an emergency operation in the

Table 3.3. The parameters of *Almaz-1* SAR.

Parameter	Value
Satellite altitude (km)	270–380
Orbit inclination (deg)	72.7
Wavelength (cm)	9.6
Polarization	HH
Radiometric resolution, single-look (dB)	2–3
Swath width (km)	40
Spatial resolution, single-look (m)	10–15

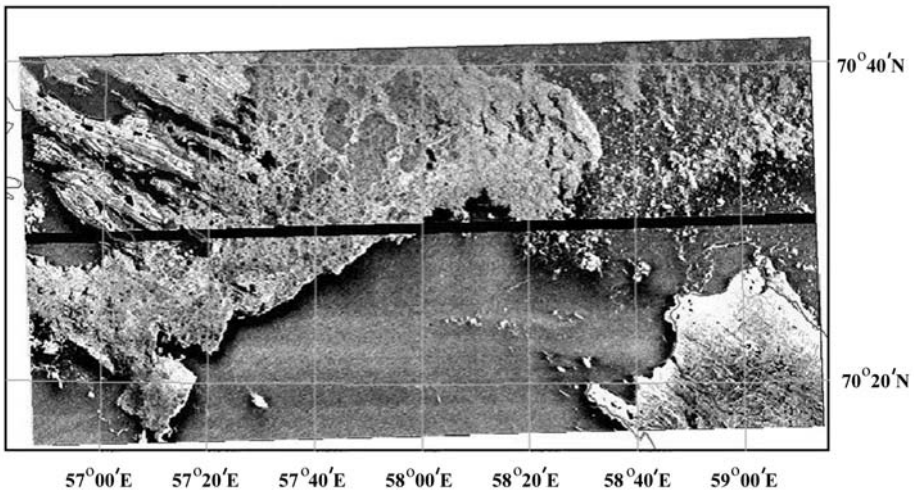

Figure 3.15. A sub-image of SAR image, obtained from *Almaz-1* for the area of the Kara Gate (orbit 1541, 06.07.1991).

Antarctic, when the R/V *M. Somov* was stuck in the ice. From these images it was possible to detect icebergs and estimate their size, as well as to recognize several sea ice parameters, such as ice extent, boundaries of stable and unstable fast ice, ice type (nilas, young and first-year ice), prevailing ice forms, ridges and areas of strongly deformed ice (Alexandrov *et al.*, 1996). In *Almaz-1*'s SAR image of the area near the Kara Gate open ice is evident to the north and east of Vaygach Island (Figure 3.15). From analysis of such images it was found that ice edge location, ice concentration, floe size, patches and stripes of ice can be determined during summer.

The first European Space Agency (ESA) European remote sensing satellite *ERS-1* with C-band SAR operated successfully for many years after launch in July 1991 and provided a means of acquisition of a large amount of data for sea ice studies and monitoring in various parts of the world. In high-resolution imaging mode, the *ERS-1* SAR provided three-look, noise-reduced images with a spatial resolution of 26 m in range (across-track) and 30 m in azimuth (along-track). Image data were acquired for a maximum duration of approximately 12 min per orbit and transmitted to ground-stations within its line of sight. *ERS-2*, the second satellite of this series, was launched in April 1995. Since mid-August 1995 both satellites operated in tandem mode for about 9 months, with *ERS-2* observing the same area as *ERS-1* 1 day later. The technical parameters of *ERS-1/2* SARs are shown in Table 3.4.

The SAR images obtained from *ERS-1/2* have been used by many researchers in a number of sea ice studies in the Arctic, Antarctic and in other ice-covered seas—for example, in the Gulf of Bothnia—(Bertoia *et al.*, 1998; Drinkwater, 1998; Kwok and Cunningham, 1994; Gill and Valeur, 1999, Sandven *et al.*, 1999a). Although *ERS* satellites are not primarily intended for operational service their data were implemented for sea ice monitoring in the U.S.A., Canada, Finland and demonstrated and evaluated in several other countries. The infrastructure for downlinking, processing

Table 3.4. The parameters of *ERS-1/2* SAR.

Parameter	Value
Satellite altitude (km)	785
Orbit inclination (deg)	98.52
Wavelength (cm)	5.66
Polarization	VV
Angle of incidence (deg)	20–26
Swath width (km)	100
Spatial resolution, three-look (m)	26×30

and distributing SAR images in near-real time from the European sector of the Arctic has been developed—for example, in Norway where the Kongsberg Satellite Service (KSAT) is capable of delivering SAR scenes to users in near-real time (Johannessen *et al.*, 2000). This infrastructure has enabled the Nansen Environmental and Remote Sensing Center in Bergen to perform several pre-operational demonstrations where interpreted SAR scenes and other SAR products have been delivered to various types of Arctic operations including research expeditions. Together, the Nansen Centers in Bergen and St. Petersburg in cooperation with ESA and the Murmansk Shipping Company conducted a series of projects to demonstrate the possibilities of *ERS* SAR data for sea ice monitoring and supporting navigation in the Northern Sea Route (Johannessen and Sandven, 1992; Johannessen *et al.*, 1996, 1997a–c, 2000, 2003). The first combined use of *ERS* SAR and real aperture radar images from Russia's *Okean* satellite, carried out during the Icewatch Project in 1995–1996, have been described by Johannessen *et al.* (2000).

Canada's *Radarsat*, launched in November 1995, is the first SAR satellite with capability to operate in several modes with different swath widths, incidence angles and resolutions—Figure 3.16a and Table 3.5. It operates in C-band and HH-polarization. Different modes make the satellite useful for several marine and terrestrial applications. For sea ice monitoring, which is one of the primary objectives of *Radarsat*, ScanSAR mode is mostly used, allowing mapping of all sea ice areas with a minimum 3-day repeat cycle. ScanSAR mode provides swaths up to 500 km wide and typically 100-m resolution.

ScanSAR images are used in operational ice monitoring in the Canadian Arctic, Greenland Sea, Baltic Sea and other areas where there is sea ice (Ramsay *et al.*, 1996; Gill *et al.*, 1997; Bertoia *et al.*, 1998, 2004). By systematic acquisition of ScanSAR images over large parts of the Arctic sea ice cover and by use of the *Radarsat* Geophysical Processor, it has been possible to estimate sea ice motion, deformation and thickness from sequential imagery over several years from 1996 (Kwok and Cunningham, 2002). Based on these products, evolution of the Arctic ice cover can be studied in terms of its area change, ice thickness growth and ice volume production. Furthermore, these ice products can be used to study the role of sea ice in the climate system, such as albedo feedback and heat flux from ocean to atmosphere through leads. In the European sector of the Arctic Ocean, especially

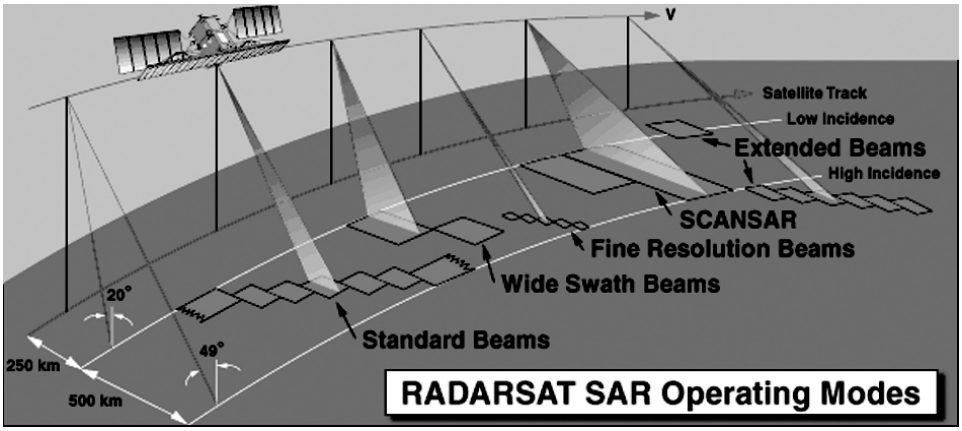

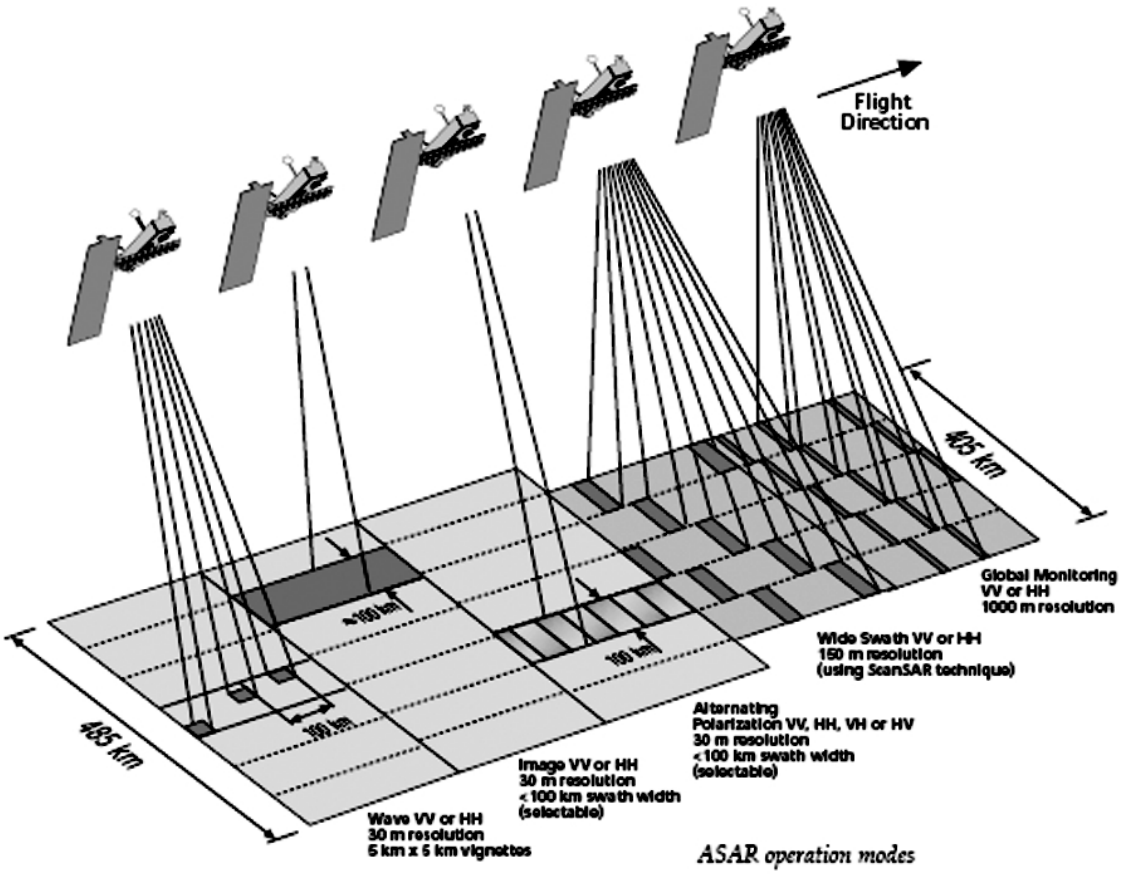

Figure 3.16. Modes of operation of contemporary SAR systems: (a) *Radarsat* SAR, courtesy of Canadian Space Agency; and (b) *Envisat* SAR, courtesy of European Space Agency (see also color section).

Table 3.5. The parameters of *Radarsat-1* and *Radarsat-2* SAR.

	Beam modes	Nominal swath width (km)	Incidence angles to left or right side (deg)	Number of looks	Spatial resolution (approx.) (m)
RADARSAT-1 modes with selective polarization					
Transmit H or V	Standard	100	20–50	1×4	25×28
	Wide	150	20–45	1×4	25×28
Receive H or V or	Low incidence	170	10–20	1×4	40×28
(H and V)	High incidence	70	50–60	1×4	20×28
	Fine	50	37–48	1×1	10×9
	ScanSAR wide	500	20–50	4×2	100×100
	ScanSAR narrow	300	20–46	2×2	50×50
New RADARSAT-2 modes					
Polarimetry	Standard quad polarization	25	20–41	1×4	25×28
	Fine quad polarization	25	30–41	1	11×9
Selective single polarization	Triple fine	50	30–50	3×1	11×9
Transmit H or V	Ultra-fine wide	20	30–40	1	3×3
Receive H or V	Ultra-fine narrow	10	30–40	1	3×3

in the Barents and Kara Seas, no systematic acquisition of ScanSAR data have been performed. Studies of sea ice signatures and processes in this area from ScanSAR data are therefore limited to a few cases during dedicated experiments (Pettersson *et al.*, 1999a; Alexandrov *et al.*, 2000b; Sandven *et al.*, 1998a, 2001).

The Advanced SAR (ASAR) onboard ESA's *Envisat* satellite has been producing images since 2002 and has many similarities to *Radarsat*. ASAR operates in five modes: global monitoring mode, wide-swath mode, image mode, alternating polarization mode and wave mode, as shown in Figure 3.16b and Table 3.6.

Wide-swath mode is similar to *Radarsat*'s ScanSAR mode and is the most appropriate for sea ice monitoring, providing acquisition of 420 km wide swath images with spatial resolution of 150 m. In image mode and alternating polarization mode high-resolution images (30-m resolution) can be obtained in 60–100-km swaths at different incidence angles ranging from 15 to 45°.

Alternating polarization (AP) mode allows acquisition of three dual polarization combinations: HH and HV, VV and VH, or HH and VV. Initial results from AP images suggest that cross-polarization will improve the potential for distinguishing ice from open water, which can sometimes be difficult with only HH or VV polarization. The co-polarization option (HH and VV) of AP mode (mainly used for research) has

Table 3.6. The parameters of *Envisat* ASAR.

Operating mode parameter	Image mode	Alternating/Cross-polarization	Wide-swath mode	Global monitoring	Wave mode
Polarization	VV or HH	VV/HH, HH/HV or VV/VH	VV or HH	VV or HH	VV or HH
Spatial resolution (along-track and across-track) (m)	28×28	29×30	150×150	950×980	28×30
Radiometric resolution (dB)	1.5	2.5	1.5–1.7	1.4	1.5
Swath width (km)	Up to 100 7 subswaths	Up to 100 7 subswaths	400 5 subswaths	$\geq$400 5 subswaths	5-km vignette 7 subswaths
Incidence angle range (deg)	15–45	15–45			15–45

shown that the co-polarization ratio may also be useful for discriminating ice from open water areas (De Abreu *et al*., 2003). It has been shown that sea ice classification largely benefits from the availability of cross-polarization data (Scheuchl *et al*., 2004), and that different polarization combinations at different incidence angle ranges need to be selected to obtain more robust results for sea ice mapping (Nghiem, 2004). Also, ice surface roughness information can be retrieved from AP images (Haas *et al*., 2004). An example of discrimination between ice and water from *Envisat* AP mode is shown in Figure 3.17.

Another advantage of cross-polarization images is for better detection of ridges and discrimination between multi-year and first-year ice as well as between level ice and deformed ice. Observations of C-band scatterometer measurements of Baltic Sea ice from aircraft quantitatively illustrated that the backscatter contrast between level ice and ice ridges is larger at cross-polarization than co-polarization (Makynen and Hallikainen, 1998). Multi-year versus first-year ice contrast is as high as 9 dB in cross-polarization data, compared with less than 3 dB in like-polarization channels.

In 2003 the Canadian Ice Service began to use ASAR wide-swath data as a supplement to ScanSAR images in the routine production of ice charts, bulletins and forecasts for Canadian waters (Flett *et al*., 2004). In the same year the European *Envisat* ASAR images were introduced in sea ice monitoring in the Norwegian Arctic (Sandven *et al*., 2004). During spring 2004 the Finnish Ice Service received the first ASAR images in near-real time and transmitted them to Finnish and Swedish ice-breakers (Vainio, 2004). Near-real time ASAR images were acquired for the Ross Sea in the Antarctic to assist ship routing (Parmiggiani, 2004). In summer 2003 several ASAR images were transmitted to the nuclear icebreaker *Sovetsky Soyuz* to support her operations in the western part of the Northern Sea Route. In February–June 2004 a series of near-real time ASAR images was transmitted to the Murmansk Shipping Company and, via the TV communication channels of the Orbita system, to the

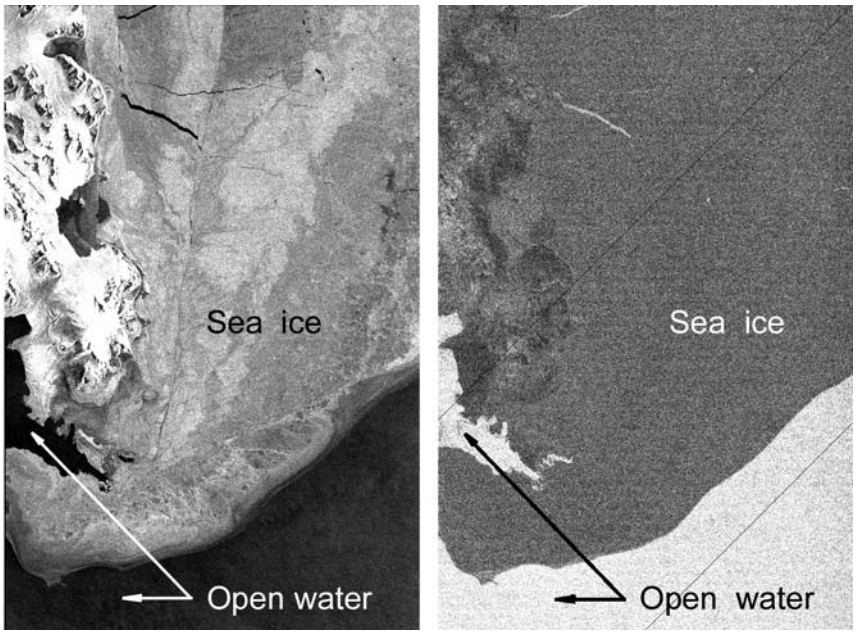

Figure 3.17. Example of *Envisat* alternating polarization image of about 100-km swath width in the Svalbard region showing: (a) HH-polarization; and (b) polarization ratio (VV/HH) where the open water and sea ice is well-discriminated (© European Space Agency).

nuclear icebreakers *Yamal*, *Sovetsky Soyuz*, *Arktika*, *Vaygach* and *Taymyr*. These images were used to selecting optimum routes in the sea ice of the Barents and Kara Seas, in the Yenisey Estuary and in the the Ob' Gulf (see Chapter 6).

ASAR's global monitoring mode offers a new opportunity to observe and monitor most of the Arctic and Antarctic sea ice as a result of being the default mode of operation, which is used when no other modes are requested. This low-energy mode provides image stripes of 500-m pixel size and a swath width of 450 km and 1-km resolution. The images require no pre-ordering and are available in near-real time from a server at ESA. This is a very convenient capability, which makes it suitable for operational monitoring because daily mosaics can be produced covering large parts of Arctic sea ice areas (Figure 3.18). Using this mode, the first ice drift retrievals have also been produced by tracking ice features from consecutive images. Further analysis of these images has not started yet, so it is not clear which other products can be derived from global monitoring mode.

Use of SAR data for sea ice observation in the Northern Sea Route started in 1991 after the launch of ERS-1. In the period from 1991 to 1997 the Nansen Centers in Bergen and St. Petersburg obtained ERS SAR data in near-real time for delivery to expeditions and demonstration campaigns. The SAR ice images were used to extract more detailed information of importance for ice navgation—such as leads, polynyas, ridges, shear zones and areas of level ice versus deformed ice. The SAR images were

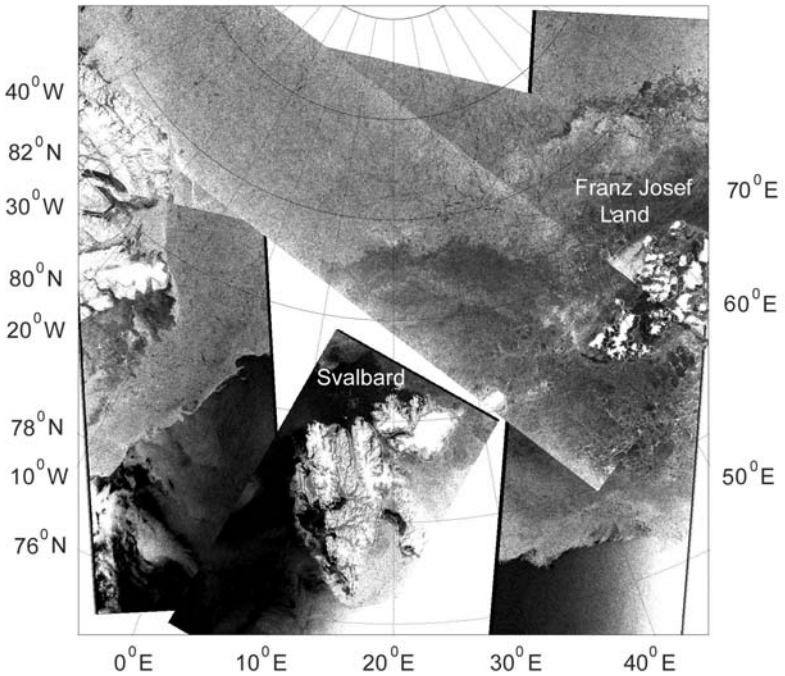

Figure 3.18. *Envisat* A-SAR regional Global Mode mosaic in the Svalbard area on 11 May 2004 at 1-km resolution (© European Space Agency).

primarily sent to Murmansk Shipping Company's icebreakers to support ice navigation and to validate the SAR information by the ice navigators on the icebreakers. Scientists from NIERSC participated in several of these expeditions to obtain validation data for the SAR analysis. In 1997 a new era started by *Radarsat* delivering wide-swath SAR images, which could cover much larger areas of sea ice compared with the ERS images. From 2003 *Envisat* ASAR started to deliver wide-swath SAR images covering the eastern Barents Sea and the Kara Sea region several times per week. This allows development of operational SAR ice monitoring in the Northern Sea Route, where the sea ice areas can be mapped with 1- to 3-day intervals. The various expeditions and demonstration campaigns from 1991 to 2005 are described in more detail in Chapter 6.

3.1.7 Passive microwave radiometry

Passive microwave radiometers have been operated on spacecraft for several decades. They detect the thermal emission of electromagnetic radiation coming mainly from the earth's surface. Although their spectral bands are far from the thermal infrared where the emission has its power peak, sensitive radiometers can detect signal variations representing about 1° Kelvin and a 0.3% change in the surface emissivity coefficient. Surfaces with variable emissivity and/or with different temperatures

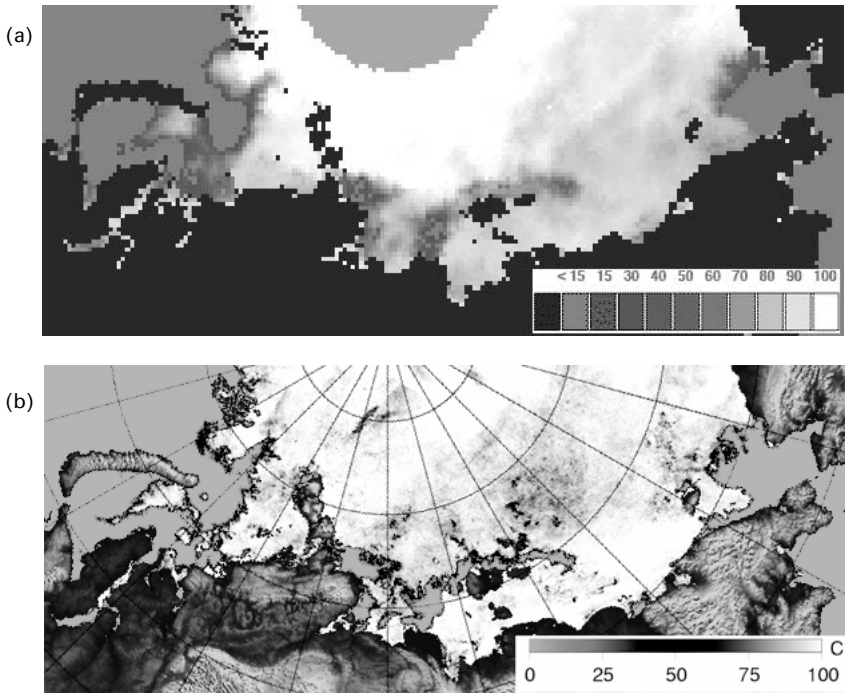

Figure 3.19. Examples of ice concentration maps in the Northern Sea Route for 3 July 2006, using (a) SSM/I data with 30-km resolution, (b) AMSR-E data with about 10-km resolution (see also color section). The SSM/I product is produced by NERSC and is used for estimation of long-term statistics (1978 to present) and for assimilation in the TOPAZ ice–ocean forecasting system. The AMSR-E product is produced by the Institute of Environmental Physics at the University of Bremen, and is used for daily mnonitoring of sea ice in different parts of the Arctic (courtesy: G. Heygster). Note that spatial resolution, scale and color-coding of the ice concentration (displayed in %) is different for the two examples.

can then be distinguished and mapped. In polar waters the emission coefficient is the main variable, and it is a fairly good signature to use for water–ice and also rough ice type discrimination. Examples of sea ice concentration maps in the NSR from the present passive microwave instruments (SSM/I and AMSR-E) are shown in Figure 3.19.

The current satellite microwave radiometers are all low spatial resolution instruments with typically a 5–100-km field of view, thus the amount of data is also much lower than for high-resolution SAR instruments. In addition, swaths can be wide, up to 1,500 km. It is therefore possible to make daily ice maps covering almost all of the polar oceans except two holes, around the North and South Poles, due to orbit inclination.

Microwave radiometers operate at several frequencies and, generally, in two polarizations, making available a number of so-called "channels" within a broad frequency range. Available channels may be from 6.6 GHz and up to 89 GHz with

Table 3.7. Emissivities of water and ice.

Frequency	Calm sea water at 0°C		First-year ice		Multi-year ice	
	V	H	V	H	V	H
19 GHz	0.62	0.34	0.95	0.90	0.80	0.65
37 GHz	0.69	0.39	0.95	0.90	0.67	0.58
85 GHz	0.75	0.48	0.94	0.89	0.58	0.54

either H (horizontal) or V (vertical) polarization. The footprint size (also called "spatial resolution") is given by the equation:

$$fp = c * sd/(ad * f) \tag{3.1}$$

where *fp* is the footprint, *sd* is the distance from satellite to footprint, *ad* is the antenna diameter, *f* is the microwave frequency and *c* is the speed of light. Its size varies greatly with channel frequency. For example, an antenna of diameter 1 m at a distance of 1,000 km will have a footprint of 45 km at 6.6 GHz and 3.4 km at 89 GHz.

Many radiometers look at a fixed angle of about 50° incidence, this together with other effects make the actual footprint (referred to as the "3-db signal decrease from the antenna boresight direction") somewhat larger. The frequencies mostly used for sea ice are between 18 GHz and 90 GHz, with associated footprints (resolution of ice features) roughly between 8 km and 60 km, depending on antenna size and choice of channels (frequencies).

Microwave emissions from sea ice differ noticeably from those of seawater, making ice, generally, readily distinguishable from liquid water on the basis of radiation. Also, water emission is quite stable in moderate wind and for polar sea temperatures. At higher frequencies, the atmosphere and its variable cloud systems has an influence, but this can be compensated for in the algorithms for sea ice concentration. Otherwise, it is a day-and-night, all-weather mapping instrument. Table 3.7 shows winter (cold ice) emissivities at V and H polarizations (Svendsen *et al.*, 1983). In the summer, the emissivity of multi-year ice is equal to that of first-year ice and the two ice types cannot be separated (Massom, 1991).

Most of the instruments have conical scan geometry, eliminating variation in the incidence angle across the swath that causes problems for active microwave SAR. This, together with the availability of many channels makes it possible to design reliable algorithms for several sea ice parameters. First, the fraction of ice area within each footprint is the main parameter to be measured, generally called "total ice concentration". Accuracy in the range 5–10% is generally achieved with the current algorithms (Svendsen *et al.*, 1983; Cavalieri *et al.*, 1984). Second, the ratio of multi-year ice and first-year ice can be measured when the ice surface temperature is well below freezing—that is, in the winter season. In the summer the signatures of these ice types are almost equal so they cannot be separated. The presence of thin ice types like nilas and young ice will be an error source in winter. Then, multi-year ice emissivity is somewhat variable, so that the accuracy of the fraction of multi-year ice in

winter is only in the range 15–25% (Cavalieri *et al.*, 1984). However, the accuracy is not well-determined and other authors give different values.

The first non-scanning radiometer was launched on a Russian *Cosmos* satellite in 1968. The first western passive microwave imager was the electrically scanning microwave radiometer (ESMR) launched on NASA's *Nimbus-5* satellite in 1972. With a footprint size of 25–50 km and a revisit frequency of every 1–3 days, it covered the whole Arctic allowing calculation of sea ice concentration, extent and temperature. An atlas of its measurements over the Arctic 1973–1976 has been published by NASA (Parkinson *et al.*, 1987). This single-channel instrument was followed by the 10-channel scanning multi-channel microwave radiometer (SMMR) onboard NASA's *Nimbus-7* satellite. The SMMR operated between 1978 and 1987 and an atlas of its measurements over both Arctic and Antarctic sea ice has been published by NASA (Gloersen *et al.*, 1992). SMMR was followed by the first of a still-continuing series of seven-channel special sensor microwave imager (SSM/I) instruments onboard the satellites of the U.S. Defense Meteorological Satellite Program (DMSP). The first SSM/I was operational in 1987—fortunately, it had a several months overlap with SMMR allowing inter-calibration of their data sets.

The Japan Space Agency also developed the advanced microwave scanning radiometer (AMSR) that has been operating on the earth observation system (EOS) *Aqua* satellite (formerly named PM-1) since 2002. AMSR has a larger antenna that allows sea ice measurements with a smaller footprint (>8 km) than that available with SSM/I instruments (>15 km). Data from both SSM/I and AMSR can readily be downloaded from servers in near-real time. On Russian satellites in the *Okean-O1* series, the instrument RM-08 was in operation from 1983 until 2000. It had a single-channel at 37 GHz (0.8 cm) with 25 km footprint and was especially important for use in cooperation with the side-looking real aperture radar onboard the same satellites. The main parameters of described microwave radiometers are presented in Table 3.8.

Most algorithms use the fact that emissivity (or emission coefficient) varies in frequency in a markedly different way for water than the main two types of sea ice—first-year and multi-year ice (see Table 3.7). For calm sea water with given temperature and salinity, the emissivity value is very predictable and increases rapidly with

Table 3.8. Parameters of satellite passive microwave sensors.

Sensor/Satellite	Channels	Frequency (GHz)	Polarization	Footprint (km)	Swath width (km)
RM/*Cosmos-243*	4	3.5–3.7		>25	?
ESMR/*Nimbus-5*	1	19	H	>25	3,000
RM-08/*Okean*	1	37	V	25	600
SMMR/*Nimbus-7*	10	6.6–37	V & H	150–30	780
SSM/I/*DMSP*	7	19–85	V & H	60–15	1,400
AMSR/*Aqua*	12	6.9–89	V & H	75–8	1,440

increasing frequency. First-year ice has a nearly frequency-independent high value about 0.95, while for cold multi-year ice the emissivity decreases with increasing frequency. In addition, a vertically polarized signal has a markedly higher emissivity than a horizontally polarized one, whereas variation with frequency is similar.

The NASA SMMR team algorithm (Steffen *et al*., 1992), developed by a joint research team for the first multi-channel sensor in space makes use of three channels (18V, 18H and 37V). It computes the area of water, first-year ice and multi-year ice (winter only) within each footprint, the size of which is determined by the lowest frequency (18 GHz) to be about 50 km. Ice temperature is also compensated by the channel combination, and a "weather filter" is included to eliminate some noise due to atmospheric effects mainly over water.

The NORSEX algorithm (Svendsen *et al*., 1983), developed at the Nansen Center for the same sensor, uses only two channels (18V and 37V) for computing ice area fraction values, the minor effect of changing ice temperature being compensated by input of its seasonal mean value. The algorithm is used with only small modifications for later instruments having essentially the same channels. The NORSEX algorithm is extended to include the high frequency of 85–89 GHz to achieve a footprint of about 15 km for SSM/I. Since the atmospheric contribution to satellite-measured signals increases rapidly with increasing frequency, this must be done using special techniques in order to keep the good performance of ice–water discrimination obtained by using lower frequency channels. In the NORSEX-85H algorithm for SSM/I, the 85H channel is added using an image sharpening technique called "unsharp masking", thus achieving both good resolution (about 15 km) and good ice/water separation (5–10%).

Data can be obtained either as calibrated brightness temperature (°K) for the various channels or as computed ice parameters. In the first case any algorithm may be applied to the data to obtain the ice parameters. The geometry of the data can be scan-oriented by giving the center latitude–longitude for each data point, or data are given as an image in a pre-defined projection. In the latter case, latitude–longitude lines and coastlines are often added so that a map-like image is obtained.

Brightness temperature from the RM-08 instrument has been available in real time (RT) at many Russian stations in APT-mode transmission (137.4 GHz) that can be received with suitable equipment. An example is shown in Figure 3.20a as a mosaic of 4 days.

Brightness temperatures from operating SSM/I instruments are available in near-real time (NRT) at the FTP server at Marshall Space Flight Center (*microwave.msfc.nasa.gov*) in the U.S.A. The delay from measurement to file is less than 1 day and the data are scan-oriented. The brightness temperature from the AMSR instrument is available on the Web in NRT from the National Snow and Ice Data Center (*nsidc.org/data/amsr*), also in the U.S.A. Daily ice concentrations on polar-stereographic projection maps from SSM/I are also available here.

Ice concentration maps are available from several websites—such as the University of Bremen (*www.seaice.de*), from the Danish Center for Remote Sensing (*www.seaice.dk*) and the Nansen Center (*www.nersc.no/Seaice-archive/*). Examples are shown in Figure 3.20.

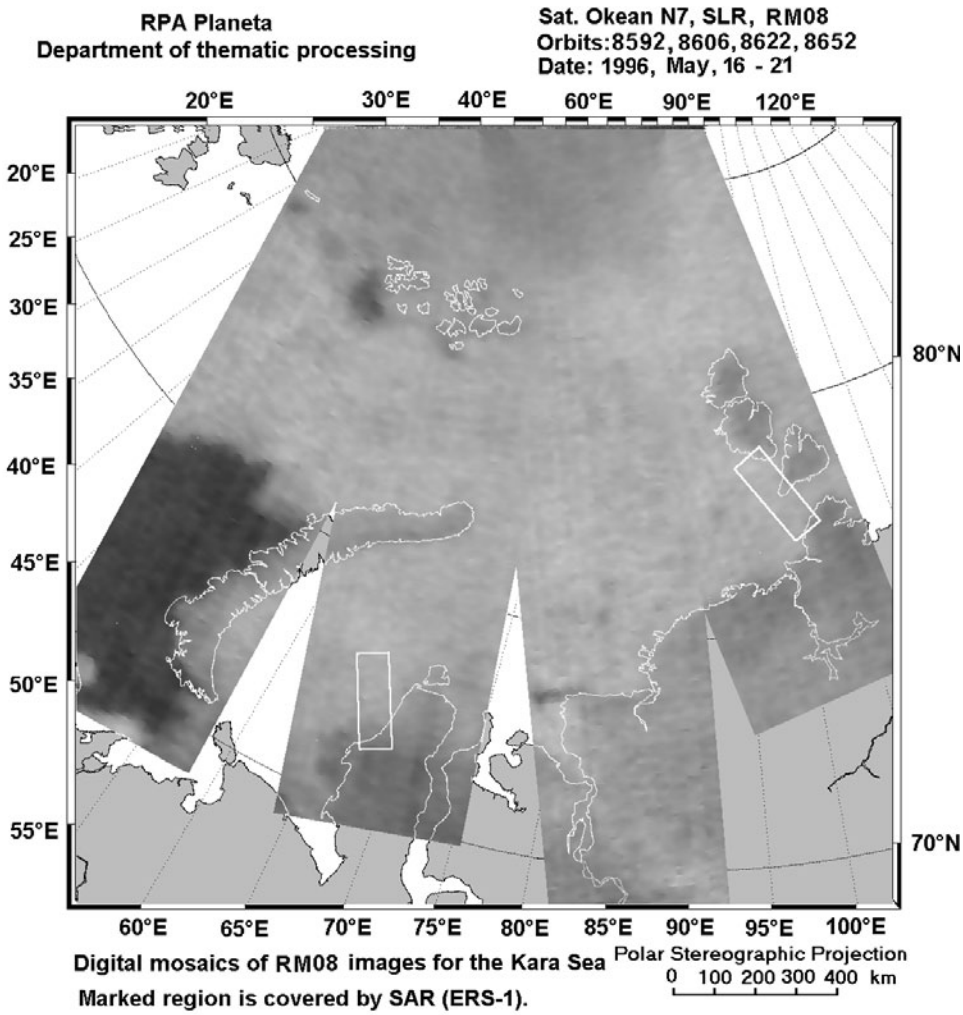

Figure 3.20(a). Example sea ice product obtained by passive microwave radiometer data: RM-08 brightness mosaic for 16–21 May 1996. Courtesy of NPO Planeta, Moscow.

For many climate-related studies, it is desirable to estimate sea ice motion, which can be achieved by use of two successive, partly overlapping images. This is possible using two 85-GHz or 89-GHz brightness temperature images obtained with a few days interval (Emery *et al.*, 1997; Martin and Augstein, 2000; Alexandrov *et al.*, 2000a). An algorithm for two-dimensional spatial correlation generally finds many reliable displacement vectors that correspond to the motion of ice features in this interval. A certain degree of filtering of erroneous vectors is required, but otherwise the method gives results that are in close correspondence with ice drift expected from wind and currents (see Figure 3.21).

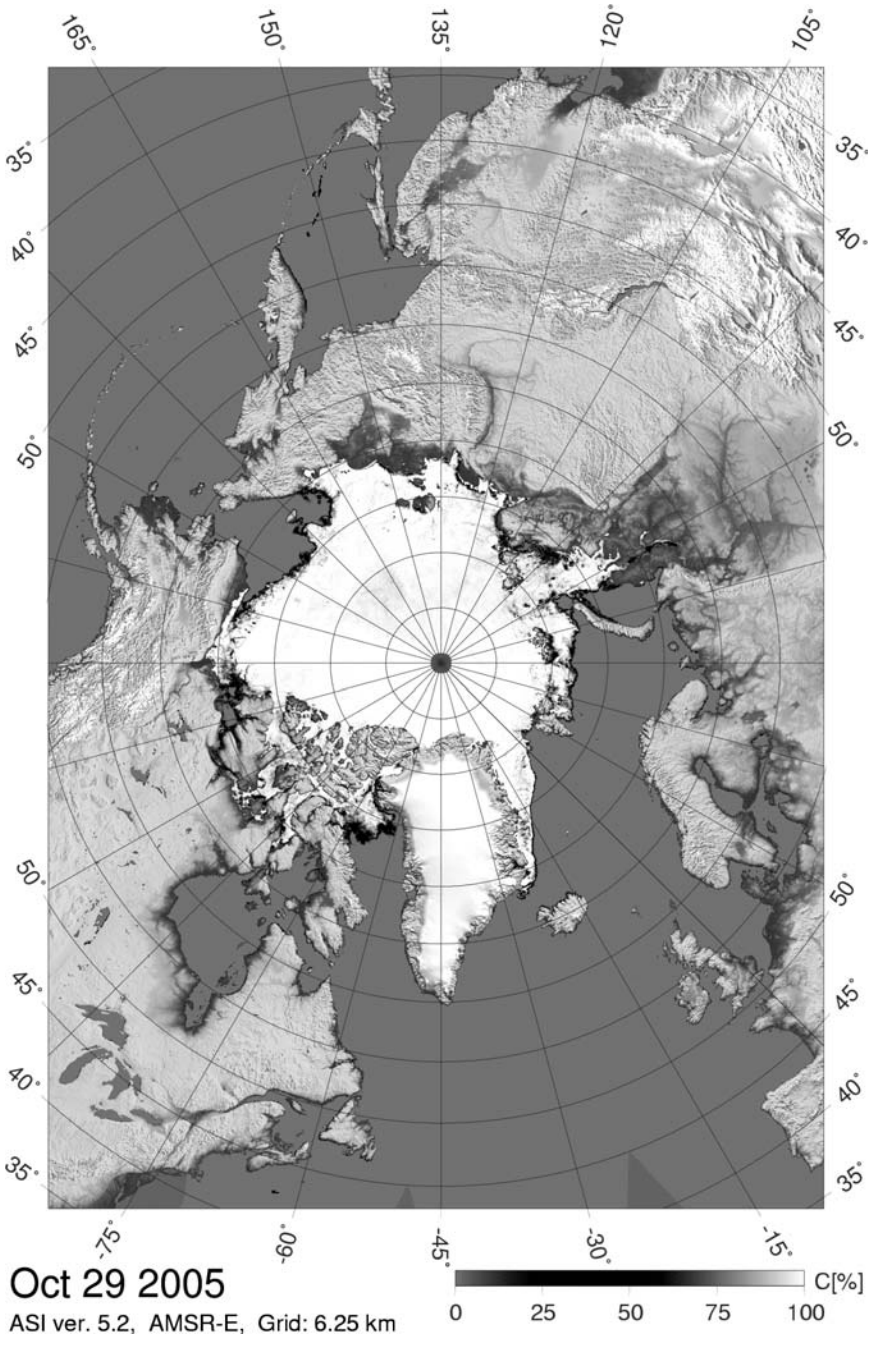

Figure 3.20(b). Example sea ice product obtained by passive microwave radiometer data: AMSR ice concentration map using ARTIST algorithm on 19 April 2004 for the Arctic Ocean. From *http://www.seaice.de*

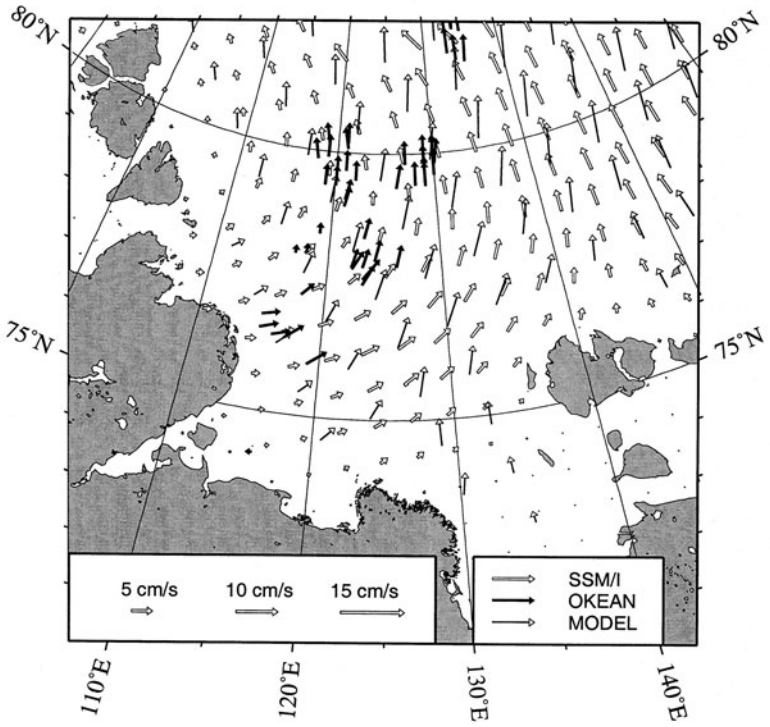

Figure 3.21. Ice drift pattern in the Laptev Sea from SSM/I over 10–30 January 1998, compared with results from model and *Okean*-derived drift vectors. From Alexandrov *et al.* (2000a).

3.2 OPERATIONAL SEA ICE MONITORING IN THE NORTHERN SEA ROUTE
(*V.G. Smirnov, V.S. Loshchilov*)

3.2.1 Organization of monitoring

With the end of regular airborne ice reconnaissance in the early 1990s, satellites present the main tool for acquisition of ice information. Russia's present-day system of sea ice monitoring in Arctic water areas, including the NSR, provides ice information acquisition, processing and dissemination to users in near-real time. It has a one-level structure and one common Center for Ice and Hydrometeorological Information (CIHMI). The Center is an operational subdivision of the Arctic and Antarctic Research Institute (AARI) and is engaged in acquisition and processing of the entire system of hydrometeorological information (including satellite data), generation of ice charts and maps of hydrometeorological conditions, forecasting the sea ice state and meteorological conditions in the NSR, and in distribution of operational and prognostic information products to users (Mironov *et al.*, 2002).

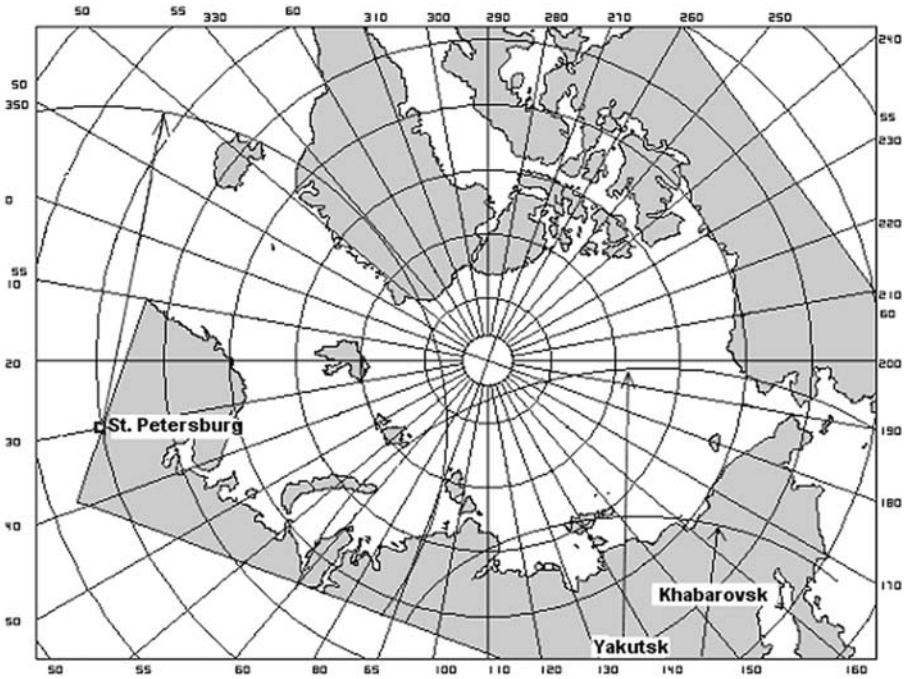

Figure 3.22. The receiving zones over the Arctic from meteorological satellites of *NOAA* and *Terra* series covered by operating Russian ground stations.

At present, there are no actively operating Russian meteorological satellites, and therefore the main source of satellite information is the available foreign meteorological satellites of the *NOAA* and *EOS* (*Terra*, *Aqua*) series. The ground-based receiving system at AARI in St. Petersburg is equipped with Telonics receiving satellite stations (U.S.A.) and ScanEx and UniScan-36 stations produced by the Russian research and development center ScanEx, and provides for receiving indicated satellite images in direct transmission mode only for the western Arctic sector including the western Laptev Sea. The UniScan-36 receiving station can be equipped with an additional module, which will allow direct receipt of *Radarsat* information.

Satellite data for the eastern sector are received at the Yakutian Administration of the Hydrometeorological Service (UGMS) in Yakutsk. The ground-station in Yakutsk is equipped with the Quorum receiving system (U.S.A.) and provides for receipt of *NOAA* five-channel optical images almost for the entire eastern sector of the Arctic (Figure 3.22).

The use of the Far Eastern Regional Data Receiving and Processing Center (Khabarovsk) for receiving information from *NOAA* and other satellites operating in direct transmission mode does not solve the problem completely. This Center is equipped with EoScan receiving stations produced by ScanEx and Telonics; however, the radio-visibility zone of Khabarovsk allows receipt of satellite data only for the coastal part of Arctic seas.

For transmission of satellite images of the eastern area of the Arctic Ocean to St. Petersburg from Khabarovsk and Yakutsk, the Internet is used. This transmission system is the most operational and rapidly developing in Russia.

The temporary absence of Russian satellites for active and passive microwave sounding restricts the list of determined ice cover characteristics and prevents monitoring on cloudy days. Nevertheless, for support of some marine operations, data from Canadian *Radarsat* and European *ERS-2* satellites have occasionally been ordered and purchased. Data from the European *Envisat* satellite are not used by AARI for operational support of marine operations. However, AARI developed data processing techniques for satellites using some images obtained in the demonstration projects Icewatch (Johannessen *et al.*, 1997a) and Icemon (Sandven *et al.*, 1997).

Ice charts published on the Internet by foreign ice centers—for example, the National Ice Center (NIC) of U.S.A.—give useful information on global and regional scales. These charts are compiled on the basis of all operating satellites including active and passive microwave data. The charts of NIC can be used as additional information for compiling weekly review ice charts of polar regions. In addition, data from the AMSR microwave radiometer and the SeaWinds scatterometer are used to produce weekly review charts.

3.2.2 Information support for users

Russia's weekly ice charts of the Arctic region are published on the Internet site of AARI on a regular basis at *http://www.aari.ru*—they are published in generalized form and contain basic information on ice conditions in Arctic seas (Figure 3.23).

This information can be used for the preliminary planning of specific sea operations. Also, weekly, detailed ice charts for each of the Arctic seas along the NSR are made. Every month one of these charts is published on the Internet site of AARI. These ice charts are available to any user but are not intended for the operational support of ice navigation along the NSR. Examples of these ice charts using national (Russian) ice symbols for winter and summer seasons are presented in Figure 3.24.

Other information of general use is also published on the AARI site—namely, prognostic information 1 to 6 days in advance including ice drift, currents and sea level elevation as well as wave forecasts for the open areas of the Arctic Ocean. An example of prognostic mean daily drift of sea ice for 2 May 2005 is presented in Figure 3.25.

At the request of users, detailed current and prognostic ice charts, recommended routes and other hydrometeorological information can be made available both over the entire NSR and any local region. Current ice charts are constructed using all available information including ground truth data and satellite data of various spectral bands. When necessary, series of *Radarsat* high-resolution images are ordered. It is also possible to order *Envisat* data that have been provided on a paid basis for their commercial use from the spring of 2004 by Eurimage and by *Radarsat*'s international companies. SAR/ASAR data are used for construction of detailed ice charts and for operational support of some transport operations in local regions under any cloud conditions (see examples in Section 4.5).

Direct transmission of operational information products (ice and meteorological

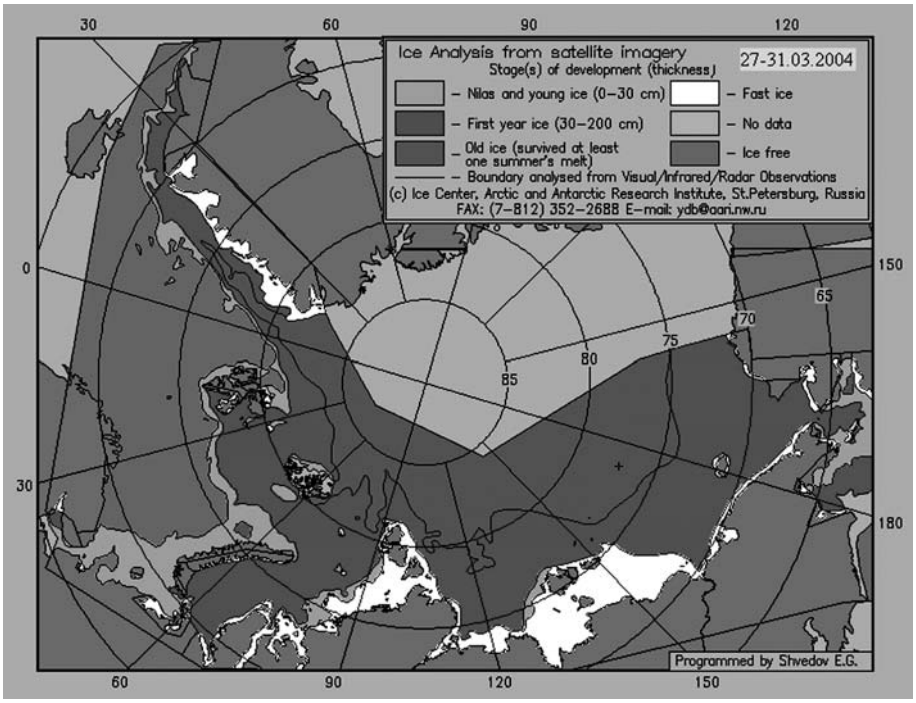

Figure 3.23. Example of a weekly ice chart distributed through the AARI Internet site (see also color section).

charts, forecasts and other information) from CIHMI to users onboard icebreakers and ships is performed using conventional and satellite communication channels. For data transmission to large ships and icebreakers equipped with *Inmarsat* communication systems and electronic cartographic navigation–information systems (ECNIS/ECDIS), a special procedure developed at AARI is used (see Section 6.4). This procedure provides for conversion of the digital ice and meteorological charts to formats compatible with ECNIS. The charts are transmitted and are depicted in ECNIS as additional information layers on top of the electronic navigation chart in the same scale and projection. In addition to *Inmarsat*, a low-orbiting Russian satellite *Gonets-D1* communication system can be used for transfer of the electronic charts to users, which can deliver digital and text information to any point on earth (Shcherbakov *et al.*, 2002). This communication system is being constantly developed and, in theory, will enable operational transfer of ice and other information to icebreakers and ships navigating at high latitudes beyond *Inmarsat* coverage.

The practice of supporting ice navigation along the NSR showed that satellite sea ice images are important for the choice of sailing route made by captains. The most convenient appears to be satellite images transformed by Mercator projection and superimposed on electronic route navigation charts. The procedures developed at AARI allow using raster satellite images in ECNIS (see Section 6.4). A significant

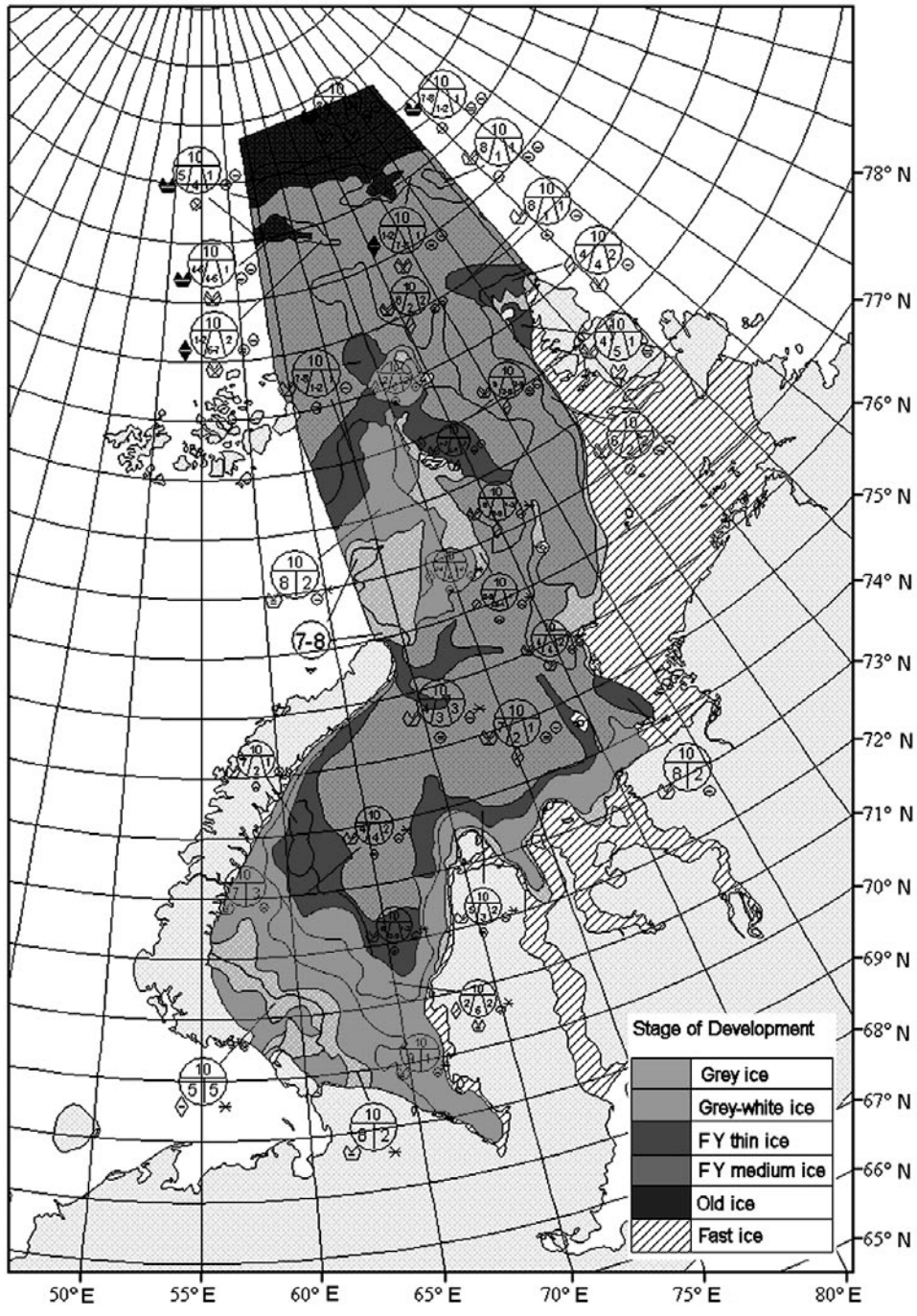

Figure 3.24(a). Weekly ice charts of the Kara Sea for the winter season (03–05.01.2005) (see also color section).

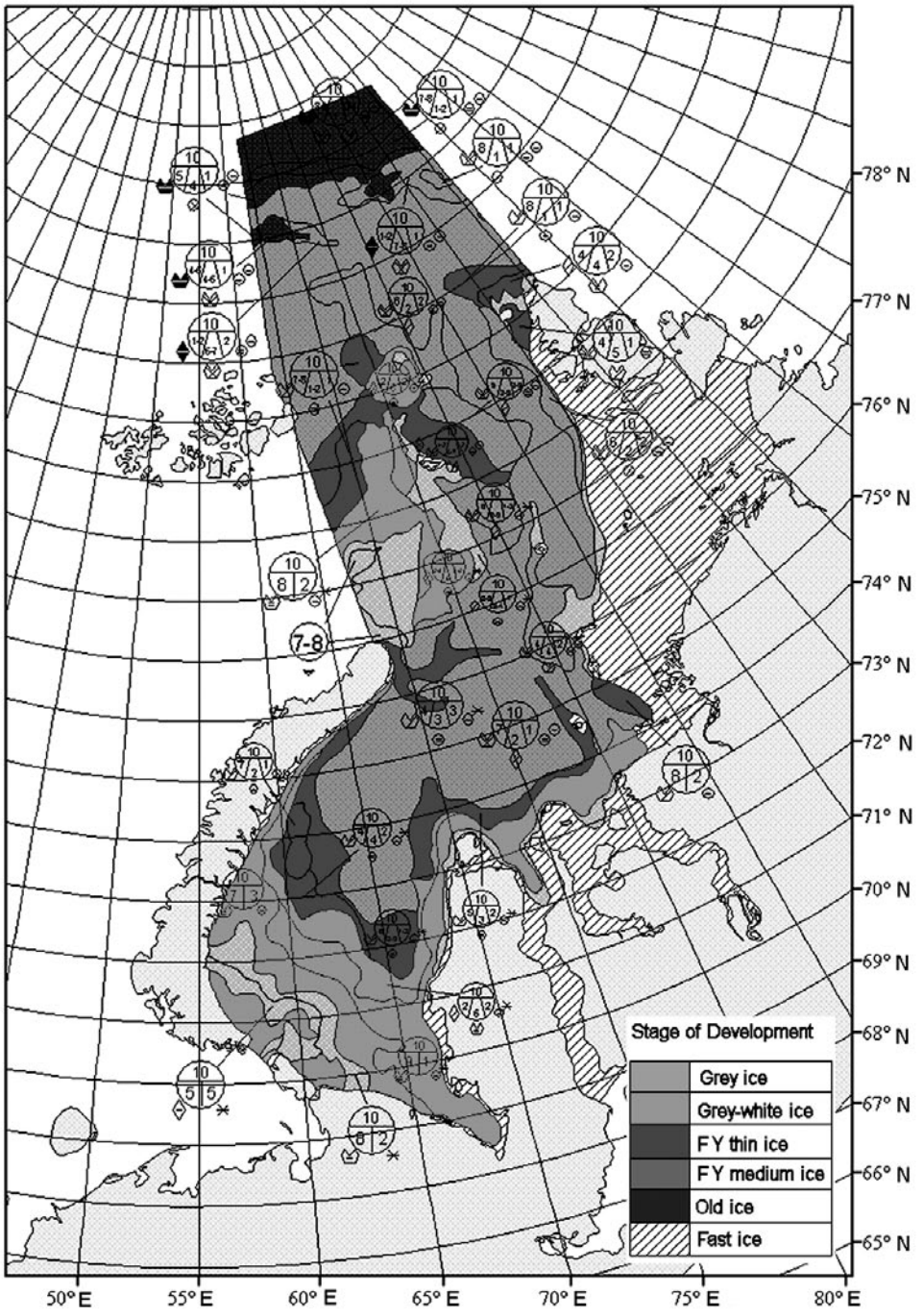

Figure 3.24(b). Weekly ice charts of the Kara Sea for the summer season (24–28.07.2005) (see also color section).

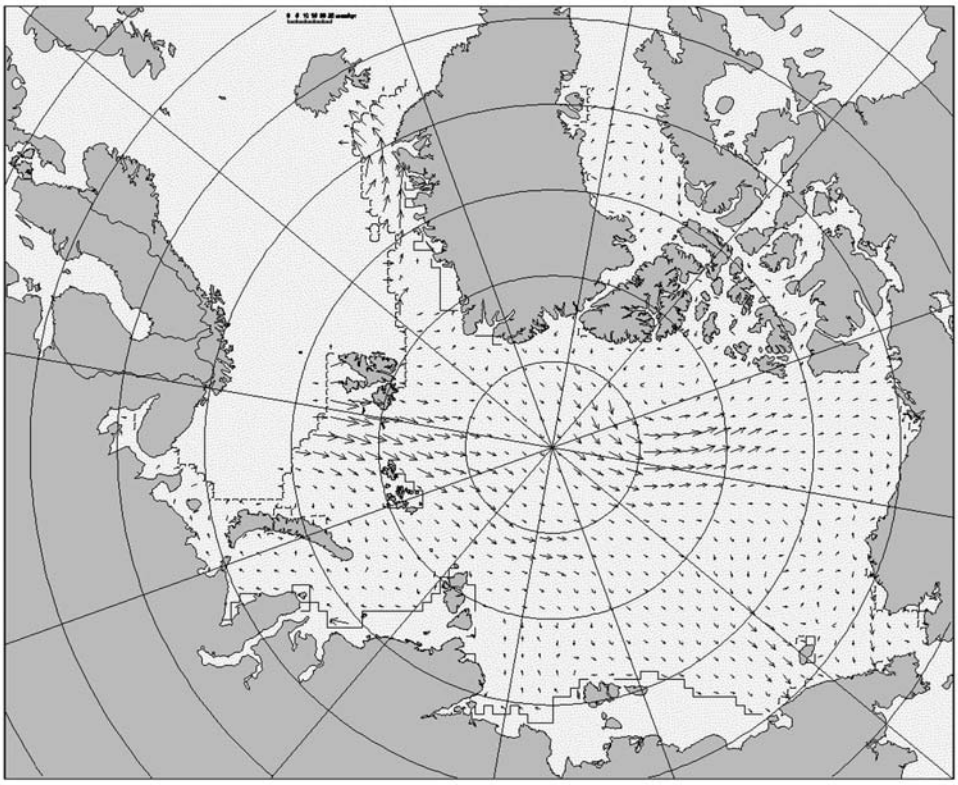

Figure 3.25. Forecast of mean daily drift of sea ice for 02.05.2005 (6 days in advance).

decrease in cargo transportation along the NSR during the last decade has reduced the number of ice information users, which in turn created some problems for implementation of information support for shipping and industrial activities in Arctic seas. On the other hand, currently observed increasing interest from several Russian and foreign oil and gas producing companies in the development of Russian Arctic fields requires the need for further development of the ice information system, which is currently funded by Russia and via commercial contracts.

3.3 USER REQUIREMENTS FOR SEA ICE INFORMATION ON THE NORTHERN SEA ROUTE

(L.H. Pettersson, N.G.Babich, S. Sandven, O.M. Johannessen, L.P. Bobylev, V.V. Melentyev, V.Yu. Alexandrov)

3.3.1 General survey of users

Elaboration of the new sea ice monitoring concepts needs a study of user requirements for sea ice information. A survey of current, potential and new users of satellite-based

sea ice information has been conducted primarily among the Russian institutions and companies with interests in the NSR and Russian Arctic waters, concerning shipping activities in the NSR and the major Siberian rivers. Users have acknowledged their benefit of using SAR data for sea ice monitoring compared with the more traditional methods, and expressed confidence that the applications of SAR data are useful. The significant interest in the future use of Earth observation data for Russian territories is identified for exploration of hydrocarbon resources—that is, increasing oil and gas exploration and production activities on- and offshore in west Siberia. Also related to these activities is the support of shipping and offshore operations in ice-covered waters (Pettersson *et al.*, 1999b).

Current users of sea ice information

In general, Russian users can be categorized in the following user groups:

- Operational users with "daily" near-real time needs in support of navigation of ships or other activities in or near ice-covered waters, including shipping and oil and gas companies.
- Consultancy services with needs for statistical sea ice information in order to plan or design future operations with different time perspectives from weeks to decades.
- Scientific users—a large community having interests in research and technical development—have the need for ice information to carry out field research programs and use in their basic research activities.

The latter group includes users whose activities relate to the development of satellite earth observation methods, as well as those who need sea ice information combined with other data collected through their research programs, including studies of climate change, as well as biological–ecological and physical processes.

Traditional Russian ice services provide composite sea ice charts and information at the mesoscale level for most parts of Russia's Arctic Shelf area as well as for the Arctic Ocean. This information is particularly important for year-round operations in relation to transport along the Siberian coast and rivers. A summary of the requirements for the three major categories of sea ice information users is given in the following sections.

Users of operational sea ice information

Sea ice parameters in combination with meteorological and hydrodynamic characteristics (temperature, wind, waves, currents, etc.) are of importance to all types of marine operations in or near ice-covered waters, including ice navigation, offshore operations, such as oil and gas extraction, fisheries, etc. All of them require reliable monitoring and forecasting of sea ice conditions.

Operational users include shipping companies with cargo and icebreaker escorting fleets. Several Russian shipping companies are responsible for ship cruising in the Russian Arctic. The largest is the Murmansk Shipping Company, which operates the

icebreaker and merchant fleet, first and foremost in the areas along the western part of the Siberian coast and in its rivers. The Northern Shipping Company Ltd and the White Sea–Onega Shipping Company have responsibilities for the marine transport activities in the White Sea region, and on the lakes and rivers between the White and Baltic Seas, respectively.

The major goal of sea ice information is to optimize and safeguard ship operations, in a time- and energy-effective way, as well as to select the safest sailing routes and reduce the risks involved. This implies the need for detailed data—in particular, on the location of most hazardous sea ice phenomena. Depending on actual ship operations, this information includes ice edge location, ice type, direction and speed of ice motion, shear zones, leads, ice roughness and icebergs. In general, sea ice information is of importance for operational activities throughout the year, but with especial focus on the period with the most severe sea ice conditions, typically from October to June/July.

Traditionally, the composite ice maps (CIMs) generated by Russian ice services are used for navigation support in the Russian Arctic. The introduction of SAR data will be beneficial for detailed elaboration of CIMs and improvement of their information content. Of more importance is a direct use of SAR images in tactical ice navigation routing, when ice pilots onboard the ships can use local ice maps based on SAR images and/or digitally enhanced images. In this respect there is a need for education and training of ice pilots in order to perform correct onboard interpretation of the sea ice in SAR images. SAR-derived sea ice information can be transferred in digital form to icegoing vessels. There are technical constraints on using the *Inmarsat* telecommunication system at high latitudes. Accordingly, there is a need for a more robust and efficient way for near-real time transfer of digital data to ships operating at these latitudes. The availability of SAR images may partly replace the use of expensive helicopters for local ice reconnaissance to optimize the sailing route.

Regular use of SAR-based sea ice information will improve routines employed to support ships navigating in ice-covered areas. In order to utilize SAR-derived ice data fully and regularly, continuity in the availability of data and derived products with appropriate time and geographical coverage is essential. Both the technical and financial aspects of such a long-term supply of both the prime data and derived sea ice information are therefore of importance. Rapid changes in the priorities and actual tasks of the icebreaker fleet also require a high degree of flexibility with respect to changes in areas for which SAR data may be requested. The area coverage provided by the Tromsø and Fairbanks receiving stations is insufficient to provide information on the entire area requested by Russian shipping companies. Taking this into account, ESA has provided two additional receiving stations, covering the Russian Arctic, located in Moscow and Khanty-Mansiysk.

The oil exploration and exploitation industry needs sea ice information to plan offshore operations and has near-real time operational requirements of this information. In particular, data about drifting icebergs is of critical importance to offshore activities. The major Russian oil and gas corporations—Gazprom, Lukoil, Rosshelf among others—are developing their activities in the Arctic and use sea ice information, including information based on microwave earth observation data. Observations

of sea ice and ocean parameters are also important for management of fishery resources and marine mammals. Regardless of the inevitable risk, fishing vessels often have to sail in severe sea ice conditions, and therefore SAR-based sea ice data could be vital for them. Long-term statistical information on key ice parameters (extent, thickness, types, etc.) needs to be improved for design, certification and insurance of vessels and marine structures operating in polar waters. Research expeditions may also temporarily need near-real time, detailed sea ice data for optimizing their field programs, and operational planning of their route and location of sampling stations.

Summarizing, we can conclude that there are three main types of users of operational sea ice information who can be subdivided according to their roles, responsibilities and tasks to be solved:

(1) Teams which are in direct contact with sea ice in their daily work and need ice information to operate ships safely and cost-effectively in ice-covered seas. Typical users are icebreaker captains and ice pilots, merchant ship captains or skippers of fishing vessels or oil platform managers, and managers of coastguard or navy vessels.
(2) Teams which are responsible for planning and implementation of sea transportation, icebreaker convoys, offshore operations and other marine operations in ice-covered areas. These teams often work on land, but have responsibilities to give directions to crews working at sea. Typical representatives of this group are shipping companies, oil companies, fishing companies, ship traffic authorities, coastguard stations and navy bases. The main challenge is to plan the best possible operations by ships and offshore platforms to minimize risks of damage and economic loss.
(3) National institutions responsible for collection of sea ice data and production of ice maps, ice forecasts and other ice information products. They are direct customers of satellite earth observation data, and they provide final sea ice information products from these data. The institutions are usually national ice centres, weather services or marine research institutes. Their main task is to collect available sea ice data and through integrated analysis deliver ice charts to other users.

Users of statistical sea ice information

These users need SAR data primarily for assessment and impact studies related to oil and gas exploration activities, for more general environmental studies and for other industrial activities in the Arctic region.

Generally, such studies are limited in geographical area, although a large number of data time series are required to map various phenomena and their typical variability for concrete applications. The cost of data, their analysis and reproduction is a limiting factor for an extensive use of SAR images. Access to a large database from which relevant data could be collected or purchased is an approach to stimulate the use of earth observation data in these activities. For some activities

there is a need to coordinate earth observation data acquisition with other types of field investigations and airborne reconnaissance. Access to simultaneous multi-spectral satellite data and other *in situ* information is also requested for many applications.

SAR data coverage should include offshore and coastal regions, estuaries, rivers, lakes and land areas in northern Russian territory. Data for all seasons are of potential use, but depend on actual needs of customers and tasks to be solved. Based on reliable sea ice statistics, an improved design of ships for Arctic operations can be achieved—for instance, great interest is shown in the access to information on various hazardous ice phenomena, their frequency and common areas of occurrence. Data acquisition for such an application can usually be planned well in advance and archived historical data may also help to satisfy user needs. Data may be processed or analysed by external experts and reported back to customers. Sometimes, electronic delivery of data is preferred. The major impediment to extensive use of SAR data is the cost of them *per se* and their analysis. The willingness of the oil exploration industry to perform studies and obtain information on sea ice conditions prior to the initiation of exploration activities are identified. Use of earth observation data may be a cost-effective information source in this respect. However, the industry has clear priorities of environmental safety aspects which need to be thoroughly considered and assessed.

Scientific users

The largest group of potential and/or actual users of satellite-derived sea ice information is the scientific community in Russia. In this respect, they provide studies of the Arctic ecology and climate, design constructions and ships to be utilized in the Arctic region, assess risk management and develop ice monitoring services including methods that use earth observation data. The diversity of this user group is very wide and covers areas such as oceanography, meteorology, sea ice studies, hydrology, glaciology, marine biology and fisheries, marine pollution and ecology. In the field of engineering research and development, applications encompass ship design, coastal engineering, risk management, marine and coastal navigation, and offshore operations.

The requirements for SAR-based ice information products range from processed image data to merged sea ice maps based on multiple SAR swaths. Generally, SAR information is required off-line, but during field investigations there is also a need for access to near-real time SAR data and derived sea ice products. For many users a combination of SAR and other multi-spectral earth observation data is required, and hence coordination in satellite EO data acquisition is necessary. Some of the applications also include process studies in which consecutive data coverage is needed. Some users are going to develop or have already built up their own expertise in SAR image processing and interpretation, but others need higher level interpreted ice information products. There is a general need for guidance and training in the interpretation of sea ice signatures in SAR imagery. Geographically, data requests cover most parts of the coastal Russian Arctic from Asia to Europe. Specific demands have also been put forward for rivers, lakes and reservoirs in Siberia. Requests for data are made through-

out the year, but most users are interested in the most dynamic periods of freezing and melting. One example is the deployment and recovery of the Russian North Pole station in 2004, where these operations were supported by *Envisat* ASAR data for identification of the appropriate ice floes for the camp and aircraft landing.

The volume and extent of Arctic sea ice, freeze-up and breakup dates for Arctic coastal ice, distances of Arctic ice edges from coastlines and width of the fast ice zone are important sea ice parameters for climate change studies. Sea ice dynamic and thermodynamic processes need to be better monitored and quantified. Estimation of net ice production and fluxes through the Fram Strait is of high priority, where satellite earth observation data and other observations can be combined.

3.3.2 Sea ice information for navigation support

Contemporary international conventions for ensuring safe navigation, safeguarding human life at sea and protection of the marine environments from pollution by ships unanimously regard hydrometeorological information as a crucial and essential part of the general system for safe navigation. Ensuring safety in Arctic navigation places special requirements on information of sea ice conditions and dynamics, and their forecast.

All forms of sea ice information for planning, organizing and managing ship operations in ice-covered seas, ensuring the safety of navigation in sea ice, publications in navigation manuals and guidelines, sailing directions and instructions for navigation in sea ice can be combined under the general name of "navigational sea ice information". Sea ice monitoring, analysis, and generation of ice charts and their dissemination among users operating in sea ice are the most important elements of navigational sea ice information supply. Dedicated ice centers—primarily that at AARI—as well as the regional and structural departments of the Russian Hydrometeorological Service implement this activity for Russian Arctic waters.

Depending on the objectives and tasks, navigational ice information is divided into three main categories: strategic, operational and tactical sea ice information.

Strategic sea ice information

Strategic ice information is used by the Federal NSR Administration (NSRA) and marine operations headquarters (MOHs), as well as by shipping companies and cargo owners to plan and manage their fleet operation. This includes:

- The composition of business plans for regular cargo transport and implementation of specific marine operations.
- The choice of ports in which cargo transport will be concentrated and locations of cargo delivery in the Arctic.
- Determination of expected sea ice conditions, terms and duration of the sea ice navigable period.
- Selection and distribution of icebreakers and merchant vessels of different ice classes according to the actual routes used for cargo transportation.

- Calculations of defined operational–economic indices of planned sea ice operations.

Sea ice charts for previous years, average long-term sea ice data and weather conditions, their forecasts for time periods ranging from 10 days to 3 or 6 months, including forecasts of sea ice formation date, ice thickness increase, sea ice melting and ice disappearance for defined areas are usually used in strategic sea ice assessment for the above tasks.

Survey ice charts are the essential part of strategic sea ice information. These ice charts cover completely or partially all water basins of the NSR, including high-latitude routes and near-pole regions, as well as adjacent parts of the Barents and Bering Seas. Survey ice maps are usually generated every 10 days during the navigable period, and outside this period they are typically produced once per month. These maps contain information on the location of ice and open water boundaries, boundaries of fast ice, recurring flaw polynyas, ice massifs and fields of different age (thickness) and ice concentration. In accordance with the scale of chosen maps, the data used for survey ice maps should be averaged. The spatial scales of averaging of sea ice characteristics can be from several thousand to tens of thousand square miles. The distance between the graphic elements (location of the boundaries of inhomogeneous ice and open water areas) on the map is usually from ten to hundreds of miles. An example strategic ice map is presented in Figure 3.23. Survey ice maps also include the following additional information: average parameters of hummocking, snow cover extent and sea ice destruction, orientation and extent of large fractures and systems of cracks in the ice massif, zones of accumulation of icebergs and grounded hummocks.

The basic data source of a strategic ice chart is satellite earth observation data at a low spatial resolution (~5–10 km) and with wide-swath coverage (e.g., SSM/I, AMSR, AVHRR *NOAA*, among others). Satellite data of higher resolution as well as data of the airborne ice reconnaissance, regular observations at polar and coastal stations and from other sources may be used as additional information to obtain more detailed estimates of sea ice concentration, thickness, hummocking, snow cover extent, sea ice destruction, icebergs and grounded hummocks.

Survey ice maps are stored in a database for scientific analysis and the management of navigation in the NSR. Usually, these maps are not distributed to ships operating in the NSR, but, if necessary, the MOHs can send them to the captains of escorting icebreakers.

Operational sea ice information

Operational ice information is used by MOHs for the following tasks:

- Choice of alternative ship navigation routes, and allocation of icebreakers to their region of operation.
- Choice of convoy formation locations, places of departure and destination of ships.

- Determination of composition of convoys (number and types of ice class ships) and development of schedules for their movement.
- Making navigation recommendations for icebreakers and ships in all stages of their voyage and operation.
- Identification of places of shelter (safe "parking" of ships) in case of unfavorable (dangerous) ice phenomena.
- Planning of sea operations for cargo delivery to non-port locations (i.e., to an unsuitable shore, by road or through fast ice) and for trans-ship cargo.
- Ensuring the safety of floating and stationary derricks and oil terminals.

Operational ice charts and weather forecasts for 1–10 days as well as forecasts of ice re-distribution, drift and compression for 3–7 days are used in the aforementioned tasks.

Operational ice charts are made during the navigable period. These charts cover the areas of Arctic seas within the NSR routes in which specific sea operations take place. For example, in the summer–fall period of navigation in the western Arctic, operational ice charts are put together for the entire region. In winter, to support fleet operation to and from Dudinka, they fully or partially cover the Barents Sea and the western part of the Kara Sea eastward to Dikson.

Operational ice maps are usually drawn every 2–3 days, or at worst every 5 days. This time period is based on the fact that the average duration of synoptic periods (i.e, coherent atmospheric circulation patterns and pressure systems) in the Arctic is about 7 days and typically varies from 5 to 11 days. Unidirectional tendencies in variations of sea ice conditions, ice drift, localization of compression areas, orientation of fracture and crack systems are accordingly developed and persists within these periods. Ice drift can vary between a few miles and tens of miles per day depending on the location. Changes in the atmospheric circulation and pressure systems lead to variations in surface wind and air temperature fields, which in turn affect the development of sea ice processes and may significantly alter sea ice state and distribution.

Operational ice maps contain many more navigation-relevant sea ice characteristics than composite ice maps. The following information is included in operational ice charts: location of ice and open water boundaries; fast ice boundaries with delineation of areas of different ice age (thickness), deformation and destruction; flaw polynyas and leads; the boundaries of ice fields of different thickness (age) and concentration; fractures and divergence in more compact ice; orientation and extent of fractures, systems of cracks and individual cracks; the amount of prevailing forms of ice in grades, separate giant or vast ice floes among smaller ice forms; local sites of increased deformation, ridges, grounded hummocks and icebergs; localization of zones of various orientations and compression in the ice cover; characteristics of snow cover; or destruction of sea ice and icebreaker-made channels in the ice.

During operational ice map production, the sea ice parameters are averaged according to the chosen scale of the baseline map. The spatial scale of such averaging can be from hundreds to several thousand square miles. The distance between the graphic elements of the map—location of the boundaries of ice of different concentration, age (thickness), local sites of increased deformation, open water areas in the

ice—usually vary from several miles and upward. As a rule, total and partial ice concentrations, deformation, snow cover, icemelt and compression are all averaged to a certain degree on operational ice maps.

The data sources for operational ice charts are satellite Earth observation data at a resolution from tens of meters to 1 kilometer, such as AVHRR *NOAA*, *Terra*. Additionally, data from visual and instrumental airborne surveys, observations at polar stations, ships and expeditions are used. During recent years, air-borne surveys have been cut to a minimum or play the role of a subsidiary source of operational ice data used for detailed assessment of some of the ice characteristics identified through other information sources. In this case, of great importance are the data of accompanying observations from ships and icebreakers due to their large number and mobility. The contribution of ice observational data from polar stations and expeditions for operational ice monitoring is negligible.

Operational ice maps and ice forecasts are transmitted to all icebreakers and ships in the region of their operation to correct sailing routes and ensure navigation safety. Operational maps are also used as a basis for making composite ice maps, and for scientific purposes—to systematize data on sea ice conditions for navigation routes, to study the general and regional dynamics of sea ice conditions.

Tactical sea ice information

Tactical ice information in needed for accomplishment of a specific sea ice operation—ship or convoy navigation, autonomous icebreaker voyage, cargo loading operations outside the ports (ship-shore, trans-ship operations). The main goal of tactical ice information is to choose the optimal course through the ice, which provides the highest navigation safety, and achieves the best time and energy efficiency. Moreover, this information is used for other tasks of ice navigation tactics:

- Specification of convoy composition and places of their formation, convoy exchange, ship destination, distances, etc.
- Choosing the means of convoy steering (towing, leading).
- Warning about phenomena particularly dangerous for navigation—intensive ice drift and/or compression, the presence of floebergs or icebergs within the route of the convoy; grounded hummocks detected in regions with inadequately mapped bathymetry, which indicates the presence of "unknown" shallow waters.
- Identification of locations of shelter for ship safety at times of extreme ice conditions.
- Examination of fast ice areas suitable for ship steering and cargo trans-ship operations.
- Study of the dynamics and tendencies of ice condition changes in regions of increased ice drift (straits, shallow coastal waters in routes, etc.).
- Ship navigation along the recommended routes in the absence of icebreaker escorting.

The major sources of tactical ice reconnaissance data are as follows:

- Airborne visual ice survey using icebreaker-based helicopters.
- Instrumental survey from aircraft equipped with the Nit' side-looking radar system (not used at present).
- High-resolution satellite earth observation data (microwave and optical).

The need for tactical sea ice information occurs episodically when there is a need to solve challenging tactical tasks of navigation in sea ice. Major users of this information are the navigators of icebreakers and ships (i.e., captains and ice pilots). Therefore, the requirement of near-real time delivery of information is quite strict. The best results in implementation of tactical sea ice information are achieved when it is received in real time during operation in the ice. The permissible delay in data delivery should not exceed more than a few hours after acquisition.

Ice reconnaissance from helicopter is carried out during the icebreaker's advance through fast ice, ice massifs and ice fields. It is performed in the most probable direction of convoy motion. The reconnaissance distance can vary from tens to hundreds of miles.

Mapping tactical ice reconnaissance data depends on how the data were acquired. The results of helicopter visual survey are drawn graphically on maps (Figure 3.26). In this case, ice parameters can be assessed with the same accuracy as is achievable by visual surveys. Usually, only sea ice characteristics of primary importance for a given operation are drawn on the map. To select the best sailing route the following information is included on maps:

- Zones of reduced ice concentration and thickness among more compact and thicker ice.
- Zones of high concentration of ice floes and individual ice floes among broken ice (i.e., small floes, ice cake and small ice cake).
- Fractures, cracks and channels in the ice (both in fast and drifting ice).
- Patches of high deformation, ridges, grounded hummocks and icebergs.
- Direction and speed of ice drift, orientation of compression areas and degree of compression.

Mapping the results of tactical ice reconnaissance is made on a scale comparable with that of marine navigation maps (e.g., from 1:100,000 to 1:1,000,000). The most frequently used is the scale of 1:100,000. The accuracy of ice mapping should practically coincide with the accuracy of determination of the ship's coordinates. The spatial scale of ice observation averaging ranges from several hundred square meters to ten square miles. The distance between the map's graphical elements depends on the practical need for detailed elaboration of navigation-significant characteristics, and usually varies from tens of meters to a few miles.

When high-resolution satellite earth observation images are used, there is no need for graphic interpretation of the imagery. Experience in using high-resolution satellite Earth observation imagery (at a resolution from several meters to hundreds of meters)

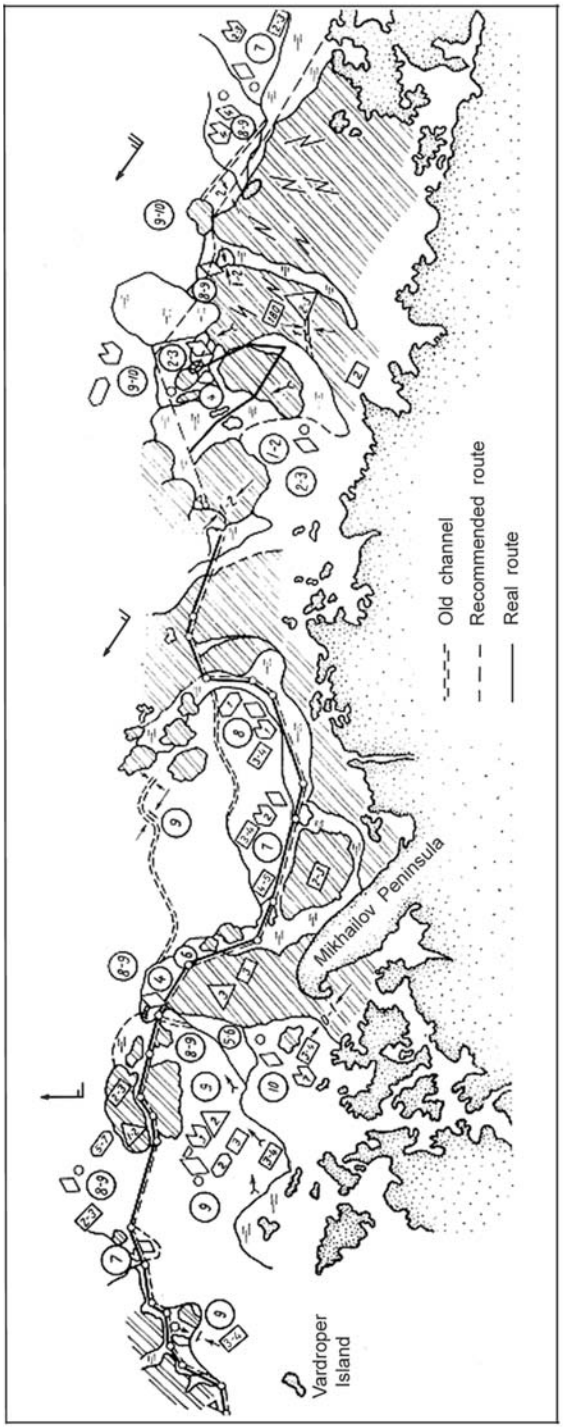

Figure 3.26. Map resulting from tactical sea ice reconnaissance.

has shown that original images with the overlaid geographical coordinate grid and coastline are sufficient in most tactical ice navigation tasks. The efficient use of such images depends on their spatial resolution and quality. As a result of receiving *ERS*, *Envisat* and *Radarsat* SAR images onboard the icebreakers, navigators rapidly learn how to interpret them and prepare an itinerary directly from the images, skirting the ice floes in open water and along extended leads in the interior of ice massifs.

Tactical ice information, obtained by visual observation or derived from satellite earth observation images, is used by an MOH scientific–operational group to supplement and improve their operational ice maps. Specialists in these groups develop image interpretation techniques, and icebreaker hydrologists teach ship navigators how to interpret satellite images.

3.3.3 Role of satellite earth observation (EO) data

In order to satisfy the requirements of operational users of sea ice information, general demands need to be formulated for satellite EO missions, sea ice information products, infrastructure and communication systems for informing users, as well as for elaborating data and pricing policy.

Satellite missions

The most fundamental requirement is to have the continuity of satellite missions that can be used to provide sea ice information. Repeat cycle, swath width, spatial and temporal resolution, all-weather capability and near-real time delivery are the essential parameters to comply with operational ice monitoring. U.S. *NOAA* AVHRR and SSM/I satellite sensors play an important role in existing Russian ice services, although they are not optimized for operational monitoring of sea ice. The European *ERS* system represented a major technological improvement, bringing a large number of high-resolution SAR ice images to many ice centers for operational evaluation. Nevertheless, the first SAR satellite fulfilling most of the requirements for ice monitoring was the Canadian *Radarsat*. Later, European *Envisat* ASAR wide-swath images, which became available in 2002, also met operational requirements. The prospects of using SAR images from future satellites for sea ice monitoring are discussed in Chapter 6.

Necessary products

Data products from satellites must provide necessary sea ice information with sufficient temporal and spatial resolution. The most important ice parameters are ice edge location, ice concentration and ice type, fast ice boundary, iceberg locations, speed and direction of ice motion, as well as leads and deformed ice areas. SAR images at a resolution of 100 m or better is the most appropriate type of satellite EO data to retrieve the abovementioned sea ice parameters. For sea ice applications, about 50% of Russian users (Pettersson *et al.*, 1999b) are able to use basic image products or a calibrated product (31%), whereas about 50% of users have their prime interest in derived sea ice information products and not necessarily the images themselves. In

order to stimulate the use of EO data by the oil and gas exploration industry it is necessary to define those end information products that are beneficial for their activities (Pettersson *et al.*, 1999b).

To generate high-quality sea ice information from satellite images, manual interpretation is needed in addition to automatic processing and classification algorithms. Manual interpretation can be time-consuming, depending on the size and complexity of ice conditions, degree to which the ice charting system is user-friendly and streamlined and experience of the ice analyst. There is a need for considerable improvements and streamlining of algorithms and processing tools for routine production of ice charts based on SAR data. In particular, better algorithms are needed for SAR ice-type classification. To utilize satellite data effectively and to improve the interpretation process the ice charting system should be able to present a range of different data types to the ice analyst (e.g., satellite data from different sensors, previous ice charts, as well as weather information). For cost-effective operational use there is a need for new products such as ice drift vector charts and automatic classification products. The system development process should not be underestimated. It is of key importance for both retaining the present customer base and attracting new potential users. A sea ice analysis and charting system must be designed to meet the requirements of the future—that is, should be easily adaptable to new satellite and auxiliary data sources (Sandven *et al.*, 1997).

Infrastructure and communication

It is of primary importance that satellite data be disseminated timely from receiving stations to ice centers, and forwarded from ice centers to operational end users. Computer networks, telephone lines and satellite communication systems are not equally well-developed in all remote regions where users of ice information need access to such data. For large data files, such as SAR images, telecommunication can be a bottleneck. In cases when the use of satellite telecommunication systems such as *Inmarsat* is the only solution, data transmission can be very expensive. For different ice regions there can be different solutions to dissemination of data and information products.

In order to achieve a level where all users at sea could get ice information in digital form, suitable end user systems must be developed which should include data transmission between ships and ship-owners, and between ships and ice service/data providers, as well as integration of sea ice information into onboard navigation systems (Sandven *et al.*, 1997).

Informing users

In spite of many pilot and demonstration projects devoted to informing users about the advantages of *ERS*, *Radarsat* and *Envisat* SAR data, there are many users of ice information who are unaware of the possibilities that can be offered by new satellites. With the increasing amount of available satellite EO data, service providers and a variety of different products and processing algorithms, there is a strong need to standardize sea ice information and make it easily available to users. In this respect it

will be important to use international ice codes also in Russian sea ice products based on EO data. This is in many cases adopted by national ice centers. Further, it will be important to include this sea ice information in developing more complex and integrated electronic cartographic navigation information systems (ECNIS) used onboard contemporary vessels (see Figure 6.21).

Data and pricing policy

The most important factor in determining international and Russian use of satellite data in operational ice monitoring is data ordering and pricing policy. The cost benefit of using satellite EO data is totally determined by the policies adopted by space agencies or national space programs for using "raw" EO data. Operation of satellite EO systems is usually funded by national governments through space agencies, space programs or organizations such as the WMO and EUMETSAT. Due to different data policies, there is a situation where some types of satellite data used for ice monitoring are free of charge such as *NOAA* AVHRR and SSM/I data, while other data such as *Envisat* and *Radarsat* SAR, *SPOT* and *Landsat* have to be purchased. Recently, space agencies have moved toward a more liberal pricing and open dissemination data policy. The availability of EO data is improving; however, the price still hampers wide use of satellite data. Agreements between space agencies and national ice services (public or private) have contributed to increased use. In Europe and Canada the European Commission and the ESA are implementing global monitoring for environment and security (GMES) in order to stimulate the use of EO data. GMES will also contribute to increased use and availability of SAR data and services for Arctic ice-covered waters.

In this regard ESA has already made large amounts of *ERS* and *Envisat* SAR data available free of charge for ice research and monitoring demonstrations. Many users worldwide have become familiar with the use of spaceborne SAR data and demonstrated their usefulness for sea ice monitoring. Commercial users such as oil and other companies have to pay a commercial price for SAR data to the EO data distributors.

Canada's *Radarsat* is operated on a more commercial basis; however, there is still an opportunity to get data free of charge for research and demonstration purposes. Some European ice services and national agencies have made agreements with *Radarsat International* in order to secure public accessibility to EO data for their use. Still, the price policy for EO data is a limiting factor for their widespread use in Europe and Russia for the NSR.

The general view among users is that an ice monitoring service is most efficient when it operates under the auspieces of national ice or weather forecasting services. The public sector will continue to play the major role in funding the basic ice services, including the use of satellite data. But, there is also increasing interest among many users to strengthen the role of the private sector in paying for special ice services and products. With growing ship traffic, oil and gas exploration, fisheries and other economic activities in ice-covered waters, there will be an increased demand for dedicated, specific ice monitoring services and products. User requirements for these services are more extensive or advanced than the standard ice charts delivered by national ice

centers. This will enable existing ice centers or other service providers to develop and deliver commercial sea ice information products, which will be supplementary to standard ice charts, the latter being either free of charge or inexpensive.

Gaps between user requirements and capabilities

Various satellite data in the visible are the common information source for sea ice monitoring and mapping of sea ice conditions. They provide the current basis to obtain strategic, operational and tactical sea ice information. Sea ice charts generated from such images formally satisfy user requirements for strategic ice information in terms of their coverage, and spatial and temporal resolution. However, in practice, sea ice information cannot be obtained for some areas of the Arctic Ocean and the NSR because of the following reasons:

- Sea ice information cannot be retrieved from such images in cloudy conditions.
- Information from visible images cannot be obtained during winter darkness.
- Information from IR images can be retrieved only when temperature falls below $-10^{\circ}C$.

Therefore, solutions to the following tasks are of high priority:

- To use SSM/I data to get strategic sea ice information. The Arctic Ocean is covered daily with SSM/I data.
- To use satellite scatterometer data to get strategic sea ice information.
- To implement the use of *Radarsat* ScanSAR and *Envisat* ASAR and global mode images for obtaining strategic sea ice information, which will require the availability of large quantities of SAR data.

Operational ice charts are characterized by the same limitations as those for strategic ice charts. User requirements of operational ice charts in terms of spatial and temporal resolution are more strict than those for strategic charts. These operational information requirements can be best met by use of *Envisat* ASAR and global mode images and the ice information products derived from them.

During the last decade, the use of helicopters from icebreakers to provide tactical sea ice information has been significantly reduced. During this period, the Nansen Center in Bergen, Nansen International in St. Petersburg and the Murmansk Shipping Company have carried out many pilot projects aimed at using high-resolution satellite SAR images to supply icebreakers with tactical sea ice information (see Chapter 6). Geolocated SAR images with overlaid geographical coordinates are regularly transmitted to icebreakers of the Murmansk Shipping Company in near-real time, and have proved highly efficient in the selection of optimal ship routes under difficult ice conditions. Whereas it is impossible to cover the NSR with the 100-km swath of the *ERS* SAR, *Radarsat* ScanSAR and *Envisat* ASAR images with swath widths of 500 km and 450 km, respectively, the entire area of the NSR can be covered in 48 hours.

3.4 OPERATIONAL SEA ICE SERVICES IN OTHER ARCTIC COUNTRIES

(*S. Sandven, V.Yu. Alexandrov, O.M. Johannessen*)

3.4.1 Introduction

Operational monitoring of sea ice and icebergs has been developed in Arctic countries over many decades to bring about safe operations in ice-covered seas. Industry and trade in Arctic countries are directly dependent on sea transportation at high latitudes, which is heavily affected by the presence of sea ice and icebergs. The *Titanic* disaster in 1912 was the direct reason for establishing the International Ice Patrol with responsibility for monitoring icebergs in the North Atlantic. Sea ice monitoring services have been established during the last century in all countries where sea ice affects navigation and other marine activities (Figure 3.27). In Europe ice services are established in Denmark, Estonia, Finland, Germany, the Netherlands, Norway, Latvia, Lithuania, Poland, Sweden and Russia. Denmark has two services, one for the Baltic Sea and another for its Greenland waters. Extensive ice services are established in the U.S.A. and Canada. In Asia, China and Japan have ice services.

National ice centers produce ice charts according to an international standard defined by the WMO. Today, ice centers are organized in the International Ice Charting Working Group (IIICWG). This Group and the Expert Team on Sea Ice

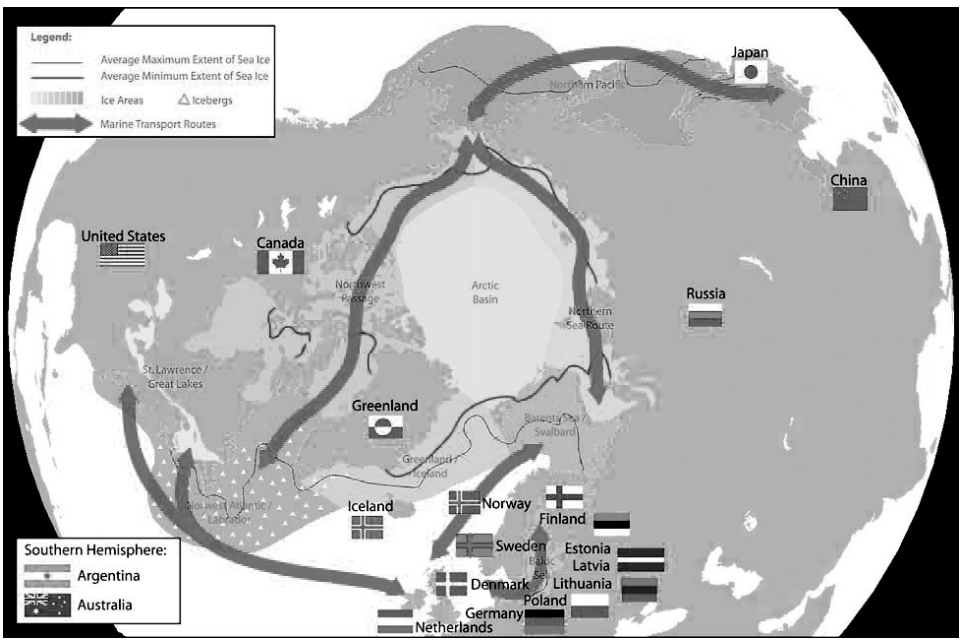

Figure 3.27. Countries with national ice services in the northern hemisphere, including ice-affected areas and the main Arctic shipping routes (IICWG, 2004) (see also color section).

(ETSI) working under the aegis of the WMO are the most important international sea ice monitoring organizations. The operational ice services provided by IICWG member organizations are based, to a great extent, on information from earth observation satellites. Earth observation is often the only cost-effective and technically feasible mean of obtaining information.

The sea ice monitoring services do more than just support sea transportation. Sea ice information is also used in weather forecasting and in climate monitoring because data on changing ice conditions are a critical component of weather and climate systems. Ice-affected regions are rich in natural resources such as oil and gas, fisheries, minerals and timber, but the harsh climate including the presence of sea ice puts severe restrictions on exploitation of these resources. Offshore operations in ice-covered seas need specific ice information, which is more detailed than the standard ice charts produced by national ice services. Search and rescue organizations dedicated to mitigation of loss of life or property due to accidents in Arctic waters need ice information to support their operations. The coastguard and the military need ice information for planning and implementation of their operations. Marine engineers need ice information for the design of safe structures and vessels that can operate in ice conditions. The polar environment and climate is heavily affected by sea ice change, especially ecosystems that are dependent on sea ice. A number of sea ice parameters are needed to report on the status and changes in the Arctic environment. People living in Arctic regions are often affected by sea ice in their daily life. Monitoring and forecasting services for sea ice are useful services to support many human activities. Finally, policy-makers need ice information to better understand and monitor polar regions for planning and decision making.

A wide variety of user requirement inventories for ice information have been developed to support different benefit areas. The key features of ice user requirements are the:

- ice parameters to be measured;
- spatial scale of the observations; and
- frequency of observation.

In addition, the time between an observation and delivery of a useful information product to the user is an important characteristic, particularly for operational users. Because ice conditions can be highly dynamic (ice drift can be up to $50\,\mathrm{km\,day^{-1}}$), users engaged in operations in or around ice require information that has a fast turnaround (1–6 h) and on a regular and reliable basis (every 6–24 h, every day). Typically, users of this information are transport ships, ferries, icebreakers, national coastguards, fishing vessels, offshore oil and gas companies, and meteorological forecast operations. The near-real time (NRT) requirement of these users has significant implications for the revisit capabilities of observation systems, and the speed and robustness of the reception, processing and delivery infrastructure. Another significant group consists of users that require access to an archive of imagery, observations and derived ice products. There is a wide range of applications for time series of consistent, objective sea ice measurements—from calculating ice

statistics for defining the best location and design of a wharf to large-scale global change climate studies.

In the following sections the major ice services in the Northern Hemisphere are briefly described, except for the Russian ice service, which has already been described in Section 3.2. More extensive information about the services can be found in *Sea Ice Information Services in the World* (2000) and at the websites of each of the services.

3.4.2 The International Ice Patrol

The International Ice Patrol (IIP), which is supported by 14 countries, has responsibility for monitoring and broadcasting information about the southern limit of icebergs in the vicinity of the Grand Banks of Newfoundland. The U.S. Coast Guard formally begins its seasonal ice observation and ice patrol service whenever icebergs threaten primary shipping routes between Europe and the U.S. and Canada. This usually occurs in the month of February and the threat usually extends through July, but the Ice Patrol is flexible and commences operations when iceberg conditions dictate. The 1992 season, the longest on record, ran from 7 March through 26 September, 203 days. Except during unusually heavy ice years, the Grand Banks are normally iceberg-free from August through January.

The addition of SLAR and *Radarsat* data improved the Ice Patrol's reconnaissance efficiency, although radar iceberg identification remained problematic even with the use of modern techniques. Therefore, for effective monitoring of iceberg location the IIP to a significant degree rely on information from vessels. During the ice season the IIP broadcasts two message bulletins each day and a daily radio facsimile chart containing ice information to inform ships of the extent of estimated limits of all known ice. Iceberg monitoring is carried out together with the Canadian Ice Service.

3.4.3 The U.S. National Ice Center

The National Ice Center (NIC) is a multi-agency operational center representing the Department of Defence (Navy), the Department of Commerce's National Oceanic and Atmospheric Administration (NOAA), and the U.S. Coast Guard under the aegis of the Department of Homeland Security. The NIC includes personnel from the National Environmental Satellite Data Information Service (NESDIS) within NOAA. The navy component within the NIC is called the Naval Ice Centre (NAVICECEN) and is a fourth echelon command reporting directly to the Naval Oceanographic Office (NAVOCEANO) at the Stennis Space Centre, Mississippi. Both NAVICECEN and NAVOCEANO are part of the Naval Meteorology and Oceanography Command, headquartered at the Stennis Space Centre. The commanding officer of NAVICECEN also serves as the director of the National Ice Center.

The main mission of NIC is to provide the highest quality strategic and tactical ice services tailored to meet the operational requirements of U.S. national interests and specialized meteorological and oceanographic services to U.S. government agencies.

Satellite imagery constitutes over 95% of the information received and integrated into NIC ice analysis products. NOAA's *Tiros-N* and *DMSP* satellites are the primary source of remote sensing data (*Sea Ice Information Services in the World,* 2000). *NOAA* and *DMSP* OLS imagery are used for global- and regional-scale mapping of ice conditions, respectively. Use of visible images is limited by the absence of natural light in winter. In summer, cloud cover precludes sea ice observation both with visible and infrared imagery for approximately 80% of time. The Fleet Numerical Meteorological and Oceanographic Centre (FNMOC) and National Centre for Environmental Prediction (NCEP) routinely process SSM/I data for ice concentration determination and transfer the results to the NIC. The main disadvantage of passive microwave data is their coarse spatial resolution. After *Radarsat*'s launch in 1995, SAR images became an important source for global and regional sea ice monitoring. In addition to satellite remote sensing data, the NIC employs U.S. Coast Guard aircraft with SLAR for special polar operations, regularly receives ice reports from visual reconnaissance missions, ships, Alaska coastal stations, and obtains information from the observational data network maintained by the International Arctic Buoy Program (IABP).

The NIC issues weekly maps of sea ice distribution in the Arctic and regional-scale ice maps on a bi-weekly basis. An example of the regional sea ice concentration map of the southwestern Kara Sea is shown in Figure 3.28. The National Weather Service in Anchorage produces a daily analysis of ice conditions in Cook Inlet, the eastern Bering, Chukchi and Beaufort Seas. Alphanumeric text messages describing ice conditions are routinely generated and distributed for U.S. Department of Defense customers. The distribution of satellite images annotated with analysis graphics is restricted to authorized users. Users may request and receive fax copies of current NIC products via the fully automated National/Naval Ice Centre Autopolling Facsimile System, which is available 24 h a day free of charge.

NIC data are the major part of the U.S. contribution to international systems of global climate and ocean observations. Data of sea ice operational analysis and forecasts are intended for the U.S. Navy, Coast Guard, Departments of Commerce and Transport, other U.S. governmental and international agencies, as well as for the civilian sector.

3.4.4 The Canadian Ice Service

The Canadian Ice Service (CIS), a branch of the Meteorological Service of Canada (MSC), is the leading authority for information about ice in Canada's navigable waters. The CIS provides reliable and timely information on ice conditions in Canadian waters for safe and efficient maritime operations and environmental protection. In summer it focuses on sea ice conditions in the Arctic and Hudson Bay region, whereas in winter and spring the Labrador Coast, East Newfoundland waters, the Gulf of St. Lawrence and the St. Lawrence Seaway are of major importance. The CIS serves as a central processing and analysis facility where satellite and airborne data, meteorological and surface observations are integrated to produce an overview of current and future ice conditions for all regions of Canada.

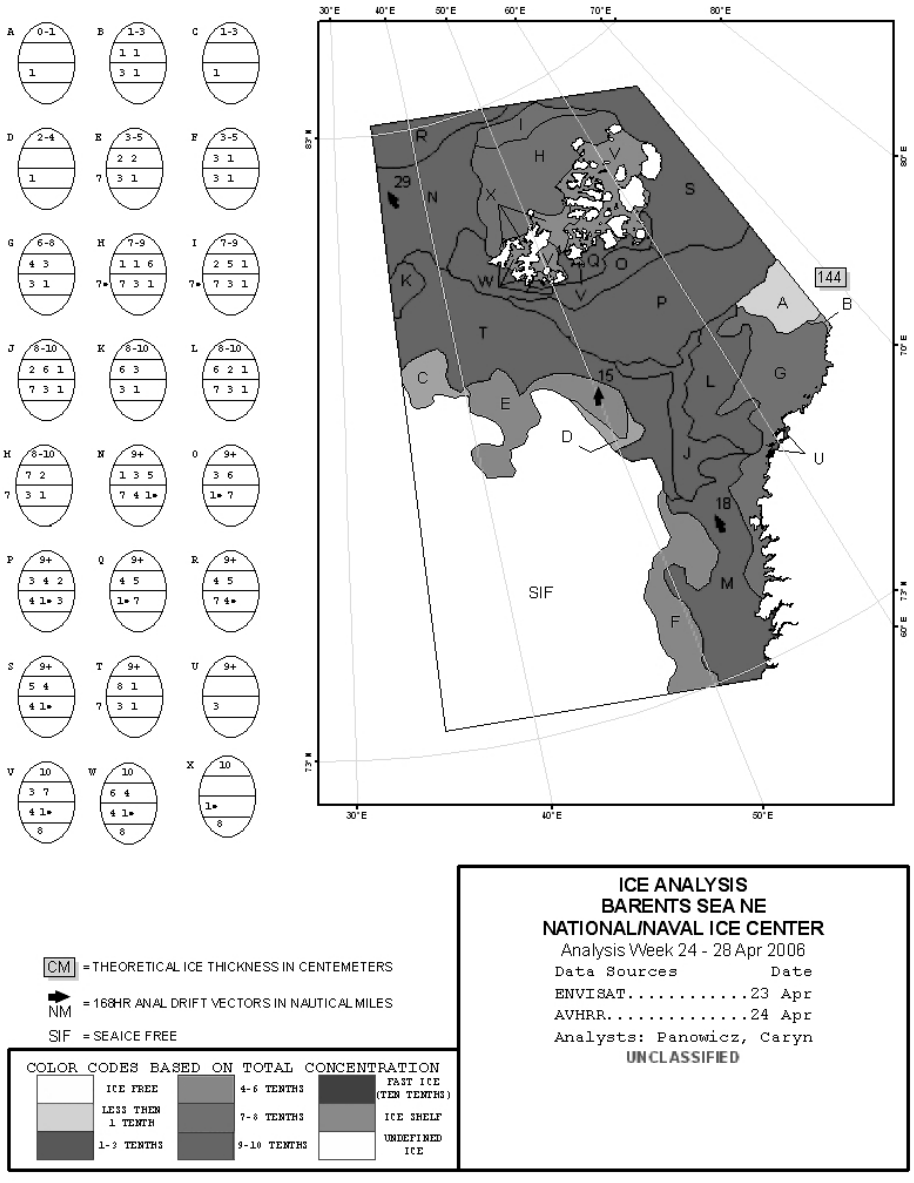

Figure 3.28. Example of regional ice chart for the southwestern Barents Sea produced by NIC for 24–28 April 2006 (see also color section).

Before the launch of *Radarsat*, the CIS employed two ice reconnaissance aircraft for data acquisition, supplemented with *NOAA* AVHRR, *ERS* SAR, SSM/I data, and ship and shore reports. Today, *Radarsat* ScanSAR wide-swath data provide daily coverage of the Canadian Arctic, and higher resolution modes are used for sea ice

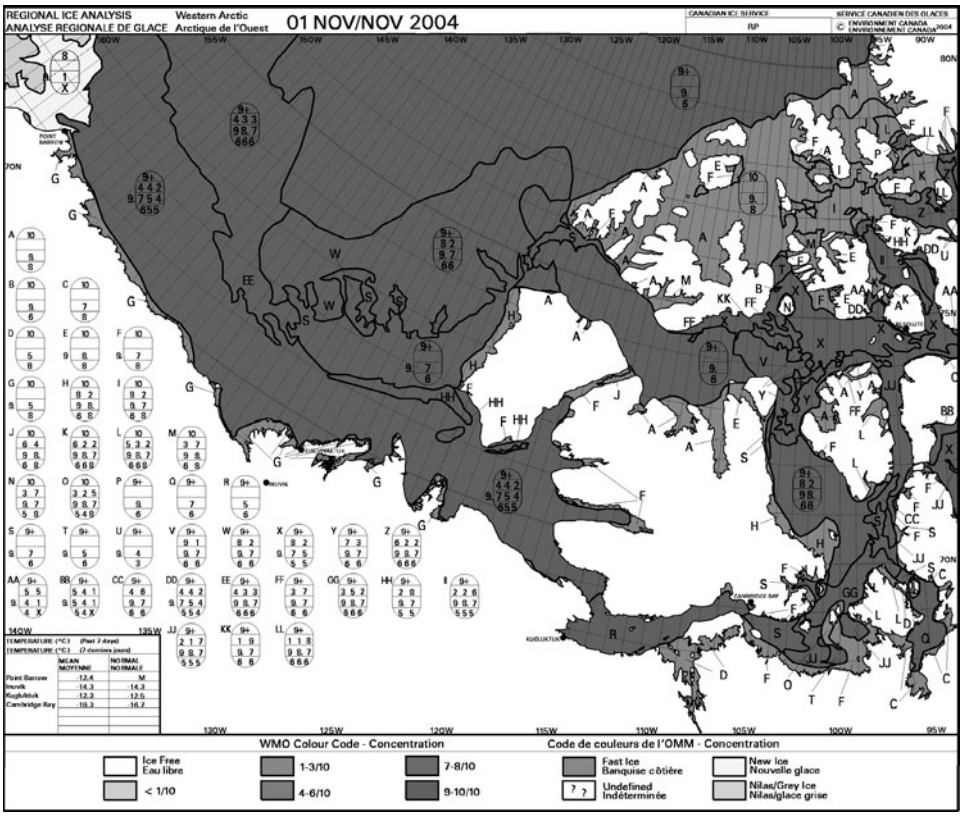

Figure 3.29. Ice chart of the western Canadian Arctic for 1 November 2004 produced by CIS (see also color section) (courtesy: CIS).

monitoring near the ports, in several selected routes and in the rivers. SAR images are produced at the Prince Albert and Gatineau receiving stations, and transmitted to the CIS in near-real time. The CIS performs ice analysis and produces ice charts for various users, primarily the Canadian Coast Guard (CCG). Sea ice monitoring is the most successful operational use of *Radarsat* images, which provide a useful mix of geographic coverage and spatial resolution. Use of *Radarsat* data is a cost-effective solution compared with airborne radar surveys, which were the main source of ice data before the launch of *Radarsat* (Edel *et al.*, 2004). Since February 1996 and until the end of 2003, the CIS has used approximately 25,000 scenes for this purpose (Flett and Vachon, 2004). An example of an ice chart produced by the CIS is shown in Figure 3.29.

In addition to mapping the sea ice, the CIS is responsible for iceberg monitoring. The method involves locating the position of icebergs using visual observations (aerial, ship and if possible satellite), and prediction of their movement for up to a maximum 30 days. A special service implemented iceberg detection and monitoring from satellite

SAR images. This service was in operation during 2003 and the International Ice Patrol was the user of this information (Flett and Vachon, 2004).

The CIS provides its clients with a variety of accurate and timely analyses of ice conditions including ice charts, bulletins, images and weather maps. Regional weekly ice charts, daily ice analysis and iceberg analysis charts, ice reconnaissance and *Radarsat* image analysis charts are available. Raw images are available to users depending on their ability to receive image data. Bulletins provide advice on ice or iceberg conditions in simple text format (*Sea Ice Information Services in the World*, 2000).

The main users of ice information are the Canadian Coast Guard, vessel traffic centers, shipping, fishing, and oil and gas industries. Others include the military, the insurance industry, scientists working on, under or around the ice, and other individuals with a need for up-to-date knowledge of sea ice distribution. Foreign ice services incorporate and exchange sea ice data with the CIS, particularly the International Ice Patrol, Greenland Ice Patrol and the U.S. National Ice Centre.

3.4.5 The Danish Ice Service for Greenland waters

The Danish Meteorological Institute (DMI) in cooperation with the Greenland Ice Service has the responsibility for monitoring sea ice conditions in Greenland waters where drifting sea ice and icebergs severely influence coastal waters and even in summer may restrict ship traffic. The most important navigation area is around Cape Farewell.

AVHRR images from *NOAA* satellites, acquired by DMI receiving stations in Greenland and near Copenhagen, have been used for operational sea ice monitoring in Greenland waters since 1991. Cloud cover often renders visible data useless, and therefore SAR data from *Radarsat* are now the main data source for sea ice mapping, and airborne reconnaissance is used as a supplement when satellite data do not provide sufficient information (Gill *et al.*, 1997; Gill and Valeur, 1999). Weekly ice charts are produced for Greenland waters in their entirety, while ice charts in the Cape Farewell area and on the east and west coasts are produced daily depending on season and requirements from ship traffic.

Users are primarily commercial vessels passing Cape Farewell and local traffic, especially in West Greenland south of 69°N. The information from the Ice Service is requested by an increasing number of sea cruise ships which are visiting Greenland waters and companies involved in exploration of oil, gas and mineral resources. Fishing vessels need information on the ice edge position. An example of a weekly ice chart for the whole of Greenland is shown in Figure 3.30.

3.4.6 The Icelandic Ice Service

The Icelandic Meteorological Office (IMO) is in charge of sea ice monitoring in Icelandic waters in the Greenland Strait (Denmark Strait) between Iceland and Greenland and in the Iceland Sea north of Iceland. Sea ice in the Denmark Strait develops from an average minimum in late September/early October, when the

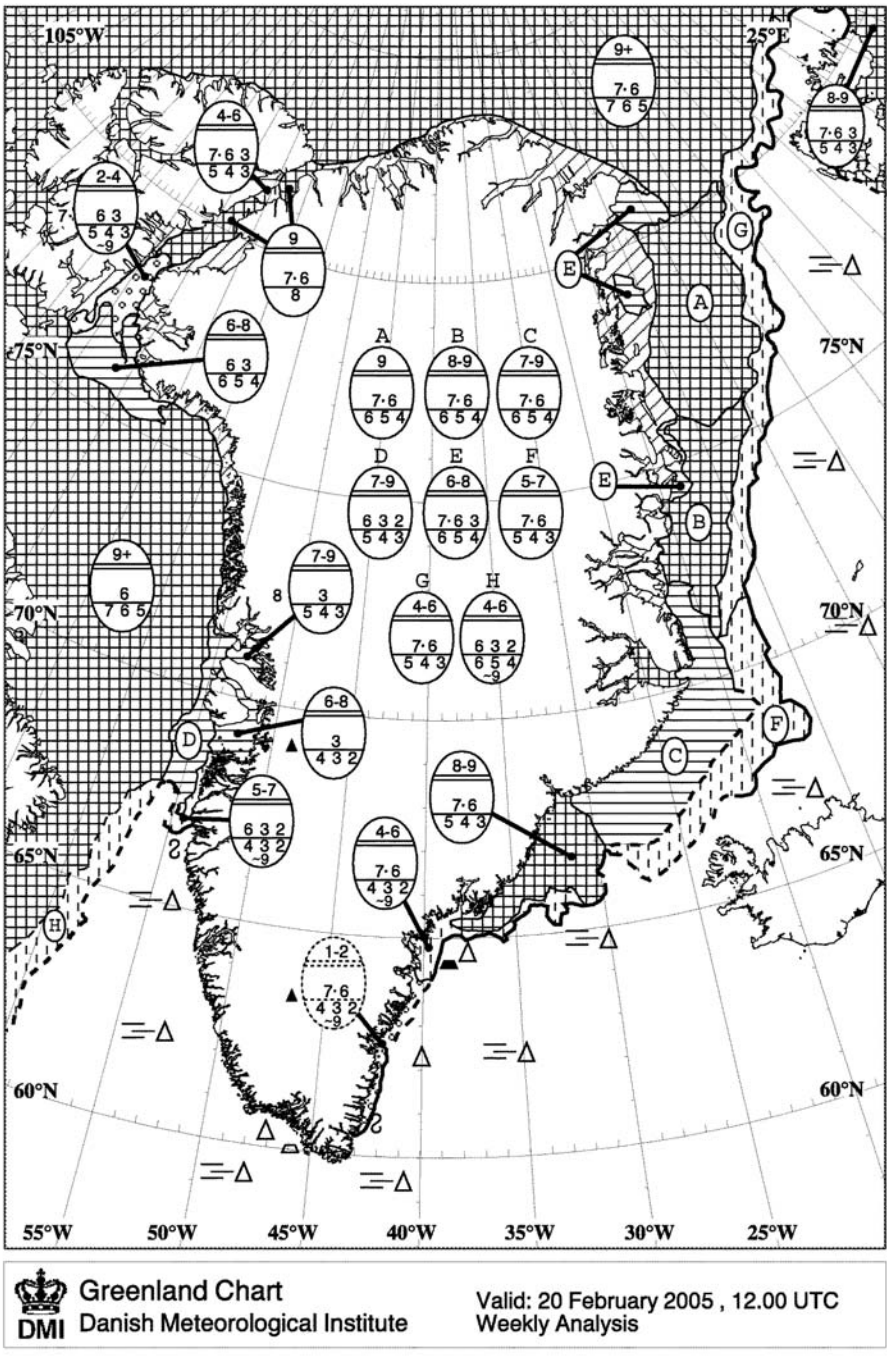

Figure 3.30. Example of weekly ice chart for the Greenland waters produced by Danish Meteorological Institute using WMO ice codes (courtesy: DMI).

average sea ice extent along the east coast of Greenland reaches Scoresby Sound, until an average maximum in late May.

For ice chart composition, IMO uses Icelandic Coast Guard (ICG) ice reconnaissance flights, visual observations from lighthouses and coastal meteorological stations, visual and radar observations made by ships and *NOAA* images. About once a week IMO receives ice charts from the Danish and Norwegian Meteorological Institutes. Although fog and cloud very often cover the sea ice edge, and it is still relatively dark in late winter and early spring, when the sea ice extent is at its maximum, use of SAR images have been considered too expensive. Icelandic sea ice charts give the ice edge location, and when available the concentration and stage of development (Figure 3.31). All maps are transmitted to ships or shipping companies by fax, and the ice edge location is sent via HF radio. Some ships can also receive satellite images via *Inmarsat*.

The traditional users of sea ice data are the fishing fleet, both trawlers and smaller coastal boats, transport vessels along coastal routes, harbour authorities, coastal and local natural hazard committees. There are also increasing numbers of requests for ice information from travel bureaus, agents of large tourist vessels and transatlantic sailing boats (mainly in summer).

3.4.7 The Norwegian Ice Service for Arctic waters

The Norwegian Meteorological Institute (met.no) produces daily ice charts for the Barents Sea, the Svalbard area and the Norwegian–Greenland Sea regions. The charts also include sea surface temperature (Figure 3.32). The main data sources are *NOAA* AVHRR images, SSM/I data and observations from ships, aircraft and meteorological observation stations at Jan Mayen, Bear Island, Hopen and in Longyearbyen. Recently, use of SAR data has been introduced to produce higher resolution ice charts to support navigation in the Svalbard area (Sandven *et al*., 2004).

The main users of ice charts produced by met.no are ship traffic and fishing vessels. Other users are coastguard vessels, the governor of Svalbard, cruise and other ship traffic and offshore activities. Marine and offshore activities are growing significantly in this region, implying stronger needs for sea ice and weather services.

3.4.8 Other Arctic ice monitoring services

In addition to the national ice services there are many universities, research institutes, space organizations and companies that are developing new monitoring systems using satellites and other observing platforms. They can provide useful supplements to operational services, especially implementation of new technologies for monitoring and distribution of data.

In Europe, daily maps of ice concentration and extent are produced by several organizations: the EUMETSAT Ocean and Sea Ice Satellite Application Facility (*http://saf.met.no*), Institute of Environmental Physics, University of Bremen (*http://www.seaice.de*) and Danish Centre for Remote Sensing at the Technical

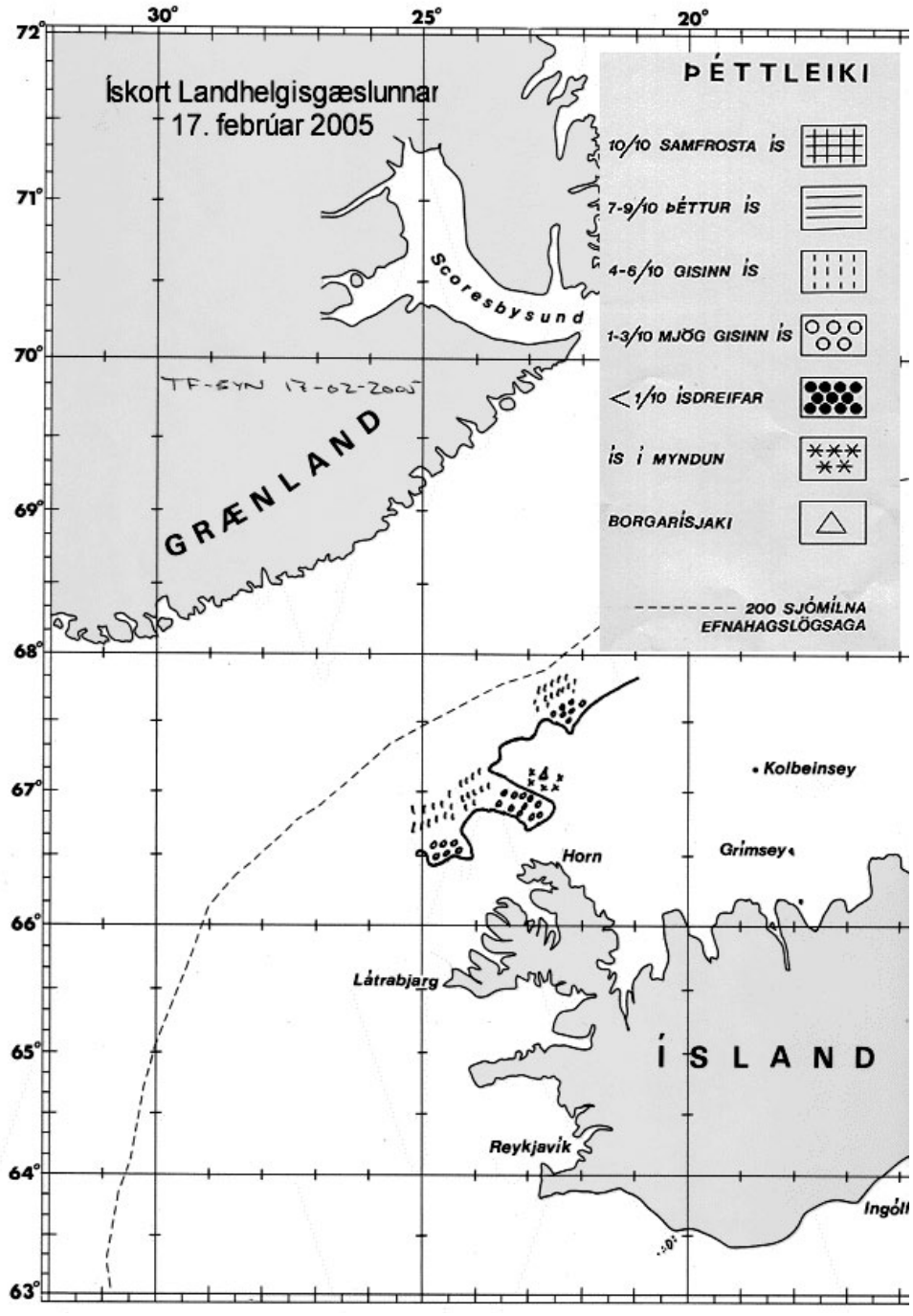

Figure 3.31. Example of ice chart produced by the Icelandic Ice Service for 17 February 2005 (courtesy: IIS).

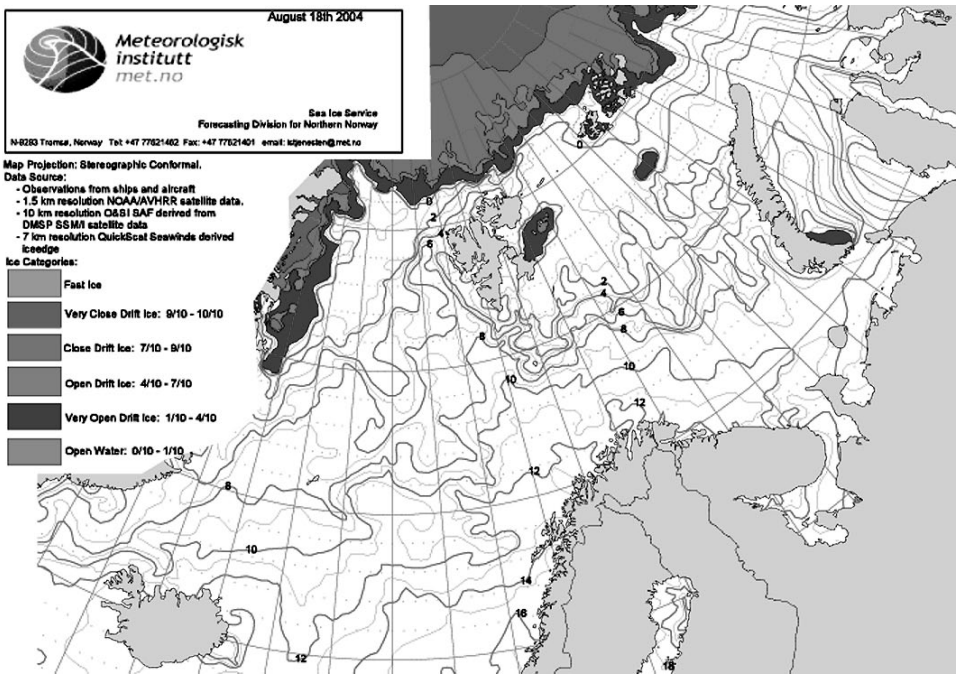

Figure 3.32. Example of ice and sea surface temperature (SST) map produced by met.no (see also color section) (courtesy: met.no).

University of Denmark (*http://www.seaice.dk*). A number of other institutions and organizations provide various types of ice information.

The International Arctic Buoy Programme (IABP) operates a number of expendable and air-dropped ice buoys, which transmit the position and meteorological parameters such as surface pressure and temperature (*http://iabp.apl. washington.edu*). The synoptic ice drift is derived from scatterometer and passive microwave data, providing a valuable supplement to the drifting buoy measurements. IFREMER (Brest, France) is a key organization in delivering these products operationally. Ice drift is also observed in areas such as Fram Strait from moorings equipped with upward-looking sonar (ULS), providing time series over several years. ULS moorings are primarily operated to measure ice thickness.

Ice drift measurements from subsequent SAR images covering the main part of the Arctic are produced by NASA's *Radarsat* geophysical processor system (RGPS) , which allows derivation of deformation fields and related data such as vortices and shear (Kwok, 1998). Maps of vortices and shear show long, narrow features, which can be caused by open water, new ice, nilas, young ice, first-year ice, rafted or ridged ice. Locally, they can be created by divergence, convergence, shear or a combination of these. Examples of RGPS products can be found at *http://www-radar.jpl.nasa.gov/rgps/radarsat.html*

Table 3.9. World Wide Web (WWW) addresses for the main ice services in the Northern hemisphere.

Ice service	Webpage URL
Canadian Ice Service	*http:://ice-glaces.ec.gc.ca*
Finnish Ice Service	*http://www.fimr.fi*
German Ice Service	*http://www.bsis-ice.de/*
Greenland Ice Service	*http://www.dmi.dk*
Icelandic Ice Service	*http://www.vedur.is/hafis/enska/*
International Ice Patrol	*http://www.uscg.mil/lantarea/iip/home.html*
Norwegian Ice Service	*http://met.no*
Russian Ice Service	*http://www.aari.ru*
Swedish Ice Service	*http://www.smhi.se*
U.S. National Ice Center	*http://www.natice.noaa.gov*

Finally, archiving and distribution of data and derived products is an important part of sea ice services. The National Snow and Ice Center in Boulder, Colorado, (*http://nsidc.org*) plays a key role as an archiving and distribution centre. NSIDC provides cryospheric data and information gathered from remote sensing instruments, ground measurements and models as well as tools for retrieval and processing of data.

4

Satellite remote sensing of sea ice

This chapter presents satellite remote-sensing methodologies for sea ice monitoring. Remote sensing of sea ice is performed in the visible, infrared (IR) and microwave spectral ranges, each having its own capabilities and limitations for sea ice mapping and derivation of ice parameters. This chapter considers electromagnetic radiation interaction with various types of sea ice in each spectral range and presents the possibilities of determining sea ice characteristics using various satellite remote-sensing methods. Section 4.1 describes visible (optical) and IR remote sensing of sea ice, currently the basis of Russian sea ice monitoring of the Northern Sea Route (NSR). Section 4.2 provides an introduction to active microwave remote sensing—namely, radar imaging. Section 4.3 presents the interpretation of sea ice characteristics in synthetic aperture radar (SAR) images. Section 4.4 describes algorithms for retrieving sea ice parameters from SAR data. Finally, Section 4.5 is a concise description of remote sensing based ice charting performed at the Arctic and Antarctic Research Institute (AARI).

4.1 OPTICAL AND INFRARED IMAGING
(*A.V. Bushuev, V.S. Loshchilov, Y.A. Shcherbakov, A.I. Paramonov*)

4.1.1 Satellites and sensors

Satellite remote sensing data in the optical spectral range have been used for sea ice monitoring and information support of shipping operations in the NSR for almost four decades. The Russian *Meteor-2* satellites provided optical images from 1970 to 2001. *NOAA* AVHRR data in the visible and thermal infrared channels have been available since 1978. As of 2005, about 20 satellites have been launched and typically at least 2 or 3 are in operation at any time. The *Terra* and *Aqua* satellites, equipped with the multi-spectral MODIS (Moderate Resolution Imaging Spectrometer) sensor,

were launched in 1999 and 2002. MODIS data are available on the Internet and since 2005 have been used for sea ice monitoring in the western part of the NSR.

AVHRR on NOAA satellites

NOAA satellites are launched in Sun-synchronous orbits with inclinations of 98.8° and altitudes of 830–870 km. Data from the Advanced Very High Resolution Radiometer (AVHRR) instrument on these satellites provide information on various oceanographic and meteorological parameters, including sea surface temperature (SST), vertical temperature profiles in the atmosphere and stratosphere, solar radiation, etc.

Sea ice observations make use of images from the AVHRR/2 radiometer, which has the following characteristics:

- spectral channels in the ranges: 0.58–0.68, 0.725–1.1, 3.55–3.93, 10.3–11.3, 11.4–12.4 μm (five channels);
- uniform scanning in look-angle;
- look-angle range of ±55.4°;
- swath width up to 3,000 km;
- spatial resolution of 1.1 km and 4 km in nadir and at the swath margin, respectively.

This information is transmitted in real time using two different modes: (1) images of two spectral channels with resolution of 4 km are transmitted in APT (137 MHz) mode, and (2) all five channels with full resolution in nadir of 1.1 km, in HRPT (1.7 GHz) mode. In Russia, the information in HRPT mode can be received using ScanEx stations, designed and manufactured by the Engineering Technological Center SCANEX. These receiving stations are installed and operate at many locations in Russia—for example, St. Petersburg (AARI Sever Center, NW UGMS), Moscow, Murmansk and Yakutsk.

The stations in St. Petersburg and Yakutsk receive images along the entire NSR taking into account the AVHRR swath width. The Sever Center in St. Petersburg can daily receive images from seven, three and one–two orbits of one satellite for the southwestern Kara Sea, the northeastern Kara Sea and the western Laptev Sea, respectively.

MODIS on Terra and Aqua satellites

These satellites have Sun-synchronous and circular orbits with inclinations of about 98° and altitudes of 705 km. The MODIS radiometer on these satellites registers reflected and emitted radiation in 36 narrow optical range channels from blue to thermal infrared (0.405 to 14.385 μm). Spatial resolutions in nadir are 250 m for channels 1–2, 500 m for channels 3–7 and 1,000 m for channels 8–36 (Table 4.1).

The spectral range of the channel and its resolution determine the information content of the corresponding satellite images. Compared with AVHRR, MODIS images have a four- and two-fold finer resolution, and at sufficient illumination of

Table 4.1. Spectral ranges and resolution of MODIS radiometer channels.

No. of channel	Spectral range (μm)	Resolution (m)
1	0.620–0.670	250
2	0.841–0.876	250
3	0.459–0.479	500
4	0.545–0.565	500
5	1.230–1.250	500
6	1.628–1.652	500
7	2.105–2.155	500
8	0.405–0.420	1,000
9	0.438–0.448	1,000
—	—	—
36	14.085–14.385	1,000

the Earth's surface can be efficiently used for sea ice monitoring in cloud-free conditions.

Channels 8–36 of MODIS are intended for observation of the ocean color and detection of phytoplankton, atmosphere temperature and humidity, temperature of land and clouds and other similar objectives. The spatial resolution of images in these channels is 1 km, similar to that of AVHRR.

Scanning is uniform in look-angles within $\pm 55^{\circ}$ of nadir, and the swath width is 2,330 km. Scanning in channels 1 and 2 is performed by a "comb" of 40 elements. Thus, a 10 km wide swath is scanned simultaneously in nadir, and its width increases to 20 km at maximum look-angle. As a result, adjacent scanning swaths overlap and the image is distorted. If elimination of this distortion is not performed by the receiving software, it should be done when the final images and maps are generated. If the sun's height in the survey area is more than 5° above the horizon, MODIS radiometer information is transmitted at 8.2 GHz frequency in direct transmission mode and can be received in real time.

4.1.2 Processing of optical satellite images

Sea ice data should be presented to users in the form of graphical (raster) and digital ice maps. For sea ice mapping from satellite images it is necessary to perform their geolocation—that is, establish the dependence between the coordinates of the image and the Earth's surface. This dependence is calculated using imaging instrumentation parameters (scanning method, etc.) and orbit parameters (eccentricity, major semi-axis, inclination angle, location of perigee, time and longitude of ascending node passage). Geolocation of satellite images is performed using developed algorithms and software.

An image on a pre-defined projection is called a "photo-chart". It is made in polar stereographic projection with resolution elements of 750 and 250 m for AVHRR and MODIS images, respectively. The coordinate reference is the North Pole. The x- and

y-coordinate axes of the Arctic Ocean photo-chart are the 110°E and 200°E meridians, respectively. The coordinate axes of the Southern Ocean photo-chart are the meridians 180° and 90°E. The Earth is assumed to be a sphere with a radius $R = 6{,}372$ km. In order not to deal with negative values, a constant value of 5,000 for AVHRR images or 20,000 for MODIS is added to coordinates x and y.

Radarsat ScanSAR and *Envisat* ASAR synthetic aperture radar (SAR) images are received by specialized centers, which also perform their initial geolocation. When information is disseminated (via the Internet or by individual applications), each image is accompanied by header data, guiding further operations for ice chart preparation using standard GIS technologies (see Section 4.5).

Optical images are transmitted in direct transmission mode without any geolocation and are received by national and regional ice centers. A detailed description of the technology developed at AARI for processing these images and further generation of single-image and mosaic photo-charts are described below.

Cutting cloud-free sub-images

Unlike SAR images, ice observations in the optical range are possible only in the absence of cloud cover. Therefore, after receiving an AVHRR *NOAA* image, cloud-free regions are delineated, and the possibility of using the image for subsequent geolocation, interpretation and compiling of ice charts is assessed.

The presence and boundaries of cloud features above compact ice are not always confidently identified from analysis of only one visible or IR channel. However, in the wintertime, a combination of channels 1, 2 and 4 allows reliable identification of fully cloud-free regions, and those with transparent clouds, where interactive interpretation is possible. Preparation of such channel-combined images is supported by the software package "SnowCat 1.0". This software can also provide automated creation of other variants of combined images (channels 1–2 and 3–4, etc.) for their visual analysis and interpretation. A single-image photo-chart is prepared for a cloud-free sub-image, which is cut using a rectangular frame and then geolocated.

Geolocation of images

Geolocation of images is performed in six steps:

(A) Image transformation to another image with an equal scale by resampling along the scanning line.
(B) Choice of initial orbital data from corresponding data bases and their preparation.
(C) Calculation of the geographical and rectangular coordinates of image corners from orbital data.
(D) Approximate image transformation using the computed corner coordinates.
(E) Improvement of geolocation using visible coastline landmarks.
(F) Final image transformation to a single-image photo-chart.

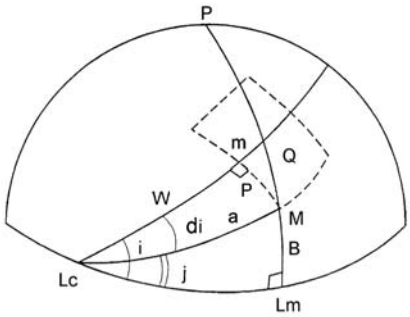

Figure 4.1. Spherical triangles solved in the geolocation process.

Step A The scanning-type satellite radiometer is uniform in look-angle, resulting in varying scale of the image (pixel size increases for *NOAA* AVHRR from the scan center to its margins from 0.78 to 4.5 km). For this reason it is transformed to an equal scale image by resampling pixels along the scanning line.

Step C The scale of an ice map in stereographic projection increases nonlinearly twice from the Pole to the Equator. Therefore, linear interpolation of the points in the middle of the sub-image boundary results in their displacement toward the Pole. This displacement depends on the average latitude and longitude of the cutout sub-image. For Arctic Seas located at 70–80°N, an interpolation error of less than one pixel can be reached if the sub-image size does not exceed 800 pixels. When the sub-image size exceeds this value, it is divided into equal parts. Then, a table of the corner coordinates of these parts (for initial and equal scale images) is prepared. At this stage the geographical and rectangular coordinates of the corners of the sub-image or its parts are determined. Based on auxiliary data (satellite type and number, instrumentation and mode), the specific parameters of the imaging instrument (scanning type, scanning angle, etc.) are entered. The orbital parameter data that are necessary for satellite image geolocation are selected from APT mode PREDIKT.NORAD.[1] The time of the first and last lines of the cutout sub-image is registered automatically.

Geographical coordinates of image corners are calculated by solving two spherical triangles *Lc m M* and *Lc M Lm* (Figure 4.1).

An arch a from the ascending node to the determined point M and angle d_i between this arch and the orbit plane are calculated by solving the first triangle. For its solution, it is necessary to calculate the arch W between the ascending node and the sub-satellite point m, by working out the time interval t between the ascending node passage and registration of this line, and then calculating the latitude of this sub-satellite point and the corresponding satellite altitude. The geographic coordinates of the determined point (sub-image corner) are calculated by solving the second spherical triangle *Lc M Lm*. The geographical coordinates of the sub-image corners are recalculated to rectangular coordinates x, y of the basic chart in the stereographic projec-

[1] PREDIKT.NORAD is a tool for satellite orbit parameter prediction.

tion. Then, formation of the photo-chart raster part begins. Each part of the cutout sub-image is transformed separately, but within the general screen coordinates that are common to the entire sub-image.

Step D Resampling image pixels to the photo-chart is performed successively by lines X, beginning with $X_{\min}$. Each line is filled in during one cycle by allocating to each pixel the element value determined by linear interpolation in m (line), n (column) of an equally scaled image. Image transformation is performed separately, but within the general system of screen coordinates. This transformation generates a photo-chart file of the entire image.

Step E The photo-chart is displayed on the computer screen with the coastlines overlaid. The difference between the coordinates of the overlaid coastlines and the shorelines visible on the image is measured. Using these differences, a system of linear correction equations is formed and the coefficients of image corners corrections are calculated. Then, repeated transformation is performed, and finally a raster photo-chart is produced (Figure 4.2).

A single image photo-chart generally includes both cloud-free and cloud-covered areas. Mosaics (called "composite photo-charts") of several cloud-free sub-images of different times can also be made. Using a developed algorithm, all sub-images have

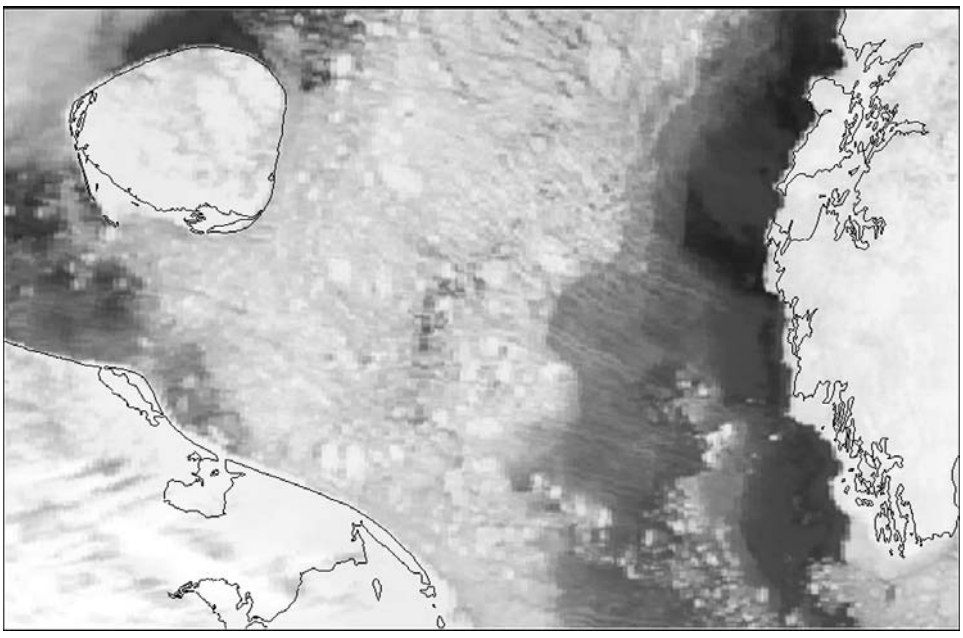

Figure 4.2. Example of a photo-chart from *NOAA* AVHRR (13 May 2004, Barents Sea) after correction of geolocation by the coastline.

undergone preliminary stages of geometric correction, transformation to a common stereographic projection and geolocation.

Single-image or composite photo-charts are used for subsequent analysis and compilation of digital ice charts in the ArcView GIS environment. The ArcView GIS can show raster images together with "shape files" (the format of vector information storage in the ArcView GIS). The photo-charts (raster images) in GIS are shown using geolocation information in so-called "world files". When a photo-chart is generated, a "world file" of geolocation is created simultaneously.

Formation of a photo-chart in Mercator projection

For operational ice navigation support in the NSR, photo-charts are prepared in Mercator projection. This facilitates the preparation procedures for raster satellite images (photo-charts) as an information layer of the electronic navigation chart in the Electronic Chart Display and Information System (ECDIS). A display of the electronic navigation chart and the raster satellite image in the same scale and projection can combine the navigation route and the detailed ice situation.

Ice charts—on which the sea ice characteristics are shown as zones of different ice concentration, ice types and forms—are used to obtain a general understanding of ice conditions and do not provide details for selecting optimal ship routes through the ice. For this purpose the navigator needs a photo-chart, on which the sailing route can be overlaid. It should be in the same projection as the navigation charts (i.e., in Mercator projection), and in real or near-real time (with a delay of no more than 4–6 h). Such navigation photo-charts are generated from AVHRR or MODIS satellite images for limited areas with a size from 200×200 to 500×500 km.

A single-image photo-chart in Mercator projection is used as an additional information layer in the electronic navigation chart, which facilitates the choice of optimal route and increases the safety of navigation through the ice. An example of such a chart is shown in Figure 4.3.

Formation of a composite photo-chart (mosaic)

Ice centers make ice charts of the Eurasian Arctic seas for defined dates with an interval of 5–10 days. However, due to clouds, ice information from optical satellite images cannot be obtained over the entire area at the same time. Therefore, the images received during periods of ice chart preparation are used for formation of composite photo-charts, which present the mosaics of cloud-free areas from several images acquired at different times. A composite photo-chart can be formed both for the entire Arctic and local areas. On their basis, composite digital ice charts are generated.

First, single-image photo-charts are formed from satellite images after their geometric correction, geolocation and transformation to stereographic projection. Then, cloud-free sub-images are chosen and put on a composite photo-chart, supplementing it or substituting zones overlapping with earlier inserted images. A special algorithm has been developed to facilitate this task, which provides cutting an arbitrary form sub-image and inserting it into a composite photo-chart. Figure 4.4

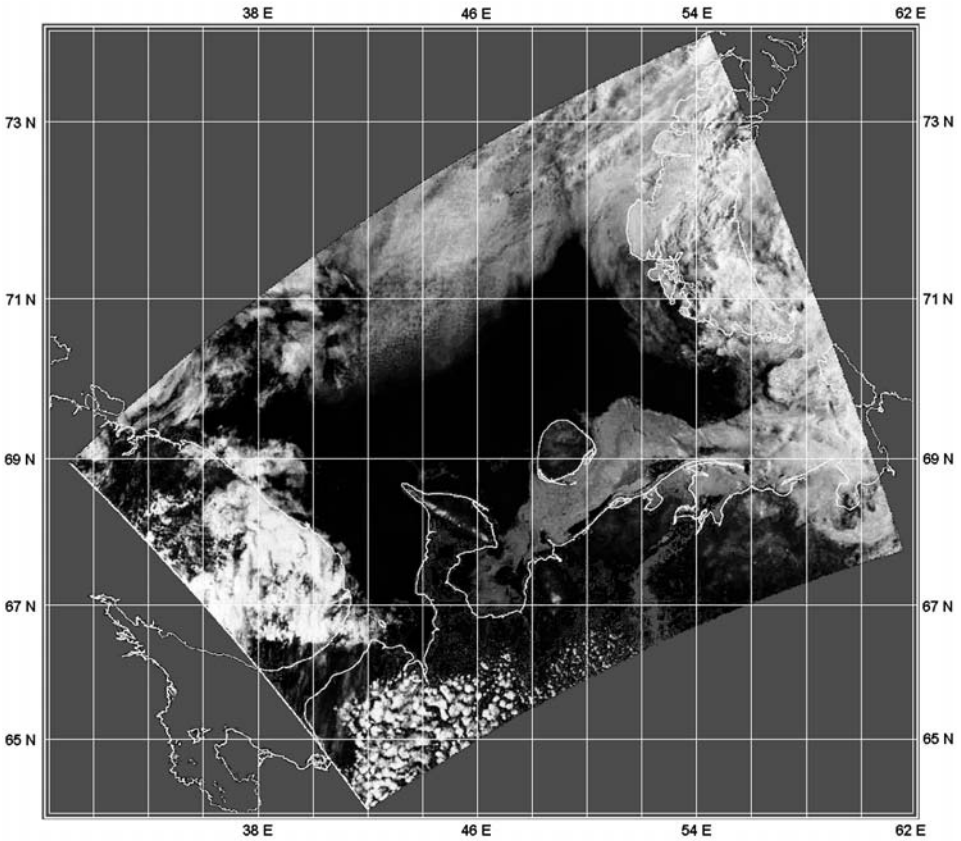

Figure 4.3. Example of a photo-chart from *NOAA* AVHRR (8 June 2002, Barents Sea) in Mercator projection.

presents an example of a composite photo-chart, composed of cloud-free areas cut out from four NOAA images over 3 days.

4.1.3 Interpretation of sea ice types and features

Optical remote sensing methods are indirect, in that the directly sensed parameters are the intensity of emitted or reflected radiation rather than the ice characteristics. The interpretation process translates image brightness values into sea ice characteristics. It includes stages of detection, recognition and interpretation of ice characteristics in the area covered by the image. Detection is simply finding the presence of ice features belonging to a defined ice class—for example, icefloe, lead (discontinuity), etc. Recognition is establishing the quantitative and qualitative characteristics of ice features by revealing relations between the properties of the image and properties of the recognized categories (ice types, icefloe sizes, width of leads, size of icebergs,

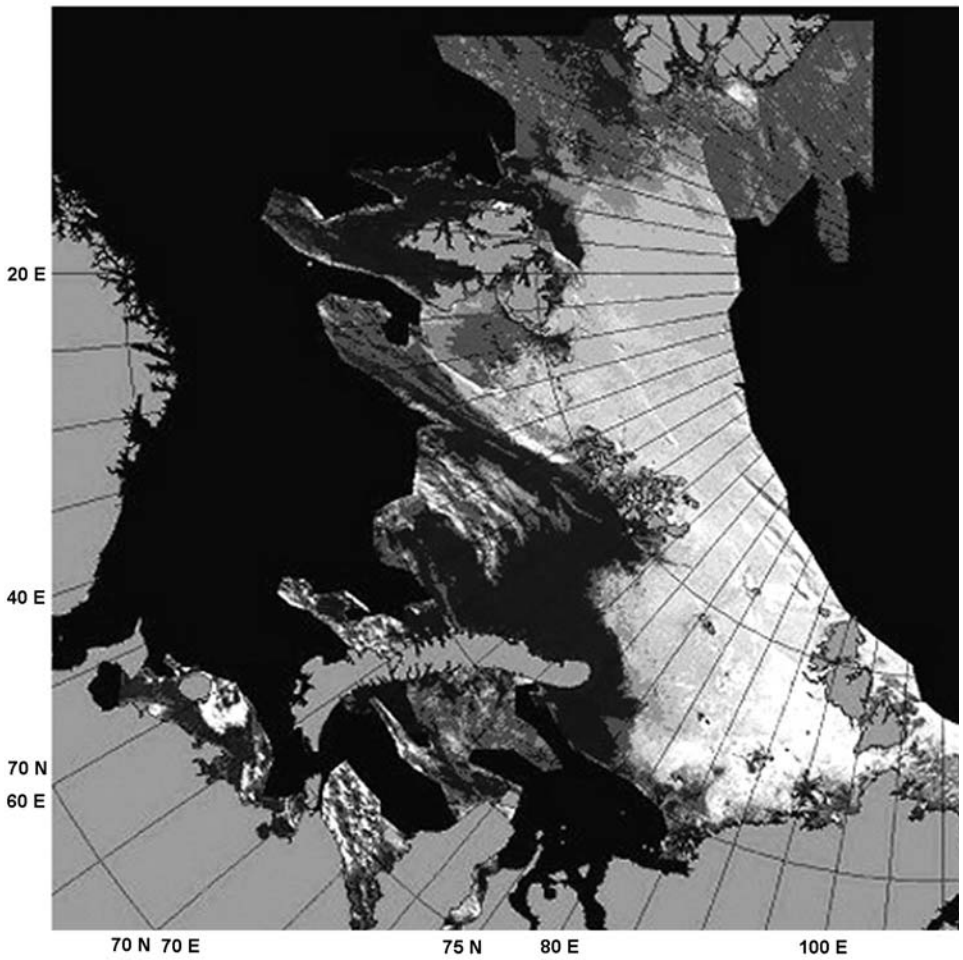

Figure 4.4. Example of a composite photo-chart for 26–28 July 2003 made by four sub-images from *NOAA* AVHRR.

etc.). Interpretation is a generalization of recognition and ascertainment of relationships between individual ice features. The interpretation process includes determination of ice concentration, partial concentration of various ice types and other generalized characteristics.

Several indicators are used for detection and recognition. They are subdivided into: (1) direct (tone, tonal image structure and texture, size and shape); (2) indirect (relation to environmental targets, preceding history of formation and decay); and (3) logical, which usually impose temporal and spatial restrictions—for example, the impossibility of young ice formation in summer. Image tone, which is a function of emitted or reflected radiation intensity, should be considered the main direct indicator.

Sea ice in visible images

In the visible range, the contrast between ice and open water or between ices of different age is determined by their albedo values. The albedo (reflection coefficient) of an ice-free sea surface is a function of the sun's height and sea surface state. The maximum albedo of seawater with moderate waves is about 20% for a sun height of about 10°. For calm seas, an albedo up to 25–30% is possible. With larger waves the maximum value decreases to 13–15%. For sun heights of more than 30°, albedo is just 4–7% (Ivanov, 1979).

Sea ice albedo is generally much higher. Due to a significant seasonal variability, it should be considered separately for the winter period (below-zero air temperatures, absence of melting, formation of young ice) and for the summer period (period of melting). For young ice it depends nonlinearly on ice thickness. The smallest values of 7–9% are observed for dark nilas. Then, it increases rapidly and for gray–white ice (15–30 cm thick) it is equal to 37%, on average. With further ice growth, albedo increase is slower and comprises only 6% for 50 cm thick ice (Grayevsky *et al.*, 1980). A more detailed description of sea ice albedo is given in Lubin and Massom (2006).

Thus, from the tone of the visible image in the winter and spring periods, it is possible to determine approximate ice thickness up to a value of 30–50 cm. For this purpose the size of uniform sea ice areas should be much more than the image pixels—for example, at least 4–5 km for AVHRR (Figure 4.5) and 2–4 km for MODIS images.

For snow-covered and deformed ice, albedo values change. Ice deformation (breakups, rafting and ridging), as well as formation of frost flowers on nilas and gray ice surfaces significantly change the albedo, especially that of youngest ice (Kuznetsov and Timerev, 1972). This complicates determination of ice age.

During the winter and spring, ice with a thickness above 20–30 cm is typically covered with snow. Snow albedo varies from 0.95 for fresh snow to 0.50 for old melting snow with the most typical values in the range 0.75–0.85. In the visible spectrum (0.4–0.7 μm) no significant spectral variation of snow albedo is observed. Its constancy for all ice older than thin first-year ice makes it possible to determine total ice concentration from visible images.

The method for automatic determination of total ice concentration (Bushuev, 1997) includes interactive selection of several separate areas with open water and compact ice. The water and ice brightness values measured are automatically averaged and used in the algorithm as tie-points. Within the selected areas the total ice concentration is calculated in hundredths and displayed. It is rounded to tenths or intermediate values ($\frac{2}{10}$–$\frac{3}{10}$; $\frac{5}{10}$–$\frac{6}{10}$; etc.), and for zones with concentrations less than $\frac{1}{10}$ or within $\frac{9}{10}$–$\frac{10}{10}$, the expert can preserve its value in hundredths. In order to save time, tie-points for water and compact ice can be determined from histograms that are plotted automatically for each area after selection of its boundary.

Before the onset of melting, the brightness of broken and deformed ice is less than that of level floes due to rafting, shades from ice ridges, standing floes and edges. Therefore, if the ice concentration in an area of broken and deformed ice is more than $\frac{7}{10}$–$\frac{8}{10}$, a correction of 5–10% should be applied to the calculated value, or it should be determined interactively using texture indications.

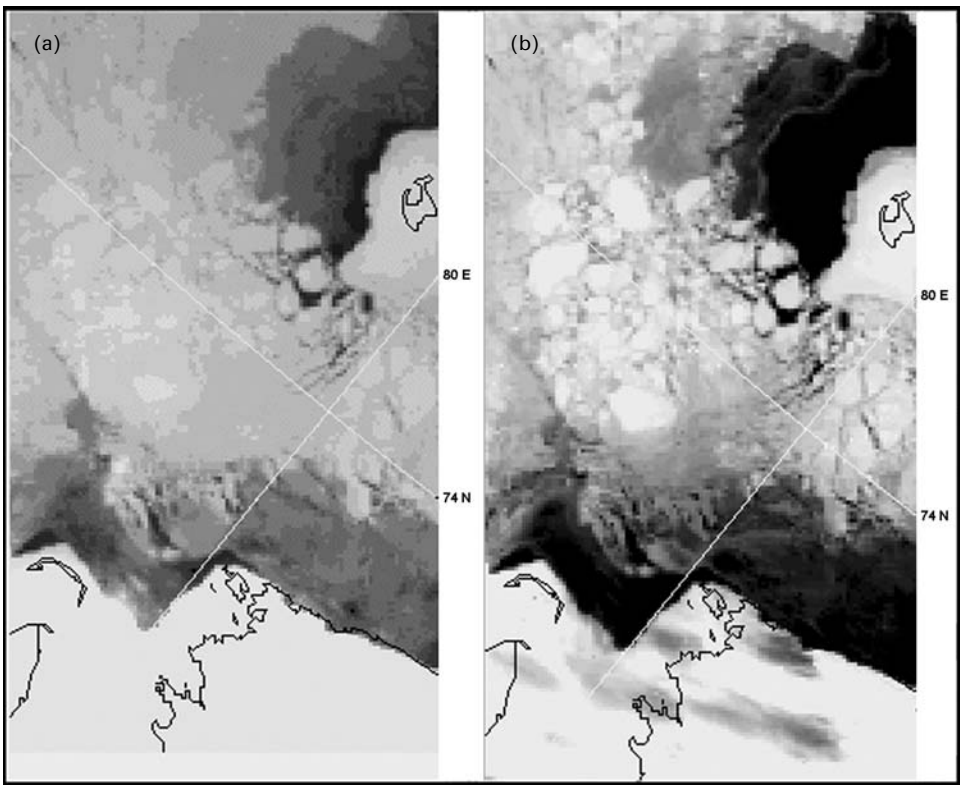

Figure 4.5. *NOAA* AVHRR images from 30 April 1998 of the Kara Sea with sea ice of different age in the IR range, channel 4 (a) and in the visible range, channel 1 (b). Such images are used to estimate the ice concentration.

In winter, an image of compact and very close ice (with concentrations of $\frac{9}{10}$ to $\frac{10}{10}$) has a "matt texture" with a slightly decreased brightness compared with fast ice and big icefloes. A spotty texture is possible when the size of separate icefloes is comparable with image pixels. At concentrations of $\frac{7}{10}$ to $\frac{8}{10}$, darker cells with open water areas usually appear in addition to spots with increased brightness.

The optical properties of snow–ice surfaces significantly change during melting (Shesterikov, 1963). During melting, three main surface types are observed: (1) water puddles; (2) wet first-year ice areas ("blue ice"); and (3) dry areas of multi-year and first-year ice crystalline upper layers with a thickness of several centimeters. Depending on (1) ice age, (2) depth of puddles and the time of their formation, (3) thickness of the crystalline ice layer and (4) other factors, the albedo of each of the three classes can have significant variations (Grenfell and Maykut, 1977). Therefore, visible images are less suited for total ice concentration determination in the summertime.

The albedo change during melting allows approximate assessment of the melting stage. Before the onset of melting, the albedo and brightness of level snow-covered

floes in images is greater than that of broken deformed ice. At the beginning of intense melting, the icefloes are covered with a melt water layer, while water from broken ice flows down and the contrast reverses—the albedo of icefloes becomes less than that of broken ice, indicating onset of the ''flooded ice'' stage. After the drainage of melt water from the floes has occurred, as a result of breakups and the formation of thaw holes, the contrast returns to the original and the stage of melting is determined. The time of onset of these stages can be assumed to be a reference time for calculations of this characteristic by models. It is obvious that—for determining this characteristic—regular observations and analysis of changes in the images of different features are necessary.

It is necessary to note that before the onset of melting the mean albedo of sea ice and its separate typical areas (zones of young and older ice, zones of different total concentrations) in the visible range are spectrally nonvarying. During the melt period, the contrast between dry parts of multi-year and first-year ice and open water significantly decreases with increasing wavelength. In the near-IR band and longer wavelengths, the albedo of all types of puddles and blue ice equals that of open water. Therefore, in images in the range of 0.7–1.1 μm, close ice can be misinterpreted as very open ice or open water. Hence, during the period of intense melting, the use of channels with wavelengths of 0.4–0.6 μm is preferable for determination of ice concentration or age.

Knowledge of the forms of floating ice is important for navigation. Icefloe size can be determined if larger than 2–3 pixels—that is, vast icefloes and big icefloes from AVHRR and MODIS images, respectively. Figure 4.6 shows *NOAA* AVHRR and *Terra* MODIS images on the same day from the Tatar Strait north of Japan. The MODIS image (250-m resolution) contains many more details of the ice cover (flaw polynyas, leads, forms and other ice features) than the AVHRR image, and has an obvious advantage for mapping ice conditions.

The possibility of determining additional characteristics of drifting ice (surface structure, snow cover, presence of mineral or organic material, etc.) completely depends on resolution. At present, for optical range satellite images, it is limited to determination of two melting stages and rafting of large young ice areas.

Fast ice albedo and its change during melting are very similar to that of big icefloes. Fast ice has a typical ''matt image'' texture, which is one of its main indicators. The fast ice boundary is most easily and accurately determined when a flaw lead or polynya is located seaward of it. However, the boundary with the drifting ice is usually identified quite reliably by their different textures and structures (see Figure 4.6).

Detection of leads is quite important for selecting optimal ship routes through the ice. Leads wider than 0.3 pixels, as well as bands of small ice cake and ridging belts, can be identified in optical images. Their width can be estimated when it is more than 2–3 pixels. Note that in some cases leads can be detected more reliably from optical satellite images than from SAR images.

Another important characteristic is ice drift. It can be determined from both visible and IR images. Each displacement vector typically terminates in small icefloes, leads and other easily recognized features. Derived ice drift vectors are used to

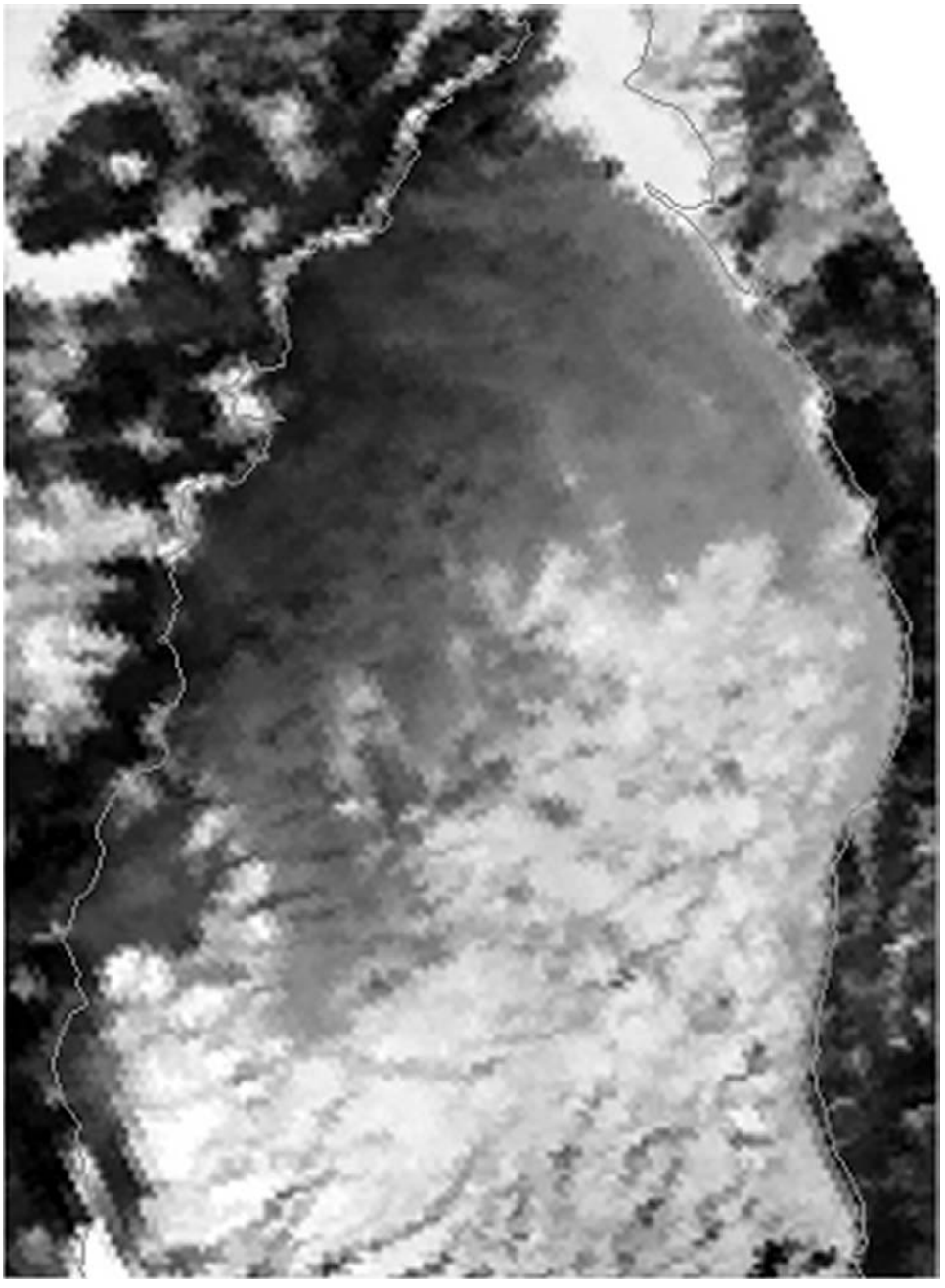

(a)

Figure 4.6(a). Optical images of sea ice in the Tatar Strait on 27 January 2002: *NOAA* AVHRR channel-1 image with resolution of 1 km.

(b)

Figure 4.6(b). Optical images of sea ice in the Tatar Strait on 27 January 2002: *Terra* MODIS channel-1 image with resolution of 250 m.

determine ice pressure areas, to relate ice observations made at one time to another given time, and to study ice dynamics, deformation and transport.

Sea ice in thermal IR images

The possibility to derive sea ice characteristics from satellite IR images is mainly determined by the difference in temperature and emissivity of ice and water surfaces in the thermal IR band: 10.5–12.5 μm. In this band one can neglect atmospheric absorption and assume that the sensor measures radiation emitted by the water, ice or clouds. The radiation power recorded by the radiometer depends both on the temperature and emissivity of the specific surface.

IR emission from sea ice originates in the thin surface layer of ice or snow (Bogorodsky and Martynova, 1978). Ice, snow and seawater have approximately equal emissivity (0.96–0.99), and therefore surface temperature determines the radiation power of all these surfaces. In winter, snow-covered sea ice is an intermediate layer between seawater that has an approximately constant temperature (-1.6 to -1.8°C) and the atmosphere. The air temperature is subjected to significant spatial and temporal fluctuations. It has been shown that under the assumption of a constant air temperature and spatially constant snow and ice thermal characteristics, the measured surface temperature of the water/ice/snow/air system will be determined by ice and snow thicknesses. Mainly, air temperature determines the value of this temperature for a given ice thickness (Doronin, 1964)—see Section 4.4.

For negative air temperatures, the surface temperature of new ice types (grease ice, shuga, slush) is close to that of seawater, thus these ice types are difficult to detect. With increasing ice thickness, its surface temperature decreases and approaches the air temperature for a ice thickness of 100–120 cm. The lower the air temperature, the greater is surface temperature contrast between ice of different thickness. Therefore, identification of areas with different ice thicknesses in IR images is in principle possible (see Section 4.1.4).

As described for visible images, determination of sea ice characteristics from IR images is performed in the same process of interpretation, using direct, indirect and logical indicators.

Accuracy of analysis

A system of indicators has been developed at AARI based on processing and analysis of simultaneous aerial photography, airborne radar surveys and sub-satellite experiments made over many years (Bushuev and Bychenkov, 1978). The possibility and accuracy of determining the main ice characteristics and different ice features from optical satellite images at different resolutions has been assessed (Bushuev, 1997). Retrieval accuracies for different sea ice characteristics from satellites used at present are presented in Table 4.2.

The presented accuracy of location of zone boundaries (which are always blurred to some extent) takes into consideration possible errors in their detection by an ice expert and their mapping as straight line segments. That is why it is larger than the accuracy of satellite image geolocation. Table 4.2 shows that from visible satellite

Table 4.2. Accuracy of sea ice characteristic determination from optical satellite images.

Instrument	AVHRR		MODIS	
Sea ice characteristic	Accuracy (tenths)	Location accuracy (km)	Accuracy (tenths)	Location accuracy (km)
Ice edge with concentration $\geq 1/10$	+	4–5	+	2–3
Fast ice and its boundaries	+	2–3	+	1–2
Total concentration and boundaries of zones with different concentration	0.5*–1.5	5–6	0.2*–0.5	2–3
Forms (partial concentration in main zones and location of some floes):				
Big ice floes	–	–	2–3	1–2
Vast and giant ice floes	2–3	2–3	1–2	1–2
Stages of ice development (age):				
Nilas and young ice	+		+	
Thin first-year	+		+	
Medium first-year and older ice	+			
Sea ice dynamics:				
Drift shear zones	+	2–3	+	1–2
Drift vectors	+	1–2	+	0.5–1
Discontinuities in the ice cover:				
Leads 0.1–0.3 km wide	–	–	+	1–2
Leads 0.3–1.5 km wide	+	2–3	0.5–1	1–2
Leads 1.5–3 km wide and more	1.0	2–3	0.3–0.5	1–2

Note: "+" the characteristic or boundary is detected; "–" the characteristic is not observed; "*" with automatic determination of total concentration.

images one can determine the most important ice characteristics. It is necessary to note that information on ice conditions of sufficient accuracy from optical satellite images can be obtained only if there is no extensive cloud cover in the region under study. On average, 80% of the Arctic Ocean is covered with clouds. It is therefore necessary to receive images from four–five orbits per day in order to obtain information at least once in any 3–5-day period.

4.1.4 Retrieval of sea ice thickness from infrared images

During winter the thermodynamic temperature of the surface of compact sea ice in the Arctic depends on its thickness. This dependence is confirmed by numerous experimental measurements and calculations using thermodynamic models. However, attempts to find a practically acceptable solution to the problem of determining sea ice thickness from satellite IR images were unsuccessful for a long time (Maykut and Untersteiner, 1971; LeSchack, 1974; Gloersen *et al.*, 1975). In recent years, with the development of new models, there has been increased interest in

deriving sea ice thickness from satellite IR images. Yu and Rothrock (1996) developed such an algorithm for up to 80 cm thick sea ice. This section presents the results of the studies and experiments on sea ice thickness determination from *NOAA* AVHRR satellite images in the thermal IR range carried out at AARI from 1979.

Classification of sea ice development stages or derivation of ice thickness from satellite images in the IR spectral range can be implemented for a cloud-free atmosphere. According to the results of experiments and calculations, the temperature of the ice surface decreases with increasing ice thickness, but after 100–120 cm does not depend on its thickness (Paramonov and Chebotareva, 1982). At low air temperatures and low wind, this limit can be reached at 150 cm. For thicker snow-covered ice, differences in ice surface temperature cannot be registered.

The pixel size of the AVHRR IR images used in this study is $\sim 1\,\mathrm{km}^2$. The characteristics of sea ice emission are averaged within each pixel, and the derived ice thickness in the pixel is called "conventional" ice thickness. The definition of "conventional" thickness is omitted in the text below.

Physical model for solution of the problem

At the lower ice surface, the ice temperature is determined by seawater's freezing temperature and can be assumed to be constant. The upper ice surface temperature is determined by heat processes occurring at the interaction of seawater with the atmosphere through the sea ice. It depends on ice thickness and snow depth, thermal conductivity, air temperature and humidity, wind speed, effective emissivity, solar radiation absorption, heat content in the ice strata and a number of other factors and effects (Bogorodsky and Martinova, 1978). Radiation from the ice surface is transferred spaceward through the atmosphere, which transforms it significantly. In theoretical models for calculation of the temperature contrast at its surface, sea ice was presented as a multi-layer medium with different thermal physical properties in each layer and rates of the processes occurring. However, for young and thin ice types, the problem can be simplified. Numerous field data allow considering these ice types as two-layer media with close to linear vertical distribution of ice and snow temperature (Bogorodsky and Gavrilo, 1980).

Thus, the retrieval of ice thickness from satellite IR images in a thermal channel is a problem for many parameters. The optimum solution of such problems contains the definition of several dimensionless parameters and relations between them.

The physical model is developed based on theoretical analysis showing a nonlinear similarity between radiation and true ice thickness fields. It is shown that the numerical values of dimensionless coefficients do not depend on air temperature, effective radiation of the underlying surface and radiation transformations by the atmosphere (Paramonov and Chebotareva, 1982; Bogorodsky and Paramonov, 1984). Based on this model, automatic composition of ice thickness charts (up to thickness values of 100–120 cm) from satellite thermal IR images can be made (Loshchilov and Paramonov, 1997; Lebedev and Paramonov, 1999, 2001; Paramonov and Lebedev, 2004).

For solving the problem, the value of one of the dimensionless parameters—connecting the depth of snow cover and the heat conductivity of snow and ice—is determined using their average values. Coefficients of regression equations for determination of IR image brightness, corresponding to ice of different thicknesses, are calculated. Deviations of sea ice physical characteristics from the average will result in a decrease in ice thickness retrieval accuracy. Therefore, the physical model represents an approximation of the actual relations between ice thickness and radiation fields. The approximation will determine this problem with an accuracy of 70–90% for cloud-free sub-images in any Arctic region, using only one initial meteorological parameter—namely, the wind speed. To increase the accuracy of ice thickness retrieval it is necessary to enter a larger number of meteorological parameters for the study period in the given region, as well as *in situ* ice thickness data.

The physical model is based on the following. The surface temperature of "thick" (more than 1.2 m) snow-covered sea ice (T_2) as measured by a radiometer does not depend on its thickness. The surface temperature of hypothetical sea ice with a zero thickness is equal to seawater's freezing temperature Θ. Therefore, in a function relating ice surface temperature and its thickness there are two boundary conditions, in which the temperature measured does not depend on ice thickness. The intermediate values of sea ice surface temperature are connected to its thickness. For a two-layer medium the heat conductivity equations can be solved in integrated form. A solution can also be found for a multi-layer medium.

Model calculations are based on solving the heat balance equation for a snow-covered ice surface subject to heat flux continuity. The use of final increments and analysis of all components results in an expression for surface temperature T_0 of sea ice as follows (Bogorodsky *et al.*, 1978; Bogorodsky and Paramonov, 1984, 1985):

$$T_0 = \frac{t_p}{\lambda + k * t_p} * \left(\frac{\lambda * \Theta}{t_p} + k * T_a - I_{ef} + I' \right) \tag{4.1}$$

where t_p is snow-covered ice thickness transformed to bare ice thickness; λ is ice heat conductivity; k is the heat exchange coefficient of the ice surface and the atmosphere; Θ is seawater's freezing temperature; T_a is air temperature; I_{ef} is effective emissivity of the ice surface; and I' is solar radiation absorbed in the upper centimeter of the snow or ice layer.

In expression (4.1) the thickness of snow-covered sea ice is transformed to the corresponding bare ice thickness t_p, which is a virtual value. Since the heat conductivity of snow is much less than that of ice, the value of t_p exceeds both the true ice thickness t_E and the snow-covered ice thickness. For transition from the transformed ice thickness to the true, a dimensionless parameter ξ is defined, connecting the ratios of heat conductivities and thicknesses of snow and sea ice:

$$\xi = \frac{\lambda_s/\lambda}{\lambda_s/\lambda + t_s/t_E} \tag{4.2}$$

where λ_s, t_s are snow heat conductivity and snow cover depth; λ, t_E are ice heat conductivity and thickness (statistical data). This coefficient is used in the paper by

Poulin, 1975). The physical meaning of this parameter is attenuation of the heat flux through the ice due to the presence of snow.

Further, a dimensionless parameter Ψ is defined:

$$\Psi = \frac{T_0 - \Theta}{T_2 - \Theta} \tag{4.3}$$

where T_2 is the surface temperature of "thick" ice.

Parameter Ψ can be calculated from satellite measurements of sea ice surface temperature, and also by use of empirical expressions for T_0 and T_2 from initial meteorological parameters:

$$\Psi = \frac{k * t_p}{\lambda + k * t_p} * \frac{k * (T_a - \Theta) - I_{ef}}{k * (T_a - \Theta) - I_2} \tag{4.4}$$

The dimensionless parameter Ψ has only a small dependence on air temperature and effective surface emissivity. The measured values of ice and water surface temperatures are close to the maximum of the Planck radiation curve, and therefore reside on a flat part of the curve. Therefore, factor Ψ is weakly dependent on atmosphere, which transforms radiation. Factor Ψ characterizes sea ice temperature or the corresponding radiation. Under identical conditions, each Ψ value corresponds to a defined ice thickness. Therefore, radiation corresponds to that of true ice thickness. This connection is nonlinear. In the model, factor Ψ is called a nonlinear "similarity coefficient" between sea ice thickness and surface temperature.

Using the dimensionless parameter ξ, factor Ψ is unambiguously connected with the true snow-covered sea ice thickness at a known wind speed. The value of parameter ξ is chosen by mean statistical values. However, if the true sea ice thickness is known, factor Ψ is unambiguously connected with the value of ξ—that is, with the ratio of thermal physical characteristics.

The expression of factor Ψ using the surface ice temperature in equation (4.3) is inconvenient. In order to avoid additional errors in determining sea ice surface temperature, a dimensionless parameter β, similar to factor Ψ, is defined:

$$\beta = \frac{\alpha_0 - \alpha_w}{\alpha_2 - \alpha_w} \tag{4.5}$$

where α_0 is brightness of the pixel for which ice thickness is determined; α_w is brightness of the pixel corresponding to seawater at freezing temperature; and α_2 is brightness of the pixel corresponding to thick, snow-covered ice.

This parameter is similar to factor Ψ, but temperature characteristics are replaced by radiation power—that is, by the energy which is assumed to correspond to the brightness of IR image pixels. Correction of the absolute error due to replacement of factor Ψ by factor β is made by substituting the calculated coefficients in the model equations. As a result, calculation error decreases to 1–2% over the entire range of the determined ice thickness. Calculation of correction coefficients was performed in the following order. The absolute errors of calculations as a result of replacing factor Ψ by factor β were computed in five ranges of air temperature changes from 0°C to −50°C. Hence, the calculations and conclusions made with respect to factor Ψ are also valid

for the dimensionless parameter β. Factor β does not depend on air temperature and effective emissivity, nor on the transmission of a uniform atmospheric layer. Factor β can be called a nonlinear "similarity coefficient" between actual sea ice thickness and satellite IR image brightness (power) (Lebedev and Paramonov, 1999), and thus can be of real use in determining ice thickness from satellite IR images.

The algorithm

In accordance with the *WMO Sea Ice Nomenclature* (1989), sea ice thickness boundaries define the stages of ice development. An arbitrary value for the ice thickness interval can be used in the model algorithm (Paramonov and Lebedev, 2004). The algorithm can be made in two different ways. It is possible to use the IR image of sea ice to calculate β and then the ice thickness.

However, it is more convenient to do it in a different way. It is possible to calculate factor β values by defining ice thickness intervals and the corresponding average snow depth, ice and snow heat conductivity and actual surface wind speed. The next step is calculation of brightness boundary values corresponding to open water and thick ice in the IR image. Then, a histogram of the selected sub-image is analyzed. In sea ice, fractures and leads with open water are constantly formed. These areas have the minimum brightness of the histogram, the values of which are entered into the algorithm. The brightness of "thick" ice ($>$120 cm) is also determined from test image areas.

Then, the regression equations relating the statistically determined entry parameters for discrete ice thickness values and the corresponding image brightness are solved. Calculation results are used for conventional coloring of determined ice thickness ranges, according to pre-defined palette colors.

The algorithm includes some preliminary interactive procedures, such as visual analysis of the image in different spectral channels, delineation of cloud-free zones and also analysis of surface wind speed data from coastal meteorological stations. Usually, image brightness is calculated for eight ice thickness intervals, ranging from $<$0.05 to $>$1.20 m.

The resulting color map shows zones with different ice thicknesses—that is, sea ice thickness distribution. Usually, zones are clearly identified by their color. Two types of uniform ice zone boundary segmentation can be used for sea ice mapping. First, zones with an approximately uniform distribution of thickest ice spots are segmented. Within the segment boundary, partial ice concentration for up to three dominating thickness intervals is determined visually. In this variant, a traditional method of analysis and interpretation is done. Mapping of ice zones is performed in interactive mode and supported by a special software module in the ArcView GIS environment.

The second variant uses a median filter with a mask size that depends on the level of detail in the processed image, and the permissible generalization of ice zone boundaries. The filter removes all small spots of size less than half the filter mask. Mapping is performed in interactive mode with only one dominant ice thickness class within the boundaries of each segment. Thus, small spots of secondary classes are eliminated by the median filter.

The classified image will show the ice thickness distribution as a color map and can be used as an ice photo-chart (e.g., for ice navigation). Also, some editing, which leads to further generalization of the resulting ice chart—is used.

Examples of sea ice thickness retrieval from IR images

Mapping sea ice thickness is possible only in the complete absence of cloud cover, and only during the cold period of the year. There are no statistics on the frequency and regions of the Eurasian Arctic seas where such favorable conditions occur. However, even infrequently obtained data on the spatial distribution of sea ice thickness for larger or smaller sea regions are of great interest for sea ice monitoring. The retrieval of ice thickness from IR images presents a unique capability in addition to other methods of ice thickness measurements. Two examples of ice thickness retrieval from IR images and its comparison with ice thickness measurements at coastal stations are presented below.

Example 1 Figure 4.7 presents an example of ice thickness retrieval from an IR image of the southeastern Barents Sea. Segmentation of uniform zones and estimation of partial concentration of different ice thickness grades within them were performed visually by an expert. The ice thickness data thus derived from the IR image were then compared with ground measurements of ice thickness made at coastal meteorological stations and from ships. All these measurements together with the meteorological data are presented in Table 4.3. Although the ice thickness measured at coastal stations near the shore may not correspond to the ice thickness in the open sea, this is the best control method so far. As can be seen from Table 4.3, ground measurements are in good agreement with ice thickness estimates from the IR image.

Example 2 Figure 4.8 presents a chart of the spatial ice thickness distribution in the Kara Sea in mid-winter. It was based on ice thickness derived from the IR image of the *NOAA-14* satellite for 8 January 1997. The boundaries of relatively large zones of uniform or prevailing ice thickness are segmented automatically. Within these zones, the small spots of thicker or thinner ice have been filtered out. This chart shows the spatial distribution of thin and medium first-year ice in the Kara Sea. This information is difficult to get from analysis of images in the visual and microwave ranges.

Table 4.4 presents near-simultaneous ice thickness measurements made at coastal meteorological stations. As can be seen from this table, these ice thickness measurements agree quite well with the ice thickness estimates from the IR image.

Analysis of the chart shows the ice formation over this area in early winter. It shows that ice thickness increases eastward. The elongated zones of relatively thinner ice near the islands are indicators of ice motion direction during the preceding period. Old ice prevails within the zones of thick ice (more than 120 cm thick) in the eastern part of the Kara Sea.

This method for automated sea ice thickness retrieval from IR images has been tested for many other cases. It has been applied to the Arctic, to some regions of the

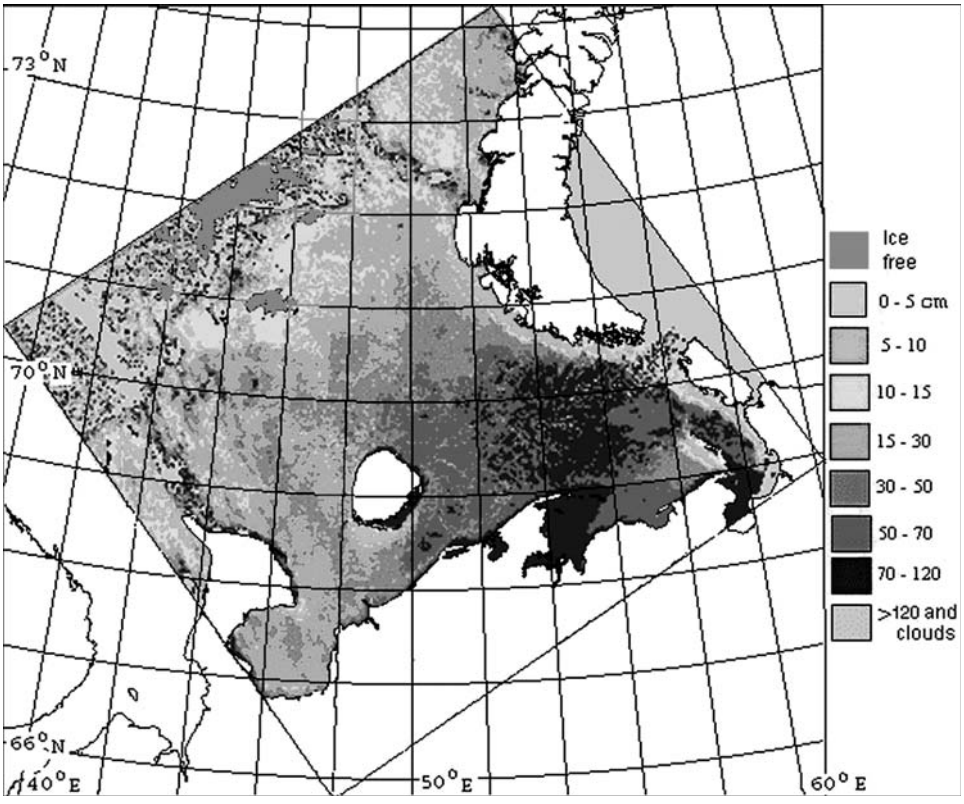

Figure 4.7. Example of ice thickness in the Barents Sea derived from *NOAA* AVHRR IR image (channel 4) taken on 4 May 2001 at 08:20 GMT (see also color section).

Table 4.3. Comparison of sea ice thickness determined from the IR image shown in Figure 4.7 with its measurement at coastal stations and onboard ships (31 March 2001).

Meteorological station and from latitude/longitude	Air temperature (°C)	Windspeed (m/s)	Ice thickness measured (cm)	Ice thickness derived IR image (cm)
Kolguev Island (north) 69°30′N/49°08′E	−16.9	4.0	120	70–120
Bugrino, (Kolguev Island, south) 68°48′N/49°20′E	−14.7	8.0	81	70–120
Cape Konstantinovsky 68°33′N/55°30′E	−16.5	3.0	102	70–120
Shipborne data, 69°26′N/57°35′E	−12.0	3.0	30	50–70

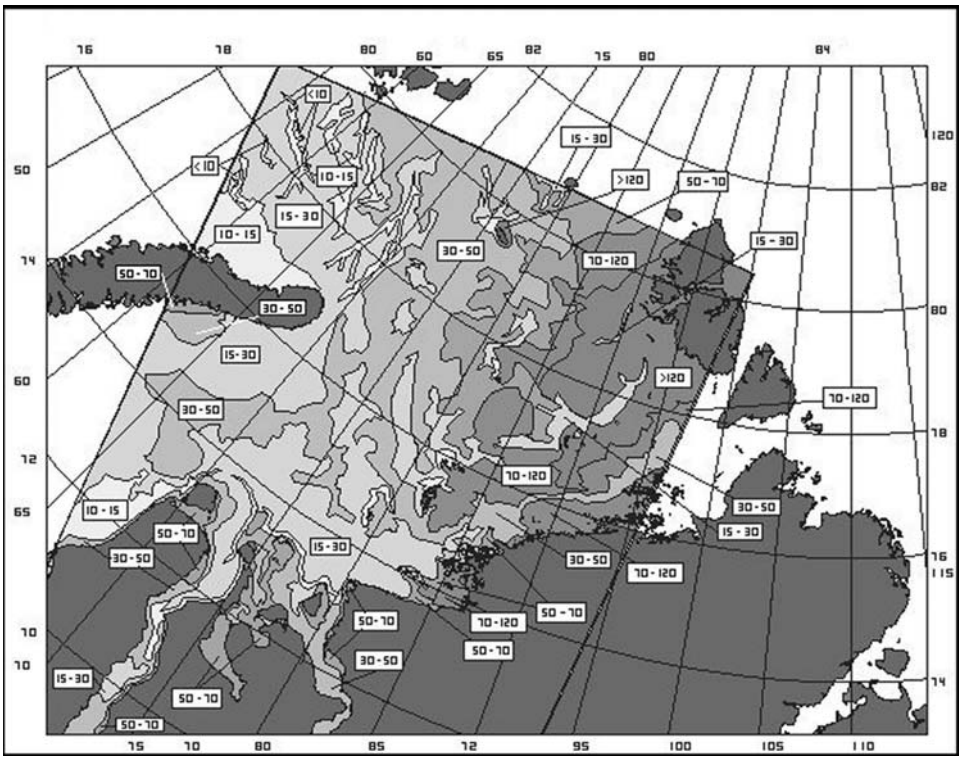

Figure 4.8. Chart of ice thickness (in cm) spatial distribution in the Kara Sea derived from *NOAA* AVHRR IR imagery on 8 January 1997 at 08:29 GMT.

Southern Ocean and to some marginal seas—in particular, the Tatar Strait. The data from *in situ* ice thickness measurements from ships, icebreakers and coastal meteorological stations confirm derived estimates in 70–90% of the cases. Hence, in spite of assumptions made in the physical model and using unknown meteorological parameters, it is reasonable to use the method for practical purposes.

It is especially efficient to use ice thickness data derived from IR images together with mapping of ice conditions from satellite high-resolution SAR images. In the wintertime, the combined analysis of these images avoids coarse errors in interpretation of sea ice in SAR images.

4.2 RADAR IMAGING
(*S. Sandven, O.M. Johannessen, K. Kloster, V.Yu. Alexandrov*)

Remote sensing by imaging radar systems on aircraft and satellites is the most important method of observing sea ice on a regional scale independent of cloud cover and daylight conditions. The radar systems used for sea ice observation are:

Table 4.4. Comparison of sea ice thicknesses determined from the IR image in Figure 4.8 with those measured at coastal stations on 31 December 1996. Data on air temperature and windspeed are for 7 January 1997 at 06:00 GMT.

Meteorological station and latitude/longitude	Air temperature (°C)	Windspeed (m/s)	Ice thickness measured (cm)	Ice thickness derived from IR image (cm)
Vize Island, 79°30′N/76°59′E	−38.0	0	82	70–120
Isvestiy Ts.I.K. Island, 75°58′N/82°58′E	−40.0	2.0	85	70–120
Dikson Island, 73°30′N/80°24′E	−39.1	5.0	62	30–50
Vilkitskiy Island, 73°30′N/75°40′E	−36.1	2.5	58	50–70
Golomyannyy Island, 79°31′N/91°02′E	−46.7	2.5	120	>120
Cape Sterligova, 75°25′N/88°40′E	−42.6	2.5	101	50–70
Amderma, 69°46′N/61°41′E	−32.6	5.0	50	15–30
Khabarovo, 69°40′N/60°20′E	−33.2	5.0	44	30–50
Sop. Karga, 71°53′N/82°43′E	−38.9	2.5	108	30–50
Marre-Sale, 69°42′N/66°40′E	−32.9	2.5	55	15–30
Kharasavey, 71°08′N/66°48′E	−39.6	2.5	41	30–50

(1) synthetic aperture radar (SAR);
(2) side-looking real aperture radar (SLR); and
(3) scatterometers.

The former two are described in more detail in this section, because they have been and are extensively used in the NSR. Use of scatterometer data for ice monitoring has been developed over the last decade for monitoring the whole Arctic and Antarctic, but not specifically used in the NSR

Imaging radar instruments provide their own source of illumination in the microwave range of the EM spectrum, at wavelengths on the order of 10,000 times longer than those in the visible spectrum. Because of this, radar instruments can operate independent of solar illumination and the long radar waves can penetrate

clouds and precipitation. This is particularly important for sea ice monitoring in the polar regions where cloud, fog and darkness significantly limit the use of visible and IR data. Imaging radar emits energy in the form of EM waves, which strike an object causing some of them to be reflected back to the radar sensor, where the amplitude and phase of reflected waves are registered as well as the return travel time. Radar images have many specific properties making them different from visible and infrared images. These include:

- radar images are sensitive to surface roughness;
- radar detects the moisture and dielectric properties of the surface, as given by its complex dielectric constant;
- radar systems use polarized signals, and the polarization dependence of the reflected microwave pulse can be measured;
- SAR images have speckle noise due to the coherent nature of radar systems;
- radar images have certain geometrical distortions in range, such as image layover and shadowing;
- SAR images are sensitive to the motion of objects in the azimuth direction.

4.2.1 Imaging radar systems

The major difference between SLR and SAR is based on the fact that SAR uses a coherent detection process, whereas real-aperture radar uses an incoherent process (Ulaby *et al.*, 1981). Satellite SAR has an advantage over SLR in that its azimuth resolution is much better that that for SLR. Additionally, the radiometric accuracy of SAR data can be more closely controlled, making calibration easier (Bertoia *et al.*, 1998). Since SAR images are the most important for observing sea ice on regional and local scales, the most common properties and parameters of SAR systems are described in the following sections.

Important parameters and properties

The overall geometry of the SAR system is shown in Figure 4.9. SAR can look to the left or to the right of the orbit, covering an area on the Earth surface well away from *nadir* (which is the ground projection of the satellite orbit). The two main directions are called *azimuth* (along the satellite orbit) and *range* (the look direction of SAR perpendicular to the azimuth/orbit). Slant range is along the line from satellite to ground, while ground range (often only called "range") is on the ground from the nadir line. Measurements of the travel time of the reflected microwaves are converted to the slant range distance:

$$R = \frac{c\tau}{2} \tag{4.6}$$

where c is the speed of light and τ is the travel time. Ground range is used in processed images and defines the location of an object in the ground- or across-track direction.

The resolution of a radar system is defined as the minimum distance between two point targets that can be observed as separate bright spots in the image. The azimuth

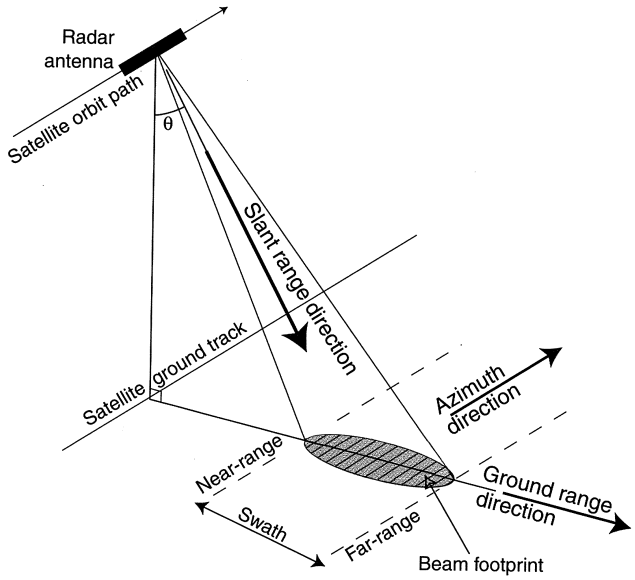

Figure 4.9. The geometry of the satellite SAR system (from Robinson, 2004).

resolution of an SLR system is much lower than that of SAR. For SLR, azimuth resolution is proportional to the beam width β of the radar, which is the angle by which the radar beam expands, defined as a function of signal frequency λ and antenna length L:

$$\beta = \frac{\lambda}{L} \tag{4.7a}$$

Along-track or azimuth resolution r_a is roughly given as:

$$r_a = R\beta \tag{4.7b}$$

This value is of the order of kilometers for satellite systems. The beam width of radar is a function of antenna length, with larger antennas producing a narrower beam. To obtain a high azimuth resolution for SLR, one must use either a very short range or a very large antenna. SAR uses the along-track motion of the satellite to simulate the data that would have been collected by a much longer antenna. SAR records both the magnitude and phase of the signal backscattered for the length of time it takes the satellite to move in its orbit. To form an image in the azimuth direction, these complex-valued signals are summed coherently with an appropriate phase shift, to simulate what an antenna would generate if it were large enough in the azimuth direction to receive all of these responses simultaneously (called the ''synthetic length'' of the antenna). This results in azimuth resolution (Wackerman, 1992):

$$r_a = \frac{L}{2} \tag{4.8}$$

Figure 4.5. Symbols for electromagnetic wavelength bands used in radar remote sensing.

Symbol of band	Wavelength (cm)	Frequency (GHz)
P or UHF	30–100	0.3–1.0
L	15–30	1.0–2.0
S	7.5–15	2.0–4.0
C	3.75–7.5	4.0–8.0
X	2.4–3.75	8.0–12.5
Ku	1.67–2.4	12.5–18.0
K	1.13–1.67	18.0–26.5
Ka	0.75–1.13	26.5–40.0
Mm	0.75	40.0

where L is the length of the antenna (i.e., its physical dimension), and thus r_a can be of the order of 10 m.

The slant range resolution r_r of both radar systems SLR or SAR is:

$$r_r = \frac{ct_p}{2} \tag{4.9}$$

where t_p is the duration of the transmitted radar pulse. This resolution is the minimum slant distance necessary between two objects for them to be separated.

Imaging radar instruments operate at microwave frequencies between approximately 400 MHz and 35.2 GHz, corresponding to wavelengths between 62 and 0.85 cm. The frequency bands are identified by symbols as shown in Table 4.5. For all but the shortest wavelengths, clouds and precipitation have no effect on wave propagation through the atmosphere. Therefore, good-quality radar images can be obtained during different weather and light conditions. For almost all current satellite systems, only one frequency (C-band, 5.6 cm) is in use. To obtain more than one channel for SAR imagery, different polarizations are in use.

Another characteristic of imaging radar systems is polarization, which is defined as the direction of the electric vector of an EM wave. The electric vector is transverse to the direction in which EM energy is transmitted. Sunlight is nonpolarized because the direction of the electric vector is randomly distributed. Radar systems emit pulses, which are either horizontally (H) or vertically (V) polarized. Radar antenna can receive either horizontally or vertically oriented return signals, or both. Until recently, only single-polarization, VV (*ERS-1/2* SAR) or HH (*Radarsat*) images were available from satellites. *Envisat* ASAR has the possibility to transmit and receive two polarizations at the same time, resulting in two images with different polarizations—for example, HH and HV (two-channel imagery). In addition, it can record simultaneous like-polarizations VV and HH. This opens up the possibility of using channel combination algorithms for retrieval of sea ice parameters.

The incidence angle—that is, the angle vertical to incident radiation–is an important variable in all SAR images. It is closely related to the ground range

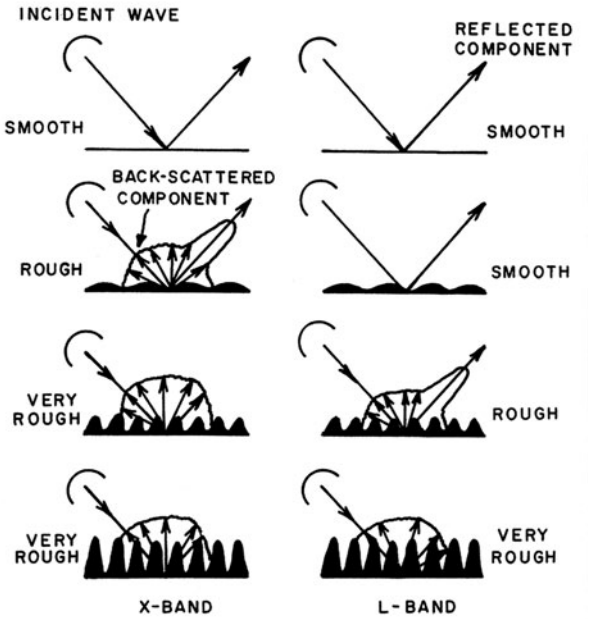

Figure 4.10. Scattering of electromagnetic waves of different bands from smooth, rough and very rough surfaces: high-frequency band (left) and low-frequency band (right) (from Onstott and Shuchman, 2004).

dimension of the image; for every range there is a corresponding incidence angle. The relation is given geometrically by the height of the satellite and the curvature of the Earth. The incidence angle may have a large variation (20–50°) if the imagery is wide-swath. It is also large variation of the mid-beam angle in many narrow-swath images. These swaths are selected from the several so-called "antenna beams" available, taken with different orientations (look-angles) of the antenna, θ in Figure 4.9. These beams are electronically steered to cover the desired swath position from the nadir line. While *ERS* only has one narrow-swath beam (100 km wide, 23° mid-beam angle, both *Radarsat* and *Envisat* have a choice of seven narrow-swath beams (60–100 km wide), each with a different swath position and corresponding mid-beam incidence angle.

In contrast to visible and infrared remote-sensing sensors, imaging radars are very sensitive to surface roughness. For very smooth surfaces, there is an almost specular reflection of the radar waves, and very little energy is reflected back to the radar. If the surface is very rough—roughness is given relative to the radar wavelength (i.e., 5–6 cm for C-band)—the radar wavelengths interact with the surface in a way that can be compared with a diffuse Lambertian surface at optical wavelengths, and thus a fraction of the transmitted energy is reflected towards the radar (Figure 4.10). The amount of roughness controls to a large extent the distribution of reflected energy and, thus, radar image intensity.

The wavelength λ and incidence angle q_1 of a radar wave determine roughness.

A surface is called "rough", if the following criterion is met:

$$\Delta h \cos q_1 > \frac{\lambda}{8} \tag{4.10}$$

where Δh is the vertical scale of surface roughness.

The basic radar equation and SAR signal processing

The measured signals need considerable processing before the result can be made available as an image product. A SAR product's basic coordinate system is equal time (in slant range direction) and equal Doppler (in azimuth direction). Most pre-processors convert from slant range to the more practical *ground range* along the Earth's surface, assuming the Earth as an ellipsoid. For surfaces with steep slopes, such as mountainous areas, radar causes several imaging artifacts (referred to as "layover" and "shadowing"). These are of little concern for sea ice imagery.

The received power P_R is given by the basic radar equation, which relates transmitted power, distance, target reflectivity and antenna characteristics:

$$P_R = \frac{P_t}{4\pi R^2} G \frac{\sigma}{4\pi R^2} A \tag{4.11}$$

where P_t is transmitted power, R is distance between the surface and the antenna, G is gain of the antenna, σ is target radar cross-section and A is antenna area.

The flux of a spherically outward propagating wave is given by the first term on the right-hand side of equation (4.11). Power is focused by the antenna such that in the desired direction it is greater by a factor of G—the second term in (4.11)—relative to that of a spherically expanding wave. The focused flux is backscattered by an object, which has a cross-section σ defined as the equivalent area of a perfectly isotropically reflecting object. The flux is reflected back as given by the third term in (4.11). Finally, the reflected flux hits the antenna area A—the fourth term in (4.11)—so that the product of the four terms produces the power received by the antenna.

In the basic radar equation, σ is defined as the area (m^2) of a discrete object. For imagery of extended surfaces, a reflection coefficient is defined called a "normalized radar cross-section" or "backscatter coefficient", σ^0. This is the radar cross-section σ per unit surface area. σ^0 is a dimensionless number and is a measure of the scattering behavior of extended surfaces. It is a function of radar frequency, incidence angle and polarization. It defines the scattering characteristics of the surface. It is unity for a surface of small metal spheres which exhibit ideal diffuse scattering (nonvarying with incidence angle). The backscatter coefficient for a typical sea ice surface is generally much smaller than unity at the most used incidence angles (20–50°). σ^0 is more often expressed in dB (that is $10 \log \sigma^0$), and for sea ice surfaces the range is from about -4 dB to -25 dB. It expresses the radar backscatter property of a given surface and can be used to compare the surfaces observed by different radar systems.

The σ^0 value for a given surface is influenced both by small-scale and large-scale geometric surface properties (relative to wavelength). The small-scale inhomogeneity in semi-transparent materials such as ice will strongly influence scattering in various directions. The large-scale geometry of semi-reflecting objects will also influence

backscatter, since the local incidence angle has a large effect on backscattered reflection.

Also important is the complex *dielectric constant* of the various materials (snow, sea ice and water), which define the reflection and absorption details of the radar EM wave for the given material. Note especially that when ice is formed from seawater, the salt content in the ice may have a large effect on the backscatter signal.

Noise and spatial resolution properties

A SAR image with the highest possible spatial resolution (using the full length of the synthetic antenna) is very noisy, due to the coherent vector summation of signals from individual scatterers in the resolution area. This radar noise is often referred to as *speckle noise*. The standard noise filtering method is to split the antenna length and to average the independent measures of these sub-lengths ("looks"). Also, averaging of pixels is used. But, this will at the same time degrade the spatial resolution. The standard deviation of the signal is reduced proportional to the inverse square root of the number of averaged measurements. This number is called the *effective number of looks*. The standard deviation of a single-look image signal is about 3 dB. This is very large, and actually comparable with its mean value. However, a single-look image has the best possible resolution, but very good feature contrast is required if this is to be used.

Averaging in azimuth using several looks is often done during the pre-processing stage, in order to reduce the standard deviation of σ^0 caused by speckle noise. If three azimuth looks are used (e.g., for the *ERS* PRI product), the resulting noise will be about ± 2 dB or about one-half of the signal mean value. At the same time, azimuth spatial resolution is also degraded by a factor of 3 (e.g., from 8 m to 25 m).

Subsequent pixel averaging in both range and azimuth is often used, mainly for two purposes: (1) to achieve a lower noise; and (2) to get a smaller image data file. This results in larger pixel size and lower resolution. Averaging an ERS PRI image to about 40 effective looks will typically give an image with a speckle noise of ± 0.6 dB (about one-fifth the signal mean value), and with a pixel size of 100 m in each direction.

4.2.2 Signal calibration, corrections and adjustment

Calibration

In order to enable comparison of the surfaces measured with the radar system and to make quantitative image interpretation of surface type, a SAR image needs to be calibrated. Radar image data are generally given as pixel values within a given range of digital values (usually 8- or 16-bit). In the process of calibration these digital values are transformed to values related to the backscatter of any given surface. They must always be given with three parameters: (1) radar frequency; (2) radar polarization; and (3) incidence angle.

Radar images can be calibrated relatively or absolutely. Relative calibration accounts for changes in radar system parameters—such as gain drift in ampli-

fiers—and provides all the information needed for studies of temporal and spatial variations of the surfaces, as long as the same system is used for all the measurements (Ulaby *et al.*, 1981). Determination of relative scattering coefficients is possible when internal calibration of the radar system is done. In this case the mathematical form of the conversion equation is known. This means that the ratio of the various σ^0 values can be found, but not their individual values. With relative calibration it is impossible to express the output in terms of the scattering coefficient.

For many applications, it is desired to convert pixel values to σ^0 values (i.e., to calibrate the SAR image absolutely). Absolute calibration must also take into account biases and the absolute gain of the antenna and receiver. To obtain σ^0 values the numerical parameters of the conversion equation must also be given and their determination may be done after external calibration of radar using known targets on the ground as references. Absolute calibration allows implementation of accurate measurements needed to compare the results from different systems. If a radar image is calibrated, the primary limiting factor in the precision of the overall measurements is the number of independent looks—that is, the speckle noise (Ulaby *et al.*, 1981). Images without a reliable given equation are uncalibrated, and here only qualitative and relative interpretation of surface type can be made.

Range corrections

For an image to be calibrated, it is thus required that a reliable and stable relation (a conversion formula) exists between the pixel value and the backscatter coefficient σ^0. It can usually be assumed that the conversion formula is nonvarying in the image azimuth direction, but not in the range (ground range) direction. The signal output by the satellite is as a rule affected by three major effects that cause the signal to vary in range direction and thus should be corrected (e.g., to a mid-range value). These are:

(1) Antenna gain—that is, efficiency in the transmitting and receiving of signals. It is a function of the instrument look-angle, as measured from nadir to the direction of the radiation, with a maximum in the boresight direction and decreasing to either side. Knowledge of the gain profile of the antenna lobes that cover the swath (several overlapping lobes are in use for ScanSAR) is required. Correction of this effect is generally included in the pre-processing of images; this is G in equation (4.11).
(2) The distance from the satellite to the target—that is, the slant range—varies within the swath. The signal strength varies as the inverse of the cube of the slant range distance, and must be corrected. Correction of this effect is also generally included in the pre-processing of images; this is R in equation (4.11).
(3) Signals are measured in the slant range direction while images are presented in the ground range direction. This introduces a third effect on the signal: the requirement to multiply the processed signal by the sine of the incidence angle to get the corrected σ^0 value. This requires knowledge of the incidence angle for every pixel. Since images are generally pre-processed for many applications—including land where the incidence angle can have large local variation—

correction of this effect is generally not included in the pre-processing of images. However, in the case of horizontal surfaces of sea ice and water, this correction is easy to apply as it only varies with incidence angle and is easily computed from the satellite geometry.

It is important to know which of the three corrections above have been applied to the received image values (usually the first two). The term "backscatter brightness" is sometimes used for images that have not been corrected by the third factor, the sine of the local incidence angle.

For very low σ^0, the internal electrical noise of the instrument must also be subtracted from the pixel values to get the correct σ^0. This is the so-called "noise-floor" of the image and will determine the lowest backscatter that it is possible to measure. In addition, it is generally a range varying value, usually between approximately -22 dB and -26 dB. If backscatter is very high and approaching 0 dB, other effects (e.g., quantization of unprocessed signals) may also introduce errors if not corrected; these, however, usually have no serious effect on standard sea ice imagery.

The form of the conversion equation between the pixel value and σ^0 varies between the various processing centers that undertake pre-processing, from the instrument raw signal to the digital image. An equation often used is to present the pixel values as the square root of backscatter brightness divided by a suitable constant called the "calibration constant". This square-root signal is also called "voltage" (since the power in the backscatter signal is proportional to voltage squared in electric systems). Such coding of values helps to minimize the range of pixel values required to represent σ^0 over its full range of possible values. This latter range is easily several powers of 10—for example, from 0 dB (near-range windy water) to -26 dB (noise-floor of *ERS*).

Images from different processing centers have different calibration constants. For *ERS-1/2* SAR in PRI format processed at ESA PAFs,[2] the values are approximately 58 dB and 60 dB, respectively (Laur *et al.*, 1997). For *Radarsat* SAR from the Canadian processing centre, a range varying calibration "constant" is used to compensate for range variation in σ^0 (different variations are used for different surfaces, as noted under "range adjustments" below). For *Envisat* ASAR, wide-swath mode (WSM) images have a calibration constant value of 68.3 dB (determined August 2004 by ESA), whereas other ASAR modes have different values.

The images are sometimes presented in 8-bit per pixel format in order to reduce file size, especially if a large geographical area is covered with a small pixel size. This may severely limit the range of values that are possible to present, and at the same time keeping radiometric resolution (the backscatter difference representing a 1-bit difference) at an acceptable value. The solution can be to code pixel values as the logarithm of the backscatter value (proportional to backscatter in dB), or to use another nonlinear coding. Since the image signal is almost always lowest in the far range, due to the fact that σ^0 for most surfaces will decrease with increasing incidence angle (see Figure 4.11), another possibility used is to apply a calibration "constant" that is a

[2] A PAF is a processing and archiving facility within the ESA.

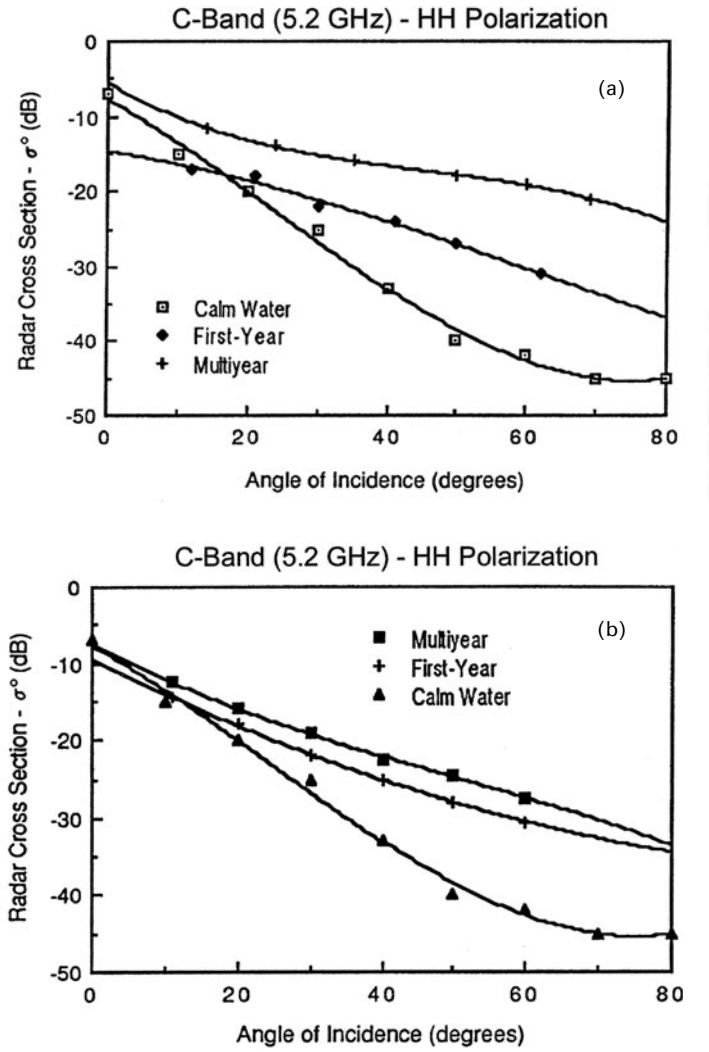

Figure 4.11. The backscatter coefficient at C-band as a function of incidence angle for two major ice types and calm water during winter (a) and summer (b) (from Onstott and Shuchman, 2004).

given (decreasing) function of range. As long as such coding is explicitly given for the images, it will be possible to convert back to σ^0, and thus the image is considered to be calibrated.

Range adjustments

Before making visual interpretation of a gray-scale SAR image, it is important to have a similar signal (gray tone) for similar surfaces independent of range. However, for

both ice and water surfaces the backscatter coefficient decreases with increasing incidence angle (Figure 4.4), and thus the gray tone varies with the range position within the image. This is especially the case with water, where a decrease in σ^0 is approximately inversely proportional to the fourth power of the sine (for vertically polarized) or tangent (for horizontally polarized) of the incidence angle. For ice, the decrease is approximately inversely proportional to the one and a half times the power of the incidence angle.

Because of this, all SAR images of the polar ocean processed with a range-invariant conversion formula between pixel value and σ^0 will be noticeably darker in the far range than in the near range. This can be adjusted by multiplying pixel values by a suitable range varying function. Because this function is different for ice and water, adjustment can be made with respect either to ice or to water. Thus, the resulting image will not generally be adjusted, but will show some areas (ice or water) with some residual range-dependent gray tone variation. This must be taken into account when image interpretation is made. Most images presented in this book have been processed using the 1.5th power range adjustment suitable for ice.

4.2.3 Radar backscatter from sea ice

Sea ice is a complex, polycrystalline composite of pure ice with random brine, air pockets and snow layers. Its backscatter depends on many physical parameters, such as surface roughness, salinity, air, crystal structure, snow cover and others. Two major mechanisms: (1) surface scattering (i.e., scattering from the layer very near the ice or snow surface) and (2) volume scattering are taken into consideration in describing the dependence of the backscatter coefficient on several sea ice properties. Selection of wavelength, polarization and viewing angle control the depth at which the backscatter from snow and ice takes place. This may help in determination of dominant scattering mechanisms (Onstott, 1992).

The penetration depth of radar waves into the sea ice is determined by its complex dielectric constant. When it is large, there is little transmission into the material, and thus little or no volume scattering can take place. The complex dielectric constant of sea ice strongly depends on the distribution of liquid brine and air pockets within the ice. Since new and young ice types retain a considerable amount of brine, microwave energy does not penetrate far into the ice and backscatter originates from the surface. Sea ice formed during the current winter contains typically from 6 to 10‰ salt, enough to limit the penetration of C-band radar waves into the ice to a few centimeters (Shokr, 1998). Therefore, the backscatter from first-year ice is dominated by surface scattering. The strength of the return signal is also to a large extent determined by surface roughness of different scales. An area consisting of many pieces of broken ice generally gives a higher backscatter than the same ice type with a level surface. Multiple reflections from two or more surfaces nearly perpendicular to each other can give the so-called *corner reflection effect*, which may enhance the return signal by up to an order of magnitude (Johannessen *et al.*, 2003).

As a result of summer melting, the surface relief of old ice has changed, and the salinity and density of its upper part are significantly reduced. Therefore, C-band

waves penetrate into it for a few tens of centimeters (Shokr, 1998). Within this layer, multiple scattering on a large number of air bubbles results in uniform scattering in most directions, including backscattering to the SAR antennae. Due to this volume scattering, cold multi-year ice with a level surface has higher backscatter than first-year ice (Johannessen *et al.*, 1997a). At C-band, surface scattering is typical for ice of high salinity and wetness (e.g., young and first-year ice), as well as summer ice, while volume scattering is typical for dry ice of low salinity (e.g., old ice in winter). Thus, many sea ice characteristics such as surface conditions, crystal structure, temperature, salinity, density and others significantly influence its radar return as expressed in its backscatter coefficient σ^0.

To describe the dependence of σ^0 on major sea ice properties qualitatively, analytical models have been developed. One that has been successful in describing homogenous conditions is that of Winebrenner *et al.* (1992). Surface scattering at the C-band may be significant, as often there are roughness features on millimeter, centimeter and larger scales at the interfaces separating air and snow, snow and sea ice, frazil and columnar ice, or infiltrated and dry snow. In the case of surface scattering the backscattering coefficient may be expressed as:

$$\sigma^0_{pp}(\theta_{ii}) = K\Gamma^2(p,f,\theta_i,\varepsilon^*_r)SF(p,f,\sigma,l) \tag{4.12}$$

which is a function of the Fresnel reflection coefficient (Γ), a shape function (SF) and a scaling constant (K). The reflection coefficient is a function of incidence angle (θ_i), polarization (p), frequency (f) and the complex dielectric constant (ε^*_r). SF is a function of polarization, frequency, root mean square surface height (σ) and surface correlation length (l) (Onstott, 1992). However, accurate quantitative descriptions of small- and large-scale properties, both in vertical and horizontal directions, that are necessary to provide input for such backscatter models are generally lacking (Tucker *et al.*, 1992).

The backscatter of multi-year ice is attributed to air bubbles in the upper portion of the ice sheet. By assuming that each bubble is characterized by a cross-section proportional to its radius to the sixth power, the total σ^0 of such ice may be expressed as the contribution from the surface and ice volume, as given by Kim *et al.* (1985):

$$\sigma^0_{pp}(\theta_i) = \sigma^0_s(\theta_i) + \gamma^2(\theta_i)\sigma^0_v(\theta_i) \tag{4.13}$$

The surface scattering contribution is identical to that described earlier. The intensity of the volume backscatter is weighted by the transmission coefficient γ, which is reasonably close to 1. The volume scattering coefficient may be expressed as:

$$\sigma^0_v(\theta'_i) = N\sigma_b \cos(\theta'_i)\left[1 - \frac{1}{L^2(\theta'_i)}\right] \Big/ (2k_t) \tag{4.14}$$

where N is the number of particles, σ_b is the scattering cross-section per particle, L^2 is the two-way loss factor and k_e is the extinction coefficient.

The number of particles is a function of the density of the layer (ρ) and the radius (r) of the particles cubed and given by:

$$N = \left(1 - \frac{\rho}{0.926}\right) \Big/ \left(\frac{4\pi r^3}{3}\right) \tag{4.15}$$

The backscatter of sea ice is influenced by snow on its surface, especially by wet snow. Snow cover insulates thin ice, increases its temperature, absorbs the extra brine and, as metamorphism proceeds, can introduce significant surface roughness (Grenfell *et al.*, 1992). The interface between snow and sea ice may be gradual, consisting of a high-density snow–ice layer. Dry snow on first-year ice can have a significant effect in some cases, depending on SAR parameters and snow characteristics, while dry snow on multi-year ice is mainly transparent and thus has little effect on backscatter (Johannessen *et al.*, 1997a). Perovich *et al.* (1998) found that σ^0 values of snow-covered ice at angles of 45° and 50° were greater by 5–10 dB than that for bare ice. Moist snow has considerable effect on backscatter. For peak melt conditions the penetration depth of C-band radiation is only 4.5 cm. Discrimination between snow-covered old and first-year ice is thus possible only during the first 2 weeks of summer (Onstott, 1992).

The backscatter of thin sea ice depends on its temperature. In a paper by Nghiem *et al.* (1998) repeatable diurnal cycles in backscatter were found with changes of 4–6 dB between night and day, which are synchronous with diurnal thermal variations and the cycles in sea ice physical parameters. During the entire experiment the air temperature remained below −10°. For *ERS* SAR, the backscatter of thin ice increased by 3–5 dB during the day, corresponding to a rise in ice surface temperature. The diurnal effect is opposite to the effect of surface wetness on thin ice, when backscatter drops in the case of surface wetness. The paper attributes this to the thermal expansion of brine inclusions and an increase in sea ice effective permittivity due to the ice warming. A similar increase in σ^0 due to increasing ice temperature is found in *ERS-1* SAR data from Arctic field experiments (Kwok *et al.*, 1998). This is particularly relevant to sun-synchronous satellites which acquire data along ascending and descending orbit paths at daytimes and nighttimes over the same area.

Dependence of sea ice backscatter on frequency, polarization and incidence angle

The backscatter of sea ice depends on radar frequency, polarization and incidence angle. Empirical regression models are made to estimate approximate values of sea ice σ^0 as a function of frequency and incidence angle (Moore *et al.*, 1980). In winter the backscatter of first-year and multi-year ice increases linearly with increasing frequency, and these ice types can be distinguished in the range of frequencies between 5 and 35 GHz (Onstott, 1992). VV and HH radar responses are quite similar for many ice types. Typical dependence of σ^0 for multi-year ice, first-year ice and calm water on incidence angle at the C-band and HH-polarization is shown in Figure 4.11. The C-band is used for imaging in *Radarsat* ScanSAR (HH) and *Envisat* ASAR (VV and HH).

Figure 4.11 shows that, for winter conditions, the difference in σ^0 between calm open water and first-year or multi-year ice increases markedly from the near- to far-range. The difference between the two ice types has much less angle variation; but they differ markedly in backscatter. For summer conditions the difference between sea ice and calm water increases in much the same way as they do with angle. Here, the two ice types have almost identical backscatter.

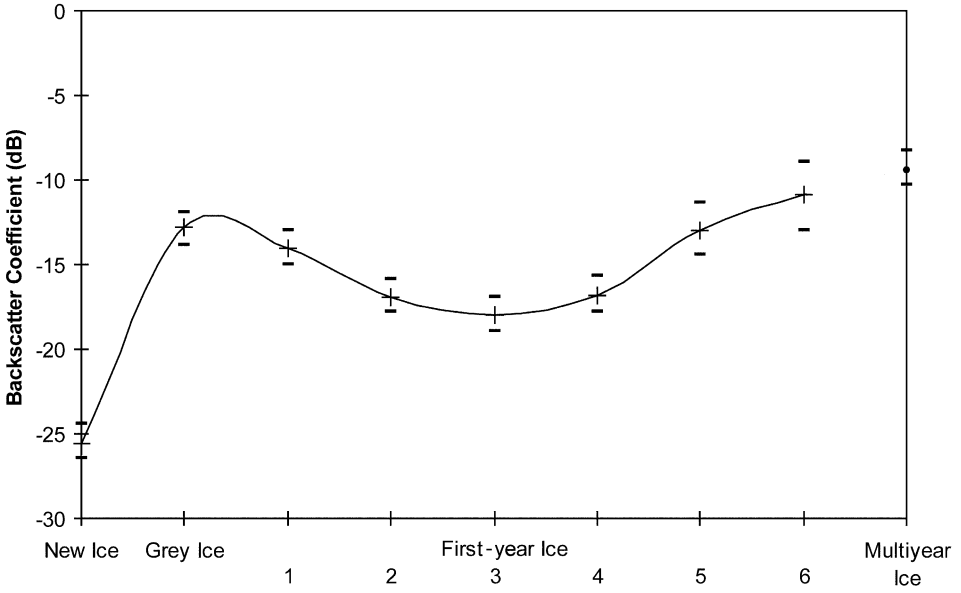

Figure 4.12. Changes in *ERS* SAR backscatter of sea ice during its evolution and deformation in the Beaufort Sea during spring: 1 = thin first-year ice; 2 = medium smooth first-year ice; 3 = thick smooth first-year ice; 4 = first-year rough ice; 5 = first-year very rough ice; 6 = first-year very heavily deformed ice (after Onstott, 1997).

Changes in sea ice backscatter during ice growth in winter

The backscatter of newly formed sea ice changes during its growth in winter. The principal features of these changes, shown in Figure 4.12, are the low backscatter from new ice and nilas, its increase for gray ice and then a slow decrease with subsequent increase in first-year ice thickness. Finally, with the beginning of a new freeze-up, it is significantly higher for multi-year ice (all ice that has survived summer melting). It is seen that the backscatter of sea ice depends on its surface roughness, and it is higher for deformed ice. The presented dependence is typical for X- and C- bands at VV- and HH-polarizations (Bushuev *et al.*, 1983; Nazirov *et al.*, 1990; Onstott, 1992; Melling, 1998).

Discussion of backscatter

The following describes some analyses made by various authors of ice backscatter and its dependence on polarization, incidence angle and other factors. Emphasis is on ERS-1/2 SAR, *Radarsat* ScanSAR and *Envisat* ASAR, which all operate at the C-band.

Calm water has very low backscatter, but even the slightest breeze is sufficient to produce roughening of the water surface and significant backscatter enhancement (Onstott *et al.*, 1998). When the wind speed is above approximately 4–5 $m\,s^{-1}$,

it becomes higher than that of sea ice (Kwok, 1998). For example, at VV-polarization σ^0 is -4.5 dB when the wind speed is $8\,\mathrm{m\,s^{-1}}$ (Sandven *et al.*, 1999a). The strong dependence of open water backscatter on wind speed and direction is used for wind retrieval from calibrated radar data (Furevik *et al.*, 2002).

New ice types—such as frazil ice, grease ice, slush and shuga—may change the backscatter significantly from that of open water. Frazil ice is the initial ice state, a suspension of fine spicules or platelets of ice, formed on the sea surface. Grease ice is the freezing of frazil ice, in which the spicules and plates of the ice have coagulated into a thick soupy layer on the water surface. These ice types have been observed to dampen capillary waves, thus producing a smoother surface than that of surrounding water. The mean σ^0 values of grease/frazil ice, as measured by a scatterometer at a 35° incidence angle, amounted to -27 dB and -28 dB for VV- and HH-polarizations, respectively (Beaven *et al.*, 1994). These values are below the noise-floor of *ERS*, *Radarsat* and *Envisat* SARs, and thus grease ice can be identified based on low intensity. However, both grease ice and calm water can have low signals. New ice may have a large range of backscatter from -23 to -5 dB (Winebrenner *et al.*, 1996). In studies by Lundhaug (2002) the mean σ^0 of new ice, derived from series of *ERS-1/2* SAR images, was -11.1 ± 1.39 dB. Bushuev *et al.* (1983) found that slush and shuga may have a high σ^0 because of their rough surface on the scale of radar wavelength.

Nilas is a thin, elastic crust of ice, easily bending in waves and swell. It has a low backscatter coefficient due to near specular reflection from its level surface. In studies by Askne *et al.* (1994) the *ERS-1* derived backscatter coefficient of smooth nilas amounted to -22 dB. Beaven *et al.* (1994) found significant difference between the σ^0 of dark (24 dB for VV- and -28 dB for HH-polarizations) and light nilas (between -19 and -20 dB for both VV and HH) at a 35° incidence angle. The σ^0 of nilas grown in the laboratory was equal to -24 dB, which is below the noise-floor of *ERS* SAR (Kwok *et al.*, 1998). However, in some cases nilas may be rafted, when its backscatter is higher (Melling, 1998).

Pancake ice is formed from grease ice, shuga or breaking nilas in wave-agitated conditions. It forms elliptically or circularly shaped pans ranging in size from 10 to 100 cm across, and as they bump against one another they force the grease ice located between them to pile up as pans edges, forming rims. Its radar backscatter is quite variable due to differences largely associated with pan diameter and rim height. Relatively high backscatter can be obtained from pancake ice, which is up to 10 cm thick and consists of generally circular pieces with raised edges, ranging from 30 to 300 cm in diameter. At the C-band and VV-polarization, its response is greater than that of bare and snow-covered ice at all angles, and may be similar to that of the open ocean (Onstott *et al.*, 1998). In the studies by Beaven *et al.* (1994) the mean σ^0 of pancake ice, measured by a scatterometer, were lower and amounted to -16 dB and -17 dB for VV- and HH-polarizations, respectively.

Significant increase in young ice backscatter, reported in a number of studies, is often caused by the appearance of frost flowers. These consist of fragile 10–30 mm high saline ice crystals that grow on the ice surface and are accompanied by formation of a 1–4 mm thick slush layer (Nghiem *et al.*, 1997). The extent and form of frost flowers depend on air temperature and the level of supersaturation of the air near the

ice surface, and therefore their contribution to backscatter can vary (Tucker *et al.*, 1992; Nghiem *et al.*, 1997). Brine from thin ice might cause a higher dielectric constant in the frost flowers than that in the ice sheet, resulting in increasing backscatter.

Melling (1998) wrote that frost flowers could contribute an additional 10–15 dB to the backscatter from thin ice. According to Hallikainen and Winebrenner (1992), the mechanism behind this phenomenon includes scattering from a rough, effective surface produced by brine absorbing the frost flowers and some kind of volume scattering effect by ice crystals within frost flowers. Askne *et al.* (1994) revealed an increase of σ^0 to -13 dB and to -6 dB, when the ice surface was covered with newly formed frost flowers and rough saline snow, respectively. In studies by Lundhaug (2002) the mean *ERS* SAR-derived σ^0 of young ice was -9.41 ± 0.83 dB.

Laboratory measurements, indicating a 3–5 dB higher σ^0 at all polarizations for the case of full flower coverage, are consistent with the backscatter increase (up to 5 dB) in *ERS-1* SAR data (Nghiem *et al.*, 1997). In the range of incidence angles from 35° to 40° flower-covered ice has a higher co-polarized backscatter ratio compared with that of bare ice. This is relevant for *Envisat* data analysis. However, no significant change in backscatter was observed when ice flower crystals were removed, and only after removal of the underlying high-saline slush layer does the backscatter level return to that of thin ice (Nghiem *et al.*, 1997). Therefore, slush patches are major contributors to observed backscatter changes (Kwok *et al.*, 1998).

Over time—with deterioration of frost flowers and accumulation of snow among them—the σ^0 of young ice gradually decreases (Onstott, 1992; Melling, 1998). Nevertheless, at the transition to thin first-year ice it is roughly 5 dB higher than that for new ice at frequencies from 1 GHz up to at least 10 GHz. According to Hallikainen and Winebrenner (1992), the backscatter effects at typical SAR frequencies (5 and 10 GHz) must result from the formation of slush at the snow–ice interface rather than from the very weak volume scattering in snow at those frequencies. The mean σ^0 of undeformed first-year ice has been derived from calibrated *ERS-1* SAR images by Kwok and Cunningham (1994), Winebrenner *et al.* (1996) and Lundhaug (2002). According to Kwok and Cunningham (1994), it amounts to approximately -17 to -18 dB with its angular decrease in the range of 0.14–0.37 dB deg^{-1}. Lundhaug (2002) and Winebrenner *et al.* (1996) found that the σ^0 of first-year ice is -13.54 ± 0.95 dB, and within the range -14 dB and -18 dB, respectively. Onstott (1992) has also found that—at the C-band and a 40° incidence angle—the σ^0 of first-year ice is at least 5 dB lower for HH- than for VV-polarization. As it grows, first-year ice experiences desalination and—due to continuous metamorphism at the snow–ice interface—the latter becomes smoother. A 2–3-dB difference in its σ^0 is found during a transition from 1.3 m to 1.8 m thick ice (Onstott, 1997).

The backscatter of first-year ice increases with deformation (i.e., with the appearance of surface roughness). Mean σ^0 values of rough ice are -13.6 dB, between -11.5 dB and -14 dB, and -10.0 ± 0.86 dB, according to Kwok and Cunningham (1994), Winebrenner *et al.* (1996), and Lundhaug (2002), respectively. The threshold between deformed and undeformed first-year ice was set at -14 dB, because above this level deformation may be seen in a SAR image. For a deformed ice surface, there is

only slight dependence of σ^0 on incidence angle and polarization. Because of the latter, ridges may be observed at higher contrast at HH-polarization (Melling, 1998).

Multi-year ice, which can attain thicknesses greater than 3 m, produces the strongest backscatter for level ice. At the C-band and higher frequencies both surface and volume scattering contribute to its backscatter, and the relatively higher contribution of the ice volume compared with the ice surface is the generally accepted physical explanation for the observed difference in σ^0 between multi-year and first-year ice (Kwok and Cunningham, 1994). A number of estimates of multi-year ice backscatter are available. In *ERS* SAR lookup tables the value of -8.6 dB is given for a standard backscatter deviation of 2.2 dB (Kwok *et al.*, 1992). According to Schwartz *et al.* (1994), the σ^0 from multi-year ice in the Beaufort Sea is typically -10 dB before melting. Gineris and Fetterer (1994) report the same value for ice in the Beaufort Sea and -10.1 dB for the East Siberian Sea. In studies by Sandven *et al.* (1999a) the *ERS-1* SAR-derived σ^0 of multi-year icefloes were typically -9.0 ± 1.5 dB, and Lundhaug (2002) report the mean σ^0 of multi-year ice of -8.42 ± 1.25 dB. As a result of volume scattering dominance, there is only a weak dependence on incidence angle over the range of incidence angles observed by *ERS-1*, with slopes ranging between -0.03 and -0.1 dB deg^{-1} (Kwok and Cunningham, 1994).

During the winter the σ^0 of old ice remains quite stable (within 0.5 dB) at a given geographic location (Kwok and Cunningham, 1994; Fetterer *et al.*, 1994). With ice aging from second-year ice to young multi-year ice and then to old multi-year ice its σ^0 increases (Barber *et al.*, 1998a, b). The possible explanation is that older ice appears to have larger and deeper hummock layers which contain larger bubble sizes spaced further apart within the hummocks. In the Fram Strait region the surfaces of multi-year icefloes can be flooded with seawater. Microwave signatures from this flooded ice can easily be confused with first-year ice (Tucker *et al.*, 1992).

Differences of sea ice backscatter related to ice position

The backscatter values of sea ice depend on its location relative to the main ice pack (Onstott, 1992; Gineris and Fetterer, 1994; Kwok and Cunnigham, 1994; Sandven *et al.*, 1999a). Figure 4.13 shows the typical σ^0 values of the major ice types in the ice edge region and in the interior pack ice, measured in the Barents Sea (Sandven *et al.*, 1999a). Backscatter coefficients have been derived from calibrated *ERS-1/2* SAR images, using *in situ* sea ice and snow measurements nearly coincident with *ERS-1* overpasses. The σ^0 of open water for different wind speeds were calculated using the CMOD4 algorithm.[3]

The ice edge zone had a combination of open water and various stages of new and first-year ice. Grease ice, which had the lowest σ^0 of all ice types, was seen to develop rapidly into pancake ice with sharp edges and high (> -7.0 dB) σ^0. Small floes of thicker first-year ice had a rough surface and a backscatter between -10.5 and

[3] The CMOD4 algorithm is number 4 of an algorithm to compute the backscatter coefficient of a C-band VV-polarized radar signal, applied to the *ERS-1/2* scatterometer and SAR wind measurements (e.g., Furevik *et al.*, 2002).

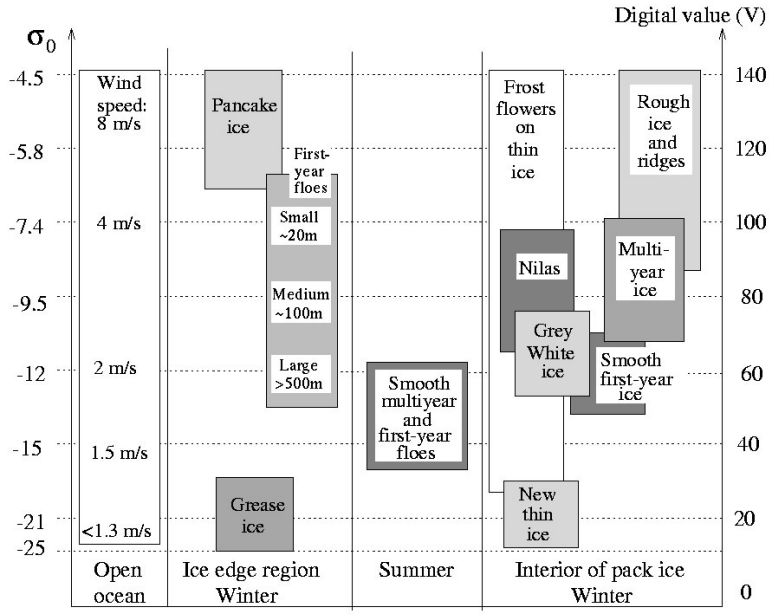

Figure 4.13. SAR backscatter as a function of ice types observed during *ERS* SAR ice validation experiments in the Barents Sea in 1991–1992. Digital value is scaled 8-bit (Sandven *et al.*, 1999a).

-6.5 dB. Multi-year icefloes could also occur in this zone, and, similar to first-year icefloes, they also tended to break up owing to the wave field.

Large areas of multi-year and first-year ice in the interior zone had typical σ^0 values of -9.0 ± 1.5 dB and -10 to -13 dB, respectively. This example shows that multi-year ice in the interior can have similar backscatter to that of small and medium floes of first-year ice in the ice edge region, whereas pancake ice in the ice edge region can have similar backscatter to that of ridged and heavily deformed first-year and multi-year ice in the interior (Johannessen *et al.*, 1997b). Thus, ice classification based solely on SAR backscatter is more challenging in the marginal ice zone than in the interior pack ice.

Several studies have shown that the backscatter of the same WMO ice types change due to differences in parameters such as deformation, and for multi-year ice due to differences in its age and melt ponding rate. Higher fractional areas of frozen melt ponds decrease overall backscatter, whereas higher fractional areas of deformed features enhance it. This is again variable from one geographical area to another. Thus, the *ERS-1* SAR-derived σ^0 of multi-year ice increases from the western Beaufort Sea to the Canadian Archipelago, as well as having a minimum at around 75°N and two maxima near 77°N and near 73°N (Kwok and Cunningham, 1994; Winebrenner *et al.*, 1996). In the East Siberian and Chukchi Seas in the period from November through April the mean *ERS-1* SAR-derived σ^0 of multi-year ice slightly decreases from east to west (Gineris and Fetterer, 1994).

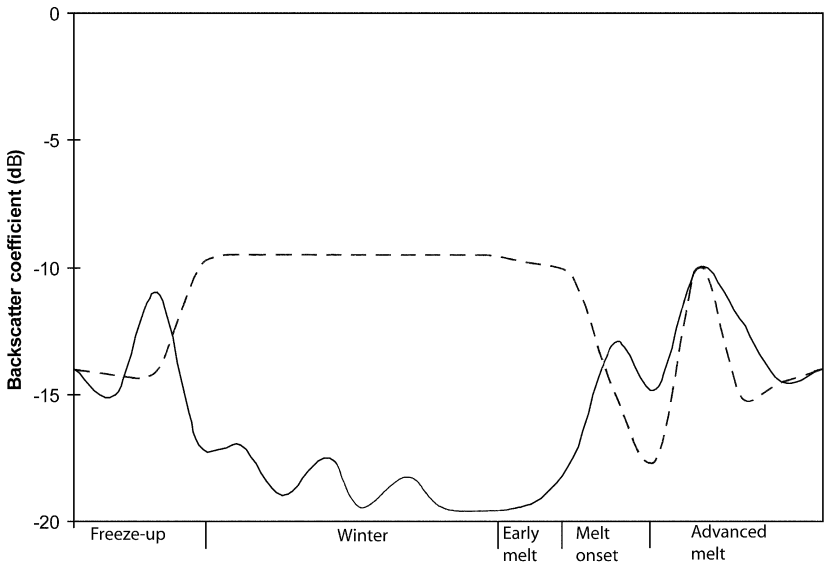

Figure 4.14. The annual cycle of the evolution of *ERS* SAR-derived σ_0 for thick first-year ice (solid curve) and multi-year sea ice (dotted curve) (after Barber *et al.*, 1998).

Changes in sea ice backscatter during melting

The real and imaginary parts of the sea ice dielectric constant increase with increasing ice temperature (Gogineni *et al.*, 1992). Also, solar insolation moistens the upper snow and changes its crystal structure. Therefore, the σ^0 of first-year and multi-year ice significantly changes during the melting period (as shown in Figure 4.14). The ASF ice classification algorithm[4] accounts for these seasonal changes by utilizing separate backscatter lookup tables for winter to early spring, late spring, early summer, mid-summer, late summer and fall (Kwok *et al.*, 1992a). Barber *et al.* (1998b) identified the following phases of seasonal evolution of sea ice backscatter: winter, early melt, melt onset and advanced melt. Changes in the σ^0 for snow-covered, thick first-year ice and multi-year ice during these periods are shown in Figure 4.14 (Barber *et al.*, 2001).

During early melt the difference in backscatter of multi-year and first-year ice does not change significantly. Volume scattering continues to dominate the σ^0 of multi-year ice, which slightly decreases but remains fairly stable. The backscatter of first-year sea ice slightly increases and presents a combination of basal layer volume scattering and ice surface scattering. Water from melted snow may percolate down and freeze on the cold ice, forming a rough layer of superimposed ice (Gogineni *et al.*, 1992). Small amounts of liquid water can cause significant diurnal variations in ice (Barber *et al.*, 1998a).

[4] This algorithm is in use at the Alaska SAR Facility in Fairbanks, Alaska. It classifies first-year and multi-year ice in SAR images, using empirically determined sea ice backscatter coefficients (Kwok *et al.*, 1992b).

The onset of melt is denoted by a rapid decrease in the σ^0 of multi-year ice. The water within the snow cover on multi-year ice effectively masks volume scattering from hummocks (Barber *et al.*, 1998b). Therefore, the *ERS* SAR-derived σ^0 of multi-year ice drops for typically 7–10 dB (Jeffries *et al.*, 1997; Winebrenner *et al.*, 1998). According to Schwarz *et al.* (1994), minimum σ^0 values occur when the area of melt ponds on icefloes is at a maximum and reaches 50–60% of the surface. The σ^0 of first-year ice, dominated by volume scattering from wet snow grains in the basal layer and by surface scattering from the wet snow surface, rapidly increases at the beginning of melt onset. After reaching a maximum, the σ^0 of first-year ice distinctly decreases (Barber *et al.*, 1998b, 2001; Kwok *et al.*, 2003).

The advanced melt stage begins when air temperatures exceed 0°C (Gogineni *et al.*, 1992). At the beginning of this stage the σ^0 of multi-year ice rapidly increases with an increase in the volume scattering component due to reduction in liquid water within the hummocks (Barber *et al.*, 1998b). Multi-year ice becomes indistinguishable from first-year ice until freeze-up. Jeffries *et al.* (1997) report an increase in its σ^0 from -14–15 dB in July, when melt pond coverage is about 30%, to roughly -13 dB by late August, and that it probably reflects a decrease in total melt pond area to an average of 10% in this period. During August, when daily air temperatures remain positive, σ^0 varies between -9.5 dB and -14 dB (Schwartz *et al.*, 1994). Winebrenner *et al.* (1996) report its high correlation with temperature variations above and below freezing. According to Jeffries *et al.* (1997), this variability in σ^0 can be additionally caused by strong winds roughening the surface of melt ponds, and occasional summer snowfall and subsequent melting. In first-year ice, σ^0 increases over the ponding period and decreases as the ice begins to drain; however, the mechanisms of first-year ice scattering during the advanced melt period are largely unknown (Barber *et al.*, 2001).

In autumn, when air temperature falls below freezing levels, liquid water freezes into the remaining ice, and due to an increase of volume scattering its σ^0 reaches winter multi-year ice values within 7 days of continually sub-freezing air temperatures (Winebrenner *et al.*, 1998). Studies in the Beaufort Sea have shown that the σ^0 of multi-year ice increases to -10 dB in early September and then remains close to that value (Schwartz *et al.*, 1994). The backscatter of newly formed ice varies widely, as described earlier.

4.3 INTERPRETATION OF SEA ICE PARAMETERS IN SAR IMAGES (*V.Yu. Alexandrov, S. Sandven, O.M. Johannessen, K. Kloster*)

Interpretation of the features and parameters of sea ice in satellite radar images includes the processes of detection, recognition and interpretation of ice parameters. Parameters and features such as backscatter value and texture, as well as the structure, size and form of objects are used for detection and recognition. Radar image brightness, which is determined by the sea ice and water backscatter coefficient σ^0, is the principal direct interpretation feature. Based on differences in backscatter, the major ice types can be detected. Differences in ice type, ice form and surface roughness modify the backscatter coefficient and produce images with various sea ice tones, thus

enabling estimation of several sea ice parameters. However, some ice types can have similar backscatter coefficients and texture, and then other information may be used for their recognition, such as connection with the hydrometeorological conditions during the preceding period, ice drift data, other remote sensing data, sea ice observations from vessels, etc. *A priori* knowledge of ice conditions may also restrict the appearance of certain ice types in different regions.

The backscatter from sea ice depends on three radar parameters: frequency, polarization and incidence angle. The signatures of several ice types in radar images at the C-band can be similar at different polarizations and incidence angles. For example, nilas is evident with a dark tone, old ice has a brighter tone than first-year ice and ridged ice is shown with a brighter tone than level ice. Signatures of some other ice types and open water can be very different. For example, at VV-polarization the backscatter of slightly rough open water and thin ice is greater than that at HH-polarization by 5–7 dB and 2–3 dB, respectively (Onstott, 1992). For interpretation, signatures of major sea ice types and features need to be known for the radar parameters used by *ERS* SAR, *Radarsat* ScanSAR or *Envisat* ASAR.

The specification of SAR signatures for various sea ice types and features has been made during many sub-satellite experiments. SAR images from *ERS*, *Radarsat* and *Envisat* satellites have been compared with observed sea ice conditions. Ice type, thickness, deformation rate, concentration and several other parameters have been visually determined from icebreakers, video- and photo-survey data. In some cases *in situ* measurements of ice thickness, snow depth and density, and some other parameters are also available. Meteorological observations are of great aid in image interpretation. A detailed description of several experiments is presented in Section 6.1. Based on sub-satellite data analysis, the possibility of deriving the most important sea ice parameters from SAR images has been assessed, and the radar backscatter signatures of typical sea ice types and features were found.

The most important geophysical parameters describing sea ice—such as ice concentration, ice type, ice thickness, floe size, size and orientation of leads, floe size, deformation rate, ice drift and areas of convergence/divergence, stage of melting and several others—are defined in the World Meteorological Organization's (WMO) *WMO Sea Ice Nomenclature* (WMO, 1989). The following description follows this nomenclature.

4.3.1 Ice development

The *WMO Sea Ice Nomenclature* defines the following principal sea ice types: new ice, nilas, young ice, first-year ice and old ice, each of which is further subdivided into more types.[5] Increase in the ice thickness and changes in its structural and salinity properties and surface roughness during its growth causes changes in its backscatter coefficient (see Section 4.2). Based on differences in backscatter and texture, most of the main sea ice types can be determined from SAR images.

[5] More detailed definitions of ice terms are presented in the Glossary (p. 427).

New ice

Sea ice recently formed on the water surface includes frazil ice, grease ice, slush and shuga. Frazil ice is formed as small, elongated crystals in the form of plates. It does not change the backscatter coefficient of the water surface, and therefore cannot be detected in SAR images. In the absence of waves, the number of crystals rapidly increases forming a continuous soupy layer called ''grease ice'', which is characterized by its low reflectivity and matt appearance of its upper surface (Weeks and Ackley, 1986). Its backscatter coefficient is often lower than the noise-floors of satellite SARs (Beaven *et al.*, 1994), and in such cases it cannot be distinguished from calm open water in SAR images. The backscatter coefficient of open water increases significantly with the formation of capillary waves on its surface when the wind speed exceeds 2–3 m s^{-1}. Grease ice inhibits the formation of capillary waves (see Figure 4.15) and can be detected by its dark signature, often among bright areas of pancake ice or wind-roughened water surface (Johannessen *et al.*, 2003). Under the impact of wind and

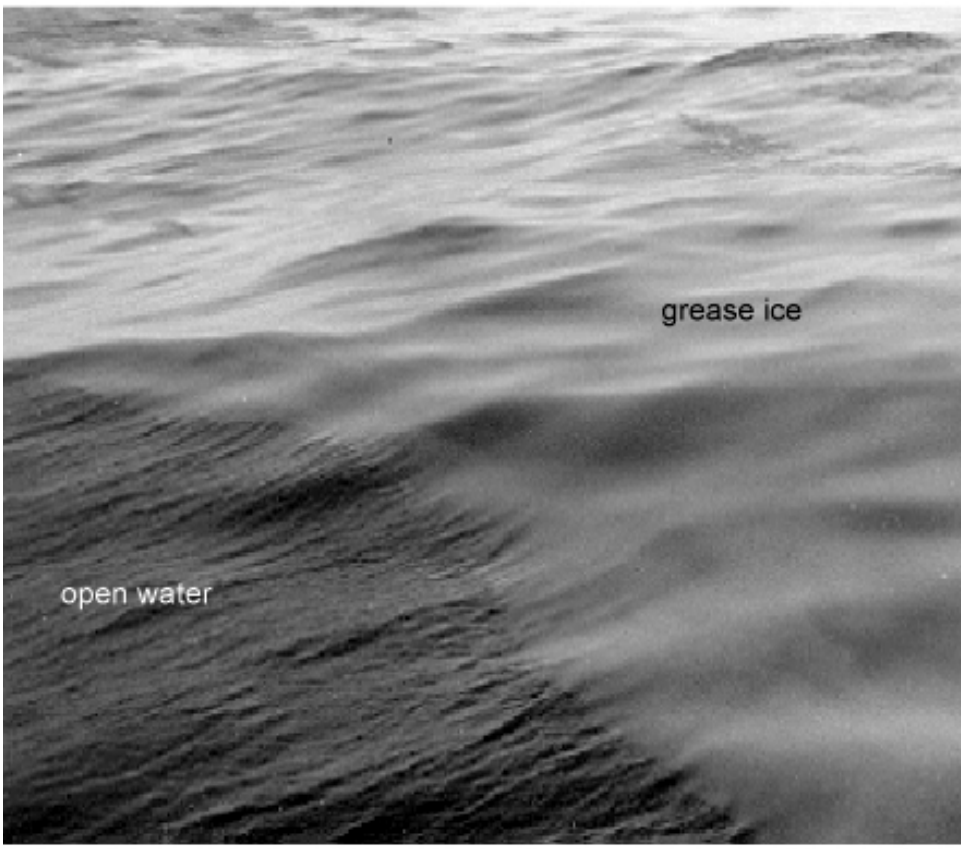

Figure 4.15. Photo of the effect of grease ice by its damping of short (a few cm) wind waves (Johannessen *et al.*, 2003).

surface currents it accumulates in areas (see Figure 4.16a), evident as dark stripes and spots in the SAR image (Figure 4.16b).

Large amounts of newly fallen snow on a freezing water surface form a viscous bulk layer called ''slush''. Porous, whitish ice lumps called ''shuga'' are formed from grease ice and slush under the impact of waves. Both slush and shuga have high

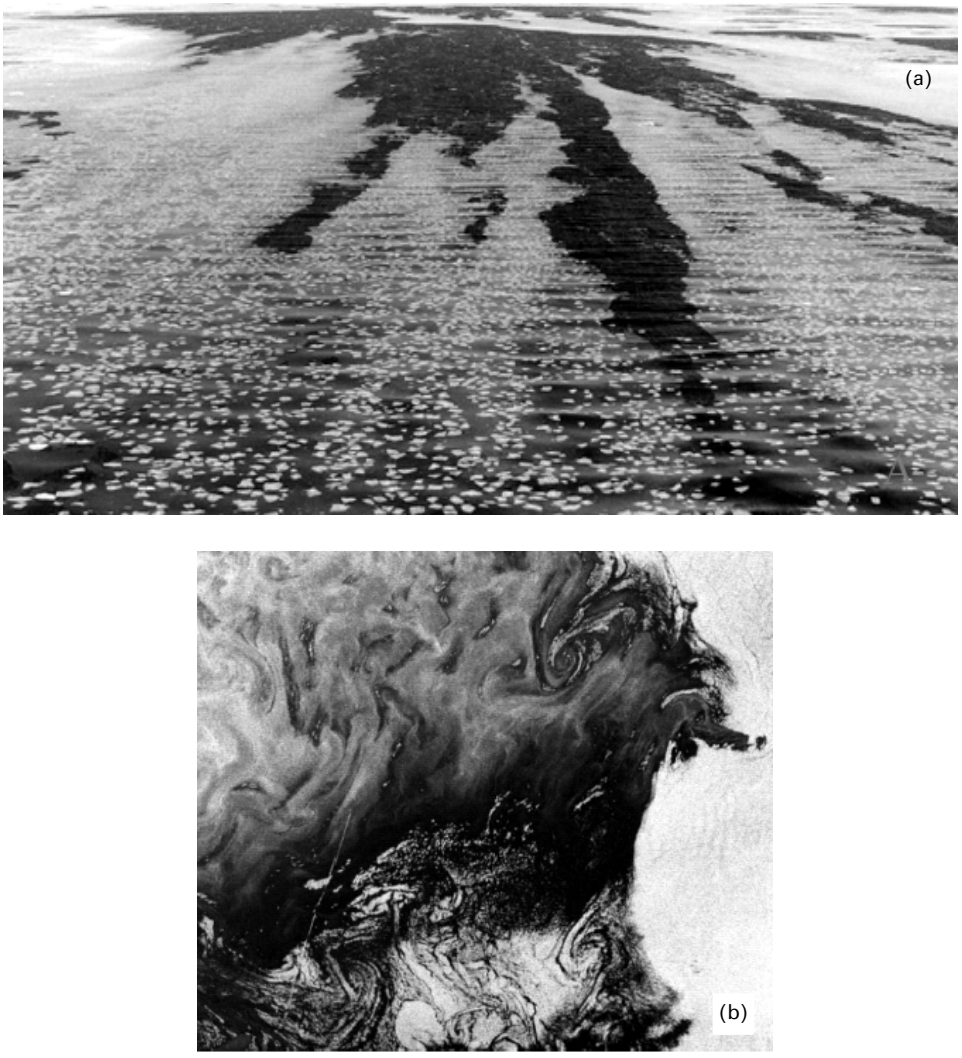

Figure 4.16. (a) Photo of typical grease ice observed in the ice edge region. (b) Sub-image of an *ERS-1* SAR scene covering about 50×50 km from the marginal ice zone, showing the characteristic signature of grease ice (dark), pancake floes (bright area in the upper left part of the image) and open water (almost white area on the right-hand side of the image generated by winds of 5–10 m s^{-1}). The SAR image was obtained in the Barents Sea during the SIZEX experiment in March 1992 (Johannessen *et al.*, 2003).

backscatter coefficients due to their rough surface on the scale of radar wavelengths. These are evident in SAR images as elongated stripes parallel to the wind direction with a characteristic light tone and a complicated texture (Bushuev *et al.*, 1983).

New ice on water can thus be detected in SAR images, although it depends on the state of the water surface. Low incidence angles, such as that of *ERS-1/2* SAR, may be preferable for their identification.

Nilas

Nilas, which is formed from grease ice and represents an elastic ice crust bending under wave and swell action, is subdivided into dark and light nilas with thicknesses of less than 5 cm and 5–10 cm, respectively. Due to the near specular reflection of EM waves from its surface, nilas has a low backscatter coefficient: in the range from −24 to −28 dB (lower than SAR noise levels), and from −19 to −20 dB for dark and light nilas, respectively (Beaven *et al.*, 1994). Its dark SAR signature can be similar to that of calm open water, and to distinguish it from water can be quite difficult (Figure 4.17). Large areas of rafting, which are typical of nilas, can be detected with a bright tone in a SAR image (Johannessen *et al.*, 2003). The surface of nilas can be covered with frost flowers, which significantly increase its backscatter coefficient.

Young ice

Young ice, which has a thickness between 10 and 30 cm, is subdivided into 10–15 cm thick gray ice and 15–30 cm thick gray–white ice. Gray ice is formed from light nilas during its growth or when circular pieces of pancake ice are frozen together (see Figure 4.18a). It has high backscatter (bright SAR tone), as shown in Figure 4.18b. Two mechanisms can be responsible for thehigh backscatter of gray ice: a continuous layer of frost flowers on its surface, or a rough upper surface.

A system of cracks dividing the gray ice area into distinct blocks is often evident in SAR images. This also helps to differentiate it from nilas (Borodachev, 1998). Compared with nilas, gray ice is less elastic and breaks as a result of sea swell. Under pressure, it usually rafts.

With continued growth, gray ice becomes gray–white ice. Typically, it forms elongated icefloes with a length in the range from 1 to 8–10 km, separated by fractures (Bushuev *et al.*, 1983). These fractures can be detected in a SAR image as dark lines. Gray–white ice has a medium backscatter value, which is lower than that of gray ice (Figure 4.19). It usually ridges under pressure.

First-year ice

All sea ice developed from young ice from the previous summer is defined as first-year ice. It is subdivided into thin, medium and thick first-year ice types, with thicknesses of 30–70 cm, 70–120 cm and more than 120 cm, respectively. In Arctic seas, thin first-year ice is common during fall. It has lower backscatter than gray–white ice. During winter ice thickness increases and thin ice becomes medium and, later, thick first-year ice.

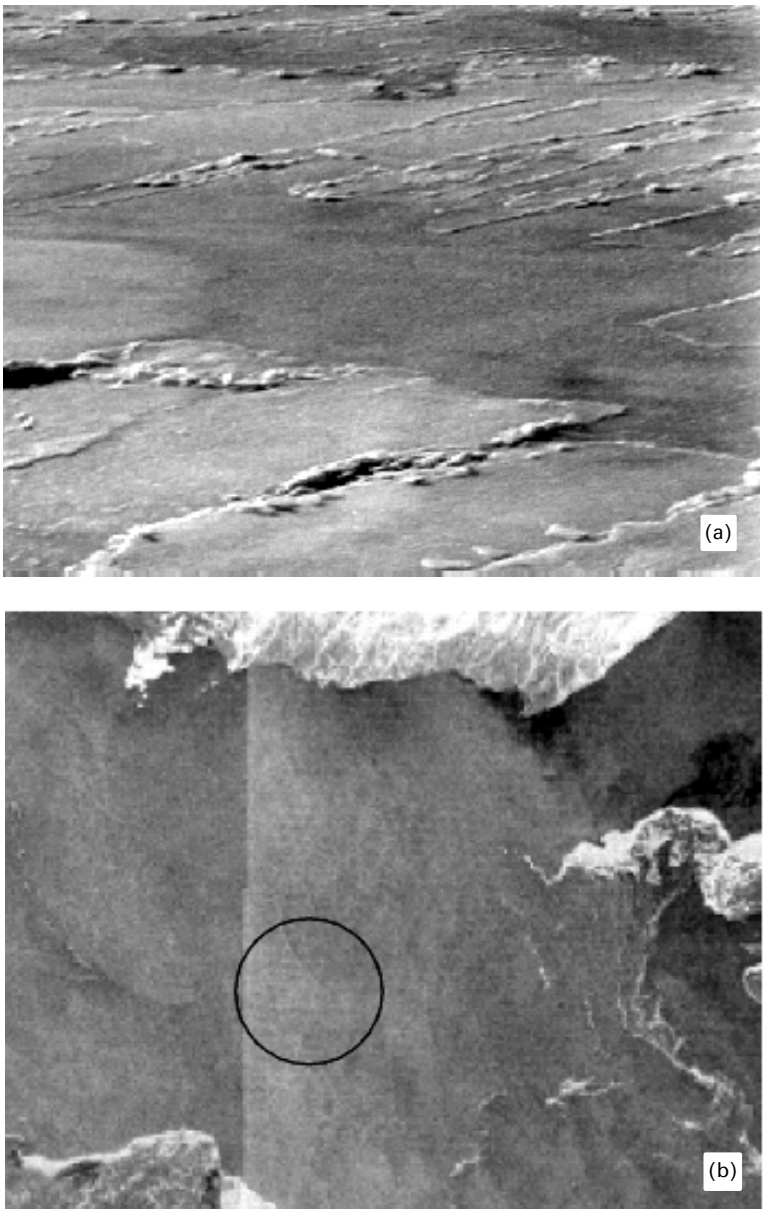

Figure 4.17. (a) Photo of nilas after pressuring, causing the formation of rafting and small ridges. Photo was taken north of Dikson in April 1998. (b) A SAR image of smooth nilas shows characteristic uniform and low backscatter within the circle of a diameter of about 30 km where the photograph was taken. The SAR image is a sub-image of a *Radarsat* ScanSAR image (© Canadian Space Agency) in Vilkitskiy Strait. Bolshevik Island is seen in the upper part of the image and Cape Chelyuskin is seen in the lower left corner. Tongues of older ice are seen as bright bands on the right-hand side of the image (Johannessen *et al*., 2003).

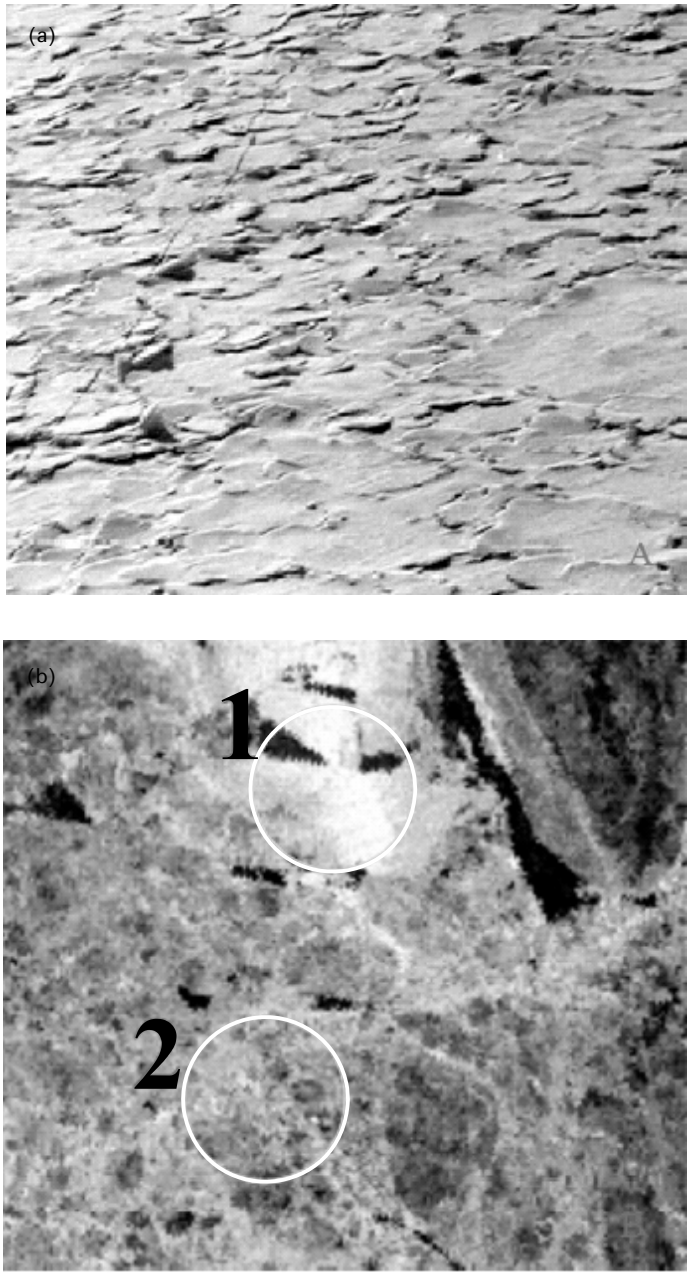

Figure 4.18. Photo of gray ice with a rough surface with many small edges (a), which gives uniform high SAR backscatter as shown in region 1 of the ScanSAR sub-image (b) (© Canadian Space Agency). The dark areas in the SAR image are nilas. The area in circle 2 shows the typical SAR signature of first-year ice with identification of floes. The data were obtained in the Kara Sea at 75°N 82°E on 30 April 1998 (Johannessen *et al*., 2003).

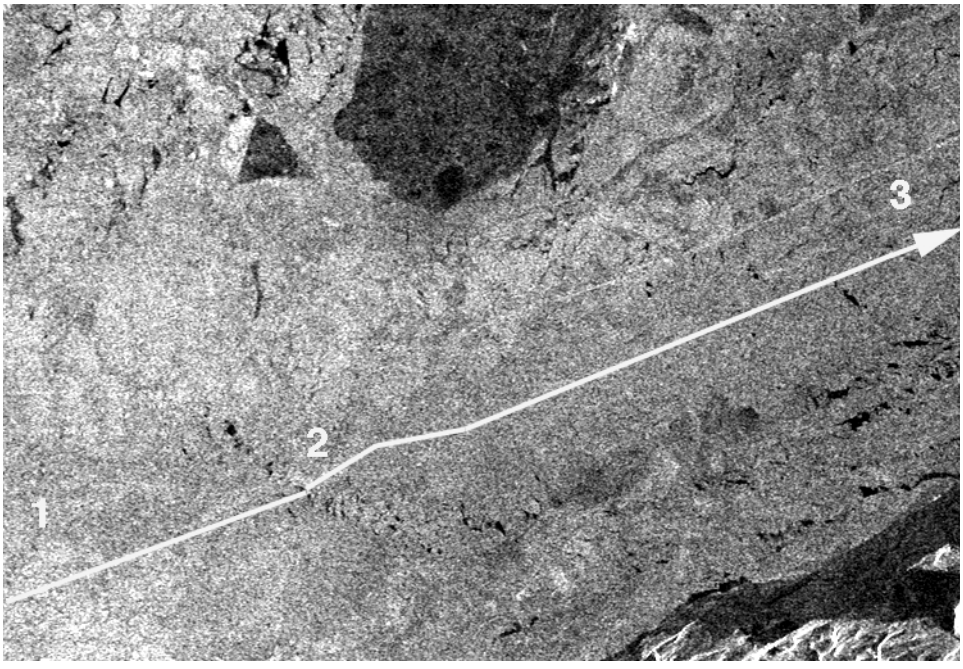

Figure 4.19. Full-resolution ScanSAR sub-image with a pixel size of 50 m from 25 April 1998. Image shows predominantly gray–white ice in the flaw polynya along the northwest coast of Novaya Zemlya. The dark area near the coast is level fast ice. An icebreaker track is evident as a thin, bright straight line above the overlaid arrow line. A large floe of first-year ice is seen as a dark area in the upper part of the image (© Canadian Space Agency).

With the increase in its thickness the backscatter of first-year ice slightly decreases. Giant and vast floes of first-year ice often represent a conglomerate of several smaller icefloes frozen together. Therefore, their SAR signature can be quite inhomogeneous, consisting of small areas with various brightnesses and textures. An example of such an icefloe is shown in the ScanSAR image in Figure 4.19. Homogenous level parts are dark and areas in-between are brighter, probably due to increased ice surface roughness.

In most cases first-year ice can be reliably separated from both young and old ice. However, it is practically impossible to separate thin, medium and thick first-year ice from each other in a SAR image. To solve this problem to some degree, additional information on the sea ice conditions in different regions and their development during the winter can be used.

Old ice

"Old ice" is the term for sea ice that has survived at least one summer's melt. It is subdivided into second-year ice and multi-year ice. Note that in remote sensing, multi-

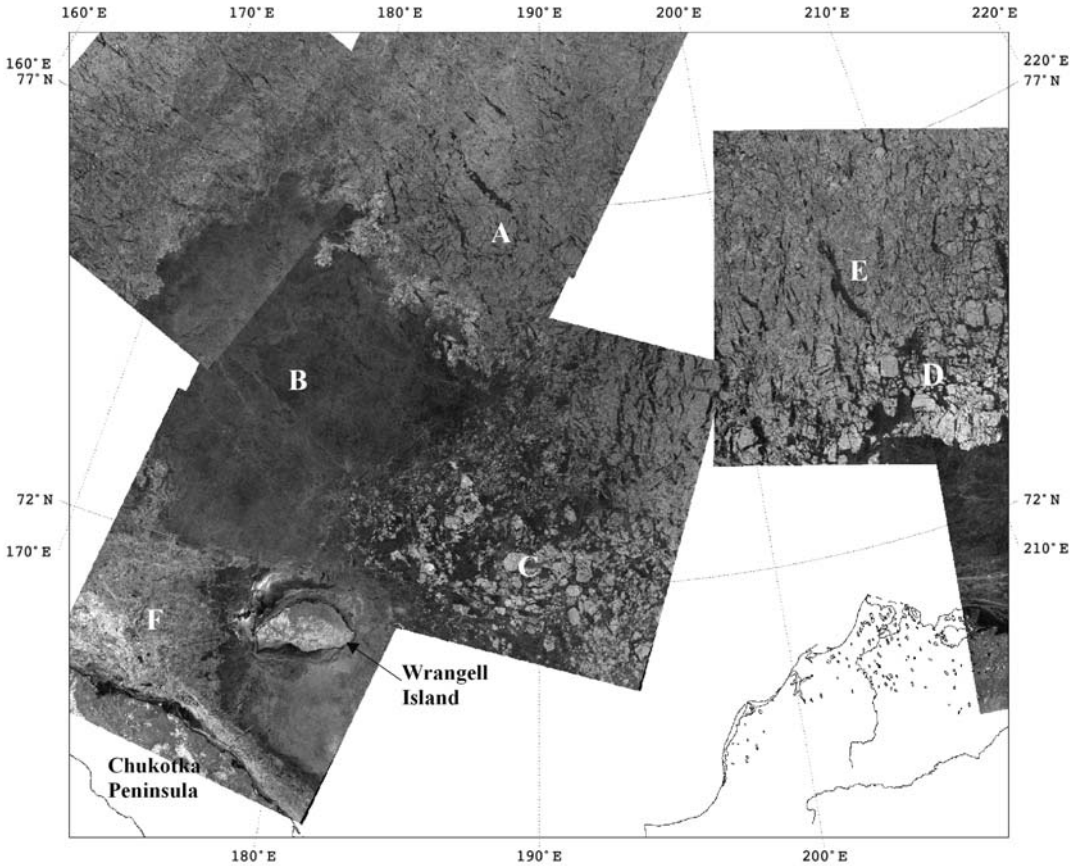

Figure 4.20. *Radarsat* ScanSAR wide image from 6 March 1998 showing old ice in the East Siberian Sea (© Canadian Space Agency). See main text for annotated areas.

year ice is generally used synonymously for old ice. Soon after the beginning of the freeze-up, old ice attains a high backscatter coefficient, which does not change significantly during the winter. The backscatter coefficients of second-year and multi-year ice are quite similar, so it is practically impossible to distinguish them.

In the SAR images in Figure 4.20, multi-year ice (area A) is reliably discriminated from first-year ice (area B) due to its brighter tone and rougher texture. Floes of old ice are generally rounded (areas C and D). The shape of giant, vast and big icefloes can be determined if their size significantly exceeds the spatial resolution of satellite SAR images. In very close old ice a number of leads can be identified (area E).

Near the ice edge, old and first-year ice is often broken into small icefloes of size less than the SAR spatial resolution of about 100 m. A photo of the sea ice near the ice edge in the Barents Sea is shown in Figure 4.21b. In this case more specific interpretation is difficult, as such areas have a homogenous and bright tone in the SAR image shown in Figure 4.21a.

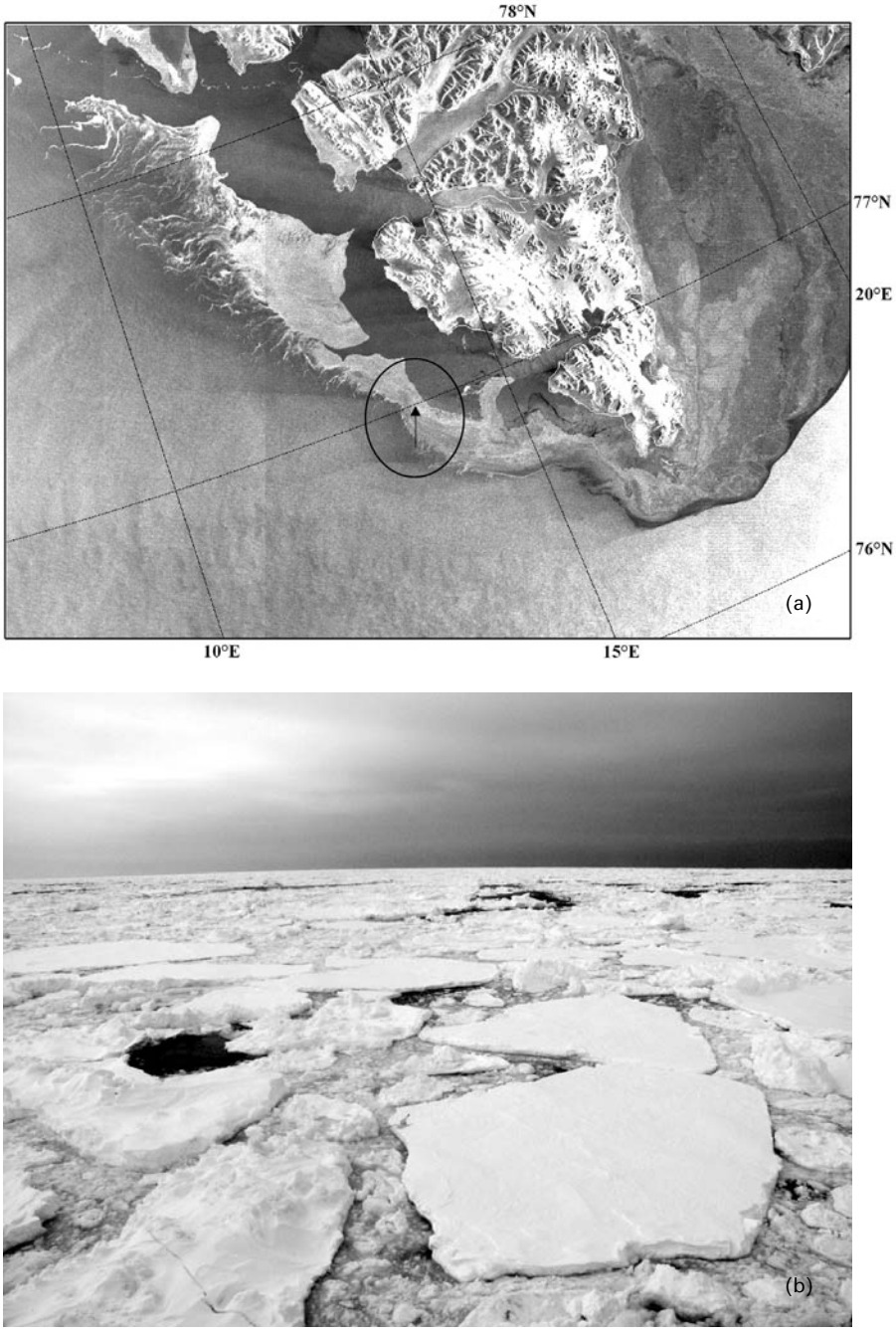

Figure 4.21. (a) *Envisat* ASAR image from 19 April 2004, covering sea ice westward of Svalbard (© European Space Agency), and (b) photo of typical sea ice conditions in the area marked by an arrow at 77°N in the image above (Johannessen *et al.*, 2001).

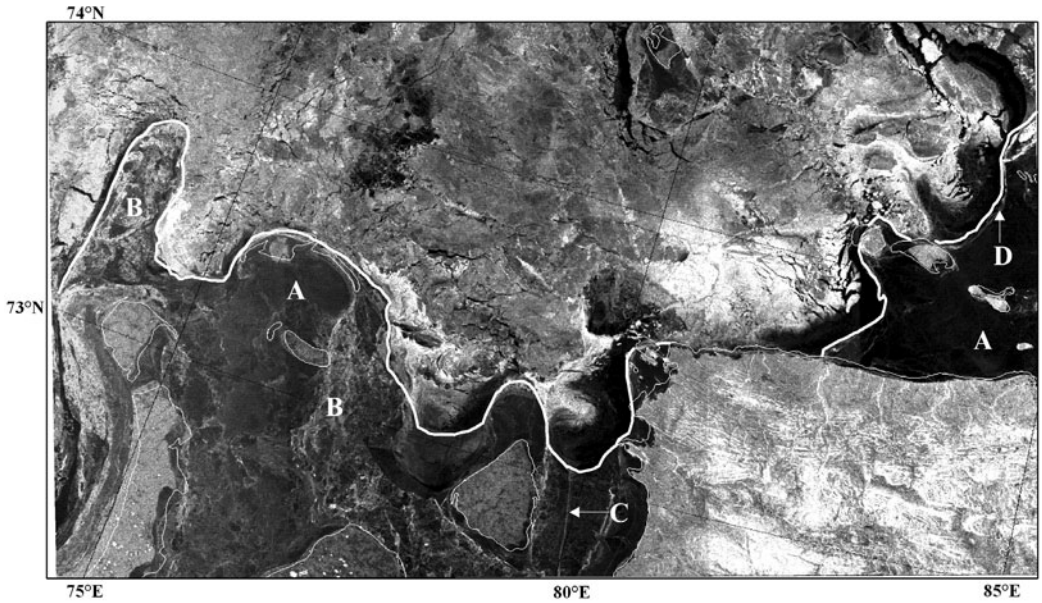

Figure 4.22. *Envisat* ASAR image from 11 March 2004, showing winter sea ice conditions in the Kara Sea. Large areas of fast ice near the coast in a dark tone are marked with the white line (© European Space Agency). See main text for annotations.

4.3.2 Forms of fast ice

Fast ice forms along the Arctic coast in autumn. It can be detected in SAR images when its width significantly exceeds the radar spatial resolution and its backscatter coefficient is different from that of the sea surface. In winter fast ice covers large coastal regions of Eurasian Arctic seas, extending up to several hundred kilometers from the coast. Mostly it is first-year ice, but may be more than 1-year-old in some regions. The fast ice boundary in the central part of the Kara Sea, detected from an *Envisat* ASAR image, is shown by the white line in Figure 4.22. The SAR signature of first-year fast ice depends on its surface roughness and to some degree on salinity, and may be similar to that of drifting pack ice. Level and deformed fast ice have dark (area A), and brighter (area B) SAR signatures, respectively. A channel in the fast ice in Yenisey Gulf, made by icebreakers, can be detected (area C). In the absence of wind, an unfrozen flaw polynya has a dark signature similar to that of level fast ice and distinguishing them is difficult. However, when ridged ice is located at the fast ice edge, it can be seen as a linear bright feature (at D). Also, the analysis of successive SAR images can be helpful if the fast ice boundary or the fast ice edge is difficult to see.

Grounded hummocks are evident as bright spots in SAR images if their size significantly exceeds radar spatial resolution. Data on sea depth and analysis of successive SAR images are necessary for their reliable identification. Grounded hummocks are located in shallow areas, and their coordinates do not change with time.

4.3.3 Forms of floating ice

The form of floating ice is one of its most important parameters that can be determined by SAR image interpretation. Smaller forms (<20 m) of floating ice include pancake ice, ice cake, small ice cake and brash ice. An icefloe is a relatively flat piece of sea ice 20 m or more across. According to their largest size floes are subdivided into: giant (over 10 km across), vast (2–10 km), big (500–2,000 m), medium (100–500 m) and small (20–100 m) (WMO, 1989).

The backscatter of a given ice type depends significantly on its composition of ice forms. Areas composed of pancake ice, brash ice, ice cake and small floes have bright homogenous SAR tones. Pancake ice is typical for the ice edge zone, where it frequently alternates with grease ice. Pancakes are developed from frazil ice and, during initial stages, present semi-consolidated slush. Wave action causes oscillatory motions resulting in repeated contact and separation between the plates and pushes newly formed frazil crystals up to form the characteristic raised pancake rims on the plate edges (Weeks and Ackley, 1986). With a diameter of disks in the range of 0.3–3 m pancake ice has a rough surface that leads to a high backscatter and a bright SAR signature (Figure 4.23).

The brash ice between icefloes has a relatively bright SAR tone. A mixture of brash ice, pancake ice and small icefloes is quite common for the ice edge, where large icefloes are broken under wave action. Sea ice in this area often has typical light-gray signature, as is evident in the *ERS-1* SAR image of the ice edge in the Barents Sea (Figure 4.24).

During the SIZEX'92 experiment icefloes identified in an *ERS-1* SAR image (Figure 4.25a) were compared with an aerial photo-survey from a low-altitude helicopter (Figure 4.25b) (Sandven *et al.*, 1999a). Average floe diameter increased from about 10 m near the ice edge to approximately 40 m and 120 m when 25 km and 50 km from the ice edge, respectively. Some 60 km north of the edge ice, icefloes of about 1–3 km in diameter with open water and new ice between them were observed. In spite of the large floe size they could hardly be detected in SAR images. When sea ice concentration exceeds 90%, they are closely connected and SAR could not detect the boundary between them, as for F1–F4, for example. Recognition of icefloes is better when fractures of several hundred meters wide separate them such as, for example, those marked by letters L1 and L2. Soh *et al.* (1998) also concluded that icefloe detection is difficult when icefloes nearly touch each other. Level icefloes with a size exceeding SAR resolution can more easily be detected among wide fractures and smaller ice forms.

During the summer, sea ice concentration decreases. Then, separate icefloes of relatively small size can be detected as dark spots on a wind-roughened water surface with a very bright tone as shown in Figure 4.26. Their detection under low-wind conditions is far more difficult.

4.3.4 Ice edge

The ice edge is the boundary between the open sea and the sea ice. It may be termed "compacted" or "diffuse" (WMO, 1989). The location of the ice edge is roughly

(a)

(b)

Figure 4.23. (a) Photo of pancake ice about 1 m in diameter, as often observed at the ice edge. (b) *ERS* SAR signature of pancake ice interleaved with open water and grease ice. The mixed bright and dark signature is typical for pancake and grease ice found at the ice edge (Johannessen *et al*., 2003).

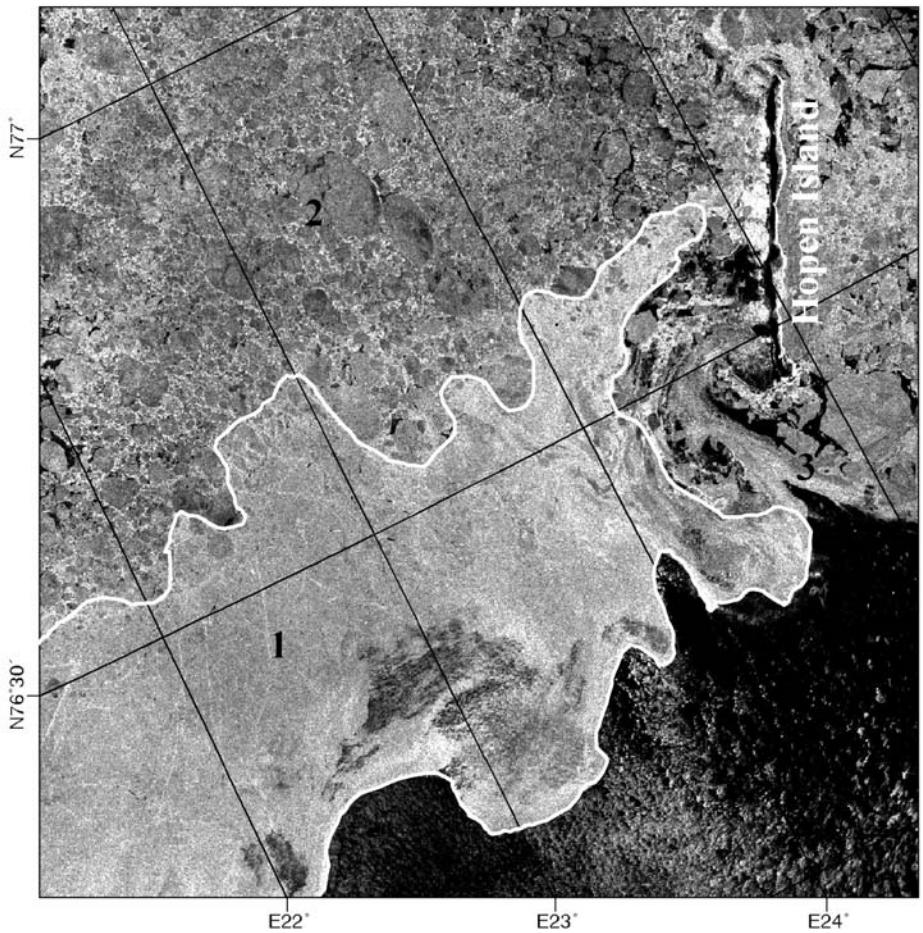

Figure 4.24. *ERS-1* SAR scene from 27 May 1994, covering Hopen Island, southeast of Svalbard: 1 = compact deformed first-year ice—the mid-gray, homogenous pattern is characteristic for floes smaller than the satellite's image resolution, and the darker area in-between is leads and fractures covered by open water and/or thin ice; 2 = compact first-year ice with floes varying from a few hundred meters up to 10 km; 3 = large openings with calm open water or thin ice (© European Space Agency).

defined by a given ice concentration—for example, 10% or 30%. The marginal ice zone is a variable transition zone between open water and areas of dense pack ice. The ice edge can be well-defined or diffuse, straight or meandering, with ice eddies and ice tongues extending into open water areas (Johannessen *et al.*, 1987, 1994; Sandven *et al.*, 1999a). Studies with airborne SAR show that it is a very useful sensor for mapping ice edge location, detailed ice edge morphology, ice edge motion and ice edge processes (Johannessen *et al.*, 1992).

ERS-1 SAR possibilities for mapping sea ice in the ice edge zone were studied during the SIZEX'92 experiment in the Barents Sea. The ice edge shown by a SAR 30-

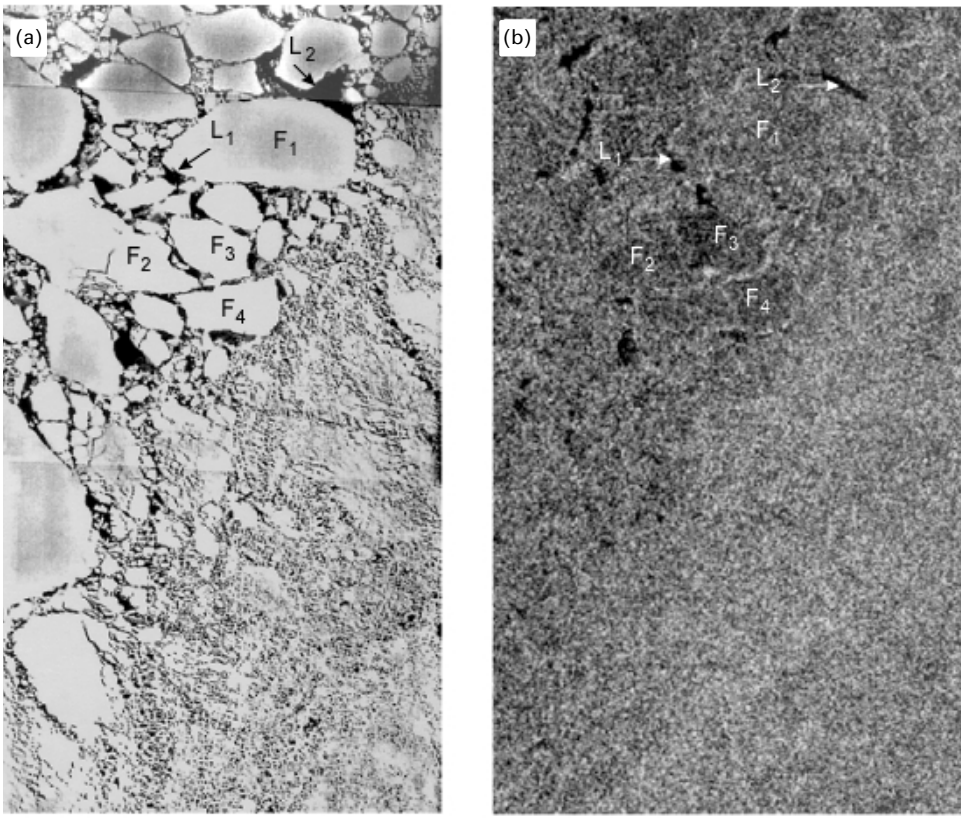

Figure 4.25. (a) Aerial photo of an 8 × 15-km area in the transition between the interior of the pack ice and an intermediate zone taken 8 March 1992. (b) Corresponding area from a full-resolution *ERS-1* SAR image (20-m pixels) taken on the same day. Floes (F_i) and leads (L_i) common to each image are marked (Sandven *et al.*, 1999a).

m resolution image was compared with aerial photography in Figure 4.27. The aerial photograph shows that the ice edge consists first of a 2 km wide band of ice cakes (<5 m in diameter) across the swath in the lower part of the photograph. Above this band a 4–5 km wide zone of mostly open water is found with some scattered bands of icefloes typically 100 m wide. North of the open water band, the ice pack consists of almost 100% concentration of small floes. The full-resolution SAR image, which covers the same area as the aerial photo, shows open water in the lower part of the image with slightly higher backscatter than the ice edge bands. Also shown clearly are long surface waves from the south that penetrate into the ice pack. Most of the smaller bands in the middle of the aerial photo are difficult to observe in the SAR image.

With frequently obtained SAR images of an ice edge area, it is possible to investigate ice edge development in major detail, as is shown by the four sequential *ERS-1* SAR images from 2 to 11 March 1992 in Figure 4.28, covering an area in which

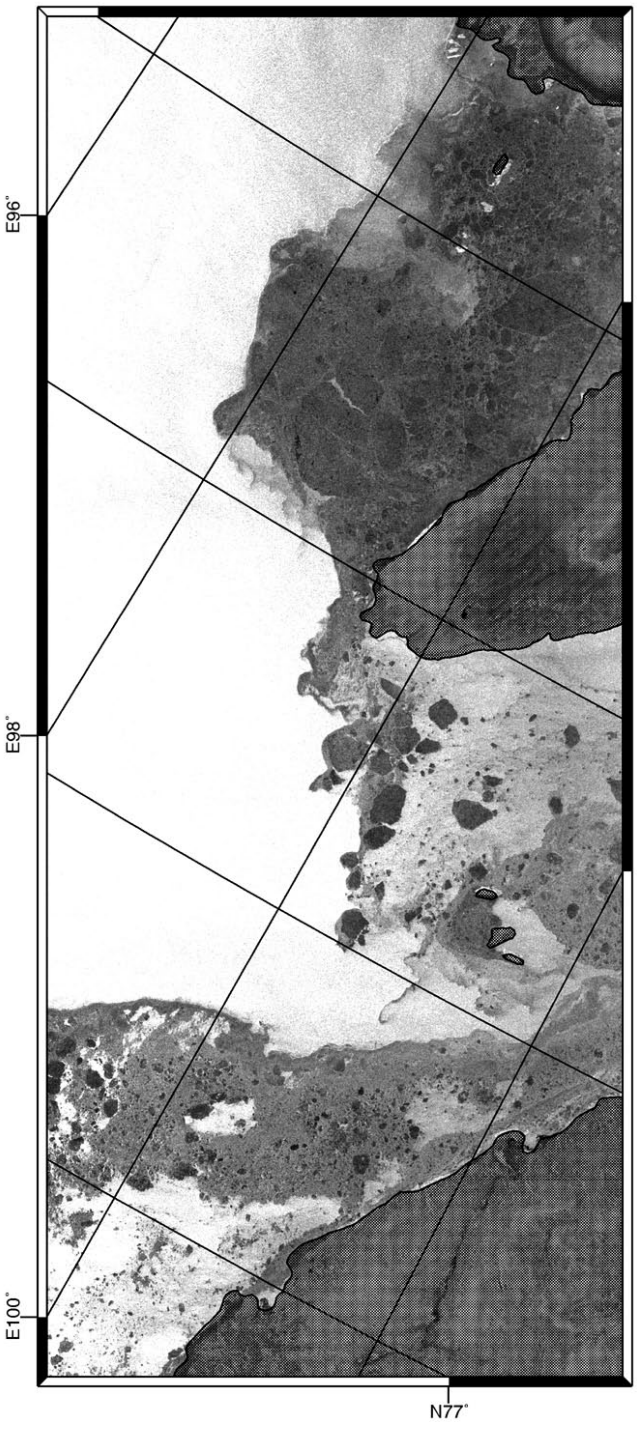

Figure 4.26. *ERS-2* SAR image of western Vilkitskiy Strait and parts of Shokalskiy Strait on 17 August 1997 (© European Space Agency) (Sandven *et al.*, 2001).

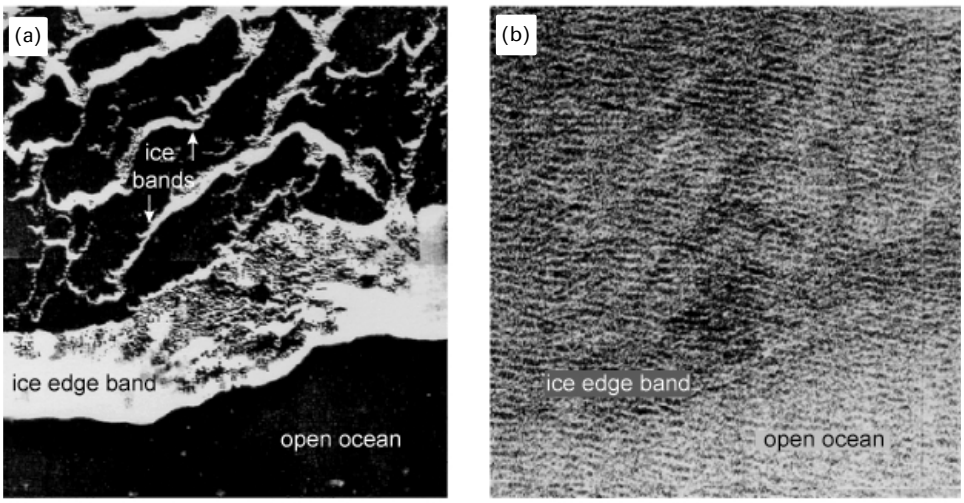

Figure 4.27. (a) Aerial photo covering an 8 × 8-km area of the ice edge region taken on 8 March 1992, a few hours after an *ERS-1* overpass. (b) Sub-image of a 30-m resolution *ERS-1* SAR image, covering the same area as the aerial photograph. Alternating bands of ice floes and open water are shown (Sandven *et al.*, 1999a).

field *in situ* observations were also made. Common to all the images is the fact that the main ice pack (top left), consisting of mostly first-year and some multi-year ice, is readily distinguished from areas of newly formed ice and open water. Within the ice pack, two different ice zones are apparent in the SAR images. The first is an intermediate ice edge zone about 20–30 km wide characterized by many small floes, broken up by the incoming wave field. It appears as a relatively uniform gray area in the SAR images without any identification of individual floes or other ice features. North of it is the interior of the ice pack, which has not been affected by surface waves. This area consists mostly of very close first-year ice with groups of large multi-year floes (light-gray image features) drifting southward from the Arctic Ocean. Three different ice zones were defined on the basis of these observations: the interior of the ice pack, the intermediate zone and the ice edge zone. The ice edge is evident in all the images.

The ice edge on 2 March 1992 was remarkably well-defined and nearly straight due to southeasterly (on ice) winds of 6–8 m s^{-1} during the preceding days. The SAR image distinguishes clearly between open water and compact ice (i.e., the ice edge) and the grease ice areas outside the ice edge. Due to predominantly southwesterly winds between 2 and 5 March 1992 the ice edge began to meander and was less well-defined in Figure 4.28b. The area of newly forming ice outside the main ice edge expanded considerably in this period, and much of the grease ice had changed into pancake ice within 24–48 hours, based on *in situ* observations. The distinction between grease ice (dark signature) and pancake ice (bright signature) is clear on the 5 March 1992 SAR image. Continued reconfiguration and relocation of the ice edge is evident in the SAR images for 8 and 11 March 1992 as shown by Figures 4.28(c) and (d). Moderate

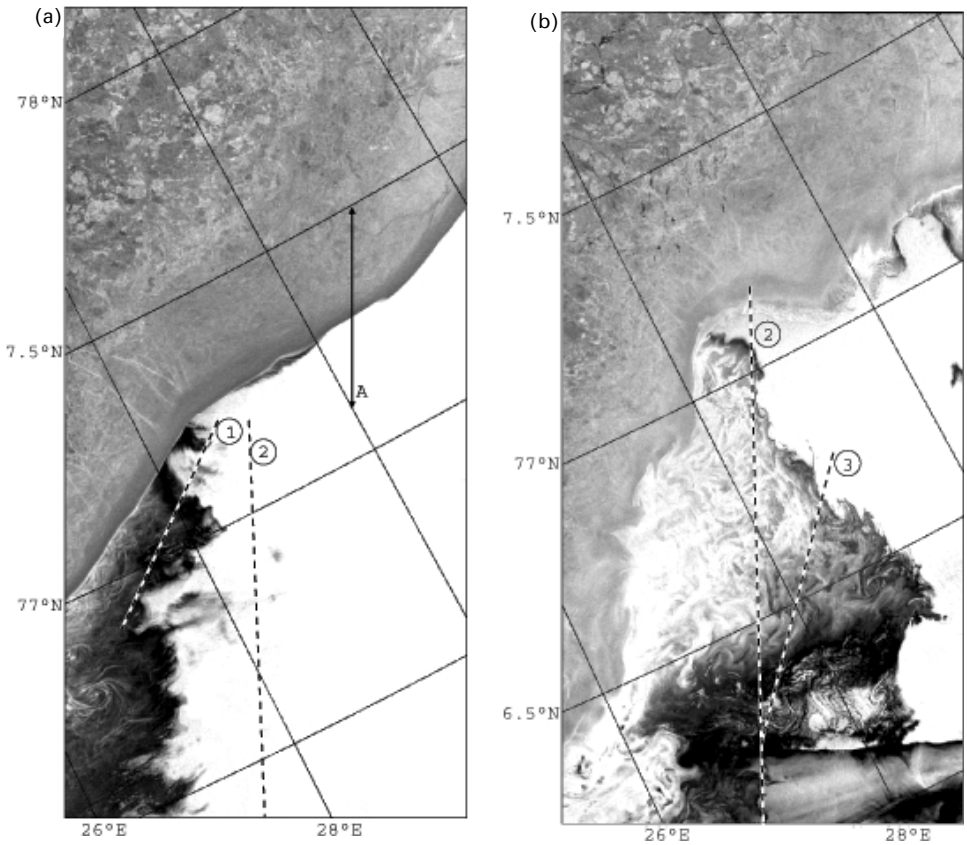

Figure 4.28. *ERS-1* SAR images acquired on 2 March (a), 5 March (b), 8 March (c) and 11 March (d) 1992, from the same descending path in the western Barents Sea. The sequence shows the movement, development, and reconfiguration of the ice edge. The locations of low-altitude aerial photographs are marked with squares in (c) (Sandven *et al.*, 1999a).

(4–6 m s^{-1}) off-ice winds caused bands of small floes parallel to the main ice edge, but these bands were not seen in the SAR images.

The availability of wide-swath SAR images from *Radarsat* and *Envisat* satellites has significantly improved the possibilities of large-scale studies of the ice, including mapping of the edge zone. The *Radarsat* ScanSAR image in Figure 4.29 shows a meandering ice edge in the eastern Barents and Pechora Seas during winter conditions. Calm open water is clearly seen as dark areas due to its low backscatter. Bright stripes of ice and ice tongues—containing pancake ice, young ice and first-year ice cake—can be seen at the ice edge.

Overall, the satellite SAR data were found to be well-suited for studying small-scale spatial variability of the ice edge. However, due to significant variability of water backscatter SAR cannot reliably distinguish open water from sea ice in some wind situations. For example, areas with a light-gray tone can be either ice or roughened

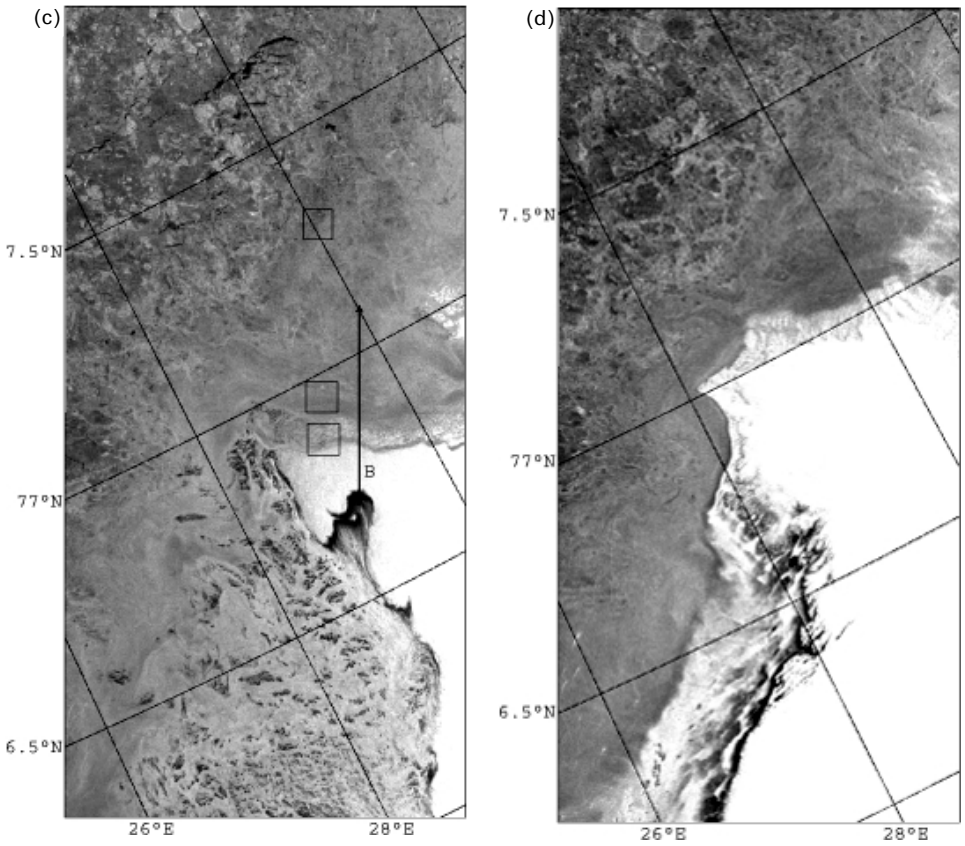

Figure 4.28 (*cont.*)

water at medium windspeed, whereas dark-gray tone areas can either be calm water or thin, smooth ice (Gill and Valeur, 1999). The location of diverging ice edges can be very difficult to determine with precision, especially during summer conditions when most ice is dark in SAR.

4.3.5 Openings in the sea ice

Identification of openings in the ice is important for navigation, such as fractures and leads. Polynyas are nonlinear-shaped openings with open water enclosed in ice, which may contain brash ice and/or be covered with new ice, nilas or young ice. Their SAR signatures can be very different. In the case of open water it often changes signature as a consequence of wind direction. Wind can create Langmuir circulation within a polynya, causing the formation of grease and pancake ice stripes approximately parallel to the wind direction. These have a bright signature (Martin *et al.*, 1992). Polynyas covered with new ice and nilas have a dark tone in SAR image, while those

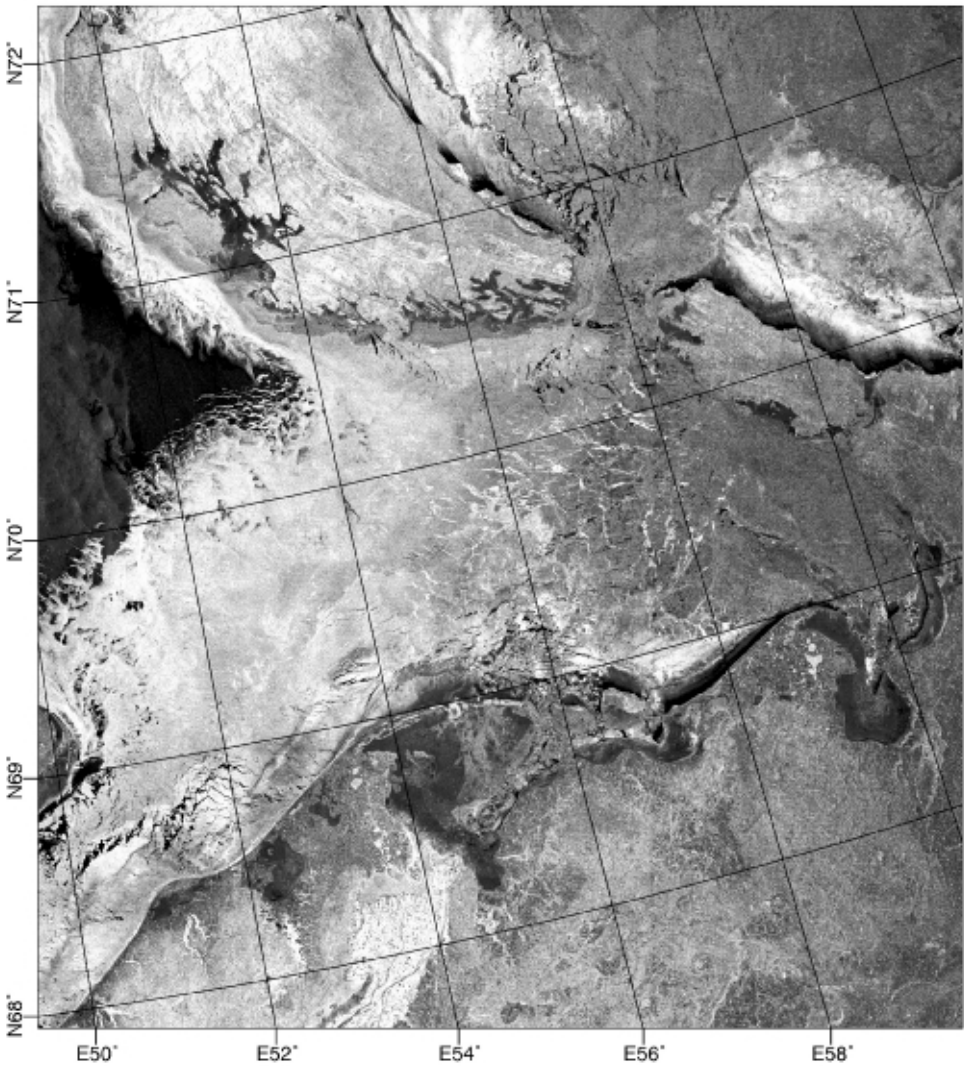

Figure 4.29. *Radarsat* ScanSAR image from 3 February 1997, covering the Pechora Sea. The meandering ice edge is clearly visible to the left (© Canadian Space Agency).

covered with young ice have a homogenous SAR tone brighter than that of drifting ice as shown in Figure 4.30, area 2. Thin first-year ice in area 3 has a darker tone than young ice and a more homogenous texture than average and thick first-year ice.

Analysis of the possible use of SAR to detect fractures has been made based on near-simultaneous sea ice observations from icebreakers. Full-resolution sub-images of the *Radarsat* ScanSAR image of 25 April with the overlaid route of the icebreaker *Sovetsky Soyuz* are shown in Figure 4.31. Compared with the first-year ice, which

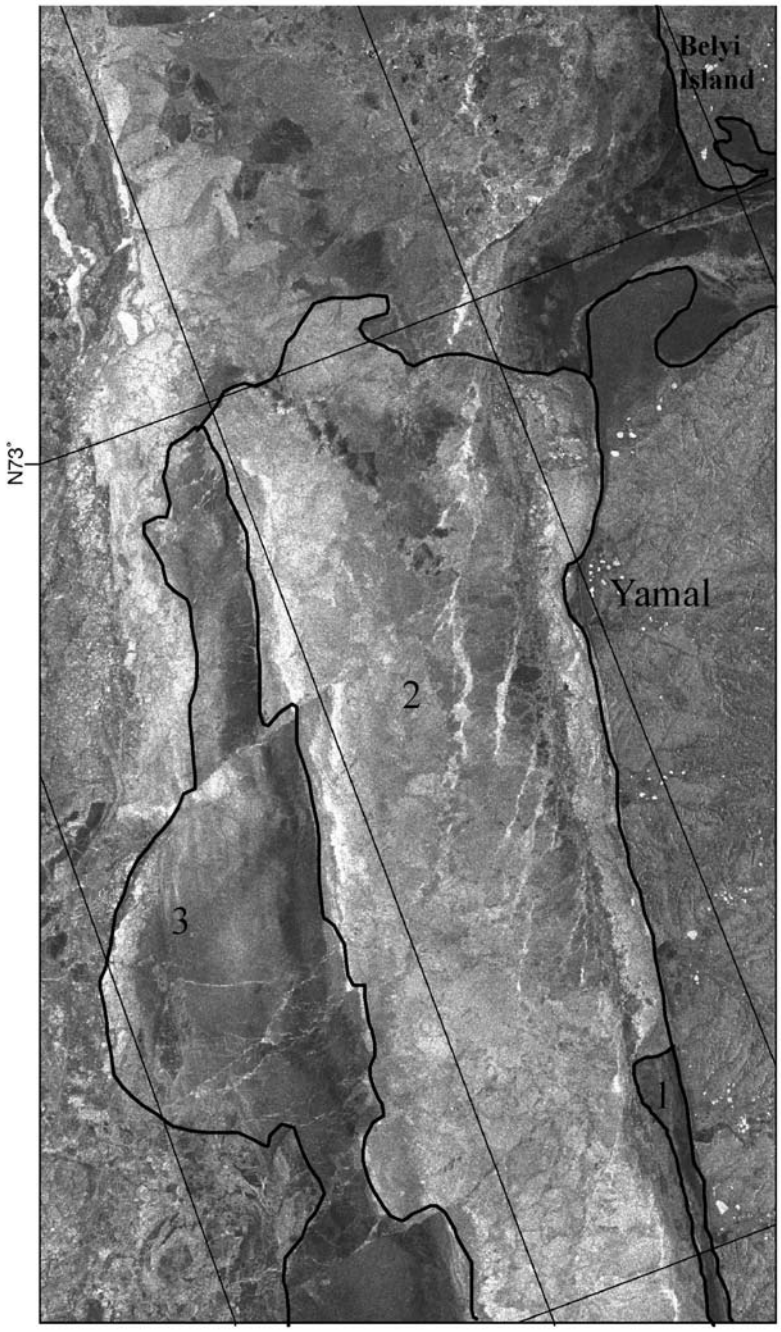

Figure 4.30. *ERS-1* SAR image from 9 January 1996, covering sea ice to the west of the Yamal coast: 1 = fast ice; 2 = young ice in Yamal's recurring polynya; 3 = thin first-year ice (© European Space Agency).

covers most of the sub-image, leads with open water and nilas—legs 1, 2 and 3, Figure 4.31(a)—have a darker signature, while refrozen leads covered by gray ice (e.g., leg 4) have a brighter signature. The non-frozen lead in leg 5, varying from 300 m to 500 m in width, can also be detected in the ScanSAR mosaic where the pixel size is 400 m. The grayish signature in leg 6 corresponds to medium/thick first-year ice of moderate roughness. Leg 7 shows another example of the high contrast in backscatter between gray and gray–white ice and nilas.

Another ScanSAR sub-image—Figure 4.31(b)—shows similar ice types but with a dominant fracture zone across the image. Legs 1 and 2 cross a wide polynya between two large first-year floes, showing characteristic differences in backscatter between first-year ice, young ice and nilas. Legs 3, 4 and 5 cross the main fracture zone with many small first-year icefloes mixed with small leads and gray and gray–white ice. Legs 6 and 7 cross through medium and thick first-year ice of moderate roughness with narrow leads and fractures.

Comparison shows that the detection of leads that are 200–300 m wide in compact first-year ice is easy in ScanSAR images, even if the pixel size is 400 m. This conclusion on sub-resolution lead detection is in agreement with visible and thermal band remote sensing (Miles and Barry, 1998). Several small-scale features, such as leads of approximately 100-m width, fracture zones and icebreaker channels were also detected in full-resolution ScanSAR images. In difficult areas it is recommended to use 100-m resolution ScanSAR sub-images in near-real time to select the optimal sailing route (Alexandrov *et al.*, 2004). Unambiguous interpretation of leads in SAR images can be difficult. A fracture shown with a light tone can be misinterpreted as a wide ridge. Leads covered with gray ice may not be detected in old ice since backscatter coefficients are similar. Fresh channels in first-year and young sea ice formed by ships are often seen in SAR images.

4.3.6 Ice surface deformations

Sea ice is divided into level ice that has not been affected by deformation, and deformed ice that has been squeezed together and in places forced upwards and downwards (WMO, 1989). The subdivisions of deformed ice are rafted, ridged and hummocked ice. The backscatter from deformed ice exceeds that from level ice, because of the roughness, including corner reflection of radar signals from some surfaces. Rafted new and young ice can be seen as a bright feature in a SAR image. The possibility to detect ridges from SAR data depends on their width relative to radar resolution. Incidence angle and polarization may also affect detection. Sometimes ridges are better detected at HH-polarization since the radar contrast between level and ridged ice may be higher than at VV-polarization.

SAR signatures of deformed, low-salinity ice were studied during a sub-satellite experiment in the Gulf of Bothnia (Sandven *et al.*, 1999b). A *Radarsat* ScanSAR narrow-swath image for 10 March 1997 in Figure 4.32 has been compared with visible *Resurs* images and with sub-satellite *in situ* data. The homogenous, dark SAR signature in areas 1 and 2 corresponds to ice with a level surface. A grounded hummock with horizontal size of several hundred meters is clearly seen as a bright

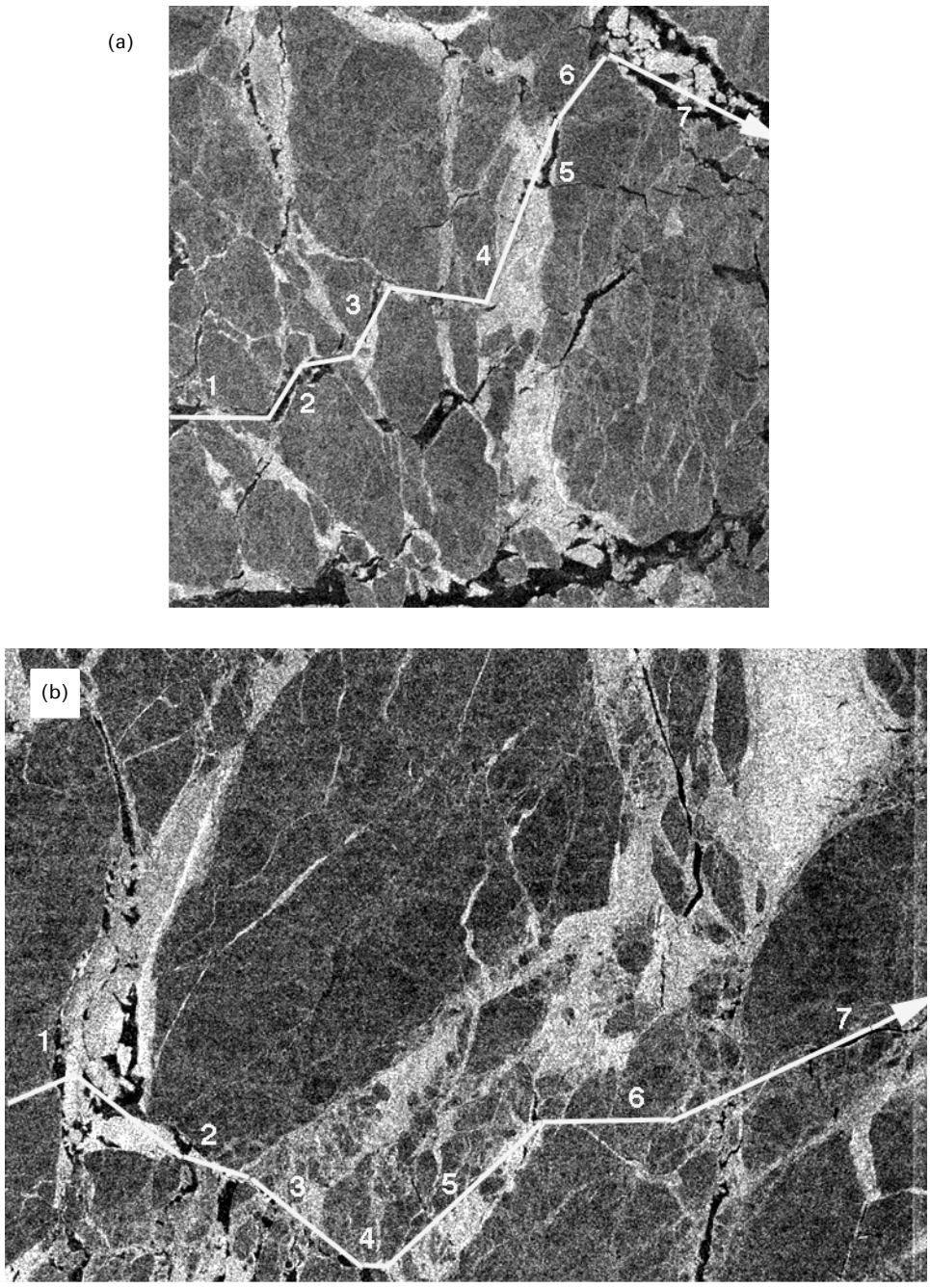

Figure 4.31. Full-resolution sub-images of *Radarsat* ScanSAR wide from 25 April 1998. The route of the NIB *Sovetsky Soyuz* and sites of sub-satellite sea ice observations are overlaid (© Canadian Space Agency).

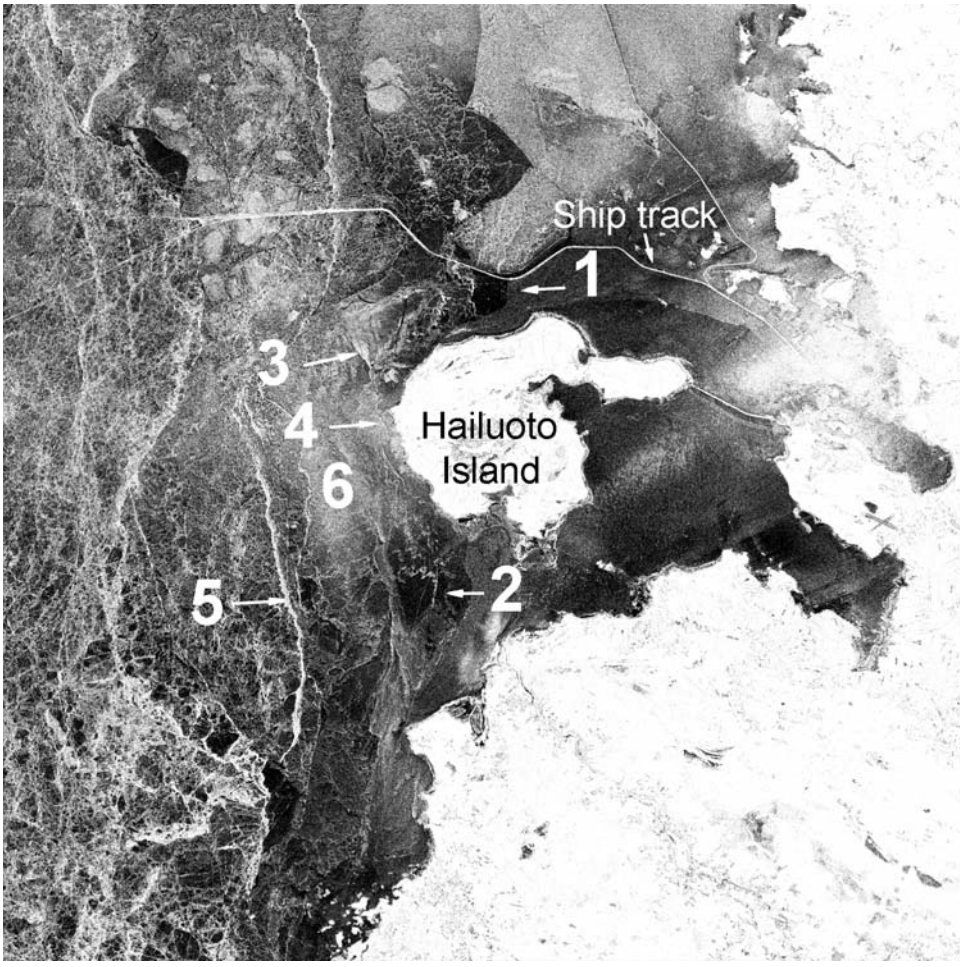

Figure 4.32. *Radarsat* ScanSAR narrow image from 10 March 1997, covering the northern part of the Gulf of Bothnia. The sites of *in situ* ice observations mentioned in the text are numbered 1–6 (© Canadian Space Agency).

spot marked by 3. A 5–7 m wide ridge can be detected in the ScanSAR image as a thin white line (4). Its width was determined during field studies. In a *Radarsat* fine-resolution image it was possible to detect ridges only 20–30 cm high and 1 m wide. A ridge approximately 1 km wide (5) is shown as a thick, white line. It was also detected in an *Okean* RAR image with a spatial resolution of about 1–2 km. The homogenous, bright SAR signature in area 6 corresponds to undeformed ice, but its surface was covered with regular rough features with a typical size of about 20 cm. According to Melling (1998), ridges in first-year ice are more difficult to detect in *ERS-1/2* SAR images compared with those of *Radarsat*, probably due to the small incidence angles and VV-polarization.

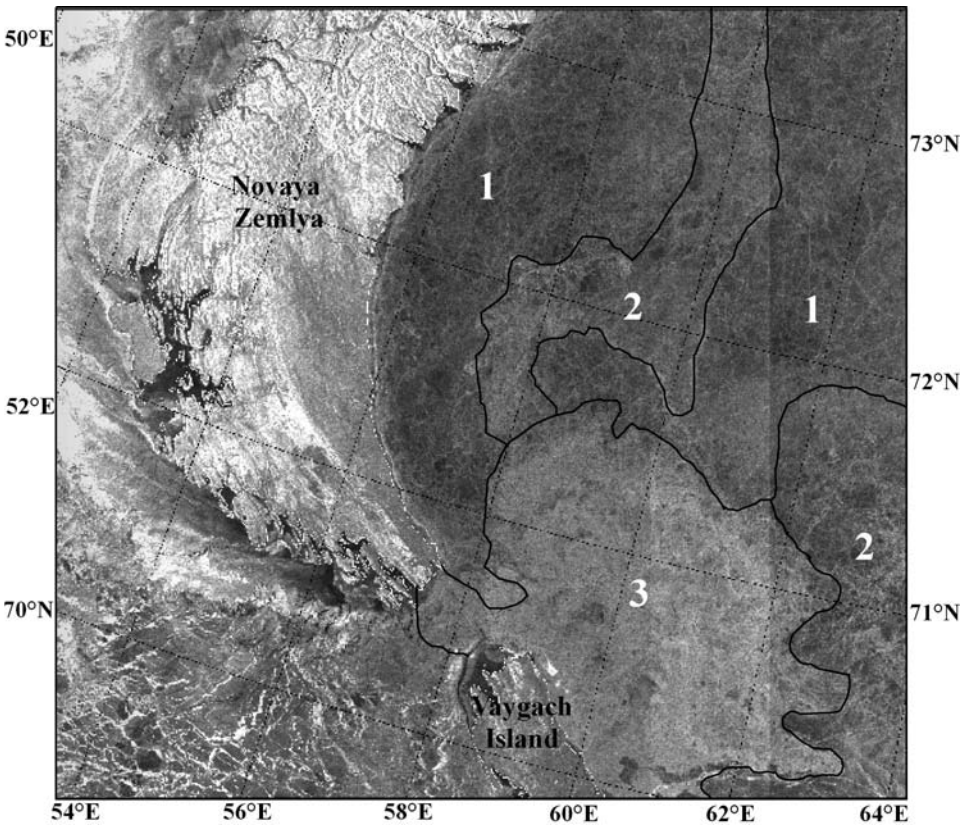

Figure 4.33. *Envisat* ASAR image from 18 February 2004 with interpretation: (1) slight deformed first-year ice; (2) moderate deformed first-year ice; (3) heavily deformed first-year ice (© European Space Agency).

In first-year ice large areas of level ice, as well as slight, moderate and heavy deformed ice can be detected from *ERS*, *Radarsat* and *Envisat* SAR images. For example, in the *Envisat* ASAR image of 18 February 2004, presented in Figure 4.33, areas of various ice deformations are marked. Image tone changes from dark for level fast ice in the bays of Novaya Zemlya to bright for heavily deformed ice.

The surface of old ice is covered with smooth hillocks, formed by the melting of ridges and hummocks during summer. Since the strong backscatter from old ice is mainly caused by volume scattering within the ice and not by its surface, its surface roughness has a small effect on SAR images.

Our analysis of successive *ERS-2* SAR images of freshwater ice has shown that during intensive melting the difference in backscatter of deformed and level ice significantly decreases, and it is impossible to distinguish them in a SAR image (Alexandrov *et al.*, 2002). Also, analysis of successive *Envisat* ASAR images of the Yenisey Gulf showed that, during melting, deformed and level fast ice became indistinguishable.

4.3.7 Icebergs

Icebergs observed in Eurasian Arctic seas are calved from outlet glaciers, located in Svalbard, Novaya Zemlya, Franz-Josef Land and Severnaya Zemlya. In the Barents and Kara Seas they are usually observed north of 74°N, but in some years (e.g., 1929) they appeared even near Murmansk and at the entrance to the White Sea (Abramov, 1996). In May 2003 an anomalously large number of icebergs (109) was detected in the eastern Barents Sea in the area adjoining the Shtokman gas deposit field (73°N, 44°E). The maximum horizontal dimensions and maximum height were 190×430 m and 20.8 m, respectively (Zubakin *et al.*, 2004). The probability of iceberg occurrence in the southwestern Kara Sea, near the western coast of Yamal is small. The southern boundary of their distribution in the northeastern Kara Sea is located at 75–76°N. Large numbers of icebergs are frequently observed in the western Laptev Sea, where the southern boundary of their distribution reaches Provideniya Bay and Preobrazheniya Island (Abramov, 1996; Zakharov, 1996; Eicken *et al.*, 1994; Alexandrov, Kolatschek, 1997). Icebergs from Severnaya Zemlya are often found in Vilkitskiy Strait (Zakharov, 1996). Icebergs are dangerous to ships and sailing along the NSR, as well as to oil installations and underwater pipelines on the Arctic Shelf (Voevodin and Popov, 1996).

High-resolution SAR may be used to detect icebergs in the NSR. Even if they are small compared with Antarctic and Greenland icebergs, their backscatter coefficient may significantly exceed that of sea ice and calm sea surfaces. Icebergs that are too big for radar resolution may be seen as bright spots in SAR images, and in some cases their tracks in sea ice can be seen (Septhton and Partington, 1998). The SAR potential for iceberg detection—depending on their size, form and the parameters of adjacent sea ice or open water—has been investigated in several experiments. Iceberg sizes were measured from aerial photo-survey data or estimated visually and imaged with SAR.

In the *ERS-2* SAR image in Figure 4.34 of 11 September 2001, covering the area east of Red Army Strait in the Laptev Sea, approximately 20 icebergs can be seen among newly formed ice in area 1. Some of the icebergs (see arrow in Figure 4.34) are within drifting sea ice, which has a higher backscatter than new ice. More than 100 icebergs were observed in this area during previous expeditions in 1989, 1993 and 1995—most of them were small (<60 m). In SAR images only the largest icebergs can be detected (Alexandrov *et al.*, 2003). Willis *et al.* (1996) show that under corresponding conditions it is possible to detect about one-half of small icebergs (15–60 m in diameter), two-thirds of average icebergs (60–120 m) and practically all large icebergs in *ERS* SAR images.

An approximately 100 m long iceberg, observed from the icebreaker *Sovetsky Soyuz*, is shown as a bright spot in the full-resolution ScanSAR sub-image of the western Laptev Sea in calm open water in Figure 4.35. Several other similar spots can be seen in this sub-image, although no other icebergs have been observed from the icebreaker in this area (Sandven *et al.*, 2001). This confirms to some degree the conclusions of Willis *et al.* (1996) and Johannessen *et al.* (1997a) that mapping of small icebergs from SAR images may result in a number of false objects. Iceberg

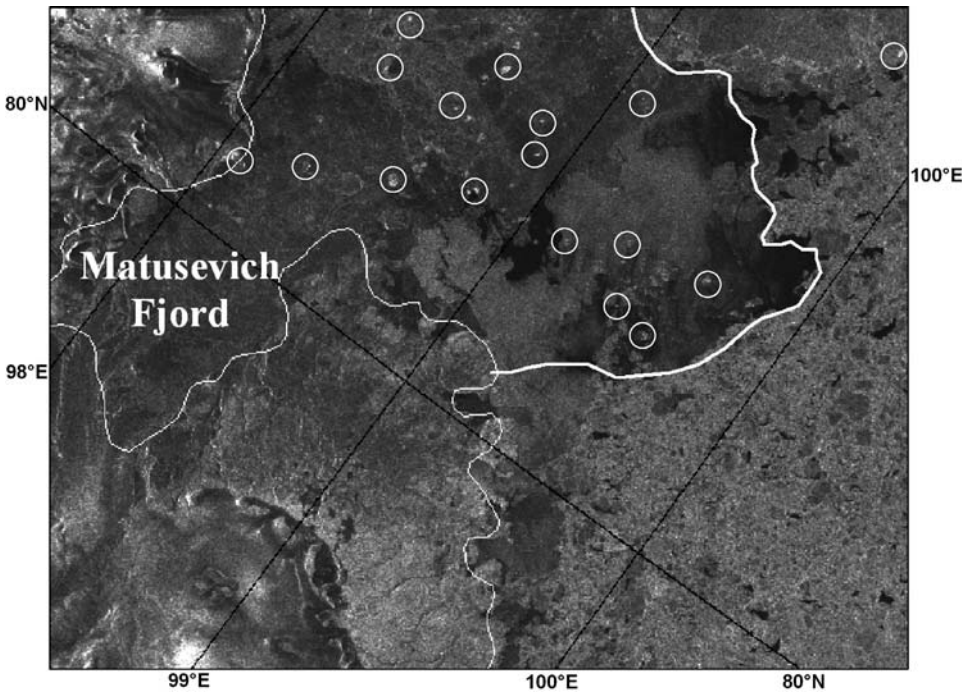

Figure 4.34. *ERS-2* SAR image from 15 September 2001, covering the eastern part of Red Army Strait in Severnaya Zemlya and an area eastward of it. Several icebergs in this area can be detected due to their bright SAR signature, as indicated by the white circles (© European Space Agency).

detection by SAR in open water is also limited by wind conditions. When wind speed increases, the backscatter contrast between icebergs and surrounding open water is reduced.

A large number of growlers, bergy bits and small icebergs occurs seaward of several outlet glaciers located in the northwestern part of Novaya Zemlya, see Figure 4.36. The areas seaward of the Vera and Bunge outlet glaciers have a homogenous, bright signature, different from that of open water in *ERS-2* SAR images, marked on the figure. The external boundary of iceberg distribution was determined by near-simultaneous sub-satellite observations from a ship. The icebergs spread seaward for several miles and correspond to the bright areas in SAR images. This is a cumulative effect of a large number of icebergs at concentrations from $\frac{2}{10}$ to $\frac{3}{10}$ of the area. Therefore, the areas seaward of these outlet glaciers with a large number of growlers, bergy bits and small icebergs, can be detected in SAR images as an integrated effect.

Only a few individual icebergs can be identified, as shown by the rightmost circle in Figure 4.34.

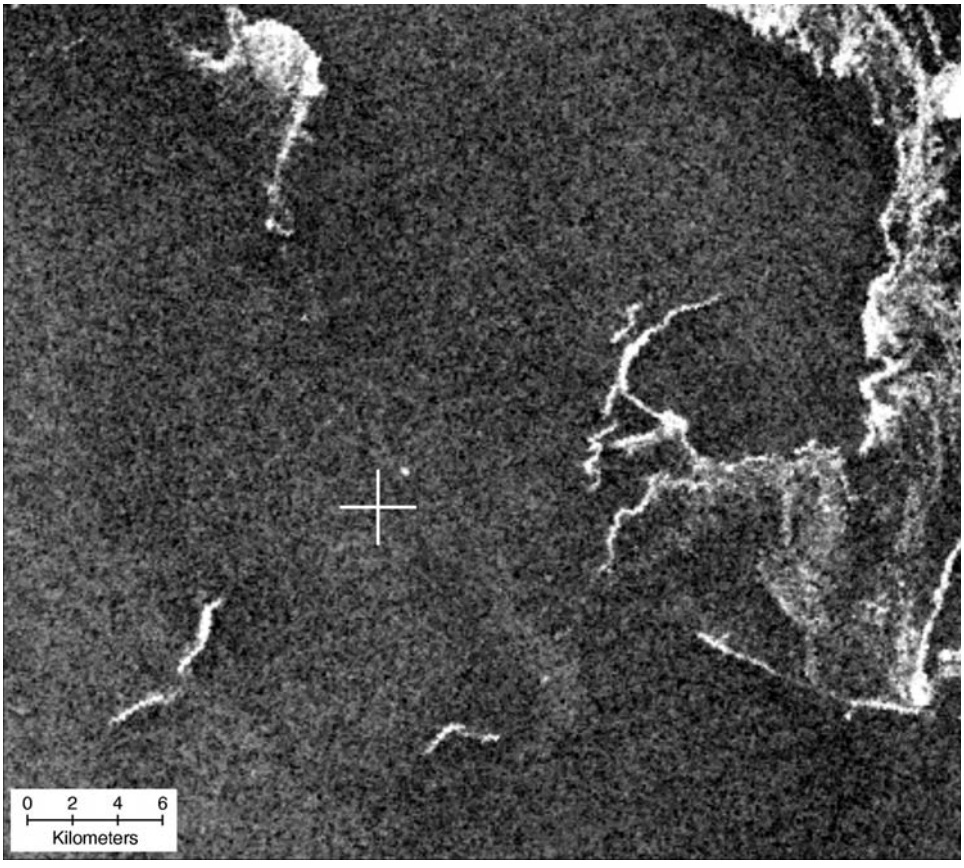

Figure 4.35. Full-resolution *Radarsat* ScanSAR wide sub-image from 7 September 1997, covering the western part of the Laptev Sea. The iceberg observed from the NIB *Sovetsly Soyuz* is up and to the right of the cross (© Canadian Space Agency).

Summary

As a result of SAR studies with sub-satellite experiments, the signatures of the principal sea ice types and features in *ERS*, *Radarsat* and *Envisat* SAR images have been specified and verified during different seasons.

During winter, several stages of ice development can be derived from SAR images, including new ice, young ice, first-year ice and old ice. For a given ice type, its SAR signatures may be different for various ice forms. Separate floes can be detected when their size significantly exceeds the spatial resolution of radar. The deformation of first-year ice can be detected and divided into level ice, slightly deformed ice, moderate deformed ice and heavily deformed ice. Shore and flaw polynyas can be identified and their width measured. The possibility of detecting leads in drifting sea ice depends on their width and also the type of ice contained in

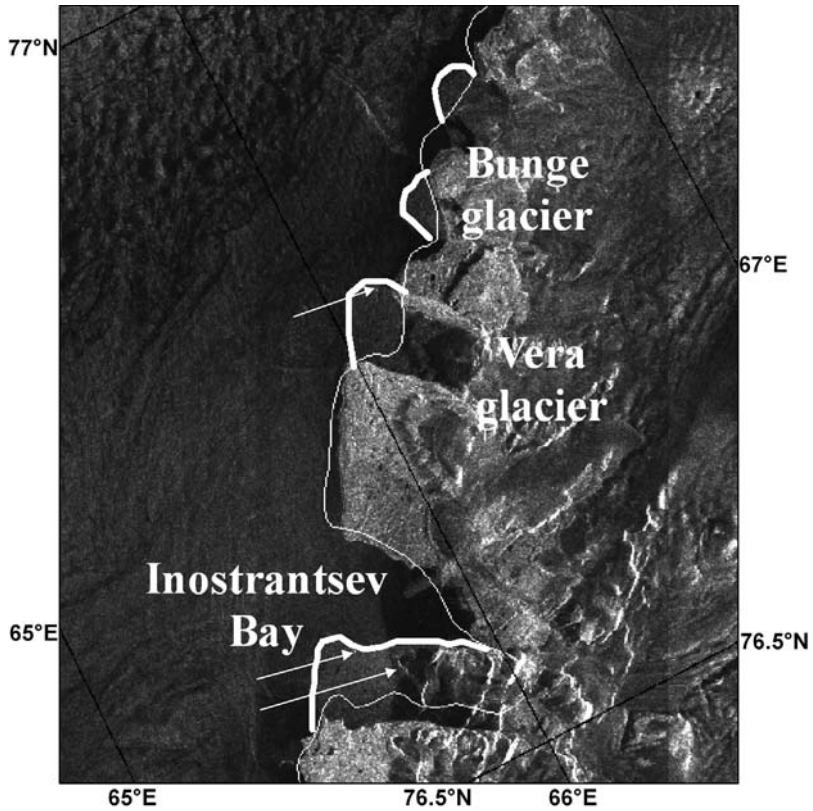

Figure 4.36. *ERS-2* SAR image of 7 September 2001, covering the outlet glaciers in the northern part of Novaya Zemlya. Areas with a $\frac{2}{10}$ to $\frac{3}{10}$ concentration of icebergs seaward of glacier boundaries are evident with a relatively bright SAR signature. These areas are shown with a white line (© European Space Agency).

them. Long leads can be seen, even if considerably narrower than the SAR resolution. Identification of a minor fraction of the relatively small icebergs occurring in the NSR is possible within certain limits. In most cases fast ice and its boundary are easily detected in SAR images. If necessary, some ambiguities can be resolved using successive images. Determination of old ice and its boundary is possible in most cases. From successive SAR images, ice displacement and vectors can be calculated.

SAR images are successfully used for mapping sea ice conditions during summer as well. The following sea ice parameters—ice edge location, sea ice concentration, large icefloes, stripes of ice in water, ice drift vectors and areas of convergence/divergence—can all be derived from SAR (Sandven *et al.*, 2001). Satellite SAR is excellent for detailed mapping of ice edge location and its changes, leads, polynyas and ice with different surface roughness.

Ambiguities in SAR image interpretation are caused by the similarity of signatures for different sea ice types and features. Without *a priori* data it is impossible to

distinguish between thin, medium and thick first-year ice, and also between second-year and multi-year ice.

4.4 SEA ICE RETRIEVAL ALGORITHMS FOR SAR
(*A.V. Bogdanov, S. Sandven, O.M. Johannessen, V.Yu. Alexandrov, L.P. Bobylev, V.S. Loshchilov*)

Visual analysis of radar and optical satellite images by an expert remains a major technique in their interpretation and is widely used, particularly when ice conditions are difficult for interpretation, such as those observed in the MIZ (Johannessen *et al.*, 2003). However, the role of automatic and semi-automatic techniques is constantly increasing, and digital image processing and pattern-recognition techniques are widely used in interpretation of remote sensing data. Among the earliest applications, computers were used for image processing during the unmanned lunar and planetary exploration missions conducted by NASA in the mid-1960s (Green, 1989). The images were converted from analog to digital format and then computer-processed. Many of the digital image processing capabilities developed at that time—such as image enhancement and thresholding—are used today. With the increased computational power and development of new algorithms for image processing and analysis, the question addressed now is how far computers can go to replacing humans in interpreting image data collected from satellites, aircraft and ground observations.

With regular acquisition of high-resolution SAR data the volume of obtained data sets increases drastically and visual interpretation of these images and retrieval of sea ice parameters becomes laborious. Therefore, significant attention was paid to the development of algorithms for automatic derivation of the main sea ice parameters: ice type and concentration (Kwok *et al.*, 1992b), icefloe distribution (Soh *et al.*, 1998), detection of icebergs (Willis *et al.*, 1996), ice motion (Fily and Rothrock, 1987) and several others. Image processing algorithms, where a computer does most of the routine work—such as image geolocation, enhancement and operator-assisted classification—are used in several sea ice information centers. These ice centers also require automated algorithms for SAR image interpretation to assist sea ice experts in extracting geophysical information. Producing ice type and ice concentration estimates automatically has been a long-standing goal of both the operational and scientific communities (Bertoia *et al.*, 1998). Automated algorithms of sea ice classification and ice drift retrieval from SAR data have been implemented at the Alaska SAR Facility. A fully automated ARKTOS[6] system that classifies sea ice images in an operational environment by mimicking the reasoning process of sea ice experts has been developed (Soh *et al.*, 2004). The intention of this section is to describe some of the techniques currently used for automatic interpretation of SAR images, provide examples of this interpretation and discuss its results, and to outline future directions in the development of these algorithms.

[6] ARKTOS is an intelligent system for satellite sea ice image analysis named Advanced Reasoning using Knowledge for Typing Of Sea-ice (ARKTOS).

4.4.1 Sea ice classification

Sea ice classification approaches: manual, semi-automatic, fully automatic

The objective of sea ice classification is to categorize SAR image pixels into several ice categories. These categories are often defined as a compromise between practical usability of classification results and information capability of satellite data to derive important characteristics of sea ice as defined by WMO (1989). The used ice categories are mainly related to sea ice development and its surface roughness. Ice thickness cannot be derived from SAR images, but can be roughly estimated from the ice development stage. Correct classification of sea ice is also an important prerequisite for estimation of other sea ice parameters—such as ice concentration, distribution of polynyas and their shapes.

Classification can be visual, semi-automatic and fully automatic (i.e., performed without human intervention). Both semi-automatic and fully automatic approaches require the involvement of experts for selecting classification system parameters (feature extraction, segmentation algorithm parameters, structure optimization, etc.) and training (selection of training regions, estimation of classifier parameters, definition of expert rules, etc.) if a supervised algorithm is used. Semi-automatic algorithms are currently most often used for sea ice classification as "a reasonable compromise between an automated scheme which is unlikely to be valid outside very restrictive circumstances and a fully manual scheme which fails to make use of any computer intelligence in assisting the user" (Sephton and Partington, 1998). The functions of an operator in such approaches are: (1) evaluating and proving the classification results, (2) selection of classification algorithm parameters and (3) interactive correction of classification results by assigning correct labels to the segments or changing their form if required. In classification tasks the operator rather than an intelligent computer program can more easily solve complex perceptual problems—such as outlining meaningful ice objects (icefloes, leads), taking into account complex relationships between objects and using his/her expert knowledge. Modern digital computers outperform humans in the domain of numeric computation and related symbol manipulation. In particular, computer-based algorithms easier accommodate subtle differences in image brightness, operate with exact quantities, and computation results can be readily evaluated at each of the processing steps. Thus, currently used techniques are based on the semi-automatic approach, combining advantages of visual interpretation with that of computer-based processing. One of the currently pursued ways is to simulate some of the human cognitive processes or low-level mechanisms of neuronal information processing in the brain and to implement them in the computers.

Classification chain

The typical image processing chain used for classification of sea ice includes: (1) image pre-processing; (2) segmentation of ice features if a segment-based approach is used; (3) computation of image (segments) parameters; (4) pixel- or region-based classification using the computed parameter sets; and, finally, (5) post-processing. Because the

information is processed sequentially in feed-forward manner, the success of the current operation depends on the fulfillment of all previous operational steps. In practice, this means that the parameters used for pre-processing, feature extraction and classification must be carefully tuned to the task at hand before operation of the algorithm.

The approaches to sea ice classification can be assigned to two main categories: region-based classification and pixel-based approaches. In pixel-based algorithms, normalized image pixel values or digital numbers (DNs) are used in classification. When multi-spectral or multi-polarization images are available, corresponding pixel values are combined in a feature vector. In region-based classification the calculated parameters of the segments are stacked in a feature vector and used for their classification.

Tonal information conveyed by separate pixels is directly related to the measured physical quantity (backscattering coefficients for SAR and reflectance for optical images), which carries information on sea ice state, type and other parameters. Single-source pixel-based classification, however, is in many cases ambiguous because several sea ice types and open water have similar tonal properties. For example, the ranges of backscatter coefficients of open water and sea ice may overlap significantly (Section 4.2 and Figure 4.13). If just a single sensor image is available, computation of texture and other local statistical parameters and their use in classification usually improves the results. Fusion of data from several sources can greatly improve the quality of derived ice information.

Pre-processing

Image pre-processing can include radiometric and geometric corrections, filtering and reduction of speckle noise and contrast enhancement. The goal of this step is to remove possible artifacts from the images and assure their relative or absolute calibration. Both types of calibration are used for automatic image classification. Absolute calibration is required when scatterometer surface-based measurements of the backscattering coefficients of sea ice are used in classification and in some sensor fusion algorithms. Relative calibration is sufficient in many cases for supervised image classification, thus guaranteeing that the radar signatures of new, incoming data will be similar to those used for training of the classification algorithm. For unsupervised image classification—aiming to find distinct clusters in feature space without their assignment to pre-defined ice classes—only the invariance of object radar signature on its position within the same image is required.

To achieve radiometric calibration the user in some cases needs to perform antenna pattern correction, range spreading loss compensation and a correction for incidence angle using known SAR parameters. For classification of wide-swath SAR images it is also necessary to account for angular dependence on the sea ice backscatter coefficient. To reduce this effect, a range-varying normalization—using empirical corrections for the surface type dominant in the image—can be applied. However, it requires *a priori* knowledge of the dominant surface type in the image and

cannot fully compensate the radiometric dependence for other surface types in the image.

Image segmentation

Segmentation is a process that subdivides the image into its constituent parts or objects (Gonzalez and Wintz, 1987). An image segment usually represents a homogenous—in terms of its tonal and textural properties—image area. Image segments may correspond to such ice objects as icefloes, leads, polynyas, areas of deformed ice, etc. The development of robust segmentation techniques is highly desirable for sea ice classification because (1) filtering and noise reduction can be done more effectively using the larger number of pixels constituting an object; (2) the segment shape can be used in subsequent classification along with texture and other image parameters; (3) information on segments can be used for higher level information processing and reasoning using knowledge bases, semantic nets, etc. for improved estimation of object properties and their classes.

Unfortunately, it is very difficult to elaborate a general algorithm capable of coping with different ice objects and ice conditions. Several segmentation algorithms are reported for detection of icefloes from the background of open water or brash ice (Banfield, 1991; Korsnes, 1993b; Soh *et al.*, 1998) and identification of polynyas. Even in these relatively well-defined sub-domains, some difficulties are encountered in developing a reliable segmentation algorithm that is able to operate in variable ice conditions. The fundamental problem with ice segmentation is that it is inherently fuzzy (Soh *et al.*, 1998) and under-constrained. The segments may not correspond to the ice objects (icefloes or polynyas) directly—contiguous icefloes can be combined together as a single segment—while, on the other hand, a polynya can be represented by several segments. Some *a priori* knowledge in the form of constraints is used to "reconstruct" ice objects from image segments. For example, the form of icefloes can resemble ellipses. Even with such constraints there are some exceptions that reduce the universality of the algorithms—for example, the edges of broken first-year ice cannot be rounded.

Region-based and contour-based image segmentation algorithms are used. Region-based segmentation is based on analysis of image regions that can be obtained as a result of unsupervised segmentation, global or local histogram analysis followed by morphological operations of erosion and dilation to smooth out segment edges. The known methods of region-based segmentation are split and merge (Gonzalez and Wintz, 1987), region growing (Beveridge *et al.*, 1989), knowledge-based methods and others. Contour-based image segmentation uses edge detection techniques—such as Laplacian and gradient-based edge detectors. Missing edge pixels can be obtained from analysis of the absolute values of image gradients and their directions: the search is performed in a direction perpendicular to the gradient direction. In the case of a high-resolution SAR image corrupted by gamma-distributed, multiplicative speckle noise, a likelihood ratio operator is an optimal detector, in the sense that it maximizes the probability of detection for a given probability of false alarm (Lopes *et al.*, 1999). In practice, the ratio of exponentially weighted averages (Lopes *et al.*, 1999), the ratio of local standard deviation to mean deviation (Sephton and Partington, 1998) and

others are used for edge detection. The surface and edges of objects represent different sides of the problem, and this redundancy can be used in hybrid approaches (Zhu and Yuille, 1996).

Examples of *ERS* SAR image (30.04.1998) segmentation using three different segmentation algorithms are shown in Figure 4.37. The image—Figure 4.37(a)—depicts (1) a flaw polynya near Arkticheskiy Institute Islands (dark patterns in the upper part of the image) containing areas of open water, nilas and deformed young/new ice accumulated in the long bright stripes; (2) small floes of young ice and ice cakes representing a bright background in the image in which (3) floes of first year ice are observed. Due to variability of the tonal and textural properties of the ice its segmentation is rather difficult.

The used segmentation algorithm—see Figure 4.37(b)—is based on finding the local minima in the image histogram, thresholding the image according to such minima, and application of the morphological operators of erosion and dilation to "smooth" object edges. Segmentation is not error-free: some icefloes are joined together in a single segment, whereas some others are only partially delineated. An advanced version of the region-based segmentation algorithm, which introduces the restricted growing concept and uses probabilistic labeling to determine object pixels, is described in Soh *et al.* (1998) for identification of icefloes in SAR images. In the later-developed ARKTOS sea ice classification system (Soh *et al.*, 2004) the authors used the watershed region-based segmentation algorithm. An example of application of this algorithm to the same image and using the same set of parameters as described in Soh *et al.* (1998) is presented in Figure 4.37c. The algorithm first finds local minima in the image and the "steepest descent" algorithm is applied to the gradient image to mark all the pixels according to the local minima they converge. The algorithm typically produces a large number of small segments, so a number of iterative region merging operations is performed using mean segment brightnesses and gradient at the border to obtain larger segments. In Figure 4.37d the result of the region-growing segmentation algorithm, which uses the ratio of means of the current segment to that of an adjacent region as a measure of similarity, is presented. The algorithm also starts by finding local minima. The adjacent region is joined to the current segment if the ratio is less than the threshold, which is in this experiment set at 2.

Feature extraction

Image features also called "image attributes" describe tonal image properties, image texture, form and shape of icefloes, border state and other properties. It is assumed that these features describe some specific properties of ice type, which helps in its separation from other ice types. Finding and selection of ice image features with the highest discrimination capacity is an important step in the design of a sea ice classification algorithm. If the selected features provide well-separated ice clusters in the feature space, even a simple "box" classifier can produce satisfying classification results. On the other hand, classification becomes very difficult in cases when the corresponding clusters are strongly overlapped. Different sets of image features

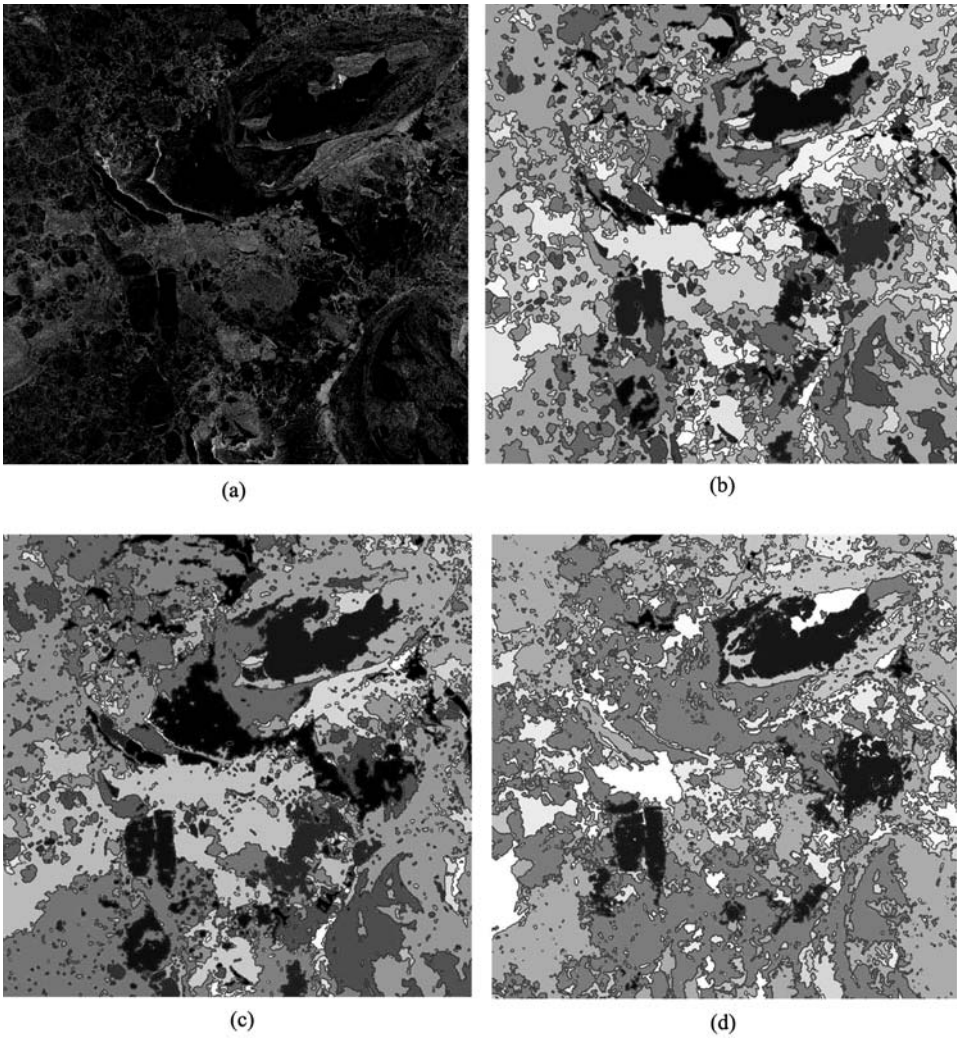

Figure 4.37. Examples of sea ice segmentation of an *ERS* SAR image (a) taken on 30 April 1998 of the Kara Sea using (b) simple histogram-based thresholding followed by application of morphological operators of erosion and dilation and iterative region merging; (c) watershed segmentation algorithm followed by iterative region merging (Soh *et al.*, 1998); and (d) image brightness-based region-growing algorithm followed by iterative region merging. The brightness of segments is proportional to the mean image brightness (image data © European Space Agency) (see also color section).

have been investigated during recent years: texture features, image moments, wavelets, etc.

Local, statistical image features can be computed within a small pixel neighborhood that is, however, large enough to obtain the required statistics. The SAR image

features used for feature vectors comprise three main groups: image moments, gray level co-occurrence matrix (GLCM) texture and autocorrelation function-based features. Texture features are often understood as a description of spatial variations of image brightness in a small image region. Some texture features can be used to describe regular patterns in the region, while others depend on overall brightness distribution. Texture has been used for a long time by sea ice image interpreters for visual classification of different sea ice types in radar images. For example, multi-year ice is characterized by a patchy image structure explained by the formation of numerous melt ponds on its surface during summer. Another example is the network of bright, linear segments corresponding to ridges in deformed first-year ice. Texture depends on the spatial resolution of the radar, the spatial scale of sea ice surface and volume inhomogeneity. There is currently a lack of information on large-scale sea ice properties and, as a consequence, the mechanisms of texture formation.

Texture features describe local, statistical image properties within a small region. They have been investigated in several studies (Holmes *et al.*, 1984; Shokr, 1991; Nystuen and Garcia, 1992; Wackerman and Miller, 1996; Collins *et al.*, 1997; Soh and Tsatsoulis; 1999), and are in general found to be useful for sea ice classification. A set of the most informative features differs from study to study, and it may depend on several factors including geographical region, ambient conditions, etc. Applying texture usually increases classification accuracy; but, it cannot fully resolve ambiguities between different sea ice types, so that incorporation of other information is required.

In supervised classification, texture features are computed over the defined training regions and the classifier is trained to recognize similar patterns in newly acquired images. Several texture patterns can correspond to one ice class, which implies the existence of several disjointed regions in the feature space for the given class. The latter, however, is not observed in our data. The structure of data in the input space is affected by several factors including definition of ice classes, selection of training regions and existence of smooth transitions between different textures. In this study, training and test data have been collected over a relatively small geographic area where image and *in situ* data overlap. In contrast to this local approach, ice texture study can be done using training regions selected over a relatively large geographic area and across different seasons based on visual image analysis (Soh and Tsatsoulis, 1999). Selection of ice types, which may have several visually distinct textures, can facilitate formation of disjointed or complex form clusters in the feature space pertinent for one ice type. Note that in this case MLP should show better results than the LDA-based algorithm.

The approach to texture computation is closely related to the classification approach adopted to design a multi-season, large geographic area classification system using: (1) a single classifier with additional inputs indicating area and season; (2) a set of local classifiers designed to classify ice within a particular region and season; and (3) a multiple classifier system. The trained classifier can be considered as a member of a set of classifiers, each of which performs a simpler job than a single multi-season, multi-region classifier.

The image moments used in this study are mean value, second-, third- and fourth-order moments and central moments computed over the distribution of pixel values

within a small computation window. GLCM-based texture features include homogeneity, contrast, entropy, inverse difference moment (Haralic *et al.*, 1973), cluster prominence and cluster shade. Autocorrelation function-based features are decorrelation lengths computed along the 0°, 45° and 90° directions. In total, 16 features are used for SAR image classification. Only the mean value was used for the optical image because of its lower spatial resolution. Texture computation parameters are selected experimentally, taking into account the results of previous studies.

There are several important parameters that need to be defined for GLCM: (1) computation window size; (2) displacement value, also called "interpixel distance"; (3) number of quantization levels; and (4) orientation. In defining these parameters we took into account that the studied region contains mixed sea ice types. With increasing window size and interpixel distance (which is related to the spatial scale of inhomogeneities "captured" by the algorithm), the computed texture would be more affected by composition of ice types within the computational window than by properties of a given ice type. Therefore, in the classification approach adopted here, we selected a smaller window size equal to 5×5 pixels and an inter-pixel distance equal to 2. This implies that we used a moderate-scale ice texture. The use of macro-texture information (larger displacement values) or multi-scale information (a range of different displacement values), recommended in the latest and comprehensive ice texture study (Soh and Tsatsoulis, 1999), would require a soft classification approach. To reduce computational time, the range of image gray levels is usually quantized in a number of separate bins. Image quantization, generally leading to the loss of information, does not strongly influence the computation of texture parameters as long as a sufficient number of bins is used (>16–32) (Soh and Tsatsoulis, 1999). In our experiments the range of image gray levels is quantified to 20 equally spaced bins. The GLCM is averaged for three different directions—0°, 45°, and 90°—to account for possible rotation of the ice. The training data set is prepared by moving the computational window within the defined training regions. For each non-overlapping placement of the window, the image features are computed in three images and stacked in a vector. The number of feature vectors computed for different ice classes is given in Table 4.6.

Supervised classification

Linear discriminant analysis (LDA) based classification algorithm

An LDA-based algorithm is proposed by Wackerman and Miller (1996) for sea ice classification in the marginal ice zone (MIZ) using single-channel SAR data. In this study it is applied for data fusion of different sensors. LDA is a known method for the reduction of dimensionality of the input space, which can be used at the pre-processing stage of the classification algorithm, to reduce the number of input features. Using this method the original, usually high-dimensional input space is projected onto a lower dimensional one. The projection of n-dimensional data vector $\vec{x}$ is done using the linear transformation $\vec{y} = V^T \vec{x}$, where $\vec{y}$ is the vector of dimension m ($m < n$) and V is the $n \times m$ transformation matrix. Elements of the transformation matrix are found by

Table 4.6. Description of ice classes and the number of training and test feature vectors for each class.

Sea ice class	Description	No. of training vectors	No. of test vectors
1. Smooth first-year ice	Very smooth first-year ice of medium thickness (70–120 cm)	150	130
2. Medium deformation first-year ice	Deformed medium and thick (>120 cm) first-year ice, deformation is 2–3 using the five-grade scale	1,400	1,400
3. Deformed first-year ice	As above, but with deformation 3–5	1,400	1,400
4. Young ice	Gray (10–15 cm) and gray–white (15–30 cm) ice, small floes (20–100 m) and ice cake, contains new ice in-between floes	1,400	1,400
5. Nilas	Nilas (5–10 cm), grease ice, areas of open water	1,400	1,400
6. Open water	Mostly open water, at some places formation of new ice on water surface	30	26

maximizing Fisher's criteria, which is a measure of separability between classes. For a two-class problem it is defined as (Fisher, 1936):

$$\frac{\vec{\nu}_{ij}^{T} B_{ij} \vec{\nu}_{ij}}{\vec{\nu}_{ij}^{T} W_{ij} \vec{\nu}_{ij}} \tag{4.16}$$

where $W_{ij} = \Sigma(\vec{x}_i - \vec{m}_i)(\vec{x}_i - \vec{m}_i)^T + \Sigma(\vec{x}_j - \vec{m}_j)(\vec{x}_j - \vec{m}_j)^T$ is the total *within-class* covariance matrix, given as a sum of the two covariance matrices of ith and jth ice classes; $\vec{m}_i$ and $\vec{m}_j$ are the mean feature vectors of classes i and j, respectively; B_{ij} is the *between-class* matrix, given by $B_{ij} = (\vec{m}_i - \vec{m}_j)(\vec{m}_i - \vec{m}_j)^T$; and $\vec{\nu}_{ij}$ is the transformation (projection) vector to which matrix V reduces in the two-class case. Vector $\vec{\nu}_{ij}$ defines a new direction in feature space, along which separation of classes i and j is maximal. It can be shown that vector $\vec{\nu}_{ij}$ maximizing the clustering metric is the eigenvector with the maximum eigenvalue λ that satisfies the equation (Lachenbruch, 1975):

$$W_{ij}^{-1} B_{ij} \vec{\nu}_{ij} = \lambda \vec{\nu}_{ij} \tag{4.17}$$

In general, case classification of vectors $\vec{y}$ can be performed using traditional statistical classifiers. The central limit theorem is applied since $\vec{y}$ represents a weighted sum of random variables and conditional PDFs of $\vec{y}$ are assumed to be multi-variate normal. The method is distribution-free in the sense that "it is a reasonable criterion for constructing a linear combination" (Lachenbruch, 1975). It is shown to be statistically optimal if the input features are multi-variate normal (Bishop, 1995). Another

assumption that needs to be satisfied when applying LDA is the equivalence of the conditional covariance matrices for each class. These assumptions are difficult to satisfy in practice. However, slight violation of these criteria does not strongly degrade the performance of the classifier (Lachenbruch, 1975).

In the limiting case, LDA can be used to project the input space in one dimension only. By projecting feature vectors of pairs of classes, the multi-class classification problem can be decomposed into two-class problems. The constructed classifier is a piecewise linear classifier.

Neural networks

Artificial neural network models have received much attention during recent decades due to their ability to approximate complex input–output relationships using a training data set, perform without any prior assumptions on the statistical model of the data, generalize well on new, previously unseen data (see Bishop, 1995 and references therein) and be less affected by noise. These properties make neural networks especially attractive for sensor data fusion and classification. Empirical comparisons of neural network based algorithms with standard parametric statistical classifiers (Benediktsson *et al.*, 1990; Paola and Schowengerdt, 1995) showed that a neural network model can outperform statistical methods as long as a sufficient number of representative training samples is presented to the neural network. It also avoids the problem of determining the amount of influence a source should have in classification (Benediktsson *et al.*, 1990). Standard statistical parametric classifiers require a statistical model and, thus, work well when the used statistical model (usually multi-variate normal) is in good correspondence with observed data. There are not many comparisons of neural network models with non-parametric statistical algorithms. However, there are some indications that these algorithms can work at least as well as neural network approaches (Eckes and Fritzke, 2001).

Several researchers have proposed neural network models for sea ice classification. Key *et al.* (1989) applied a back-propagation neural network to fuse the data of two satellite radiometers. Sea ice was among 12 surface and cloud classes identified on the images. Hara *et al.* (1995) developed an unsupervised algorithm that combines learning vector quantization and iterative maximum likelihood algorithms for the classification of polarimetric SAR images. Total classification accuracy, estimated using three ice classes, comprised 77.8% in the best case (P-band). Karvonen (2004) used a pulse-coupled neural network for unsupervised sea ice classification in *Radarsat* SAR images. Although these studies demonstrated the usefulness of neural network models when applied to sea ice classification, the algorithms still need to be extensively tested under different environmental conditions using ground-truth data. It is unclear whether neural network models outperform traditional statistical classifiers and generalize well on the test data set. It is also unclear which input features and neural network structure should be used in classification.

In our experiments (Bogdanov *et al.*, 2005) we used a multi-layer feed-forward neural network trained by a standard back-propagation algorithm (Werbos, 1974; Rumelhart *et al.*, 1986). Back-propagation neural networks also known as

"multi-layer *perceptrons*" (MLPs) are structures of highly interconnected processing units which are usually organized in layers (Rosenblatt, 1958). An MLP can be considered as a universal approximator of functions that learns or approximates a nonlinear input–output mapping function using a training data set. During training the weights between processing units are iteratively adjusted to minimize root-mean-square (RMS) error function. The simple method for finding weight updates is the *steepest descent* algorithm, in which weights are changed in the direction of the largest reduction in error—that is, in the direction where the gradient of the error function with respect to the weights is negative. This method has some limitations (Bishop, 1995) including slow convergence in areas characterized by substantially different curvatures along different directions in the error surface—such as in long, steep-sided valleys. To speed up convergence, we used a modification of the method that adds a momentum term (Rumelhart *et al.*, 1986) to the equation:

$$\Delta w_\tau = -\eta \nabla E_\tau + \mu \Delta w_{\tau-1} \tag{4.18}$$

where Δw_τ is the weight change at iteration τ, ∇E_τ is the gradient of the error function with respect to the weights evaluated at the current iteration, η is the learning rate parameter and μ is the *momentum constant*, $0 \leq |\mu| < 1$. Due to inclusion of the second term, changes of weights having the same sign in steady downhill regions of the error surface are accumulated during successive iterations, which increases the step size of the algorithm. In regions where oscillations take place, contributions from the momentum terms change sign and, thus, tend to cancel each other, reducing the step size of the algorithm. The gradients ∇E_τ are computed using the known back-propagation algorithm (Werbos, 1974; Rumelhart *et al.*, 1986).

Results and discussion

Examples of sea ice classification in the Kara and Barents Seas using the MLP algorithm are presented in Figure 4.38. The MLP algorithm has been trained using samples (image moments and texture) from three radiometrically corrected *Radarsat* images including those shown in Figure 4.38. The images show ice conditions in the Kara and Barents Seas in late April 1998. Due to dominant easterly and southeasterly winds in the region before and during image acquisition, the ice drifted westwards, creating polynyas with open water, very thin ice and young ice characterized by different (bright and dark) signatures in radar images (letters A, B, C).

The results of classification visually correspond to expert interpretation with the distinction that a number of small-scale features, which are usually omitted or generalized into larger regions in expert classification, are identified by such an automatic approach—Figure 4.38(b), (d). Examples of such features is classification of young ice in leads between floes of first-year ice in Figure 4.38(a), classification of big (500–2,000 m) floes of first-year ice and regions of deformed first-year ice. Two separate classes have been used for open water areas with bright and dark signatures in the images, assuming only low- and high-windspeed values during image acquisition.

Quantitative comparison of LDA and MLP algorithm performances in the Kara Sea showed that the MLP algorithm performs slightly better than the LDA with total

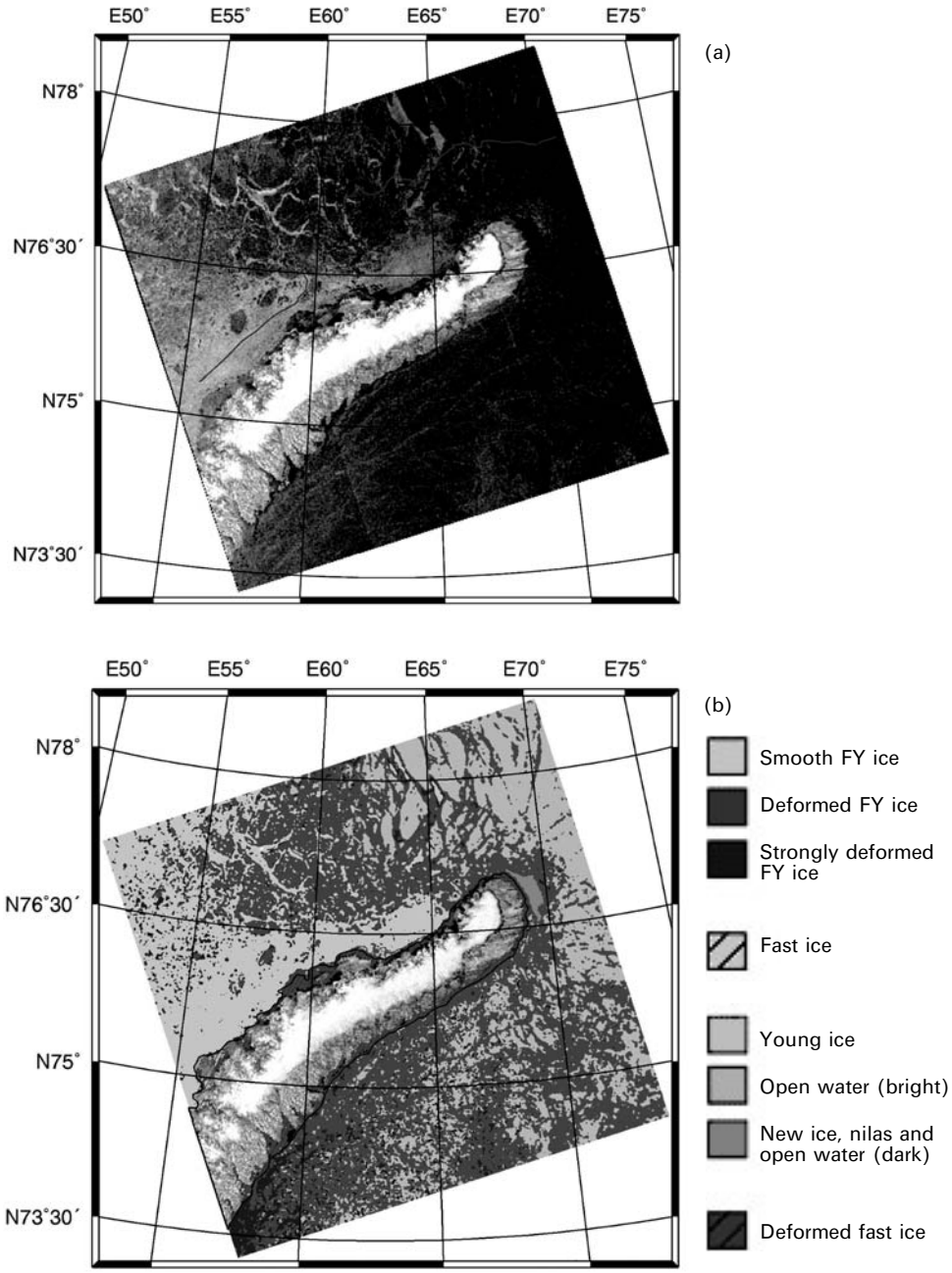

Figure 4.38. Examples of MLP-based sea ice classification of two *Radarsat* ScanSAR images (© Canadian Space Agency) acquired over the Kara and Barents Seas. Separation of drifting and fast ice is done manually: (a) ScanSAR image of 25 April 1998; (b) classification of 25 April image (see also color section).

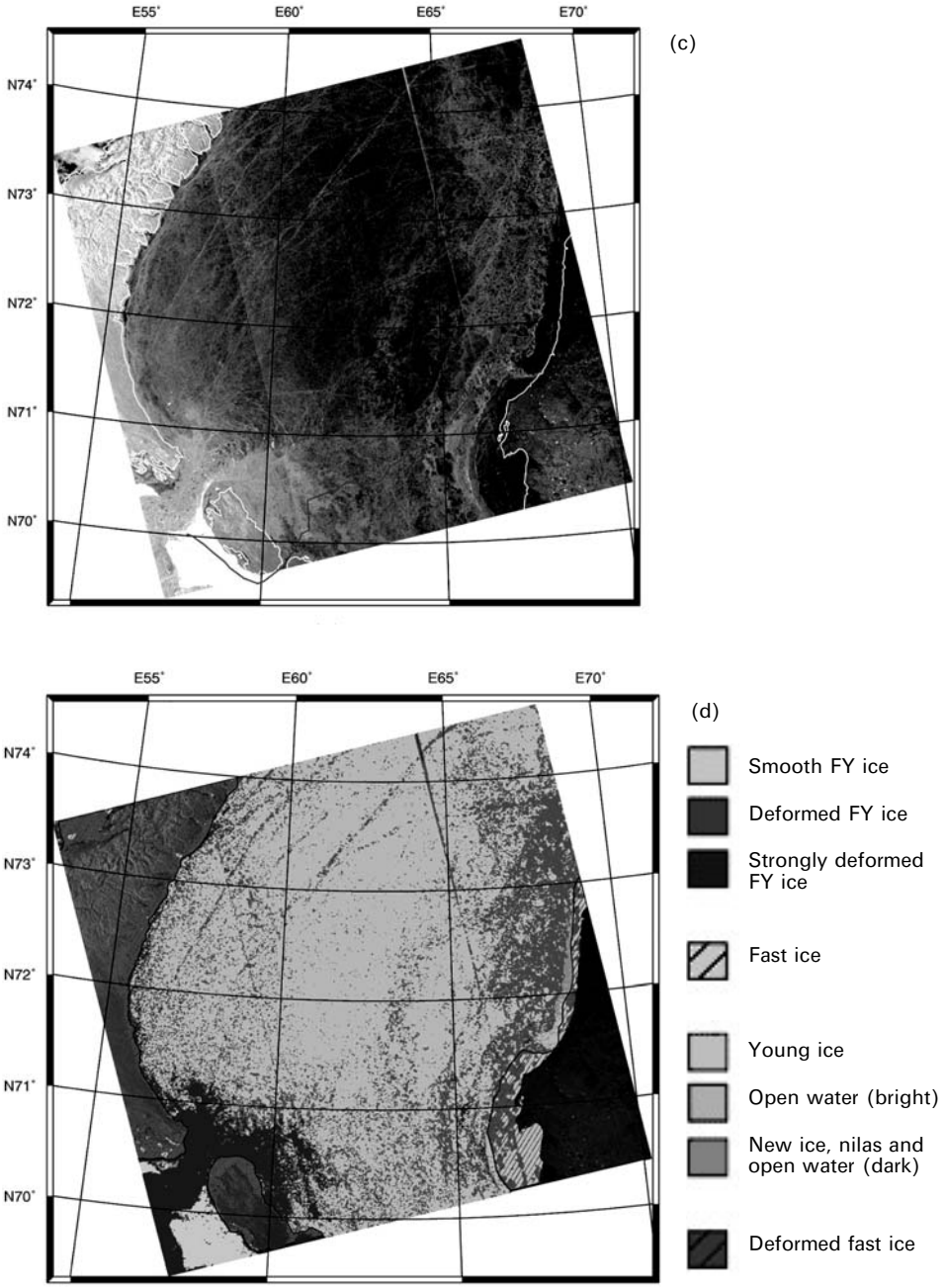

Figure 4.38 (*cont.*). Examples of MLP-based sea ice classification of two *Radarsat* ScanSAR images (© Canadian Space Agency) acquired over the Kara and Barents Seas. Separation of drifting and fast ice is done manually: (c) ScanSAR image of 8 May 1998; (b) classification of 8 May image (see also color section)..

classification accuracies of 71% and 68%, respectively, but requires a longer training time (Bogdanov *et al.*, 2005). In addition to the *Radarsat* image, *ERS* and *Meteor-3/5* low spatial resolution images acquired near-simultaneously have been combined in classification. The joint use of *ERS* and *Radarsat* image features increases the number of correctly classified test vectors to a value of about 84%—improvements are observed for all ice classes. The classification accuracy of open water is much higher, due to incorporation of polarimetric information. Classification of dual-polarization data (VV and HH) not only facilitates separation of classes with large polarization ratios, but also those with relatively small ratios, which have similar tonal signatures on *ERS* and *Radarsat* images. The improvement in classification of young ice, medium and rough first-year ice with a pronounced texture can be due to incorporation of texture features in the classification.

Fusion of *ERS*, *Radarsat* SAR and *Meteor* visible images improves estimated accuracy up to 91%. Incorporation of clear sky optical data helps in discrimination of nilas and open water and, theoretically, can reduce the effect of variable open water radar signatures on classification accuracy, making it (less) invariant to wind speed. The increase in classification accuracy gained by fusion of a single polarization *ERS-1* SAR with *Landsat* TM images has already been demonstrated by using a maximum likelihood classifier (Steffen and Heinrichs, 1994). The results of Bogdanov *et al.* (2005) confirm that visible images are useful in combination with multi-polarization SAR data.

Direct comparison of the sea ice classification results of the described algorithms and those reported in the literature is rather difficult. The reasons for this are that: (1) there is currently no common, generally available satellite data set which can be used for cross-validation of different algorithms; (2) developed algorithms usually incorporate a piece of expert knowledge which is difficult to reproduce; (3) the seasonal and spatial variability of sea ice precludes the development of general approaches applicable in different polar regions and seasons.

4.4.2 Sea ice concentration

Ice type is considered to be the most important sea ice parameter for navigation in winter, while ice concentration is more important in summer when the sailing route is selected through areas with low values. Presently, sea ice concentration for the Arctic Ocean is routinely derived from satellite passive microwave SSM/I and AMSR data. However, satellite passive microwave data have low spatial resolution, thus concentrations are too coarse for some regions, particularly near the coast. High-resolution satellite SAR systems are quite efficient for detection of small sea ice features and open water areas. Their use for determination of sea ice concentration has significant interest, and several algorithms for its derivation have been developed (Sandven *et al.*, 1991, 2001; Dokken, 2000; Dokken *et al.*, 2000; Markus and Dokken, 2002).

Sea ice/Open water discrimination

Both open water and sea ice have a wide range of backscatter. The difference in backscatter between them can vary significantly depending on wind speed and sea ice properties. This difference also depends on SAR wavelength, incidence angle and polarization. The most critical step in ice concentration determination is to distinguish windy open water from the various ice types.

For *ERS-1/2* SAR—with C-band, VV-polarization and incidence angles of 20°–26°—the backscatter of open water in low wind is mostly significantly lower than that of sea ice (see Table 4.7 for the backscatter data presented in Onstott, 1992). Calm water can therefore be reliably distinguished from most multi-year and first-year sea ice. Note however that during late summer their discrimination can be ambiguous, and that—even at onset of freeze-up and during winter—new ice and nilas can have a backscatter similar to that of calm water.

The backscatter of open water increases with increasing wind speed and becomes similar to that of sea ice when the wind speed is above approximately $2\,m\,s^{-1}$. With its further increase to over $5\,m\,s^{-1}$, the backscatter of open water becomes larger than that of most sea ice types. Open water can thus be distinguished in either very low or very high wind in a SAR image. During summer the sea ice has low backscatter (less than -12 dB), and when the wind speed is greater than $5\,m\,s^{-1}$ the backscatter difference between sea ice and open water exceeds 4 dB (Soh *et al.*, 1998). According to Sandven *et al.* (1999a), in many cases open water in *ERS* SAR images had higher backscatter than any of the observed ice types, from -4.5 to -3.0 dB.

Within drifting ice, the backscatter of wind-roughened open water may be lower than that in the ocean due to wave dampening and wind shadowing by icefloes. Therefore, when wind speed is in the range $3–10\,m\,s^{-1}$, open water cannot be reliably discriminated from ice using single-channel radar data (Steffen and Heinrichs, 1994). However, in many cases *ERS* SAR can be used to separate open water from sea ice during the melt season. The open water signature is darker than that of sea ice in the case of low wind and brighter in the case of strong wind.

Radarsat ScanSAR operates at HH-polarization and in the range of incidence angles from 20 to 50°. Compared with *ERS*, HH-polarization reduces open water backscatter and at greater incidence angles the difference in backscatter between ice and calm open water increases. According to Dokken (2000), analysis of *Radarsat* images indicate that open water and sea ice separates fairly well and shows better contrast in first-order texture and backscatter values than those of *ERS*. However, taking into consideration that the backscatter of calm open water can be well below

Table 4.7. Backscatter contrast between calm open water and sea ice for *ERS-1* SAR (Onstott, 1992).

	Winter	Late spring	Early summer	Mid-summer	Late summer	Fall
Difference in dB	>6.4	>6.5	>6.6	>6.6	>1.3	>7.2

the noise-floor and that the backscatter of sea ice decreases with incidence angle, distinguishing them in the mid- and far-ranges of the *Radarsat* ScanSAR swath can be complicated. New ice types and nilas have relatively low backscatter and could not be distinguished from open water (Sandven *et al.*, 2001). As a result, in the freeze-up period, sea ice concentration can be estimated only for thicker ice types. *Envisat* ASAR can operate both at VV- and HH-polarizations and has an incidence angle range in WSM mode rather similar to that of *Radarsat*. Therefore, at HH-polarization its capability to separate sea ice from open water does not differ from that of *Radarsat*.

Open water has a much larger polarization ratio than sea ice, except for thin new ice. Thus, using the VV- to HH-polarization ratio, sea ice and open water can be discriminated, in spite of ambiguities caused by the wind-induced roughness of the sea surface (Remund *et al.*, 2000). Also, HV-polarization data should show this ability (Soh *et al.*, 2004).

Several algorithms for derivation of ice concentration from *Radarsat* and *ERS* SAR images are based on mean ratio, local threshold and wavelet methods (Crane and Anderson, 1994; Markus and Dokken, 2002). In the mean ratio method, the ice concentration for a large area is determined by relating average backscatter to typical open water and sea ice values. In the dynamic local threshold method, it is determined by adapting the threshold between ice and open water, based on local intensity distributions. In the wavelet-based method, the edges around icefloes are detected and linked (Dokken, 2000).

Radarsat's Geophysical Processor System determines the summer open water fraction within each cell using the wind-dependent characteristics of open water (Kwok, 1998). It computes the expected σ^0 of open water using the surface wind speed and its direction relative to the radar look direction at each point. Two backscatter thresholds are used to determine whether a pixel belongs to the open water category—that is, if the open water σ^0 is well above or below than that of sea ice. If the backscatter of open water and ice overlap the pixel is not classified.

The algorithm for sea ice concentration retrieval from *ERS* SAR images, described in Johannessen *et al.* (1997b), also uses two threshold values to separate open water from thick ice. In the case of strong wind the "high" threshold is used and all higher image values, representing mostly wind-roughened open water, are marked as ice-free pixels. In the low-wind case, pixel values lower than the "low" threshold values are marked as ice-free areas—that is, grease ice and calm open water. Pixels with values between "low" and "high", representing sea ice, are set to 100% ice. Using meteorological data, it is possible to determine when ice and water signatures can be similar and the pixel class cannot be determined (Sandven, *et al.*, 1991). This algorithm is briefly described below.

Algorithm of sea ice concentration retrieval from ERS *SAR images*

SAR images contain speckle noise that may result in single pixels being classified as ice in the open water. In order to reduce speckle, the image is averaged—for example, from 12.5- to 100-m pixels. Computation of ice concentration from *ERS* SAR is based

on thresholding. First, each pixel is classified as ice or open water and, then, $M \times N$ pixels are combined to get ice concentration as a percentage.

Therefore, the main steps of the algorithm are the following:

(1) Computation of the image histogram and determine the "low" and "high" peaks.
(2) Classification of each pixel $p_{i,j}$ as:
    - ice if "low" $\leq p_{i,j} \leq$ "high"; or
    - open water if $p_{i,j} <$ "low" or $p_{i,j} >$ "high".
(3) Calculation of sea ice concentration within the rectangular areas of $M \times N$ pixels from the classified image by averaging.

Sea ice concentration estimates depend critically on selection of the "low" and "high" thresholds, which vary with wind, season and geographic area (Kwok *et al.*, 1992; Sandven *et al.*, 1993; Drinkwater *et al.*, 1994). To optimize estimates in different areas according to the wind, these thresholds must be adjusted. Within an *ERS* SAR scene of 100×100-km size, the wind speed may not change significantly, and then a single histogram peak is present. In low wind the histogram peak is defined as "low", and "high" is set to 255—that is, no water pixels with high backscatter values. For high wind the peak in the histogram is defined as "high" and "low" is set to 0.

Algorithm for sea ice concentration retrieval from Radarsat ScanSAR images

Estimation of total ice concentration using the described approach has been made using ScanSAR images acquired in the Laptev Sea in September 1997. In addition, the SSM/I-derived ice concentrations of the same day, sub-satellite sea ice observations and meteorological data were used. The threshold values "high" and "low" separating ice from open water can be found from the ScanSAR image without the need of absolute calibration, but backscatter range correction must be applied. Then, water–ice discrimination is possible across the whole image using the same threshold value. For all the analyzed images, water pixels within the sea ice have lower backscatter values than ice pixels, thus a "low" threshold is used. In areas close to the ice edge the assumption that a lower and upper threshold can discriminate water from ice fails. Such areas are identified in the SAR image and then masked out.

An original ScanSAR image was first averaged to 500-m pixel size in order to reduce speckle noise. All land areas were masked and open water regions masked out using ice concentration estimates from SSM/I, obtained by the NORSEX algorithm (Svendsen *et al.*, 1983). A threshold of 20% was used for this operation. By analyzing the histogram of the remaining SAR-pixels two distinct peaks were found that were assumed to correspond to the ice and water areas within it. The pixel value at the local minimum between the two peaks was chosen as the threshold value for separating them: all pixels with values above the threshold were set to ice and all other pixels to water. By averaging over a certain unit area, defined by $n \times n$ pixels, the ice concentration was estimated. A unit area of 6.5×6.5 km was used (13×13 pixels). The results of the analysis of the SAR image of 7 September 1997 are shown in Figure 4.39a,

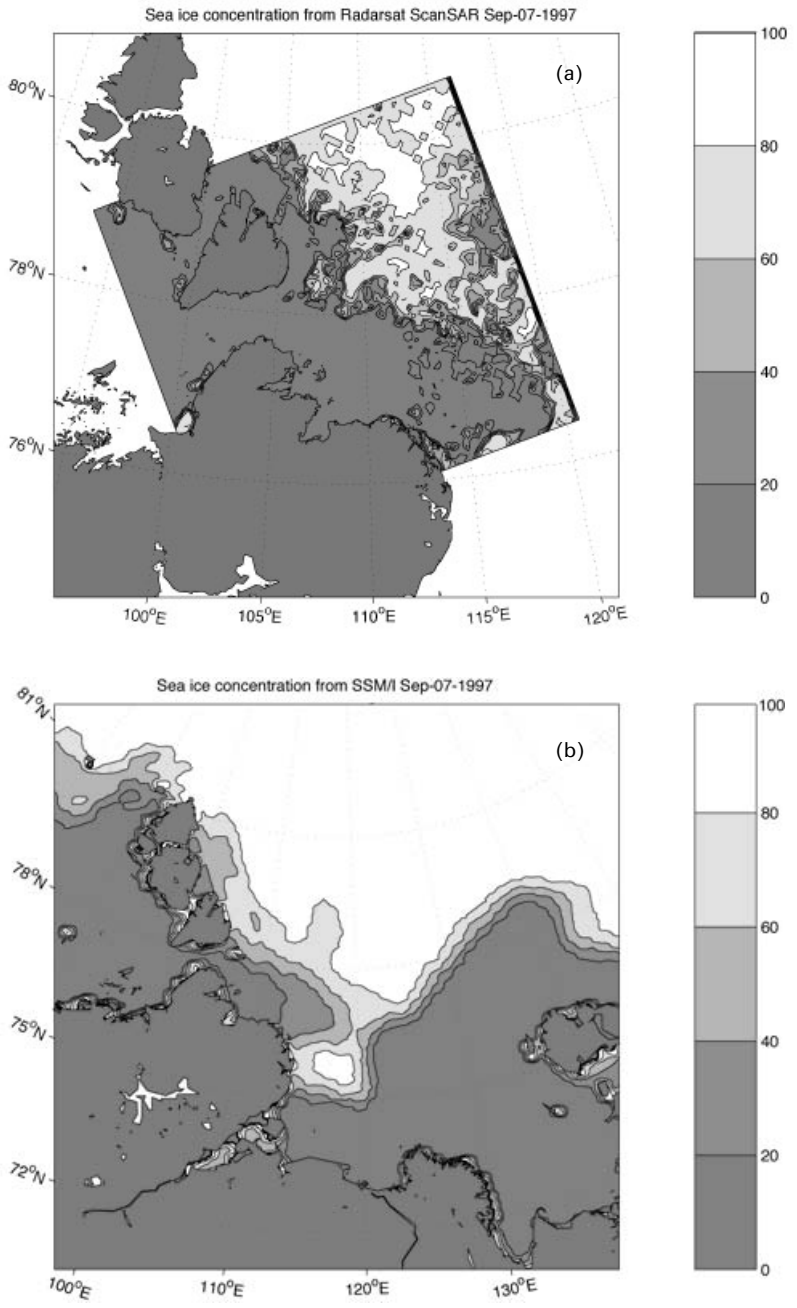

Figure 4.39. Ice concentration analysis from: (a) ScanSAR image data (© Canadian Space Agency) of 7 September 1997, presented with a spatial resolution of about 6 km; (b) SSM/I data on the same day using the NORSEX algorithm (Svendsen *et al.*, 1983) using the 85-GHz channel (Sandven *et al.*, 2001) (see also color section).

while the SSM/I concentration for the same day is shown in Figure 4.39b for comparison.

This result shows that ice concentration can be mapped in detail down to about 6 km with SAR data. In comparison, SSM/I data do not show details less than 10–20 km. Linear regression analysis was also made on a profile in the two data sets, containing altogether 328 pixels. It showed a correlation of 0.76 and a RMS of 12.4. Although the two data sets agree fairly well on an overall basis, the *Radarsat* algorithm tends to overestimate ice concentration compared with SSM/I data. Taking into account the difference between SAR and SSM/I data both radiometrically and in spatial resolution, it is not surprising that the two data sets give somewhat different results. Comparing SSM/I-derived ice concentrations with *in situ* observations from the I/B *Yamal* indicates that both data sets agree well for this particular case, although the coarse resolution of SSM/I data does not reflect smaller scale features.

Note that thin ice types—such as grease ice and nilas—may have low backscatter, similar to that of calm open water (Sandven *et al.*, 1999a). This means that in several cases these ice types will be classified as open water, and the ice concentration will be estimated only on the basis of first-year ice and other thicker ice types with backscatter signatures well above the threshold value. For practical purposes of navigation in ice, this is not a severe drawback.

The accuracy of sea ice concentration retrieval from SAR images has been addressed by several studies. For the icebreaker *Oden* (Dokken, 2000) during the Arctic Ocean Expedition 1996, the SAR-derived estimates agreed with sub-satellite observations within ±3%. When compared with *Landsat* TM, *ERS* SAR show an error of 5 to 8% for high ice concentration regions during winter, and the main source of these errors is misclassification of ice-free and smooth first-year ice areas (Steffen and Heinrichs, 1994). This error increases for areas of lower ice concentration. According to Johannessen *et al.* (1992), SAR ice concentration estimates have an accuracy of about 20%. Overestimation by 5 to 10% has resulted from *Radarsat* imagery using the ARKTOS system, with a mean absolute error of 8.4% (Soh *et al.*, 2004). However, these values may well reflect the uncertainty in ice concentration values on ice charts, rather than real error in ARKTOS. Several authors have mentioned that low image contrast and some backscatter inversion (where water pixels appear darker in the image, due to the wind-roughened water surface during summer) play a large role in classification error during the summer.

An important task is definition of the image area where ice concentration is calculated. *WMO Sea Ice Nomenclature* (WMO, 1989) defines ice concentration as "the ratio expressed in tenths describing the amount of the sea surface covered by ice as a fraction of the whole area being considered." Usually, image areas, in which sea ice is distributed approximately homogenously, are marked in interactive mode, and within them ice concentration values are calculated or estimated visually.

An automated approach to mark or segment different ice concentration zones can be taken by low-pass filtering the image with a defined window size. The result is a smoothed image where the brightness of each pixel is equal to the average brightness within the selected window. In this image, use of a re-classification algorithm can mark

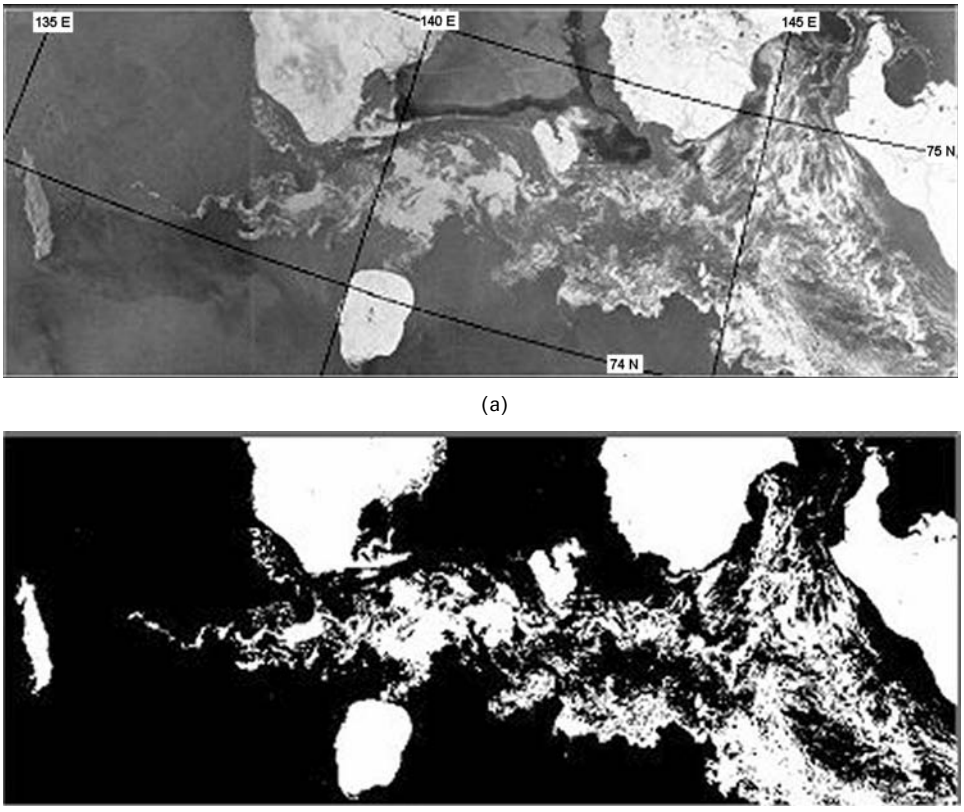

Figure 4.40. Sequence of procedures for ice concentration retrieval from *Radarsat* image (© Canadian Space Agency) of 4 September 1997, covering Sannikov Strait: (a) initial image (500-m resolution); (b) image after ice/water thresholding.

the zones of chosen ice concentration intervals. This method of sea ice concentration retrieval from SAR image is shown in Figure 4.40.

Filter window size depends on the scale of the resulting ice charts and the necessity to show small spatial details of ice concentration. The disadvantage of this algorithm is the smearing of boundaries of sharply defined ice features. This effect can be eliminated in further processing and analysis of the classified image and in the composition of a vector ice map.

4.4.3 Sea ice motion

The retrievals of sea ice motion from two successive satellite images are made by comparing common ice features. Since this may be a time-consuming procedure, several automated techniques for sea ice tracking in SAR images have been developed. The earliest methods were based on area correlation (Daida and Samadani, 1990).

(c)

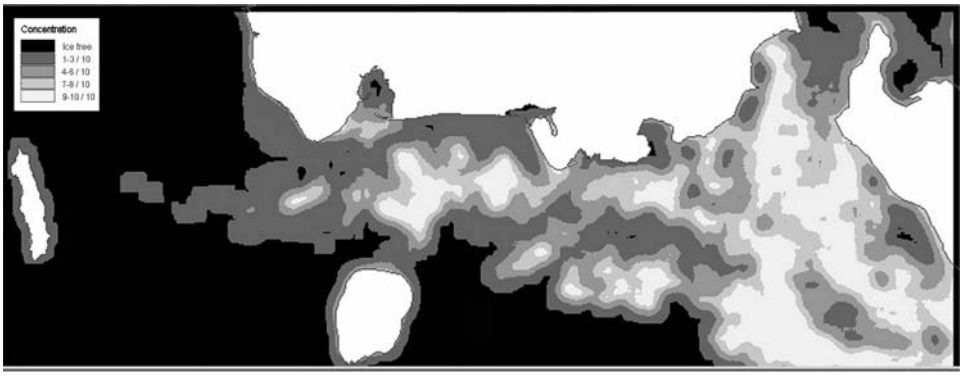

(d)

Figure 4.40 (*cont.*). Sequence of procedures for ice concentration retrieval from *Radarsat* image (© Canadian Space Agency) of 4 September 1997, covering Sannikov Strait: (c) The result of low-pass filtering with a 15×15 pixel window; (d) the result of classification within the ice concentration levels in tenths ($\frac{1}{10}$ $\frac{3}{10}$, $\frac{7}{10}$ $\frac{8}{10}$ and $\frac{9}{10}$ $\frac{10}{10}$).

Fily and Rothrock (1987) have used a cross-correlation approach, previously used for cloud-tracking by Collins and Emery (1988). Their algorithm was designed for use on *Seasat* SAR images with a spatial resolution of 25 m. The method is, first, to find tie points at a coarse resolution and, then, to use them as centers about which to search for tie-points at a higher resolution, proceeding through a hierarchy of stages. This algorithm is suitable for use in central Arctic regions with compact sea ice. It performs not so well on highly fragmented ice and when there are large rotations of icefloes.

Several algorithms of ice drift retrieval have been developed, based on feature-tracking. The first step in these algorithms is SAR image segmentation and vectorization of segment boundaries. Then, various techniques have been used to match the segment in successive images. Vesecky *et al.* (1988) matched floe–lead boundaries as straight line segments. The approach by McConnel *et al.* (1991) includes selection of a candidate segment from one image and searching for the best match in the second

image by shifting the segment along all features with similar characteristics and finding their one-dimensional cross-correlation. Banfield (1991) used a stochastic approach for matching icefloes.

An operational system for ice motion extraction from SAR imagery at the Alaska SAR Facility includes a combination of feature-based and area-based techniques for the tracking of icefloes that undergo translation and rotation between imaging passes (Kwok *et al.*, 1990). In the central Arctic, where sea ice motion is predominantly translational, area correlation for matching corresponding image patches works reasonably well. However, as rotation increases, the correlation peak broadens and eventually becomes statistically insignificant. Therefore, in the ice margin the algorithm uses feature-tracking and the matching is done by the one-dimensional cross-correlation of segments. The weakness in applying feature-based approaches to SAR images is that the extraction of image features (floe–lead boundaries, individual floes, etc.) is inaccurate, due to speckle and low contrast in SAR images (Sun, 1992).

In the case of strong rotations, a polar coordinate system can be introduced, and in the new coordinates the rotation parameter becomes a translational parameter; this allows the cross-correlation technique to be applied to the transformed power spectra to obtain the rotation angle. After removing relative rotation, the peak in cross-correlation will increase, and the first-order motion vectors related to the rigid motion (translation and rotation) can be derived (Sun, 1994). For non-rigid motion the "optical flow" method can be applied, which, unlike feature-based approaches, deals with deformation by using local partial derivatives of brightness values (Sun, 1992). The key to the algorithm is a method by which the changes in brightness among neighboring points in both spatial and time domains are used to derive motion vectors. This method can be used to retrieve ice deformation, which is of special interest in sea ice studies since it is responsible for the production of ice ridges/open leads. A drawback of the optical flow method is that it does not properly reconstruct the displacement field at discontinuities of the motion.

The MCC or cross-correlation algorithm by Fily and Rothrock—described above and by Vesecky *et al.*, (1988)—is much used for ice motion studies in Eurasian Arctic seas. It was further developed for use with SAR data at NERSC (Fleshe, 1988; Kloster *et al.*, 1992). The MCC cross-correlation method builds an image pyramid with levels of resolution and computes the ice kinematics on each level, starting at the coarsest. Results on one level are used as initial values on the next (finer) level. On each level the method uses a two-dimensional binary search in a window of size d, and a displacement of up to $d/2$ pixels up/down/left/right can be found. The correlation between blocks of pixels from image 1 and image 2 can be given by:

$$c = \frac{\sum_{i=1}^{w}\sum_{j=1}^{w}(B_1[i][j] - m_1) \times (B_2[i][j] - m_2)}{v_1 \times v_2} \tag{4.19}$$

The value of the correlation factor c is between -1.0 and 1.0. The pair of blocks with the highest correlation is kept, and the corresponding displacement provides an estimate of ice motion. In order to remove false vectors, median filtering of the

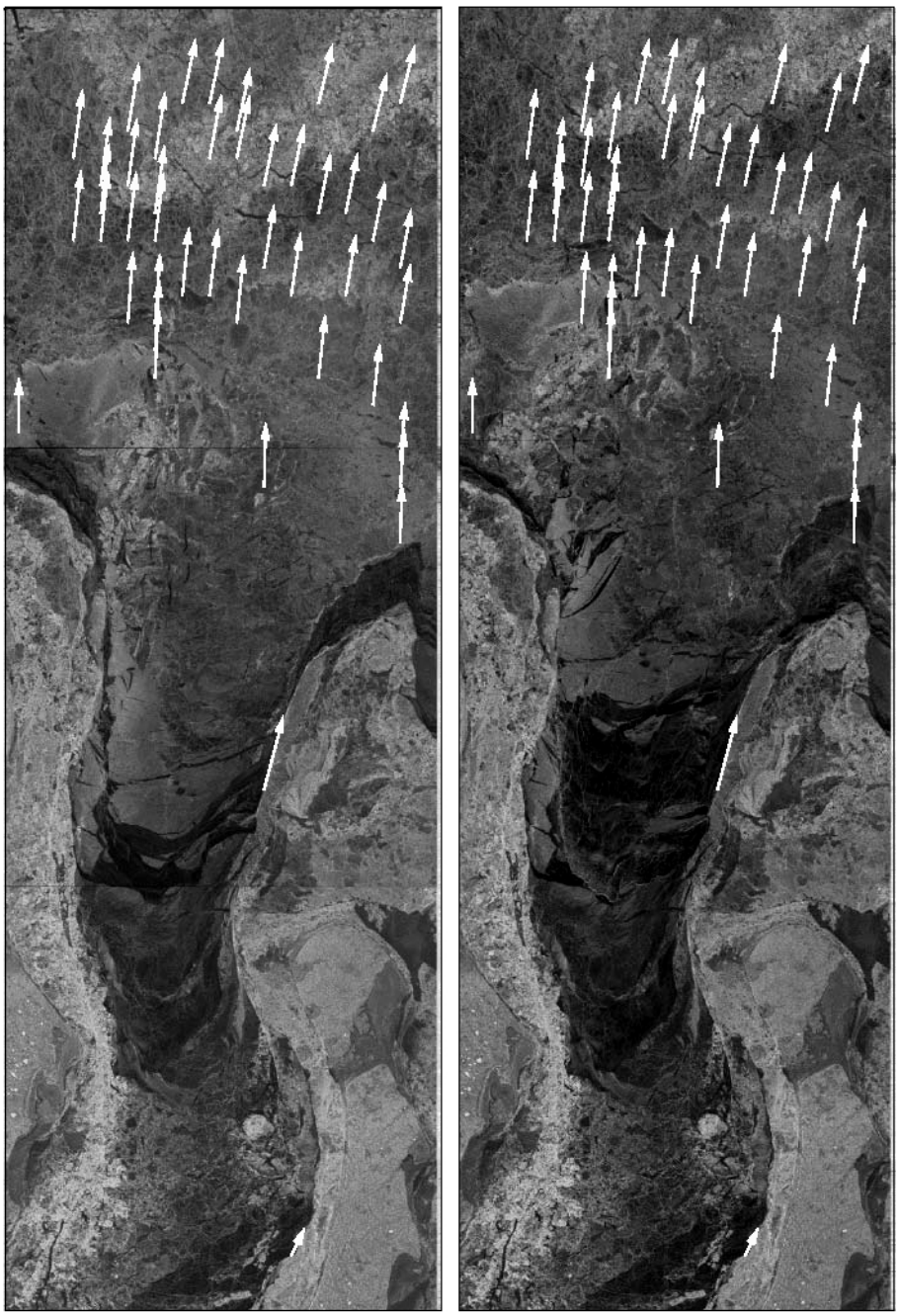

Figure 4.41. Ice motion in the estuary of the Ob' River, computed from *ERS-1* SAR images on 24 and 27 February 1994. Mean displacement is 14.7 km over a 72-h period, providing a mean ice speed of 5.7 cm s^{-1} (Johannessen *et al.*, 2003).

displacement vectors is performed after the binary search. This procedure replaces each vector by the median of nine vectors.

Two SAR images covering the same area taken at a time interval of a few days are used. Their dimension must be divisible by 4 for successful generation of an image pyramid. An initial displacement can be given to start the program. The user can also set the size of search window and the block size. The multiple cross-correlation method produces a vector file containing the computed ice motion vectors, one for each block. Each vector has a correlation factor c indicating how reliable the vector is. The vectors are finally plotted on top of the images by an auxiliary program.

Figure 4.41 shows an example of ice motion computed by the MCC method in the estuary of the Ob River using *ERS-1* SAR data from 24 and 27 February 1994. Only vectors with correlation factor $c \geq 0.75$ are plotted. Ice motion is uniform in the upper part of the images, and thus the MCC method gives a good estimate. In the lower part of the image, ice motion is either too large to be found with the given search window or there is fast ice which does not move (there is also land and an island in the lower part of the image).

The MCC method is well-documented and is a much used method for estimating ice motion. The algorithm has been tested successfully on both AVHRR and SAR data (Sandven *et al.*, 1991; Kloster *et al.*, 1992; Moctezuma Flores *et al.*, 1994). The methods use simple computations, and each computed displacement vector has a correlation factor telling how reliable it is. This allows vectors with low correlation to be marked or filtered out during plotting. The user may give an initial displacement to start the search, and the block size and search window can be chosen.

4.5 ICE CHART COMPOSITION AT AARI
(*A.V. Bushuev, V.S. Loshchilov*)

Information on sea ice conditions is transmitted to users and recorded in the data bases as digital raster and vector ice charts. The main purpose of ice charts is to accurately show the spatial distribution and characteristics of sea ice—that is, zones of different total ice concentration, partial ice concentration of the major ice types, forms of icefloes, leads, fractures and other phenomena and features. Satellite images are interpreted by visual inspection in order to produce accurate ice charts.

General principles of sea ice mapping

The segmentation of images and subsequent interpretation and mapping of ice conditions are carried out by ice experts. They make their visual analysis as quantitative estimates based on computer screen imagery. Interactive mapping of ice conditions is supported by software developed at AARI for ice chart generation, based on ArcView.

The electronic ice chart is generated as a set of layers presenting the distribution of various data describing sea ice conditions. The data layers depend on the geometric properties of the features defined and can have several forms: polygons (area), lines or

points. The polygons are defined according to zones of different concentration and/or ice age. The line features represent cracks and leads. The points represent features that are small at the chart scale—such as stamukhas and icebergs.

Each layer of the electronic ice chart is written in a separate shape-file format. The structure of the attribute data has also been developed. It includes the different codes of winter and summer codes for total concentration and ice types. Objects in each layer are connected to the attribute data by means of a universal identifier (ID), which establish the relationship between the data layer ice feature and its characteristic attributes.

The ice chart is constructed by defining closed polygons of similar ice forms. The boundaries of the closed polygons are traced by an operator interactively, based on his visual analysis of the image (single or a mosaic of several images) on the computer screen. Removal of overlapping areas of polygons is made automatically at the final stage of ice chart composition.

The ice chart is stored in shape-file format. It can also be exported and stored in raster Windows Meta File (*.WMF), Windows Bitmap (*.BMP) and other formats. Before being stored in raster format, WMO standard egg-code[7] symbols are drawn on the ice chart. For each polygon this is automatically filled in from corresponding attribute tables. The software graphics module determines the egg symbol size, its location on the chart and, if necessary, creates an arrow to indicate the polygon to which this symbol refers. Identification of polygons can be made by letters and corresponding egg symbols can be located at chart margins in this case.

4.5.1 Generation of ice charts from optical images

Preliminary preparation of images

For composition of ice charts from *NOAA* AVHRR multi-channel images, one uses images of those spectral channels or their combinations that are most informative and least influenced by distortions from cloudiness and atmospheric haze. The preparation of combined images from different spectral channels is done using the software package named "SnowCat 1.0". Automatic creation of combined images is made by an algebraic procedure combining images from different spectral channels—for example, creating them as the difference between two channels (1 − 2) or (4 − 4), or a combination of channels 1, 2 and 4 by false-coloring the images using RGB colors. Practice shows that false-colored RGB images facilitate their visual analysis and interpretation to a great extent.

With the described software the following processes are performed in order to generate vector ice charts in "GIS ArcView": (1) the geographical linking and transformation of NOAA AVHRR images to a given stereographic projection; (2) the formation of a single image or a mosaic of several images; and (3) the creation of a so-called "world file".

[7] An egg-code symbol is used for description of: (1) total and partial ice concentrations, (2) stages of development of ice and (3) forms of ice. Defined in WMO (1989).

Generation of single-image ice charts

In accordance with the terminology adopted at AARI, an individual ice chart is a chart that is prepared from one satellite image (at one satellite pass) and presents the ice conditions at a specific time. Individual ice charts are the main elements, showing instantaneous ice conditions, for use in ice monitoring. They are primarily intended for operational support of shipping and other activities at sea. The swath width for *NOAA* AVHRR satellite images can be up to 3,000 km, and therefore these individual ice charts contain information over an extended area.

The process of image analysis and interpretation consists of tracing closed polygon boundaries, each containing uniform ice by concentration or by type. For each polygon, attribute data on important sea ice parameters are entered in a template (''pop-up'' window) in the form of the WMO international egg symbol for sea ice charts (as shown in Figure 4.42). This information is stored internally in information tables. Also, the color code of polygons is stored automatically. The color depends on ice concentration or ice type. The ice chart color code is defined in WMO (2004).

Figure 4.43a presents an example of an individual ice chart prepared in the GIS ArcView environment, based on the analysis of *NOAA* AVHRR images.

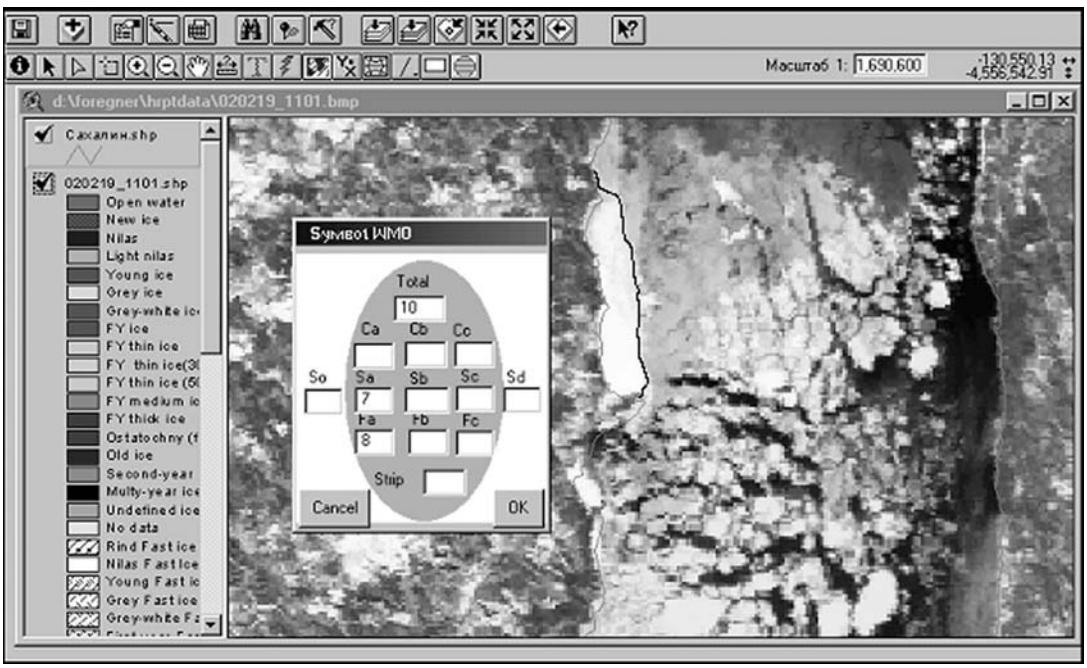

Figure 4.42. Example of the working window used in interactive ice mapping in GIS ArcView. The ''pop-up'' template with the egg symbol for marking of attribute data on sea-ice parameters in a given polygon is shown.

Generation of mosaic image ice charts

Composite or mosaic ice charts are based on several images received at different times—for example, over a 5-day period. These charts usually include very large areas—for example, the entire Arctic Ocean. Preparation of such charts has several uses: (1) the need for regular (e.g., every 5 days) monitoring of ice conditions; (2) the study of ice conditions over a large area; (3) obtaining initial data for medium- and long-range ice forecasts; and (4) climatic studies.

The composite ice chart can in principle be constructed by combining (superimposing) charts based on single satellite images of different times. This, however, requires performing a non-trivial procedure for editing individual ice charts compiled by different operators. Therefore, the method chosen makes a composite image or mosaic formed from several *NOAA* AVHRR images taken at different passes and times. The algorithm for generating such a composite mosaic image in a given map projection is described in Section 4.1.2.

A composite ice chart is usually prepared from a composite image by a single specialist, in order to minimize subjective errors and the need of further editing. Usually, use of a 5-day period for combining initial satellite images does not introduce serious errors due to ice changes. The same period is used in sea ice mapping by ice services in a number of other countries. It is however important to use images with a minimum of cloud.

The analysis, interpretation and preparation of a composite ice chart are also made in the GIS ArcView environment using a suitable software module and the same procedure as explained before. Figure 4.43b presents an example of a composite ice chart by combining four images over a 3-day period.

In the analysis of optical images, other information may also be used. That may include: (1) satellite high-resolution SAR images; (2) ice charts made earlier; (3) meteorological and ice observations made at coastal stations, icebreakers and data from drifting buoys.

4.5.2 Generation of ice charts from SAR images

The advantages of SAR images from *ERS*, *Radarsat* or *Envisat* are their high spatial resolution and independence on weather conditions and sunlight. These advantages are important for navigation through the sea ice along the NSR. Due to the narrow swath width of *ERS* SAR (100 km) and moderately narrow swaths of *Radarsat* ScanSAR (500 km) and *Envisat* ASAR (400 km), they are most efficiently used on a regional scale for detailed analysis and mapping of ice conditions. High-resolution SAR images enable detailed and accurate mapping of zones with different ice concentration, ice type, broken or strongly deformed ice, icefloes, fractures and large leads as well as determination of ice drift vectors.

Radarsat and *Envisat* satellite images are currently used for operational mapping of the ice conditions in the NSR, but only sporadically (every 3–7 days) in limited regions. Images from these satellites are usually used by the Murmansk Shipping Company (MSC) to support transport operations from the Barents Sea to the mouths

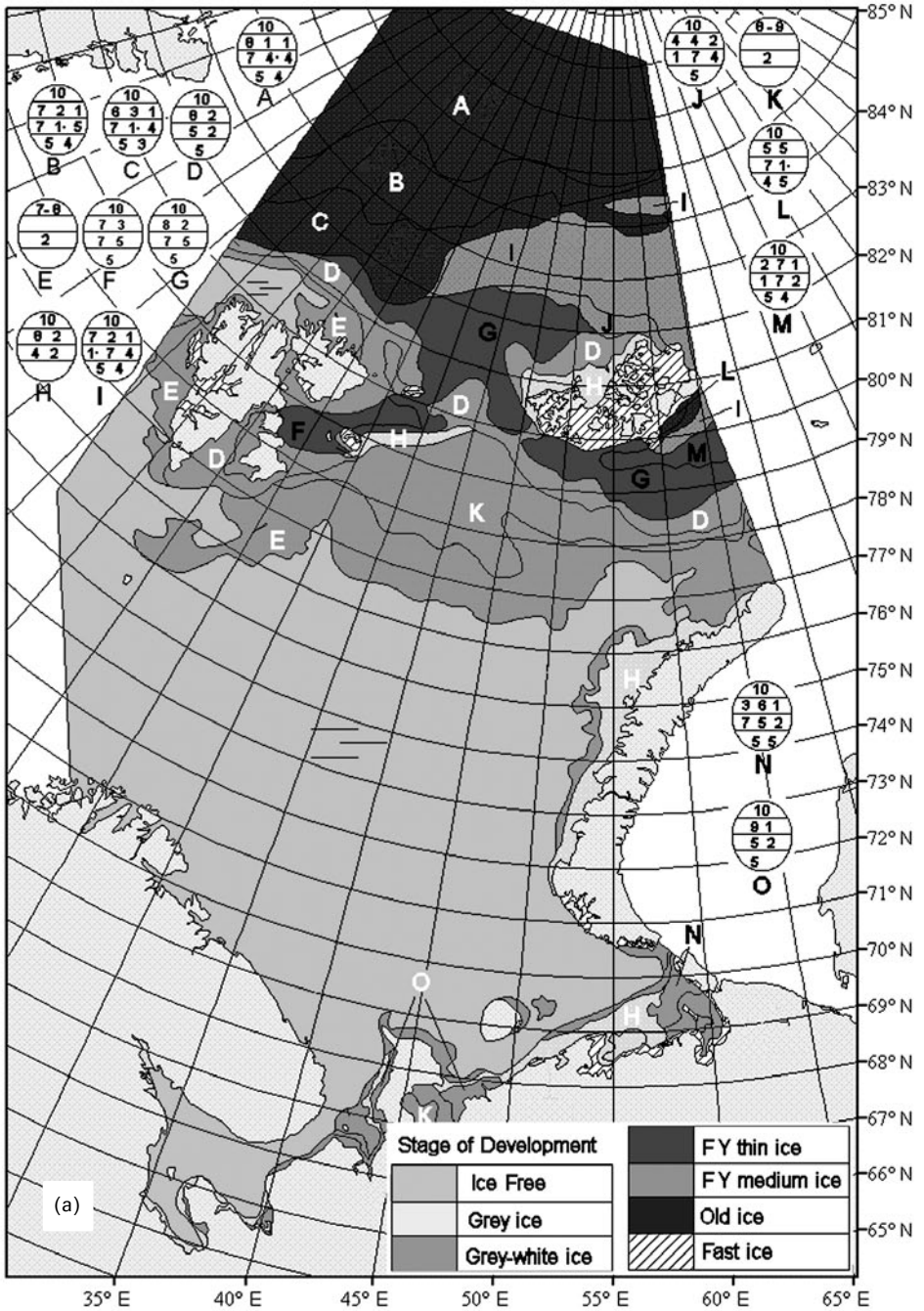

Figure 4.43. Examples of ice charts, composed from visible satellite images: (a) an individual ice chart of the Barents Sea made from analysis of the *NOAA* AVHRR image for 3 January 2005 (see also color section).

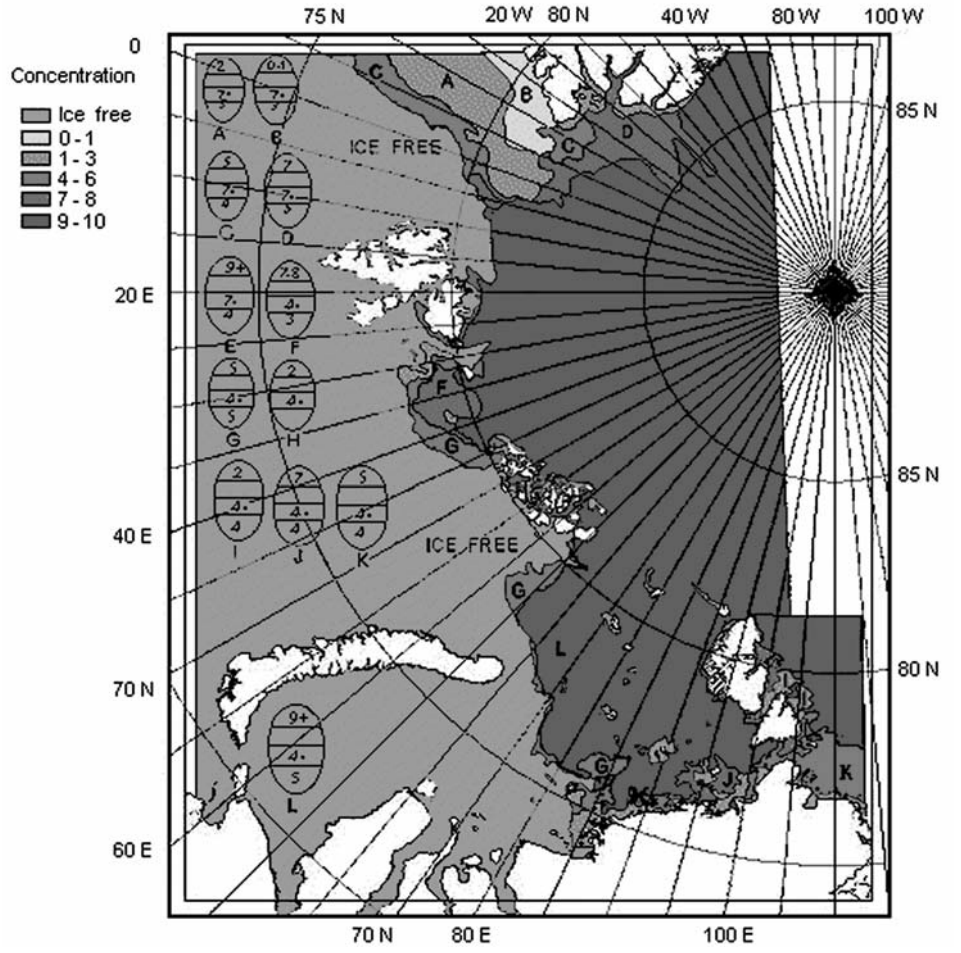

Figure 4.43 (*cont.*). Examples of ice charts, composed from visible satellite images: (b) composite ice chart of the Barents and Kara Seas made from a composite image (mosaic) of four AVHRR images for 26–28 July 2003 (see also color section).

of the Yenisey and Ob' Rivers in wintertime and early spring. In the Kara Sea region, heavy ice conditions have built up by the end of winter, requiring constant and detailed ice mapping to select optimal ship routes. SAR images have not been provided regularly in this region, but they have been used occasionally for making operational and strategic ice charts.

To make ice charts from SAR images, the same methodology that was developed for optical images is used. This methodology, which includes software modules based on ArcView, is used for interactive preparation of digital ice charts. Some problems with the interpretation of sea ice types from SAR images in wintertime are partly eliminated by combining the analysis with optical and IR images. Experience shows the possibility of better SAR image interpretation, and especially identification of

young or relatively thin first-year ice zones using such image analysis. These zones are used for selection of the optimal ship routes through the ice. For combined analysis, images no more than 3–5 days apart should be used.

Several examples of ice charts, composed at AARI by means of expert analysis and interpretation of SAR images from *ERS-2*, *Radarsat* and *Envisat* satellites both in winter and summer are presented in Figure 4.44. Also, optical images from *NOAA* satellites were used for their analysis. SAR images were received in near-real time onboard expedition ships or nuclear icebreakers for selecting optimal sailing routes through the ice. During voyages, research teams carried out a wide range of measurements and observations of the different sea ice types seen in these images.

Figure 4.44a presents an ice chart of the area around the Arkticheskiy Institute and Izvestiy Ts.I.K. Islands, composed from an *ERS-2* SAR image acquired on 30 April 1998 (Figure 4.37a). The boundaries of fast ice around the islands and the young ice zones that are elongated westward are marked on the chart. These zones serve as indicators of the ice drift direction in this area for the preceding 5–7 days. Thick first-year ice of seven-tenths concentration and medium first-year ice of two-tenths concentration dominate in the pack ice. Compared with the ice chart, many more ice types can be observed on the SAR image, but some are difficult to classify as map symbols.

Figure 4.44b presents an ice chart composed from the *Envisat* ASAR wide-swath image of 24 February 2004. The corresponding image is shown in Figure 6.16c. For ice chart preparation, the ASAR image of 14 February was also used to determine the ice drift vectors for a 10-day period. The average drift velocity is 12 cm/s. Presentation of ice drift vectors based on an earlier image helps the user to analyze and more accurately understand the processes occurring in sea ice, and to interpret the prognostic and meteorological information received.

Figure 4.44c presents an ice chart composed from the *Envisat* ASAR image of 27 June 2003 in the region near Dikson. The corresponding image is shown in Figure 6.15b. The image was received during a period of intense ice melting. Some problems with correct interpretation of the striped and spotted effects of melting ice in open water are caused by weak image contrast and various open water signatures in the SAR image.

Figure 4.44d presents a composite ice chart prepared using *Radarsat* SAR images from 4 and 6 September 1997. It covers the NSR segment between 135° and 165°E in the East Siberian Sea. On the SAR image of 6 September, internal waves were clearly observed in the open water, their location and orientation being indicated on the ice chart.

These digital ice charts were all prepared by an expert and sometimes based on a combined analysis of images in different spectral ranges. They are accurate and well-suited for the support of navigation. Many SAR images were received onboard the icebreakers in near-real time. However, professional interpretation of images onboard icebreakers is not always available and can lead to erroneous tactical decisions for navigation in ice. Ice charts prepared by specialists at ice centers are often of good quality. However, they can also sometimes contain erroneous results of interpretation. The present procedures for SAR image interpretation and the mapping of ice conditions are all based on visual analysis and estimates. A more automated

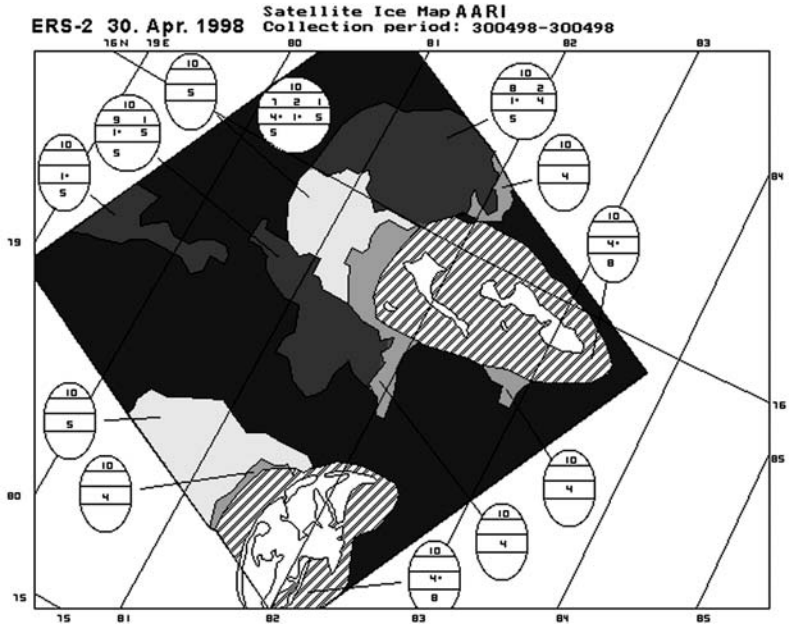

(a)

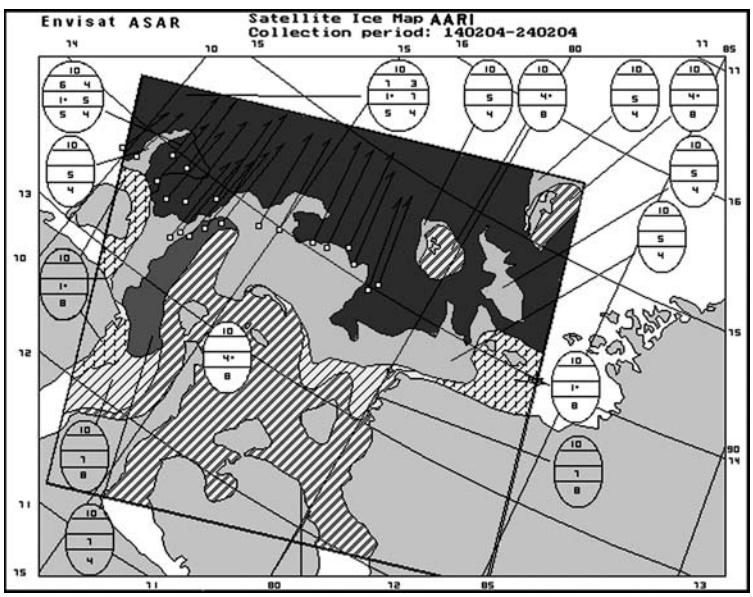

(b)

Figure 4.44. Examples of ice charts compiled from satellite SAR images: (a) ice chart compiled from an *ERS* SAR image of sea ice in the Kara Sea, 30 April 1998; (b) ice chart compiled from an *Envisat* ASAR image of sea ice in the Kara Sea, 24 February 2004) (see also color section).

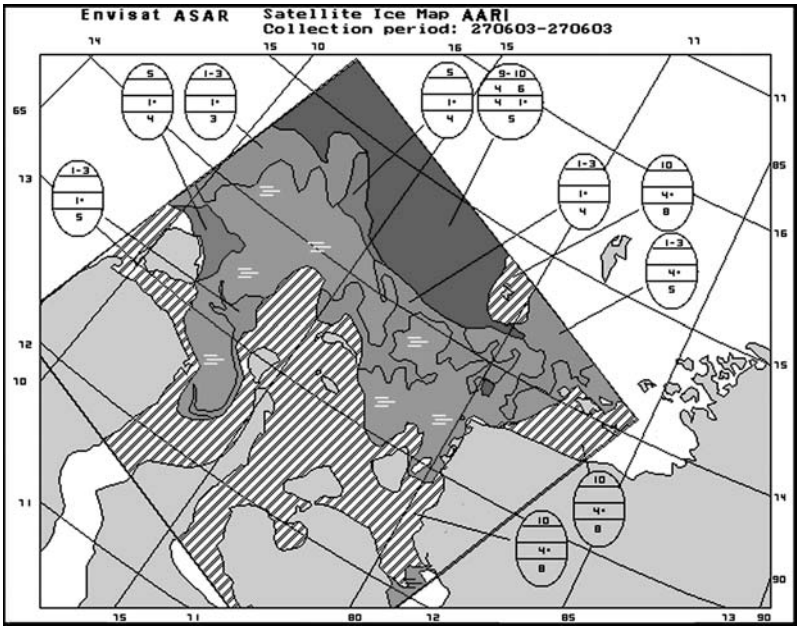

(c)

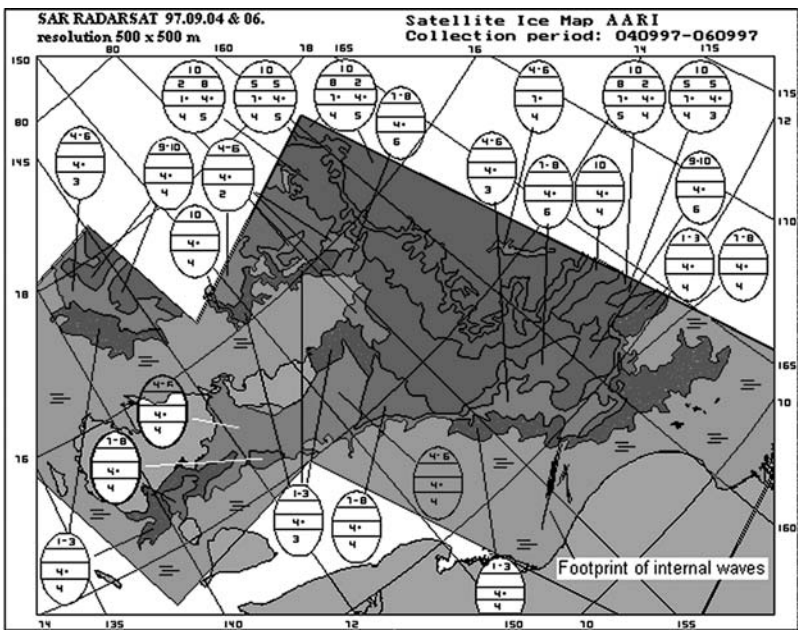

(d)

Figure 4.44 (*cont.*). (c) Ice chart compiled from the *Envisat* ASAR image of sea ice in the Kara Sea, 27 June 2003); (d) composite ice chart (mosaic) compiled from two *Radarsat* SAR images in the East Siberian Sea, 4 and 6 September 1997 (see also color section).

interpretation of the main sea ice characteristics from satellite images is desirable—such as ice types and ice concentration. The development of automatic classification algorithms (see Section 4.4) has not yet provided robust procedures which can be applied in operational monitoring. Ice analysis by human experts is therefore still the best method for producing operational ice charts based on SAR data.

5

Sea ice conditions observed from satellite remote-sensing data

Detailed quantitative information on seasonal changes of ice edge position, ice massifs, ice drift variability, fast ice and flaw polynyas in the Northern Sea Route (NSR) has been determined using multi-year, multi-sensor satellite data sets. In this chapter—as elsewhere—the NSR may be divided into western (Barents and Kara Seas) and eastern (Laptev, East Siberian and Chukchi Seas) regions. Section 5.1 describes remotely sensed sea ice conditions in the western part of the NSR, whereas Section 5.2 describes the eastern part. Section 5.3 presents recent studies of sea ice characteristics using satellite synthetic aperture radar (SAR) image data.

5.1 WESTERN PART OF THE NORTHERN SEA ROUTE (*Ye.U. Mironov, I.Ye. Frolov, V.A. Spichkin, V.P. Karklin, I.D. Karelin, Y.A. Gorbunov, S.M. Losev*)

The western part of the NSR comprises the Barents and Kara Seas, both of which are Arctic Shelf seas. The Barents Sea is delimited by the Greenland and Norwegian Seas to the west, and the Kara Sea and Novaya Zemlya in the east (Gorshkov, 1980). Based on its geographical location and natural conditions, the Kara Sea is subdivided into two large areas—the northeastern and southwestern—in which ice conditions are poorly related.

An important distinguishing feature of ice conditions of the Barents Sea is that, unlike the Kara Sea and other Siberian Shelf seas, it is never completely ice-covered. In the winter the ice area in the Barents Sea usually comprises 55–60% of the total sea area (Mironov *et al.*, 1994). In winter the entire Kara Sea is covered with close drifting ice with fast ice occupying large areas in the coastal regions (Mironov *et al.*, 1994). Its southeastern part is covered by ice of local origin with a predominant thickness up to 1.5 m for 8–10 months a year, whereas in summer it is usually completely ice-free. The northeastern part is not completely free of drifting ice during summer.

Regular use of satellite images for monitoring the Barents and Kara Seas began in the early 1970s. After 1991, when regular airborne ice reconnaissance ended, satellite imagery became the main information source for charting sea ice. From 1992, AARI began issuing composite ice charts based completely on *Meteor* (optical range), *NOAA* (IR range) and *Okean* side-looking radar (SLR) satellite images. In spite of their low resolution, the ice edge position, boundaries of fast ice and polynyas, and zones of different ice concentration and age can be determined from these images with sufficient accuracy.

5.1.1 Ice edge position

The constant presence of non-freezing areas in the Barents Sea means that a zero heat-budget zone is located in this region in winter (Mironov, 2004). To the south and west of this zone, a constant flow of warm Atlantic water to the surface water layers compensates for radiation cooling and cold advection by air transport, and prevents ice formation (Figure 5.1a). After reaching the seasonal ice extent maximum (April), the ice edge successively retreats northwards (Figure 5.1b).

Freeze-up of the southwestern Kara Sea usually occurs in October, in the absence of residual ice. In the northeastern part, young ice forms among residual ice in September (Figure 5.1a). After that until summer, the Kara Sea is covered with close drifting ice. Thus, the ice edge in the Kara Sea is present for only a short time—from July to October (i.e., about 3 months).

For spatial analysis of ice edge location in the Barents Sea, two methods of recording were used: at specified longitudes or latitudes or at regular grid points. A multi-year series of ice edge positions was formed for the period from 1972 to 1996 with the main statistical characteristics calculated for each month at specified longitudes or latitudes (Figure 5.2a).

Three areas can be distinguished by seasonal changes in ice edge position, their seasonal amplitude and multi-year variability (Figure 5.2a). The first one is located in the western Barents Sea at 20–30°E longitude and is characterized by the smallest seasonal amplitude. The seasonal maximum and minimum in this area are observed in March–April and September, respectively. The smallest and largest multi-year variabilities are recorded in the winter–spring and summer–autumn periods, respectively. The largest seasonal amplitude with a pronounced seasonal maximum is observed in April, and the minimum in September in the northeastern Barents Sea at longitudes of 50–60°E. The smallest and largest multi-year variabilities are recorded in the summer–autumn and winter–spring periods, respectively. The area at 35–45°E longitude occupies an intermediate position between the aforementioned areas and is characterized by an approximately equal multi-year variability in all seasons (Mironov, 2004).

The minimum multi-year variability of ice edge position in winter–spring in the western part of the Barents Sea is determined by the influence of the northern branch of the Nordkapp Current. Its warm waters prevent sea ice spreading in the vicinity of 20–30°E longitudes. The presence of open water "bays" (areas found at 30–35°E and 45°E) is also determined by the influence of warm current systems, which are seen on charts of mean multi-year ice edge location.

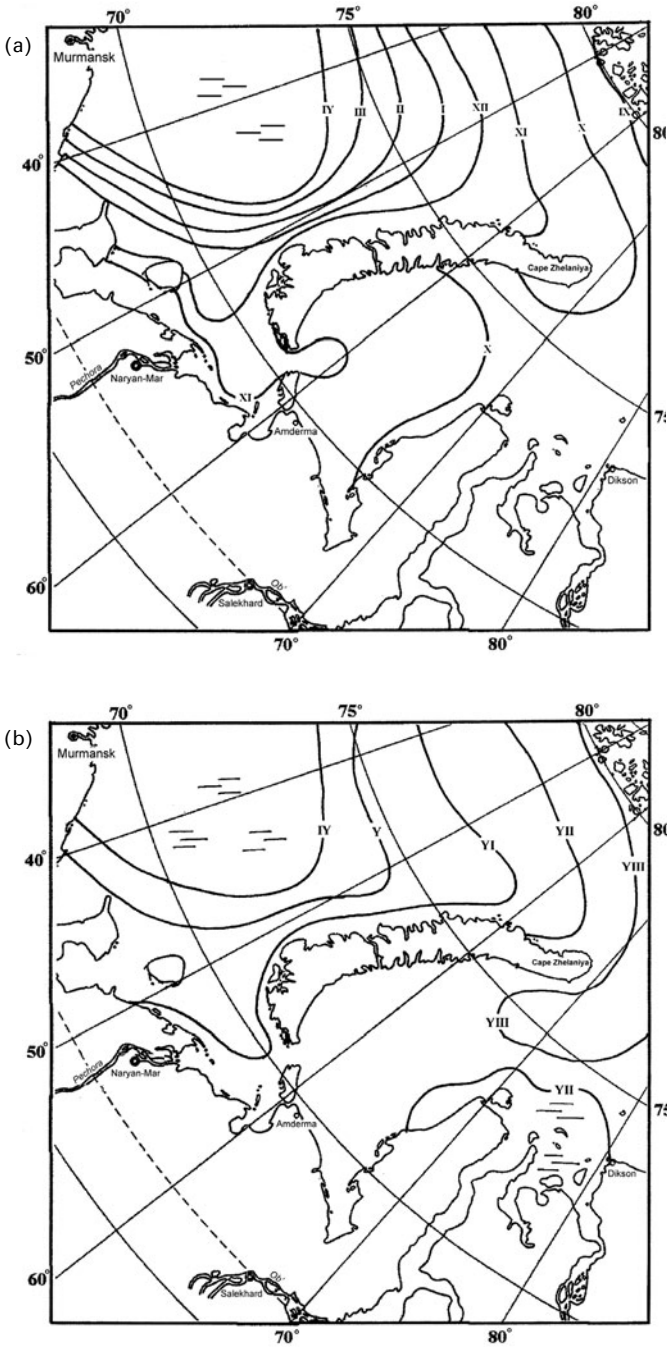

Figure 5.1. Mean annual location of ice edge in the eastern Barents Sea and the southwestern Kara Sea in the middle of the month: (a) during the period of sea ice growth; (b) during the period of sea ice decay.

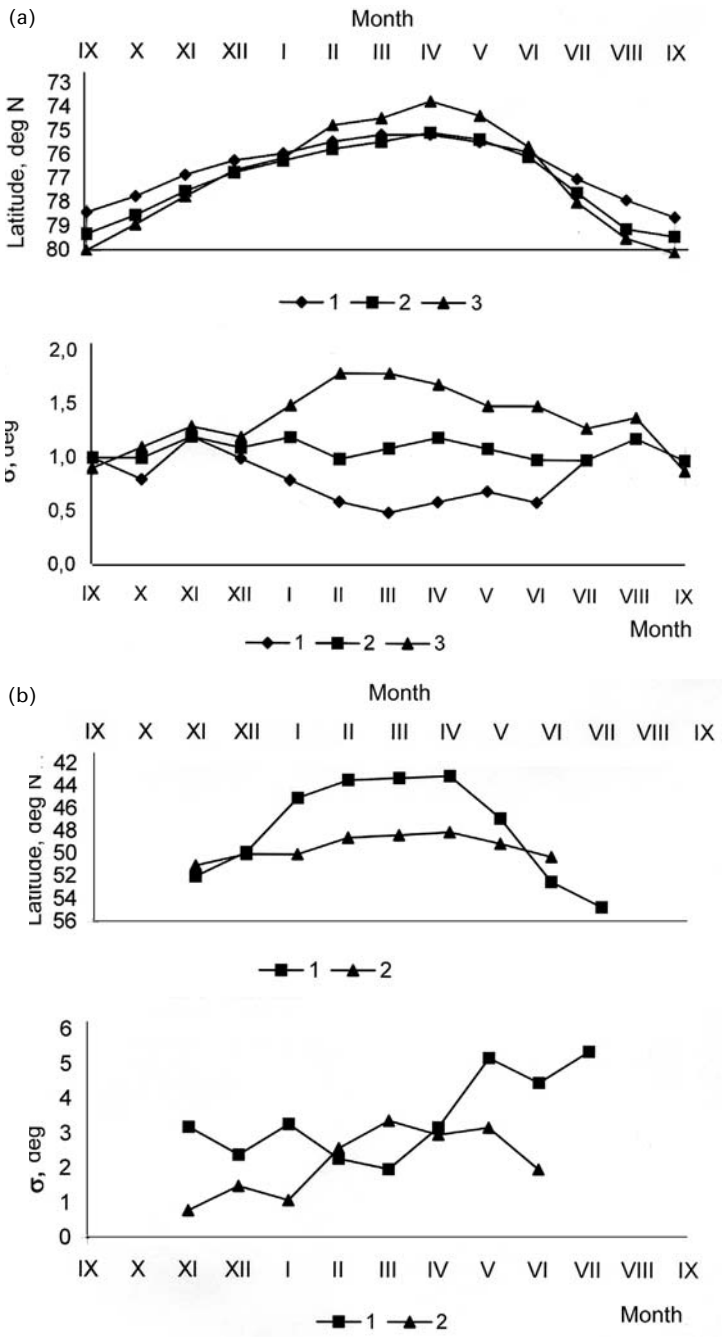

Figure 5.2. Seasonal variability in ice edge position (upper) and its standard deviation (lower) at typical longitudes in: (a) northern Barents Sea (1: at 25°E; 2: at 40°E; 3: at 50°E); (b) south-eastern Barents Sea (1: at 69°E; 2: at 72°E).

On average, in the southeastern part of the Barents Sea, sea ice completely disappears in July and young ice forms in November. The seasonal maximum of ice edge position is noted in April, while the largest seasonal amplitude and multi-year variability (Figure 5.2b) are observed at southern latitudes (69° and 70°N). In severe years, the entire southeastern part of the Barents Sea is ice-covered. The largest multi-year variability of ice edge position is noted in spring–summer (Figure 5.2b) due to the different intensity of the processes of melting and ice clearance (Mironov, 1996).

5.1.2 Ice massifs

Ice massifs are manifested as extensive accumulations of close or very close ice that are found in the same region every summer. Two ice massifs are located in the area of active shipping in the Kara Sea—Novozemelsky and Severozemelsky—their sizes comprising several hundreds of square kilometers at maximum development (Gudkovich *et al.*, 1972). Their location is steadily preserved for a long time until the sea is cleared of ice.

Characteristics of the Novozemelsky ice massif

The Novozemelsky ice massif is located in the southwestern Kara Sea and consists of local first-year ice. The thickness of very close sea ice in this region reaches 1.6–1.8 m by May. In June thin ice starts melting and the region is cleared of ice continuously. Usually, by late June the Novozemelsky ice massif occupies about 80% of the southwestern Kara Sea. A summer change in its partial area, as well as the close ice area for uniform sea regions, is presented in Figure 5.3.

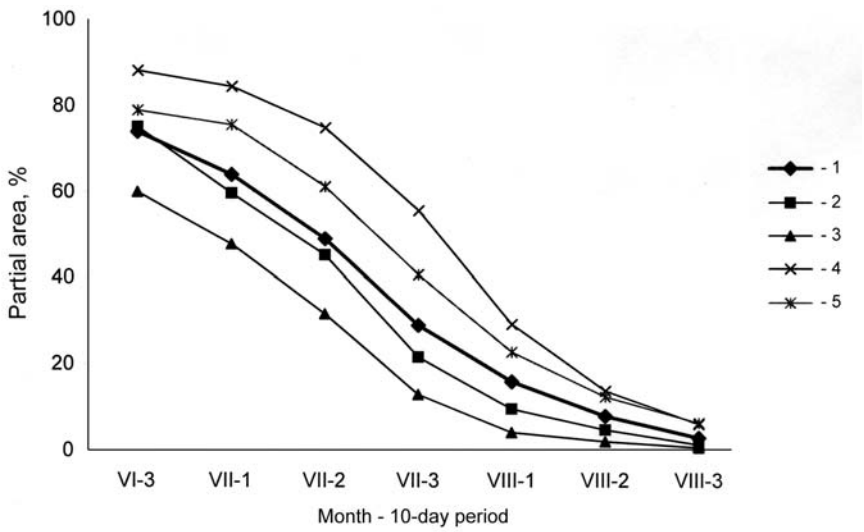

Figure 5.3. Variability of the close ice area in southwestern Kara Sea (1), Yamalo-Yugorsky (2), Ob'–Yenisey (3), Novozemelsky northern (4) and Novozemelsky southern (5) regions.

In late June, close ice steadily prevails in the western part of the sea with the massif core located in the central part north of 71°N latitude (as shown in Figure 5.4a). Near the northern part of the Yamal coast and to the north of the Belyy Island–Dikson Island line, open ice and open water predominate.

The spatial nonuniformity of close ice distribution in the initial period of melting determines a specific displacement of the Novozemelsky ice massif and a decrease in its area. Four regions were delineated in the southwestern Kara Sea (Yegorov and Spichkin, 1994) with the typical change in the close ice area as given in Figure 5.3. Throughout the entire summer period, the amount of close ice in western regions is greater than that in eastern regions. The largest and smallest close ice areas are usually located in the northern Novozemelsky and Ob'–Yenisey regions, respectively. A decrease in area of the Novozemelsky ice massif and close ice in the Yamalo–Yugorsky region to 50% usually takes place in the middle of July; in the Ob'–Yenisey and northern Novozemelsky regions this takes place 10 days earlier and 10 days later, respectively. In mid-July the massif core moves to the northern island of Novaya Zemlya and its area significantly decreases (as shown in Figure 5.4b). In Novozemelsky regions the frequency of close ice occurrence is greater than 50%, while in the eastern parts it is less than 50%. In the Ob'–Yenisey region the frequency of close ice occurrence is less than 25% over a large area.

By mid-August, the areas of the Novozemelsky ice massif and close ice in all regions are usually less than 20%. In late August the Novozemelsky ice massif disappears with a frequency of occurrence of about 80%, although in some years this can be in late July or delayed until late September. Preservation of close ice at sea in September occurs in rare years with a frequency of occurrence of about 5%, with its area at this time being less than 10%.

The area of the Novozemelsky massif and its location change from year to year, but remains substantially typical for each summer season. Five types of ice conditions can be identified in the southwestern Kara Sea based on the durations of the partial area of close ice. Typical changes in close ice areas in the summertime are shown in Figure 5.5. The differences between these types of ice conditions are minimal at the beginning of active melting, and then increase. The greatest differences between them are manifested from the middle of July until early August.

Easy ice conditions (types 4 and 5) have the largest frequency of occurrence, comprising 60% and 40% in the eastern and Novaya Zemlya regions, respectively. The frequency of occurrence of heavy ice conditions (types 1 and 2) comprises 20% and 40% in the eastern and Novaya Zemlya regions, respectively. Average ice conditions (type 3) occur in about 20% of all regions. Both a strong and weak development of the Novozemelsky ice massif in the entire southwestern Kara Sea occur in about 25% of cases. Various combinations of close ice types in its four ice regions are observed approximately in 50% of cases.

Two characteristics of the close ice distribution in the southwestern Kara Sea are important for navigation. First, connection of the Novozemelsky and Severozemelsky ice massifs makes shipping difficult along the Cape Zhelaniya–Dikson route. These ice massifs separate in the second half of July, on average. In years with easy and heavy ice conditions, they separate in the first half of July and the first half of August,

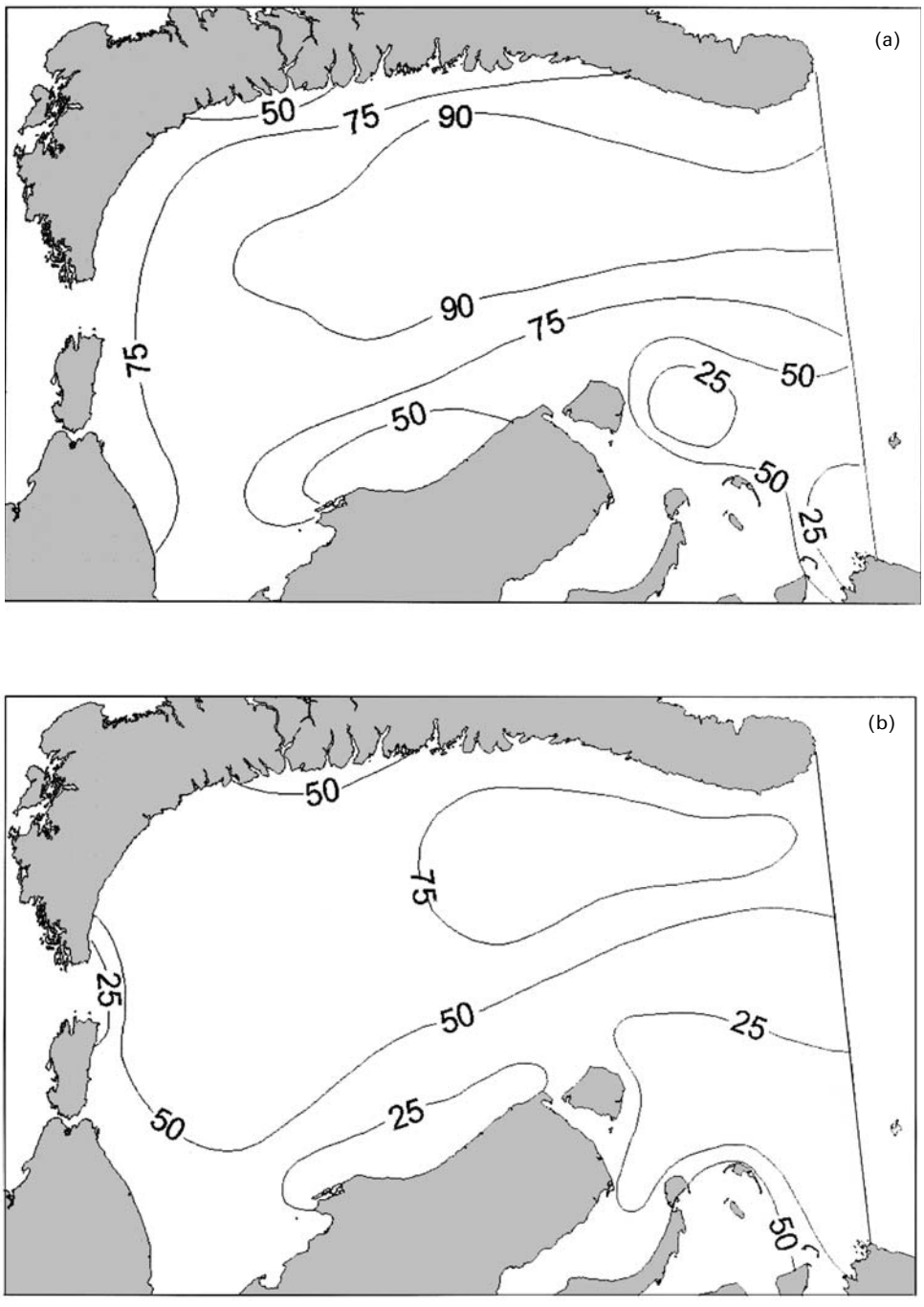

Figure 5.4. Frequency of close ice occurrence (%) of the Novozemelsky ice massif: (a) in late June; (b) in mid-July.

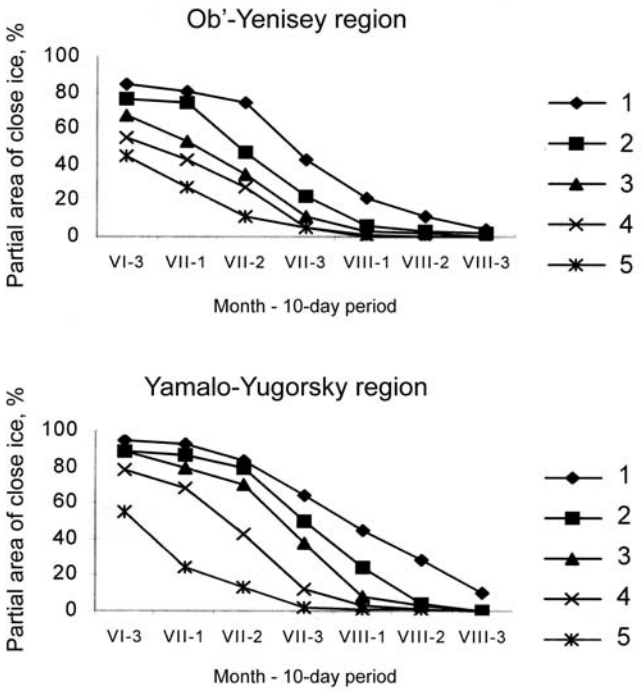

Figure 5.5. Typical partition of close ice areas in the Ob'–Yenisey and Yamalo–Yugorsky regions. Ice types 1–5 explained in the main text.

respectively. Second, the presence of close ice near Kara Gate Strait in the absence of ice in the Yamalo–Yugorsky region complicates navigation from the Pechora Sea to the Kara Sea. This ice usually moves southward along the southern island of Novaya Zemlya. The frequencies of occurrence of close ice near Kara Gate Strait together with open water (very open ice) and open ice in the Yamalo–Yugorsky ice region are 15% and about 10%, respectively. Sea ice is most frequently located near Kara Gate Strait from the middle of July to late August, when the main mass of drifting ice in the Yamalo–Yugorsky ice region melts. The ice can be located near Kara Gate Strait during one, two/three and even four 10-day periods with frequencies of occurrence of 50%, 40% and 10%, respectively.

Characteristics of the Severozemelsky ice massif

The annual summer accumulation of close ice in the northeastern Kara Sea along the Taymyr coast and Severnaya Zemlya is identified as the Severozemelsky ice massif. It is formed of local first-year fast ice about 2 m in thickness (Gudkovich *et al.*, 1972). The close ice of this massif is usually located in the western and eastern Severozemelsky regions (Yegorov and Spichkin, 1994). The western and northern boundaries of these regions correspond to the maximum boundary of fast ice extent. The western boundary passes from Dikson to Sverdrup Island, then eastward to Voronin Island

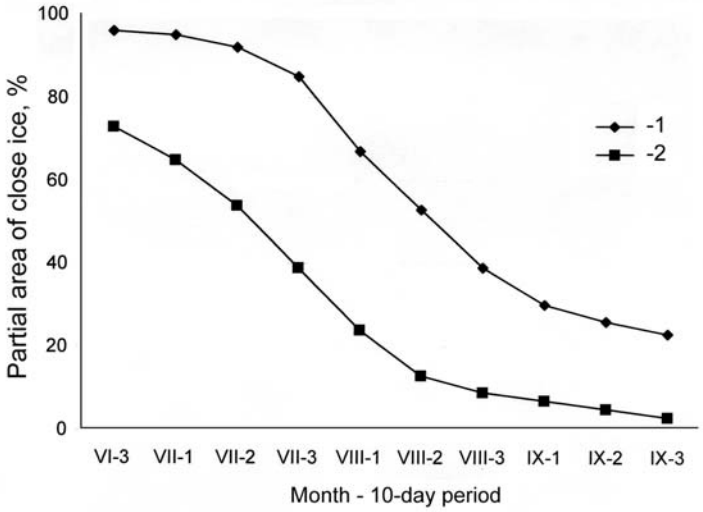

Figure 5.6. Typical partition of close ice in the Severozemelsky ice massif western (1) and eastern (2) regions.

and farther northward to the Sedov Archipelago. Major shipping routes are located in the western and eastern Severozemelsky regions. The boundary between them passes from Cape Sterligov along longitude 88°E.

In May, fast ice and close drifting ice are located almost over the entire area. In June—with thin ice melting, ice concentration decreasing and clearance of ice—the close ice of the Severozemelsky ice massif begins to separate. By late June, it usually occupies about 70% and more than 90% of the western and eastern Severozemelsky regions, respectively. The change in partial area (proportion) of close ice in these regions during summer is presented in Figure 5.6.

An isoline of the presence of close ice with a frequency of occurrence of 90% passes from the Kamennye Islands along coastal islands and then coincides with the fast ice boundary in the eastern Severozemelsky region (shown in Figure 5.7). An isoline of close ice presence with a frequency of occurrence of 75% passes northward of it at a distance up to 50 km. In July the rate of decrease in the close ice area is much greater in the western than in eastern Severozemelsky regions. In summer the partial area of close ice in the western Severozemelsky region is 30–50% less than in the eastern region, where the ice massif core is located. The areas of close ice in the western and eastern Severozemelsky regions usually decrease by as much as 50% in mid-July and mid-August, respectively. The boundary of close ice moves from west to east (as seen in Figure 5.7).

In early August the frequencies of close ice occurrence in the western and eastern Severozemelsky regions are less than 50% and more than 50%, respectively. The ice massif core is located to the west of the southern island of Severnaya Zemlya with a 75% frequency of occurrence. To the south of 75°N open water prevails and the frequency of close ice occurrence is about 10%. In early September, the close ice area

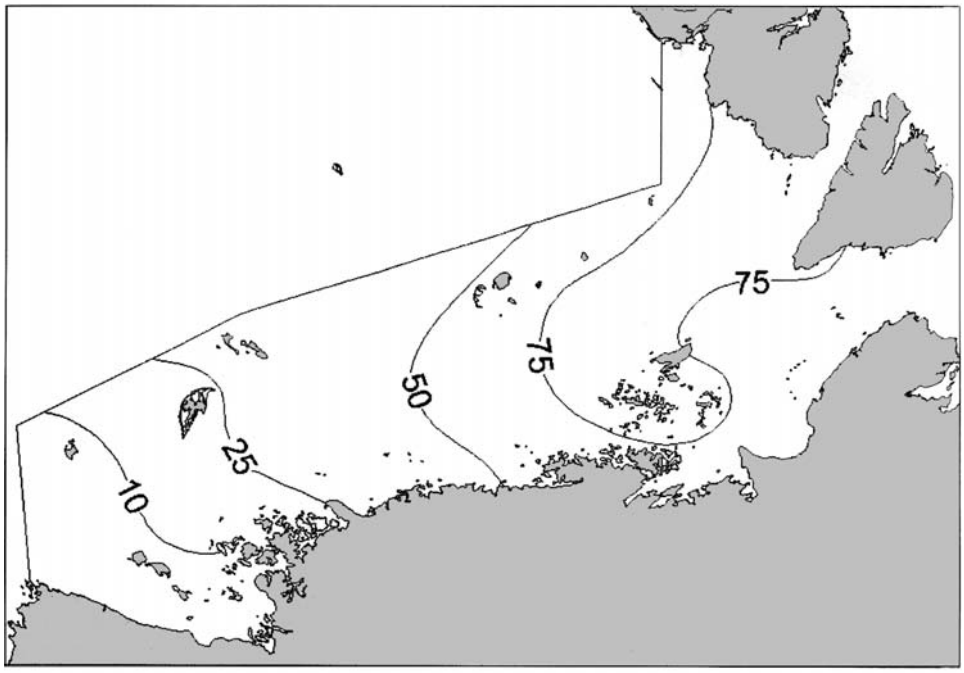

Figure 5.7. Frequency of occurrence (%) of close ice of the Severozemelsky ice massif in early August.

decreases much less. On average, in September it is less than 10% and 30% in the western and eastern Severozemelsky regions, respectively (as shown in Figure 5.8). The frequencies of close ice occurrence in the western and eastern Severozemelsky regions are less than 10% and 30–40%, respectively. There is no pronounced ice massif core. In the western Severozemelsky region ice usually melts completely, while in the eastern region it can be preserved until the autumn freeze-up and comprise significant areas of residual and then multi-year ice, especially near the coast and in the straits of Severnaya Zemlya.

The area of the Severozemelsky ice massif changes from year to year, but its typical features are preserved throughout the summer season. Based on the durations of close ice dominance—which change from zero to ten 10-day periods in different regions—five and seven types of summer decrease in the close ice partial area were identified in the western and eastern Severozemelsky regions, respectively (Yegorov and Spichkin, 1994). The types of close ice area that decrease in the summertime are given in Figure 5.8.

In the western Severozemelsky region seasonal changes in the close ice area follow a regular pattern, while in the eastern region they are rather specific. In the western Severozemelsky region, the close ice area comprises 50% from late June to mid-August. In the eastern Severozemelsky region more than 80% of the close ice partial area is preserved at type 1 throughout the entire summer season. At other types the

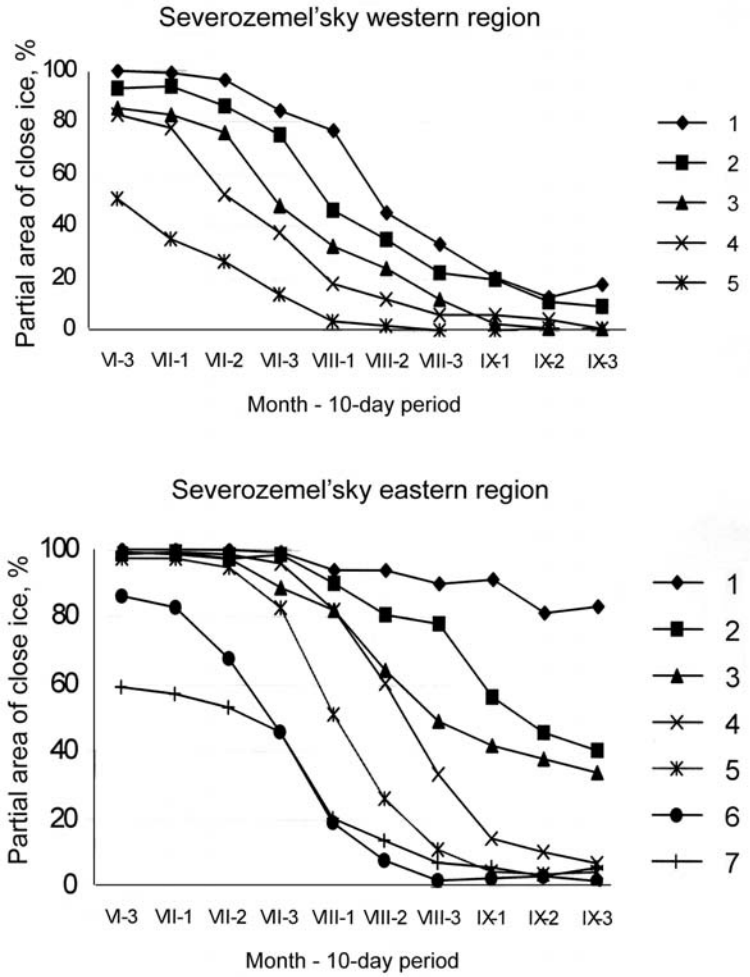

Figure 5.8. Typical variability in the partial area of close ice in the Severozemelsky western and eastern ice regions. Ice types 1–7 are explained in the main text.

close ice area reaches 50% and stays at this level for a considerable time—from late July to mid-September. For types 2 and 3, close ice is preserved because of the onset of new ice formation in 40% of the area. At other types, residual close ice has a partial area less than 10% by the end of summer. The largest interannual changes in the close ice area in the western Severozemelsky region comprise approximately 70% and can be seen from early July to early August. In the eastern Severozemelsky region the greatest differences between the types of ice conditions in the close ice area are 80–90% from early August to late September.

In the western Severozemelsky region, easy (type 5) and heavy (types 1 and 2) ice conditions occur in 45% and 30% of cases, respectively. In the eastern Severo-

zemelsky region, heavy (types 1, 2 and 3) and easy (types 6 and 7) ice conditions have a frequency of occurrence of about 50% and 15%, respectively.

From mid-July to mid-August, close ice is transported for a short time from and to the western Severozemelsky region with a frequency of occurrence of about 60% over each 10-day period. Close ice is exported with a frequency of occurrence of about 30%, with large exports comprising 15% when the decrease in close ice area for each 10-day period is more than 50%. Close ice is transported to the region with the same frequency of occurrence—about 30%—with transports of large amounts comprising 20% when the increase in close ice area over each 10-day period is more than 70%. In 5 years the entire ice-free area in mid-August was covered completely by close ice for each 10-day period.

In the eastern Severozemelsky region seasonal changes in close ice occur more steadily with a frequency of occurrence of its short transport to and from the region comprising about 30%. There are no large changes in ice area. Export of close ice is mainly in August with a frequency of occurrence of about 30% and the decrease in its area for each 10-day period is usually less than 20%. Close ice is transported to the region in September with a frequency of occurrence of about 10% and the increase in its area for each 10-day period is less than 15%.

5.1.3 Fast ice distribution

General characteristics of fast ice formation

In the western Eurasian Arctic from Cape Kanin Nos to Cape Arkticheskiy, fast ice forms annually along almost the entire continental shoreline and around the islands. It begins to form almost simultaneously with the onset of stable ice freeze-up near the shore. It has three typical stages, as described in the following paragraphs.

In the first stage, young coastal ice forms by the freezing of floating new and young ice in shallow areas at depths up to 5 m, where natural land irregularities facilitate its cohesion to the shore. At this stage, fast ice usually extends up to 3 km from the coast at large depths and about 6–8 km in shallow zones. Even the insignificant, external impacts of changes in sea level, wind, wave and swell, young coastal ice may break up, but it is capable of freezing again rapidly. As its thickness increases to 0.3–0.4 m, the stability of fast ice also increases.

In the second stage, fast ice extends further from the coast, usually up to 6–8 km at relatively large depths, as a result of the freezing of large ice floes, which are about 0.5 m thick at their edges. The width of fast ice increases particularly rapidly in coastal shallow water at depths of about 5 to 10 m when there is significant shore irregularity and the presence of shoals, banks and islands near it. Fast ice comprised of thin first-year ice may also break up with sea level change, wind impact and swell, and as a result of the pressure and piling of drifting ice. Fast ice forming at the second stage is usually ridged.

In the third stage, the fast ice width increases due to the freezing of about 1 m thick large ice floes to its edge. In shallow water it spreads up to 15–20 m depths and extends

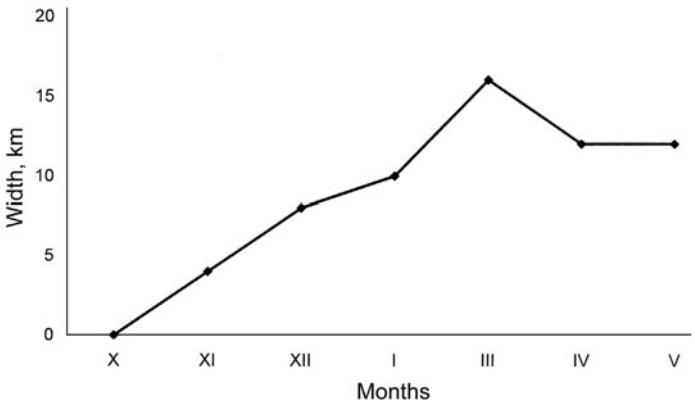

Figure 5.9. The average extent of fast ice during its development near the Yamal Peninsula shore.

up to 10–20 km and over several tens of kilometers from the shore in deep and shallow waters, respectively. Fast ice development lasts for several months (Figure 5.9).

Near the shores of the Yamal Peninsula in 90–100% of cases a fast ice width of 2–4 km and 4–6 km is achieved in 1–2 months and 2–3 months, respectively. With a frequency of occurrence of about 90% the maximum fast-ice area is usually reached in January–February.

Fast ice in the southeastern Barents Sea is narrow and unstable. Fast ice in the Kara Sea is stable; it is narrow in its southwestern part and wide in its northeastern part. Its width varies significantly from year to year. The location of its boundary changes nonsimultaneously in different regions. Therefore, simultaneous extreme locations of fast ice boundaries in all regions from Cape Kanin Nos to Cape Arktichesky are unlikely to occur.

Location of fast ice boundary in the southeastern Barents Sea

In the southeastern Barents Sea the dates that coastal areas freeze up and fast ice forms are significantly different. Fast ice formation dates are most unstable in the Kola region. In the Pechora region they are more stable, especially in Pechora and Khaipudyrskaya Bays. In years of intense cyclonic activity, fast ice constantly breaks up and stable fast ice is not observed at offshore deep waters. Its distribution in the southeastern Barents Sea is shown in Figure 5.10.

An indented coastline is typical for the 900-km section from Cape Kanin Nos to Cape Russky Zavorot. The prevailing syzygial[1] tide (3–4 m and 1–2 m in the west and east, respectively), sea swell and sustained southerly winds are capable of stopping fast ice formation and clearing the area of ice for an extended period.

[1] A syzygial tide is the maximum tide, when Sun and Moon culminate simultaneously and the tide-generating forces of the Moon and Sun act along the same direction.

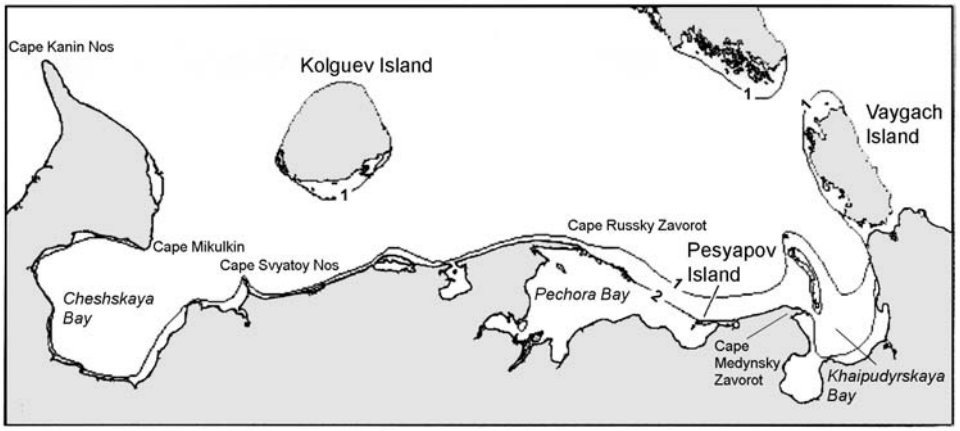

Figure 5.10. The smallest and greatest fast ice boundaries in the southeastern Barents Sea.

There is usually no fast ice over much of the Kanin coast, even during severe winters. In the section from Cape Mikulkin to Cape Svyatoy Nos, it annually forms only in the mouths of the many tundra zone rivers. Over the entire coast of Cheshskaya Bay, it forms only during severe winters. At times of its greatest extent, fast ice in the western and southern parts of Cheshskaya Bay extends predominantly about 3–5 km from the coast and in its eastern part about 10 km. Near Kolguyev Island, fast ice forms annually only in the inlet in the southeastern side of the island.

In the section from Cape Svyatoy Nos to Cape Russky Zavorot, morphological and hydrometeorological conditions do not facilitate fast ice formation. It develops only during severe winters, when its width can reach 5 km. Fast ice is established annually in the shallow waters of Pechora Bay from Cape Russky Zavorot to Pesyakov Island. Under favorable and average hydrometeorological conditions, its boundary passes along the Gulyayevskiye Koshki Islands. During severe winters, the fast ice boundary moves northward by as much as 10–20 km. Along the Varandey coast from Pesyakov Island to Cape Medynsky Zavorot in mild and average winters fast ice extends only 2 km from the coast. During severe winters, fast ice with a predominant width of about 15–20 km covers most of the area and connects the eastern islands with the Varandey coast. In winter, persistent southwesterly winds are capable of clearing the ice for an extended period.

Khaipudyrskaya Bay is annually covered with fast ice. Near the western islands and along the Yugorsky coast, its width is 3–5 km. Under average meteorological conditions in winter, fast ice occupies the greater part of the water area of Khaipudyrskaya Bay. In severe winters, its boundary is located approximately 50 km from the southern shores and 15–20 km from the western islands and the eastern mainland coast.

Fast ice annually forms near the Novaya Zemlya coast. Its boundary usually passes along the capes or in immediate proximity (up to 5 km) to the shores. Near the southwest and northeast shores of Vaygach Island, fast ice forms every year and extends 1–2 km from the shore irrespective of winter hydrometeorological conditions.

In Kara Gate Strait, it usually forms only along Vaygach Island and the southern part of Novaya Zemlya. Its width in the strait is mainly less than 10 km. The entire Yugorsky Shar Strait is annually covered with fast ice.

Fast ice boundary in the Kara Sea

The fast ice characteristics in the Kara Sea are given on the basis of satellite observation data over the period 1979–2003. An example of a satellite image, used for determination of the fast ice boundary in the northeastern Kara Sea, is shown in Figure 5.11. The Central Kara and Western Severozemelskaya flaw polynyas can also be clearly seen in the image.

Fast ice in the Kara Sea forms from late September in its northern part until late January near the coast of Vaygach Island. According to satellite observations, multi-year variation in its formation dates in the Kara Sea regions is from 2–3 to 8 weeks. Therefore, provision of an accurate average date of its formation is meaningless as it has low probability. An estimate of the most probable duration of fast ice has a greater probability. Fast ice formation in the northeastern Kara Sea occurs in mid-October to early November with a probability of 70–90%.

In the Ob'–Yenisey region—freshened by river water—fast ice formation dates change less than in all other regions. In 80–90% of cases, fast ice forms here between the third 10-day period of October and the first 10-day period of November. The most probable period of its formation along the Yamal coast (including Baidaratskaya Bay) is November. In this month 90% of instances of its formation are observed. The largest variation in fast ice formation dates is observed near the Amderma coast and Vaygach Island, where it lasts 8 weeks: from mid-November to late January. According to satellite data of 25 years, it is impossible to determine the most probable time interval of its formation here, as it can form in any week of this 8-week period.

The intensity of fast ice growth and the period of its maximum extent in the regions of the Kara Sea noticeably differ. As noted (Section 2.2.3), fast ice reaches its greatest extent in its northeastern part. From the moment of its formation and until late January, it spreads comparatively quickly, and then the rate of its increase diminishes. In the central part of the northeastern Kara Sea between November to January the fast ice width increases by 25 km and then only by 5–7 km each 10-day period. Substantially, its development in this area is finished by late March (Figure 5.12). At the center of the northeastern Kara Sea in March–April, the range in fast ice width variation is 140–240 km. In some years, Sverdrup, Arctic Institute, Izvestiy Ts.I.K, Isachenko, Kirov and Voronin Islands are located within the fast ice. Its area during the period of maximum development varies within 39,000–139,000 km^2 with an average value of 116,000 km^2.

Fast ice in the southwestern Kara Sea develops least of all along the Amderma and Yamal coasts. It lasts until April with the most intense growth during October to November. Except for Baidaratskaya Bay, the greatest fast ice extent is observed in the vicinity of Belyy Island, where it extends 35–40 km from the coast. The multi-year variability of its width along the Yamal coast is small, and reaches 20 km during the period of its maximum development.

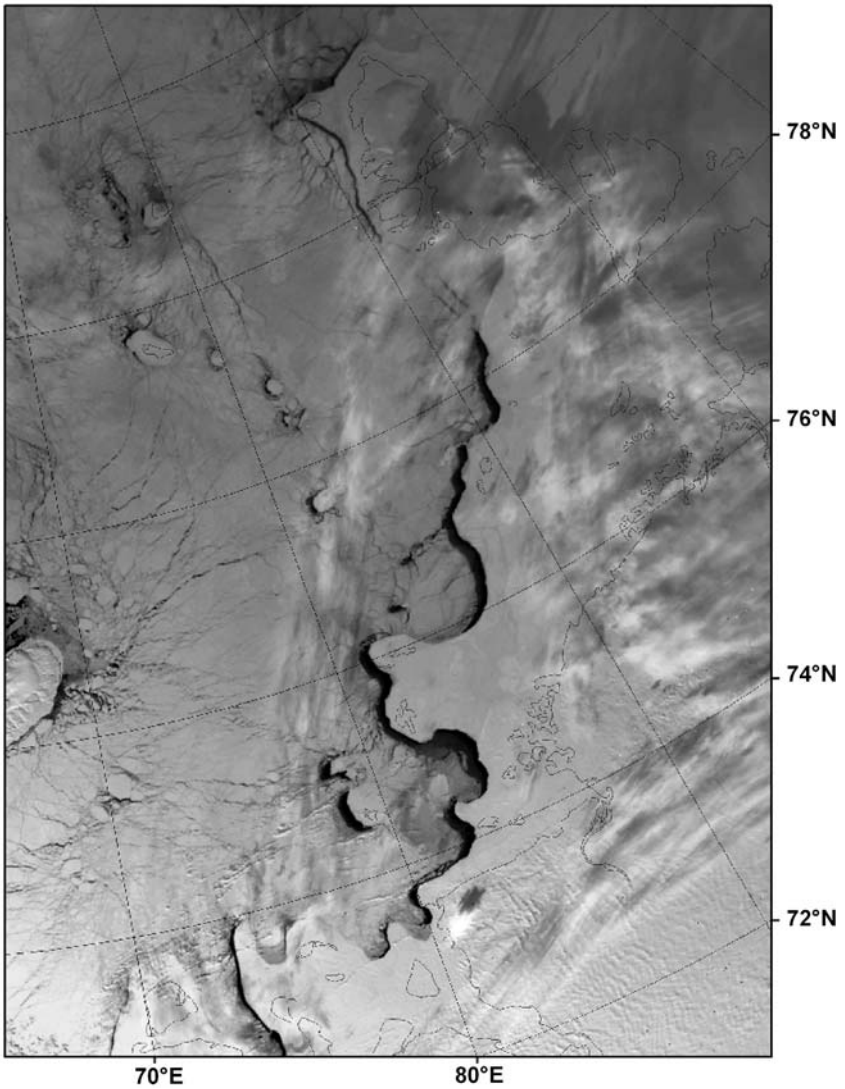

Figure 5.11. Satellite TV image of the northeastern part of the Kara Sea for 23 March 2004.

The Ob'–Yenisey region, which is influenced by runoff from the Ob' and Yenisey Rivers, is characterized by the comparatively low variability in the dates of stable ice freeze-up and fast ice formation. Fast ice formation is most intense in its southern part in Gydanskaya Bay. Even by October its average width in the vicinity of Oleniy Island comprises 30 km, and by January the fast ice boundary reaches Vilkitskiy Island. Its development in the Ob'–Yenisey region occurs comparatively intensively until December–January, and then its width increases slowly until May by 1–2 km per month. Multi-year changes in the fast ice boundary in the Ob'–Yenisey area occur

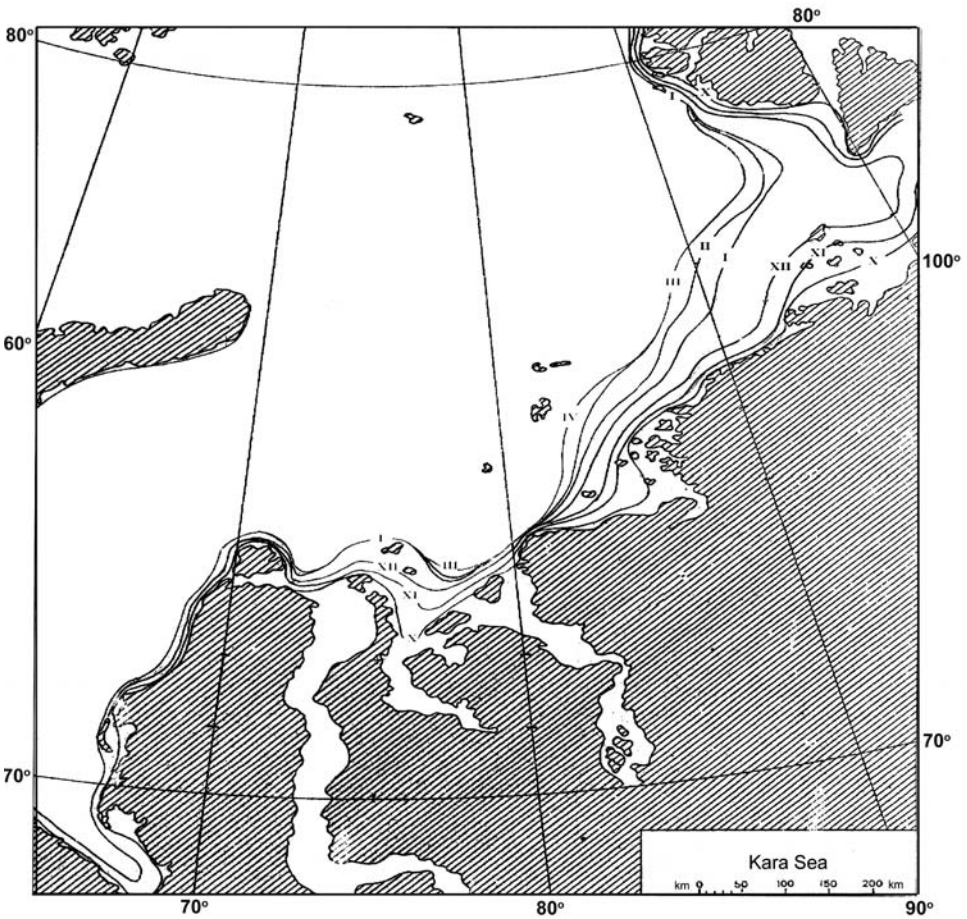

Figure 5.12. Average position of fast ice boundaries in the Kara Sea during its period of growth—October (X) to April (IV)—based on satellite data from 1979 to 2003.

within the 10-m isobath, although shallow water at depths up to 30 m spreads much more northward here. In some studies, significant tides and tidal currents are pinpointed as the cause of this peculiarity of fast ice extent in this region (Borodachev, 1998). On the other hand, the Ob'–Yenisey region is under the prevailing influence of offshore southern winds. Due to these winds, the Ob'–Yeniseyskaya flaw polynya steadily persists during the entire winter period. The influence of offshore winds in restraining fast ice development and decreasing its width has been noted in a number of studies (Skokov, 1985; Batskikh *et al.*, 1987; Yulin, 1997).

In March, under average conditions 97% and 96% of the fast ice area forms in the northeastern and southwestern parts of the Kara Sea, respectively (Table 5.1). It has completely formed by April. Under favorable conditions for its development, the fast ice area in December is close to the size of that which forms under average conditions

Table 5.1. Mean and extreme areas of fast ice during the period of growth in the Kara Sea in the middle of the month from satellite data from 1980 to 2002 (in thousands of km^2).

Region	Area	Month							
		Oct.	Nov.	Dec.	Jan.	Feb.	March	April	May
Southwestern	Mean	0	20.1	26.4	29.8	34.6	35.0	36.7	35.5
	Max	1.0	29.3	35.8	44.6	50.2	50.3	56.2	54.8
	Min	0	1.7	17.3	17.6	18.7	18.1	18.1	17.5
Southeastern	Mean	23.2	31.1	49.9	90.7	109.7	121.3	124.6	122.7
	Max	39.8	48.6	112.8	154.3	162.7	163.9	164.1	167.3
	Min	0.4	3.1	14.9	28.1	32.6	34.4	36.2	39.2
Entire sea	Mean	23.2	51.2	76.3	120.5	144.2	155.3	161.3	158.2
	Max	40.8	77.9	148.6	199.0	212.9	214.2	220.2	222.1
	Min	0.4	4.8	32.2	45.7	51.4	52.5	54.3	56.7

in May. Interannual variations in fast ice area are especially large in the northeastern Kara Sea, comprising 128,000 km^2 in April.

The breakup of fast ice and its final decay occur first in its boundary. Between Dikson and the Arctic Institute Islands it has completely disappeared by the middle of June, earlier than in other regions. In late July the only unbroken fast ice remains around the Nordenskjöld Islands, which then disappears in early August. In some years, fast ice in this region does not break up until the onset of new ice formation. Interannual differences in the dates of fast ice decay in the northeastern Kara Sea range from 1 to 3 months.

In the southwestern Kara Sea, fast ice decay begins in early June near Vaygach Island and the Amderma coast. In the second half of June, fast ice begins to decay in Baidaratskaya Bay. By the middle of July, the entire Yamal coast up to Belyy Island becomes ice-free. Fast ice in the Ob'–Yenisey region breaks up very rapidly. Early breakup dates in this region are observed in the first 10 days of July and in the second 10 days of the month, when its decay is final.

5.1.4 Flaw polynyas

Seven polynyas can be identified in the Kara Sea: Northern Novozemelskaya, Southern Novozemelskaya, Amderminskaya, Yamalskaya, Ob'–Yeniseyskaya, Central Kara and Western Severozemelskaya (Karelin, 1997). The regions where they form are shown in Figure 2.14. The formation of polynyas is related to offshore winds, and their existence is in practice dependent on wind flows in corresponding regions. The location and length of polynyas change with fast ice extent and configuration of its boundary.

Changes in the Yamal and Ob'–Yeniseyskaya polynyas from late April to mid-May of 2003 can be seen in satellite TV images (Figure 5.13). It is evident that by mid-May the Yamal polynya was full of drifting ice, whereas the size of the Ob'–

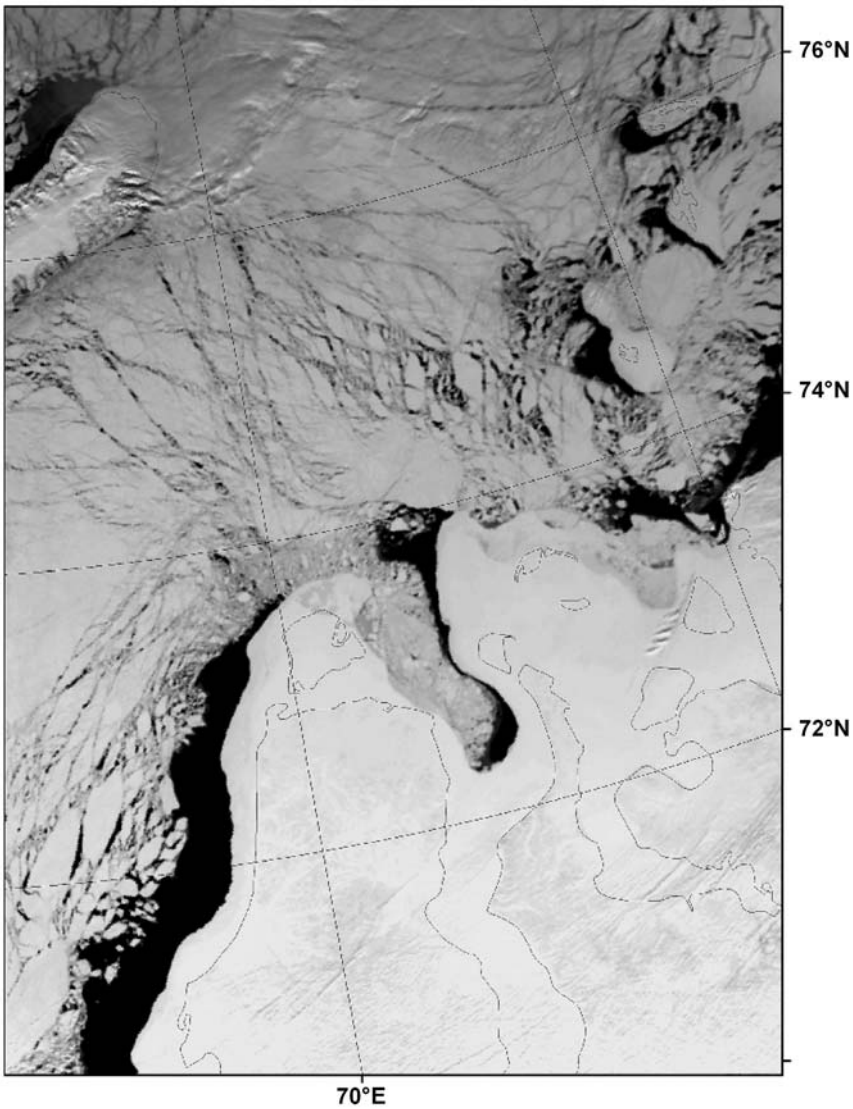

Figure 5.13(a). Satellite TV image of the southwestern part of the Kara Sea for 29 April 2003.

Yeniseyskaya polynya increased. Satellite data over the period 1979–2004 allow the development of Eurasian Arctic seas polynyas during winter to be characterized. Their length and width can be determined from ice charts—with a scale of 1 : 5,000,000—that are weekly produced at AARI. The accuracy in determining their boundaries is 2–3 km. In cases where the polynya width changes over its entire length, its average value is determined by taking into account the contribution of the lengths of uniform polynya segments.

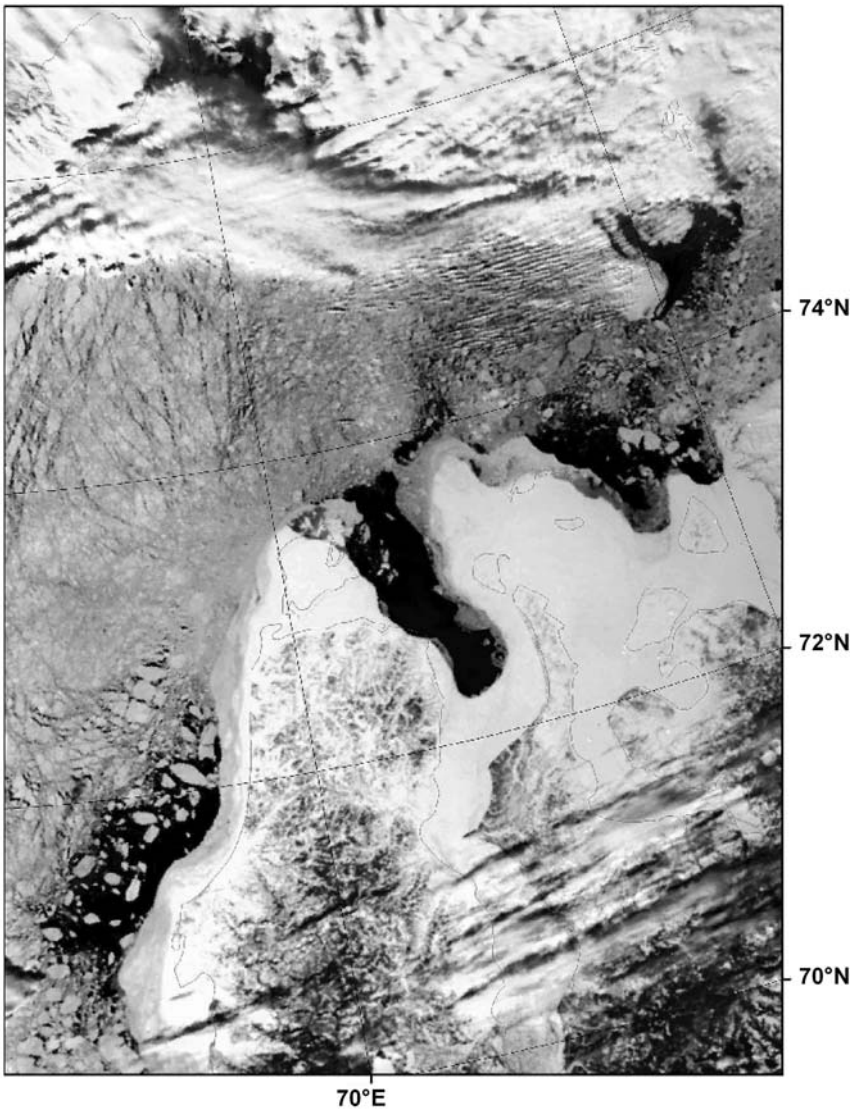

Figure 5.13(b). Satellite TV image of the southwestern part of the Kara Sea for 16 May 2003.

In accordance with the adopted classification (Section 2.2.3), the Ob'–Yenisey-skaya and Central Kara polynyas belong to the category of stationary polynyas on average over the whole winter season, all other polynyas of the Kara Sea belonging to the category of stable polynyas—that is, their frequency of occurrence is more than 50%, but less than 75% (Table 5.2). The ranges of variability in their length and width are significant and their maximum areas are more than 100 times greater than their minimum values.

Table 5.2. Mean frequency of occurrence—*P* (%)—and characteristics of polynyas of the Kara Sea observed from satellite data from November to June 1979–2003.

Polynya	*P* (%)	Characteristic					
		Length (km)		Width (km)		Area (thousand km^2)	
		Mean	Range of changes	Mean	Range of changes	Mean	Range of changes
N. Novozemelskaya	59	341	50–630	28	2–110	9.9	0.5–66.0
S. Novozemelskaya	58	271	60–350	42	2–160	11.3	0.5–17.2
Amderminskaya	69	287	40–470	32	2–127	9.8	0.4–58.7
Yamalskaya	66	420	80–670	28	2–137	12.9	0.6–69.7
Ob'–Yeniseyskaya	88	281	50–560	44	2–190	12.9	0.4–65.2
Central Kara	78	479	50–920	36	2–138	18.3	1.0–121.9
W. Severozemelskaya	66	259	50–620	29	2–170	8.1	0.4–56.1

The mean monthly frequency of polynya occurrence differs sometimes substantially from the average value over the entire season. In all months the Ob'–Yeniseyskaya polynya remains stationary with a frequency of occurrence within 77–98%. The Central Kara polynya—being stationary—on average enters the category of stable polynyas in February and March (Table 5.4). A stable—on average—Amderminskaya polynya exists as stationary in December–March and is close to becoming an episodic polynya in May. In two months—January and June—the frequency of occurrence of the Yamalskaya polynya is 78% and 82%, respectively, and in these months it is stationary. It is interesting to note that increased frequency of occurrence of the Yamalskaya polynya causes the frequency of occurrence of the Southern Novozemelskaya polynya to decrease—and *vice versa*—which is in agreement with wind conditions over the southwestern Kara Sea (Table 5.3).

Table 5.3. Mean monthly frequency of occurrence of polynyas in the Kara Sea observed from satellite data from 1979 to 2003 (%).

Polynya	Month							
	Nov.	Dec.	Jan.	Feb.	March	April	May	June
Northern Novozemelskaya	—	53	59	55	60	65	55	78
Southern Novozemelskaya	—	61	50	69	59	70	52	55
Amderminskaya	—	90	81	79	76	60	50	60
Yamalskaya	—	68	78	56	66	54	63	82
Ob'–Yeniseyskaya	93	90	94	88	89	77	80	98
Central Kara	84	83	78	68	58	86	76	88
Western Severozemelskaya	56	55	60	65	63	80	74	72

Table 5.4. Inter-annual variability in frequency of occurrence of polynyas in the Kara Sea, observed from satellite data from 1979 to 2003 (%).

Polynya	Mean frequency of occurrence	Gradations of frequency of occurrence		
		$P < 50$ (episodic)	$75 > P > 50$ (stable)	$P > 75$ (stationary)
Northern Novozemelskaya	59	36	32	32
Southern Novozemelskaya	58	36	44	20
Amderminskaya	69	16	40	44
Yamalskaya	66	12	60	28
Ob'–Yeniseyskaya	88	–	4	96
Central Kara	78	12	28	60
Western Severozemelskaya	66	36	24	40

The formation and development of polynyas depend on hydrometeorological conditions. Therefore, their stability from year to year can differ significantly from their mean multi-year stability. For the analysis of multi-year variability in polynya stability, their frequency of occurrence was calculated for each year as a ratio of the number of 10-day periods in which a polynya was observed to the total number of 10-day periods in November–June. The results are presented in Table 5.4.

As can be seen from Table 5.3, except for the Ob'–Yeniseyskaya polynya—which is almost always stationary—all other polynyas throughout November–June can form episodically. In 36% of cases, the Northern and Southern Novozemelskaya, as well as the Western Severozemelskaya, polynyas appeared occasionally. In 12–16% of the observation years, the Amderminskaya, Yamalskaya and Central Kara polynyas appeared only episodically. The same polynyas can be stationary. The Central Kara polynya existed as stationary more often—in 60% of the observation years. The other polynyas were stationary in 20–44% of cases. In all other years, these polynyas existed steadily with a frequency of occurrence of 50–75%.

Polynyas in the Barents Sea that form near the southern and southwestern coasts of Franz Josef Land and along the shores of Novaya Zemlya are stable (Zakharov, 1996). Those forming along the entire southern shore of the Pechora Sea are episodic. Their existence varies between 1 and 22 days. On average, the duration of polynyas in different areas of the Pechora Sea varies from 2 to 4 days.

5.1.5 Fractures in the sea ice

Discontinuities—hereafter collectively called "leads"—are a typical structural element of the ice cover of Eurasian Arctic seas in the winter and spring periods. They form as a result of sea ice deformation related to the spatial nonuniformity of its drift (Gorbunov *et al.*, 1986a). Such nonuniformity is mainly determined by the drift field variability and morphometric characteristics of the region, including the spatial difference of ice thickness. The result is the appearance of leads (Gudkovich and Doronin, 2001).

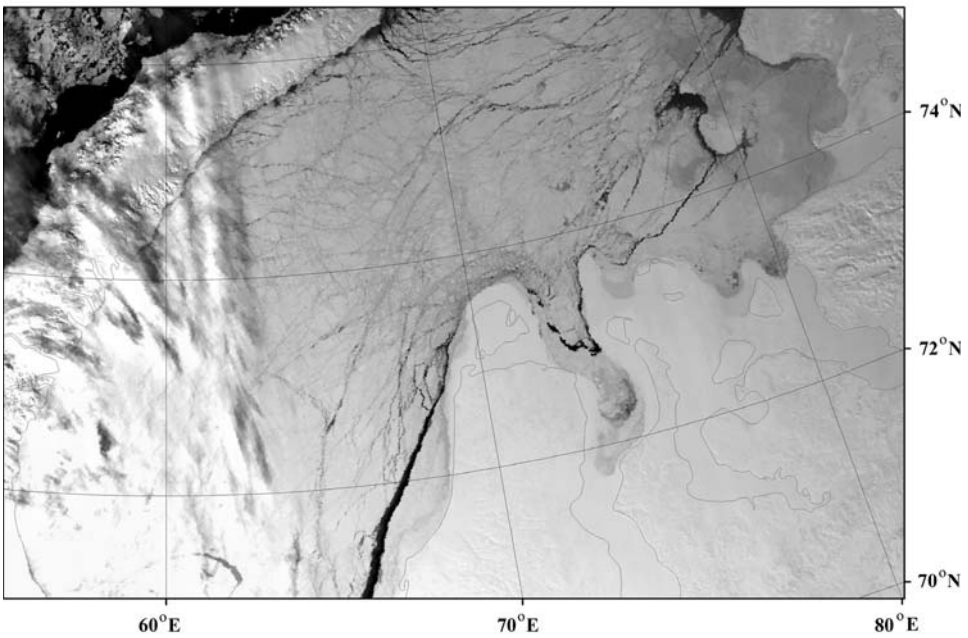

Figure 5.14. *NOAA* AVHRR image (11 April 2004) showing a system of leads in Kara Sea ice.

The first data on leads were obtained from visual observations made during airborne ice reconnaissance and ship voyages in the ice. Aerial photography and SLR surveys estimated all the parameters of leads and obtained their statistical characteristics. Since the early 1970s, satellite images have been a major source of information on leads. Due to the significant coverage by satellite images, it was determined that leads in sea ice form specifically ordered systems (Figure 5.14). By their shape and mutual location, arched, quasi-parallel and polygonal systems are most frequently identified. A quasi-parallel system of leads is characterized by the presence of leads close to their orientation. In the polygonal system there are bi-modal directions of leads and the ice cover is divided into segments in the shape of parallelograms and rhombuses (more rarely, as rectangles). An arched system of leads is typical of pre-strait areas.

Based on satellite imagery, studies of leads in the sea ice of the Arctic Ocean were carried out as early as the 1970s (Kupetsky, 1973; Provorkin, 1975; Bushuev and Bychenkov, 1978) and were substantially expanded in the 1980s. Some results of these studies were published in several articles (Karelin, 1985; Gorbunov *et al.*, 1986b).

Interest in studying leads is primarily determined by their practical significance. They are often used for the escort of ships by icebreakers in difficult areas. The history of navigation in the Eurasian Arctic provides many such examples. For instance, in 1954 in mid-October the diesel–electric ship *Yenisey* was escorted via a system of leads through close ice from Pevek Port to the eastern boundary of multi-year ice. In 1997 the research–expedition ship *Mikhail Somov* that supplied polar stations in the Laptev

Sea left the operation area in early December, when ice was reaching the stage of thin first-year ice. Under these conditions, the captain, choosing existing leads in the sea ice for transit, was able to bring the ship to Vilkitskiy Strait independently (i.e., without icebreaker assistance). Since 1990, high-latitude voyages in the summertime have been much more frequent, including icebreaker cruises to the North Pole. They are made by taking advantage of *en route* leads and fractures (Brigham, 1995; Frolov, 1997a, b; Frolov and Klyachkin, 2001).

Considerable attention has been paid to the study of lead characteristics in the sea ice of the Kara Sea, which is governed by regular voyages of ships in winter along the Kara Gate Strait–Dikson and Cape Zhelaniya–Dikson routes. As a result of these studies, the presence of orderly systems of large leads here in winter was revealed and three types of their spatial structure were determined (Adamovich, 1987; Karelin, 1998). Six uniform regions were delineated and quantitative values of lead orientation and density in these regions were obtained (Adamovich, 1987). The significant stability of lead orientation for time intervals up to 20 days and the relationship between how they change and wind direction change was found (Karelin, 1998). It was shown that in the regions of ice navigation along the Kara Gate Strait–Dikson and Cape Zhelaniya-Dikson routes, leads' modal orientation is close to the general direction of ship routes (Brestkin *et al.*, 1995). A method of diagnostics and forecasting the characteristics of large leads in the sea ice of the Kara Sea has also been proposed (Gorbunov *et al.*, 2001). Initial information for the Kara Sea was derived using a database generated from satellite low-resolution images for an incomplete period of 18 years (1979–1984, 1986, 1987 and 1991–2004). Leads wider than 500 m can be detected in the images. Calculation of lead characteristics was performed from November to May by studying 100×100 km grid squares. The coordinate axes on which the grid was constructed are located parallel to longitudes 40°E and 130°E. This lead mapping approach, as well as measurements of lead density and orientation (see below), is comparable with those independently developed and applied to the Beaufort, Chukchi and East Siberian Seas using thermal and visible band satellite imagery between 1979 and 1986 (Miles and Barry, 1998).

For estimating the density of leads, their specific length l^* was used. This presents a total length of leads in the square $\sum_{i=1}^{n} l_i$ referred to the area of this square Q:

$$l^* = \frac{1}{Q} \sum_{i=1}^{n} l_i$$

Three fields of this characteristic—referring to the beginning, middle and end of the period under consideration—are presented in Figure 5.15. Analysis of the fields revealed that from November to May the sea ice of the Kara Sea has zones of relatively increased and decreased density of leads whose location is rather stable. Zones of increased density are observed between Novaya Zemlya and the Yamal Peninsula, between Cape Zhelaniya and Graham Bell Island, between Cape Zhelaniya and the Artic Institute Islands and sometimes between the Franz Josef Land and Severnaya Zemlya archipelagos. Relatively decreased values in the specific length of leads are observed along the coast of Novaya Zemlya and the mainland (along the fast

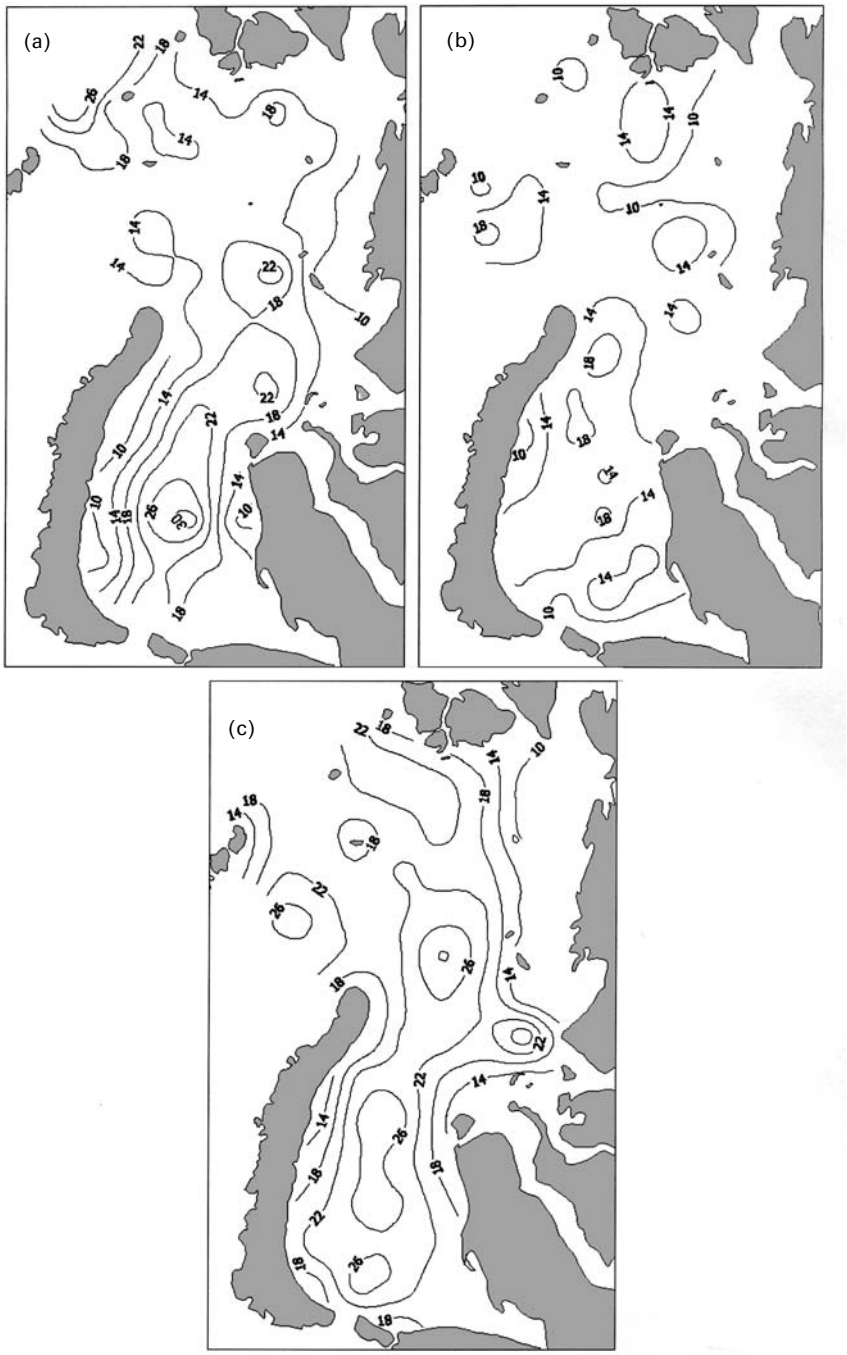

Figure 5.15. Estimates of specific length of leads (m/km^2): (a) November; (b) February; (c) May.

Table 5.5. Monthly mean and maximum specific lengths of leads (discontinuities) in the ice cover of two regions of the Kara Sea (m/km^2).

Month	Northeastern region		Southwestern region	
	Mean	Max.	Mean	Max.
November	15.8	50.6	17.3	45.6
December	16.0	59.9	18.7	74.7
January	17.9	69.9	16.4	62.5
February	12.8	38.7	15.5	57.8
March	18.8	73.5	16.8	53.0
April	19.8	61.2	16.9	64.3
May	24.7	78.8	24.7	69.8

ice boundary or beyond flaw polynya limits), and also in the vicinity of Vize Island. Near the mainland, their density is mainly 10–12 m/km^2. Near Vize Island these are 12 m/km^2 from December to February, 14 m/km^2 in November, March, April and 18 m/km^2 in May.

Seasonal variability in the average specific length of leads in the Kara Sea corresponds in general to the existing understanding of variability in the degree of the ice cover breakup in Arctic seas (Gorbunov *et al.*, 2001). In November–January, the changes in average specific length of leads are insignificant and are determined by changes in the size of zones with increased density of leads (Table 5.5). February is characterized by their minimum density. In the northeastern part of the Kara Sea (to the northeast, north of the Cape Zhelaniya–Dikson Island line), they are smaller than in the southwestern area (see Figure 5.15b, Table 5.5). From March a gradual increase in the specific length of leads occurs, both in zones with relatively increased density and in general over the sea. In May the density of leads achieves its maximum in the entire Kara Sea comprising 24.7 m/km^2, on average. Correspondingly, in zones of increased density their specific length achieves 26–30 m/km^2 (see Figure 5.15c).

To study variability in the orientation of leads, mean monthly values of modal orientation α_m of leads and their probability for three months were calculated in each grid square. Figure 5.16b presents the modal orientation of leads by means of grid squares calculated for the same months as the specific length. It is represented by segments whose orientation corresponds to the orientation of the first and second mode, if the latter exists. The length of the segments is proportional to the probabilities of intervals $\alpha_m \pm 20^\circ$.

Analysis of data on lead orientation in the sea ice of the Kara Sea showed that in spite of the large spatial variability in prevailing direction, mean monthly values of modal orientation of leads change little throughout the entire winter–spring period in a significant part of the grid squares. Thus, from November to May, the modal orientation of leads in 50% of the grid squares changed from month to month by no more than 30°, and in 28% of the squares for the same period a change by more than 30° was only observed once. Quite remarkable in this respect appears to be the

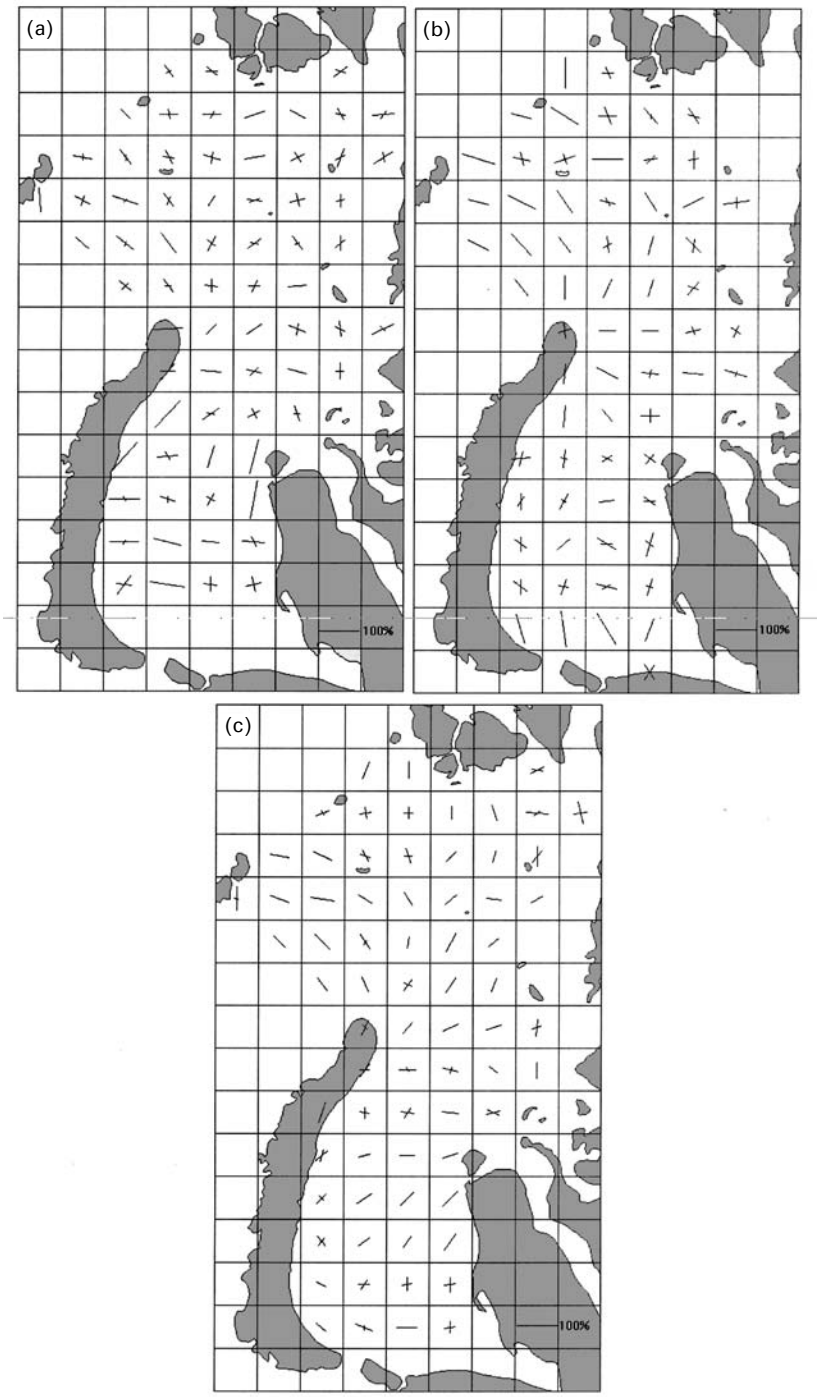

Figure 5.16. Modal orientation of leads: (a) November; (b) February; (c) May.

Table 5.6. Mean and maximum lengths of leads (discontinuities) in the ice cover of the whole Kara Sea in different months (km).

Month	Mean	Maximum
November	94	474
December	86	636
January	95	516
February	67	692
March	94	503
April	84	697
May	98	601
November–May	91	697

region between Cape Zhelaniya and Graham Bell Island. Here, a stable system of arched leads is observed. In each of the ten squares of this region, the values of the first mode of lead orientation from November to May can be considered constant. A deviation from the modal direction of leads, calculated over the entire period, is no greater than 20° in each month. The probability of interval $\alpha_m \pm 20$ (modal interval) in these squares is more than 50% and comprises 63% in two of them, which further testifies to the stability of the prevailing direction.

Of interest is a change from month to month in the number of squares with a uni- and bi-modal distribution of lead orientation. A bi-modal distribution was noted in most squares (68%), indicating the dominance of the polygonal system of leads in the sea ice. The second mode in this month was even recorded in some squares of the zone of stable lead orientation between Cape Zhelaniya and Graham Bell Island. During winter with increasing ice thickness, the frequency of occurrence of a bi-modal distribution of lead orientation gradually decreases, and in March–May a uni-modal distribution of lead orientation becomes prevalent (58–59%).

Analysis of the length of all recorded leads showed this characteristic to be quite stable during the ice period (Table 5.6). Especially stable appear to be the mean monthly values of the lead length, which have practically no seasonal variations while their maximum length is determined by the size of the region.

In summary, the study of generalized characteristics of large leads in the sea ice of the Kara Sea using a multi-year database obtained from satellite imagery allowed us to reveal the presence of quasi-stationary zones of increased and decreased density of leads, estimate seasonal variability and confirm the existence of regions with a stable lead orientation.

5.2 EASTERN PART OF THE NORTHERN SEA ROUTE (*V.P. Karklin, I.D. Karelin, Y.A. Gorbunov, S.M.Losev*)

The characteristics of ice conditions in the eastern part of the NSR are presented here, based predominantly on satellite observations from the early 1970s to present.

5.2.1 Ice edge position

The decay of sea ice begins with the spring melt processes. Ice melt in Eurasian Arctic seas begins in mid-May and continues to the second 10-day period of June. Under average melting conditions, ice has melted by the end of the summer, except for thick first-year ice whose thickness decreases to 20–40 cm, and old and ridged ice. The clearance of ice from the seas is directly connected with melting as a result of dynamic processes.

Timing of the ice-free season depends on the geographical location of the regions. The southern Chukchi Sea becomes ice-free earlier than the other regions. Due to advection of comparatively warm Bering Sea water, up to 10% of ice in the southwestern sea area melts as early as in late May, on average. Under the influence of warm river runoff in the Laptev Sea basin, the clearance of sea ice begins in mid-June. The role of warm runoff from the large Indigirka and Kolyma Rivers is insignificant, their influence spreading only in near-mouth areas (Gudkovich *et al.*, 1972). Ice melting in the East Siberian Sea begins only under the influence of solar radiation heat and advection of atmospheric heat. Sea ice begins to clear, on average, in July.

The most intense clearance of the seas occurs in August and ends in late September before the onset of ice formation. However, it occurs at different intensities, which are related to the characteristics of each region in the Arctic Seas. By the end of the melting period, 80% of the eastern Laptev Sea and the southwestern Chukchi Sea become ice-free, on average. Approximately 50% of the western Laptev and East Siberian Seas are ice-free before the onset of ice formation. The eastern East Siberian Sea is less ice-free that the other regions (Table 5.7).

The spatial character of Eurasian Arctic sea clearance of ice under average ice conditions is illustrated by the average location of ice edges in late July, August and September (Figure 5.17). Calculation of average edges and the characteristics of their variability was determined from the latitude of their position at longitudes with an interval of 2.5°.

Variability in ice edge location from year to year is connected with the variability of ice conditions, which in turn are determined by multi-year changes in hydrometeorological processes. Multi-year variability in ice-edge location was characterized

Table 5.7. Ice-free area during the third 10-day period of each summer month in different regions of eastern Eurasian Arctic seas (%).

Region of sea	Month			
	June	July	August	September
Western Laptev Sea	10	24	45	51
Eastern Laptev Sea	10	33	69	80
Western East Siberian Sea	0	10	31	49
Eastern East Siberian Sea	0	6	17	27
Southwestern Chukchi Sea	27	57	75	85

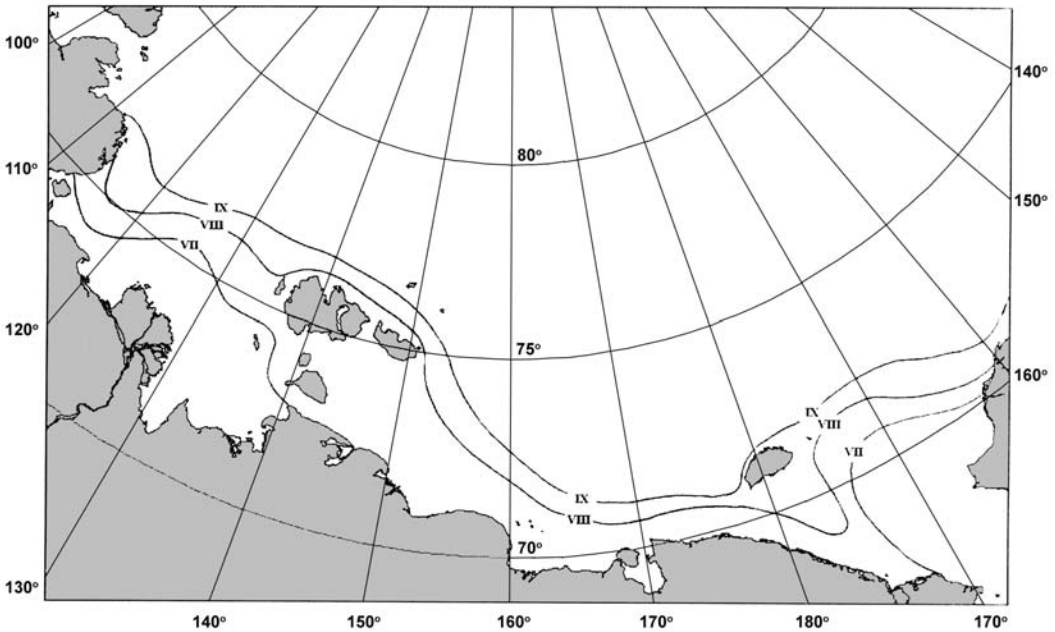

Figure 5.17. Average ice edge location in eastern Arctic seas in July (VII)–September (IX) from data of 1973–2003.

by calculating standard deviations at longitudes—every 5°—between 100° and 190°E.

Variability in ice edge location in the Laptev Sea significantly increases from west to east in all summer months (Figure 5.18a). Within the sea, multi-year changes in ice edge by latitude are within ±0.2–2.8° or ±22–310 km. The ice edge location near the Taymyr coast (between 100 and 105°E) is the least variable. In the central Laptev Sea, it varies by ±200 km. The most significant ice edge changes are typical of the New Siberian Islands (between 135 and 140°E), where their standard deviation can comprise ±300 km, on average (Figure 5.18a).

In the East Siberian Sea, multi-year changes in ice edge location occur in accordance with the characteristics of its areas. In its western part (to the west of 160°E), which is more intensively ice-free, multi-year changes in ice edge location are within ±200–250 km. Ice in the eastern sea area is located on average quite close to the coast and its edge to the north of Cape Shelagsky varies by latitude by only ±50 km. The ice edge variability range increases to ±250 km in September (Figure 5.18b). In August and September, sea ice can reach the Chukchi coast or be located to the north of Wrangel Island. The standard deviation of variability in ice edge latitude in these months comprises 180 km and 200 km, respectively.

In the Chukchi Sea the most significant changes in ice edge location occur in its northern areas, where they are characterized by a standard deviation of 150 km and 250 km in August and September, respectively (Figure 5.18b).

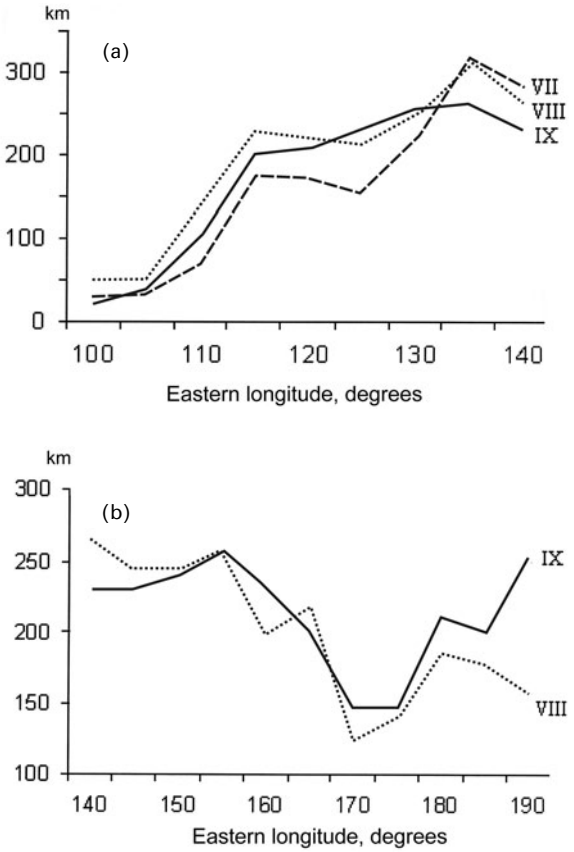

Figure 5.18. Changes of standard deviations of ice edge location from 1973 to 2003: (a) in the Laptev Sea in July (VII)–September (IX); (b) in the East Siberian and Chukchi Seas in August (VIII) and September (IX).

5.2.2 Ice massifs

During the melt and disappearance of ice in seas, open and very open ice appears, located predominantly in the marginal zone. Large areas of close and very close ice are defined as ice massifs. At the eastern part of the NSR, five ice massifs are identified in the Laptev, East Siberian and southwestern Chukchi Seas (Figure 5.19).

The Taymyrsky and Ayonsky ice massifs are spurs of the Arctic Basin ice massif. The Taymyrsky ice massif mainly occupies the western Laptev Sea and often blocks Vilkitskiy Strait from the east. The Ayonsky ice massif is the largest spur massif in the Eurasian Arctic. It is located in the eastern East Siberian Sea. Depending on its location (western, central or eastern), the massif blocks the central sea areas or Long Strait from the west (Gudkovich *et al.*, 1972).

The other ice massifs—Yansky, Novosibirsky and Wrangelevsky—are mainly comprised of ice of local origin. The Yansky and Novosibirsky ice massifs while they

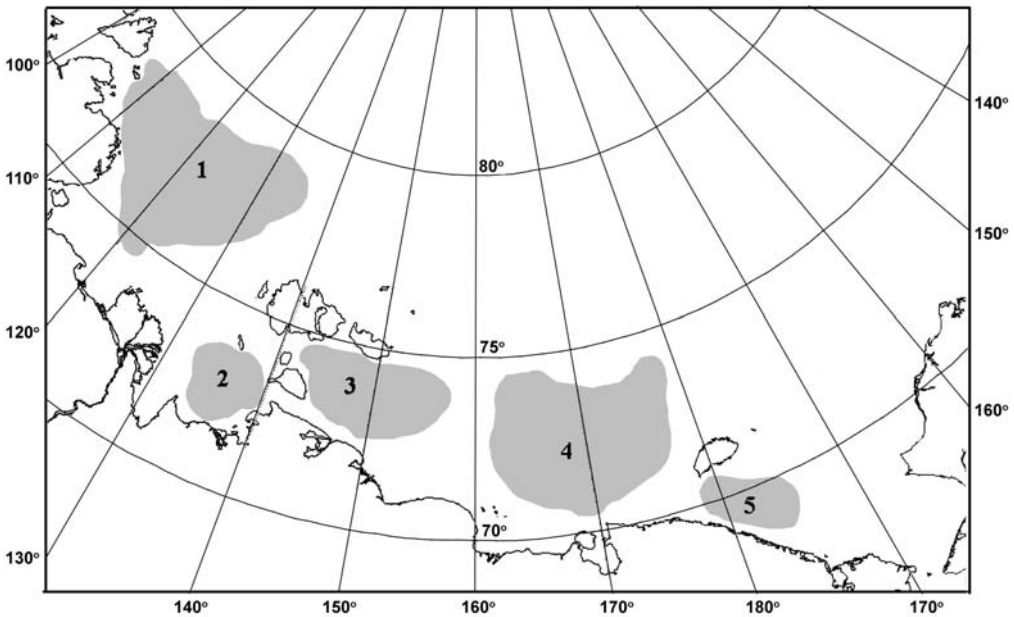

Figure 5.19. The location of ice massifs at the eastern part of the Northern Sea Route (1 = Taymyrsky, 2 = Yansky, 3 = Novosibirsky, 4 = Ayonsky, 5 = Wrangelevsky).

last block the New Siberian Straits (Sannikov and Dmitry Laptev). The Wrangelevsky ice massif blocks the eastern approaches to Long Strait and is often supplied by ice from the Ayonsky massif. Ice melting in most massifs begins in June, but at different intensities (Figure 5.20).

The Wrangelevsky ice massif area, whose ice begins to melt as early as May, decreases more rapidly than others. By late July, slightly more than 20% of its close ice remains in the southwestern Chukchi Sea. On average, from the middle of July a sharp decrease in area of the Yansky and Novosibirsky ice massifs begins (Figure 5.20). By mid-August their areas decrease by 70% and 60%, respectively. Under average conditions of melting and sea clearance of ice, the area of the Taymyrsky ice massif decreases by half by late July. The Ayonsky ice massif decreases more slowly than the others. Under average conditions, about 50% of its area remains in the sea before the beginning of new ice formation in late September.

In spite of the stability of the Ayonsky and Taymyrsky ice massifs, in rare cases they disappear at the end of the ice melting period (Table 5.8). There have been occasions when they completely disappear as early as mid-August: the Taymyrsky massif completely disappeared in 1995 and the Ayonsky in 1990. In 1990 the Taymyrsky massif got very close to disappearing (its area was only about 5%). Similar situations were observed in 1945 and 1968.

The least stable are the Novosibirsky and Yansky ice massifs. In 50% of cases, the Novosibirsky and in 80% the Yansky massifs disappeared in late September. Cases of complete disappearance of the Yansky ice massif in early August are frequent. In 1990

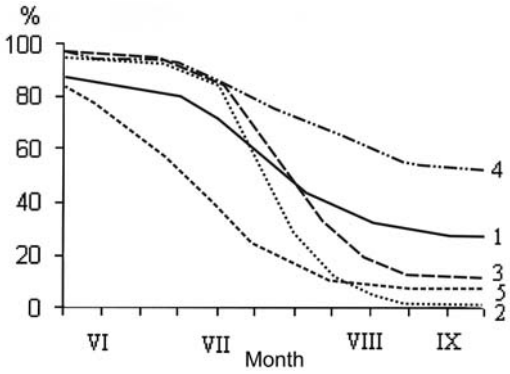

Figure 5.20. Average fraction of ice massifs at the eastern segment of the Northern Sea Route during the period of melting from data for 1973–2003: 1 = Taymyrsky; 2 = Yansky; 3 = Novosibirsky; 4 = Ayonsky; 5 = Wrangelevsky.

the Novosibirsky massif disappeared in late July (Table 5.8). Standard deviations of 10-day values of ice massif areas (characterizing their multi-year variability) have typical seasonal variations. The time of maximum variability in ice massif area depends on the characteristics of the regions of their location. Thus, the maximum variability of the Wrangelevsky and Ayonsky massif ice massifs is observed in June and September, respectively (Table 5.9). The maximum variability of the other ice massifs in eastern Eurasian Arctic seas falls in July and August (Table 5.9).

The amplitude of multi-year variations in ice massif areas (the difference between the maximum and minimum values in the observation series) is significant. The largest amplitude is observed in the multi-year variability of the Ayonsky massif area in August and September, when it can either disappear or occupy almost the entire eastern East Siberian Sea. The range of multi-year variation in area of the Yansky and Nobosibirsky massifs in July is also large (Table 5.9).

Table 5.8. Occurrence of complete disappearance of ice massifs over the period 1973–2003 (%).

Ice massif	July (10-day period)			August (10-day period)			September (10-day period)		
	1	2	3	1	2	3	1	2	3
Taymyrsky	—	—	—	—	3	3	10	13	3
Yansky	—	—	—	10	23	55	77	81	81
Novosibirsky	—	—	3	3	13	29	39	52	52
Ayonsky	—	—	—	—	3	3	3	—	—
Wrangelevsky	—	—	—	3	16	32	42	45	45

Table 5.9. Mean and extreme areas of ice massifs and their standard deviations (σ) in the third 10-day periods of months for 1973–2003 (% area of sea region).

Ice massif	Area	Month			
		June	July	August	September
Taymyrsky	Mean	84	59	33	26
	Max	100	88	67	73
	Min	51	20	0	0
	σ	**11**	**19**	**20**	**19**
Yansky	Mean	95	57	5	1
	Max	100	100	34	17
	Min	88	10	0	0
	σ	**3**	**22**	**9**	**3**
Novosibirsky	Mean	94	67	17	11
	Max	100	98	70	72
	Min	38	0	0	0
	σ	**13**	**25**	**22**	**20**
Ayonsky	Mean	94	79	60	52
	Max	100	97	94	84
	Min	72	43	0	0
	σ	**8**	**14**	**22**	**26**
Wrangelevsky	Mean	64	24	8	6
	Max	95	47	39	42
	Min	23	4	0	0
	σ	**21**	**12**	**10**	**11**

5.2.3 Ice drift variability based on remote-sensing observations

Ice drift observations have been carried out for many decades and have made it possible to obtain (often unique) data for studying ice motion variability in Eurasian Arctic seas. These observations from the shore allowed, in particular, studies into the influence of sea ice characteristics (dimensions of ice features, ice concentration, hummock and ridge concentration and thickness) on the ice drift and ice motion characteristics in the coastal zone (Gordienko, 1941). Radar ice drift observations from the shore were carried out in the early 1980s near Cape Schmidt. Some results of the studies based on the material obtained were published in Komarov and Shchukin (1985).

An important role in the studies of ice motion in open sea regions belonged to observations of drifting radio-buoys using directional transmitters (Gorbunov and Moroz, 1972). In the 23 years of using this system, more than 400 automated stations were deployed on drifting ice in the Arctic Ocean and more than 45,000 determinations of radio-buoy coordinates were obtained. About 45% of all cases refer to Eurasian Arctic seas, most of them in the East Siberian Sea. Data on radio-buoy

drift served as a basis for the *Atlas of Ice drift in Arctic Seas* (Gorbunov *et al*., 1979b) and were used in many studies of ice conditions (Gudkovich and Nikolayeva, 1961; Nikolayeva, 1970; Gorbunov, 1981).

Photographic and radar surveys of sea ice from aircraft had great importance in the study of ice drift regularities in Eurasian Arctic seas. Aerial photography with the purpose of making ice drift measurements was conducted in the East Siberian and the Chukchi Seas in 1965, 1968, 1969, 1971 and 1977. The first radar surveys for the same purpose were made in spring of 1969, and in the 1970s and 1980s they were carried out in all Eurasian Arctic seas. Data obtained as a result of the surveys were used in studies of the meso-scale structure of ice drift fields (Gorbunov and Losev, 1978a, b), spatial variability of ice motion velocity (Gorbunov and Losev, 1979), influence of obstacles on ice motions (Gorbunov and Losev, 1977, 1978a, 1998; Gorbunov *et al*., 1977), ice exchange through the straits (Gorbunov, 1979) and of other problems (Gorbunov, 1967; Gorbunov and Losev, 1974; Gorbunov *et al*., 1979a, b).

From 1979 automated buoys were used for ice drift observations in the Arctic Ocean, their coordinates being determined by satellites. Data obtained using this information source are rather few for Russian Arctic seas and were not widespread in ice drift studies (Gorbunov and Losev, 1994; Alexandrov *et al*., 1994).

The possibility of using satellite images for ice motion studies was demonstrated by Provorkin (1972). However, this method was not widely applied in the Russian Arctic, although it is obviously very promising in general. Some results of ice drift studies in Eurasian Arctic Seas based on data collected using remote-sensing methods are presented below.

Ice drift variability in the southeastern Laptev Sea from airborne side-looking radar

For studying variability in ice drift velocity, data obtained from airborne radar sea ice surveys in July–August 1976—in the framework of the *POLEX-Sever-76* full-scale experiment—were used. A total of 13 surveys were performed at the polygon in the southeastern Laptev Sea that allowed 12 drift vector series that lasted from 2 to 6 days to be obtained. The total number of drift vectors was about 700.

From the moment of fast ice breakup to mid-August, the onshore drift prevailed: from 9 to 31 July from west to east, and then up to 15 August from north to south. Ice drift velocity changed over a wide range: from values close to 0 to 32.6 km/day. The average ice motion velocity in the open sea over the entire observation period was 7.4 km/day, and in 86% of cases the drift velocity was no greater than 12 km/day. The modal velocity range is equal to 4–8 km/day (Figure 5.21).

Data on ice drift velocity in the open sea were also estimated separately for each period. The average and extreme values of this ice drift velocity significantly change from period to period (Figure 5.22). There is however a tendency for an increase in the average and maximum ice drift velocity from the moment of fast ice decay (first 10 days of July) until the ice almost completely disappears. This tendency is probably caused by the decrease in ice floe size, ice thickness and ice concentration. Spatial changes in ice drift velocity in the southeastern Laptev Sea are significant in that they are determined by an indented coastline, presence of islands, straits and numerous

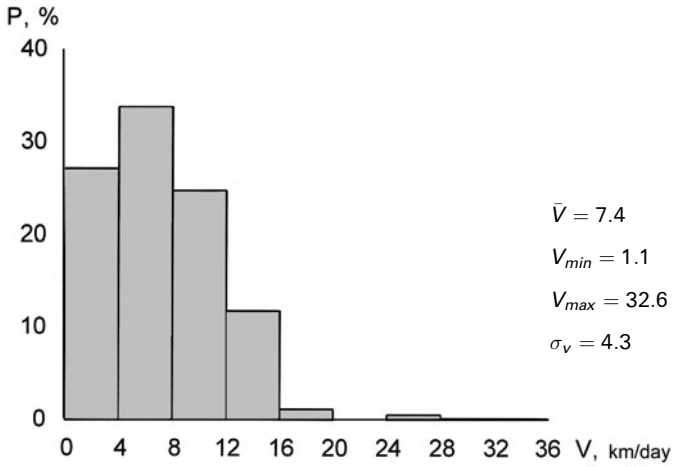

Figure 5.21. Distribution of ice drift velocity in July–August in open areas of the southeastern Laptev Sea.

banks with stamukhas on them. The ice drift velocity fields for some periods present a complicated pattern of alternating zones of increased and decreased values. Zones of slower drift are noted in coastal areas and in the shallow waters of the open sea. The average ice motion velocity in coastal areas is only 1.9 km/day. In 65% of cases, ice drift velocity was no greater than 2 km/day. Within the coastal zone it increased with increasing distance from the shore.

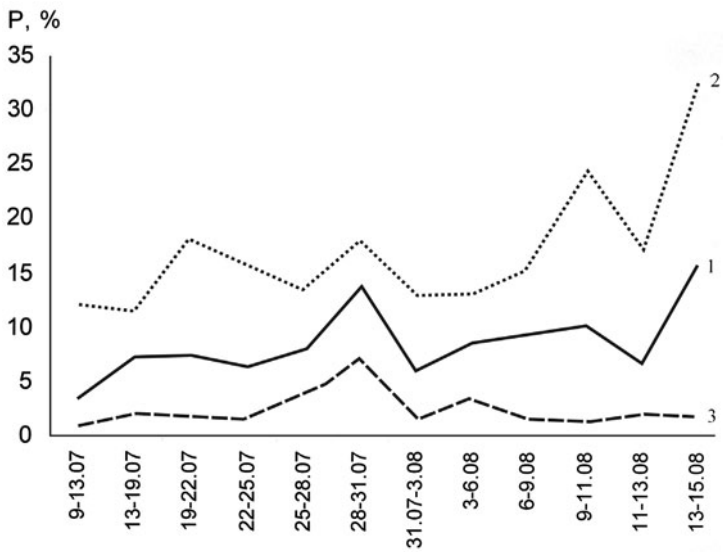

Figure 5.22. Temporal variability of average and extreme ice drift velocities in July–August 1986 in the southeastern Laptev Sea: 1 = average; 2 = maximum; 3 = minimum.

Zones of increased ice drift velocity are observed in Dmitry Laptev and Sannikov Straits and along the strait axis between Stolbovoy and Kotel'nyy Islands, it accelerated 1.6 times faster than the open sea. After 5 August, increased ice drift velocity is also observed in other parts of the region, due to formation of extensive zones of very open and open ice and decreased ice floe sizes.

In general, radar surveys made in the summer of 1986 allowed a number of the ice drift characteristics in the southeastern Laptev Sea to be revealed. However, no further ice motion studies were conducted here, so no estimates of climatic variability in ice drift in this area are available.

Ice drift variability in the East Siberian Sea from observations of drifting radio-buoys

For studying variability in ice drift velocity, data from 110 radio-buoys (spar-buoys and drifting automatic radio meteorological stations—DARMS) during stable drift direction periods in 1954–1972 were used, and a total of 630 drift vectors were collected. In all cases, ice concentration was between nine-tenths and ten-tenths, and sometimes ten-tenths consistently. The average duration of stable drift direction periods was 7 days. Buoy speeds changed over a very wide range from a value close to 0 up to 82 km/day (Figure 5.23). However, high speeds were rarely observed; the occurrence of ice drift speeds greater than 40 km/day and greater than 30 km/day were observed only 0.45% and 1.9%, respectively, of the time. The speeds were less than 20 km/day and less than 10 km/day in 90% and 53% of cases, respectively. The most common range of occurrence of the drift speed of close ice was 5–10 km/day.

Seasonal changes in ice drift velocity are noticeably manifested in variations of the most probable values, which increased from 6.7 km/day in January–March to 8.1 km/day in October–December (Table 5.10). The maximum ice speed (82 km/day) was recorded in July–September.

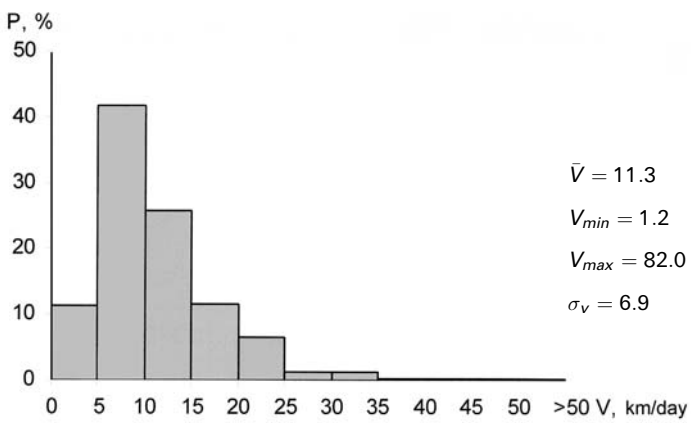

Figure 5.23. Distribution of ice drift velocity in the East Siberian Sea.

Table 5.10. Statistical characteristics of ice drift speed in the East Siberian Sea (km/day).

Period	No. of cases	$\bar{V}$	V_{min}	V_{max}	σ_v	Modal range	Mean in the modal range
January–March	35	12.0	2.2	35.6	8.4	5–10	6.7
April–June	270	11.4	1.7	48.2	6.7	5–10	7.6
July–September	204	10.5	1.4	82.0	7.1	5–10	7.7
October–December	121	12.5	1.2	33.0	6.2	5–10	8.1
January–December	630	11.3	1.2	82.0	6.9	5–10	7.7

Table 5.11. Statistical characteristics of ice drift speed in the East Siberian Sea.

Drift direction	No. of cases	$\bar{V}$	V_{min}	V_{max}	σ_v
North	71	10.4	1.4	29.6	5.5
Northeast	37	11.0	2.6	30.6	5.9
East	54	10.4	1.7	33.0	5.4
Southeast	91	11.5	2.9	82.0	9.3
South	43	10.4	1.2	27.8	5.2
Southwest	39	11.1	2.2	33.9	6.5
West	65	10.5	3.0	24.1	5.3
Northwest	230	12.3	2.3	48.2	7.3

Average ice drift speeds differ as a function of drift direction (Table 5.11). Average annual velocities of northwestern and southeastern ice motion are higher than those of southwestern and northeastern by 11%. The difference in maximum ice motion speed in different directions is especially large.

Spatial variability in ice drift velocity in the East Siberian Sea clearly indicates the significant influence of Long Strait. The ice drift speed within the strait increases in the southeast, west and northwest directions. In summer the difference between ice drift speed in Long Strait and in the central part of the sea can be large (twofold and more). In the wintertime, spatial differences in ice drift velocity are determined not only by the influence of Long Strait, but also by the impact of fast ice in the western part of the sea. In the adjoining water area, ice drift in the northwest, west, southwest and south directions is slower. There are very few observations of ice motion in the shallow western sea area. Satellite information could probably be used to identify the ice drift characteristics in this region after fast ice decay.

5.2.4 Fast ice distribution

In the wintertime the most extensive fast ice forms in the eastern part of the NSR. Its larger portion is located on both sides of the New Siberian Islands in comparatively

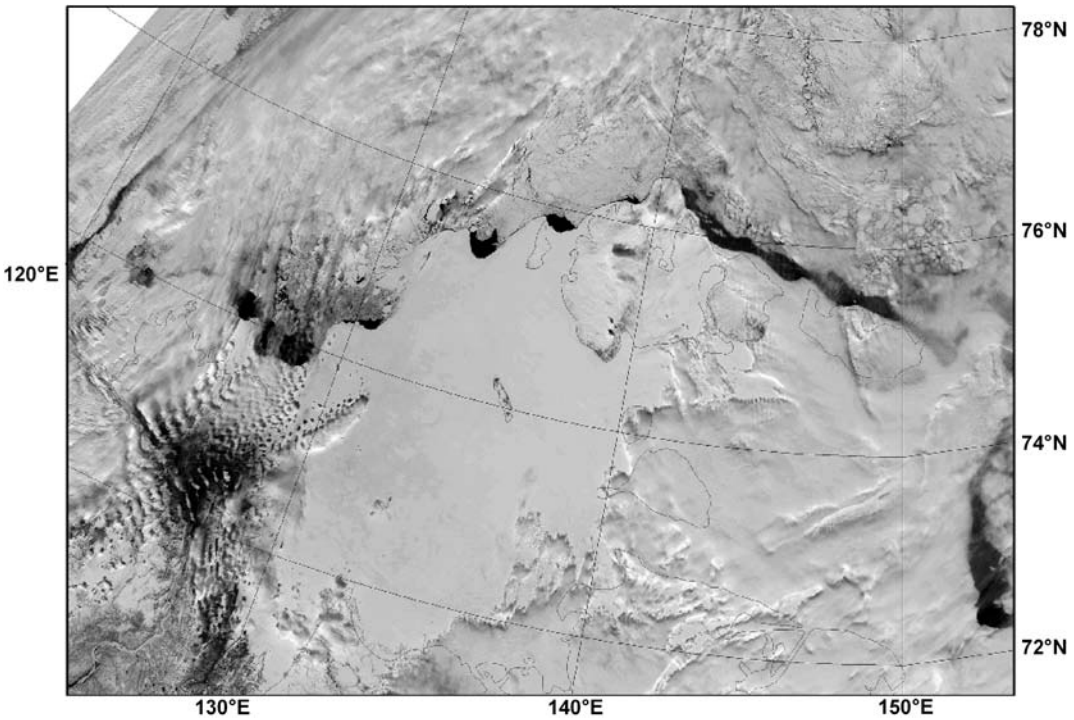

Figure 5.24. Satellite TV image of the eastern Laptev Sea and the western East Siberian Sea for 25 May 2003.

shallow water areas of the eastern Laptev and western East Siberian Seas (see Figure 5.24). The fast-ice boundary in the eastern part of the Laptev Sea, to the north of the New Siberian Islands, and in the western part of the East Siberian Sea is clearly seen in the image. Along almost its entire boundary, fast ice is separated from drifting ice by polynyas.

Fast ice of the Laptev Sea

The earliest fast ice formation in the Laptev Sea is observed during the third 10-day period of September along the coasts of Severnaya Zemlya archipelago and the Taymyr Peninsula. Early fast ice formation is more frequently connected with the presence of ice from the Taymyr massif that has not melted over the summer and becomes part of fast ice. During the first 10 days of October, fast ice forms along the Taymyr coast, in Khatanga, Anabar and Olenek Bays, in the Lena Delta and farther eastward to Cape Svyatoy Nos. At the same time, it forms in shallow inlets in the New Siberian Islands. It completely covers Dmitry Laptev and Sannikov Straits during the first and second 10-day periods of November, respectively.

Four main Laptev Sea regions with different fast ice spreading rates are discriminated: Severozemelsky, Taymyrsky, Anabaro-Oleneksky and Yansky. Along the

Severnaya Zemlya and Taymyr coasts, fast ice typically extends beyond a 10-m isobath, within 25–50 km of the coast. The southern and eastern sea regions are characterized by an extensive shallow zone with depths less than 25 m (Gordienko, 1971) and by well-developed fast ice. In the area of Oleneksky and Anabarsky Bays, its width can be more than 200 km. An extensive shallow water zone allied with spreading of water from the Lena and Yana Rivers facilitates formation of a wide fast ice zone in the eastern Laptev Sea (Karelin, 1945). The extent of the shallow zone from the Buor-Khai Gulf northward reaches 500 km, on average, and 550 km in some years. To the north of this region, near Kotelny Island, its width achieves 20 km on average and 50 km in some years.

Fast ice develops quickest from October to January and is most intensive in the eastern Laptev Sea (Figure 5.25). The fast ice extension here stops in March or early April, by which time its boundary has reached the 20-m isobath. Its development in the Anabaro-Oleneksky region in winter occurs more slowly (Figure 5.25), and its boundary moves northward in April–early May. There is an intense increase in fast ice

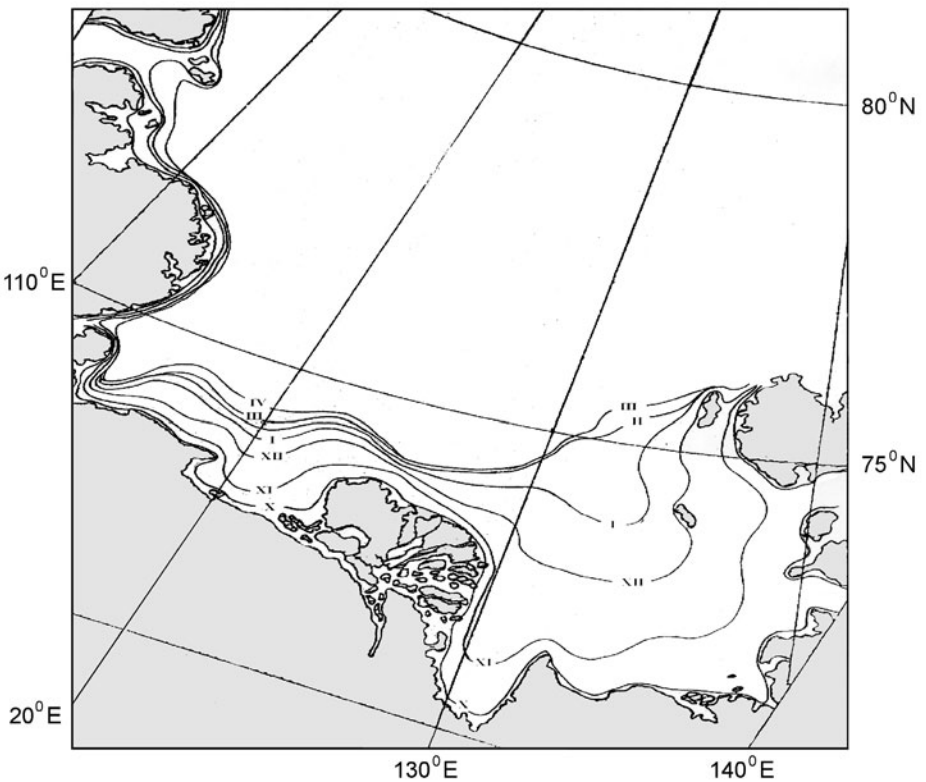

Figure 5.25. Average location of fast ice boundaries during the period of its growth—October (X) to April (IV)—from satellite data over 1980–2003 in the Laptev Sea.

Table 5.12. Mean and extreme fast ice areas during the period of growth in the Laptev Sea in the middle of the month, based on satellite data from 1980 to 2002 (thousand km^2).

Region	Area	Month							
		Oct.	Nov.	Dec.	Jan.	Feb.	March	April	May
Western	Mean	15.13	29.90	31.28	45.51	49.66	54.40	56.13	57.50
	Max	28.60	43.32	63.70	66.76	72.07	80.38	81.54	83.60
	Min	2.70	10.32	15.36	26.30	27.70	27.72	27.49	30.03
Eastern	Mean	19.89	51.36	108.48	131.76	141.6	146.23	148.32	148.32
	Max	33.69	122.64	148.56	154.08	154.32	161.04	160.08	162.72
	Min	7.53	10.79	30.48	98.16	109.44	132.00	132.72	133.92
Entire sea	Mean	35.02	81.26	39.76	177.27	191.26	200.63	204.45	205.82
	Max	62.29	65.96	12.26	220.84	226.39	241.42	241.62	246.32
	Min	10.23	21.11	45.84	124.46	137.14	159.72	160.21	163.95

area until January, by which time about 80% and 90% of its area forms in the western and eastern parts of the Laptev Sea, respectively (Table 5.12).

Fast ice in the eastern Laptev Sea does not depend significantly on interannual changes in hydrometeorological conditions. Its minimum area at the end of the growth period comprises 67% of its maximum area. The amplitude of interannual variations in fast ice area is equal to 28,800 km^2, which comprises about 19% of its average area. In the western part of the sea, the fast ice area is much more variable. The range in interannual variations is equal to 53,600 km^2, which comprises about 93% of its average area. The maximum fast ice area is 2.8 times greater than the minimum area.

The final period of fast ice decay in the Laptev Sea occurs, on average, during the second half of July, and 70–85% of all cases fall within this period. The dates of fast ice decay in the Laptev Sea vary within 1–1.5 months.

Fast ice of the East Siberian Sea

The most extensive fast ice forms in the East Siberian Sea, mainly in the western part, which is relatively shallow. The western region has depths less than 25 m which occupy about 56% of the entire region (Gordienko, 1971).

The average dates of fast ice formation in the western and eastern parts of the East Siberian Sea are observed during the second/third and third 10-day periods of October, respectively. Early fast ice formation in the western and eastern parts can occur during the third 10-day period of September and the first 10-day period of October, respectively. Its late formation was observed during the first and third 10-day periods of November in the western and eastern parts, respectively.

As a rule, fast ice in the East Siberian Sea forms in open water. However, in years when residual ice remains in the sea, fast ice forms almost 2 weeks earlier and with incorporates this ice (Karelin, 1949). In the area of the New Siberian Islands, the

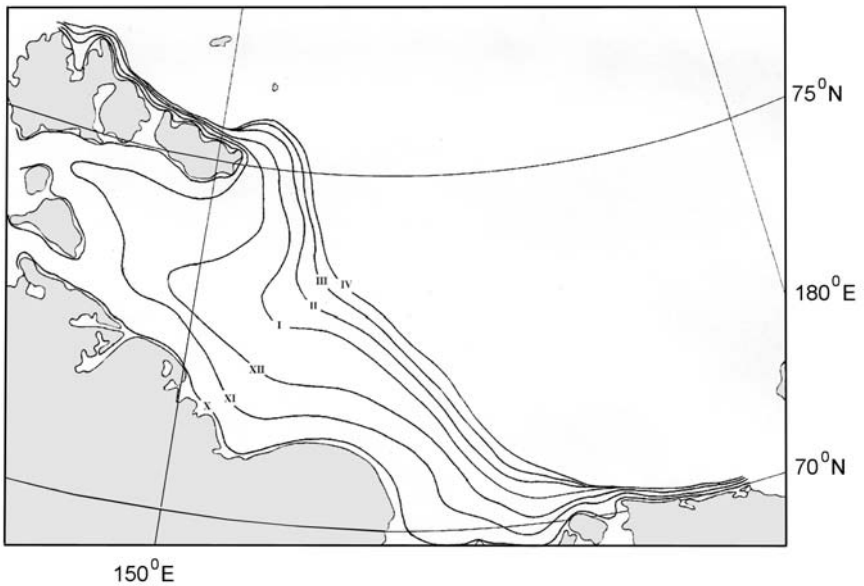

Figure 5.26. Average location of fast ice boundaries during the period of its growth based on satellite data from 1980 to 2003 in the East Siberian Sea.

formation of new fast ice sometimes occurs in the presence of old—unbroken from the previous year—fast ice (Karelin, 2001).

From the moment of stable fast ice formation, its boundary moves seaward and, depending on winter conditions, reaches its maximum extent from the coast in April (sometimes in May) (Figure 5.26). In some regions its external boundary is retained by stamukhas that form as a result of strong onshore winds.

The rate of fast ice growth is unsteady throughout the winter. In Dmitry Laptev and Sannikov Straits, its boundary moves very quickly eastward. Over a month—from November to December—the boundary at the Sannikov Strait latitude moves over 300 km, on average. Then, the intensity of the advance of the fast ice boundary decreases. In March its position stabilizes to the north of the New Siberian Islands and near the Chukchi coast and in April in central sea regions.

On average, the distance between the fast ice boundary and the mouth of the Indigirka in a northeastern direction reaches 290 km. To the north of the New Siberian Islands, the maximum distance of the fast ice boundary from the coast during the period of its greatest development (March–May) reaches 50–80 km. On average, it extends no more than 25–30 km from the Chukchi coast.

Under the average conditions of fast ice formation in the East Siberian Sea, its area grows very intensely from October to February. By February 92% and 65% of its area forms in its western and eastern parts, respectively (Table 5.13).

Interannual changes in fast ice area in the western sea region in different months of its growth period vary within 120,000–135,000 km^2, which comprises 33–37% of

Table 5.13. Mean and extreme areas of fast ice during the period of growth in the East Siberian Sea in the middle of the month, based on satellite data from 1980 to 2002 (thousand km^2).

Region	Area	Month							
		Oct.	Nov.	Dec.	Jan.	Feb.	March	April	May
Western	Mean	26.7	48.3	105.2	140.3	174.2	185.1	189.3	184.4
	Max.	56.4	120.3	178.2	209.4	230.4	231.7	231.7	228.9
	Min.	0	11.3	44.3	87.9	104.9	112.6	112.6	105.2
Eastern	Mean	8.4	28.7	30.9	54.2	58.4	69.8	87.4	90.1
	Max.	24.6	68.6	75.0	78.2	104.6	117.1	133.9	122.0
	Min.	0	2.0	14.8	31.2	32.2	29.7	35.2	32.2
Entire sea	Mean	34.1	77.0	136.1	194.5	232.6	254.9	276.7	274.3
	Max.	81.0	188.9	253.2	287.6	335.0	348.8	365.6	350.9
	Min.	0	13.3	59.1	119.1	137.1	142.3	147.8	137.4

the region's area. In the eastern part, interannual changes in fast ice area are less significant ranging within 17–24% of the region's area in February–April.

The final fast ice breakup at sea occurs throughout July, on average (Figure 5.27). By the end of the month, it is preserved at the eastern approaches to Sannikov and Dmitry Laptev Straits. The range of its breakup dates in sea regions varies from four to seven 10-day periods.

Fast ice of the Chukchi Sea

Fast ice in the Chukchi Sea forms along the Chukchi and Alaskan coasts. Due to deepwater in the coastal zone, it is not greatly developed in the southwestern Chukchi Sea. On average, it forms in late October–early November. In accordance with the dates of stable ice formation, its latest formation is observed near the easternmost Chukotka coast. The most intense growth of fast ice is in December–January. Near the Chukchi coast it achieves its maximum extent by mid-March and does not change again until the onset of melting (Figure 5.28).

In March the average fast ice width reaches about 12 km near Cape Schmidt and can vary within 5–20 km. Then, more eastward it increases to 30 km in the area of Koluchinskaya Gulf, where it can comprise 70 km in some years. Farther eastward, it decreases to 10 km.

The fast ice area near the Chukchi coast after reaching about 6,000 km^2 in early November slowly increases to about 11,000 km^2 in March, holding this size until the onset of melting. In years favorable for fast ice development, its area is more than twice its average value (Table 5.14). The average area of Chukchi fast ice at the end of its development comprises 6% of the southwestern sea area. It can occupy 13% and only 3% of the sea area in years of its maximum and minimum development, respectively.

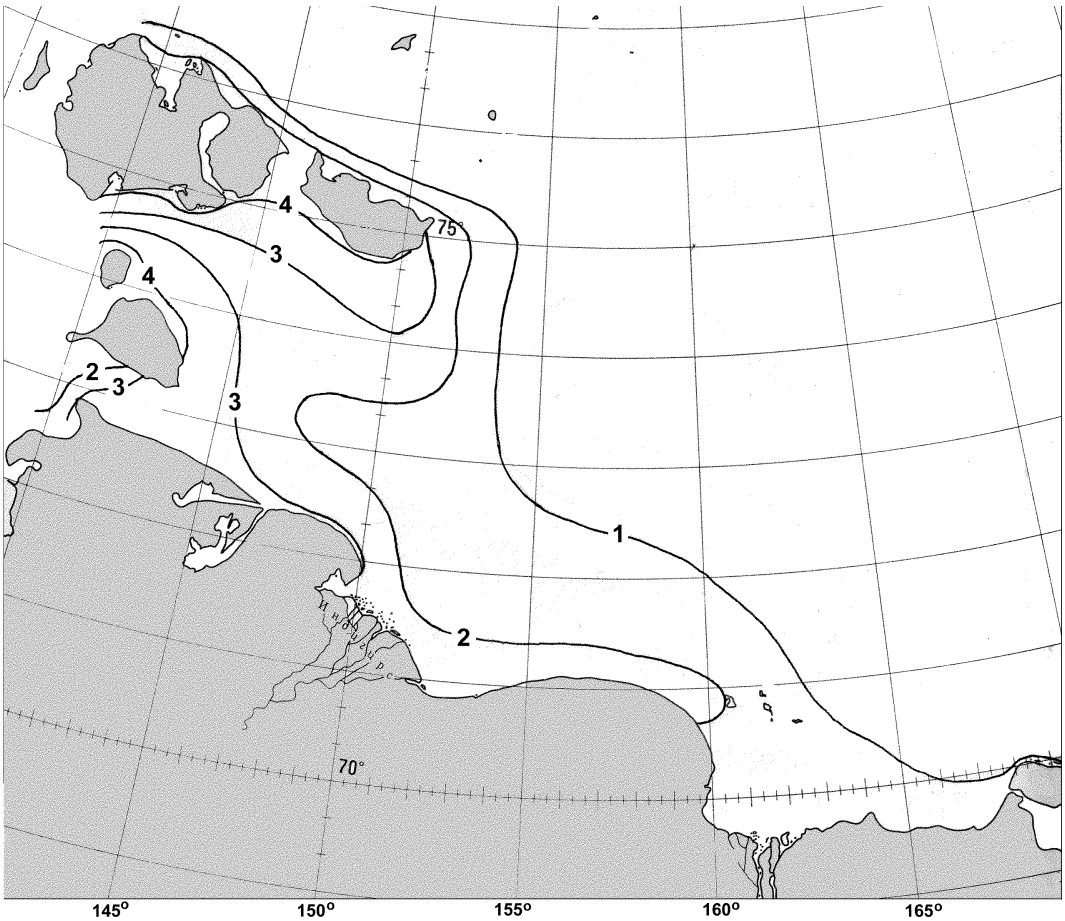

Figure 5.27. Location of fast ice boundaries in the East Siberian Sea during decay: 1 = first 10-day period of July; 2 = second 10-day period of July; 3 = third 10-day period of July; 4 = first 10-day period of August.

Fast ice around Wrangel Island is more developed than that along the Chukchi coast. Its maximum development is achieved in the second 10-day period of April. Its average width comprises 23 km near the northwest coast (ranging from 10 km to 110 km), 33 km near the northern coast (20–55 km) and 13 km along the southern coast of the island (7–22 km). Mean multi-year area of fast ice around Wrangel Island during its maximum development is equal to 9,000 km^2, which comprises 5% of the area of the southwestern Chukchi Sea and can achieve 14% in extreme years.

Near the Alaskan coast, between Cape Hope and Cape Barrow, fast ice formation begins in mid-October, on average. In the third 10-day period of October, it spreads to regions adjoining Kotsebu Bay and Bering Strait. By the time of its maximum development, the fast ice width along the section from Bering Strait to Cape Lisbern can reach 5–65 km, and farther northward to Cape Barrow 10–40 km.

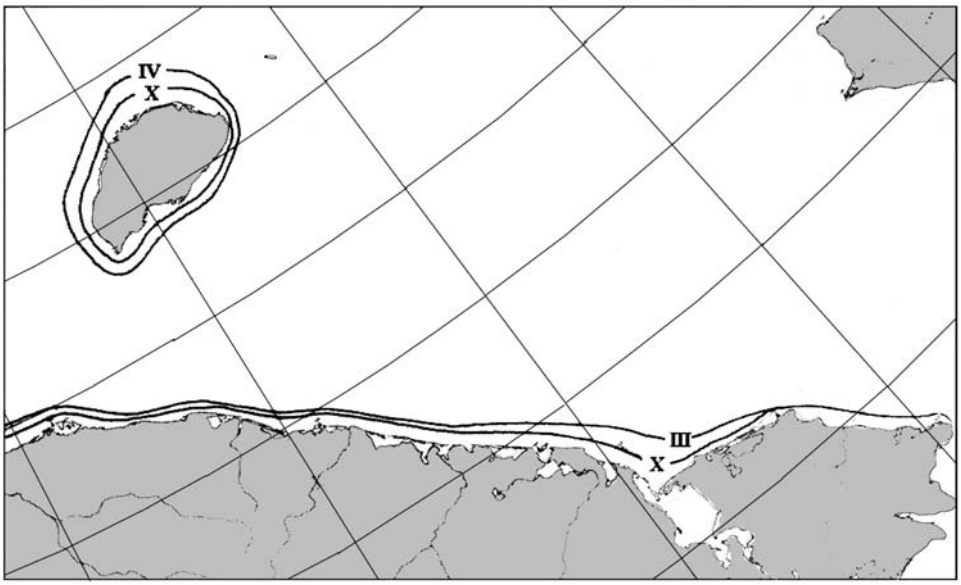

Figure 5.28. Average location of fast ice boundaries during its growth in the Chukchi Sea from satellite data from 1980 to 2003.

The onset of fast ice decay in the Chukchi Sea is observed in the southern sea area during the second 10-day period of May, when—under the influence of Bering Sea water—the early sea clearance of ice starts. It completely disappears from the sea during the third 10-day period of June, on average. The exception is the Kolyuchinskaya Gulf where it can persist in some years until mid-July.

5.2.5 Flaw polynyas

There are 12 polynyas—differing in stability (frequency of occurrence)—that form in eastern Eurasian Arctic seas during the winter: five of them are identified in the Laptev Sea: Eastern Severozemelskaya, Northeastern Taymyrskaya, Eastern Taymyrskaya, Anabaro-Lenskaya and Western Novosibirskaya; five more are observed in the East

Table 5.14. Mean and extreme areas of fast ice during the period of growth in the southwestern Chukchi Sea in the middle of the month from satellite data from 1980 to 2003 (thousand km^2).

Area	Month							
	Oct.	Nov.	Dec.	Jan.	Feb.	March	April	May
Mean	5.7	7.3	7.6	9.8	10.6	10.9	10.9	10.9
Max	8.8	14.3	15.5	17.2	18.7	23.4	23.4	23.4
Min	2.3	2.5	2.0	4.7	5.1	5.1	5.1	5.1

Table 5.15. Mean frequency of occurrence—*P* (%)—and characteristics of the polynyas of eastern Arctic seas from satellite data over the period November–June 1979–2003.

Polynya	*P*	Characteristic					
		Length (km)		Width (km)		Area (thousand km^2)	
	(%)	Mean	Range	Mean	Range	Mean	Range
E. Severozemelskaya	64	323	50–540	26	5–75	9.1	0.4–53.3
NE Taymyrskaya	70	180	50–350	36	5–165	6.4	0.3–36.3
E. Taymyrskaya	57	209	30–430	26	5–165	5.5	0.4–35.8
Anabaro-Lenskaya	84	371	60–750	40	5–200	14.7	0.4–71.1
W. Novosibirskaya	82	381	70–1170	42	6–235	16.6	0.8–82.2
N. Novosibirskaya	77	321	50–480	32	5–125	10.6	0.4–44.4
E. Novosibirskaya (west)	44	244	30–650	25	5–187	6.7	0.5–69.2
E. Novosibirskaya (east)	37	297	80–530	24	5–163	7.7	0.5–58.8
Ayonskaya	38	225	50–440	24	5–108	5.4	0.4–26.9
W. Chukotskaya	25	182	40–440	21	5–73	4.1	0.3–16.6
E. Chukotskaya	29	350	9–780	22	1–126	9.3	0.4–98.3
Chukchi lead	76	485	50–1040	24	4–52	13.9	1.0–45.6

Note: The characteristics of the Chukchi lead (an Alaskan polynya) are based on data from 1994 to 2003.

Siberian Sea: Northern Novosibirskaya, Eastern Novosibirskaya (west), Eastern Novosibirskaya (east), Ayonskaya and Western Chukotskaya (Figure 2.14); and a further two polynyas are located in the Chukchi Sea: the Eastern Chukotskaya and that forming along the Alaskan coast (called the "Chukchi lead"). The range over which their size and area varies is significant. The sizes of well-developed polynyas are tens of times greater than those formed during periods unfavorable for their development (Table 5.15).

According to their average frequency of occurrence in November–December, stationary polynyas include the Anabaro-Lenskaya and the Western and Northern Novosibirskaya polynyas (Table 5.15). The Northern Novosibirskaya polynya was first detected at the beginning of the 19th century by the Russian Hydrographic Expedition. The expedition participants were thunderstruck when they saw open water during winter at such high latitudes. Their observations resulted in the concept of an open northern ocean to the north of the New Siberian Islands—an idea that was refuted in the early 1880s by survivors of the *Zhannetta* drift under the command of De Long. It became clear that open water on top of fast ice forms under the influence of offshore wind and presents here a "Siberian polynya" (Vize, 1939; Zakharov, 1996).

It was determined by later studies that stationary polynyas also form to the west of the New Siberian Islands over fast ice in the area of the Lena and Anabar estuaries. Analysis of satellite data shows that in 80% of cases all three polynyas exist simultaneously and in favorable years can form a through-passage seaward of fast ice extending approximately 2,000 km. Thus, three polynyas comprise the "Siberian polynya".

Table 5.16. Mean monthly frequency of occurrence of polynyas in eastern Eurasian Arctic seas from satellite data from 1979 to 2003 (%).

Polynya	Month							
	Nov.	Dec.	Jan.	Feb.	March	April	May	June
Eastern Severozemelskaya	68	66	62	75	63	52	45	77
Eastern Taymyrskaya	75	75	69	83	66	48	61	80
Northeastern Taymyrskaya	73	63	58	72	62	40	37	50
Anabaro-Lenskaya	84	83	77	88	84	78	80	94
Western Novosibirskaya	79	78	68	78	76	79	95	96
Northern Novosibirskaya	67	87	67	64	77	76	90	91
Eastern Novosibirskaya (west)	32	57	44	43	49	46	29	50
Eastern Novosibirskaya (east)	28	42	32	42	46	44	34	38
Ayonskaya	22	41	42	38	45	39	29	44
Western Chukotskaya	18	10	20	20	19	28	30	51
Eastern Chukotskaya	24	23	19	28	26	18	38	61
Chukchi lead	—	76	50	79	72	86	85	—

The Anabaro-Lenskaya polynya is the most stable of them. During winter, its frequency of occurrence exceeds 80% decreasing to 77–78% only in January and April. The frequency of occurrence of the Western Novosibirskaya polynya in January and of the Northern Novosibirskaya polynya in November, January and February drops to 64–68% (Table 5.16).

Polynyas form less frequently over fast ice of the Severnaya Zemlya archipelago and the Taymyr coast than in the southern and eastern Laptev Sea. Their average frequency of occurrence is more than 50%, but less than 75% (Table 5.15). The Eastern Severozemelskaya polynya is stationary in February and June, while the Eastern Taymyrskaya polynya is stationary in November, December and February. Their frequency of occurrence exceeds 75% (Table 5.16).

The flaw polynyas of the East Siberian Sea to the north of the New Siberian Islands form episodically. Their average frequency of occurrence decreases from 44% to 29% the farther one goes along the Chukchi coast. However, in some months, polynyas are stable and their frequency of occurrence is slightly more than 50% (Table 5.16).

The climatic frequency of Eastern Chukotskaya polynya (Chukchi flaw lead) occurrence in June is about 60%. In years of active shipping along the NSR, the flaw lead was used for early routing of ship convoys to Pevek and Kolyma. In the eastern Chukchi Sea near the Alaskan coast, a stationary polynya forms (Table 5.16) that is called the "Chukchi lead" (Smirnov, 1974; Buzuev *et al.*, 1988). The stability of this polynya slightly decreases in January (to 50%), when the frequency of occurrence of easterly winds decreases. In April–May, its frequency of occurrence is greater than 80% (Table 5.16), and it often serves as an initial ice clearance source in the Chukchi Sea.

Table 5.17. Annual variability in frequency of occurrence of the polynyas of Eastern Arctic seas from satellite data from 1979 to 2003 (%).

Polynya	Mean frequency of occurrence	Gradations of frequency of occurrence		
		$P < 50$ (episodic)	$75 > P > 50$ (stable)	$P > 75$ (stationary)
Eastern Severozemelskaya	64	28	44	28
Eastern Taymyrskaya	70	8	52	40
Northeastern Taymyrskaya	57	20	68	12
Anabaro-Lenskaya	84	—	32	68
Western Novosibirskaya	82	4	24	72
Northern Novosibirskaya	77	—	44	56
Eastern Novosibirskaya (west)	44	56	36	8
Eastern Novosibirskaya (east)	37	68	28	4
Ayonskaya	38	76	24	—
Western Chukotskaya	25	96	4	—
Eastern Chukotskaya	29	84	16	—

Note that the average stability of polynyas for a given season can change significantly from year to year and, on average, even stationary polynyas can form less frequently in some years—and, *vice versa*, episodically forming polynyas can be stable. Thus, the polynyas comprising the stationary "Siberian polynya" are stationary for 56–72% in winter seasons. In other seasons, their frequency of occurrence is less than 75%. The most stable Western Novosibirskaya polynya is observed only episodically in 4% of cases (Table 5.17). At the same time, polynyas in the East Siberian Sea, episodic by average frequency of occurrence, are found to be stable in 16% to 36% of these seasons. The exception is the Western Chukotskaya polynya, which has been found to be stable only once (Table 5.17).

5.3 SAR STUDIES OF SEA ICE CONDITIONS (*K. Kloster, M. Lundhaug, V. Alexandrov, S. Sandven*)

Coverage of the Northern Sea Route by *ERS-1/2* SAR images is variable in space and time; it was most frequent between the autumn of 1993 and the spring of 1998 in connection with the "Icewatch program" (Johannessen *et al.*, 2000). With the launch of *Radarsat* in 1996 and 4 years later of *Envisat*, wide-swath SAR images with a resolution of about 100 m became available over much larger areas and with shorter observation intervals than was possible with *ERS* SAR. SAR images from these four satellites—as well as SLR images from *Okean* satellites—have been used for studies of a number of sea ice parameters, such as fast ice, polynyas and ice drift. Some examples of studies of these three ice parameters are described below.

5.3.1 Fast ice

SAR image analysis for fast ice

Fast ice in SAR images often has a quite uniform tone within relatively large dark areas. This is in contrast to pack ice with its mixture of ice types and floe sizes, which generally has more variable backscatter with larger spatial variance. However, the backscatter of fast ice depends on its surface roughness, salinity and other factors, and it is often different for ice formed at different times and under various weather conditions. At the ScanSAR mid-range incidence angle of 35°, smooth and young fast ice has a low backscatter value (<-20 dB), while old and rough fast ice (e.g., fast ice formed from the freezing of smaller ice pieces and ridged fast ice) can have high values (>-10 dB). Due to this large backscatter variability—and because of overlapping values for water, fast ice and drifting ice—the detection of fast ice is based mainly on feature identification. Reliable indicators of fast ice are: (1) the existence of a flaw line or a flaw polynya at its outer boundary; and (2) the absence of ice motion. Small backscatter variations within typical fast ice areas may also be an indicator. Information on bathymetry is important in the analysis, as fast ice generally forms in shallow areas.

Flaw lines and polynyas can usually be seen in a SAR image. Abrupt backscatter changes often correspond to the position of the fast ice boundary, but not in all cases, as the backscatter of fast ice, drifting ice and open water may be similar in some cases. Mapping the fast ice boundary is done using a combination of several indicators:

(1) As all fast ice must be connected to a shore and/or to grounded ice in shallow waters, all ice close to land and ice enclosed in bays and between islands is considered fast ice out to where a flaw signature is detected. Here, the fast ice edge borders on the pack ice or open sea, or on an area forming a flaw polynya.
(2) The signature of a large flaw polynyas is generally quite smooth (with low spatial variance), either dark if it is filled with new ice and/or calm water or with a typical wind-streak texture if filled with open water and/or scattered ice.
(3) Image comparison is made with the most similar images taken at an earlier and/or later date. Areas with detected ice motion are considered to be pack ice, while fast ice features remain stationary.

Comparing two sequential SAR images taken with a suitable time interval allows detection of fast ice as areas with immovable ice features. Analysis of successive images of the same area from the onset of freeze-up to stable winter conditions allows its temporal formation to be studied. During this period the fast ice boundary generally moves seaward. Later in the winter it remains stationary.

Mapping fast ice in the Kara Sea by Radarsat

Mapping the fast ice boundary in the western part of the Eurasian Russian Arctic was done in the "Amethyst Project" (Sharov, 2002) by *Radarsat* ScanSAR images taken in March 1997 and March 1998 using about 34 scenes each year. In March, fast ice

usually reaches its maximum width (Volkov *et al.*, 2002). Out of the list of several hundred scenes available in the Alaska SAR Facility archive within this large area, one to three scenes were selected along each swath to cover the area of interest. The main objective was to cover all of the western Russian Arctic coastal areas in March of these 2 years at least once and, if possible, to compare imaged areas with a time interval of days or weeks. The satellite has a 24-day/343-orbit repeat period, with near-repeats after 3 days (3.2° to the east) and 7 days (1.0° to the west). For March of the two selected years, all major coastal areas were covered and many were covered repeatedly with intervals ranging from 1 day to several weeks.

The maps presented in Figure 5.29 show the *Radarsat*-derived fast ice boundary for March 1997 and 1998. The following overall results can be listed for the five regions marked 1–5 in Figure 5.29a:

(1) Along Novaya Zemlya, fast ice forms in the fjords down the western and eastern coasts. In March 1997 large areas of open water persisted west and north of Novaya Zemlya, but fast ice cannot be distinguished from calm open water in the *Radarsat* images, although it could have been present in some of the bays. The stable fast ice boundary was located at a maximum 15 km from the coast. Figures 5.33 and 5.34 show typical large flaw polynyas. Along the eastern coast of Novaya Zemlya a very narrow stripe of fast ice can just about be detected in the March of both years.
(2) Along the Amderma and Yamal coasts, fast ice usually sticks close to the shore. A narrow strip, surrounding Vaygach Island, can be detected for both March 1997 and 1998. In Yugorsky Shar Strait a light SAR signature in March 1997 and a darker one in 1998 corresponds to deformed and more level fast ice, respectively. A narrow strip of fast ice existed along the Amderma coast in both years, widening to about 40 km in the inner bay. The fast ice boundary then continued north, about 20 km from the Yamal coast, with no significant difference in the 2 years. Here, areas of alternating level and rough ice can be detected. Level ice with a dark tone covers the areas close to the shore. Near the northern part of Yamal the ice is strongly deformed and has a brighter SAR signature. The polynyas that occasionally open in this region along Yamal (see Section 5.3.2) can be up to 40 km wide, but in 1998 they were generally quite narrow, about 10 km.
(3) In the Ob'–Yenisey region, fast ice is located over the wide shallow zone between the river estuaries seaward of Vilkitskiy and several other islands. Its boundary, derived from *Radarsat* imagery, was approximately at the same location in both years, with some variations: in March 1998 its width around Belyy Island was larger and reached 15 km, and in the Ob' Bay it was located more to the north than in March 1997. The fast ice here is mainly rough (bright), although large areas of level ice (dark) are found in both years, but in different places. North of the fast ice, wide polynyas are seen in both years.
(4) In the eastern Kara Sea, a very large fast ice area can be sen from the image between Dikson in the west and Severnaya Zemlya in the east. A typical SAR image of this region is shown in Figure 5.30. Here, the fast ice boundary can be

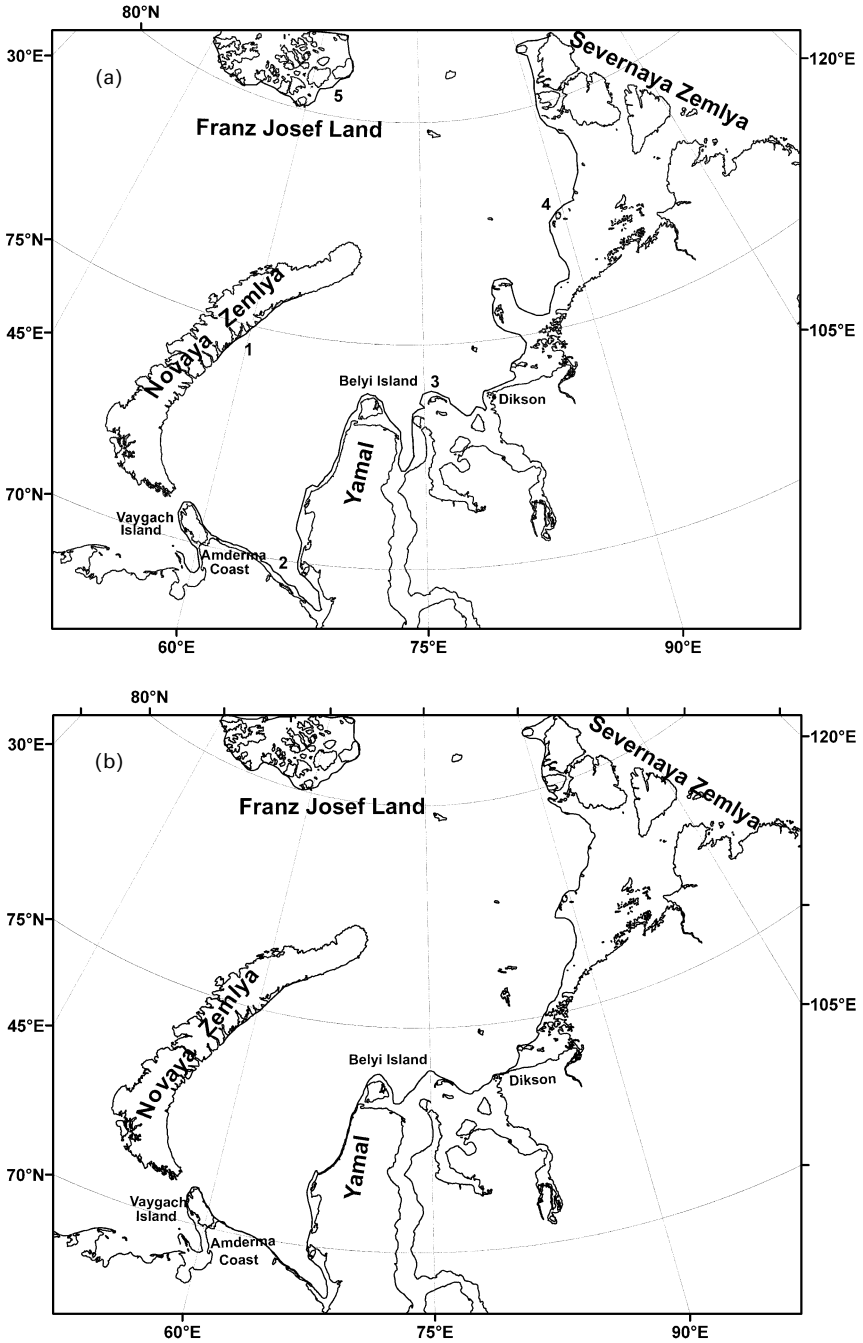

Figure 5.29. The extent of fast ice in the western part of the Eurasian Arctic derived from *Radarsat* ScanSAR images for March 1997 (a) and March 1998 (b) (© Canadian Space Agency).

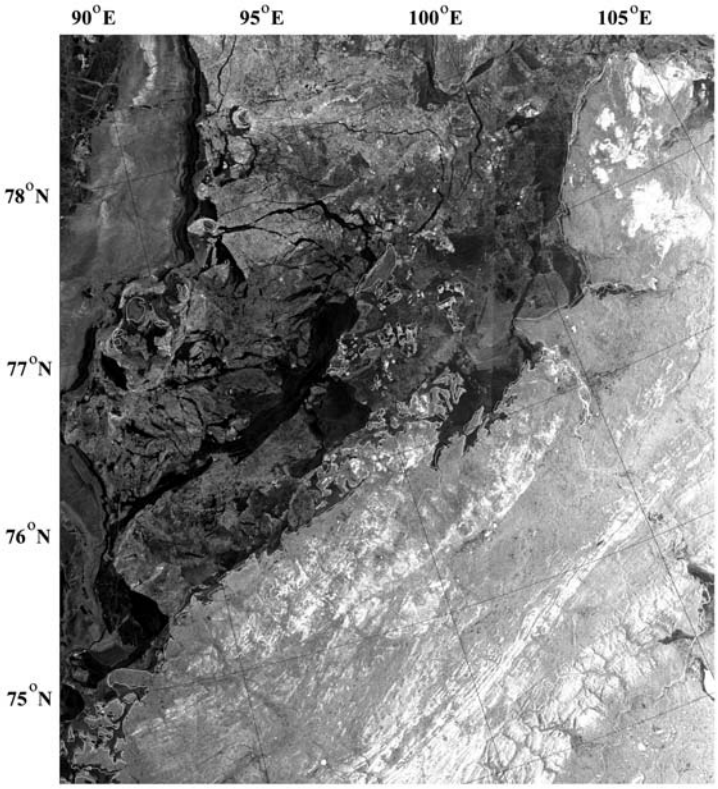

Figure 5.30. *Radarsat* ScanSAR image for 24 March 1997, showing fast ice in the eastern part of the Kara Sea more than 200 km out from the Yamal coast (© Canadian Space Agency).

seen in the upper left part (just north of the chain of islands from Sverdrup Island and northeastward past Kirov and Voronina Island toward Severnaya Zemlya). This was the general situation in both years. *Radarsat* data show that the fast ice signature here is very variable, corresponding to the variable degree of sea ice deformation. The area is very complex, especially in 1997. As multi-year ice has a brighter SAR signature than first-year ice, it is possible that some of the bright areas in Figure 5.30 is multi-year fast ice (formed from ice surviving from last summer). In 1998, large areas of level fast ice are seen near the mainland, around the Nordenskjöld archipelago and in Shokalskiy Strait. In some parts the fast ice boundary can be clearly detected in *Radarsat* images, whereas in other parts sequential images have to be analyzed for this purpose. Flaw polynyas up to 30 km wide are sometimes found seaward of the fast ice boundary.

(5) A narrow band of fast ice surrounds the Franz Josef Land archipelago. Its boundary follows the shoreline of the outer islands closely, less than 10 km offshore. Polynyas of width up to 40 km are sometimes seen, the widest are

found in the western part. A more detailed study of the fast ice at Franz Josef Land—using a large number of *Radarsat* ScanSAR images—is described in the following sections.

Mapping fast ice at Franz Josef Land

The extent of fast ice at Franz Josef Land was studied and mapped using 111 *Radarsat* ScanSAR wide-B mode images taken in 1996–2002 (Sharov, 2002). Each of the images has a center latitude of 80°55′N and covers nearly the whole Franz Josef Land archipelago. The mean repetition interval is 13 days for the period of December 1996–November 1997 (29 scenes), 14 days for the period of December 1997–February 1999 (33 scenes) and 24 days for March 1999–April 2002 (49 scenes). Figure 5.31 shows an example of the *Radarsat* ScanSAR imagery used for fast ice analysis.

Figure 5.31. Example of *Radarsat* ScanSAR image for Franz Josef Land on 14 March 2001 (© Canadian Space Agency).

As a result, maps showing the fast ice boundary and also major flaw polynyas for the early, middle and the late ice season have been drawn for 1996 to 2002. The extent of fast ice for March (middle of the ice season) for these winters is shown in Figure 5.32. Here, the fast ice and polynya boundaries are marked. The degree of uncertainty of the lines is variable, as analysis strongly depends on the presence of fast ice indicators.

5.3.2 Coastal polynyas

Identification of the shore and flaw (fast ice edge) polynyas is important for navigation in the Northern Sea Route: sailing time is shortened if these areas of thin ice/open water can be followed (Johannessen *et al.*, 2000; Mulherin *et al.*, 1994). Several studies show that successive satellite radar images can be used for detecting polynyas and for studying their development during a time interval of days or weeks. For example, *ERS-1* SAR data have been used for studies of the North-East Water polynya northeast of Greenland (Gudmansen *et al.*, 1995), in Tatarskiy Strait in the Japan Sea (Martin *et al.*, 1995) and in the area of Commonwealth Bay in Eastern Antarctica (Wendler *et al.*, 1997). Further, Dokken *et al.* (2002) have investigated areas in the Arctic with a focus on Franz Josef Land, and the Storfjorden polynya in Svalbard has been studied by Haarpaintner *et al.* (2001) using a time series of SAR images.

Analysis of a shore polynya at Cape Zhelaniya

Polynyas in SAR images show a marked difference in backscatter with respect to their surroundings and can easily be identified by means of visual inspection. This difference may be both in absolute values of σ^0 and in texture (spatial variation). Open water in polynyas has a large wind-dependent variation in σ^0, whereas nilas and young ice often have a low σ^0, but this may change rapidly to a high value if frost flowers form. Figure 5.33 shows four sequential radar images of the northern part of Novaya Zemlya, the first obtained on 24 April 1998 at 03:06 GMT by *Okean* RAR. The three others were obtained on 25 April: *Radarsat* ScanSAR at 02:48, *ERS-2* SAR at 09:30 and *Radarsat* ScanSAR at 12:46 GMT. These images show changes in a shore polynya off Cape Zhelanya during this period of 35 hours (Johannessen *et al.*, 1999b). The *Okean* image has low resolution, but shows in the polynya (Figure 5.33a) as a diffuse feature consisting of a mixture of darker and brighter signatures than the surrounding first-year ice. The polynya has a homogeneous grayish feature in (Figure 5.33b) the first *Radarsat* ScanSAR image, a very bright tone in the *ERS-2* SAR image (Figure 5.33c), acquired about 6 hours later and after a further 3 hours it showed very low backscatter in the last *Radarsat* ScanSAR image in Figure 5.33d.

Meteorological data indicate that during 23 April and in the morning of 24 April the wind was quite weak and variable in direction. From the afternoon of 24 April until the following afternoon, south–southwesterly winds prevailed with speeds of 5–6 m s^{-1}. This wind had generated the flaw polynya, but since the windspeed was stable it cannot explain the large temporal variability in SAR signature. However, both polarization and incidence angle determine radar backscatter. As the polynya was observed at not too different incidence angles in the first *Radarsat* ScanSAR (28°) and

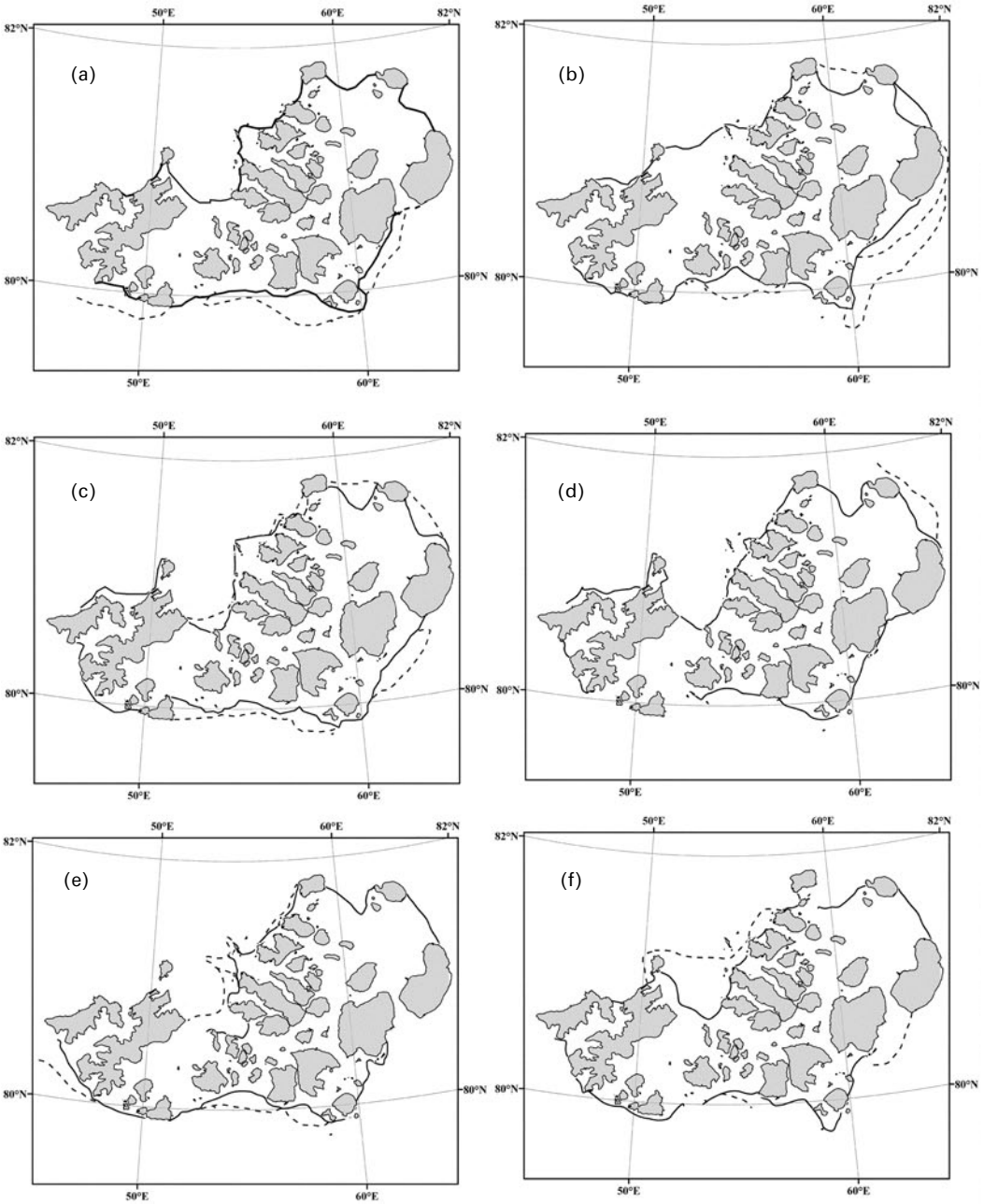

Figure 5.32. Franz Josef Land fast ice extent in March as derived from *Radarsat* images. Solid line: stable fast ice. Dashed line: flaw polynyas. (a) 18 March 1997, (b) 13 March 1998, (c) 25 March 1999, (d) 19 March 2000, (e) 14 March 2001; (f) 9 March 2002.

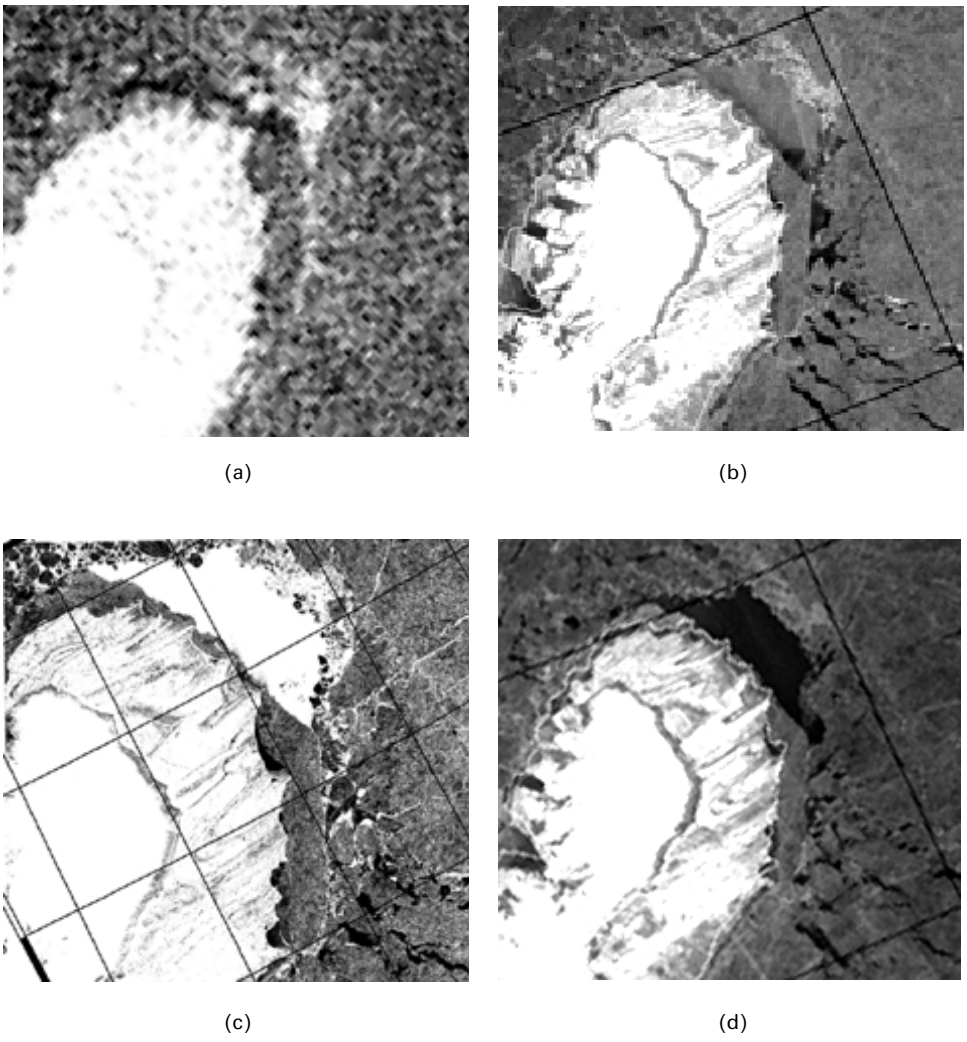

Figure 5.33. A series of four radar images, covering the polynya at Cape Zhelaniya of Novaya Zemlya in 1998: (a) *Okean* RAR (VV) at 03:06 GMT on 24 April; (b) *Radarsat* (HH at 28° incidence angle) at 02:48 GMT on 25 April; (c) *ERS-2* (VV at 23° incidence angle) at 09:30 GMT; (d) *Radarsat* (HH at 43° incidence angle) at 12:46 GMT. Each image covers about 100 × 100 km. © Canadian Space Agency (b), (d); © European Space Agency (c).

the *ERS-2* SAR (23°) images, the large difference in signatures is explained by the fact that the σ^0 of wind-roughened sea at VV-polarization significantly exceeds that at HH-polarization. The larger signal at VV-polarization for a given wind has been documented in several studies (Onstott, 1992; Drinkwater *et al.*, 1992). The large difference between the two *Radarsat* images in Figure 5.33(b) and (d) is explained by

the large difference in incidence angle, since open water backscatter decreases rapidly with increasing incidence angle for both VV- and HH-polarizations.

Large difference in σ^0 between VV-polarization (*ERS-2*) and HH-polarization (ScanSAR) has been found for gray ice with frost flowers (Johannessen *et al.*, 1999b). However, Ulander *et al.* (1997) have shown that frost flower build-up on top of young ice—when air temperature is in the range from -5° to -8°C—will take several days. Full coverage of frost flowers, as observed by Nghiem *et al.* (1997), required 2 days of ice growth with temperatures of about -28°C. Thus, frost flowers are not the cause of observed variations. Also, the changes in radar signatures in this polynya cannot be explained by variations in the wind velocity during the studied period. Thus, this example clearly shows how the radar signatures of polynyas change significantly due to polarization and incidence angle differences.

Analysis of flaw polynyas in the Kara Sea

Polynyas in the Barents and Kara Seas were mapped using *ERS* SAR and *Radarsat* ScanSAR images (Lundhaug, 2002b). The study covers a large area: Vaygach Island, the Pechora Sea, Yamal coast, the Ob' and Yenisey estuaries, Taymyr coast, Novaya Zemlya, Severnaya Zemlya, Franz Josef Land and Vize and Ushakova Islands. The first data set was drawn from repeated passes over the same areas with 3-day intervals from *ERS-1* during its ice orbit in March 1994. The second data set was taken from *ERS-1/2* images obtained in February/March 1996 during the *ERS-1/2* tandem phase, when repeat pass data were obtained with 1-day intervals. Archived *Radarsat-1* ScanSAR data from the Alaska SAR Facility for March 1997 and 1998 were selected for study as a consequence of their good spatial and temporal coverage of the large area. A total of 94 *ERS-1/2* SAR scenes and 71 *Radarsat* ScanSAR wide scenes were acquired and analyzed. Also, bathymetry data along with wind and temperature from global NCEP reanalysis data, both for the time of imaging and for the preceding days, were used in the analysis.

For each polynya, its width was measured on the computer screen as the mean distance from land or from the fast ice to the far edge of the pack ice, usually first-year ice. For this purpose the cursor was positioned at two image points: at the land/fast ice border and at each ice edge border. This measurement was done for all polynyas where a reasonable mean width could be found. In areas where repeated SAR images were available, the same polynya was measured several times during its development. A total of 125 measurements were obtained.

The *Radarsat* ScanSAR image for 2 March 1998 in Figure 5.34a shows the polynya at the northwestern coast of Novaya Zemlya. Its dark signature in the SAR image represents grease ice or nilas, which forms quickly as the polynya opens up during low air temperatures of -22°C. If windspeed had been very low (less than $3\,\mathrm{m\,s^{-1}}$) the dark signature of the polynya could also have indicated open water. But with a windspeed of $7\,\mathrm{m\,s^{-1}}$, found from the NCEP data for this time, this would have created higher backscatter. The thin, brighter signature is the transition zone between grease ice/nilas and thicker first-year ice, where thin ice has piled up or rafted at the ice

edge. Fast ice areas up to 10 km wide are also visible between the coast and the polynya.

This polynya closed up as a result of changing wind direction and remained closed for the next 2 weeks due to the dominance of westerly and southwesterly winds. As a consequence of this, a polynya on the eastern side of southern Novaya Zemlya and Vaygach Island opened up. This is a very typical situation for this area, with southwesterly winds blowing first-year ice away from the coast. The *Radarsat* ScanSAR image for 18 March 1998, presented in Figure 5.34b, shows the polynyas clearly as large, dark areas along the coasts. The dark signature is due to grease ice and nilas, while the bright lines along the edge of first-year ice is thin ice that has piled up. Maximum polynya width is about 38 km. The wind was about $9\,m\,s^{-1}$ and the air temperature was about $-8^{\circ}C$ on this day. During the period from 17 to 24 March, the wind direction shifted between westerly and southerly with a speed of 5 to $11\,m\,s^{-1}$. After 24 March these polynyas closed up when the wind turned north–northeasterly. The air temperatures in this period varied between $-1^{\circ}C$ and $-9^{\circ}C$.

Based on all 165 SAR images for the selected winter periods during the years under study, the mean and standard deviations of polynya widths have been determined. They are presented in Table 5.18. In 1994 and 1996, estimates were done solely for the Pechora Sea and the southwestern Kara Sea from *ERS-1/2* SAR data. In 1997 and 1998, polynya widths were measured for the larger study area using *Radarsat* images.

As shown in the table, the largest polynyas were found along the Taymyr coast with a mean width of about 40 km. Typical polynya widths along the western coast of Yamal Peninsula and near the outlets of the Ob' and Yenisey Rivers ranged from 20 to 30 km, with a standard deviation of more than 20 km. A high value for mean polynya width is generally accompanied by a high standard deviation value. Wide polynyas were also measured in the Vaygach area (mean value about 25 km) and around Franz Josef Land (mean value about 23 km). The polynyas near Vize and Ushakova Islands had lesser width. SAR observations were few in number for the Yamal coast (8), Taymyr coast (7) and the Ob'–Yenisey area (8). Thus, table values of polynya widths are less certain for them. A significant variability in mean width for different years was observed. The maximum value, as well as maximum standard deviation, was found in 1997. An important limitation of this study is that SAR observations were sparse and uneven in time. Fast changes of polynya signature and width during its freezing and due to changes in wind direction cannot be captured by sampling intervals of 3 days and longer.

5.3.3 Ice drift in the Laptev Sea

The Laptev Sea is a major source area for sea ice in the Eurasian sector of the Arctic Ocean and for supplying the Transpolar Drift (Karelin, 1945; Zakharov, 1966, 1976; Timokhov, 1994; Emery *et al.*, 1997). On average, sea ice is exported to the Arctic Ocean during autumn, winter and spring. During summer, ice circulation is more variable and sea ice is generally imported from the Arctic Ocean in June and July.

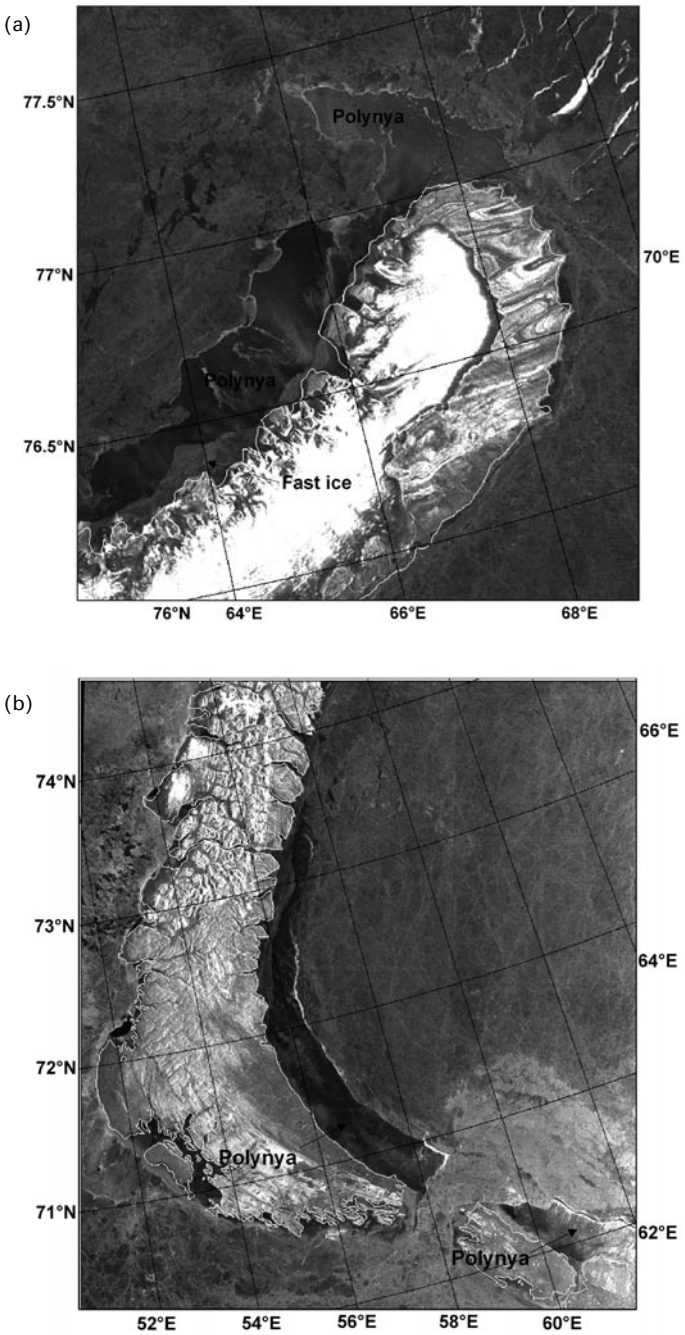

Figure 5.34. *Radarsat* ScanSAR images of polynyas near Novaya Zemlya coast: (a) for the northern part, 2 March 1998; (b) for the southern part, 18 March 1998 (© Canadian Space Agency).

Table 5.18. Mean and standard deviation of polynya widths as determined from SAR images. *ERS* SAR was used in 1994 and 1996 and *Radarsat* ScanSAR was used in 1997 and 1998 (from Lundhaug, 2002b).

Area	Mean (km)	Standard deviation (km)
Vaygach area	24.8	20.5
Pechora Sea	15.2	17.3
Yamal coast	29.8	25.8
Ob/Yenisey estuaries	21.3	20.4
Taymyr coast	40.8	27.3
Novaya Zemlya	18.9	16.0
Severnaya Zemlya	19.8	18.1
Franz Josef Land	22.9	20.2
Vize/Ushakova Islands	10.1	7.3

Studies of short-, medium- and long-term ice drift in the Laptev Sea have been conducted using successive SAR images from *ERS-1/2* and *Radarsat* satellites and SLR images from the *Okean* satellite (Alexandrov *et al.*, 2000a; Sandven *et al.*, 2001). Ice displacement vectors for the period between acquisitions of several images have been calculated from the geographical coordinates of the same ice features that could be recognized in these images. *ERS* SAR and *Radarsat* ScanSAR images have been used to produce short-term ice drift estimates for August–September 1997 (Sandven *et al.*, 2001). Their high-resolution and accurate geolocation enables displacements to be found for periods of several days with high accuracy. The narrow swath of *ERS-1/2* SARs makes recognition of the same ice features difficult during longer time periods, since often different sea ice areas are imaged. However, in wide-swath *Okean* and ScanSAR images the same ice features can more often be recognized after a significantly longer time period—in some cases even after several months. In the winters of 1987/1988 and 1994/1995, 48 and 27 ice displacements, respectively, were retrieved from many *Okean* SLR images for periods that vary from 3 days to 7 months. Ice drifts for medium-term and long-term periods are described in Alexandrov *et al.* (2000a). Long-term ice drift patterns have also been determined for winter 1997/1998—this from successive ScanSAR images. In what follows the term "drift speed" is used for the value obtained by dividing displacement distance by time period.

Short-term ice drift patterns

Radarsat ScanSAR and *ERS-2* SAR images, covering the Vilkitskiy Strait area and parts of the Laptev and East Siberian Seas over the period from 11 August to 7 September 1997, have been used to obtain short-term ice motion patterns (Sandven *et al.*, 2001). The *ERS-2* SAR image for 11 August showed a stream of eastward drifting ice floes in the central and southern part of Vilkitskiy Strait, whereas its northern part was mainly ice-free. The ScanSAR image for 14 August, presented in

Figure 5.35a, shows the eastward ice drift in the Vilkitskiy Strait, composed of ice from the northwestern side of Bolshevik Island, where the fast ice of Shokalskiy Strait started to break up and drifted southward. From the ScanSAR scenes for 14 and 15 August, ice displacement of 38 km over a period of about 24 h was found, corresponding to a drift speed of $0.44\,m\,s^{-1}$. In the eastern Vilkitskiy Strait and in the Laptev Sea, ice drifted to the southeast at a drift speed of $0.20\,m\,s^{-1}$, as shown by the ice motion vectors in Figure 5.35a.

The western parts of Vilkitskiy and Shokalskiy Straits were covered with three consecutive *ERS-2* images from 14 and 20 August. As for ScanSAR images, the ERS image for 17 August (see Figure 4.26) showed that the ice north and west of Cape Neupokoeva (78°N, 100°E) drifted southwards into Vilkitskiy Strait and then merged with eastward flowing ice coming from the southwest. A group of large floes observed north of the cape on 14 August had moved about 60 km and were located south of the cape 3 days later, corresponding to an ice drift speed of $0.23\,m\,s^{-1}$. A giant ice floe, located northwest of the cape on 14 August, moved 20 km towards the southeast in the same period, corresponding to a drift speed of $0.08\,m\,s^{-1}$. The ice along the Taymyr coast also drifted eastwards, as can be recognized by open water on the leeward side of the small islands. The floe displacement in this region between 17 and 20 August corresponds to an ice drift speed of $0.03\,m\,s^{-1}$.

The ScanSAR image for 26 August indicated a reduction in ice in Vilkitskiy and Shokalskiy Straits, as compared with the previous ScanSAR survey, and several well-developed ice edge eddies and vortex pairs in the region west of 100°E longitude. Ice edge eddies and vortex pairs have been previously studied in the Greenland Sea (Johannessen *et al.*, 1994a), where the mixed barotropic/baroclinic instabilities of the currents were found to be a probable generating mechanism for these phenomena. Analysis of successive ScanSAR images, covering the Vilkitskiy Strait and the western Laptev Sea on 26 and 31 August, showed that in the western Laptev Sea the thick icepack drifted to the southwest at a drift speed of $0.05\,m\,s^{-1}$, while open water/new ice areas persisted east of Severnaya Zemlya. Ice drift in Vilkitskiy Strait was estimated from SAR images for 24, 26 and 27 August. The first image pair showed that two floes located near the northern coast of the strait moved southwards at $0.06–0.08\,m\,s^{-1}$ in a period of easterly winds. In the central part of the strait floes moved eastwards at drift speeds up to $0.17\,m\,s^{-1}$ even though the winds continued to be easterly at $4–8\,m\,s^{-1}$. This suggests that eastbound currents, which appear to dominate in the central and southern parts of the strait, captured the floes. Ice displacements in the central part of the Laptev Sea, measured on ScanSAR images for 3 and 6 September, gave a southeastern ice drift speed of $0.15\,m\,s^{-1}$.

Three ScanSAR images, obtained in the area of the New Siberian Islands and parts of the East Siberian Sea, were used to make a mosaic and to calculate the ice drift speed for the period 4 to 6 September, which varied from 0.10 to $0.20\,m\,s^{-1}$, as shown in Figure 5.35b.

Analysis of a sequence of *ERS-2* and *Radarsat* ScanSAR images during late summer conditions in 1997 shows that ice motion in the Laptev Sea was mainly in a south–southeastern direction and that the ice drifted eastward through Vilkitskiy Strait as shown in Figure 5.35c. The few images from the area around the New

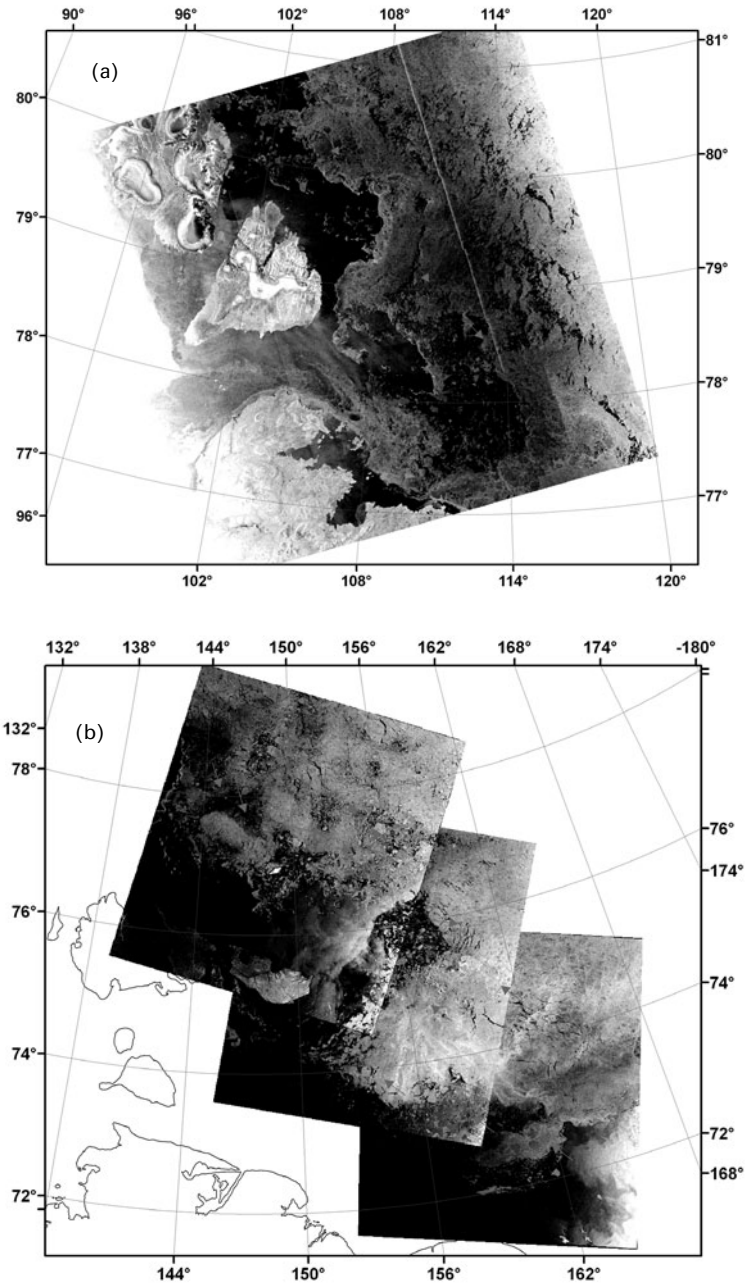

Figure 5.35. Ice drift in the Laptev Sea in August–September 1997: (a) *Radarsat* ScanSAR image of 14 August 1997, with ice drift vectors until 15 August superimposed (© Canadian Space Agency); (b) Mosaic of *Radarsat* ScanSAR images taken in the area of New Siberian Islands from 4 to 6 September 1997, with 1-day ice drift vectors superimposed (© Canadian Space Agency) (see also color section).

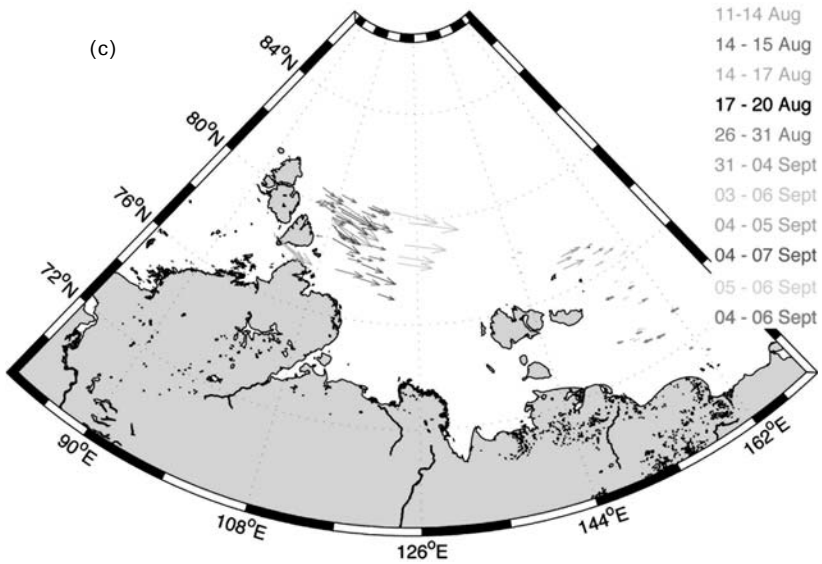

Figure 5.35 (*cont.*). Ice drift in the Laptev Sea in August–September 1997: (c) composite of all ice drift estimates from successive SAR images analyzed for the period from 11 August to 7 September 1997 (see also color section).

Siberian Islands show an easterly drift north of 76°N while it turns westerly between 76°N and the mainland.

Circulation patterns in Vilkitskiy and Novosibirskie Straits are complex due to the effects of ice–coastal interaction and the role of currents. The motion depends mainly on the prevailing wind. SAR imagery provides a unique capability for mapping ice drift in straits and near the coasts where other methods may provide little information. Their analysis shows that in August–September 1997 the sea ice in Vilkitskiy Strait moved eastward with drift speeds between 0.06 and 0.44 $m\,s^{-1}$. Westward ice drift was observed in Sannikov Strait between 3 and 6 September, transporting ice from the East Siberian Sea into the Laptev Sea. The prevailing wind was then westerly, but the wind speed was low (less than 10 $m\,s^{-1}$) over the whole period.

Medium-term ice drift

Here also the term "ice drift" is used for ice displacement, and ice drift speed is obtained by dividing the displacement distance by the (longer) time period. Analysis of a series of SLR images from the *Okean* satellite for winters 1987/1988 and 1994/1995 shows significant interannual variability in ice drift during periods of several weeks (see Figure 5.36). From 11 to 28 January 1988 the data indicate a north–northeastern ice drift in the eastern part of the Laptev Sea with a drift speed of 4.8 $km\,day^{-1}$—see Figure 5.36(a). Between 16 February and 13 March 1988 the data show the opposite with a strong onshore component and ice import from the Arctic

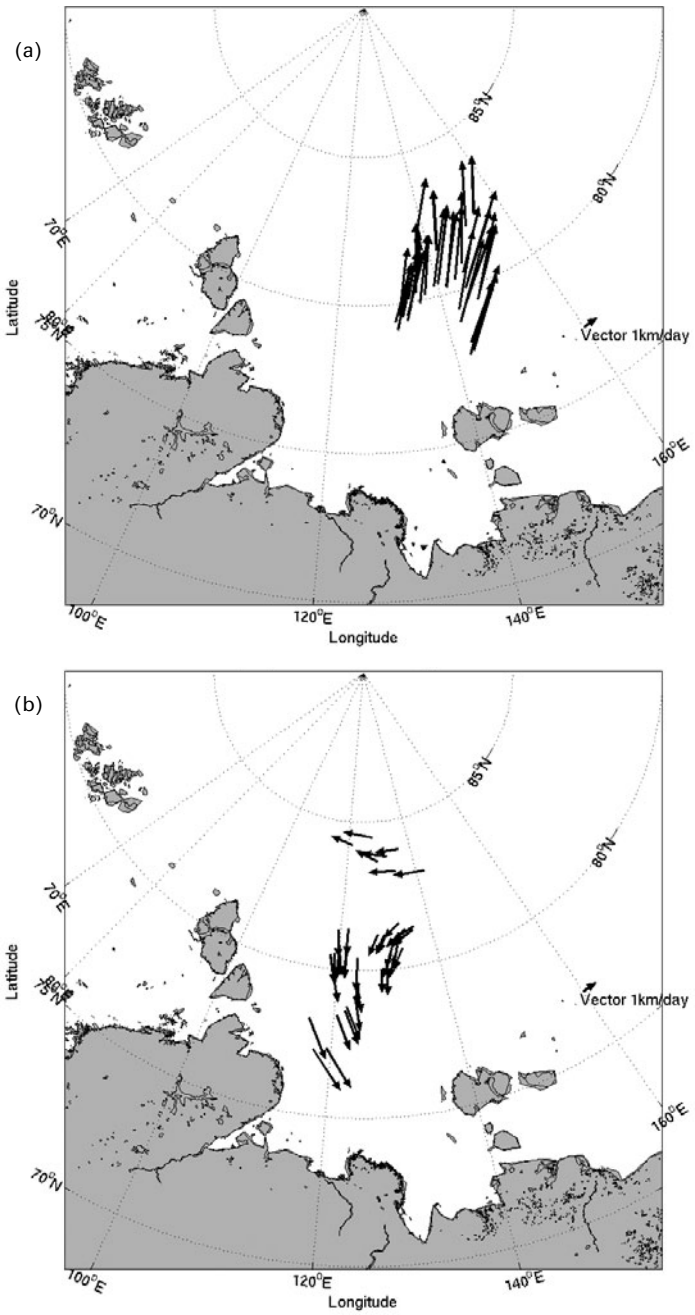

Figure 5.36. Patterns of scaled (see unit vector at right) ice drift speed (km/day) in the Laptev Sea derived from *Okean* RAR images for medium-term time intervals during the winter of 1987/1988. The vectors show the scaled drift speed of selected ice features, keeping their start points: (a) 11–28 January 1988; (b) 16 February 1988 to 13 March 1988.

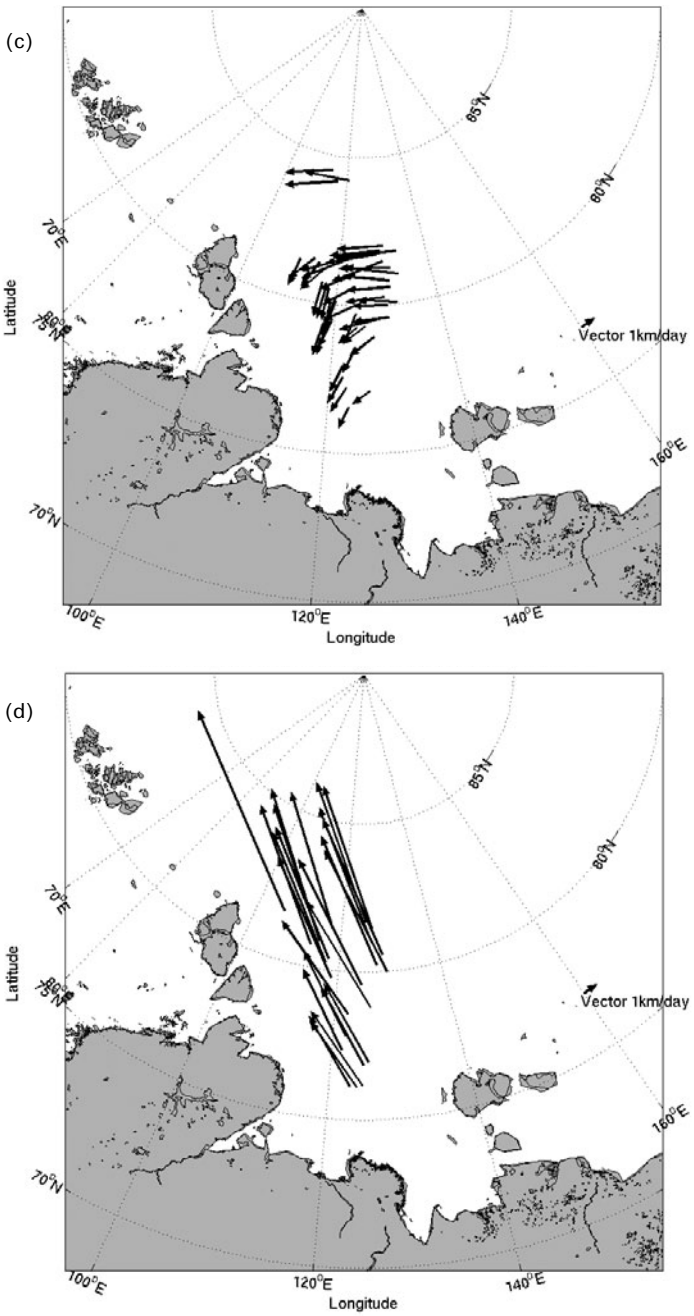

Figure 5.36 (*cont.*). Patterns of scaled (see unit vector at right) ice drift speed (km/day) in the Laptev Sea derived from *Okean* RAR images for medium-term time intervals during the winter of 1987/1988. The vectors show the scaled drift speed of selected ice features, keeping their start points: (c) 29 March 1988 to 12 April 1988; (d) 12 April 1988 to 6 May 1988.

Ocean. The ice drift speed in this period is equal to 1.9 km day^{-1}. North of the Laptev Sea, the speed of westward ice drift reaches 1.7 km day^{-1}—see Figure 5.36(b). A similar pattern was found between 29 March and 12 April, with sea ice moving southwestward to the Laptev Sea at a drift speed of 2.4 km day^{-1}. North of the Laptev Sea it moves mainly to the west—Figure 5.36(c). Between 12 April and 6 May the ice motion pattern changes and sea ice moves to the north–northwest at a drift speed increasing from 6.2 km day^{-1} in the areas to the south of 80°N to 9.7 km day^{-1} in the northernmost parts of the Laptev Sea—see Figure 5.36(d).

Figure 5.37 shows the detailed ice drift trajectories of several ice floes in areas near Severnaya Zemlya and to the north of the New Siberian Islands in September–November 1987. The positions of these ice floes have been measured in two *Okean* image sequences: 14 images for the western part of the Laptev Sea from 17 September to 11 November, and 5 images for its eastern part from 10 September to 18 November. These show that ice motion can be significantly different in different areas. Near

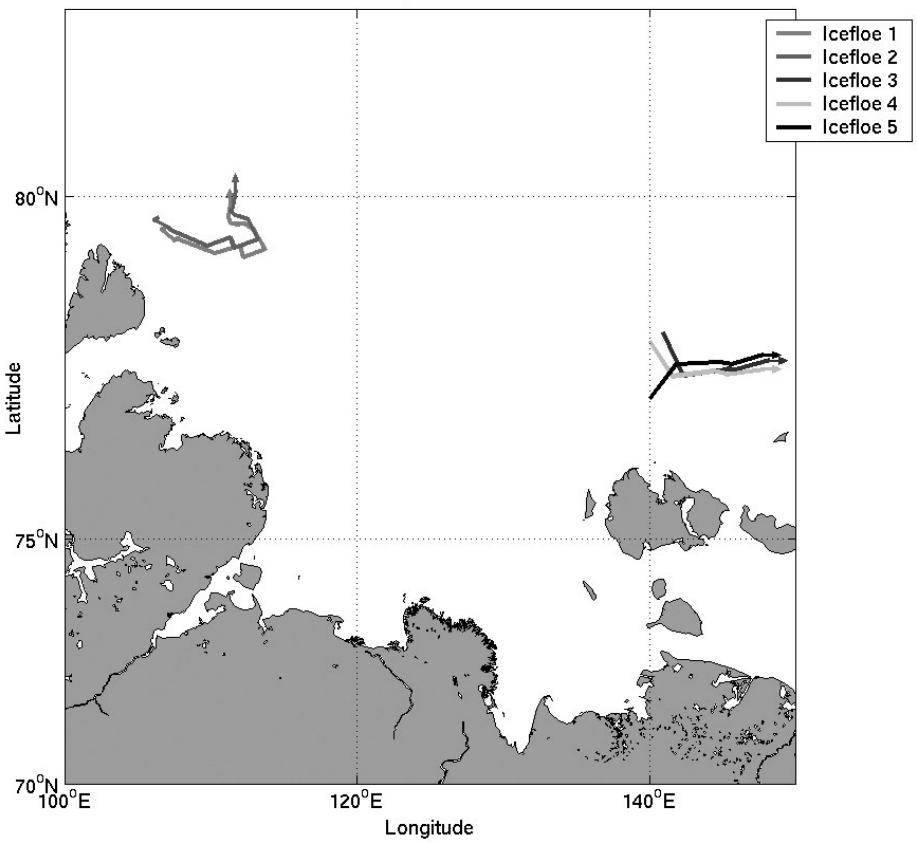

Figure 5.37. Detailed ice drift trajectories of selected ice floes in the Laptev Sea measured from *Okean* RAR images over several months (September–November 1987).

Severnaya Zemlya, sea ice drifts to the east–southeast until the last 10-day period of October and after that generally turns northwest, whereas at the eastern border of the Laptev Sea it generally moves eastward.

Long-term ice drift

Long-term ice drift from November to March has been measured from *Okean* images for winters 1987–1988 and 1994–1995 and from *Radarsat* images for winter 1997–1998 (as shown in Figure 5.38). For these three winters, some of the ice features detected in the images for November have also been recognized in images for March of the next year. Measured displacements of several large and persistent ice floes made calculation of ice drift speed during these long periods possible.

All three patterns in Figure 5.38 show that—from November to March—sea ice moved from the Laptev Sea to the Arctic Ocean in a general north–northwestern direction. In winter 1994/1995 the ice drift direction changed from northeastern in the southern part to north–northwestern in the northern part of the Laptev Sea—Figure 5.38(b). Significant interannual variability in ice drift is found. Thus, drift speeds during November–March 1987–1988—Figure 5.38(a)—and 1994–1995—Figure 5.38(b)—amount to 2.2–2.5 km day^{-1} and 1.1–3.2 km day^{-1}, respectively. The largest drift speed of 3.2–3.9 km day^{-1} was found in winter 1997–1998—Figure 5.38(c). This is approximately 1.5 and 3 times faster than in the same periods in 1987–1988 and 1994–1995, respectively.

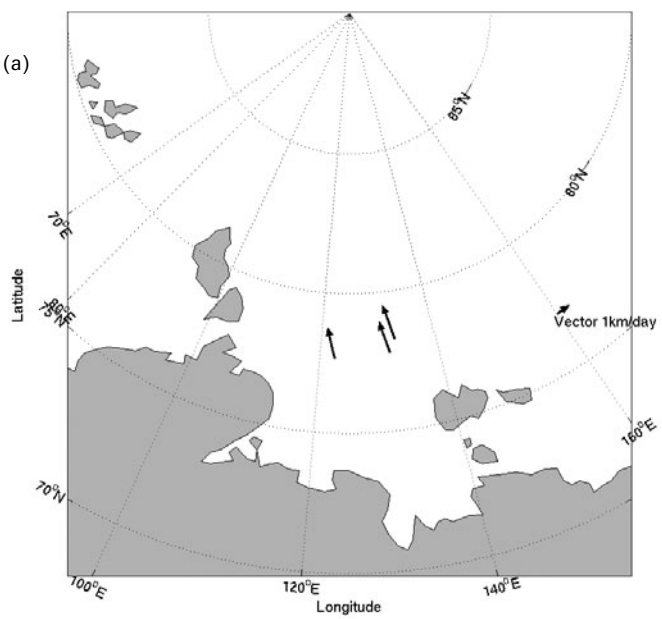

Figure 5.38. Vectors of scaled ice drift speed (km/day) in the Laptev Sea: (a) *Okean* RAR, winter, from 8 November 1987 to 13 March 1988.

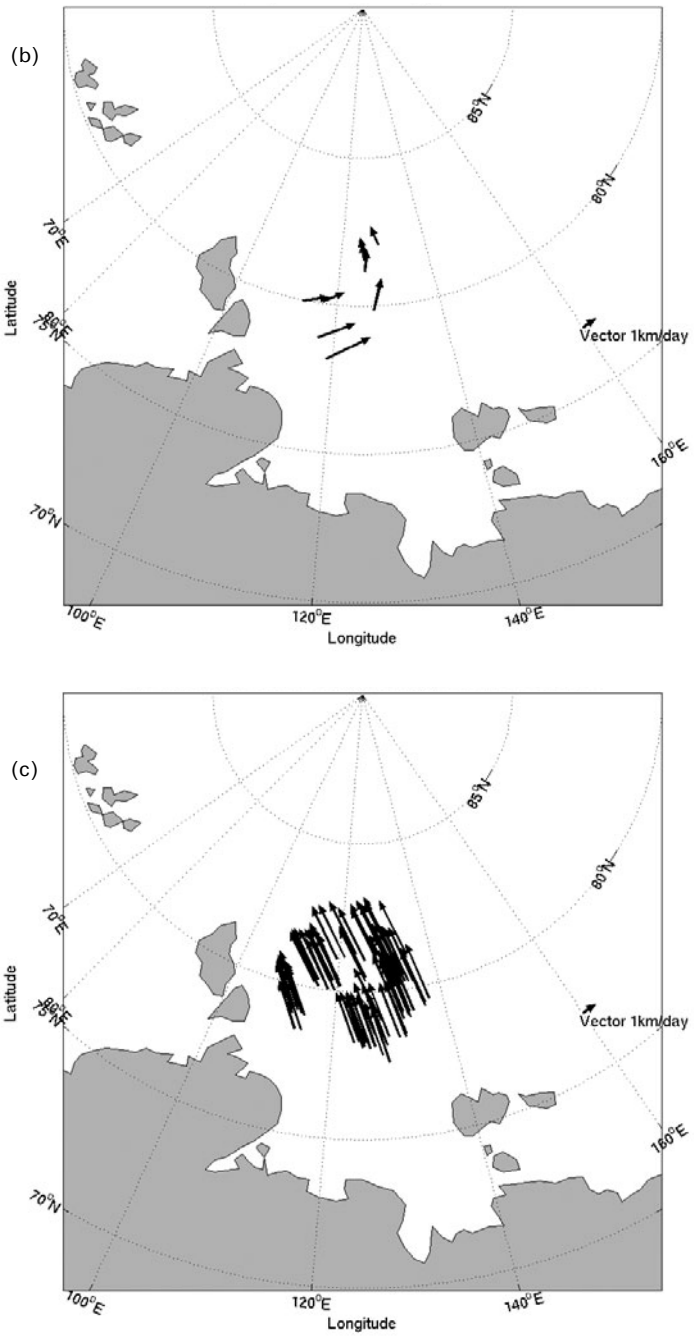

Figure 5.38 (*cont.*). Vectors of scaled ice drift speed (km/day) in the Laptev Sea: (b) *Okean* RAR, winter, from 28 November 1994 to 10 March 1995; and (c) *Radarsat* ScanSAR, winter, from 28 November 1997 to 6 March 1998.

Vectors showing the scaled ice-drift speed for the longer period from November to May for winters 1987–1988 and 1994–1995 have been measured from pairs of *Okean* SLR images and are shown in Figure 5.39. From early November 1987 until early May 1988, sea ice drifted to the north–northwest. An icefloe located in early November at 75°N moved northwards with a drift speed of $2\,\mathrm{km\,day^{-1}}$. The ice drift speed for this period, found from the displacements of ice floes located at approximately 77°N, vary between $3.2\,\mathrm{km\,day^{-1}}$ in the central part of the Laptev Sea and $4.0\,\mathrm{km\,day^{-1}}$ in its eastern part, which significantly exceeds the drift speed for the period November 1987–March 1988. This indicates the significant ice outflow to the Arctic Ocean from March to May. Figure 5.39(b) shows the latitudinal dependence of ice drift direction. It changes from north–northeast at 78°N–80°N to north at about 81°N, and to north–northwest at 83°N–84°N. Ice drift speed increases from 1.8–$2.2\,\mathrm{km\,day^{-1}}$ at latitudes between 78°N and 81°N to $2.5\,\mathrm{km\,day^{-1}}$ at 84°N.

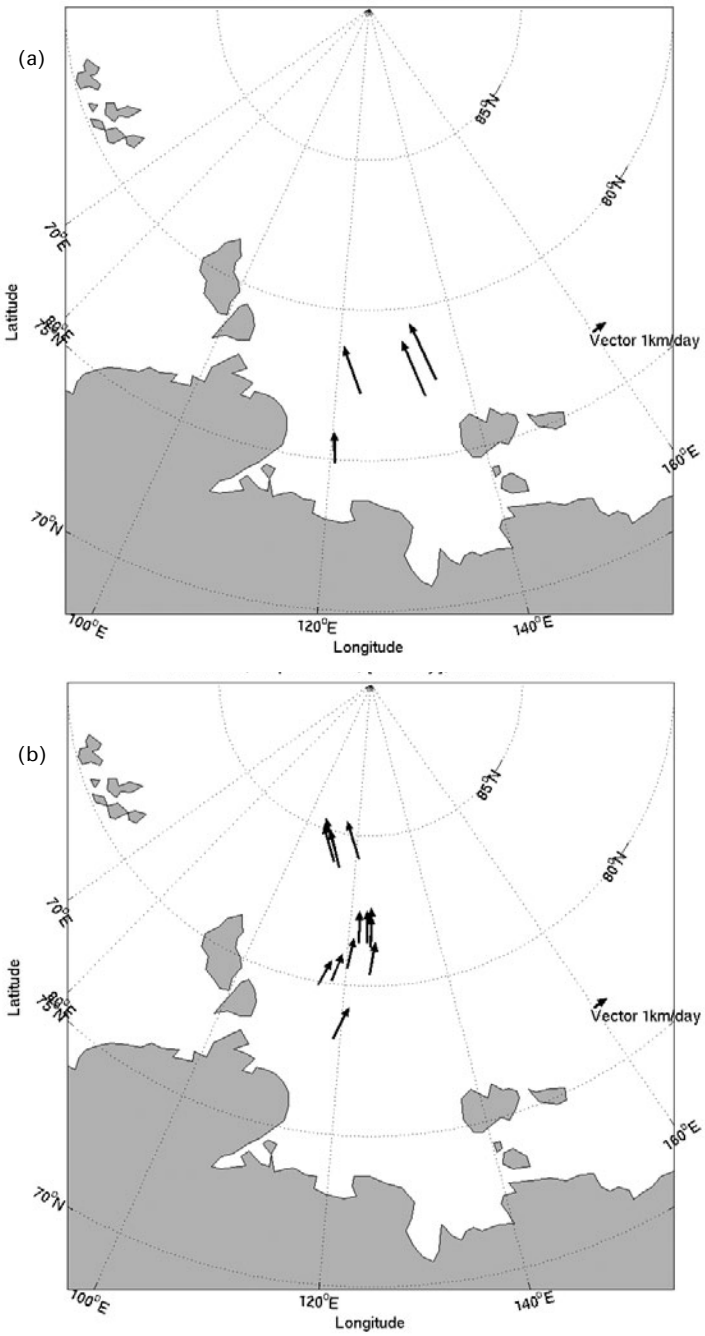

Figure 5.39. Vectors of scaled ice drift speed (km/day) in the Laptev Sea from *Okean* RAR images: (a) winter, 8 November 1987 to 6 May 1988; and (b) winter, 19 November 1994 to 21 May 1995.

6

Application of SAR for ice navigation in the Northern Sea Route

Remote-sensing techniques including synthetic aperture radar (SAR) have been used successfully for supporting navigation in the Northern Sea Route (NSR). Section 6.1 presents the first series of demonstration campaigns, starting in 1991, using SAR image data from *ERS-1*, *ERS-2* and *Radarsat*. Section 6.2 is a description of the campaigns from 2003 to 2005, which included the use of advanced synthetic aperture (ASAR) data from the *Envisat* satellite. Section 6.3 is a discussion of the use of SAR data onboard icebreakers in the NSR. Section 6.4 describes the use of complementary data—namely, optical images onboard icebreakers. An assessment of the use of satellite images for ice routing in the NSR is provided in Section 6.5. Finally, the future prospects for further development of sea ice monitoring are discussed in Section 6.6.

6.1 USE OF SAR IMAGES DURING EXPEDITIONS—PRE-*ENVISAT* (*O.M. Johannessen, V.V. Melentyev, S. Sandven, L.H. Pettersson, L.P. Bobylev, V.Yu. Alexandrov, K. Kloster, L. Zaitsev*)

In August 1991, just 3 weeks after the launch of the first high-resolution SAR sensor onboard the European Space Agency (ESA) European remote-sensing satellite (*ERS-1*), images were acquired and transmitted to the French vessel *L'Astrolabe* to support her voyage from Europe to Japan through the NSR (Johannessen and Sandven, 1992; Johannessen *et al.*, 1992a, b). This experiment was found useful, and in 1993 the Nansen Centers in Bergen (NERSC) and St. Petersburg (NIERSC), together with the Murmansk Shipping Company (MSC) started extensive demonstration campaigns for sea ice monitoring (Johannessen *et al.*, 1994b, 1996). During the 1993/1994 winter season, more than a hundred *ERS-1* SAR images were transmitted to marine operation headquarters (MOHs) and to nuclear icebreakers operating along the Siberian coast (Table 6.1). In addition to supporting ice navigation this

Table 6.1. SAR sea ice demonstration campaigns in the Northern Sea Route.

Vessel	Period	Area	Satellite SAR	Number of images*
L'Astrolabe	August 1991	Through-voyage	*ERS-1*	15
NIB *Sovetsky Soyuz*	November 1993	Through-voyage	*ERS-1*	29
NIB *Vaygach*	February–March 1994	Barents and Kara Seas	*ERS-1*	20
NIB *Taymyr*	September 1994	Kara and Laptev Seas	*ERS-1*	20
Kandalaksha	August 1995	Through-voyage	*ERS-1*	18
NIB *Vaygach* and *Taymyr*	January–February 1996	White, Barents and Kara Seas	*ERS-1/2*	13
NIB *Sovetsky Soyuz*	September 1997	Laptev Sea	*Radarsat*, *ERS-2*	21
NIB *Sovetsky Soyuz*, I/B *Kapitan Dranitsyn*, M/T *Uikku*	April–May 1998	Barents and Kara Seas	*Radarsat*, *ERS-2*	17
NIB *Sovetsky Soyuz*	June–July 2003	Barents and Kara Seas	*Envisat*	6

* *Note*: one image can be a composite of two scenes.

ESA project accomplished the scientific objectives of validation and thematic interpretation of sea ice information from *ERS-1* SAR data, studying various sea ice processes and phenomena. In summer 1995 a similar acquisition and transmission of SAR images was done to support the voyage of the ice going cargo vessel *Kandalaksha* from Japan to Norway through the NSR (Sandven *et al.*, 1995).

After these successful experiments, the European and Russian Space Agencies cooperated in 1995 by launching the "Icewatch Project" with the purpose of using *ERS* SAR together with other remote-sensing data for sea ice monitoring in the NSR (Johannessen *et al.*, 1997a, b, 1999c, 2000). In winter 1996, SAR data were again used in conjunction with the nuclear icebreakers *Taymyr* and *Vaygach* operating in the White, Barents and Kara Seas, and in the Yenisey River up to the port of Dudinka.

With the launch of the Canadian *Radarsat* in November 1995, the NSR could be covered with 450–500 km wide-swath SAR images—also denoted "ScanSAR" images—every 1–2 days. The first use of ScanSAR images in the NSR took place during an expedition to the Laptev Sea by the icebreaker *Sovetsky Soyuz* in August–September 1997. In this expedition it was demonstrated that ScanSAR data could improve the mapping of larger sea ice areas much more effectively than *ERS* data, mainly because of improved coverage. Several sea ice parameters necessary for navigation have been derived from these images, such as ice types, leads and polynyas (Sandven *et al.*, 1998a). In the following winter, ScanSAR images were used to map sea ice in the eastern Barents Sea and the Kara Sea as far east as Dikson.

ScanSAR images were found to be particularly important for navigation in severe sea ice conditions, because leads, ridged areas and level ice areas could be identified (Alexandrov *et al.*, 1999). A brief summary of these demonstration campaigns, as well as a later one using data from *Envisat* (Section 6.2) is presented in Table 6.1.

In all these experiments, scientists from the Nansen Center and collaborating institutes were onboard the icebreakers—receiving images, interpreting sea ice conditions and collecting visual observations for validation of SAR ice images. The experience gained from these experiments has been used to establish operational procedures for SAR ice monitoring in the NSR.

6.1.1 The first SAR ice routing experiment with *L'Astrolabe* in 1991

After Amundsen's *Maud* expedition in 1918–1920, *L'Astrolabe* was the first civilian foreign ship to obtain permission to sail through the NSR. The purpose of the voyage was to reopen this route to international ship traffic and to gain experience for future sailings. This expedition took place only 3 weeks after the launch of *ERS-1*, and the first SAR image was produced at the same time as *L'Astrolabe* started the voyage. The European Space Agency, which launched and operated the *ERS-1* satellite, provided a set of SAR images covering the sailing route of *L'Astrolabe*. This was done in a project established by NERSC in cooperation with ESA, Mers Magnétique, the Norwegian Space Center and the Alaska SAR Facility (ASF) to provide near-real time SAR-based sea ice information for *L'Astrolabe*'s voyage (Johannessen and Sandven, 1992; Johannessen *et al.*, 1992a, b).

L'Astrolabe's route

L'Astrolabe left Murmansk on 6 August and sailed alone to the ice edge located north of Dikson. From the ice edge she was escorted eastwards by the icebreaker *Kapitan Dranitsyn*. In this period most of the ice along the NSR was limited to the area between Dikson and Cape Chelyuskin (see Figure 6.1). From the western part of the Laptev Sea *L'Astrolabe* sailed alone in open water to an area near Wrangell Island. Thick floes of drifting multi-year ice were encountered in this area where the icebreaker *Kapitan Khlebnikov* acted as an escort on 22 August. Farther east, only scattered pieces of ice were observed, and the ship reached Provideniya in the Bering Strait on 25 August.

Data acquisition

When planning *ERS-1* SAR data acquisition, two main factors were deemed important: ordering of data for the appropriate areas on the correct days according to the eastward voyage, and transmission of essential SAR ice information to *L'Astrolabe* in time to be used for navigation. The SAR scenes of ice-covered areas were requested from ESA based on large-scale ice maps from SSM/I data showing the location of sea ice in the planned sailing route (Figure 6.1).

The diagram for SAR and SSM/I data flow during the expedition is shown in Figure 6.2. *ERS-1* SAR data in the areas west of about 110°E were received by the Kiruna ground-station and transferred by computer link to ESA ESTEC, where an ice

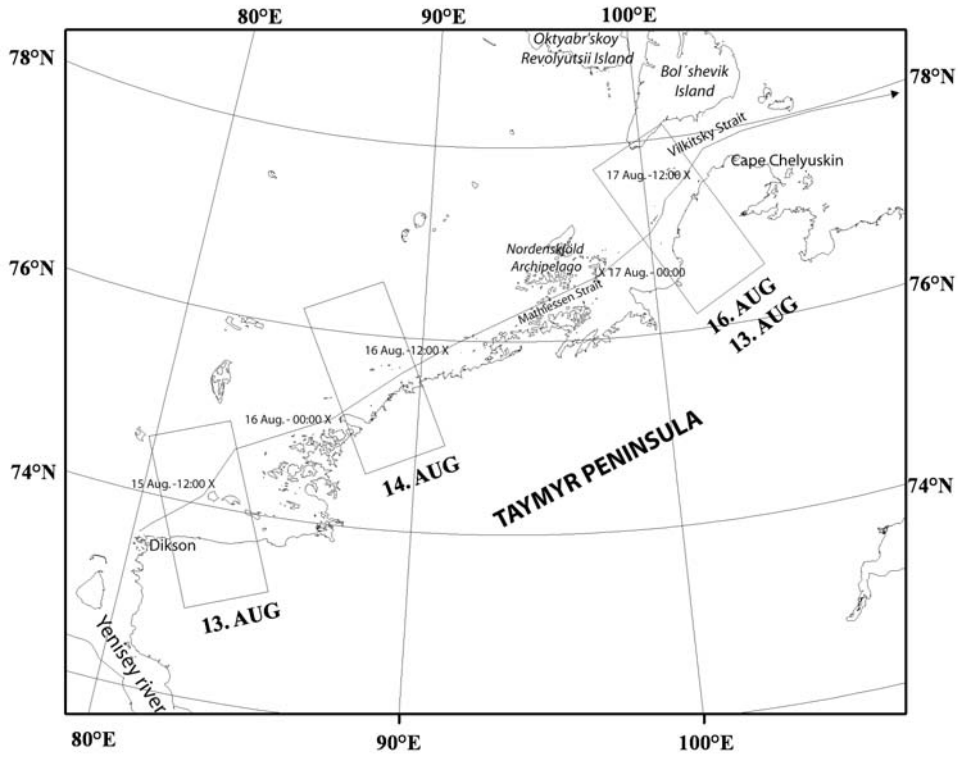

Figure 6.1. The coverage of four SAR images from ascending orbits of *ERS-1* between Dikson and Cape Chelyuskin during *L'Astrolabe*'s voyage. The ship track and its daily positions at 00:00 and 12:00 as well as dates of SAR image acquisitions are shown.

expert from NERSC analyzed the ice conditions in the images. The Laptev Sea was not covered by any ground stations, but east of 130°E SAR data were received and analyzed by the Alaska SAR Facility in Fairbanks. After analysis, SAR images and analyzed sea ice maps were transmitted to the ship by fax using Inmarsat.[1] In a similar way, large-scale ice concentration maps were produced from SSM/I data and transmitted to the ship.

SAR image interpretation and their use for ship routing

The first SAR image (Figure 6.3(a)) of the ice-covered area east of Dikson was acquired on 13 August and received onboard *L'Astrolabe* the following day. Ship observations showed that the bright, homogenous radar signature corresponded to open water, while the darker patches were mostly smooth first-year ice. The next SAR

[1] Inmarsat is a company that owns and operates a global satellite communication system.

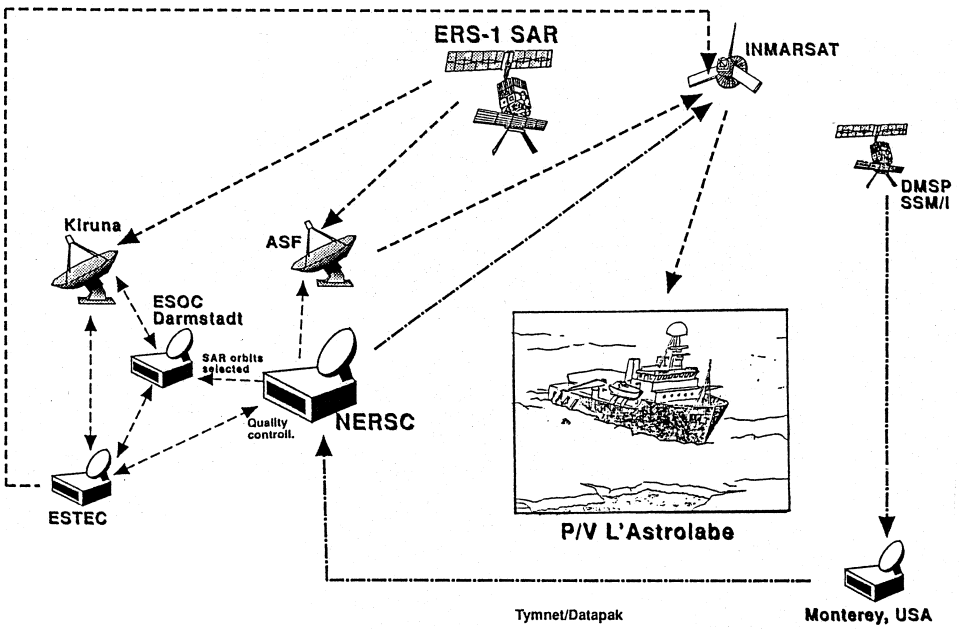

Figure 6.2. Communication lines during the voyage of *L'Astrolabe* through the Northern Sea Route.

image (Figure 6.3(b)) on 14 August covered the area from 87° to 90°E. The image was received onboard the ship a few hours before she moved into the area. Ship observations showed that the ice concentration varied from 50 to 100% and most of the ice was first-year with both smooth and rough surfaces.

The easternmost SAR images obtained from the Kiruna Station were near Cape Chelyuskin. The first SAR image in this area (Figure 6.3(c)), obtained on 13 August, showed mostly giant ice floes (typically 10 km in diameter) with low backscatter due to their smooth surface or, possibly, melt ponds. Areas of high backscatter between the floes were shown to be broken-up ice with a rough surface. The image was repeated 3 days later (Figure 6.3(d)), on 16 August, which was less than a day before the ship sailed through the area. In addition to the ice features observed earlier, this image also showed a ship track from a previous icebreaker expedition.

When this image was received onboard the *L'Astrolabe* the next day, the ship had already moved through the area using the same track as shown in Figure 6.3(d). Comparison between SAR signatures and ship observations confirmed that the gray areas were smooth first-year ice with melt ponds, while the bright areas were first-year ice broken into small floes.

On 19 August *L'Astrolabe* approached the New Siberian Islands, an area covered by the Alaska SAR Facility. A total of 11 SAR images were acquired by ASF, but these did not cover any sea ice areas along the sailing route. The images were faxed onboard, and rapid transmission was useful in planning the ship route.

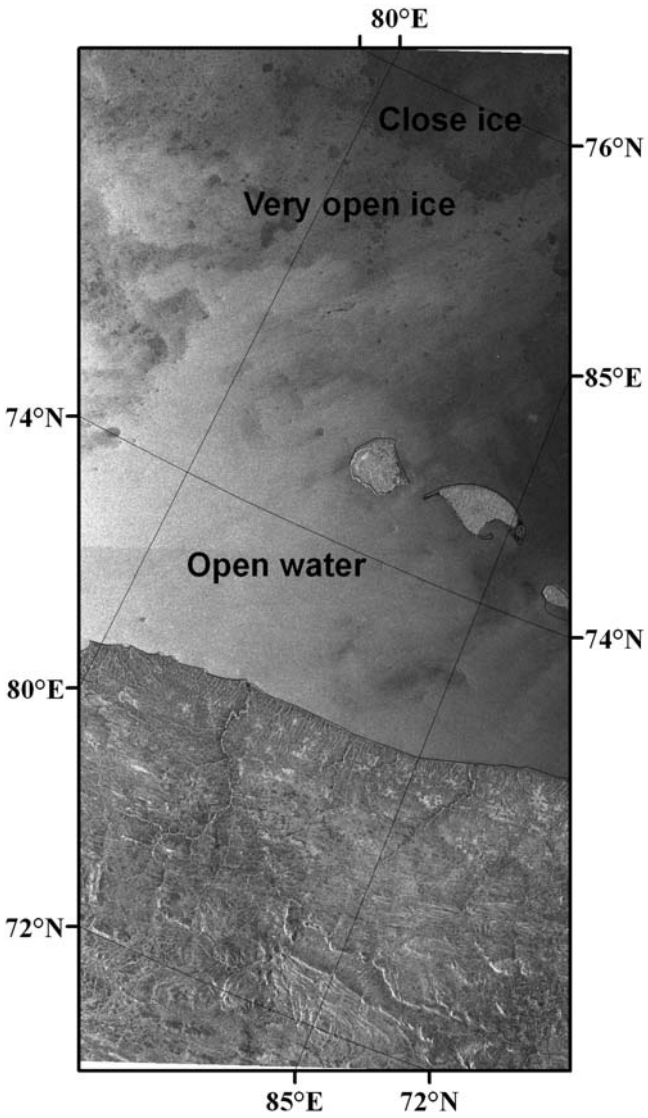

Figure 6.3(a). The first *ERS-1* SAR images, acquired during *L'Astrolabe*'s voyage between Dikson and Cape Chelyuskin: 13 August 1991 near Dikson showing mostly open water (© European Space Agency). Location see Figure 6.1.

Conclusion from L'Astrolabe's voyage

ERS-1 was an exploratory research satellite for Earth observation, especially not designed for regular sea ice monitoring. With a swath width of 100 km and 14 orbits per day, there are significant gaps between the SAR swaths on any given day. A ship sailing along the NSR will move in and out of the SAR swaths as shown in Figure 6.1.

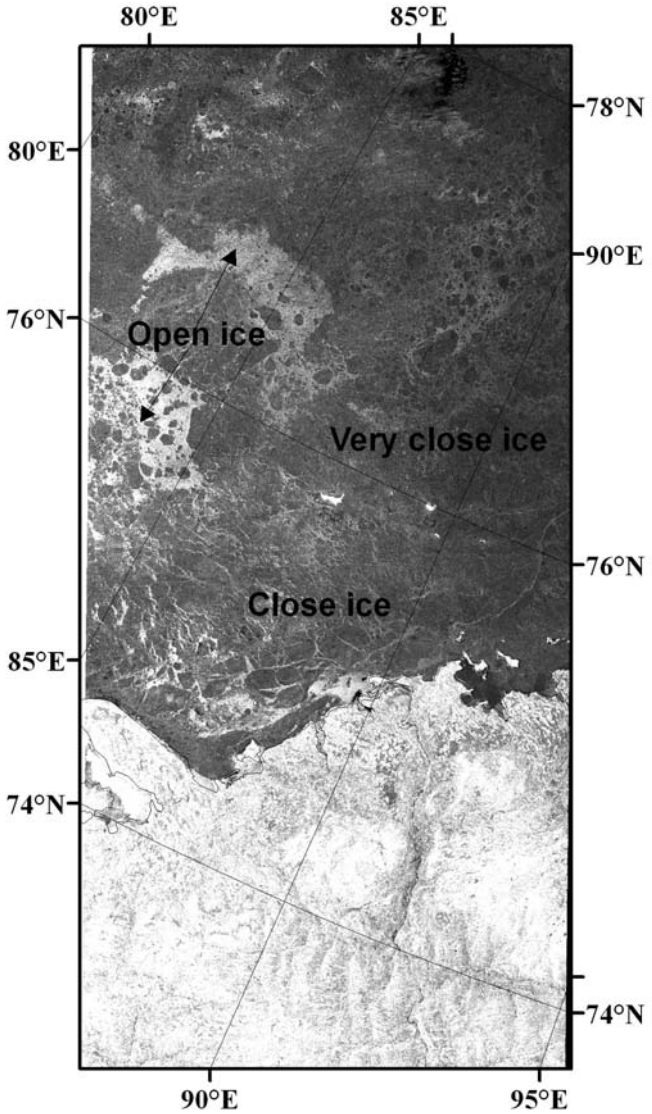

Figure 6.3(b). SAR images, acquired during *L'Astrolabe*'s voyage between Dikson and Cape Chelyuskin: 14 August (© European Space Agency). Location see Figure 6.1.

However, optimal coverage can be obtained by careful planning of SAR acquisition according to the sailing schedule. During *L'Astrolabe*'s voyage between Dikson and Cape Chelyuskin, eastward moving swaths matched fairly well with daily ship positions.

The transmission of SAR images direct to the ship by fax via the Inmarsat system could not reproduce the high quality of SAR images. Therefore, interpretation of the

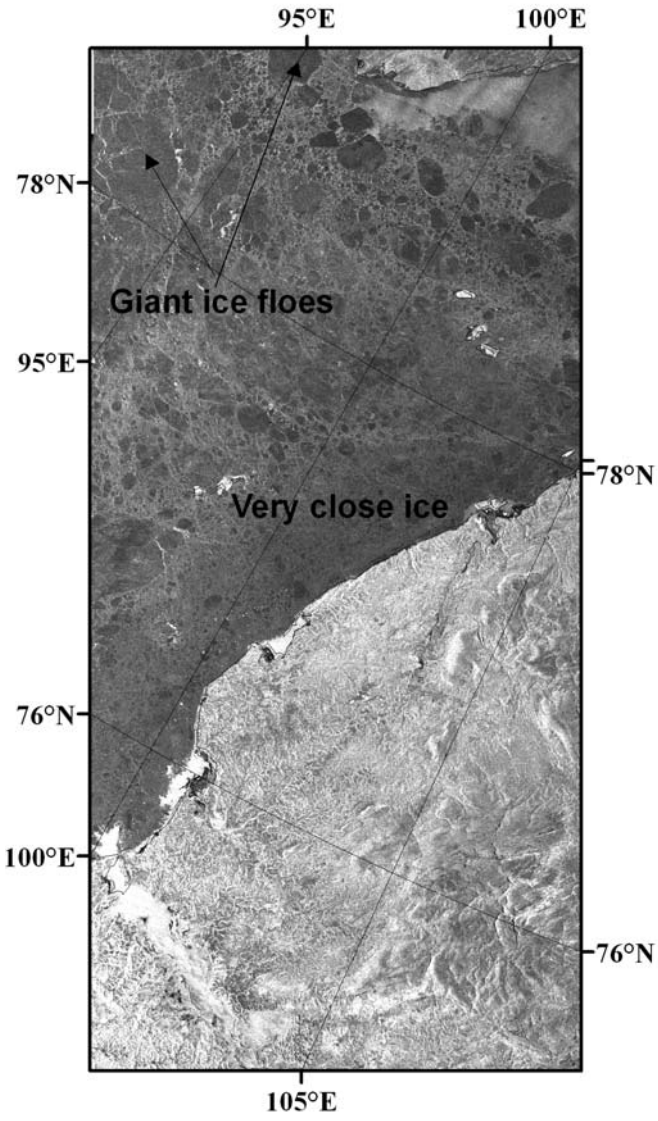

Figure 6.3(c). SAR images, acquired during *L'Astrolabe*'s voyage between Dikson and Cape Chelyuskin: 13 August near Cape Chelyuskin (© European Space Agency). Location see Figure 6.1.

images received onboard was not optimal. A crucial factor in SAR ice routing is the time delay between image acquisition and delivery onboard the ship. At the ASF, downlink, processing and analysis of the SAR images were carried out at one and the same place, making it possible to deliver images and interpretations within 12 to 24 h. In Europe, SAR data were transmitted from Kiruna in Sweden to ESTEC once a day, and the time delay from acquisition to reception onboard was usually 1–2 days.

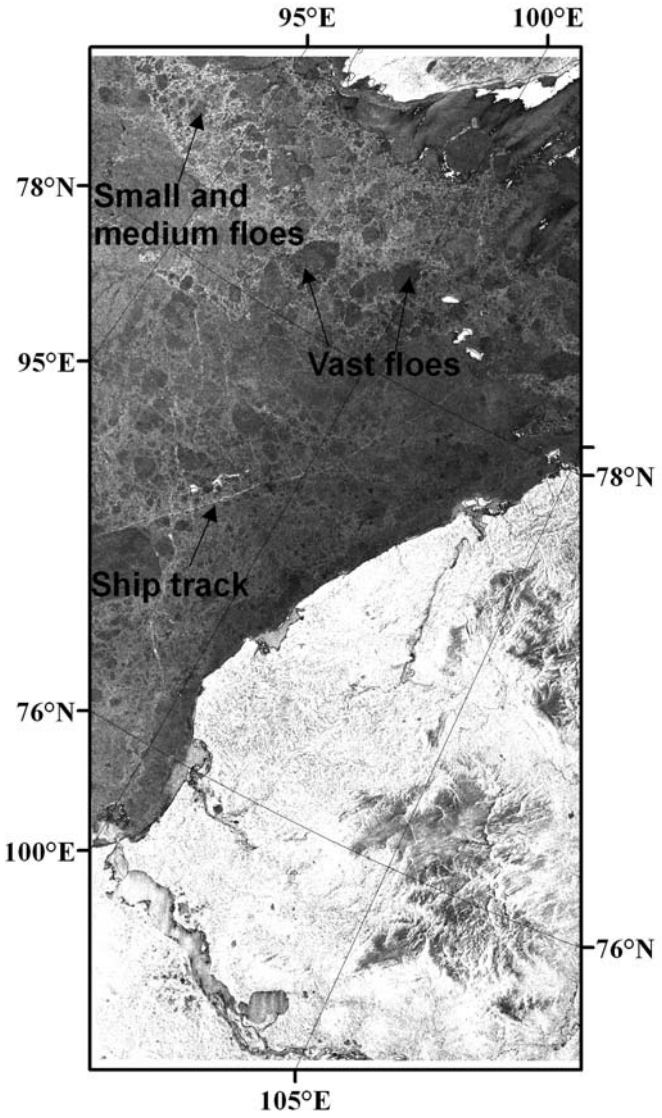

Figure 6.3(d). SAR images, acquired during *L'Astrolabe*'s voyage between Dikson and Cape Chelyuskin: 16 August, same area as in (c) (© European Space Agency). Location see Figure 6.1.

The successful launch of *ERS-1* and the possibility to produce high-resolution SAR images along the sailing route was a unique new method to provide detailed sea ice information for the *L'Astrolabe* expedition. The ordering and acquisition of SAR data was not designed for near-real time delivery, but ESA was very helpful in providing images along the sailing route. In future ice routing systems, it is important that SAR image ordering is flexible and can be adjusted to the different possible sailing

routes (Johannessen and Sandven, 2002). SAR data transmission by fax via the Inmarsat communication system functioned better than anticipated, and most of the NSR, except for the Laptev Sea, was within range of Inmarsat. The time delay between image acquisition and its reception onboard the ship varied from 6 to 48 hours. With better ground processing facilities, the time needed for processing and distribution of SAR images should be reduced to 1–2 h. The quality of the SAR images transmitted via fax was not optimal, although distinct ice features were well reproduced onboard the ship. With state-of-the-art communication systems, SAR data can be transmitted digitally and the problem of reduced image quality can be solved.

6.1.2 Voyages in the period 1993/1994

To continue the use of *ERS-1* SAR data in ice navigation, NERSC and NIERSC performed several demonstration campaigns: November 1993, February–March 1994 and in September 1994.

The Sovetsky Soyuz expedition in November 1993

During the period October 30–December 2, 1993, the icebreaker *Sovetsky Soyuz* escorted a convoy from Murmansk to Bering Strait (Figure 6.4) (Johannessen *et al.*, 1994b; Sandven *et al.*, 1994). Most of the time it operated in the Kara Sea. ESA scheduled intensive SAR acquisition for the western part of the NSR, mainly between

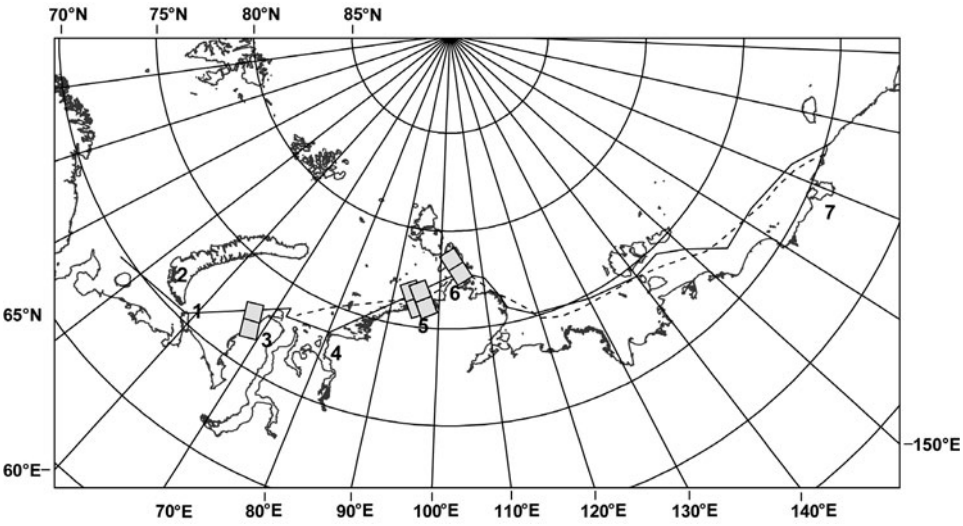

Figure 6.4. The track of the icebreaker *Sovetsky Soyuz* during her sailing in November 1993. The eastbound voyage is marked by a solid line and the westbound by a dashed line. Some major locations are indicated: 1 = Kara Gate; 2 = Novaya Zemlya; 3 = Yamal peninsula; 4 = Dikson; 5 = Taymyr; 6 = Cape Chelyuskin and Vilkitsky Strait; 7 = Pevek. Locations of the analyzed *ERS-1* SAR scenes described in the text are indicated by gray boxes.

Table 6.2. Number of received *ERS-1* SAR images/orbital passes during the 1993 demonstration campaign. Several images may be acquired during one orbital pass.

Area	During entire period	During expedition period	Transmitted onboard NIB *Sovetsky Soyuz*
Kara Gate	54/22	37/15	8/3
Yamal	21/9	13/5	8/4
Dikson	62/21	42/15	32/11
Taymyr	57/20	52/18	16/6
Chelyuskin	37/15	22/9	11/4
Other areas	6/2	3/1	3/1
Total	*237/89*	*169/63*	*78/29*

the Yamal coast and Cape Chelyuskin. Compared with the pioneer voyage of *L'Astrolabe*, when only a few images were obtained, several hundred SAR images were ordered for the *Sovetsky Soyuz* expedition, as shown in Table 6.2.

Satellite data and *in situ* observations from the *Sovetsky Soyuz* expedition provided unique material for studies of sea ice in the freeze-up season. Some characteristic sea ice features and processes are described in the following examples:

The ice edge during freeze-up

The *ERS-1* SAR image for 29 October (Figure 6.5a) covers a part of the Yamal coast as the sea ice is in the stage of formation.

Open water has a fairly uniform bright area in the SAR image due to high windspeed. The linear features observed in the open water area (marked with black arrows in Figure 6.5a) indicate a wind direction perpendicular to the ice edge. Grease ice is evident with a dark signature whereas pancake and gray ice have a much brighter signature. Their backscatter level is similar to that of a wind-roughened ocean surface, but the open water signature is more homogenous. Gray ice along the shoreline of the Yamal peninsula is also clearly evident and forms a meandering ice edge. Similar SAR signatures have been well-documented in other Arctic regions (Johannessen *et al.*, 1994a; Sandven *et al.*, 1999a).

Old ice in Vilkitsky Strait

The SAR image of 4 November (Figure 6.5b), covering Vilkitsky Strait, was used for selecting the sailing route for the eastward voyage. The image shows examples of different ice types which are characteristic for this region: gray and gray–white ice, thin first-year ice about 40 cm thick and multi-year ice about 3–4 m thick. These ice types were observed from the icebreaker *Sovetsky Soyuz*, which passed through the area 4 days after the image was acquired.

Old ice, also denoted "multi-year" ice, is often found in this area and can cause significant difficulties for navigation. It has a high backscatter and is represented by a light gray to bright signature in the SAR image (A and B in Figure 6.5b), in contrast to the darker radar signature of thin first-year ice (D). A flaw lead along the Taymyr

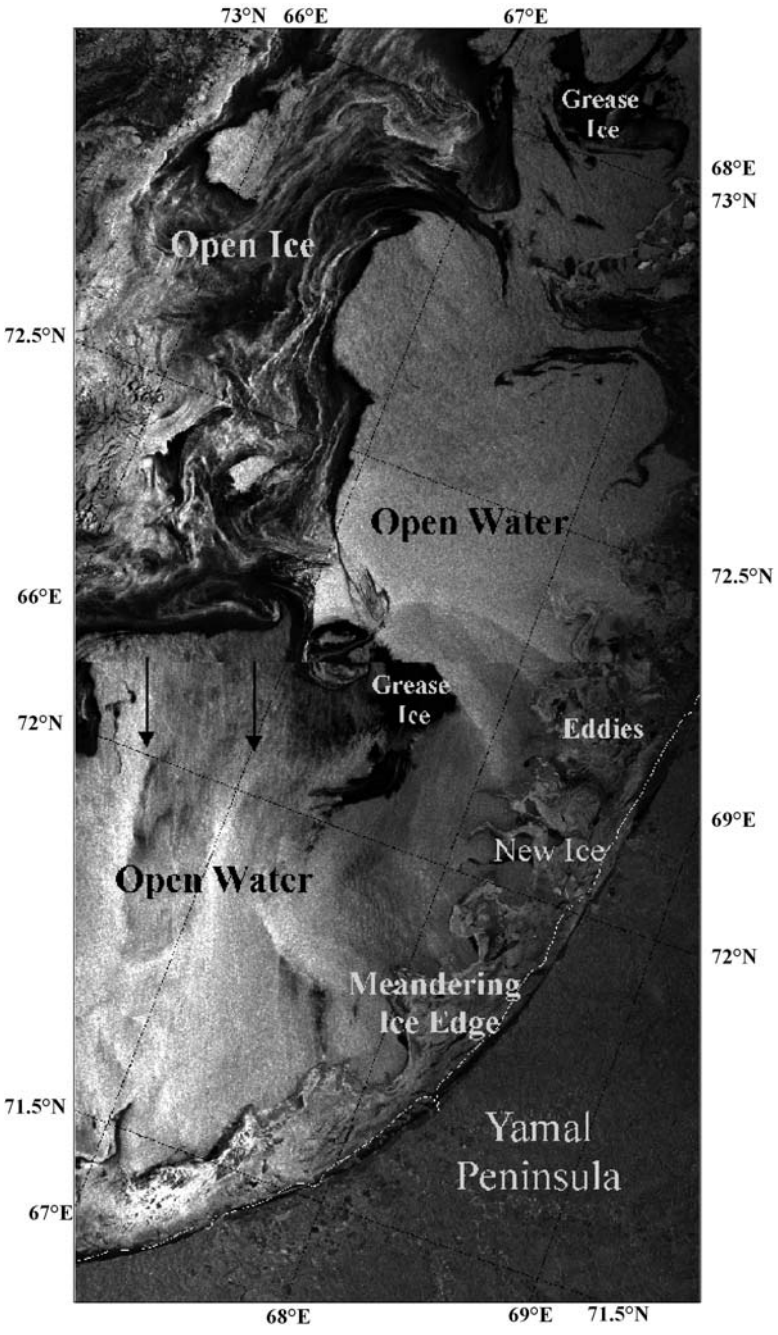

Figure 6.5(a). *ERS-1* SAR image of 29 October 1993 covering part of the Yamal coast with annotation of the main ice features. The *Sovetsky Soyuz* passed through the northwesterly corner of the image during the morning of 1 November 1993 (© European Space Agency).

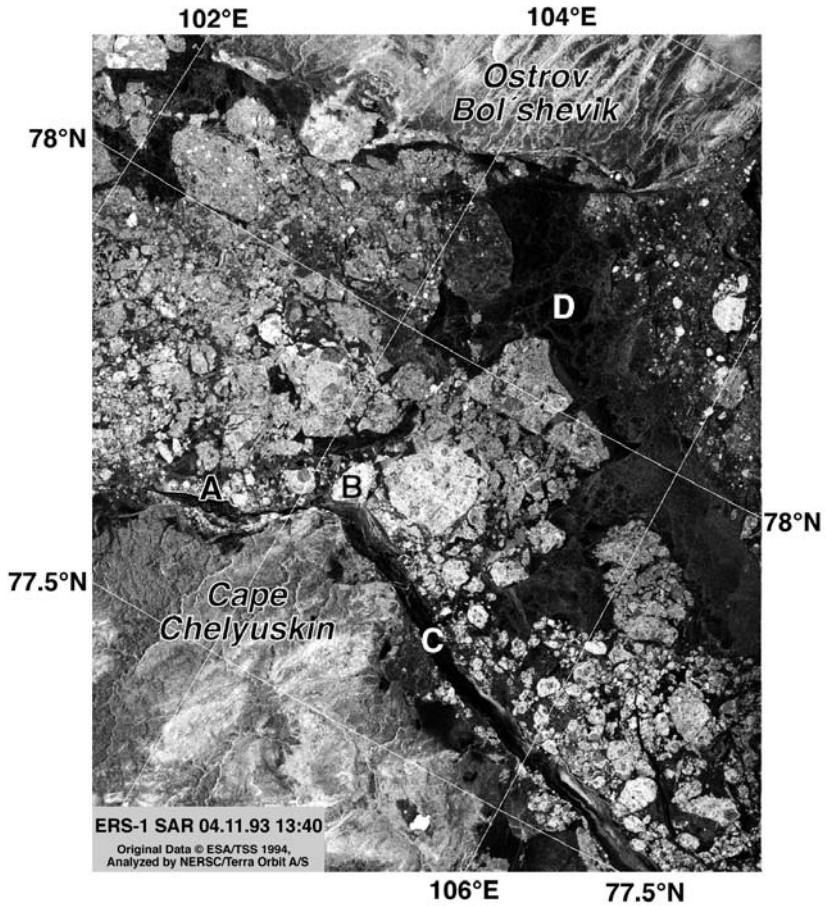

Figure 6.5(b). *ERS-1* SAR image in Vilkitsky Strait on 4 November 1993 with annotation of the main ice types as described in the text. The icebreaker followed the shoreline some 3–4 days after acquisition of the SAR image (© European Space Agency).

coast (C) is shown by a darker signature. On the onshore side of site C, first-year fast ice with a thickness of 50 cm was observed, and the SAR backscatter is slightly higher than that of ice in the flaw lead. Also, old ice offshore of site C is evident as bright spots in the SAR image. Further eastward, relatively large areas of old fast ice can be identified.

First-year ice along the Taymyr coast

Fast ice in the northeastern part of the Kara Sea can be heavily ridged causing problems for navigation. The SAR image (Figure 6.5c) covering Mathiessen Strait in the Nordenskjöld archipelago on 15 November was received onboard the *Sovetsky Soyuz* before she entered the region and was used for planning the westward voyage.

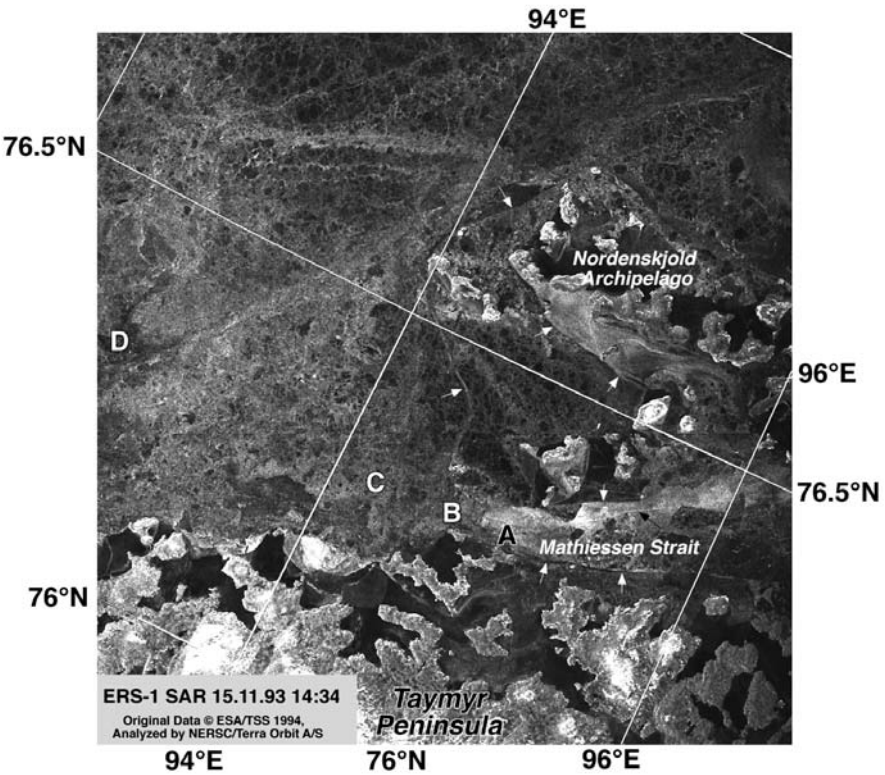

Figure 6.5(c). Annotated *ERS-1* SAR image of Mathiessen Strait on 15 November 1993. The ship track passing from the east to west through the region is visible along A, B, C and D. White arrows indicate the boundaries between fast ice and pack ice (© European Space Agency).

The location of the fast ice boundary around the islands of the Nordenskjöld archipelago is indicated with white arrows. The icebreaker crossed this boundary at A, where the ridge index was estimated to be 3–4 on a scale from 0 to 5. Even more ridged, thin first-year ice was observed at B. Farther west (at C) the ice was fairly inhomogenous with a ridge index of 3–4, consisting of nine-tenths thin first-year and one-tenth gray–white ice. The SAR signature of these ridged regions is a mixture of brighter and darker areas. From C to D the icebreaker sailed in ice of varying roughness, which corresponds to the variable brightness in the image. The thin first-year ice at D has a homogenous dark tone.

Another SAR image of Mathiessen Strait was obtained on 28 November, shown in Figure 6.5(d), after the icebreaker had passed through the area. Several ice types and ice features can be identified in the image: (1) the track of the *Sovetsky Soyuz* in the ice during her westward voyage 2 weeks earlier, observed as a bright line in the image marked by black arrows; (2) the boundary between thin first-year ice with different degrees of ridging (A) and the fast ice surrounding the islands of the Nordenskjöld archipelago; (3) a region of young ice (B) that has a bright signature; (4) new, frozen,

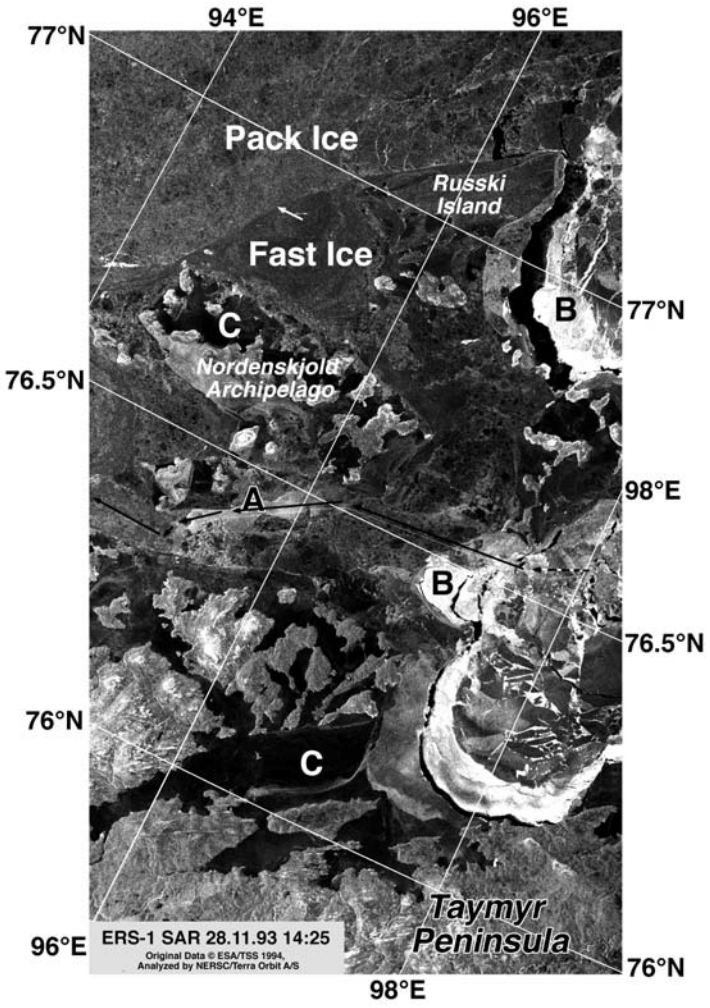

Figure 6.5(d). Annotated *ERS-1* SAR image off the Taymyr coast on 28 November 1993. The icebreaker convoy passed through this SAR swath 1 week earlier and, due to stable ice conditions, the ship track is still visible in the image. The track is located near the black arrows (© European Space Agency).

level fast ice in bays, inlets and estuaries, which is resolved as dark homogenous areas (C); and (5) drifting ice, shown in the northern part of the image, is mainly thin first-year ice with floe sizes from several hundred meters to a few kilometers. The bright, narrow lineaments correspond to open leads in this ice massif, where the wind caused surface roughening.

The SAR studies during the *Sovetsky Soyuz* expedition showed clearly the potential capability as well as limitations of *ERS-1* SAR images in ice navigation during late fall ice conditions. The most important sea ice parameters derived from

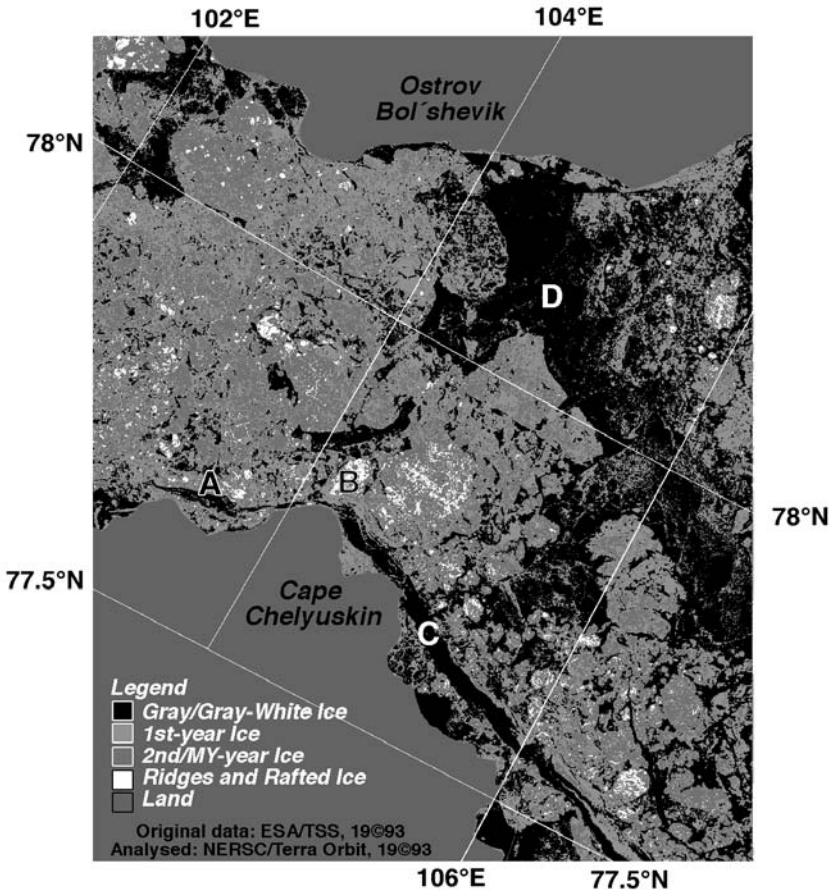

Figure 6.5(e). An example of a simple threshold classification of radar backscatter intensity in order to determine the various sea ice types. The SAR data are from 4 November 2003 shown in Figure 6.5(b) (see also color section) (© TerraOrbit AS/European Space Agency).

these images were: ice edge location, ice types (new, young, first-year and old ice), flaw leads, fast ice boundary and areas of ridged ice. Ice observations made onboard the icebreakers were used to verify the interpretation of SAR images.

The Vaygach and Taymyr expeditions in 1994

In February–March 1994 the shallow-draft NIB *Vaygach* was used for SAR ice studies during winter conditions, when the sea ice is thicker and more difficult for ice navigation (Johannessen *et al.*, 1999c). Shallow-draft icebreakers are used to sail up the Yenisey River to Dudinka Port for escorting cargo vessels transporting nickel to Murmansk. During February 1994 southerly and southeasterly winds—with air

temperatures from −20° to −40°C—prevailed in the Kara Sea. In early March the wind changed to southwesterly with warmer air masses with temperatures from 0°C to −10°C. In late March the wind was again southeasterly with temperatures from −15°C to −25°C. Wind and temperature conditions are very important contributors to ice conditions and determine how ice navigation will be performed. For example, winds blowing from the mainland form the coastal polynya (comprising the Amderma, Yamal, Dikson and Severnaya Zemlya flaw polynyas) and navigation will take place in this coastal polynya.

In the period of SAR ice monitoring, the *Vaygach* steered four convoys between the Pechora Sea and Dudinka on the Yenisey River: 24–28 February (eastward), 8–12 March (westward), 14–19 March (eastward) and 23–25 March (westward), all sailing through Yugor Strait. Four parts of its route: the Kara Gate/Yugor Strait, Cape Kharasavey, Ob' Gulf and Yenisey Gulf were covered by SAR images every 3 days. From January to March 1994 *ERS-1* was in a 3-day repeat cycle, which enabled regular SAR monitoring of the same area every 3 days (see Figure 4.41).

A SAR image was obtained on 25 February, a few hours before the icebreaker passed through the area (Figure 6.6a). It shows deformed first-year ice to the northwest of Vaygach Island and a polynya at the eastern entrance to Yugor Strait. Various stages of new and young ice in the Yamal polynya can be identified in the SAR image on 26 February (Figure 6.6b). When the *Vaygach* passed the area of the SAR image on the same day, the wind was easterly 5–12 m/s and air temperature below −30°C. As the ice was advected from the coast and open water was exposed to cold air, new ice formed immediately. The various stages in new and young ice in the polynya can be identified by different backscatter in the SAR image.

During the winter, thick fast ice grows in Yenisey Gulf. Icebreaker convoys make channels in the ice that are kept open and used repeatedly during the winter season. SAR images give information about the areas of level ice (dark radar signature) and deformed ice (bright radar signature) which are important for the selection of icebreaker channels (shown in Figure 6.6c). In this expedition about 40–45% of ordered SAR images were of immediate, practical use for the icebreakers because they covered the areas of operations and were available within hours. The possibility of receiving images onboard the *Vaygach* was dependent on the ship bearing. The vessel has "shadow zones" when Inmarsat communication is interrupted. This interruption takes place at ship headings of 182°, 270° and 350°. As a result, several SAR images obtained and processed at the Nansen Center were not received by the icebreaker.

In the late summer of 1994, difficult sea ice conditions prevailed in Vilkitsky Strait. In this period, cargo vessels required icebreaker support between the ice edge in Mathiessen Strait in the Kara Sea and the entrance to Khatanga Bay in the Laptev Sea. This was another opportunity to demonstrate the use of SAR images to support ice navigation. SAR images acquired in this period were processed and transmitted to the Marine Operations Headquarters in Dikson where an ice expert analyzed the images to make recommendations for the icebreakers. Direct data transmission of images to *Taymyr* was not possible because the ship was often beyond Inmarsat coverage. A field campaign was conducted onboard the *Taymyr* from 9 to 30

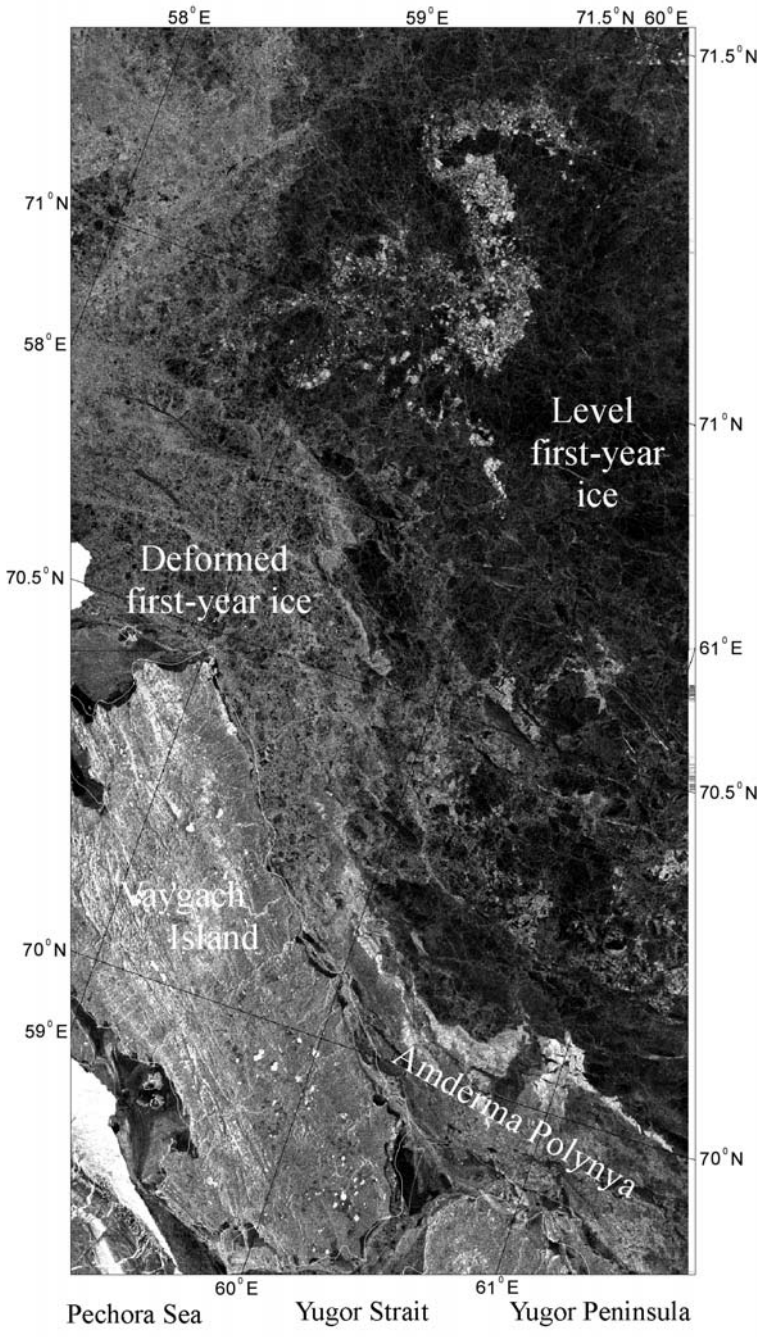

Figure 6.6(a). Annotated *ERS-1* SAR image from the Yugor Strait, between the Barents and Kara Seas on 25 February during the *Vaygach* voyage in February–March 1994 (© European Space Agency).

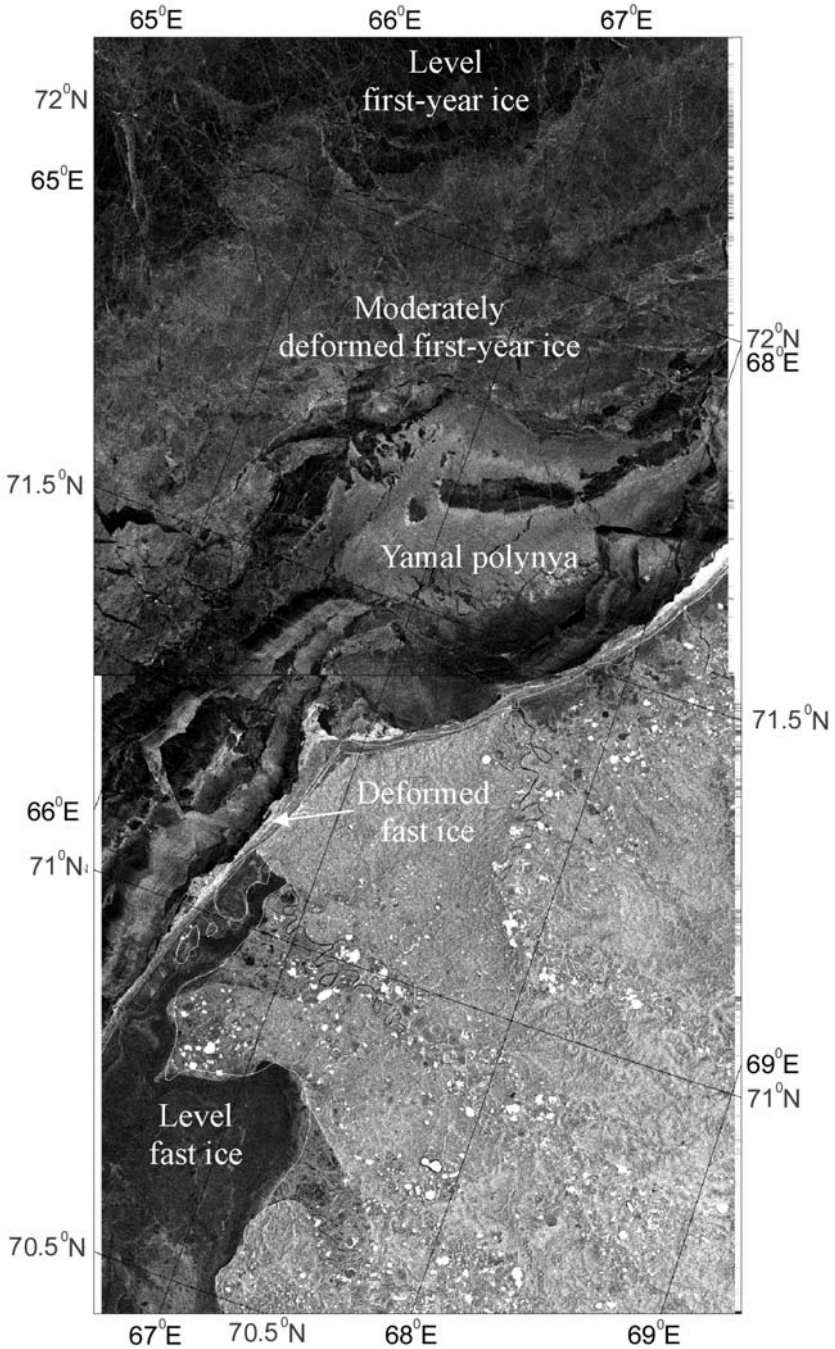

Figure 6.6(b). Annotated *ERS-1* SAR image of the Yamal coast on 26 February 1994, obtained a few hours after the *Vaygach* passed through the area (© European Space Agency).

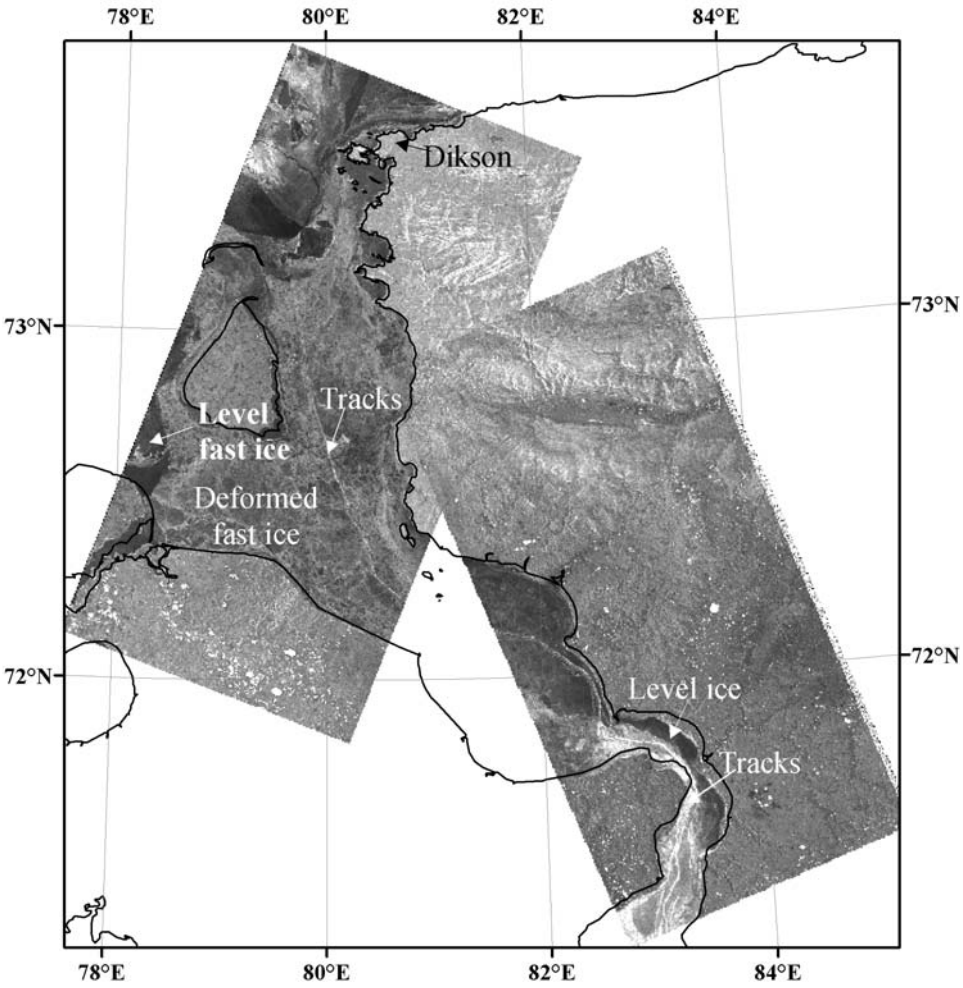

Figure 6.6(c). Annotated *ERS-1* SAR image of the Yenisey Gulf from 18 to 23 March 1994 (© European Space Agency).

September when the vessel made five voyages through Vilkitsky Strait. The western and eastern ice edges were located at 94°E and 115°E, respectively. The SAR image of 9 September shows compact first-year ice in the western and northern part of Vilkitsky Strait and more scattered ice in its southern part (Figure 6.7). Since the wind was light when the image was taken, 5–6 m/s, open ocean has a relatively dark grayish signature in the image. All acquired SAR images showed a mixture of low-concentration ice and areas of compact ice in the Vilkitsky Strait region. SAR images were used to identify ice edges, areas of compressed ice, large floes, ice tongues and ice bands.

Experience from the 1993 and 1994 expeditions

The demonstration campaigns conducted in 1993 and 1994 showed both the advantages and limitations of *ERS-1* SAR for sea ice monitoring and navigation support (Johannessen *et al.*, 1997d). The major advantage is the ability to obtain high-resolution sea ice images in near-real time independently of natural light and clouds. However, SAR images are hampered by substantial spatial and temporal gaps in data coverage. When icebreakers sail at a speed of 15–17 knots, which is common in light and medium ice conditions, it takes only a few hours to sail across the 100 km wide SAR images. Full spatial coverage of the Kara Sea can be obtained only if mosaics are built up over several days using the optimal acquisition configuration. Therefore, general sea ice mapping was made using lower resolution satellite data, and the *ERS-1* SAR images were mostly used for mapping critical areas, such as the Kara Gate or Vilkitsky Strait.

The *ERS* SAR capability to map key ice parameters—such as ice edge location, ice concentration, ice type, fast ice boundary, polynyas and leads—was demonstrated (Kondratyev *et al.*, 1995; Melentyev *et al.*, 1997). SAR only indirectly determines ice thickness. Furthermore, it is difficult to distinguish between thin, medium and thick first-year ice, as well as between second-year and multi-year ice in SAR images. In order to build up knowledge in image interpretation it was recommended to develop a SAR sea ice signature atlas and backscatter look-up tables (Johannessen *et al.*, 1997c).

SAR images have been successfully used in tactical navigation in difficult ice conditions. However, operational use of SAR in tactical navigation requires that SAR images are obtained at least once per day. During rapid changes in sea ice conditions two SAR acquisitions per day would be needed. Data delivery to the icebreaker can be done within 2–3 hours of acquisition, if the need for real time data is urgent and the communication line is working. A critical part of a near-real time ice monitoring service is the transmission of images and SAR-derived maps to ships. Use of the Inmarsat system for this purpose has significant limitations in high-latitude regions. In the last few years the digital transfer of images to ships in polar regions using Iridium[2] has been established. This has to a large extent solved the problem of data communication in the Northern Sea Route.

6.1.3 The *Kandalaksha* voyage from Japan to Norway

The ice-strengthened SA-15-type cargo vessel *Kandalaksha* sailed from Yokohama in Japan to Kirkenes in Norway via the Arctic Ocean in August 1995 (Sandven *et al.*, 1995). During her voyage large-scale mapping of ice extent and concentration was done from SSM/I data, and near-real time *ERS-1* SAR data were used for detailed mapping of potentially difficult areas.

One month before the expedition, SAR data acquisition was requested from ESA in three areas where ice navigation was considered to be most critical: Long Strait,

[2] Iridium is a satellite communication system offering complete coverage in the Arctic (*www.iridium.com*).

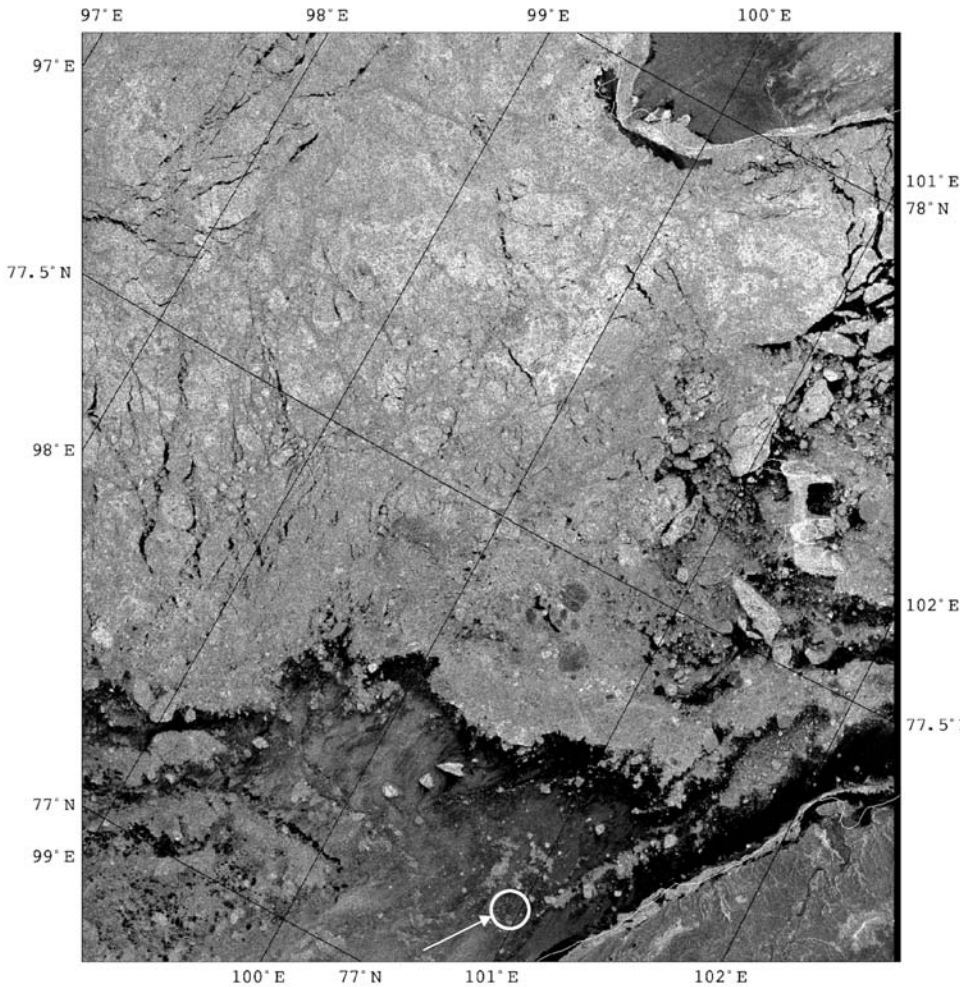

Figure 6.7. *ERS-1* SAR image showing extensive ice cover in the western entrance to Vilkitsky Strait on 9 September 1994. The navigation route along the coast has mostly open water and scattered ice. The position of the *Taymyr* is marked with a circle (© European Space Agency).

New Siberian Islands and Severnaya Zemlya (Figure 6.8). The Alaska SAR Facility acquired all imagery for areas south of New Siberian Islands and in Long Strait. The images were transmitted to the Nansen Center at 100-m resolution. Images for the Severnaya Zemlya area were obtained from Tromsø Satellite Station in Norway. At the Nansen Center the images were resampled, geolocated and transmitted to *Kandalaksha* together with SSM/I sea ice maps.

Before the expedition started, a modem and PC were installed onboard the *Kandalaksha* and connected to an Inmarsat-A station. The communication software enabled the operator onboard the ship to dial up the computer at the Nansen Center

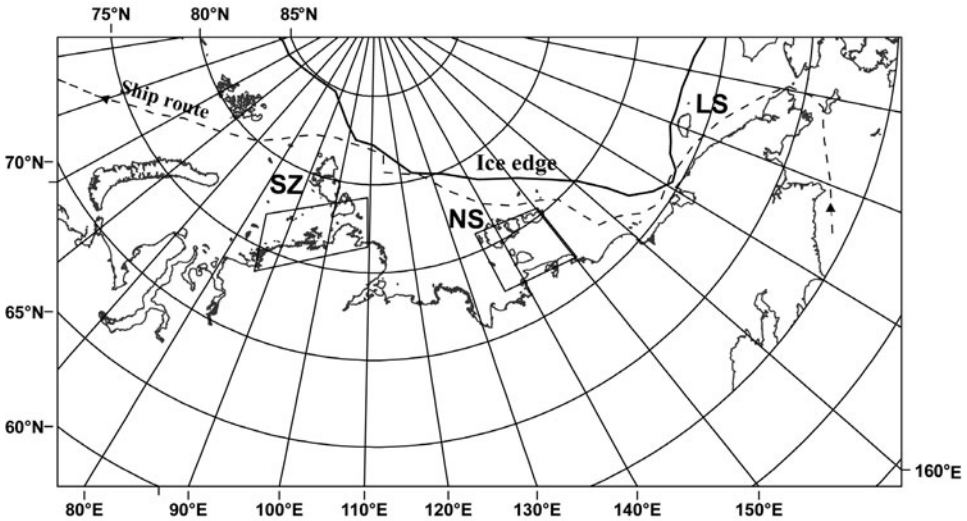

Figure 6.8. Route taken by the *Kandalaksha* (dashed line), the main ice edge location and the three selected areas for SAR acquisition: SZ = Severnaya Zemlya; NS = New Siberian Islands; LS = Long Strait are indicated.

and request transfer of files. The image files were compressed using JPEG to minimize file size and transmission time. Satellite data transmission from the Nansen Center to the ship was tested before the expedition started. A software package was used onboard for decoding, display and printout of displayed images.

SSM/I-derived maps for the Chukchi Sea showed normal ice conditions in this region until mid-July. In late July and early August an unusually rapid and strong ice retreat was observed in the whole Russian Arctic. The ice edge was located far to the north, which allowed the ship to sail north of the New Siberian Islands and Severnaya Zemlya. SAR data acquisition was planned in areas where ice conditions were expected to be difficult. But, these areas were all ice-free and there was no need to use most of the SAR data that were transmitted to the vessel.

A total of 18 SAR stripes, each consisting of 2–4 scenes, were produced to support this voyage. The delay between SAR acquisition and its reception at the Nansen Center was 1–3 hours and 1–2 days for data delivered by the Tromsø Satellite Station and the Alaska SAR Facility, respectively. All these data were made available for file transfer to the ship. South of about 70°N, both fax and file transfer were used without any difficulty, while connection at high latitudes was difficult. In the northernmost part of the sailing route the ship was beyond Inmarsat range.

One of the SAR images covering the sailing route was acquired on 25 August north of Severnaya Zemlya (Figure 6.9). The image showed mainly open water and very open ice north of 81°N. This area of low concentration was also confirmed by SSM/I data and ship observations on the same day as the SAR image was obtained. After the ship had passed north of Schmidt Island, she was directed to go in almost a straight line through the Barents Sea to Kirkenes in Norway.

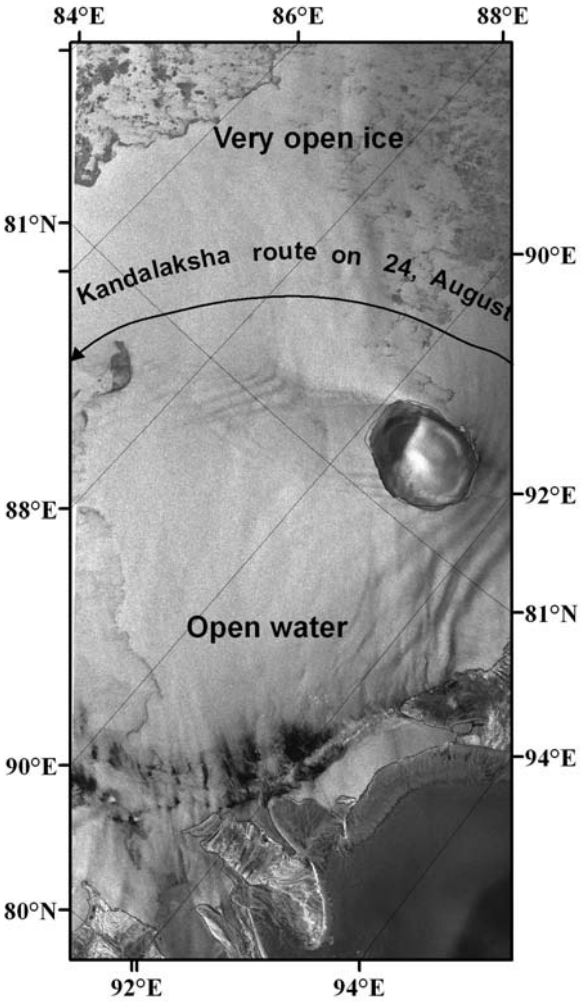

Figure 6.9. Annotated *ERS* SAR image of 25 August 1995, covering the area northwards of Severnaya Zemlya. The sailing route of the *Kandalaksha* is shown and sea ice concentrations are indicated (© European Space Agency).

The whole expedition was completed without the need for icebreaker assistance, and the sailing time from the Bering Strait to Kirkenes was only 13 days. The ship sailed in ice for a total of 8 days and reached the latitude of 81°22′N, north of Severnaya Zemlya.

6.1.4 The Icewatch expedition in winter 1996

Icewatch was the first joint project between the Russian Space Agency (RKA) and the European Space Agency (ESA) in the field of Earth observation (Johannessen *et al.*,

1996, 1997a, 1999c, 2000). The project started in 1995 and had an overall objective to promote the use of *ERS* SAR, *Okean* RAR and other satellite remote-sensing data to support navigation in the NSR. The Icewatch expedition was carried out in January–February 1996 onboard the *Vaygach* and *Taymyr*, both operating between Murmansk and Dudinka on the Yenisey River.

At this time *ERS-1* and *ERS-2* SAR were operating in the Tandem Mission, giving an opportunity to have more intense data acquisition. Furthermore, the tandem operation provided coverage over the same area with only a 1-day interval. This was a significant improvement in temporal coverage. Hundreds of *ERS-1* and *ERS-2* SAR images along the coast between Belyi Island and the Yenisey Gulf were provided in this period. Most of the images were put on the NERSC computer as JPEG files ready for transmission at the request of ships. In addition, hardcopies of the images were faxed to the icebreakers and to Marine Operations Headquarters (MOH).

Even though the number of acquired SAR images had increased from previous expeditions, it was still difficult to obtain optimal spatial and temporal matches between SAR coverage and ship location. In a few cases an optimal match between SAR coverage and ship position was obtained. One case was on 26 January in the area west of Dikson, when a SAR image was received onboard *Vaygach* less than 6 hours after its acquisition. The icebreaker was then operating in relatively heavy ice and tactical ice information from SAR became essential in selecting the optimal sailing route. The SAR image with the ship track superimposed in Figure 6.10 showed that the roughest ice had bright signatures while smoother and thinner ice had darker signatures. The optimal sailing route was therefore through the relatively smooth and thin ice. During this expedition 13 image files were received onboard the icebreaker *Vaygach* using Inmarsat. The transmission rate for data transfer varied between 2,400 and 9,600 baud, with the corresponding connection time varying from 2 to 13 min per file. The delay between satellite data acquisition and image reception onboard varied from 5 to 48 h. The quality of data transmission to icebreakers varied, depending on the orientation of their antennas. The sea ice conditions were also of importance for data transfer, as stable connection was difficult when the ship was moving through rough ice.

6.1.5 First use of *Radarsat* on *Sovetsky Soyuz* during summer 1997

The Canadian *Radarsat*, launched in November 1995, provided access to a variety of SAR modes with different incidence angles, resolution and swath width. ScanSAR images at 100-m resolution and swath widths up to 500 km provided significantly improved capability to map sea ice by SAR. The first experiment using *Radarsat* data to support navigation in the NSR was performed onboard the *Sovetsky Soyuz* in August 1997 (Sandven *et al.*, 2001). The expedition took place in Vilkitsky Strait and the Laptev Sea where the ice conditions in summer can be dominated by the Taymyr ice massif. This is thick multi-year ice, which can be a great obstacle to navigation even in the summer (Sandven *et al.*, 2001). The *Sovetsky Soyuz* arrived in Vilkitsky Strait on 10 September, while the first ScanSAR images had been obtained a few days earlier.

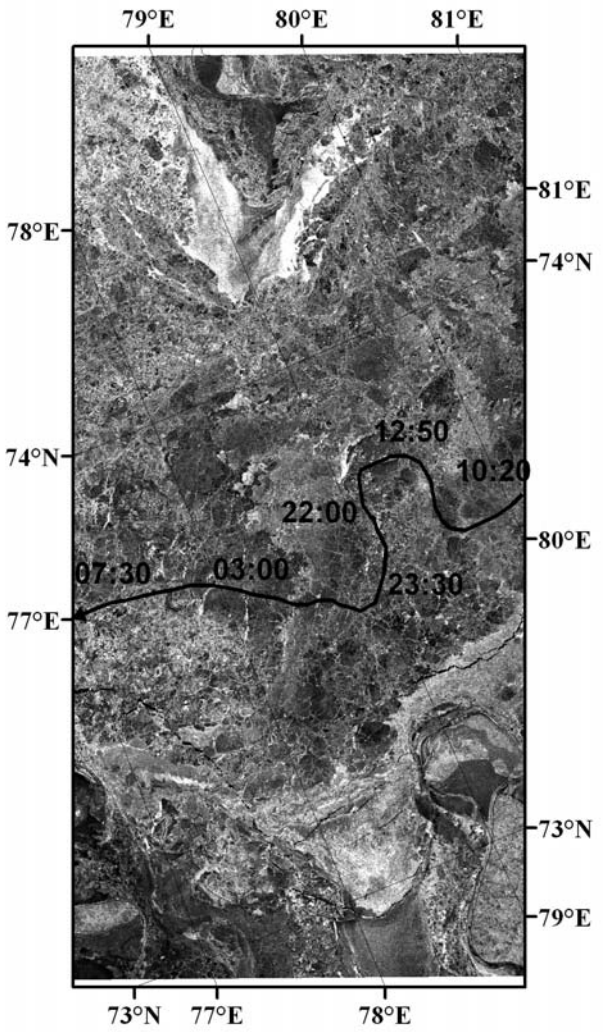

Figure 6.10. *ERS-1* SAR image transmitted in near-real time to the icebreaker *Vaygach* in the area west of Dikson on 26 January 1996. A black line indicates the ship route with sailing times in GMT. The image was used to select an easier route through very heavy ice conditions (© European Space Agency).

Data transmission to the icebreaker was not possible because the Inmarsat system did not cover this region. ScanSAR data were therefore primarily used for sea ice studies where *in situ* observations from the icebreaker were used to validate SAR observations.

Detailed analysis of ice signatures in the 7 September ScanSAR image shown in Figure 6.11(a) was made using visual ice observations, series of photographs, ice charts from helicopter and meteorological observations taken from the icebreaker.

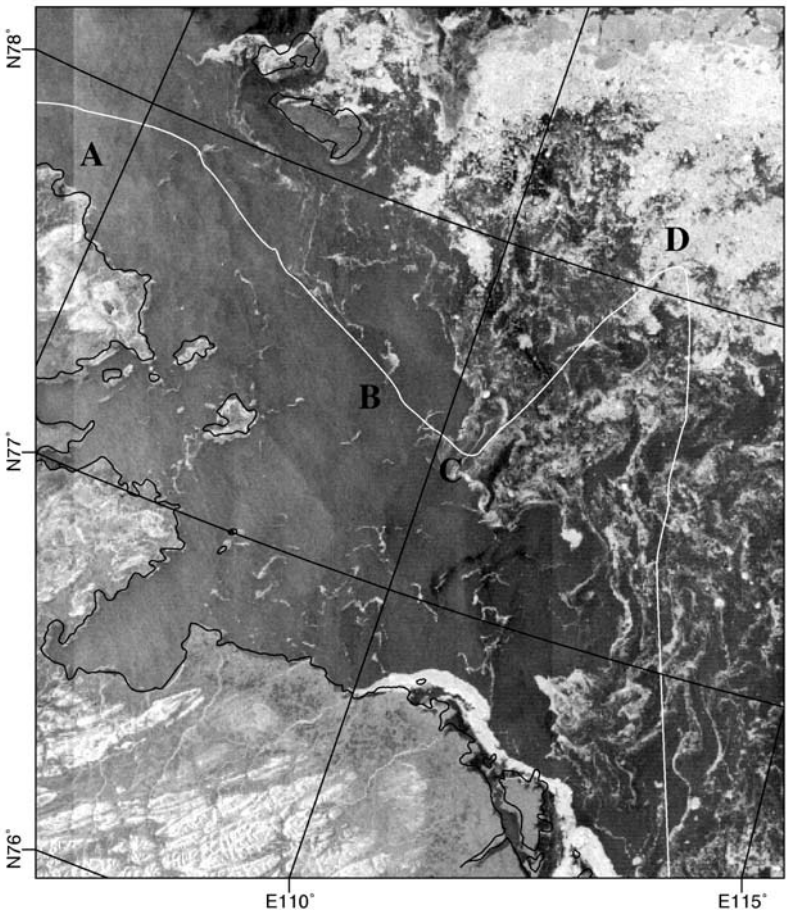

Figure 6.11(a). Subset of *Radarsat* ScanSAR image on 7 September 1997, showing the area east of Vilkitsky Strait. The line marks the track of the icebreaker *Sovetsky Soyuz*, which sailed in the area on 10–11 September. The points A–D mark different characteristic ice conditions documented by observations onboard the icebreaker (see Figure 6.12) (© Canadian Space Agency).

The area west of 110°E, between points A and C, was dominated by open water and new ice. Also, nilas and pancake ice were observed. A number of photographs of the different ice types were taken and are presented in Figure 6.12. Due to low wind velocities (3–4 m s^{-1}) open water had a similar low backscatter to that of grease ice and nilas, and this area appears as a homogenous grayish signature in the SAR image. Several bands of thick first-year ice were observed here, and the largest can be seen as bright meandering features against a darker background in the SAR image. Following the icebreaker track east of 110°E from point C in Figure 6.11(a), both total ice concentration and partial concentrations of nilas and first-year ice increased to more than 60–70%. Sea ice concentration and floe size increased to 80–90% and 50–200 m, respectively, and the ice thickness was about 100–150 cm. The SAR signature of first-

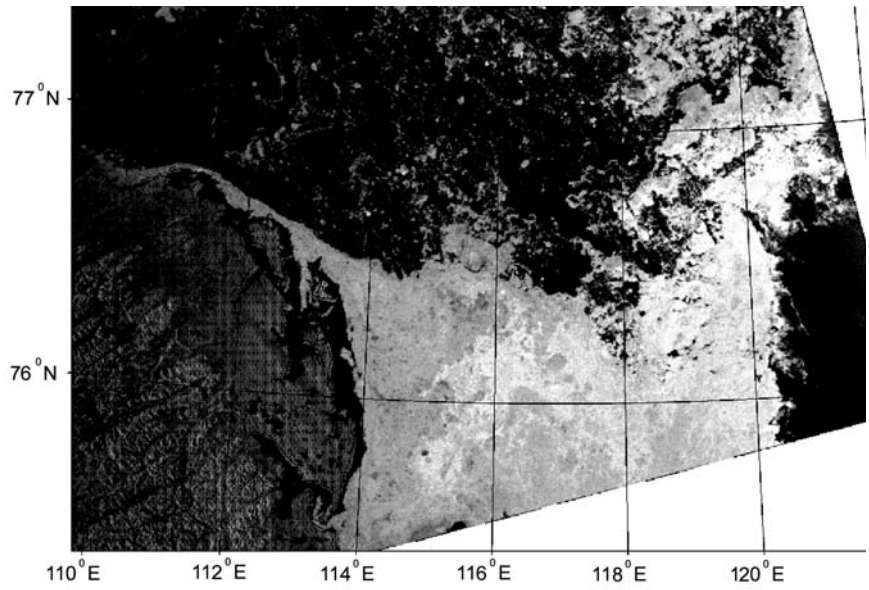

Figure 6.11(b). Subset of *Radarsat* ScanSAR image on 4 September, showing the area east of Vilkitsky Strait where the Taymyr ice massif reaches the mainland coast (© Canadian Space Agency) (see also color section).

year ice is relatively bright and can be well-distinguished. Following the *Sovetsky Soyuz* track south of 78°00′N, the sea ice consisted of grease ice, nilas pancake ice and first-year ice, and the fraction of the latter was down to 10–20%.

A subset of the ScanSAR image of 4 September, presented in Figure 6.11(b), covers a part of the Taymyr ice massif—with an ice concentration of 90–100—which extended towards the coast at 114°E and south of 76°30°N. The icebreaker *Yamal* sailed through this area on 4 September, and the icebreaker *Sovetsky Soyuz* crossed it 1 week later. The helicopter ice reconnaissance, conducted on 10 September, showed that this ice band moved eastwards 20–30 km compared with the SAR image of 4 September. This information was used to minimize the sailing route in compact sea ice.

The conclusion of this first experiment with wide-swath SAR images was that such images are very useful as supplements to traditional ice maps. ScanSAR provides much better coverage than *ERS* SAR and the selection of scenes corresponding to a given ship route is simplified. Ice edge position, ice concentration, large ice floes, ice bands in open water and ice drift vectors can be determined from ScanSAR data (Sandven *et al.*, 2001).

6.1.6 The Ice Routes and ARCDEV expeditions in 1998

Sea ice conditions in the Kara Sea during the winter of 1998 were heavier than average and the need for high-resolution SAR images in ice navigation was more pronounced

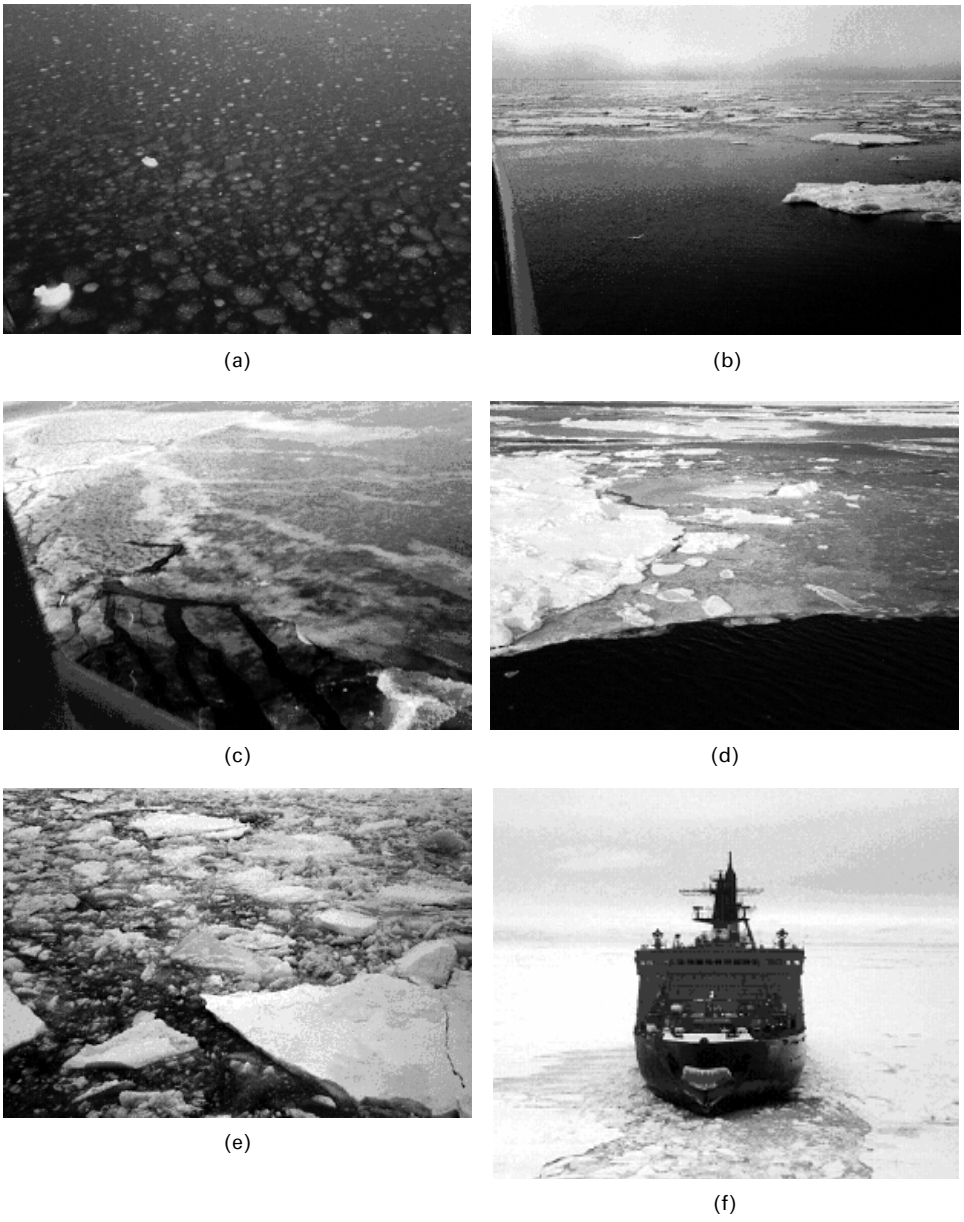

Figure 6.12. Photographs of different ice conditions observed by icebreaker *Sovetsky Soyuz* on 10–11 September within the SAR image of 7 September: (a) and (b) were taken along the section A–C in Figure 6.11(a), showing new ice and floes of first-year ice, respectively; (c) and (d) were taken at point C; and (e) and (f) were taken at point D where up to 1.5 m thick first-year ice dominated. The icebreaker *Sovetsky Soyuz* had a *rendezvous* with icebreaker *Yamal* (f) at this position.

than in previous expeditions. In April the ice conditions in the Kara Gate were severe and difficult even for the largest icebreakers which ran the risk of becoming stuck in the ice. Based on meteorological and sea ice information, the MOH for the area decided to use the route north of Novaya Zemlya for steering convoys between Murmansk and the Yenisey and Ob' estuaries. This route was significantly longer than that through the Kara Gate, but the ice conditions were more favorable. *Radarsat* ScanSAR and *ERS-2* SAR data were acquired to support two expeditions following the route north of Novaya Zemlya. One was with the icebreaker *Sovetsky Soyuz*, escorting convoys from the ice edge in the Barents Sea to the Yenisey Gulf (Alexandrov *et al.*, 1998). The other expedition took place at the same time (the ARCDEV expedition) with the Finnish tanker *Uikku* escorted by *Kapitan Dranitsyn*. This expedition started in Murmansk and had as its destination Sabeta in the Ob' estuary. Both expeditions used SAR images to support winter navigation ice conditions and conduct sea ice observations for later use in SAR image interpretation. The Arctic Demonstration and Exploratory Voyage (ARCDEV) expedition was a scientific expedition supported by the EU with the aim of exploring the technical and logistic challenges for transport of gas condensate (LNG) from the Yamal Peninsula to the market in Europe (Pettersson *et al.*, 1999a, b).

ScanSAR images covering most of the sailing routes were obtained before and during the expeditions. Transmission of images was done regularly since the ships were within range of Inmarsat for the duration of the expeditions. Compressed images with a file size of 200–300 KB and a resolution of 250 m were transmitted in a few minutes. This procedure made it possible to have SAR images onboard icebreakers within 5–6 h of the satellite overpass.

The expedition with the Sovetsky Soyuz

The sailing route of the *Sovetsky Soyuz* is overlaid on a mosaic of *Radarsat* ScanSAR and *ERS* SAR images in Figure 6.13, providing an overview of all SAR images used in the expedition. The images were used to map polynyas, leads, areas of level and ridged ice, and other ice features which were important for route selection. In the severe ice conditions to the north of Novaya Zemlya and in the central part of the Kara Sea, the use of SAR imagery was supplemented by helicopter ice reconnaissance (Alexandrov *et al.*, 2000b). Visual sea ice observations, photographs and video-recordings—made onboard the icebreaker—were used to describe the SAR signatures of various ice types and features evident in the ScanSAR mosaic. New, young and thin first-year ice was observed between the ice edge in the Barents Sea and the coast of Novaya Zemlya. The rather bright SAR signature of area E corresponds to gray–white and thin first-year ice with typical floe sizes of approximately 10 m. SAR signatures of polynyas (areas A) can change considerably depending on sea ice type and deformation. The shore polynya west of Novaya Zemlya (area A1), covered with young ice, is evident as a homogenous light tone. Rough young and first-year ice was observed in the Yamal polynya as a light tone and has an inhomogenous texture (area A2). Wind-roughened water in the polynya west of Vaygach Island has the highest backscatter (area A3).

Thick and medium first-year ice observed to the north and east of Novaya Zemlya

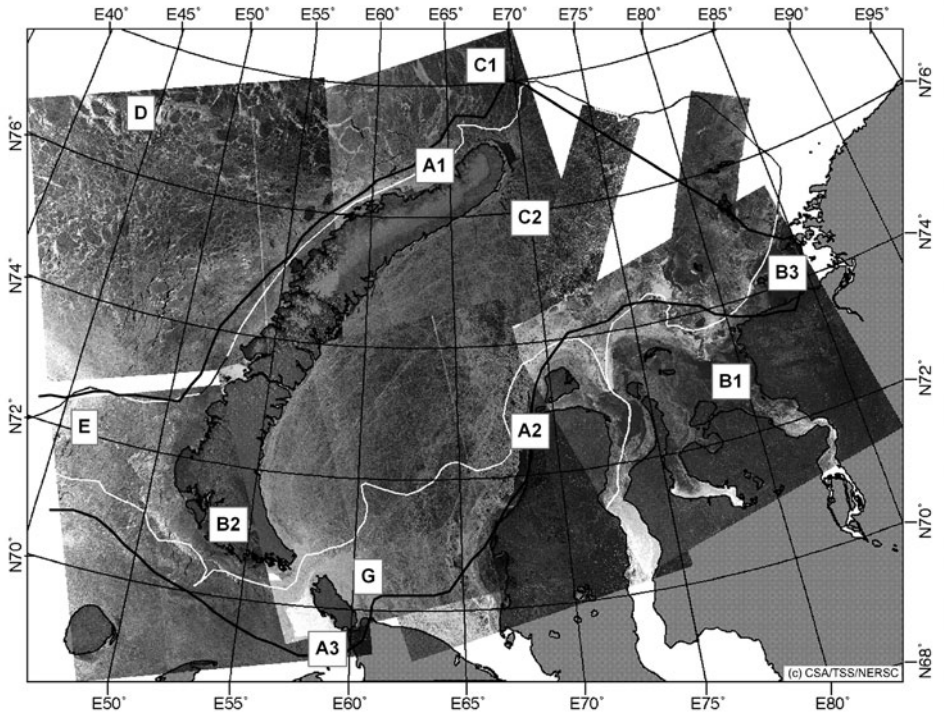

Figure 6.13. Mosaic of six ScanSAR and two *ERS* scenes for the period 23 April–8 May 1998. Sailing routes are shown for the *Sovetsky Soyuz* expedition (black line) and the ARCDEV expedition (white line). Description of the characteristic ice areas (A, B,. . ., G) is presented in the text.

(areas C1 and C2) has a homogenous dark signature for level ice and a lighter one for deformed ice. Level first-year fast ice (areas B1 and B2) is evident as a dark tone similar to that of calm open water. Ridged river ice can be distinguished from level ice by its bright tone. Giant first-year ice floes in the eastern part of the Barents Sea (area D) can easily be detected from surrounding leads. New and young ice, interleaved with medium and thick first-year ice, were observed along the sailing route from Dikson to Belyi Island. Medium and thick first-year ice prevailed in the southwestern part of the Kara Sea. East of Vaygach Island (area G) heavily ridged first-year ice can be detected by its light tone.

SAR image analysis has shown that several important sea ice parameters—such as new, young, first-year and old ice types, old and fast ice boundaries, flaw polynyas, wide leads, giant, vast and big ice floes, and large areas of rough ice—can be detected in *Radarsat* ScanSAR images. It was found that the radar backscatter signatures of different ice types could be rather similar—as, for instance, those of young ice and deformed first-year ice. Further analysis revealed that full-resolution ScanSAR images are particularly suited for discrimination of narrow leads and level areas in compact sea ice. It was therefore recommended to use full-resolution sub-images

onboard icebreakers during their operations in compact thick ice, if possible, for operational reasons (Alexandrov *et al.*, 2004).

The ARCDEV expedition

The main objective of the ARCDEV (Arctic Demonstration and Exploratory Voyage) expedition was to investigate the possibility of year-round ship transportation of gas condensate from Sabeta on the Ob' River to the European market (Pettersson *et al.*, 1999a, b). The expedition onboard the Finnish ice class tanker M/T *Uikku* was the first winter ice navigation operation of a merchant tanker to the Ob' estuary. The icebreaker *Kapitan Dranitsyn*, which escorted *Uikku*, was also used as a research platform for the ARCDEV project. About 80 scientists onboard *Kapitan Dranitsyn* performed extensive sea ice and ship performance studies. During the first part of the expedition the ARCDEV convoy followed the same route as the *Sovetsky Soyuz*. The same set of ScanSAR images was transmitted to the *Kapitan Dranitsyn* to support the navigation in ice.

Ice navigation in the Ob' estuary was extremely hard, especially in the winter of 1998. Freshwater ice is usually harder than more saline ice, and shallow water depths hamper the removal of broken ice and ridges when icebreakers plow their way through the ice cover. In shallow estuaries sea ice vessels' keels can easily strike the sea floor. The areas of deformed river ice can cause serious difficulties for icebreakers. It is therefore necessary to avoid ridged ice in estuaries. Optical satellite instruments cannot detect ridges or ridged areas. SAR images, on the other hand, can discriminate between level and deformed ice and also detect individual ridges. For this purpose, several SAR scenes, particularly from the Ob' estuary, were acquired before the voyage for use in planning the optimal route through the estuary; these images included ERS images with higher resolution than ScanSAR images. Large parts of the sea ice in the estuary are level fast ice with a very dark radar signature, as shown in Figure 6.14. Farther into the estuary the ice gets more ridged as shown by the brighter signatures. An optimal sailing route was selected through areas with level ice, avoiding heavy deformed ice. Ice experts at the marine operations headquarters for the area found SAR to be vital for detailed route planning in the estuary. They sent a list of geographical positions for the optimal route to the captain of the icebreaker *Vaygach*, who had the task of preparing a channel through the heavy fast ice before the *Uikku* and *Kapitan Dranitsyn* arrived in the area. The *ERS-2* SAR image for 6 May in Figure 6.15 was acquired after the *Kapitan Dranitsyn* and the *Uikku* had sailed to Sabeta using the prepared channel. *In situ* ice observations from the *Kapitan Dranitsyn* confirmed that the optimal route with easier ice conditions had been selected.

The Ice Routes and ARCDEV expeditions documented *Radarsat* ScanSAR images as being particularly important for supporting navigation during the heavy ice conditions encountered in April–May 1998. The navigational speed of the convoy is a good measure of the efficiency of navigation. Speed depends heavily on local ice conditions and detailed route planning in these areas. During the ARCDEV expedition, the convoy speed was below 5 knots for 30% of the expedition time. However, areas of low convoy speed were confined to relatively short distances along the overall

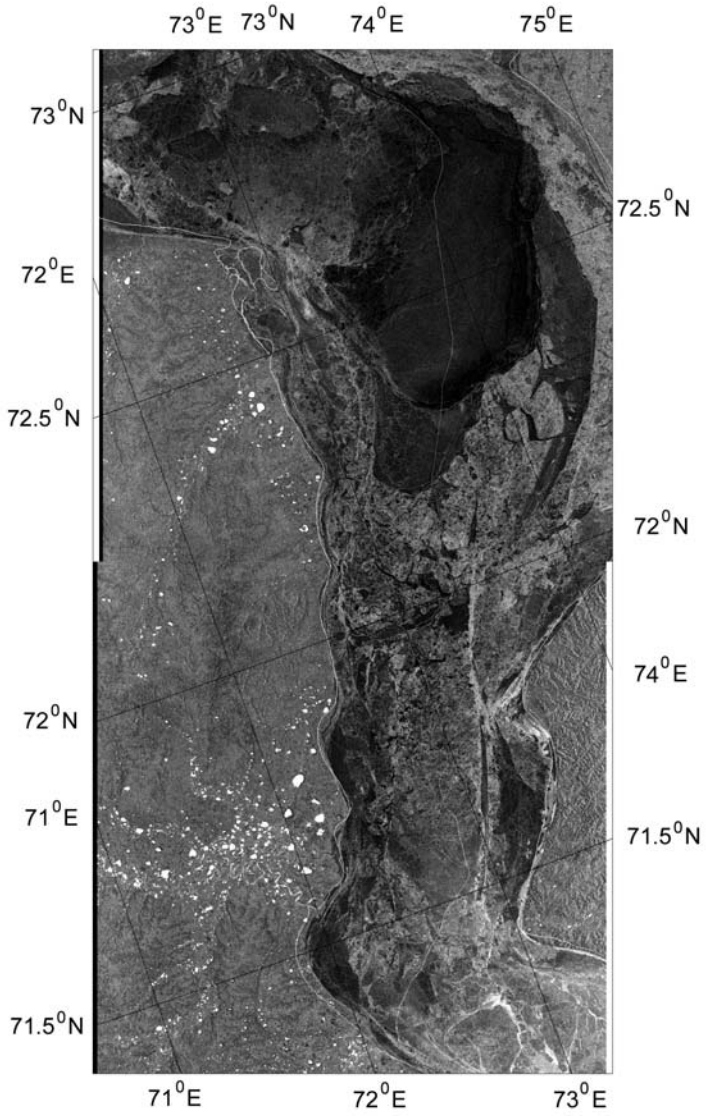

Figure 6.14. *ERS-2* SAR of 6 May 1998, covering the Ob' estuary. The ice channel of the ARCDEV convoy is seen as a bright line in the image (© European Space Agency).

sailing route. Detailed analysis of SAR and other satellite data and use of the ice information for planning sailing routes improved the general convoy speed by a factor of at least 2. In other words, the sailing time for the convoys would have been twice as long without the detailed ice information provided by satellite data. This factor was higher in the Ob' estuary, because the sailing time could easily become much larger here due to the risk of getting stuck in ridges.

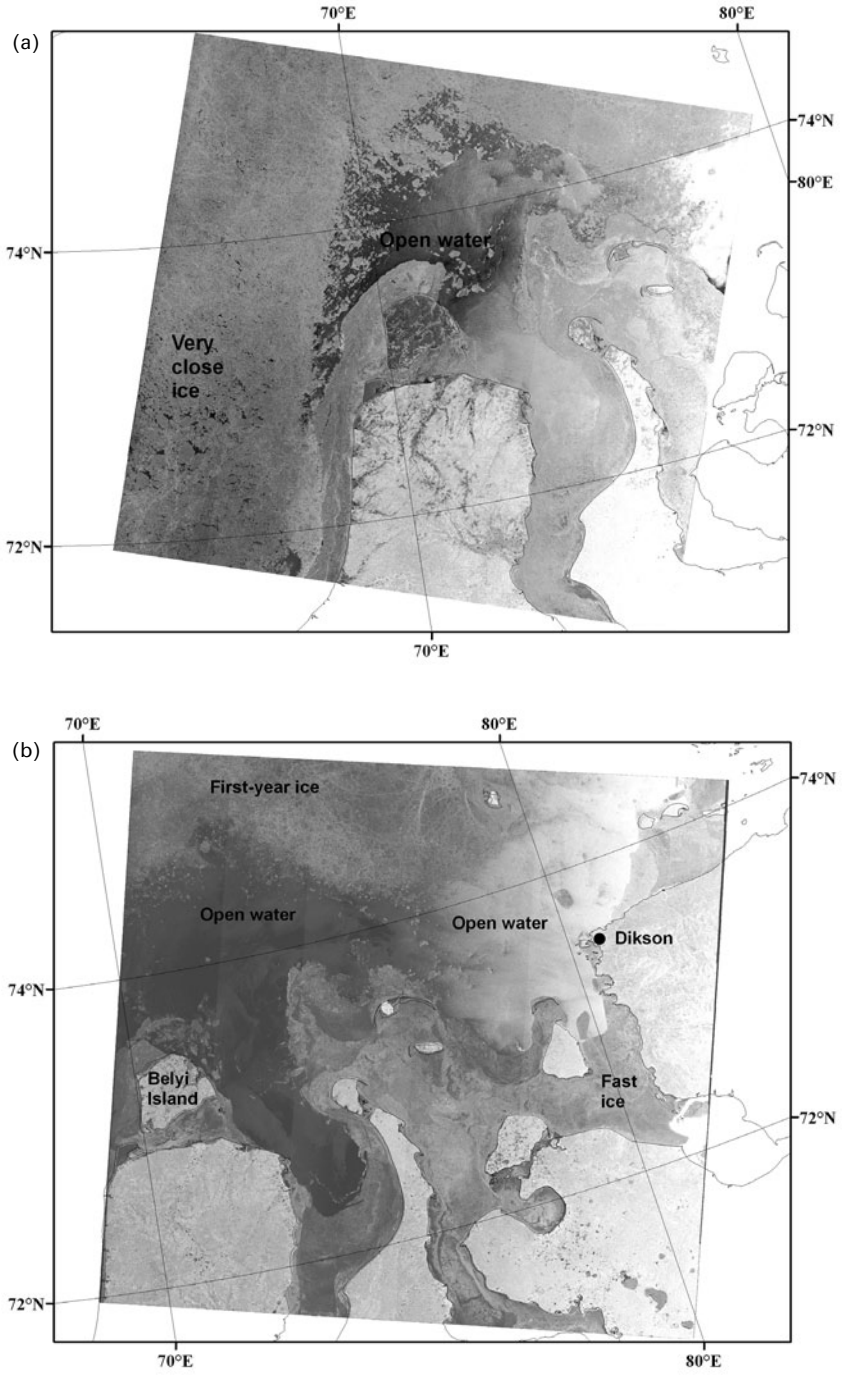

Figure 6.15. Annotated *Envisat* ASAR scenes of the Kara Sea for 20 June (a) and 27 June (b) 2003 (© European Space Agency).

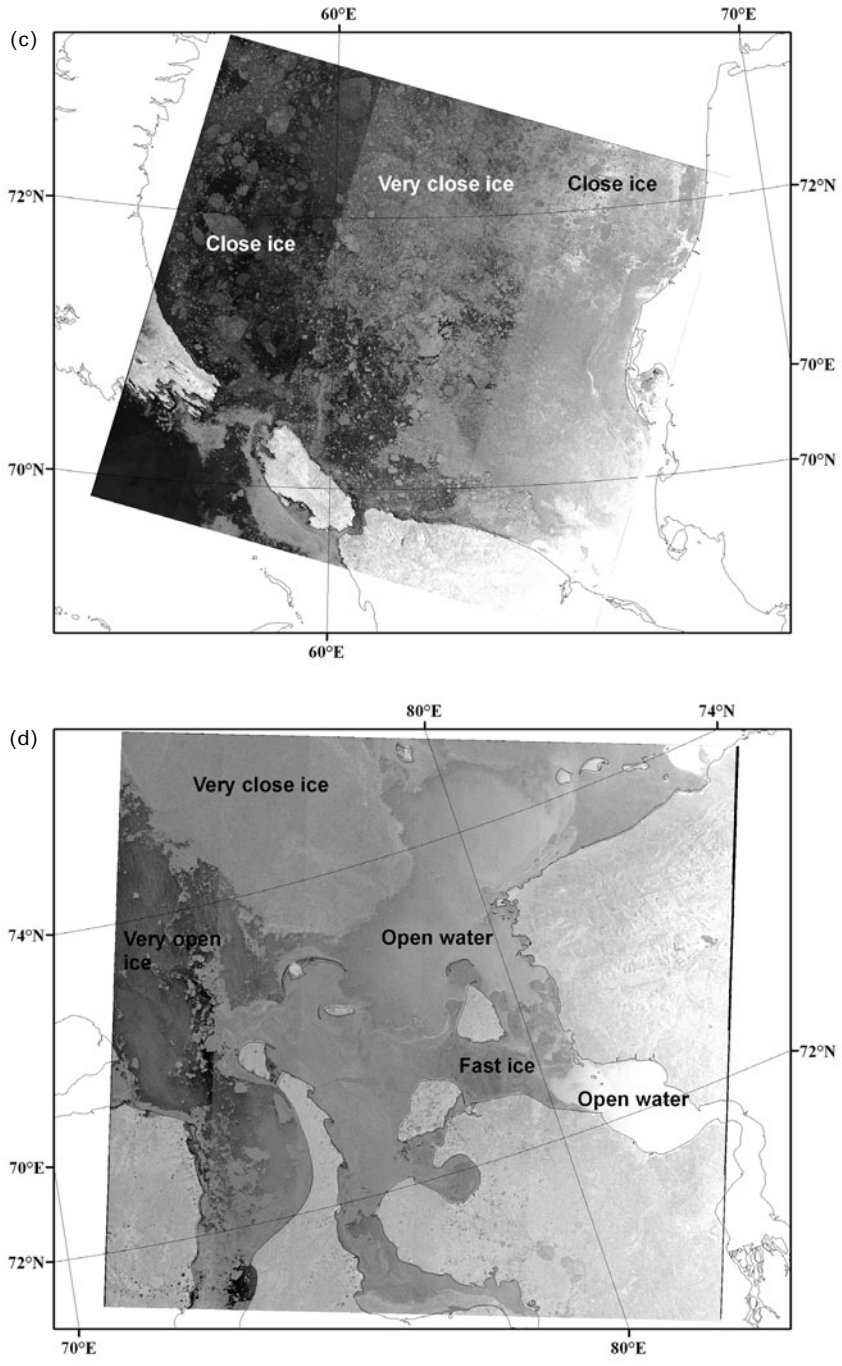

Figure 6.15 (*cont.*). Annotated *Envisat* ASAR scenes of the Kara Sea for 5 July (c) and 10 July (d) 2003 (© European Space Agency).

6.2 *ENVISAT* ASAR PERIOD FROM 2003 (*O.M. Johannessen, S. Sandven, K. Kloster, N.G. Babich, V.Ye. Alexandrov, L.P. Bobylev, M. Babiker, L.H. Pettersson*)

The advanced synthetic aperture radar (ASAR) on *Envisat*, launched in March 2002, provides several new modes of operation, including dual-polarization which represents a further technological development of spaceborne SAR systems. *Envisat* ASAR has improved the capability to map sea ice using wide-swath SAR data. The swath width of ASAR in wide-swath (WS) mode is 420 km. With a 35-day repeat cycle and a sub-cycle of 3 days it is feasible to cover most sea ice areas every 3 days using ASAR. With both HH-polarized *Radarsat* images and VV-polarized ASAR images, the possibility to observe sea ice in the NSR has increased. In addition, ASAR provides alternating polarization images in 100-km swath width.

6.2.1 *Envisat* demonstration in summer 2003

In summer (June–July) 2003, ASAR images were used for the first time in the NSR during an expedition onboard the *Sovetsky Soyuz* in the Kara Sea to the Yenisey Gulf (Sandven *et al.*, 2004). During this period, six *Envisat* wide-swath ASAR images were acquired and transmitted to MSC Headquarters and directly to the icebreaker. Descending orbits were preferred since they are acquired in early morning and thus processed for distribution on the same day. ASAR images were transformed to polar stereographic projection, resampled to 300-m pixel size and compressed to about 100 KB. Transmission to the *Sovetsky Soyuz* was done by Inmarsat as in previous expeditions. Several examples of ASAR images transmitted onboard the icebreaker are shown in Figure 6.15. The image from 20 June shows large areas of open water and low-concentration ice in the central part of the Kara Sea and very closed ice westward of Belyi Island. Another image from 27 June also shows large areas of open water in the central Kara Sea between Belyi Island and Dikson. Both images show the fast ice in the Ob' and Yenisey estuaries. In the images of 5 and 10 July it can be seen that the fast ice in the Yenisey Gulf has broken up. Using this information the icebreaker *Sovetsky Soyuz* steered the convoy from Dikson to the Kara Gate. ASAR images proved to have the same capability to observe sea ice features for ice navigation as the ScanSAR images in previous expeditions. Most of the sea ice features in HH-polarized ScanSAR images are also recognized in C-band ASAR data.

During the expedition, a sea ice specialist from AARI composed ice charts from ASAR images. The ice charts were produced using ArcView software, and presentation of the charts was done using the electronic navigation information system (ECNIS) onboard the icebreaker. The ECNIS system is used by the navigator to find icebreaker positions overlaid on the satellite images and ice charts. The system is used to assess sea ice conditions and select the optimal ship route.

Two winter experiments using *Envisat* ASAR images were performed in 2004 and 2005 in connection with icebreaker expeditions in the Kara Sea region. ASAR wide-swath images were obtained from Tromsø Satellite Station and from ESA's receiving

station in Kiruna. The images were averaged to 600-m resolution, geolocated and compressed to about 200 KB before transmission to the MOH for the area. The images were used by the MOH to make route plans for all the icebreakers and convoys operated by the Murmansk Shipping Company. The images and the results of ice analysis were transmitted to the nuclear icebreakers *Yamal*, *Sovetsky Soyuz*, *Arktika*, *Vaygach* and *Taymyr* via TV channels of the Russian "Orbita" system. This is a satellite system used between the MOH and all the icebreakers.

6.2.2 Winter–spring 2004

Starting in February 2004, ASAR images for the Kara Sea region were obtained about once per week. The images were used in navigation which took place mainly along the coast through the Kara Gate, to Belyi Island and then to Dikson. The ASAR images in early February showed large areas of open water south of Novaya Zemlya and very close ice in the southwestern part of the Kara Sea. A series of ASAR images obtained from February to May, shown in Figure 6.16, were used to analyze the ice conditions. The fast ice boundary and areas of various degrees of deformation can be observed in the images. Furthermore, thin first-year ice located north of fast ice is clearly evident in the images from February. The icebreakers *Arktika* and *Sovetsky Soyuz* were steering convoys from the west to Dikson and to the icebreaker *Taymyr*, operating on the Yenisey. The wide flaw polynya in the Ob'–Yenisey region, covered with young ice, can clearly be seen in the ASAR image of 24 February. The image on 11 March shows that first-year ice moved northward in this period and young ice prevailed south of 75°N. Using this information, the *Sovetsky Soyuz* steered a convoy from Dikson through this ice and then in a lead along the western coast of the Arctic Institute and Izvestiy TSIK islands to Cape Zhelaniya. The 11 March images show that another possibility was to sail in the area between 74°N–75°N and 72°E–76°E. The ASAR image for 23 March showed that gray–white ice and thin first-year ice prevail in the Ob'–Yenisey region. Based on this information the convoy selected the route to Tambey along a lead on the eastern side of the Ob' Gulf. Images of the Yenisey Gulf can distinguish between level and deformed fast ice including the ice channel made by the icebreakers.

The acquisition of *Envisat* images for delivery to the MSC continued in May and June 2004. Examples of images from this period when the ice is melting are shown in Figure 6.17. On 23 May the polynya north of Belyi Island and in the Ob' Gulf can clearly be seen by the bright signature representing open water. Wide areas of open ice can be seen north of the fast ice in the central part of the Kara Sea on 11 June. The SAR signature of fast ice became homogenous, implying that areas of level and rough ice cannot be distinguished. On 17 June the advance of melting is evident with large areas of open water and very open ice. On 24 June most of the image shows open water while the fast ice boundary is almost unchanged. The Yenisey Gulf is an exception, revealing fast ice broken into large floes which are drifting in the open water near Dikson.

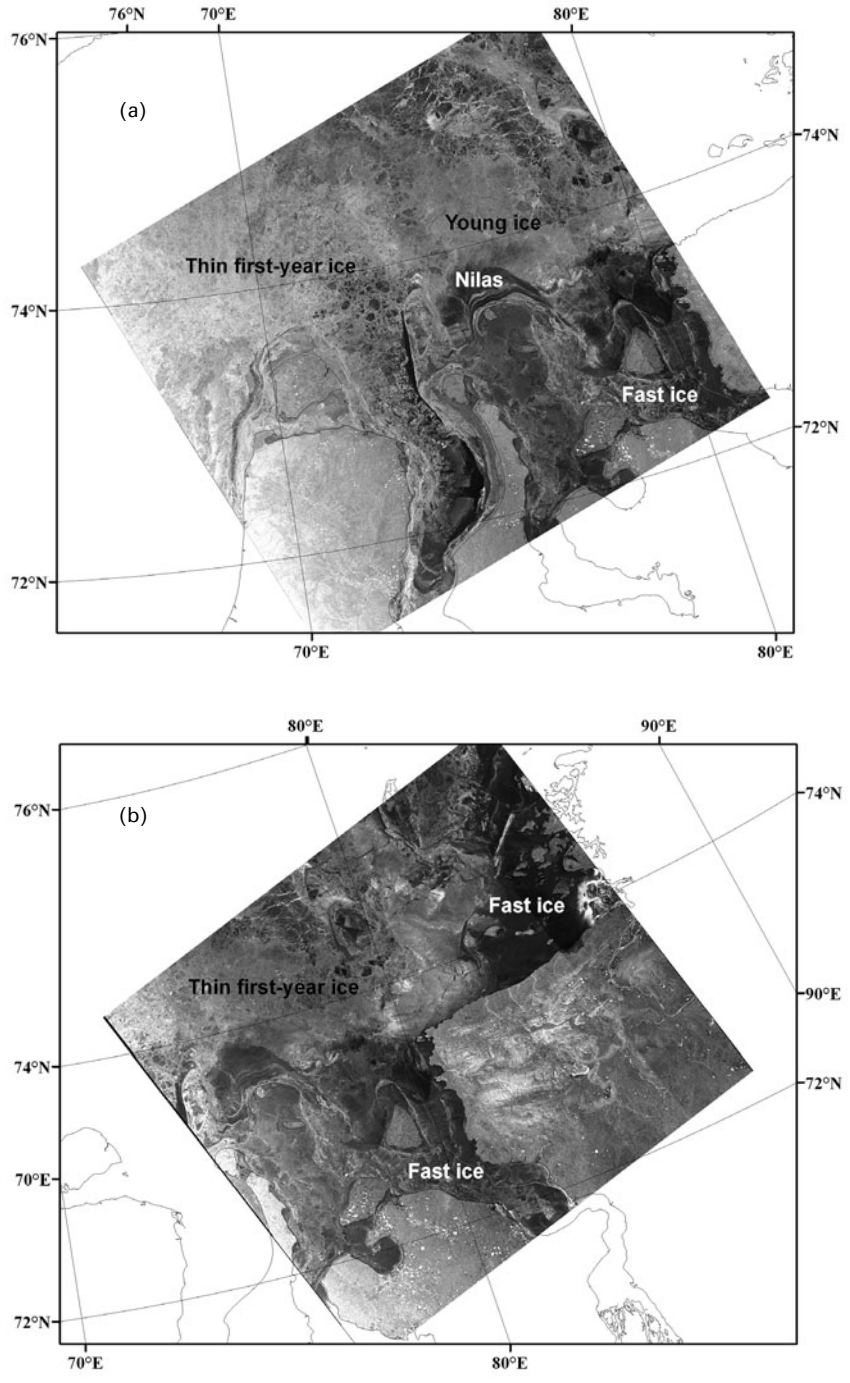

Figure 6.16. *Envisat* ASAR images in the Kara Sea during winter–spring 2004: (a) 14 February; (b) 18 February (© European Space Agency).

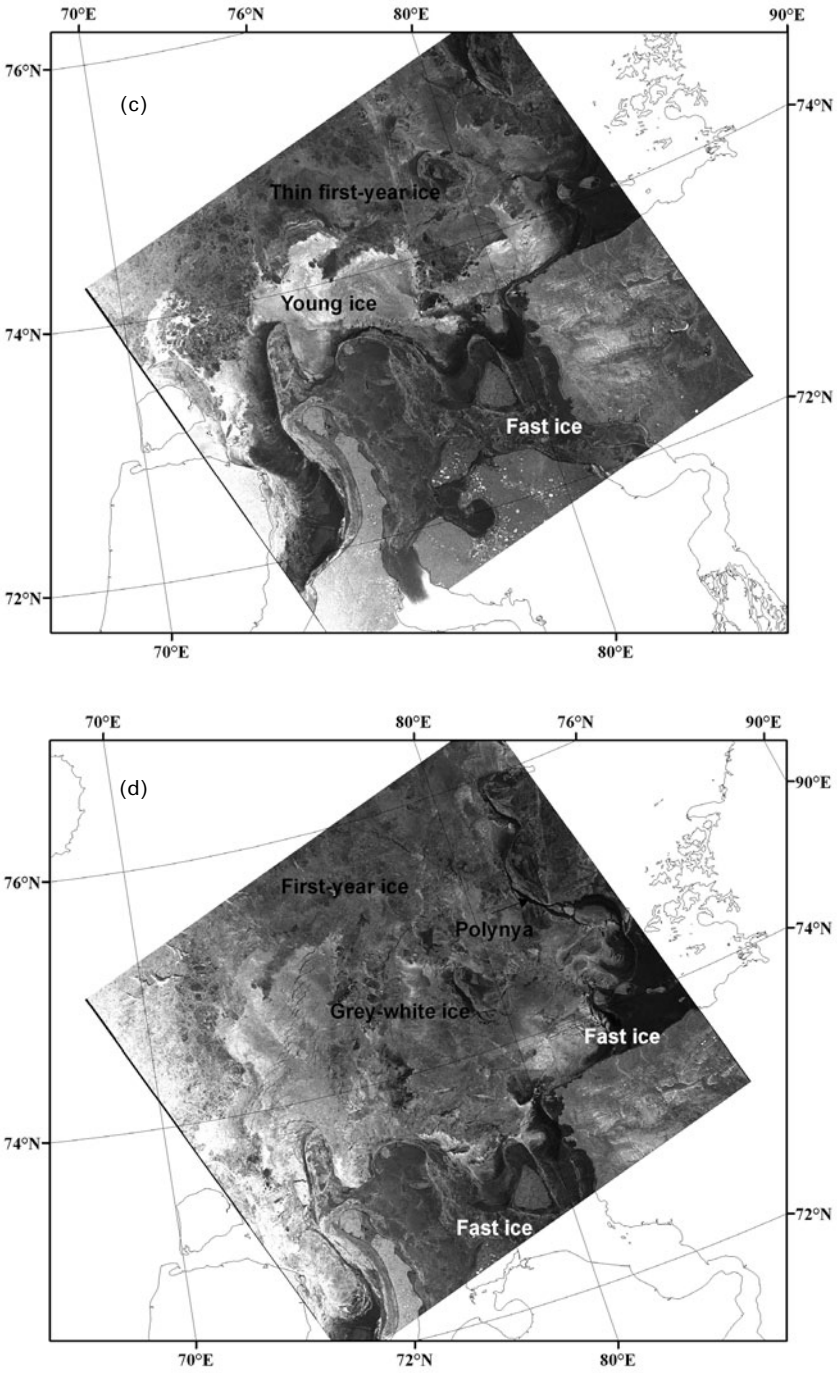

Figure 6.16 (*cont.*). *Envisat* ASAR images in the Kara Sea during winter–spring 2004: (c) 24 February; (d) 11 March (© European Space Agency).

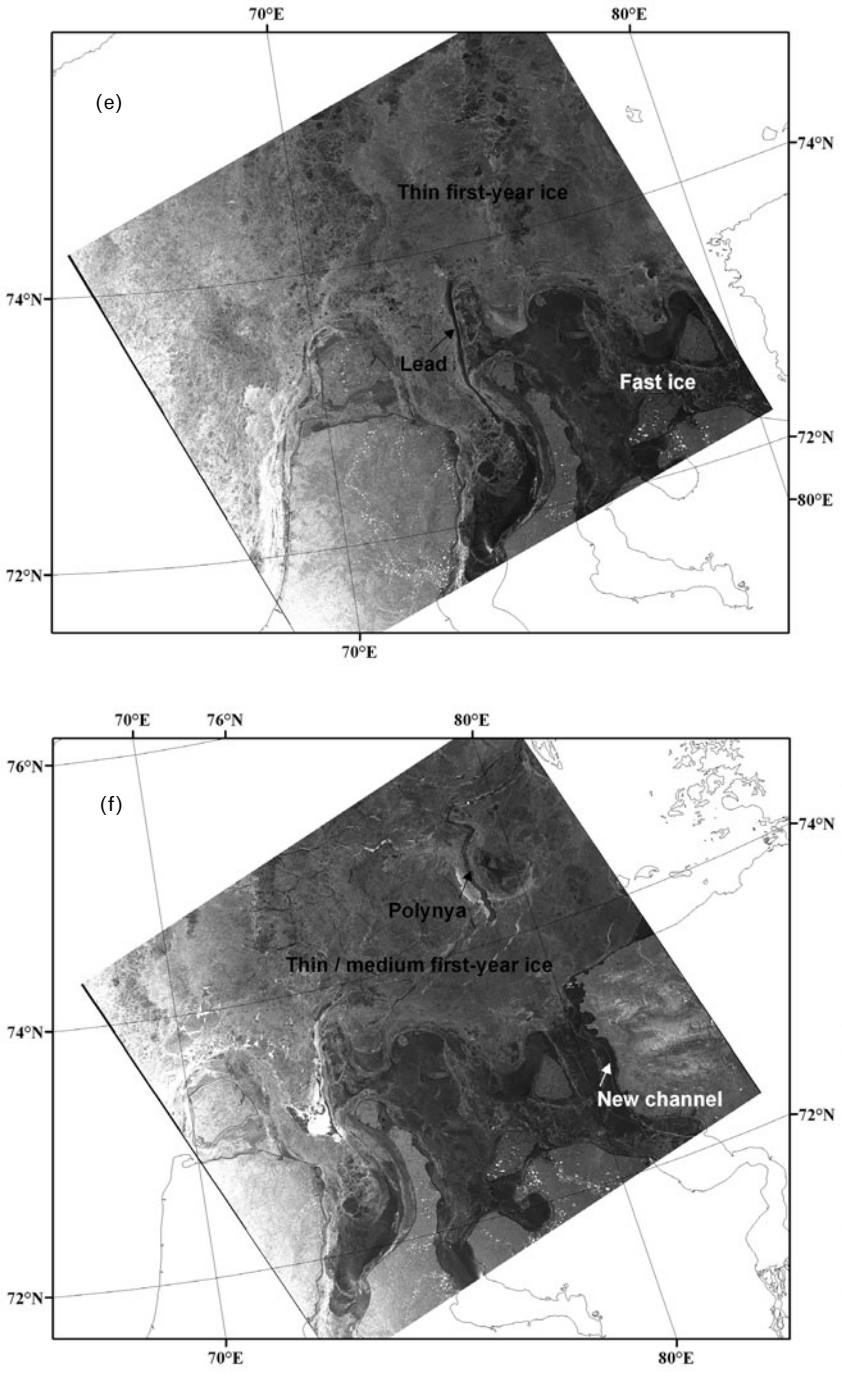

Figure 6.16 (*cont.*). *Envisat* ASAR images in the Kara Sea during winter–spring 2004: (e) 23 March; (f) 7 May (© European Space Agency).

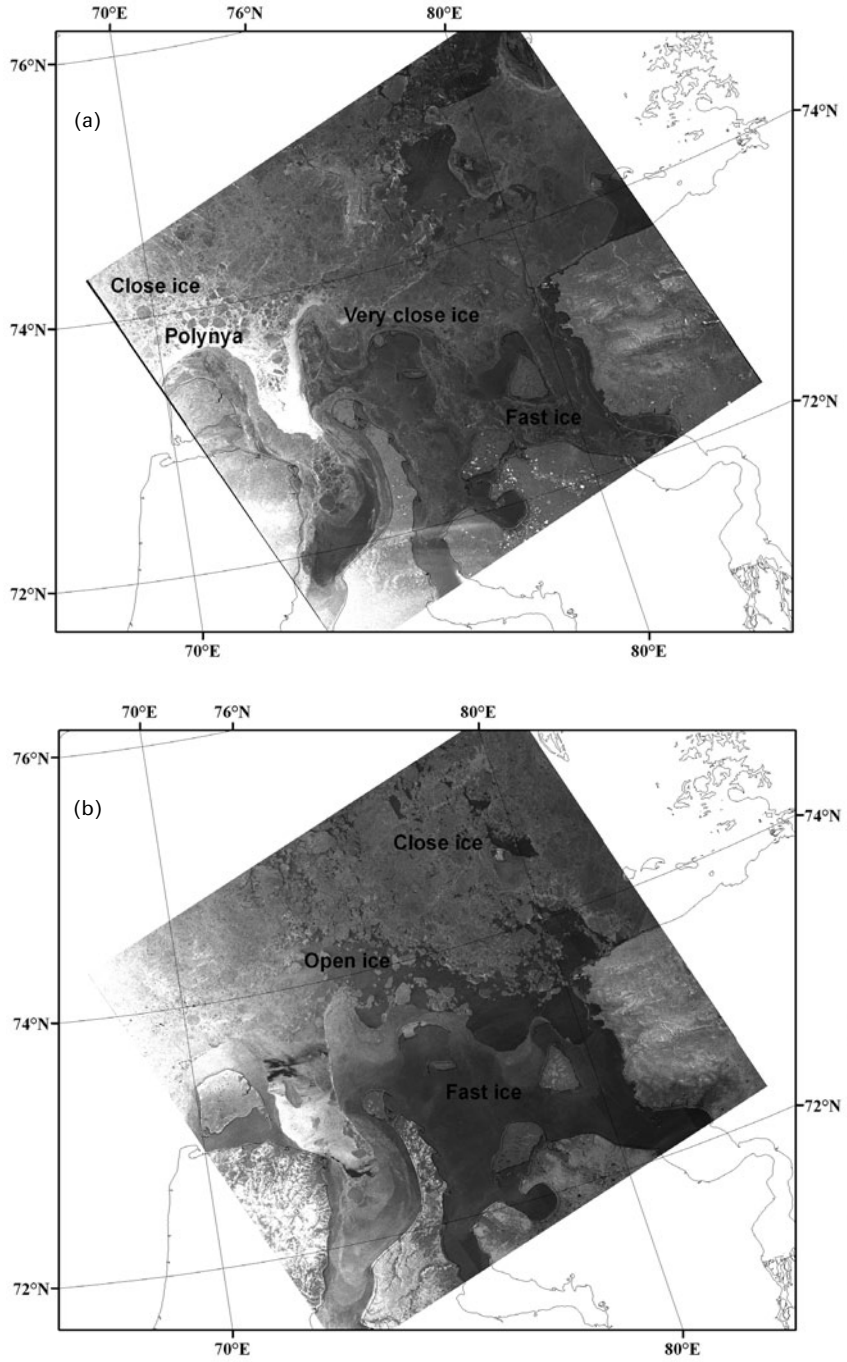

Figure 6.17. Examples of *Envisat* ASAR images in the central part of the Kara Sea during the melt season of 2004: (a) 23 May; (b) 11 June (© European Space Agency).

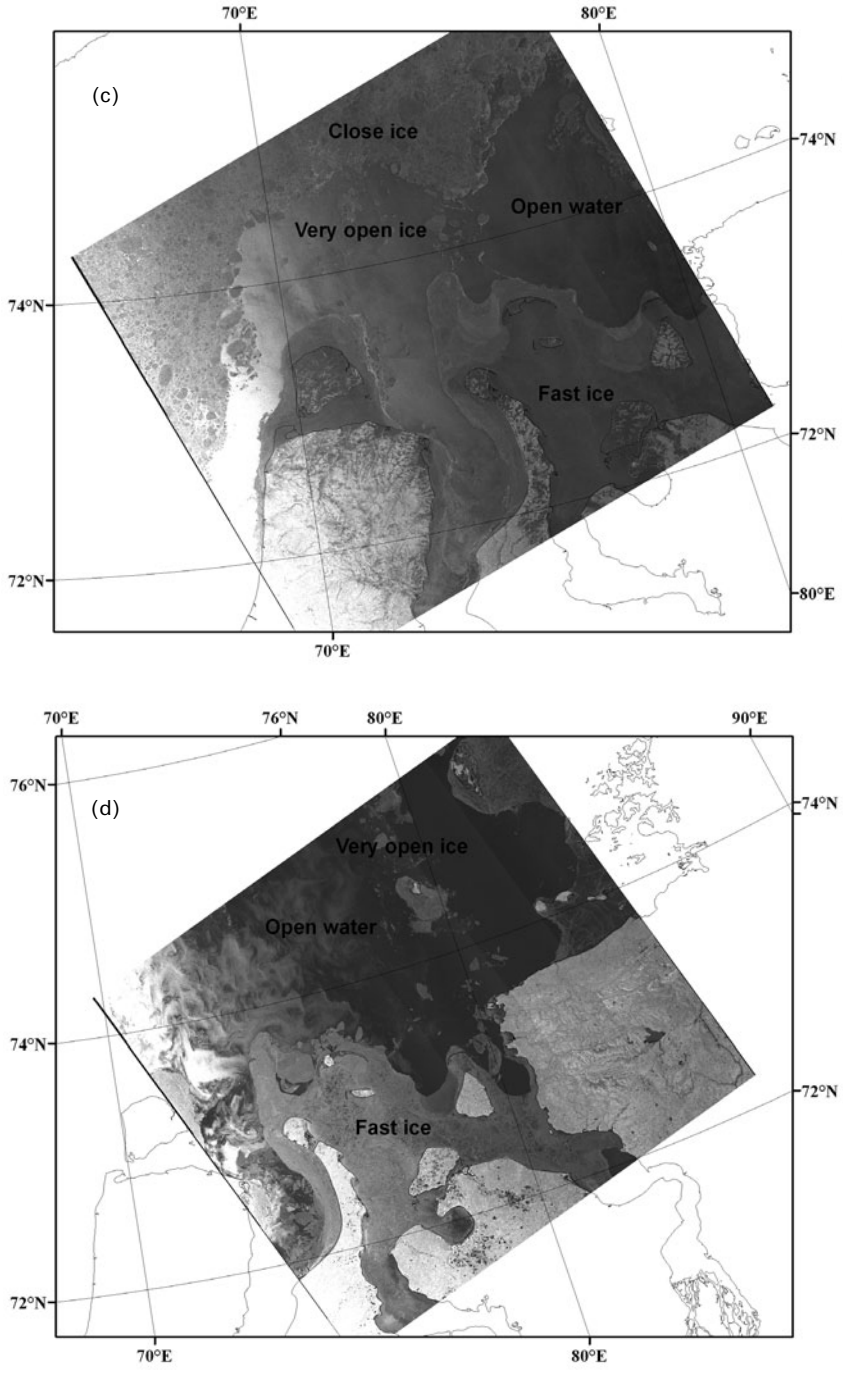

Figure 6.17 (*cont.*). Examples of *Envisat* ASAR images in the central part of the Kara Sea during the melt season of 2004: (c) 17 June; (d) 24 June (© European Space Agency).

6.2.3 *Envisat* demonstrations, winter–spring 2005

The freeze-up in the western part of the Kara Sea started in mid-October 2004. At that time, icebreakers began to support cargo vessels transporting nickel from Dudinka to Murmansk. In the following months the ice conditions were normal and transportation followed the common route through the Kara Gate Strait, along the coast northward of Belyi Island and then eastward to the Yenisey Gulf. Use of ASAR images to support navigation began in early February 2005. Several ASAR image stripes were obtained every week, which made it possible to produce image mosaics more or less regularly in the following months. This was a considerable improvement in data coverage over the ScanSAR mosaic made in 1998 (Figure 6.13). The ASAR images were used for two purposes. The first task was to determine general sea ice conditions of importance for navigation. This included accurate delineation of the fast ice boundary and zones of different types of drifting ice, flaw polynyas and areas of ice diverging, localization of deformation areas in ice massifs due to formation of cracks and fractures resulting from ice drift and compaction. The second task was to determine convoy formation sites and plan optimal routes for crossing ice areas.

The ASAR images were sent to the MOH and not directly to the icebreakers. This was done in agreement with the MOH in Murmansk, where sailing routes for different icebreakers were planned centrally. Recommended routes were transmitted from the MOH to the icebreakers as way-points.[3] The routes made maximum use of flaw polynyas; additionally, areas of thinner and less deformed ice were preferred. It was also important to avoid zones with the highest probability of thick ridged ice. For this purpose, synoptic weather maps and weather forecasts for 3–5 days in advance were used in combination with ice charts.

At the beginning of February the ice massif in the Kara Sea had shifted from the Novaya Zemlya side to the east, forming an area of strong ridging along the western coast of the Yamal peninsula and Belyi Island. Therefore, the MOH selected a new sailing route from the Kara Gate to Dikson along fracture zones avoiding the ridged ice along the Yamal coast. This sailing route is shown in the mosaic of ASAR images for the period 26–28 February in Figure 6.18. In the last week of February the icebreakers *Arktika* and *Taymyr* steered the nuclear cargo vessel *Sevmorput* to Dikson, and *Arktika* steered the vessel *Kandalaksha* in the opposite direction. ASAR images together with sea ice observations from the icebreakers showed that young ice covered vast areas east of Novaya Zemlya (area 1 in Figure 6.18). Moderately deformed, thin first-year ice prevailed further to the east (area 2), while an area of fractures extending in a northeasterly direction is observed in the center of the Kara Sea (area 3). The use of ASAR images contributed to an increase in the average speed of convoys by up to 40% in February, according to the MOH.

In early March *Arktika* steered the tanker *Varzuga* from the Kara Gate to the Ob' Gulf for shipment of gas condensate from the port of Tambey. The most important part of this operation was ice navigation in the Ob' Gulf. By using ASAR images, *Taymyr* made a channel through level fast ice, avoiding ridged areas. Again, it was

[3] Way-points are geographical coordinates defining the navigation route for a ship.

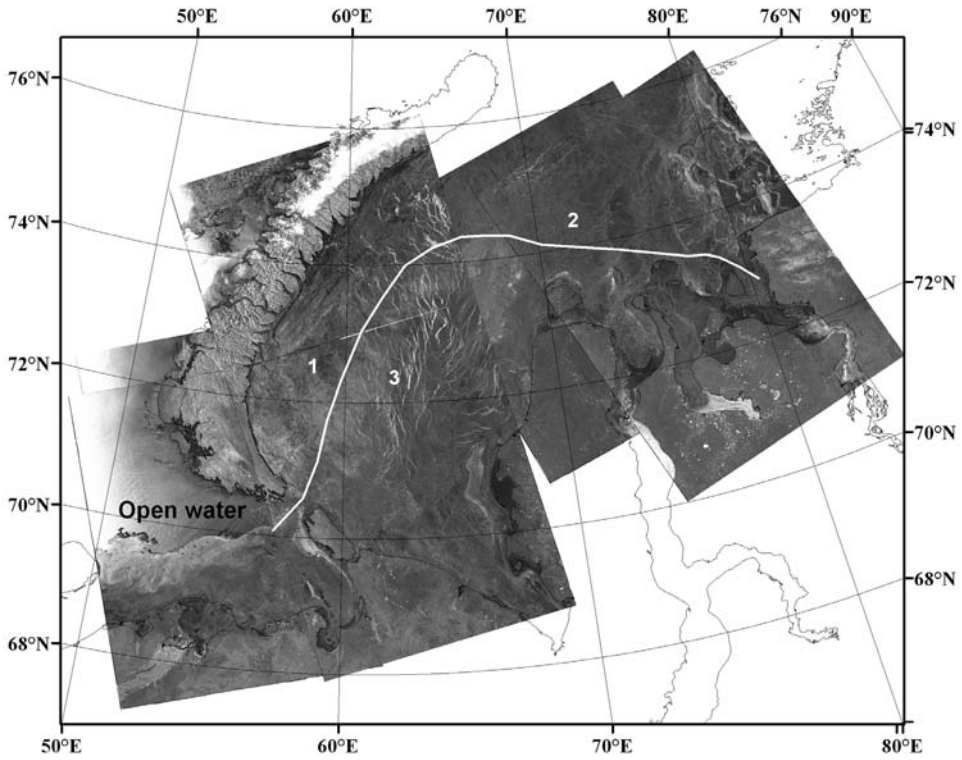

Figure 6.18. Mosaic of *Envisat* ASAR images for the Pechora and Kara Seas for 26–28 February 2005 with overlaid route of convoys: (1) area with gray and gray–white ice; (2) area with prevailing thin first-year ice; (3) area of fractures in ice cover (© European Space Agency).

confirmed that SAR images provide reliable discrimination of level and rough ice. The convoys between the Barents Sea and Dikson continued to use the route shown in Figure 6.18 during March. In late March, sea ice conditions changed in the central part of the Kara Sea, where the ice massif blocked the route north of Belyi and Vilkitsky Islands. As a result the average speed of convoys in this period decreased from 11 to 9.7 knots. The same route with minor changes was still used in early April. However, based on available *NOAA* images it was decided to navigate around Cape Zhelaniya as a consequence of ice conditions in this area being analyzed from ASAR images.

In the second part of April, convoys sailed from Dikson to the Arctic Institute and Izvestiy TSIK Islands, where easterly winds formed wide polynyas, and from here to Cape Zhelaniya across relatively level ice. This route is shown in the ASAR mosaic in Figure 6.19. Cargo ships could navigate without icebreaker support along the wide flaw polynyas on the west coast of Novaya Zemlya. This route was also used during May. The radar signatures along the sailing route in Figure 6.19 have been compared

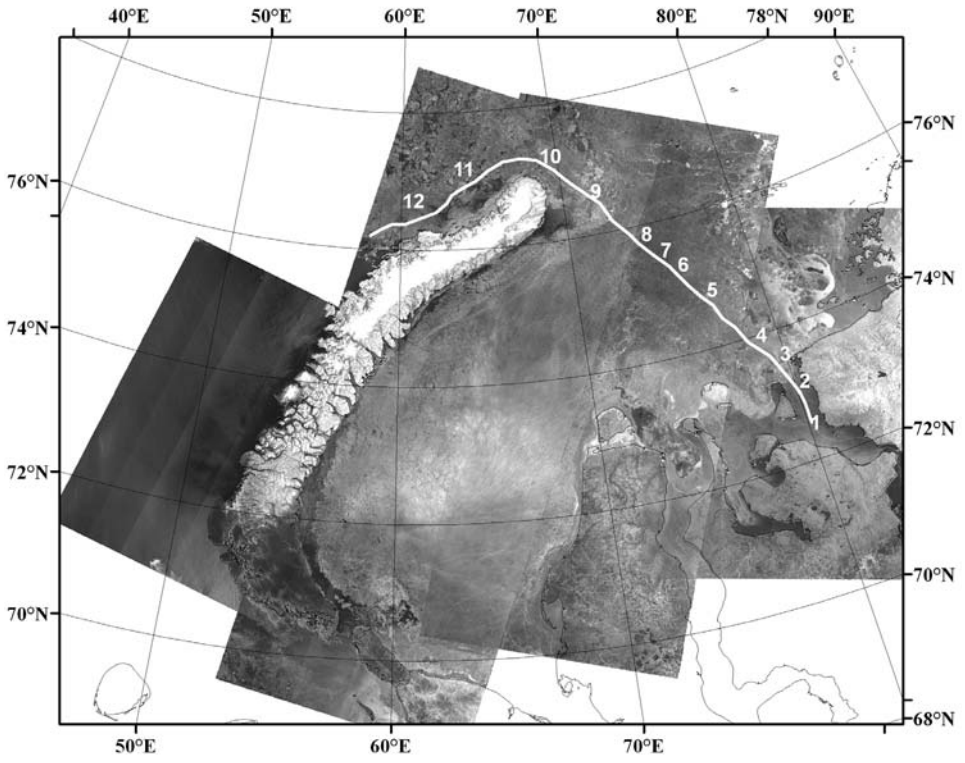

Figure 6.19. Mosaic of *Envisat* ASAR images for the Pechora and Kara Seas for 21–24 May 2005. The route of the convoy steered by the icebreakers *Arktika*, *Yamal* and *Vaygach* and points of *in situ* ice observations are overlaid (© European Space Agency).

with ship observations of sea ice. Starting in the Yenisey Gulf (point 1 in Figure 6.19), the thick first-year fast ice is characterized by a dark signature with a clearly visible boundary. The drifting ice north of the fast ice boundary has a brighter signature and consists of thin first-year and young ice (points 2–5). Farther north, the darker signature corresponds to very close ice. Here, first-year ice prevails, and variations in the signature from dark to slightly bright are caused by differences in surface roughness due to ridging and icefloe size (points 6–10). Thus, ice breccia and small floes of medium first-year ice (point 9) are shown as a brighter tone in the image. West of Novaya Zemlya, ice concentration decreases and some open water areas can be detected in the image (points 11 and 12).

Since sea ice conditions in the Kara Sea during the winter–spring of 2005 were easier than average conditions, the efficiency of using ASAR images was less pronounced. Nevertheless, the average speed of convoys through the ice was estimated by the MOH to increase by 30–40% as a result of using SAR data in navigation.

6.3 USE OF SAR DATA ONBOARD ICEBREAKERS (*K. Kloster, O.M. Johannessen, V.Yu. Alexandrov, S. Sandven, L.H. Pettersson*)

A methodology for using SAR and other remote-sensing data for icebreaker routing in sea ice has been developed since the first expedition with *L'Astrolabe*. The methodology includes SAR image ordering, production and delivery, processing and transmission to the icebreakers, as well as presentation and planning of the sailing route.

6.3.1 Processing of SAR images and transmission to icebreakers

SAR images need to be ordered in advance for *ERS*, *Envisat* and *Radarsat* data. The relevant ground-station handles scheduling and ordering procedures and receives raw SAR data. When raw data are downlinked to the receiving station, the processing involved in producing an image is normally also done at this station. The image is normally further processed at an image-processing center. When image products are ready, they are transmitted to the user, either directly onboard a ship or indirectly to a shore-based user. Processing steps are described in the following sections.

Processing of raw SAR data to make SAR images

SAR data transmitted from a satellite to the receiving station consist of a signal data set including instrument and satellite parameters for processing. This data set is called "raw data" and can be processed to make a SAR image using special algorithms running on fast computers in a few minutes. The resulting SAR image is presented in a coordinate system of ground range (across-track or "range") and azimuth distance (along-track), with square pixels. This projection is called "path-oriented" since its centerline is at a fixed distance from the satellite ground path.

SAR images are also characterized by the amount of speckle noise, given in dB or, alternatively, given as number of "equivalent looks". This characteristic noise in SAR images can be reduced only by increasing pixel size. Images may therefore be delivered at different pixel sizes, depending on the required file size and acceptable amount of speckle noise. The smallest pixel size delivered is defined by instrument resolution. It is often chosen to be one-half the resolution of the sensor. A suitable number of looks is applied to azimuth processing. For an *ERS* SAR full-resolution image (FRI), resolution is approximately 25 m with three looks in azimuth, which corresponds to 2-dB speckle noise.

Very high-resolution images with one look are also available. *Radarsat* provides an image product with a resolution better than 10 m in a one-look image. These may be used for local studies of very high contrast ice features, but they are limited by high speckle noise. Most ice features can best be observed by using larger pixel sizes and reduced speckle noise. For example, *ERS* SAR images with approximately 100 m in pixel size can be produced by pixel-averaging the FRI product. These images have speckle noise that corresponds to about 40 looks, which is equivalent to about 0.7 dB

noise. These low-resolution images (LRI) have the additional advantage of much smaller file size than the 12.5-m pixel FRIs.

For sea ice mapping on the regional scale, ScanSAR or wide-swath mode is the most appropriate. In this mode the instrument combines several sub-swaths to cover a large total swath. Wide-swath mode on *Envisat* (WSM) has a swath width of 420 km and uses five sub-swaths, while the equivalent mode on *Radarsat* has either a 450-km or a 500-km swath that uses four sub-swaths. Wide-swath data are processed to make images with pixel size of 50 m or 75 m with 8–12 looks (approximately 1.2-dB noise), corresponding to a resolution of 100–150 m. For many applications, pixel size can be further increased with an accompanying decrease in speckle noise.

The images are represented by either 8- or 16-bit pixels. The relation between pixel value and backscatter coefficient varies from station to station. Images may be calibrated, allowing absolute σ^0 to be computed. In many cases uncalibrated data are used, which means that the pixels represent relative values. In principle, every delivered image should have information about range corrections and the general equation between backscatter and pixel value: 16-bit images are often coded as "voltage" or "square root intensity", while 8-bit images may use logarithmic coding or a range-dependent equation in order to make the best use of the limited range of values (0–255). In many cases these characteristics are not well-known, which means that the image is uncalibrated.

A characteristic feature that often occurs in wide-swath images is range-striping. This is a sudden jump in the calibration equation at one or several given range values, caused by the difficulty of achieving smooth range-processing, especially at sub-swath borders. Large striping effects can be eliminated in subsequent image processing.

Processing of SAR images

Most delivered images from a receiving station—such as the Kongsberg Satellite Services (KSAT) in Tromsø, Norway or the Alaska Satellite Facility (ASF) in Fairbanks, Alaska—need to be further processed in order to be useful for end users such as icebreakers. This is done at remote-sensing centers, such as the Nansen Center in Norway. When a path projection image with 16-bit voltage-calibrated pixels is delivered from the receiving station, the following six processing steps may be required:

(1) *Conversion to an 8-bit pixel image, usually by application of a range-dependent scaling factor*. Operations on single-channel SAR images are generally performed using 8 bits per pixel because this is sufficient to represent the radiometric range of the data. Most SAR images of sea ice, especially if large water areas are present, have a characteristic decrease in pixel values with increasing range. To have an image showing equal gray tones for the same ice types independent of range, a range-dependent scaling factor is applied. The factor may be chosen differently for images with respect to ice and to water. In the NSR an ice-scaling factor is used. This means that open water tends to be bright in the near range and dark in the far range.

(2) *Averaging of image pixels, thereby reducing speckle noise and file size*. This can be done by simple block-averaging. However, for best results it should be preceded by low-pass filtering.
(3) *Determining a suitable set of geo-parameters to find the geographic NE-coordinates of each image pixel* (image geolocation). The satellite has a well-defined orbit between its northern and southern extremes as given by its inclination and nodal period. By using the distance between the satellite nadir line and SAR swath boundaries, which is given by the instrument description and swath mode selected, the NE-coordinates of all pixels can be uniquely defined based on the NE-positions of only one (reference) pixel. A suitable reference can be the NE-coordinates of the image center pixel. This is the method used for most images for the NSR processed by the image-processing software "Gopgrid" at the Nansen Center. Alternatively, the four corner pixel NE-coordinates can be used as reference; they are given by most suppliers of SAR images. These can be used in other geolocation programs without the need to know the satellite orbit.
(4) *Conversion from a path projection image to another agreed projection (e.g., polar stereographic)*. This is an optional step that is taken if a specified map projection is required by the end user. For high latitudes a polar stereographic projection is often preferred with specified center latitude, center meridian and a reference pixel size. As the path image is geolocated in step 3, resampling of image pixels from path projection to the desired projection is made. If a mosaic of several images is required, all are converted to the commonly defined projection and combined, usually with the most recent image on top.
(5) *Annotation of gridlines, shorelines and other information on the image*. For most end users, the drawing of gridlines for, say, every degree latitude and 5-degree longitude, as well as drawing shorelines is useful for subsequent image analysis onboard the ship. This also makes for a useful check on coordinate accuracy when shorelines can be compared with those visible in the SAR backscatter image.
(6) *Coding the image to an agreed file format and file size (e.g., to JPEG format of approximately 150-KB file size), suitable for transmission*. Many standard file formats are used for coding and transfer of images—such as TIFF, GIFF, JPEG, HDF and others. As transmission to icebreakers at high latitudes is generally very difficult using geostationary satellites (Inmarsat) and also very time-consuming using communication satellites (Iridium), a fairly low limit to file size is preferable. Coding in JPEG is often used because of its ability to compress files, making them more than five times smaller than an uncompessed file—for example, a TIFF file. This reduction can generally be done without losing essential ice information from the image.

Transmission to icebreakers and other users of SAR

The following three methods of transmission have been used:

(1) *Facsimile transmission using an Inmarsat telephone line to the ship*. This analog link was widely used in the 1980s and 1990s, before the widespread use of digital

transmission. A high-contrast print of the image was made, with added messages and annotation as required. A gray tone image is difficult to transmit by standard fax as it often gives very low quality (dark) output; therefore, techniques such as dithering—where uniform gray areas are replaced by small black-and-white dots—were found useful. In addition, Inmarsat offers a special setting aimed at gray tone transmission. Fax transmission of SAR was used in the expeditions described in Section 6.1.

(2) *Transfer of a digital file by FTP from a server at the processing facility*. This may be used for ships with access to the Internet. The user needs to know when a new file is available and then connects to the server. The method can be efficient, especially for larger files. This method was used from 1995 up to quite recently.

(3) *Attachment of a digital file to an email message sent to the ship*. This is currently the most used method since most vessels now have email as standard. Image products are sent as attachments and additional information about the image and other subjects can be transmitted as well. However, the size of the attached file must be kept fairly low (e.g., below 150–200 KB) and some extra data are added in the transmission. The probability of poor transmission by Inmarsat increases rapidly with ship latitude, and Iridium is presently the best system for transmission to high latitudes. Land-based users generally have Internet connections, allowing method (2) to be used. Additional information about file access, image parameters and other information may be sent by email or fax.

6.3.2 Use of SAR data onboard icebreakers for route selection

Satellite SAR images can be obtained for the whole Northern Sea Route with various time delays. The western part is covered by the KSAT station in Norway and the ESA station in Kiruna, while the eastern part is covered by the ASF in Alaska. No receiving stations cover the Laptev Sea area, but SAR data from this area can be stored onboard satellites and downlinked a few hours after the satellite overpass. Both *Radarsat* and *Envisat* provide onboard storing of SAR data. Transmission of processed SAR images to icebreakers is done via Inmarsat or Iridium communication satellites. Distribution of weather forecasts, sea ice data and other information from MOHs to icebreakers has been done by means of satellite TV broadcasting (Lavrov and Golubtsov, 2002). All nuclear icebreakers have Ekran TV receivers and VPI decoders for receiving graphical information (Kuzmichev, 2002). In summer 2003 *Envisat* ASAR images were received onboard the icebreaker *Sovetsky Soyuz* via this system.

The most common system has been the Inmarsat system, although there are geographical limitations to its use in the NSR. The quality of received images depends on satellite height over the horizon and antenna installation, which can be slightly different from icebreaker to icebreaker. Quality also depends on atmospheric conditions and ship movement during icebreaking. Inmarsat has a limit to the amount of data that can be transmitted within a reasonable time period, thus large data files cannot be transmitted. SAR images generally need to be averaged to a coarser resolution with less noise and compressed using JPEG for transmission. Iridium has the advantage that there is no geographical limitation, implying that data can be

transmitted to any area, but the amount of data to be transmitted is limited. Satellite TV broadcasting also limits file size to a few hundred KB. The transmission capacities of high-latitude telecommunication systems are one of the main drawbacks to using SAR images onboard icebreakers in the NSR.

An important factor for successful use of satellite data in ice routing is the time delays between image acquisition by the satellite and its availability onboard the ship. The shorter time delay the better it is for tactical navigation. During demonstration expeditions this delay varied from about 6 h to 2 days, depending on many factors such as the time of day and the processing time at the ground-station. In optimal cases, the time needed for processing and distribution of SAR images was as short as about 2 h.

Because SAR data for ice areas had to be ordered in advance—up to 14 days for *Envisat*—it was necessary to forecast convoy position for the time of image acquisition. For *ERS* data acquired from a 100-km swath width it was very difficult to get a good match between the data and the location of icebreakers. Even if hundreds of images were ordered, only a few were really coincident with the actual ship route. *ERS* SAR data were most useful when they were used in limited areas such as Kara Gate, Vilkitsky Strait, the Ob' Gulf and the Yenisey Gulf. With the advent of wide-swath images from *Radarsat* and *Envisat*, the possibility to cover ice areas with SAR images coincident with the ship route was significantly improved. In all experiments using wide-swath SAR, most sailing routes could be mapped by SAR on the same day or 2–3 days before or after the ship had sailed through the area.

The short time delay between SAR acquisition and delivery onboard the icebreakers increases the value of data for tactical navigation. Sea ice can be very dynamic and rapid changes can occur as a result of changes in wind conditions and tidal currents. Therefore, high-resolution information from SAR data can quickly become outdated and without value in ice navigation. If ice conditions are more stable, SAR data can be be useful several days after image acquisition.

Onboard icebreakers, navigators use SAR images for interpretation of sea ice conditions and select sailing routes where ice conditions are the most favorable. In case of severe ice conditions, helicopter ice reconnaissance is used in addition to SAR imagery. In compact sea ice it was important to identify areas of level ice. Identification of leads is particularly important because sailing in leads is more effective than breaking through ice. Mapping of level areas was also important in fast ice areas. In the Yenisey Gulf—where year-round navigation takes place—icebreakers prepare sailing channels in level ice and avoid areas of deformed ice. From SAR images several grades of ice surface roughness can be determined. Optical satellite instruments, such as AVHRR, cannot detect ridges or ridged areas in sea ice. For the ARCDEV expedition in April 1998, several SAR scenes were acquired before the voyage to plan the route through the fast ice in the Ob' estuary.

The usefulness of SAR images can be improved by inserting the images in the electronic chart display information system (ECDIS) onboard the icebreakers. This is done by including SAR imagery together with navigation data, bathymetric and meteorological information. By integrating all the important data in one system, the navigator can quickly select the safest and easiest route. In order to utilize sea

ice information derived from SAR data, continuous availability of data and derived products in near-real time is essential.

6.4 USE OF OPTICAL IMAGES ONBOARD ICEBREAKERS (*V.G. Smirnov, Y.A. Shcherbakov, V.S. Loshchilov*)

Use of optical satellite images received directly onboard icebreakers and research vessels for ice navigation started in the mid-1970s. Satellite images were first received on photographic film where continuous image transmission was made from satellites flying over the ships. This method provided real time images showing fractures, leads and open ice zones of importance for route planning. The first satellite images were medium-resolution optical images from *Meteor* with a spatial resolution of 3 km and *NOAA* APT mode images with a spatial resolution of 4 km. Data transmission was performed at a frequency of 137–138 MHz. In recent years, research vessels and some icebreakers have been equipped with receiving stations for *NOAA* HRPT images with a spatial resolution of about 1 km, transmitted at a 1.7-GHz frequency. Up to six *NOAA* images could be received daily onboard ship during operations at sea. The images with least cloud cover were used for ice analysis. In addition, series of repeated cloud images were used to update weather forecasts received from meteorological centers. In addition to optical range images, side-looking radar (SLR) images from the *Okean* satellites were received using the same equipment. SLR images, with a spatial resolution of about 2 km, were an important supplement to optical images because they were independent of cloud cover and light conditions. The processing of satellite images included rectification, geolocation, inclusion of coastlines as well as ship positions. The navigation route was planned using sea ice information derived from the image on the computer display, on which the ship's geographical coordinates were marked. Planned way-points were then transferred to a navigational sea chart. The images were also used to prepare a detailed ice chart for the area of the planned sailing route.

This technology was successfully used during the Russian–Norwegian expedition in the Kara Sea onboard R/V *Ivan Petrov* in August–October 1994 and during a Russian expedition onboard the same ship in the Barents and Kara Seas in August–September 1995. The same technology was used in subsequent expeditions onboard the R/V *Mikhail Somov* and the icebreaker *Kapitan Dranitsyn* in April–May 1998, and onboard the R/V *Akademik Fedorov* in September–October 2000. Also, later expeditions onboard a number research ships and icebreakers in the Arctic and Antarctic used the method.

Optical images have both advantages and disadvantages compared withh SAR images when used for sea ice analysis to support navigation in ice. The disadvantage is primarily the limitation due to cloud and darkness. To minimize the problem of cloud cover, mosaics of cloud-free parts in successive images are compiled, providing a time-averaged image over some days. Optical images from *Meteor* and *NOAA* AVHRR also have lower spatial resolution than SAR data. The spatial resolution of AVHRR data is 1 km, which in most cases provides useful information for navigation. The fact

that images are received onboard the ship several times per day in real time increases the usefulness of the information. The swath width of AVHRR images is about 3,000 km, which covers large areas of sea ice in the NSR. This is a significant advantage over narrow-swath images—such as SAR images from the European *ERS* satellite. Another advantage is that AVHRR data can be received free of charge, while SAR data have a significant cost.

The efficiency of using optical satellite images was demonstrated in April 1998 during the voyage of the Finnish tanker *Uikku* escorted by the *Kapitan Dranitsyn* and further assisted by the nuclear icebreaker *Rossiya* during operations in heavy ice. Both optical range and SAR satellite data were used in planning the sailing route. For example, the final decision to use the western Novozemelsky polynya for transit of the convoy to the Kara Sea—*en route* to its final destination in Ob' Bay—was made after receiving a *Meteor-3/5* image onboard the ship (Figure 6.20(a)). Optical images identifies open water very well as dark signatures compared with the bright signature of sea ice. This information was also used to identify the open water areas in the coastal polynya shown in Figure 6.20(b).

The wide swath (2,600 km) of *Meteor 3/5* images made it possible to map ice conditions simultaneously for the entire operation area. A detailed description of the use of optical range satellite information and SAR data for providing support for convoy-routing in the ARCDEV cruise is presented in Smirnov *et al.* (1999) and Smirnov (2000).

Use of optical imagery in ECDIS for icebreaker routing

Satellite communication systems—such as Inmarsat, GlobalStar and the "Moskva" television system—offer possibilities for receiving various ice and meteorological information as well as satellite images onboard ships. Research vessels and icebreakers have recently been equipped with ECDIS and global positioning systems (GPS/GLONAS). The ECDIS system has become standard on modern ships and offers the possibility of including operational ice and meteorological information in the same system as navigation information. Since 2001 several experiments using the ECDIS system for navigation support in ice conditions have been carried out. Sea ice charts and meteorological information are inserted as additional information layers, supplementing navigation layers (Figure 6.21(a)). At present, there are no procedures for presenting ice and hydrometeorological information in the S-57 standard[4] agreed at the international level. However, software such as dKart has provided a means of integrating sea ice and navigational data, as shown in Figure 6.21 (Shcherbakov *et al.*, 2002).

A method of preparation, transmission and depiction of ice information in combination with navigational data was demonstrated by the *Krasin* in the Tatar Strait in February–March 2003. It was also demonstrated by the *Sovetsky Soyuz* in the Kara Sea in June–July 2003. Examples of information received onboard the ice-

[4] A standard for electronic hydrographic charts defined by the International Hydrographic Organization.

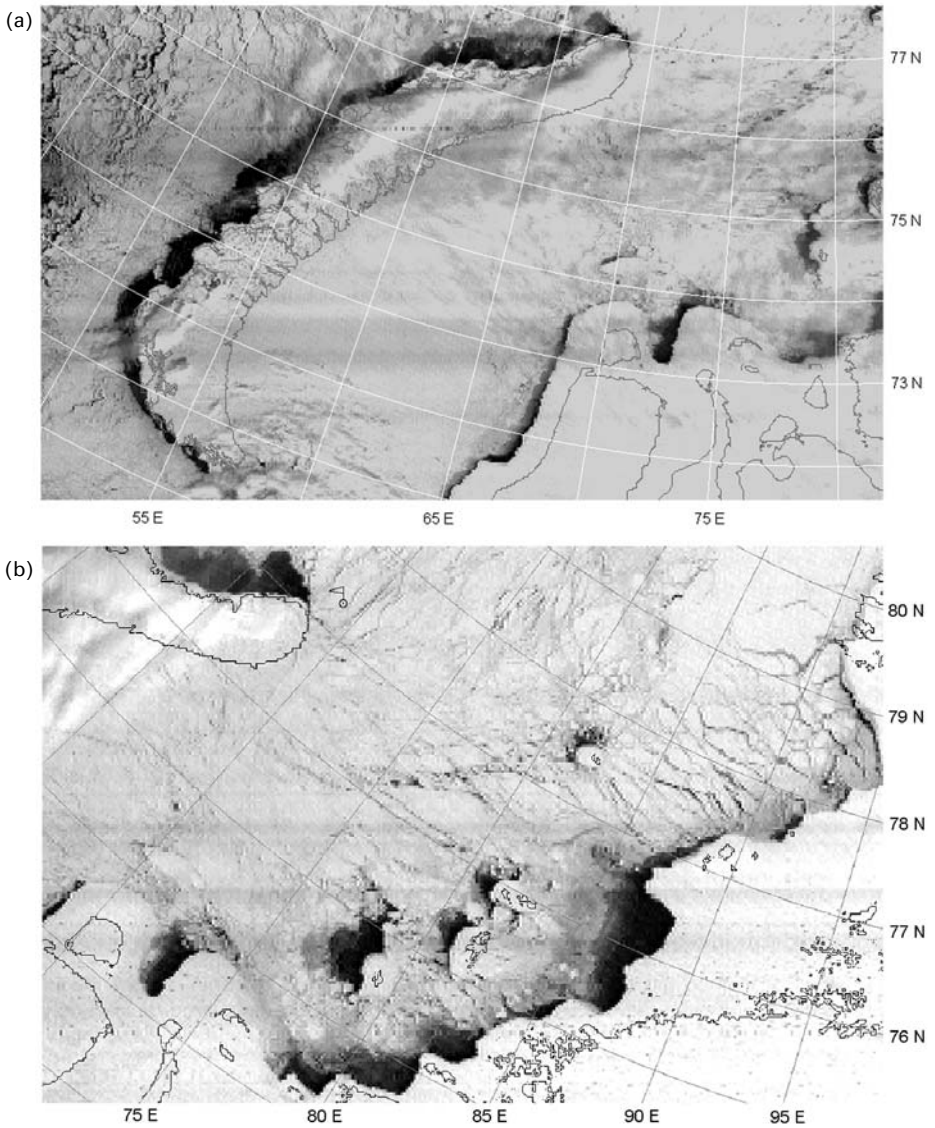

Figure 6.20. (a) *Meteor 3/5* image, 28 April 1998; (b) *Meteor-3/5* image for 30 April 1998.

breakers are presented in Figure 6.21. Ice information was transmitted to icebreakers from the "Sever" Center at AARI using satellite communication channels. This technology was also used by R/V *Akademik Fedorov* in the high Arctic in August–September 2004. This method of providing operational ice information for navigation of ships was held in high esteem by the captains of icebreakers and ships.

With ice charts included in the ECDIS system, captains of ice-going vessels have a good tool to plan tactical maneuvers in ice and select the easiest and safest transit

(a)

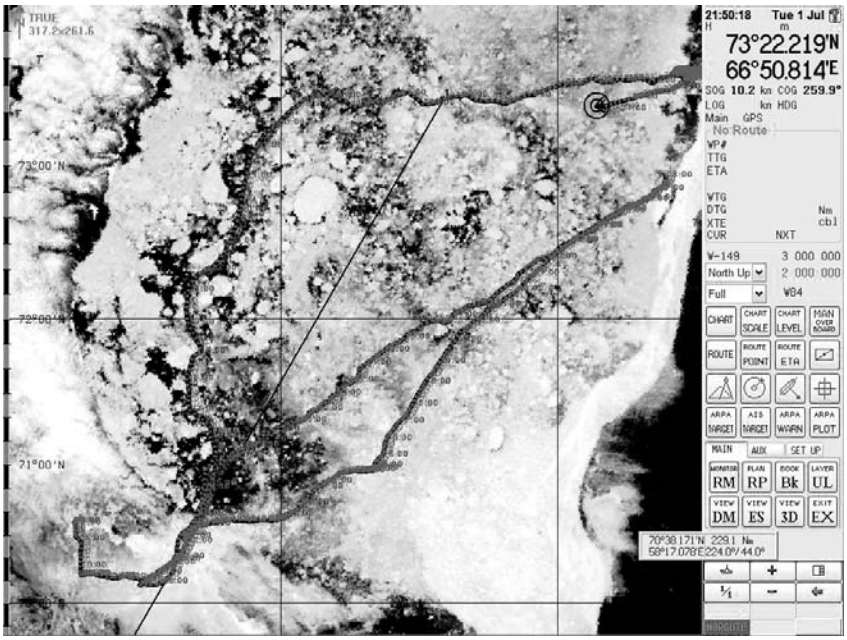

(b)

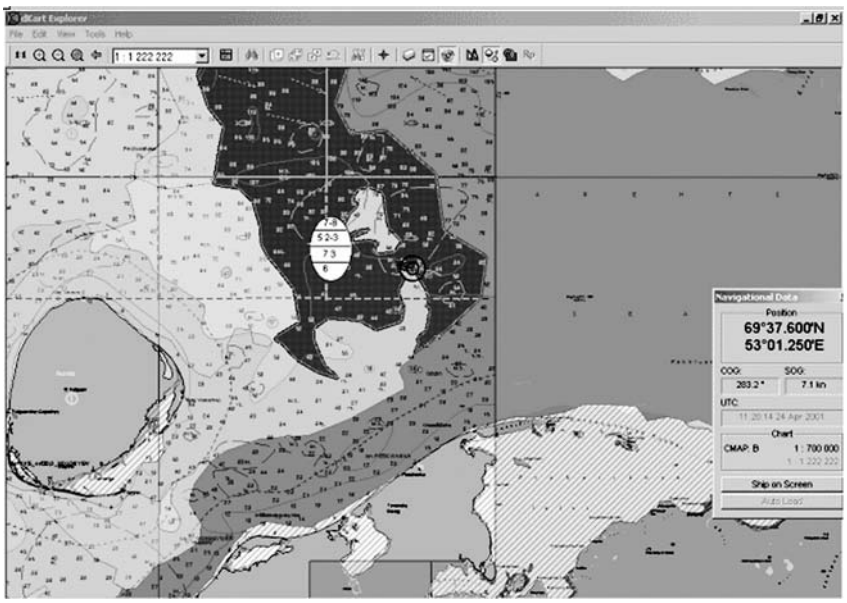

Figure 6.21. (a) Example of a combined depiction of the *NOAA* raster image and the navigation chart in ECDIS (the nuclear icebreaker *Sovetsky Soyuz*, the Kara Sea, June–July 2003). (b) Example of a combined depiction of the ice chart and the navigation chart in ECDIS (see also color section).

route to the destinations. In most cases, satellite images of sea ice are understood by ice captains and do not need professional interpretation. The most important factor in sea ice analysis for navigation is timely delivery of images. The delay between image acquisition and reception onboard should not exceed 3–4 hours. This requires satellite data downlinked directly to the ship, or data transfer via a land-based ground-station capable of delivering satellite images to the vessels within this time limit. This implies that there are reliable communication systems with sufficient bandwidth to transfer the amount of data represented by satellite images. At present, in Russia satellite TV broadcasting can deliver a data volume up to 10 MB. These systems can be used for transmitting satellite images to ice-going vessels in the NSR. Satellite retranslators have sufficiently large servicing zones in the north of the country; these zones also cover the southern areas of Eurasian Arctic seas, including the whole NSR.

6.5 ICE ROUTING AND ASSESSMENT OF SATELLITE IMAGES (*N.G. Babich, S. Sandven, L.H. Pettersson*)

Provision of sea ice monitoring data is essential for choosing the best sailing route in ice for different types of vessels and convoys. The MOH is responsible for analysis of route alternatives and decision-taking about routes. The decision is made based on information from satellite images, strategic and operational ice charts, as well as weather and ice forecasts. The criteria for selecting the optimal sailing route are (1) minimum sailing time, (2) minimum power consumption and (3) the highest safety of navigation under all sea ice and meteorological conditions. Final decisions for selecting the optimal route are made by icebreaker or ship captains based on tactical ice information and hydrometeorological information. In practice, the actual sailing route often differs significantly from the route planned beforehand. The reason is that captains obtain local ice information that is not included in the ice charts received from land. Observation of local ice conditions depends on good visibility as well as on the ice conditions themselves: in close level ice up to 1.2 m thick the observation range is 2–3 miles, in close ice up to 2.5 m thick with medium ridge concentration the range is up to 1 mile and in strongly ridged ice the range is less than 0.5 miles. Visibility is also reduced due to snowfall, drifting snow and fog. During the polar night, visibility is only within the range of illumination of the vessel. In addition, the navigator uses ship radar to assess sea ice characteristics, but interpretation of radar patterns can be quite difficult. The range of ship radar is from 3–5 miles. The resolution of the data for tactical ice information should be from tens to hundreds of meters.

The sailing route is usually chosen through areas of lower ice concentration and/or thinner ice, along polynyas, fractures and cracks. The route should avoid ice congestions, vast and medium-sized icefloes, barriers and ice ridges. When navigation takes place in ice under pressure, the sailing route should be chosen parallel to, or close to parallel to, the ice drift vector and perpendicular to the pressure axis. Pressure generates fresh cracks in ice massifs oriented parallel to the axis of pressure. The cracks can be used be for sailing as shown in Figure 6.22. The orientation of pressure

Figure 6.22. Photo of icebreaker forcing orthogonal to the front of ice pressure.

axes in the ice massif is an important navigation parameter, one which should be derived from satellite images.

The experience of using satellite SAR images onboard icebreakers for route selection from 1994 to 2004 showed that these images were used successfully for ice navigation without a preliminary graphical interpretation. Experienced navigators quickly learned to interpret the sea ice parameters of importance to navigation—such as cracks, polynyas, fractures, level or slightly ridged ice, zones of lower concentration, ridged features, small- and medium-sized icefloes, fresh openings and cracks formed by ice pressure. The importance of tactical ice information is assessed in Figures 6.23–6.25, based on the long-term experience of icebreaker operations in the Arctic. First, relative increase in mean convoy speed in ice is estimated as a function of the resolution of ice information (Figure 6.23). By assuming that strategic ice charts of 20-km resolution correspond to 100%, factor K increases exponentially up to about 300% as the resolution of ice information approaches 0. Therefore, the greatest improvement in convoy routing speed increase is achieved by using high-resolution images for route selection.

Figure 6.23 also provides quantitative criteria for the data resolution needed to produce strategic, operational and tactical ice charts. With the implementation of new technologies for the scientific–operational services involved in Arctic shipping, the criteria can be changed in the future to satisfy the requirements for safe and efficient navigation in ice.

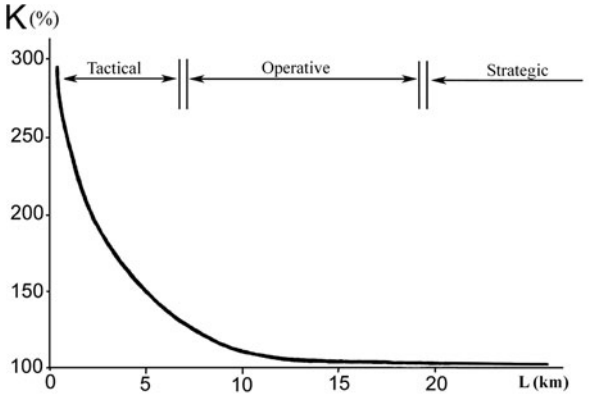

Figure 6.23. Relative increase in mean convoy routing speed in ice (K, %) as a function of resolution of ice information (L, km).

Ice thickness is the main factor determining the speed of convoys in ice. Figure 6.24 illustrates the speed of convoys as a function of ice thickness for *Arktika*-type icebreakers in the case of using tactical ice information (V_1) and in the case of not using such information (V_0) in close ice in the summer season. Figure 6.24 also shows how the routing speed factor (K) can be estimated by using tactical ice information as a function of thickness. A result of this estimate is that the efficiency of tactical ice information increases significantly with increasing ice thickness. Estimates are based on information provided by visual ice reconnaissance from icebreaker-based helicopters, SLAR surveys, and from high-resolution *ERS* and *Radarsat* SAR images.

Seasonal variability in convoy speed is presented in Figure 6.25. V_0 shows convoy speed in the absence of tactical ice information, and V_1 is with the benefit of such information. Estimates are monthly mean speeds of convoys routed by *Arktika*-type

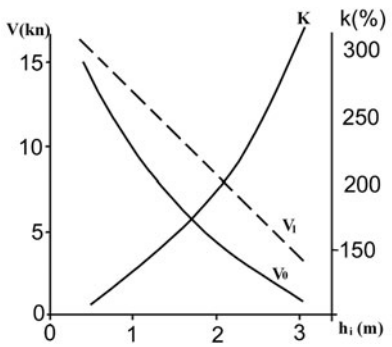

Figure 6.24. Speed of convoys (knots), routed by *Arktika* type icebreakers, depending on the thickness (meters) of close ice during the summer season in absence of tactical ice information (V_0) and using it (V_1). The relative increase of routing speed (K, %) is due to use of tactical ice reconnaissance data.

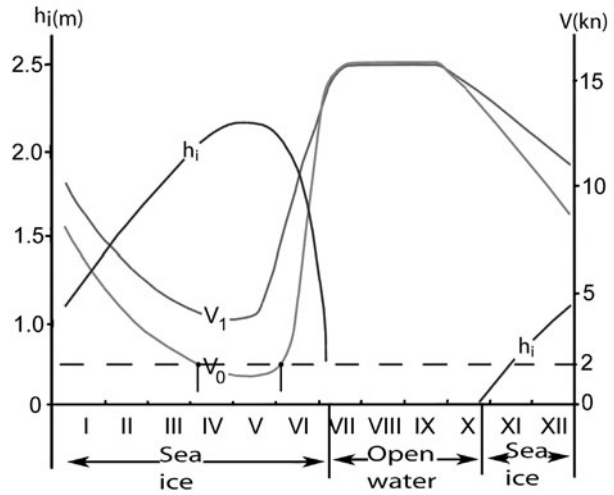

Figure 6.25. Seasonal change in mean speed of convoys when tactical ice reconnaissance data are used (V_1) and when such data are not used (V_0) for year-round navigation in the Kara Sea; the mean monthly ice thickness in the region is also indicated.

icebreakers in the Kara Sea between 70°N and 75°N. Figure 6.25 also shows the monthly mean weighted ice thickness h_i (taking into account hummocks and ridges) from freeze-up until complete ice melting.

Figure 6.25 shows the high correlation between ship speed and ice thickness. It also shows that high-resolution tactical ice information makes it possible to increase the speed of convoys in ice two- to three-fold during the winter–spring months when ice thickness is at maximum. This factor has a large impact on the number of escorted ships and the amount of cargo transported along navigation routes. When the speed of ship routing is below 2 knots the ice route is considered inefficient and noncompliant with shipping safety requirements (dashed line in Figure 6.25). Convoy speed can be below 2 knots in April and May if tactical ice information is not used. However, convoy speed can increase to 4–5 knots if such information is used. Therefore, high-resolution satellite images for tactical ice information are important for extending the dates of the navigation period and increasing transport efficiency and safety.

An assessment of using SAR images for ice navigation can be summarized as follows:

(1) High-resolution SAR images are preferable and the most promising data source for strategic, operational and tactical ice information.
(2) The advantages of using SAR for tactical navigation are: regular monitoring is possible independent of cloud and light conditions, near-real time transmission to vessels and possibility to analyze images to retrieve sea ice information of importance for navigation, and experience shows that convoy speed increases by a factor of 1.5–2.0, navigation safety increases and the accident rate decreases as a result of using SAR data.

(3) SAR data can be used to make strategic and operational ice charts for planning icebreaker operations and in fleet management.

For tactical navigation onboard icebreakers it is recommended that original images in digital format are used with the corresponding software for presentation as an information layer in ECNIS. This will enable navigators to retrieve sea ice information of importance for navigation. Near-real time transmission of images to ships and icebreakers should be provided with a minimum time delay (i.e., 2–3 h).

(4) Any future sea ice monitoring system should be based on satellite images with a resolution of 50–100 m or finer. Operational ice charts based on these images should be prepared by ice centers and transmitted to vessels operating in ice. In addition, original images without interpretation should be transmitted to vessels.

6.6 FUTURE DEVELOPMENT OF SEA ICE MONITORING (*S. Sandven, V.Yu. Alexandrov, O.M. Johannessen, L.H. Pettersson, A.V. Bogdanov, V.G. Smirnov*)

6.6.1 Prospective satellite systems

While passive microwave systems are the backbone of global sea ice monitoring, wide-swath SAR systems will become the main data source in regional ice monitoring, where detailed observations of ice dynamics and properties are required to support ice navigation and other marine operations. With more systematic acquisition and access to wide-swath SAR data with high resolution (~100 m), it will be possible to perform detailed mapping of sea ice processes in the whole Northern Sea Route with a 1–3-day interval. The launch of *Radarsat-2*, planned in 2007, will secure access to wide-swath SAR data following up the *Envisat* mission. In the next 10 years, ESA plans to launch a series of GMES[5] missions dedicated to operational monitoring of the environment. One of these missions—*Sentinel-1*—will carry C-band SAR and thereby ensure continuity of the SAR systems of the *ERS* and *Envisat* programs. Like all planned new SAR systems, *Sentinel-1* will offer multiple polarizations, which will improve retrieval of sea ice parameters.

Dual-polarization SAR data from *Envisat* and later from *Radarsat-2* and other planned SAR missions is expected to improve sea ice classification and feature extraction (i.e., edge detection, ridge detection) and reduce some of the ambiguities and uncertainties that exist in single-polarization SAR data. Other new spaceborne SAR systems will contribute to ice observation in the next few years—such as the L-band, polarimetric *ALOS* PALSAR, and the X- and L-band polarimetric *TerraSAR* (Table 6.3). The chance of having SAR data in several frequencies (X-, C- or L-band) in combination with several polarizations (VV, HH, VH, HV) offers

[5] GMES: Global Monitoring for Environment and Security (*http://gmes.info*)

Table 6.3. Summary of past, present and future planned satellite SAR systems.

Sensor	Agency	Satellite	Launch year	Swath (km)	Resolution (m)	No. of modes	Frequency and polarization
SAR	ESA	*ERS-1/2*	June 1991/ May 1995	100	25, 100	2	C-band, VV
RADARSAT	CSA	*Radarsat*	1996	500	25, 100	6	C-band, HH
ASAR	ESA	*Envisat*	March 2002	450	25, 150	11	C-band, VV/HH/VH
RADARSAT-2	CSA	*Radarsat-2*	March 2007	500	5, 25, 100	8	C-band, HH/VV
PALSAR	JAXA	*ALOS*	2006	450	25, 150	11	L-band, VV
SAR	ESA	*Sentinel-1*	2010+	400	5, 10, 50,	10	C-band, VV,HH,VH, HV
TERRA-SAR	DLR	*Terra-SAR X*	October 2006	5, 10, 30, 100	1, 2, 3, 16	2	X-band, single- and dual-polarization
SAR	Italy	*Cosmo-Skymed*	2006+				X-band
SAR	Argentina		2006+				
SAR	NRCSS, China		2006+	40, 80, 400	5, 20, 50		L-band HH

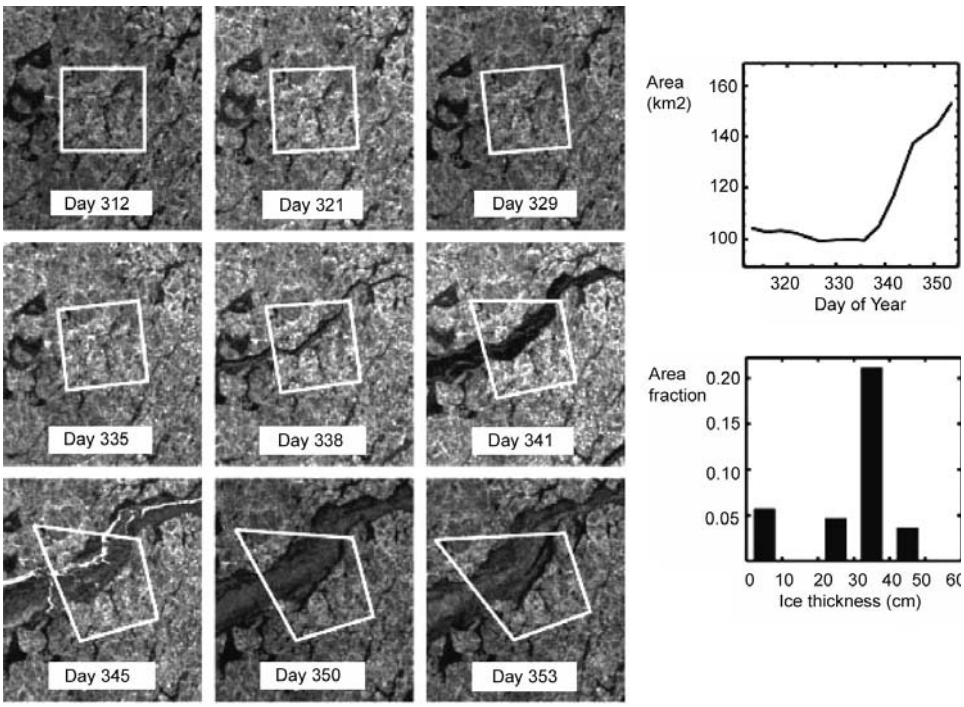

Figure 6.26. Example of ice drift and deformation of a grid cell observed in a sequence of SAR images. The grid cell is initially 10×10 km and grows through the ice season—in this case where a lead is opening up and new ice is formed. The thickness distribution of new ice is calculated as freezing progresses (courtesy: R. Kwok) (Kwok and Cunningham, 2002).

unique opportunities to extract more information about various ice classes and ice features from SAR (Table 6.3).

When SAR data from several SAR systems can be obtained for the Northern Sea Route, combining wide-swath images of about 100-m resolution with narrow-swath images with resolution down to 1–5 m, it will be possible to observe sea ice processes and quantify ice dynamics in more detail than has been done so far. With systematic coverage of the Arctic Ocean with wide-swath SAR images every 3–6 days, ice drift and deformation fields can be estimated according to the approach of the *Radarsat* Geophysical Processor System (RGPS) developed by Kwok (1998). For each cell in which ice drift is calculated, the formation and aging of new ice as well deformation (ridge formation) during the freezing season is followed in the time series of images. This allows determination of various stages in new and young ice that are difficult to classify by backscatter alone. Discrimination between the multi-year and first-year ice area is done by image classification based on backscatter. The age distribution of young ice can be converted to a thickness distribution using a simple empirical relation between accumulated freezing days and thickness (Figure 6.26).

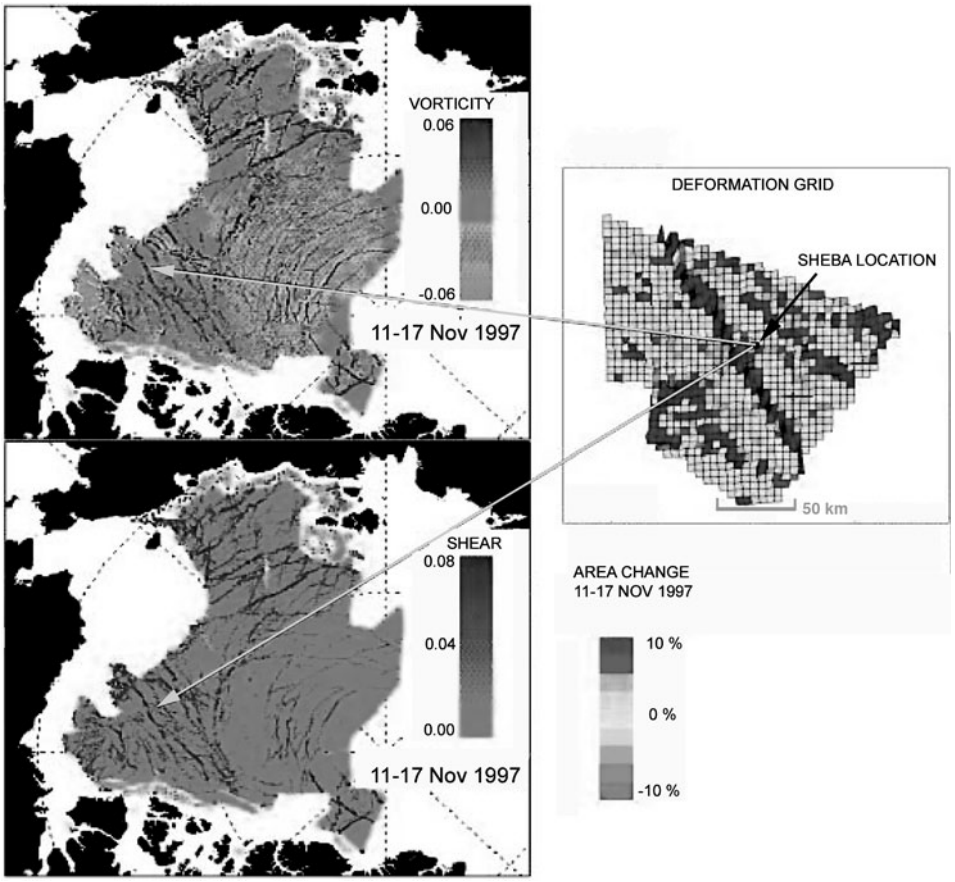

Figure 6.27. Sea ice vorticity and shear fields are examples of a linear kinematic field calculated from 6-day interval mosaics of the Arctic ice cover using the deformation grids explained in Figure 6.26 (see also color section) (courtesy: R. Kwok) (Kwok and Cunningham, 2002).

The RGPS can therefore be used to estimate the thickness distribution of ice volume produced by openings and closures of the ice cover since the beginning of the freezing season. Other products from the RGPS are maps of thin ice categories and map of various linear kinematic features (LKFs) derived from ice drift vectors (Figure 6.27). LKFs include long, narrow features irrespective of whether they contain open water, new ice, nilas, young ice, first-year ice, rafted ice or ridged ice. Locally, they can be created by divergence, convergence, shear or a combination of these. Examples of LKFs and other RGPS products can be found at *http://www-radar.jpl.-nasa.gov/rgps/RADARSAT.html*

Mapping of ridges can be done directly using high-resolution SAR and optical satellite images as shown by Sandven *et al.* (1999c) during a sea ice experiment in the northern Baltic Sea. Fine-resolution *Radarsat* images with a pixel size of about 10 m

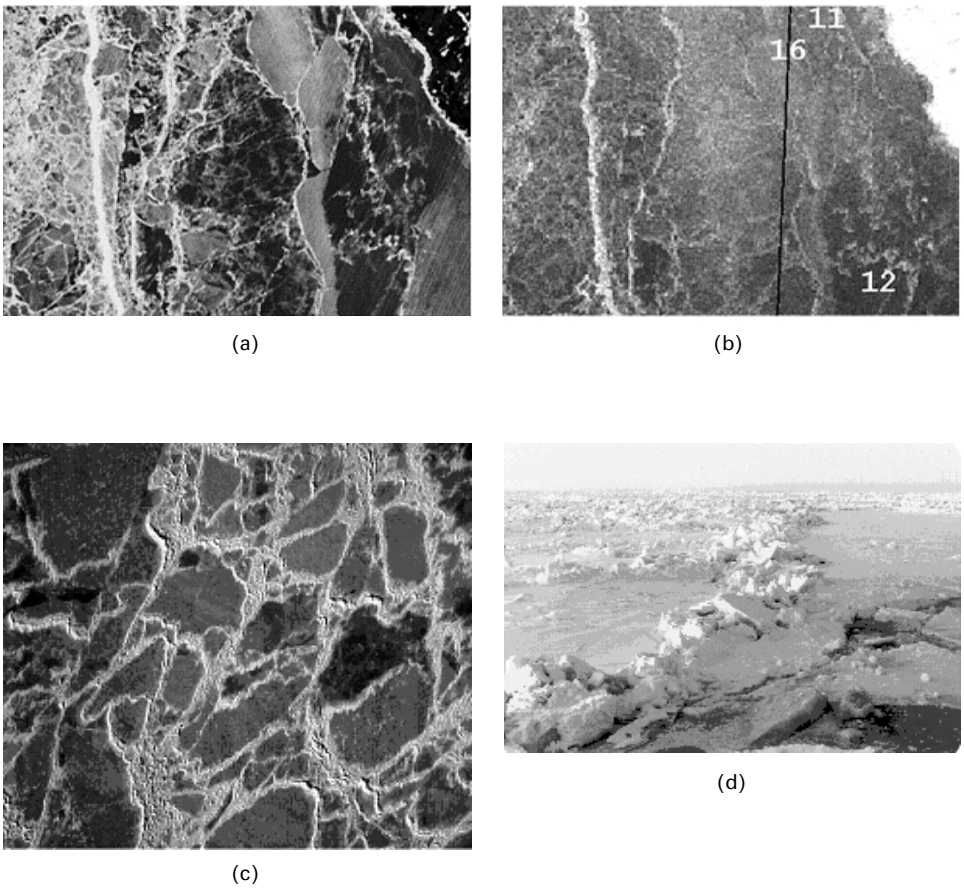

Figure 6.28. Examples of ridge mapping in the Gulf of Bothnia (Sandven *et al.*, 1999c): (a) high-resolution optical satellite image (10×15 km) from the MSU-E scanning imager onboard the Russian *Resurs-01* satellite; (b) *Radarsat* fine-resolution image of the same area as shown in (a) where the numbers indicate sites where *in situ* measurements of ridges were made. Typical ridge heights observable in SAR were 0.3–1.0 m. The wide bright line to the left in (a) is a 100 m wide ridge zone (© Canadian Space Agency); (c) vertical photograph of the ridges in an area of 1×1 km; (d) characteristic picture of ridges in first-year ice.

were used to identify various ridges in the coastal area in the Gulf of Bothnia. An example of a subset of a *Radarsat* image of 10-m resolution and an optical image of 40-m resolution is shown in Figure 6.28. High-resolution optical images have been used to verify ridges observed as bright line features in SAR. In future monitoring of ridges in the Northern Sea Route, this combined use of SAR and optical images can be implemented in operational ice services to support ice navigation. Both *Radarsat-2*, *TerraSAR-X* and the future *Sentinel-1* missions will provide SAR images with resolution better that 10 m (Table 6.3).

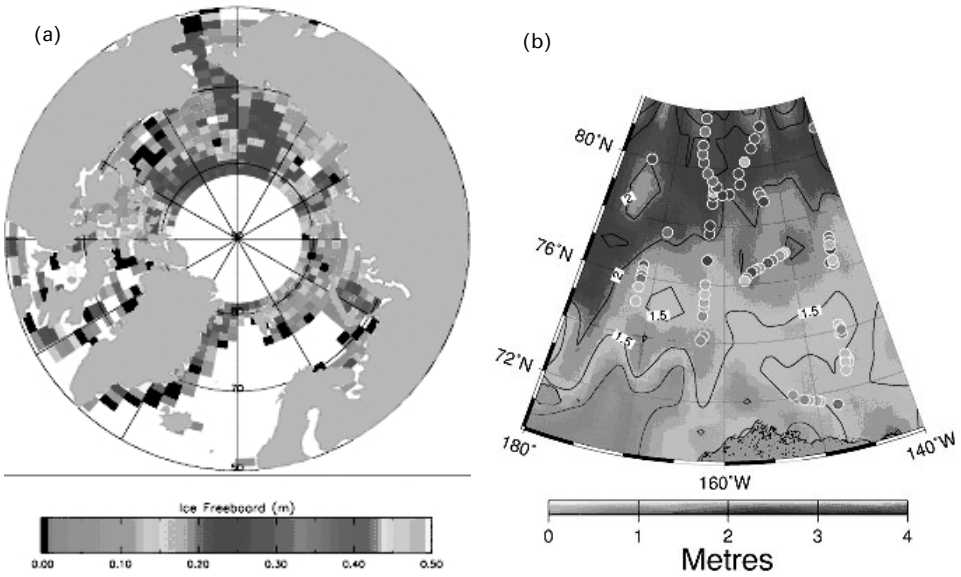

Figure 6.29. (a) Sea ice freeboard from one 35-day cycle of *ERS* radar altimeter data (cycle 97); (b) ice thickness map of the Beaufort Sea area where dots represent validation data from submarine sonar profiles. The products have been developed by University College London (UCL) (see also color section) (courtesy: S. Laxon, UCL).

A method of ice thickness retrieval from radar altimeter data has been developed by Laxon *et al*. (2003); it is based on *ERS* altimeter data obtained up to 81.5°N since 1992. The method is based on separation of radar altimeter return pulses from sea icefloes, open water or thin ice in leads, and then calculation of ice freeboard which is translated into thickness based on climatological estimates of snow cover and ice density. Ice thickness estimates are the result of averaging all the data to monthly means values in, typically, 100×100-km grids. This method will be used to retrieve freeboard and ice thickness from *CryoSat-2*, due for launch and operation from 2009. Examples of products retrieved from *ERS* altimeter data are shown in Figure 6.29.

ERS-derived ice thickness estimates for the period 1992 have thus been produced, while products from *Envisat* ASAR, covering the period since 2002 are planned for 2005–2008. *IceSat*, which was launched in 2003, has started to provide ice surface height measurements from laser altimeter, which can be used to retrieve ice thickness. An example of 10-day mapping of the Arctic ice surface height from *IceSat* is shown in Figure 6.30. When ice thickness data from *IceSat* are combined with information on ice dynamics and ice types from SAR, it is expected that new estimates of ice volume and fluxes can be retrieved and ice dynamics observed better.

6.6.2 Use of airborne and *in situ* systems

The thickness of sea ice needs to be measured by different techniques that include *in situ*, airborne and underwater systems. Most recent ice thickness data have been

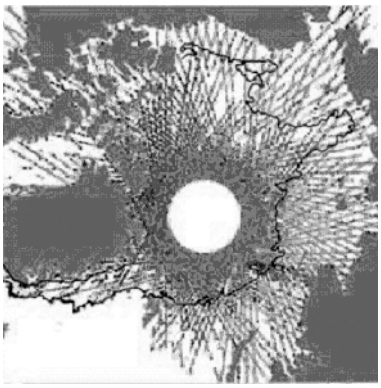

Figure 6.30. Ice surface height from *IceSat* for the period 10–18 March 2003. Red shows high values of surface height, while blue shows low values. The gray line is the extent of multi-year ice retrieved from scatterometer data (see also color section) (courtesy: R. Kwok) (Kwok *et al.*, 2004b).

gathered by upward-looking sonar (ULS) measurements from nuclear submarines (Rothrock *et al.*, 1999; Wadhams, 1994) and from oceanographic moorings equipped with ULS (Vinje *et al.*, 1998). Recently, the first trials of ULS mounted on floats suggest that wider spatial coverage can be achieved from floating systems. However, at present there is a serious lack of synoptic observations for ice thickness across the Arctic Ocean. Satellite radar altimeter data can provide an important contribution to ice thickness observations in the Arctic (Laxon *et al.*, 2003), but presently satellite data are mainly intended to provide climate information and not directly support marine operations. It is therefore important to have a number of observing systems that are not space-based capable of providing data to support ice operations.

Recently, electromagnetic (EM) sounding from helicopter flights has become a well-established technique for measuring ice thickness on local and regional scales. Large data sets representative of regional ice regimes can be gathered for determination of ice thickness distribution as shown in Figure 6.31 (Haas and Eicken, 2001). EM technology is undergoing further development and will allow repeated systematic surveys in regions where helicopters can operate.

Another innovative technique to observe sea ice freeboard from aircraft surveys is possible as a result of improvements in Arctic gravimetry and global positioning system (GPS). The basic idea is to use kinematic GPS in combination with lasers to map the surface of ice down to 10-cm accuracy over longer distances, including variations in geoid and sea surface topography (Hvidegaard and Forsberg, 2002). By using results from airborne gravity and all other gravity sources, the geoid can be obtained at the same accuracy—at least at wavelengths below 200 km. The height difference between the geoid and laser/GPS can be equated as sea surface topography plus ice freeboard. Ice thickness can then be derived from the freeboard if snow and ice density and snow thickness is known. Several field campaigns have been conducted in the Fram Strait and north of Greenland, where ice freeboard data have been obtained

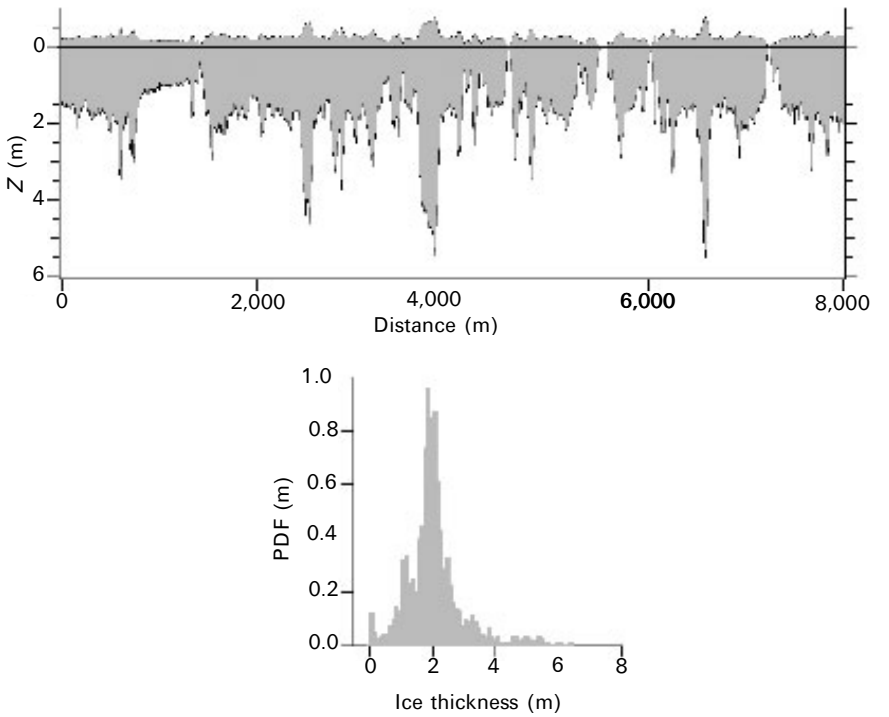

Figure 6.31. (a) Example of profile of ice thickness and surface height derived from electromagnetic induction measurements from helicopter flights; (b) ice thickness distribution function derived from the profile data in (a) (courtesy: C. Haas, AWI).

from laser altimeter data and compared with EM data from helicopters (Sandven *et al.*, 2005). Examples of these data are shown in Figure 6.32.

During the 1990s ice thickness was monitored by moored ULS—in areas such as the Fram Strait at 79°N—by the Norwegian Polar Institute (Vinje *et al.*, 1998) and in the east Greenland Currrent—at 75°N—by the Alfred Wegener Institute and others (Figure 6.33(a)). A number of other ULS systems are in operation in the western Arctic (Figure 6.33(b)). The mean and variability in ice thickness are recorded at fixed locations because ice drifts continuously southwards in this region. The data are important to estimate ice flux out of the Arctic Ocean and to validate the ice flux estimated by ice–ocean models. Data are not readily available in near-real time, but they can provide important statistics of ice thickness including the maximum draft of ice keels, which are of relevance for ice navigation and offshore operations.

A well-established autonomous system to measure ice drift consists of buoys deployed on sea ice by the International Arctic Buoy Program (IABP). They are normally expendable and air-dropped, and transmit location and meteorological parameters such as surface pressure and temperature via ARGOS. The positions of the buoys in operation in September 2005 and their trajectories for the previous

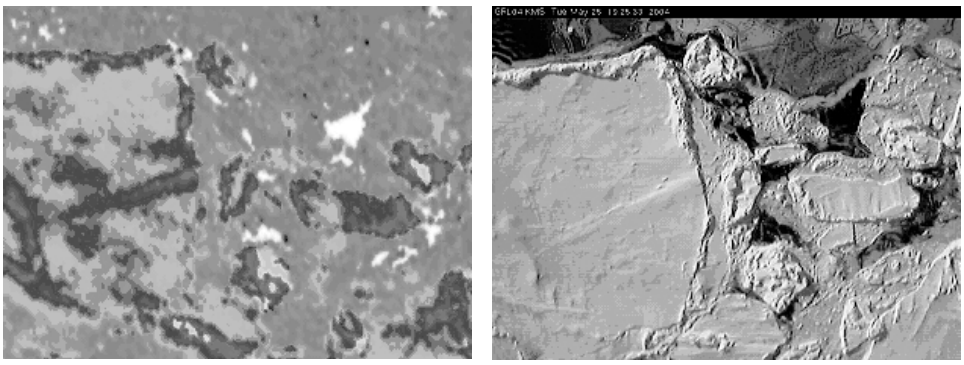

(a) (b)

Figure 6.32. (a) Ice freeboard image from scanning laser in which dark blue is thin or open water and ridges having up to 2-m freeboard are yellow–red; (b) same area as in (a) observed by a vertical video-camera. The size of the area is about 100×100 m (see also color section) (courtesy: R. Forsberg).

60 days are shown in Figure 6.34. Most buoys are located in the deep Arctic Basin, but a few buoys are located on the Russian Shelf.

The most important and classical method of getting thickness data is to drill holes in the ice. This method is laborious and can only provide very limited amounts of data. But, the method can always be used to control other methods. A more efficient way of measuring thickness *in situ* is to use ground-penetrating radar (GPR) from a sled.

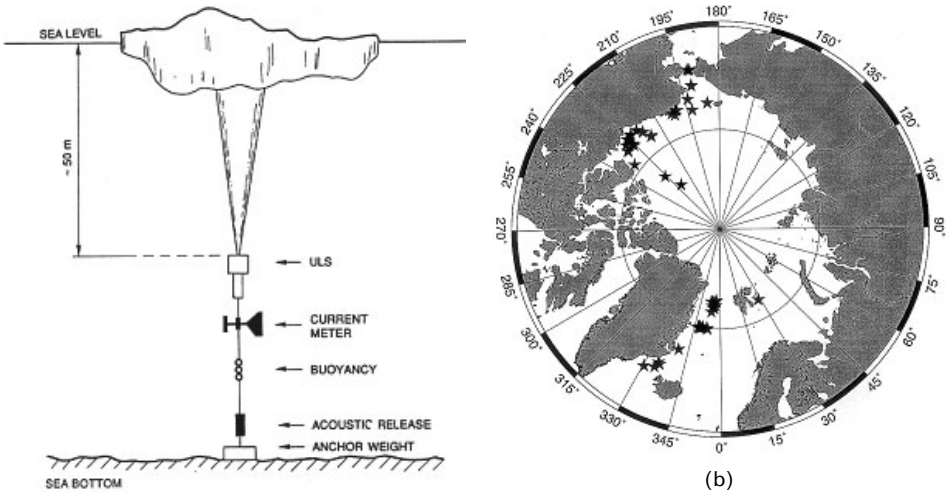

(a) (b)

Figure 6.33. (a) Illustration of upward-looking sonar (ULS) mooring deployed under the ice; (b) map of ULS moorings deployed in various parts of the Arctic Ocean (courtesy: Norwegian Polar Institute (NPI)).

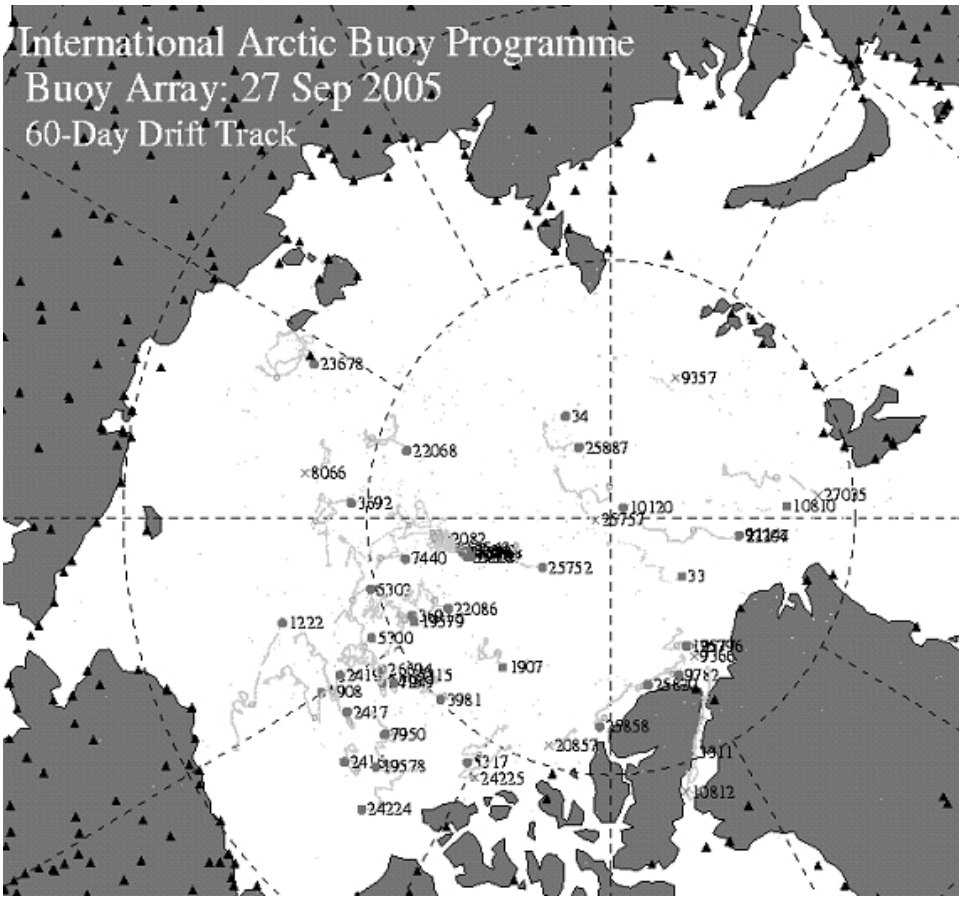

Figure 6.34. Location and drift trajectories for IABP buoys in operation in September 2005. More information can be found at *http://iabp.apl.washington.edu/*

GPR uses electromagnetic pulses at frequencies at about 50 MHz, which penetrate through the ice. If there are changes in the dielectric properties of the media on distinct horizontal layers, EM pulses are partly reflected from these layers. An example of such a horizontal layer would be the ice underside where the media changes from ice to water. To interpret the signal, traces of every shot are plotted next to each other in a radargram similar to the methodology of seismic surveys (Figure 6.35). The grayscale displays the amplitude of the received waveform. After the reflected waveform of the ice underside is identified, the travel time of the reflected wave can be derived (between 20–30 ns in this example). With the help of drilling information or using standard values for propagation velocity, travel time can be converted into ice thickness. In Figure 6.35 the bars represent drilling information.

The propagation speed depends on the dielectric permittivity of the media. Reflectivity is related to changes in dielectric properties, determining the velocity.

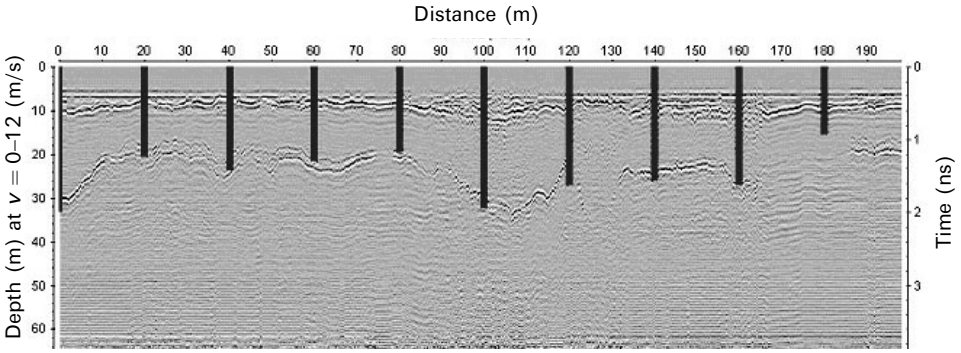

Figure 6.35. GPR section (radargram) obtained from a sled covering a distance of 200 m on a multi-year ice floe north of Svalbard. Data from drilling holes are plotted as green bars (courtesy: C. Haas, AWI) (see also color section).

Apart from wave travel velocity, damping of the wave depends on conductivity of the media and the antenna frequency (50 MHz up to 1.5 GHz). Damping increases with frequency and conductivity. In Figure 6.35 a dominant reflector corresponds nicely to the drilling information. A second reflector at around 10 ms maps the snow–ice interface as the antennas are pulled over the snow surface. Only where the ice gets too thick or consists of many little broken pieces is it difficult to find a reflected signal in the data. GPR is a useful supplement to drilling holes and can be used very efficiently if ice conditions allow a sled to be pulled. It there are heavy ridges and wide cracks in the ice, the method is not feasible.

GPR profiles can be used in combination with EM profiles from helicopters. GPR data can serve as validation data for EM profiles over shorter distances, as shown in Figure 6.36. EM data supplement GPR data because they cover much larger distances and can measure the thickest ridges that are not possible to measure with GPR

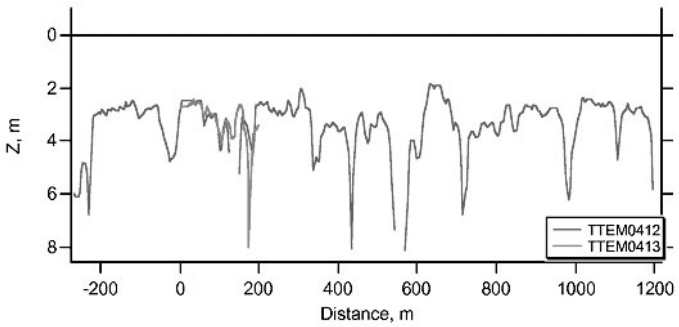

Figure 6.36. Example of a comparison of EM draft data from a helicopter (red curve) with ground penetrating draft data from a sled (blue curve). The data were obtained during the *Polarstern* expedition north of Svalbard in April 2003 (courtesy: C. Haas, AWI) (see also color section).

operated from a sled. Figure 6.36 shows a 1,400 m long profile of ice draft, obtained using both systems, taken during an experiment north of Svalbard onboard the *Polarstern* in 2003. Additional validation was performed by drilling holes along the profiles, as shown in Figure 6.35.

6.6.3 Combined use of different remote-sensing data

Use of satellite C-band SAR data is an important step in the development of sea ice monitoring, providing new capability to observe sea ice conditions independently of natural light and weather. Although C-band SAR has been most extensively used for ice observation, other radar channels (e.g., X-band, L-band) can also be used for ice monitoring. Many important sea ice parameters—such as stages of ice development, multi-year and fast ice boundaries, flaw polynyas, wide fractures and ice drift—can be derived from SAR images. However, the radar signatures of some sea ice types and features can be ambiguous, so the interpretation of ice types from SAR images is not straightforward. SAR has good capability to discriminate new, young, first-year and multi-year ice types, but more advanced classification of thin, medium and thick first-year ice, as well as multi-year and second-year ice is difficult. Discrimination between sea ice and open water is possible, but in many cases the backscatter from open ocean and ice are similar, making automated classification difficult. Therefore, significant errors may occur when a wind-roughened water surface is located close to old ice since both may have the same high backscatter (Carsey *et al.*, 1998). In addition, level fast ice and calm open water may have the same low backscatter, making it difficult to distinguish them. Large ridges and narrow leads, covered with gray ice, can have similar SAR signatures, etc. Therefore, several methods are needed to interpret ice conditions in SAR images.

In general, a combination of different data from multiple sources will improve the interpretation of satellite images (Collins, 1992). In sea ice monitoring, visible and IR satellite images are widely used, and inclusion of SAR data can improve the capability to interpret and classify ice types. Integrated use of radar and optical images requires data to be obtained near simultaneously and the acceptable difference in acquisition time should therefore correspond to the typical speed of ice drift. In areas with a high drift speed the time interval should be 1 day. In areas where the ice is stationary or moves very slowly, the time difference can be more than 1 day. In IR and visible satellite images, leads and areas of new ice can be observed more reliably than in SAR images because of the strong contrast in temperature and albedo between snow/ice and open water/thin ice. Also, the boundary between fast ice and calm open water can be detected unambiguously, whereas in some cases it is difficult to see it in SAR images. Icefloes are more clearly identified in visible images than in SAR images. *Terra* MODIS images with pixel sizes as low as 300 m are a good choice for comparison with SAR. Areas of first-year ice can be detected in SAR images, while stages of ice development can be detected from IR images based on temperature.

An example of the combined use of *Radarsat* ScanSAR and *NOAA* IR images to support the experimental ARCDEV voyage onboard the icebreaker *Kapitan Dranitsyn* in April and May 1998 is shown in Figure 6.37.

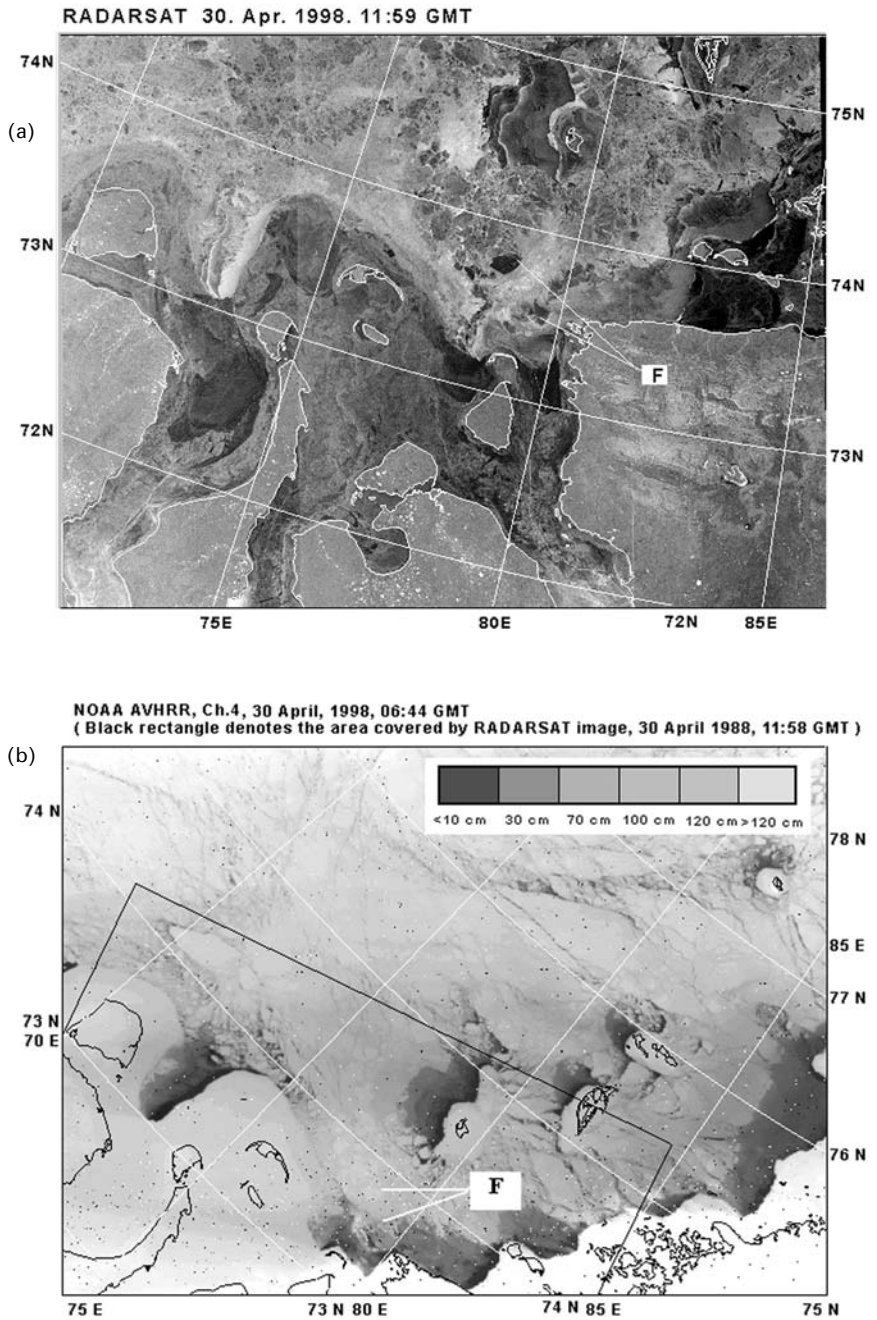

Figure 6.37. Example of combined interpretation of SAR and optical satellite images: (a) *Radarsat* ScanSAR image of the Kara Sea (30 April 1998, 11:59 GMT) (© Canadian Space Agency); (b) *NOAA* IR image of the Kara Sea (30 April 1998, 06:44 GMT).

The two areas, marked by *F* in this figure, have a dark tone in SAR images, which in combination with a light wind on 30 April (windspeed of about $4\,m\,s^{-1}$) indicates open water or ice covered with nilas. However, analysis of the near-simultaneous *NOAA* image identifies these areas as covered with thick first-year ice (see Figure 6.37(a)). The area covered by the *Radarsat* image is marked with black lines in the *NOAA* image, and a scale of sea ice thicknesscan be obtained by means of the earlier described AARI algorithm (see Section 4.1). The air temperature was about $-15^{\circ}C$ at image acquisition time, which corresponds to the conditions of using the aforementioned algorithm for ice thickness derivation from IR satellite data. Knowledge of sea ice conditions and long-term experience of studies in this region confirm that the areas marked by *F* are vast floes of level, thick, desalinated fast ice, transported to the sea from the Yenisey Gulf. The areas of thin ice are located northward and eastward of these areas (large dark areas seen in both images). Use of this or similar radar images for route selection through the areas marked by *F* in the absence of satellite data in other spectral bands can cause serious errors in interpretation.

Fusion of SAR with other remote-sensing data is carried out experimentally in some ice centers. For a longer perspective, this can be performed automatically, using statistical methods, probability functions, fuzzy logic and fuzzy set theory, neural networks and expert systems (Hall, 1992). Some of these methods have been successfully applied to sea ice classification (Collins, 1992). Artificial neural networks are especially attractive for the fusion and classification of data in different spectral bands due to their ability to approximate complex input–output relationships using a training data set, perform without any prior assumptions on the statistical model of the data, generalize well on new data and be less affected by noise.

Using an algorithm based on a multi-layer neural network, fusion of a set of spatially overlapping *ERS-2* SAR, *Radarsat* ScanSAR and *Meteor 3/5* low-resolution visible images, acquired on 30 April 1998, and classification of the sea ice types in them were made (Bogdanov *et al*., 2005). Radiometric correction, spatial alignment and co-registration of images from these sensors was done before their fusion. The selection of image test and training regions is based on *in situ* observations made onboard the icebreaker *Sovetsky Soyuz*. Used image features include image moments, gray-level co-occurrence matrix texture and autocorrelation function based features for SAR images and mean brightness for visible images.

The efficiency and advantages of this approach are illustrated by the sea ice maps produced by the MLP-based algorithm (Bogdanov *et al*. 2005) from these images and presented in Figure 6.38. *ERS* and *Radarsat* image classification maps are visually rather poor, regardless of the algorithm used. Empirical assessment of algorithms via an independent test data set showed that the performance of MLP in this case is 66% and 71% for *ERS* and *Radarsat* SAR, respectively, even if texture features are used for classification. Some parts of the polynya (regions A and B in Figure 6.38) are misclassified as first-year ice and, conversely, some areas of the first-year ice are misclassified as nilas.

A substantial improvement in sea ice classification is achieved by combining *ERS* and *Radarsat* SAR images obtained at different polarizations (VV and HH) (see Figure 6.38(c)). Fusion of these two SAR data types increases classification accuracy

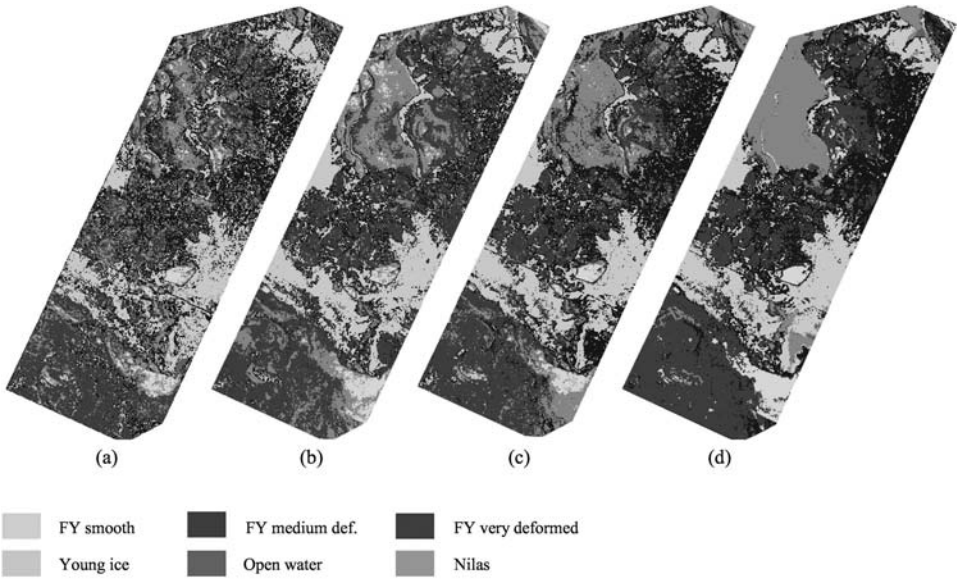

Figure 6.38. MLP sea ice classification (see Section 4.4.1) maps obtained using (a) *ERS*, (b) *Radarsat*, (c) *ERS* and *Radarsat* and (d) *ERS*, *Radarsat* and *Meteor* images (see also color section).

up to 84%. Such a noticeable improvement is observed for all ice classes. Thus, open water, young and first-year ice are much better delineated using dual-polarization information.

The classification of sea ice using three data sources (Figure 6.38(d)) in general corresponds well to visual expert classification, but in more detail than the usual manually prepared sea ice maps. Estimated total classification accuracy reaches 91% when low-resolution visual data are combined with the dual-polarization data set. In many cases, the incorporation of low-resolution visible information reduces noise in the classification, while preserving small-scale ice features, and provides additional information, especially on nilas and open water classes. Although the presented results should be treated with caution, because of the relatively small geographical region and short time period, they clearly show that fusion of satellite data in different spectral bands allows higher quality sea ice information to be obtained. The detailed presentation of information in automatically produced sea ice maps can be useful for tactical ice navigation, where small-scale ice information is needed.

Conclusion and recommendations

Sea ice can be observed by several satellite sensors, and there are services that deliver sea ice information products to many users. However, products used in operational monitoring are generally of low resolution and provide data on a fairly limited number of sea ice parameters. SAR images have proven to be capable of delivering

much more information. Operational ice services using SAR have been established on a regional basis, but there are large areas of the Arctic Ocean that are not covered by such a service yet. Regular SAR ice monitoring services are recommended as an integral part of a network of services using other satellite data (passive microwave, infrared radiometer and scatterometer). Based on SAR data from *Envisat*/*Radarsat* a number of products can be provided—such as high-resolution maps of ice extent, concentration, age (stage of development), freezing rate, deformation/ridging, drift, leads and polynyas as well as processes in the marginal ice zone related to wind, waves, eddies, freezing and melting. Derived products—such as thickness, divergence/convergence fields, linear kinematics features—can also be provided. This has been demonstrated by the *Radarsat* Geophysical Processor System. Maps of sea ice can be provided for the whole Arctic Ocean, on regional and local scales at time intervals from daily to weekly coverage. Any NSR service needs to be able to deliver near-real time products for use in operational ice charting as well as hindcast products for observation of climate processes. With the forthcoming *CryoSat-2* altimeter satellite, Arctic ice thickness data will be incorporated as a new element in ice monitoring, allowing estimation of total ice volume from space data. Because sea ice is closely linked to atmospheric and oceanic conditions, it is envisaged that real time data on air, ice and ocean must be integrated in some way in order to deliver services that meet the needs of various user groups. An NSR service needs to develop an integrated network of services, where several providers deliver information products on ice, ocean and atmosphere at high latitudes to a wide range of users.

7

Climatic variability of sea ice in the Arctic

Understanding, detection and prediction of the long-term climate variability of sea ice in the Arctic is of both scientific and practical importance, because there is a need to foresee ice conditions in the interests of shipping and other offshore economic activities—such as fisheries, gas and oil exploration and production. Section 7.1 considers the 20th century variability from century-scale historical observational records developed and analysed primarily by Russian investigators. Section 7.2 describes the spatio-temporal variability of Arctic sea ice over the past quarter century, as derived from passive microwave satellite remote-sensing data. Section 7.3 presents sea ice scenarios for the 21st century using statistical models based on observed climate variability, developed from a Russian perspective. The AARI co-authors of this chapter predict that ice extent will vary with a dominant cycle of 50–60 years, reaching maximum around 2020–2040 and 2095, with a minimum between, superimposed on a slightly decreasing linear trend. Section 7.4 presents 21st century sea ice scenarios based on results from numerical models that include increasing atmospheric concentrations of greenhouse gases (GHGs). Based on two coupled global climate models, Johannessen *et al.* (2004) predict that ice cover will reduce by about 80% during summer, assuming a doubling of CO_2 in the atmosphere at the end of this century, with a 20% reduction during wintertime. This is in contrast with Russian results, although it should be mentioned that the internal variability of the climate system is determined not only by its chaotic nature (Bengtsson *et al.*, 2006), but also by the presence of natural components of climatic changes due to external and internal causes (Gudkovich *et al.*, 2005). This can offset the ''greenhouse prediction'' of the decrease of sea ice in the 21st century (Johannessen *et al.*, 2004) and predicted warming of the atmosphere (ACIA, 2004; Bengtsson *et al.*, 2004).

7.1 LONG-TERM VARIABILITY OF SEA ICE IN THE EURASIAN ARCTIC
(*I.Ye. Frolov, Z.M. Gudkovich, V.P. Karklin*)

In the context of the hypothesized polar amplification of global warming, a number of numerical modeling studies have predicted a drastic reduction in Arctic sea ice cover—even as far as the complete disappearance of summer sea ice by the end of the 21st century (e.g., Johannessen *et al.*, 2004; ACIA, 2004, see also Section 7.4.1), caused by an expected increase in greenhouse gases in the atmosphere. However, it may be contended that—when 20th century sea ice variability is considered—the problem of the future state of sea ice cover is not as unambiguous as it may seem to advocates of the dramatic consequences of warming, as expressed, for example, by Johannessen *et al.* (2004) and ACIA (2004).

Therefore, analysis of long-term—multi-decadal to century-scale—climate variability is essential to provide the necessary perspective. Determining secular trends and quasi-periodic oscillatory signals and separating them from background noise is of key importance to understanding the climate system. Internal climate system interactions between the atmosphere, ocean and cryosphere may also create feedback across a range of time and space scales. Although not strictly periodic, such feedback may lead to quasi-cyclical behavior in climatic records including sea ice. External influences—such as astronomical (e.g., earth–sun relationships and solar variability), volcanism and anthropogenic effects (e.g., increases in GHGs)—may be superimposed on this internal variability of the climate system across a range of time and space scales.

Therefore, long, continuous, observational data sets are necessary to investigate the range of climatic fluctuations of cryospheric variables including sea ice extent (Walsh, 1995). There exists an extensive number of multi-decadal to century-scale sea ice datasets, stretching from Nordic seas to Siberian marginal seas, as described and analysed in the following sub-sections.

7.1.1 Sea ice data

Sea ice data acquired and analysed at the Arctic and Antarctic Research Institute (AARI) in St. Petersburg, Russia, are the most comprehensive available for the Northern Sea Route region. The AARI data are based on both airborne and satellite observations. The most regular and reliable data belong mainly to the period since 1940. From 1940 to 1979 ice charts were constructed from airborne reconnaissance data, whereas charts of the period 1980 to 1989 were made from airborne and satellite observations, and from 1990 to the present using satellite observations only. Before this period, data on the ice extent[1] in Russian Arctic seas were collected in August

[1] Throughout Chapter 7, the terminology used for sea ice coverage from historical data is ice "extent", rather than ice "area", in order to be as consistent as possible with the precisely defined sea ice parameters used for passive microwave satellite retrievals (Section 7.2). This is consistent with the IPCC terminology used in the forthcoming Fourth Assessment Report.

between 1924 and 1939 by the well-known polar investigator V. Yu. Vize (1940) on the basis of ship and airborne observations of ice edge position. Even earlier, the ice extent values in the Eurasian Arctic for 1900–1923 were reconstructed on the basis of observations during the voyages of expeditions and cargo ships (Karklin *et al.*, 2001). Sea ice data for individual years were calculated using a physical–statistical model (Kovalev and Yulin, 1998). Data from the Greenland and Barents Seas cover the last third of the 19th and nearly the entire 20th century, except for World War II. In this period data were reconstructed by Lebedev and Mironov (2001) based on ice extent correlation with different hydrometeorological characteristics. These data sets presented the possibility of conducting a comparative analysis of the changes in ice extent in the seas of a vast region (about 5×10^6 km^2)—from the Greenland Sea to the Chukchi Sea—throughout the entire 20th century. The length of this data set is nearly comparable with the so-called Nordic seas (Greenland and Barents Seas) data set, 1865–2000, developed and analysed by the Norwegian Polar Institute (e.g., Vinje, 2001). The AARI data set has an advantage *vis-à-vis* Vinje data in that Siberian seas to the east of Nordic seas are included.

The ice regimes of the Greenland and Barents Seas are significantly different from those of Siberian Shelf seas, because parts of these seas remain ice-free even in winter. This particular aspect of the Greenland and Barents Seas allows investigation of the interannual fluctuations of ice extent in these seas in all seasons, not only summer. In contrast, Siberian Shelf seas have complete ice cover in winter and adjacent seasons; therefore, interannual variability in ice extent is recorded only in summer. To investigate seasonal differences in long-period fluctuations of ice extent, data from April were used when ice extent is at its maximum and in August when it is close to its annual minimum. For the assessment of Siberian seas, data for August correlate closely with Greenland and Barents Seas data in July and September (Gudkovich *et al.*, 1972).

7.1.2 Linear trends in sea ice extent

Interannual and decadal fluctuations of ice extent in Arctic seas in the 20th century occurred against a background of gradual decrease from the beginning to the end of the century. Figure 7.1 presents these changes in the form of linear trends. As can be seen from the figure, the character of changes in ice extent in the summer in the so-called western (Greenland, Barents and Kara) and eastern (Laptev, East Siberian and Chukchi) Arctic seas differs significantly. Analysis shows that the largest changes described by linear trends occurred in the Greenland and Barents Seas in winter—total ice extent decreaseing by -547×10^3 km^2 (linear trend contribution to total variance here exceeds 40%). The total changes that take place in the summer period in the Greenland, Barents and Kara Seas (-513×10^3 km^2) are comparable with the changes in April in the first two seas (the contribution to variance in August comprises 24%). The linear trend in the Laptev, East Siberian and Chukchi Seas is an order of magnitude less, and its contribution to variance is just 3% and therefore not statistically significant.

There are no century-scale observational data sets for other Arctic seas, although there are sufficient data from the Beaufort Sea to construct a multi-decadal time series.

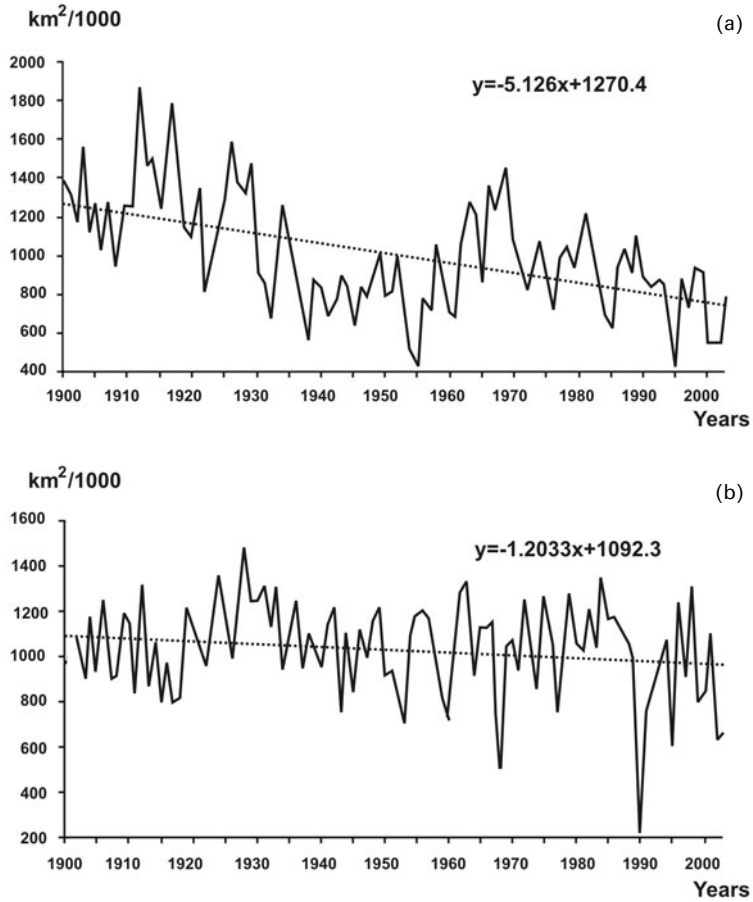

Figure 7.1. Linear trends of the ice extent in western (a) and eastern (b) Arctic seas from 1900 to 2003 (August).

An AARI analysis of Beaufort Sea ice extent in August 1968–1998 (Figure 7.2) indicates a slight, statistically insignificant negative trend. On the other hand, in subsequent years, Beaufort Sea ice extent has declined dramatically, particularly in summer (see Figure 7.11). This exemplifies the problem of temporal sampling and underscores the need for longer time series.

The trend of sea ice extent in Arctic seas varies not only spatially, but also temporally. Figure 7.3 presents the linear trends of changes in total ice extent in August for the three western seas and three eastern seas for two time intervals: (1) from the beginning of the century to 1945 (end of the warming period of the Arctic) and (2) from 1945 to the end of the 20th century.

As can be seen from Figure 7.3, the intensity of ice extent decrease in the western region from the first to the second half of the century changed significantly, almost seven-fold. It was maximum in the first half of the century and minimum in the second.

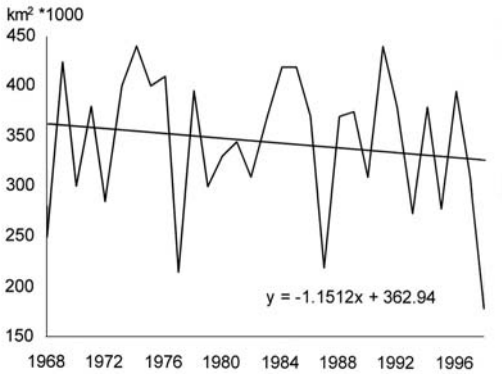

Figure 7.2. Linear trend of ice extent in the Beaufort Sea in August from 1968 to 1998.

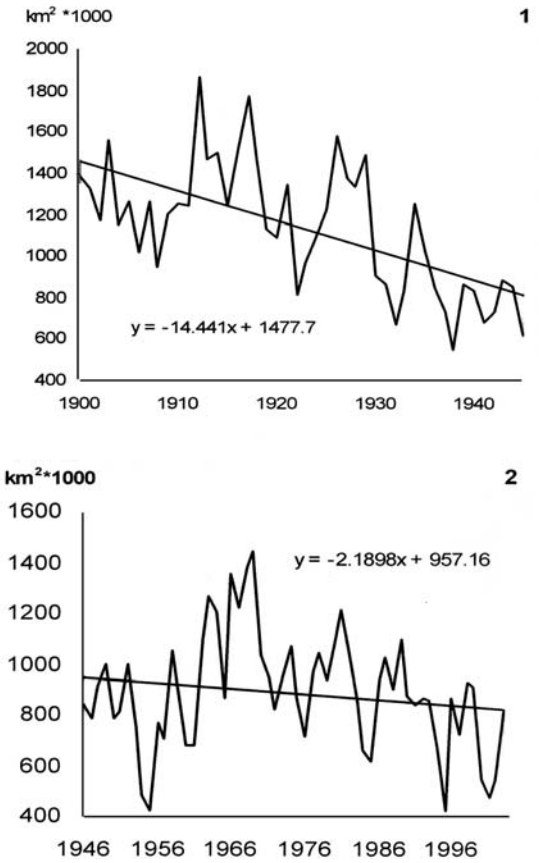

Figure 7.3. Linear trends of total ice extent in August from 1900 to 1945 and from 1946 to 2003 in western (1, 2) Arctic seas.

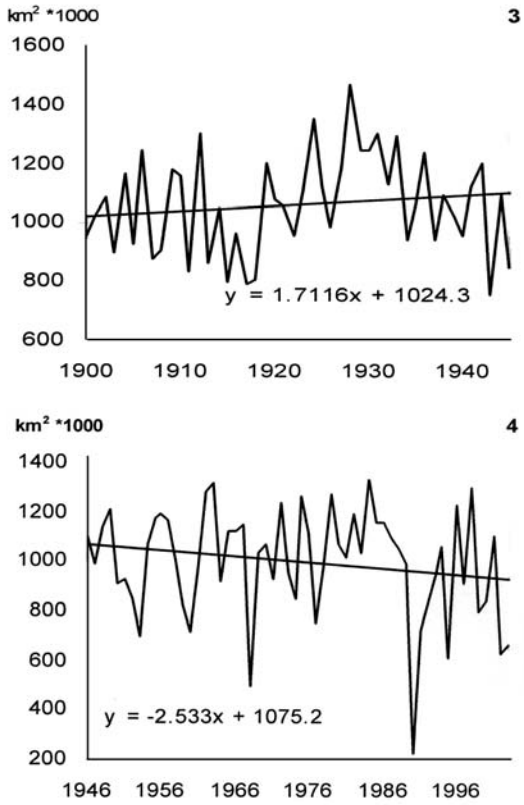

Figure 7.3 (*cont.*). Linear trends of total ice extent in August from 1900 to 1945 and from 1946 to 2003 in eastern (3, 4) Arctic seas.

The greatest changes occurred in the Kara Sea where the linear trend decreased almost 12 times. The changes in ice extent of the European Arctic in April had the same features; however, differences in the values of trends for the first and second half of the century were much less. In seas of the eastern region, from the first to the second half of the century there was a change in linear trend sign: before 1945, ice extent in the region increased and then decreased until the end of the century (by 140×10^3 km^2). In comparison, Vinje's (2001) analysis of historical data from the past 135 years (up to 2000) found that overall sea ice extent in winter (April) has reduced in Nordic seas (essentially the so-called "western seas" minus the Kara Sea) by 790×10^3 km^2 (33%). Nearly half of this reduction took place between 1860 and 1900—that is, before the AARI series began—see Figure 7.3.

Seasonal differences and intra-secular changes in the linear trend of ice extent require more detailed study of this phenomenon. The available data of observations in the Barents Sea in the second half of the 20th century allow us to calculate linear trend values in this sea for each month. Calculations show that in the second half of the 20th century, a decrease in ice extent in the Barents Sea was noted only during the

spring–summer period (March–September), while during the autumn–winter period (October–February), there was an increase in ice extent. A linear change in mean annual ice cover extent was essentially negligible (0.004×10^3 km^2/year). However, note that calculation of linear trends depends strongly on the time interval over which the trend is determined, as demonstrated in Gudkovich and Kovalev (2002) and Polyakov *et al.*'s (2003) analyses of sea ice and Arctic temperature trends. Ignoring this fact can lead to detection of spurious trends, which are absent in the phenomenon under consideration.

7.1.3 Quasi-periodic variability of sea ice extent

Variability in the ice extent of the Arctic can be characterized as having quasi-periodic behavior on interannual to multi-decadal time scales, conceptually consistent with the so-called "natural" time scales of climate variability in the Arctic (Venegas and Mysak, 2000). AARI data analysis found that the structure of these variations is characterized by quasi-periodic fluctuations over 2–3 years, 5–7, 8–12 and about 20 and 50–60 years, although the robustness of the 50–60-year cycle is uncertain because of the length of the time series. These fluctuations are manifested differently in different regions. As can be seen in spectrograms (Figure 7.4), the frequency structure of ice extent fluctuations in western and eastern Arctic seas differs significantly. A typical feature of western seas is the significant contribution of low-frequency fluctuations, while for eastern seas relatively high-frequency fluctuations play a larger role.

Ice extent in western seas has cycles lasting about 50–60 and 20 years. Their contribution to total variance comprises 25% and 15%, respectively, and exceeds significantly (eight times) the total contribution of these cycles to the total variance of these cycles in eastern seas. At the same time, in eastern seas a more significant contribution to total variance falls on cycles of about 9–12 and 7–8 years; their contribution being twice as large as the total contribution of cycles of the same duration in western seas. Thus, one can see that western seas make the main contribution to long-term (climatic) fluctuations in total ice extent in the marginal seas of the Arctic Ocean.

Analysis of ice cover extent for the 20th century in different regions of the Eurasian Arctic (Zubakin, 1987; Zakharov, 1996; Mironov, 2004) indicated that the periods of these cycles were approximately 50–60 years. These results are reasonably consistent with recent results from an independent analysis of 19th and 20th century Vinje data from the Greenland and Barents Seas, which found oscillations with periods of about 20–30 years and 60–80 years (Divine and Dick, 2006).

Karklin *et al.* (2001) data on interannual changes in total ice cover extent of Siberian Arctic seas in the 20th century were approximated by a 6th-power polynomial. The period of the cycle was 55–60 years, which is close to mentioned estimates. Similar fluctuations were detected in air temperature changes in the zone of 70–85°N (Figure 7.5).

Rates of air temperature increase (linear trend coefficient) at the time of first warming of the Arctic in the 20th century (0.45°/decade) were typically 1.5 times as high as at the time of the second warming (0.16°/decade). Karklin *et al.* (2001) note

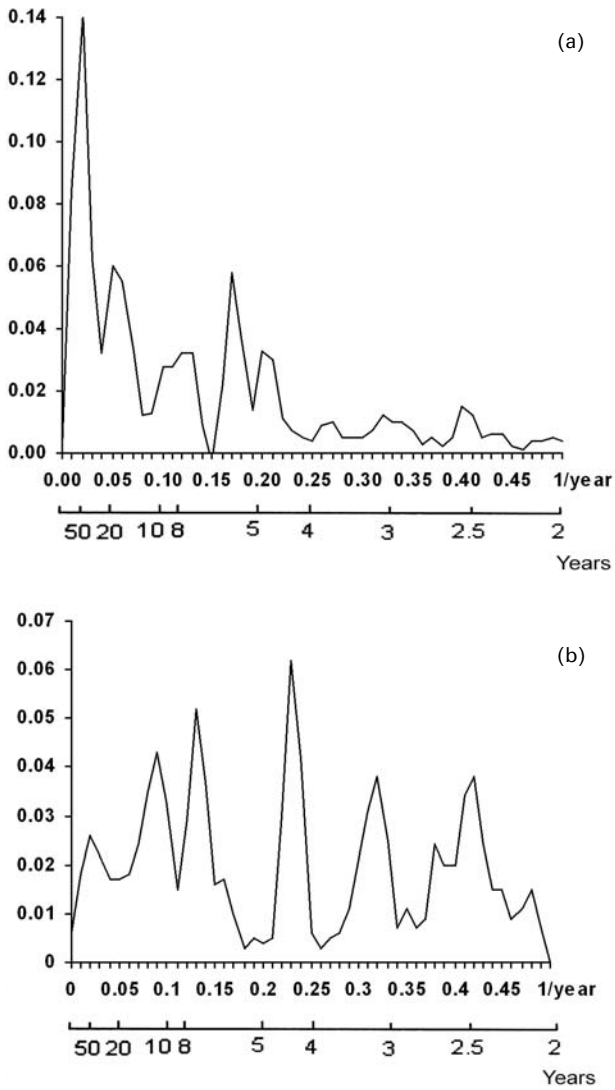

Figure 7.4. Functions of the spectral density of total ice extents in August in western (Greenland, Barents and Kara) seas (a) and in eastern (Laptev, East-Siberian and Chukchi) seas (b).

that—unlike shorter-period fluctuations—long-term fluctuations in ice extent in Arctic seas are the same for western and eastern regions, indicating a common nature.

A low-frequency oscillation (LFO) lasting about 60 years has also been detected in different hydrometeorological and biological indices (Klyashtorin and Lyubushin, 2003), Arctic air temperatures (e.g., Polyakov *et al.*, 2003), sea level pressure (SLP) and sea ice in the Atlantic Arctic region (Venegas and Mysak, 2000) and sea ice in the

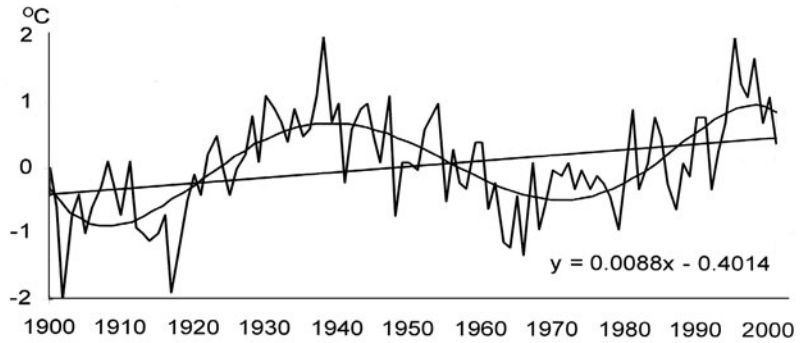

Figure 7.5. Anomalies of mean annual air temperature in the Arctic zone (70–85°N) from 1900 to 2003: straight line = linear trend; smooth line = polynomial approximation.

Greenland and Barents Seas (Divine and Dick, 2006). Here, a similar polynomial approximation was made for changes in total ice cover extent of the Greenland and Barents Seas in April and total ice cover extent of three western seas (Greenland, Barents and Kara Seas) and three eastern seas (Laptev, East Siberian and Chukchi Seas) in August (Figure 7.6).

In all regions quasi-periodic 50–60-year fluctuations were indicated. However, the amplitudes of these fluctuations differ significantly with the phases of fluctuations, being slightly displaced between western and eastern seas. Calculations show that the role of this cycle in total ice cover extent variability for western seas in winter and for seas located to the east of Severnaya Zemlya is small in summer (3–7%), while this fluctuation plays the largest role (up to 25%) in seas of the western region in summer.

In addition to this "half-secular cycle", shorter cycles lasting about 20 and about 10 years are present in long-term changes in ice cover extent. Higher frequency cycles are not considered here, since they can hardly be referred to as "long-term climate fluctuations". In order to investigate "20-year" and "10-year" cycles, spectral analysis of the ice extent series of these seas was performed for 1933–2003. All periodograms of different seas and seasons have some common features: for example, the noticeable increase in amplitude of fluctuations between 18–22-year and 8–13-year periods. However, the ratios between the amplitudes of fluctuations in the first (18–22 years) and second (8–13 years) ranges are different for different seas.

Periodograms of the ice extent in August for western and eastern regions differ as follows: first, while in the western region the amplitude of 20-year fluctuations is much larger than 10-year fluctuations, they differ little in the eastern region. The ratio between the amplitudes of the former to the latter fluctuations generally decreases from west to east. Second, the contribution of "decadal" cycles to total variance in ice cover extent for western seas (2–3%) is much less than for eastern seas (3–8%)—and *vice versa* for "20-year" cycles: in western seas it is almost twice as large as the average value typical of eastern seas.

Table 7.1 presents the values of contributions to total variance of the linear trend and long-period cycles for each region. Values for the total contribution of all

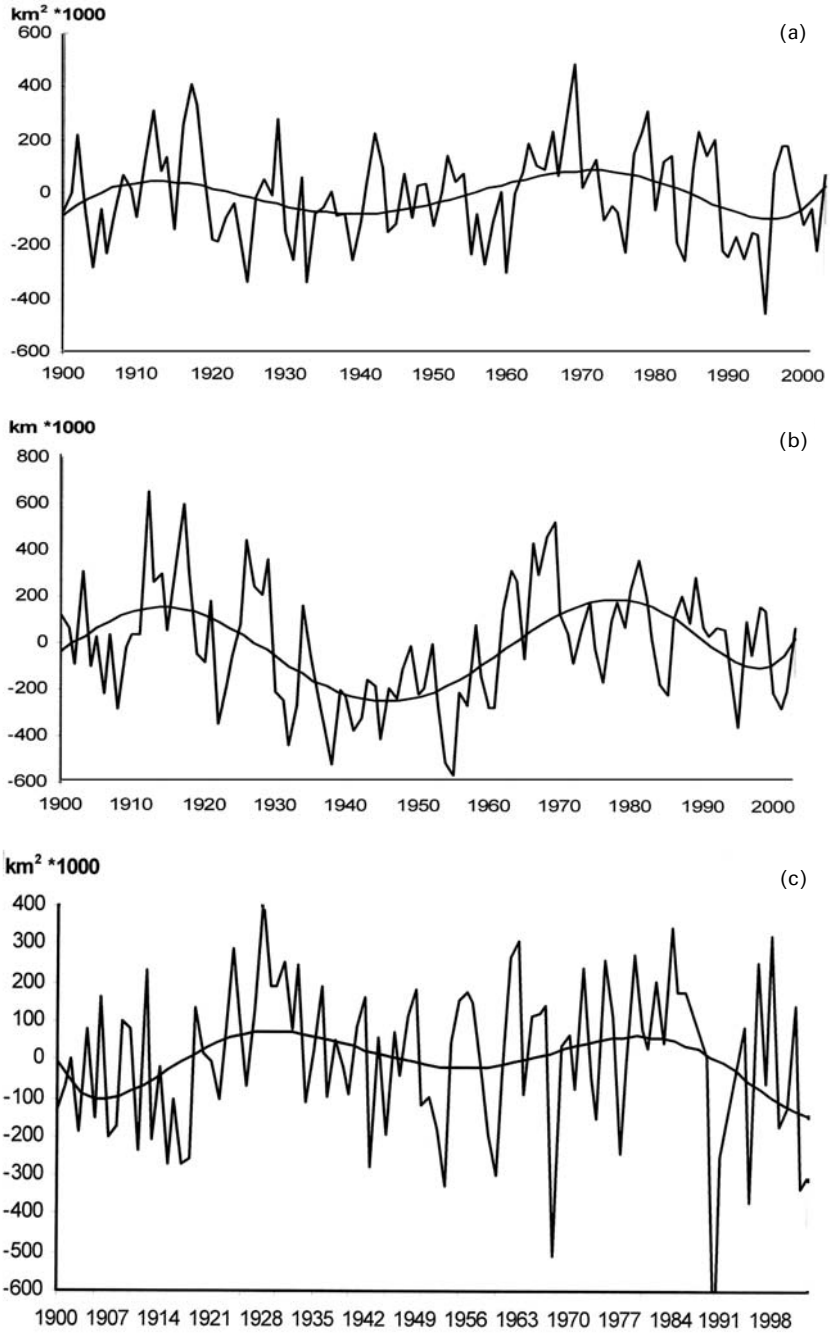

Figure 7.6. Fluctuations of total ice extent in the Greenland and Barents Seas in April (a); Greenland, Barents and Kara Seas in August (b); Laptev, East Siberian and Chukchi Seas (c) in August from 1900 to 2003 (linear trends are excluded).

Table 7.1. Contribution of climatic components to total variance of fluctuations in total ice extent in the regions (%).

Region	Month	Duration of cycles (years)				
		Linear trend	50–60	20	10	Total contribution
Greenland and Barents Seas	April	43	5	4	4	56
Greenland, Barents and Kara Seas	August	24	25	15	6	70
Laptev, East Siberian and Chukchi Seas	August	3	7	5	12	27

considered components are also presented. The values in Table 7.1 confirm that the total contribution to ice extent variance of the linear trend and long-period components in the western region is more than 2.5 times greater than in the eastern one. The contribution of a 10-year cycle to variability in ice cover extent of the eastern region is twice as high as that of the western region.

7.1.4 Causes of quasi-periodic fluctuations in ice extent

The underlying causes of these quasi-periodic fluctuations on different temporal scales have not yet gone beyond the realm of scientific hypothesis, and therefore require further detailed research. It is however obvious that most of the quasi-periodic behavior detected in sea ice cover must involve processes in the atmosphere and the ocean—components of the climate system that are influenced by both "external" and "internal" factors.

Plausible external factors may include helio-geophysical impacts such as solar activity, tidal and nutation phenomena, earth's rotation speed, fluctuations in the solar constant under the influence of varying distance between the earth and the center of masses of the solar system, fluxes of energy and charged particles from space and other astronomical factors. Internal factors include hydrometeorological processes such as internal variability of the climate system.

The phenomenon of the change in pressure anomalies in the north polar region that has been called the "Arctic Oscillation" (AO) or "North Atlantic Oscillation" (NAO) can serve as a possible cause for the "10-year" cycle of sea ice extent fluctuations. The NAO has been shown to influence ice conditions in Eurasian Arctic seas (Deser *et al.*, 2000; Hu *et al.*, 2002). The total duration of two phases of this oscillation (anticyclonic and cyclonic circulation regimes) comprises about 10 years, on average, which coincides with average 20th century durations of the 11-year cycle of solar activity periods, expressed by Wolf numbers (the so-called "Schwabe–Wolf"). The distribution of atmospheric pressure anomalies, typical of each of these AO phases, is close to atmospheric pressure field changes at high and temperate latitudes throughout the corresponding solar activity cycles revealed by Karklin (1978). The physical mechanism behind solar activity's influence on changes in atmospheric pressure fields is probably related to the intrusion of charged solar wind particles to upper

atmospheric layers at high earth latitudes. This induces the experimentally detected effect of atmosphere heating and expansion in the zone of intrusion of particles, the related appearance of horizontal gradients of atmospheric pressure and corresponding redistribution of air masses.

A "20-year" cycle of ice cover extent oscillations may also be connected to the known 22-year changes in solar activity (Hale's Law), manifested in the change of sign of magnetic fields on the sun; however, there are no convincing hypotheses about the possible mechanisms underlying such relations. Therefore, internal climate system processes may be invoked. Gudkovich and Kovalev (2002) proposed—based on analysis of long-term changes in ice extent in the Greenland Sea, the salinity of its waters and an index of cyclonic activity intensity in the Nordic seas region—a self-oscillating mechanism as responsible for the occurrence of cyclic changes in the ocean–ice cover–atmosphere system occurring about every 20–25 years. Periodic oscillations in atmospheric pressure occurring ion this time scale propagate from this zone to the east and northeast, causing corresponding changes in the ice cover extent of the Arctic Ocean. The attenuation of "20-year" cycles in changes in the ice cover extent of Arctic seas with increasing distance from Nordic seas eastward confirms the plausibility of this mechanism. Quasi-periodic oscillations in atmospheric pressure over the Norwegian Sea, caused by this mechanism, influence the westerly airflow over the North Atlantic, which is indicated by the NAO index. The inflow of Atlantic water to the Norwegian Sea and farther to the Arctic Basin, the Barents and other seas also depends on the intensity of this transfer.

The underlying causes of the pronounced 60-year cycle of ice cover fluctuations and corresponding hydrometeorological characteristics in the Arctic are not clear. There are two different hypotheses: (1) external forcing—namely, a solar variability hypothesis favored by the Russian co-authors of this book and others (e.g., Soon, 2005)—and (2) internal forcing, of a multi-decadal oscillation with a source in the northern North Atlantic, as evident in numerical model experiments (e.g., Delworth and Mann, 2000).

The external forcing hypothesis is based on the 60-year cycle of a change in solar radiation anomalies that could be the main cause of 60-year air temperature fluctuations. This is confirmed by the close coincidence of air temperature maxima in the northern hemisphere from 1579 to 1983 (reconstructed in Groverman and Landsberg, 1979). A solar forcing hypothesis for multi-decadal oscillation in Arctic temperature and Greenland Sea ice has also recently been put forth by Soon (2005) and Lassen and Thejll (2005), respectively.

The internal forcing hypothesis is based on observational evidence of enhanced expression of multi-decadal (60–80 year) cycles in air and sea temperature around the northern North Atlantic (e.g., Schlesinger and Ramunkutty, 1994), as well as indications of internal variability on the same time scales seen in many numerical model experiments, which indicate that ocean circulation in the northern North Atlantic, especially the Greenland Sea, may be the source (e.g., Delworth and Mann, 2000).

Notwithstanding the remaining uncertainties in the underlying mechanisms, the very existence of quasi-periodic variability across a range of time scales has important implications for understanding: (1) recent variability and trends in Arctic sea ice cover

observed during the microwave satellite era—1978 up to the present (Section 7.2)—and (2) future trends in sea ice cover in the 21st century (Sections 7.3 and 7.4).

7.2 RECENT ARCTIC SEA ICE VARIABILITY FROM SATELLITE DATA (*O.M. Johannessen, M.W. Miles, C. Myrmehl*)

7.2.1 Arctic sea ice concentration, area and extent, 1978–present

Sea ice concentration (percent ice area per unit sampling area) can be reliably retrieved from multi-channel, passive microwave satellite sensor measurements, as summarized in Section 3.1.7 and described more comprehensively in monographs—for example, Carsey *et al.* (1992); Gloersen *et al.* (1992) and Johannessen *et al.* (1994). From ice concentration data, additional sea ice parameters can be derived, such as ice extent (the area within the ice–ocean margin, usually delimited using the 15% ice concentration isopleth) and ice area (extent minus open water area). Sea ice data sets derived from passive microwave data are among the longest continuous satellite-derived geophysical records, extending over the last quarter century. The *Nimbus-7* scanning multi-channel microwave radiometer (SMMR) provided data from 1978 to 1987, and the follow-up special sensor microwave/imager (SSM/I) onboard a series of Defense Meteorological Satellite Program (DMSP) satellites has provided data since 1987. Newer sensor systems such as the advanced microwave scanning radiometer (AMSR-E) are now providing measurements in parallel with SSM/I, though AMSR-E data are not routinely used in place of SSM/I. The SMMR–SSM/I brightness temperature (T_B) data are resampled as 25×25 km grid cells and issued by the National Snow and Ice Data Center (NSIDC) in Boulder, Colorado, providing a standard data set for use in the application of ice parameter retrieval algorithms.

Analyses of SMMR–SSM/I data have shown that the winter maximum ice area is typically about 14×10^6 km^2 and the summer minimum ice area is about 6×10^6 km^2 (Figure 7.7), while Figure 7.8 shows the spatial patterns of 1978–2005 mean ice concentration in winter (a) and summer (b).

The seasonal cycle can be removed statistically, leaving a series of anomalies from which irregular variability and trends can be determined. The first trend analysis based on SMMR data found a slight negative trend in Arctic sea ice extent from 1978to 1987 (Gloersen and Campbell, 1991). The 3.2×10^4 km^2 yr^{-1} decrease (2.4% per decade) was found to be statistically significant. Data from the subsequent SSM/I have provided the basis to follow up SMMR trends. Johannessen *et al.*'s (1995) analysis of SMMR and SSM/I records—taken separately—revealed a greater reduction in Arctic sea ice area and extent during the SSM/I period—decreases from 1987 to 1994 were ~4% per decade compared with ~2.5% per decade from 1978 to 1987. However, large interannual variability, coupled with the brevity of individual SMMR and SSM/I records compelled scientists to produce longer time series for more robust trend estimation. Merged SMMR–SSM/I time series have since been produced and analyzed, establishing trends more robustly (Bjørgo *et al.*, 1997; Cavalieri *et al.*, 1997). The merging of SMMR and SSM/I data involves inter-comparison and

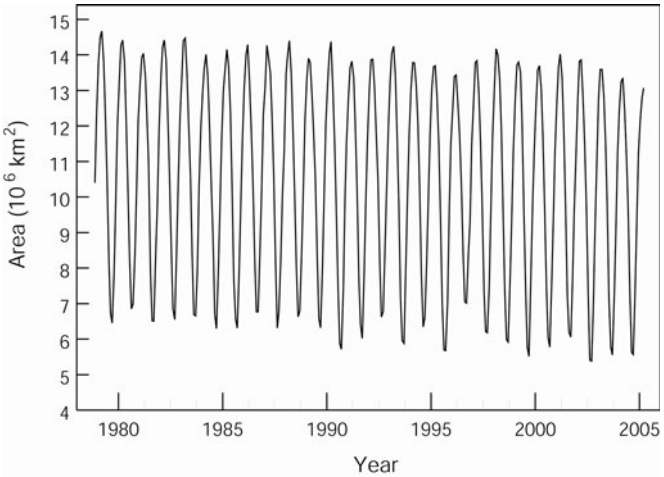

Figure 7.7. Arctic sea ice area, derived from satellite passive microwave sensor data, 1978–2005. *Source*: NERSC, Bergen, Norway, updated from Johannessen *et al.* (2004).

adjustments (i.e., inter-calibration) based on the 6-week overlap period in 1987 when both sensors operated. Two independent analyses of merged SMMR–SSM/I data established the trend in Arctic ice area and extent (1978–1995) to be about 3.0×10^5 km^2 per decade, corresponding to ~3% per decade (Bjørgo *et al.*, 1997; Cavalieri *et al.*, 1997). The SMMR–SSM/I time series were updated in 2003 (Johannessen *et al.*, 2004), indicating a decrease of $\sim 8.1 \times 10^5$ km^2 or, once again, 3% per decade in northern hemisphere annual sea ice area from 1978 to 2003. These data were updated in 2005 at the NERSC (Figure 7.9), giving the same trend.

Sea ice decreases in recent decades have been larger in summer, as first noted by Chapman and Walsh (1993) and subsequently updated and quantified by Parkinson *et al.* (1999). More recent calculations by Johannessen *et al.* (2004) indicate a 9.4×10^5 km^2 (14%) decrease in September vs. 6.8×10^5 km^2 (5%) in March (1978–2003). Parkinson *et al.* (1999) identified the seasonal and geographic patterns of variability and trends in ice concentration data, 1979–1997, finding winter reductions concentrated in the Barents and Greenland Seas, with summer reductions more pronounced in Siberian seas. Maslanik *et al.* (1996) investigated reductions in Arctic ice cover using SMMR–SSM/I data (1979–1995), with reductions in the 1990s found to be most pronounced in the Siberian sector in summer and record low Arctic ice minima in 1990, 1993 and 1995. As mentioned above, summer 2002 set the 25-year record for minimum ice extent and area (Serreze *et al.*, 2003), since surpassed (Stroeve *et al.*, 2005).

Figure 7.10 indicates the spatial patterns of linear trends in winter (a) and summer (b) sea ice concentration from 1978 to 2005, as updated by Johannessen *et al.* (2004). During this period, decreases in winter (a) were most pronounced (as large as ~50%) in the Barents and Greenland Seas. In contrast, summer decreases (b) have been greater than 50% in some areas of the Beaufort and Chukchi Seas, and as large as

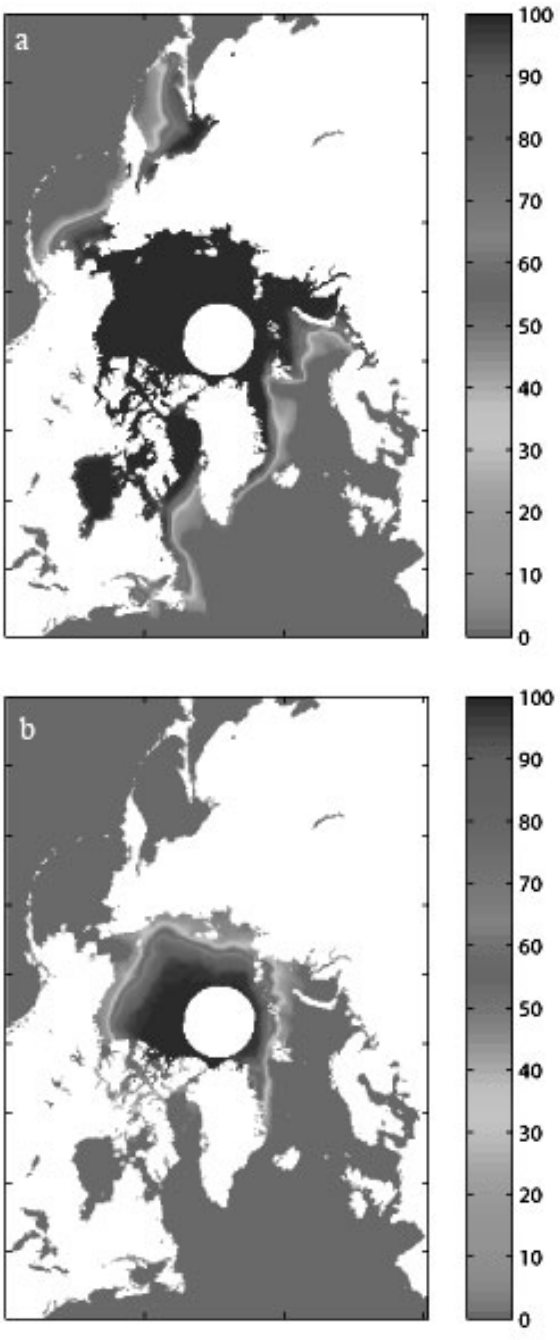

Figure 7.8. Mean sea ice concentration in the Arctic, derived from satellite passive microwave sensor data, 1978–2005, in (a) winter and (b) summer. *Source*: NERSC, Bergen, Norway, updated from Johannessen *et al*. (2004) (see also color section).

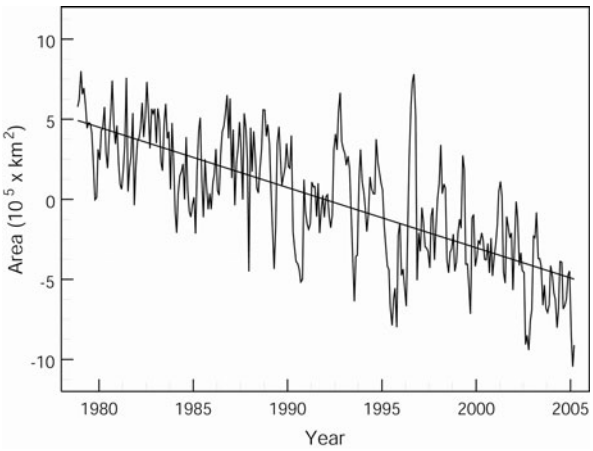

Figure 7.9. Linear trend for Arctic sea ice area anomalies, derived from satellite passive microwave sensor data, 1978–2005. *Source*: NERSC, Bergen, Norway, updated from Johannessen *et al.* (2004).

~30–50% in Siberian marginal seas (i.e., the Northern Sea Route). These summer patterns are in agreement with the independent analysis of ice cover minima from 1978 to 1998 (Comiso, 2002). The patterns reflect to some degree the extreme low amounts of sea ice in Siberian seas in the 1990s (e.g., 1998).

Johannessen *et al.*'s (2004) time series through September 2002 indicates that the record negative anomaly in summer ice cover reported by Serreze *et al.* (2003) was indeed unprecedented in the near quarter century satellite record. The record low 2002 minimum occurred from anomalous, warm, southerly winds in spring followed by low SLP and high SAT in the Arctic in summer, as found by Serreze *et al.* (2003). Furthermore, another large negative ice anomaly was observed in summer 2003, setting a new record for sea ice area, as unusually low ice concentration was apparent in the central Arctic Ocean. On the other hand, a large, positive anomaly also occurred recently, during the summer after an extreme, but temporary, reversal in the NAO index in the winter 1995/1996 (Johannessen *et al.*, 2004). Stroeve *et al.* (2005) report that summer ice in 2004 was near the record low. The summer ice extent in 2005 was again lower than the previous record low mentioned above, amounting to less than 6.3×10^6 km^2. Here we have added 0.22×10^6 km^2 to represent the area around the pole that is not imaged by SSM/I. Spatial variations in minimum ice extent in 2005 (Figure 7.11(a)) show that most of the NSR is free of ice, but with significant intra-annual variability. Figure 7.11(b) also shows the minimum ice extent for September from 1978 to 2005 and generally indicates increasing negative changes, consistent with model simulations.

7.2.2 Thick multi-year ice area

Statistical analysis of variability and trends in the previous sub-section concerned total ice cover, regardless of perennial (multi-year) vs. seasonal (first-year) ice. The

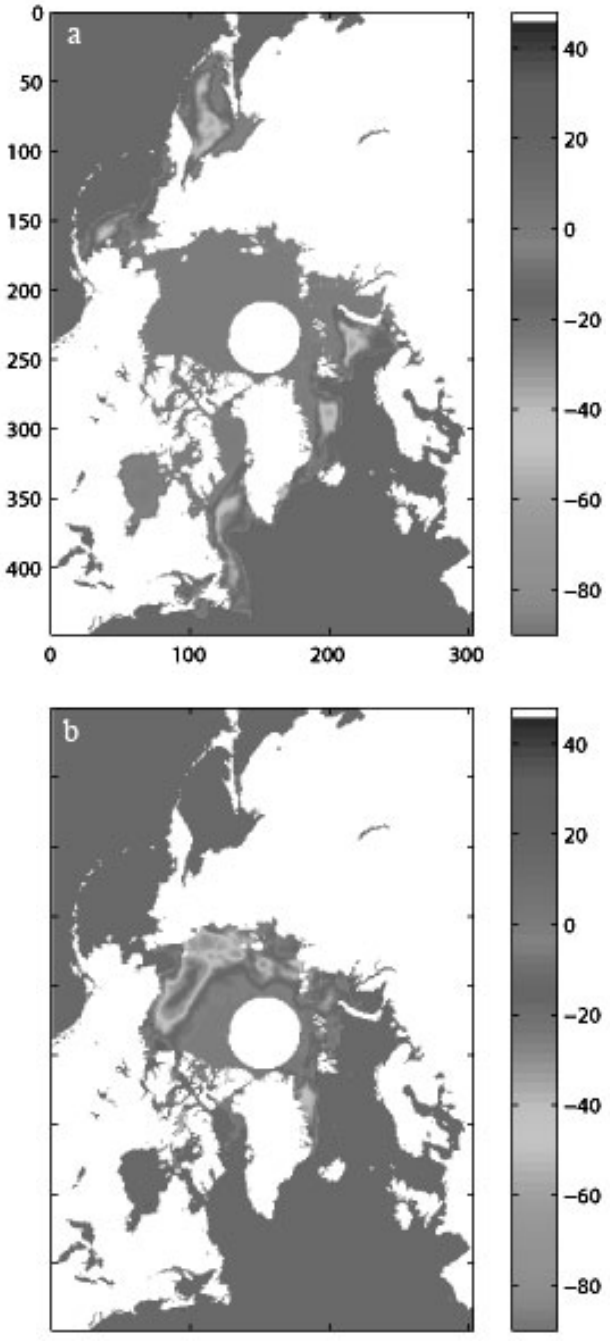

Figure 7.10. Linear trends in Arctic sea ice concentration, derived from satellite passive microwave sensor data, 1978–2005, in (a) winter and (b) summer. *Source*: NERSC, Bergen, Norway, updated from Johannessen *et al*. (2004) (see also color section)..

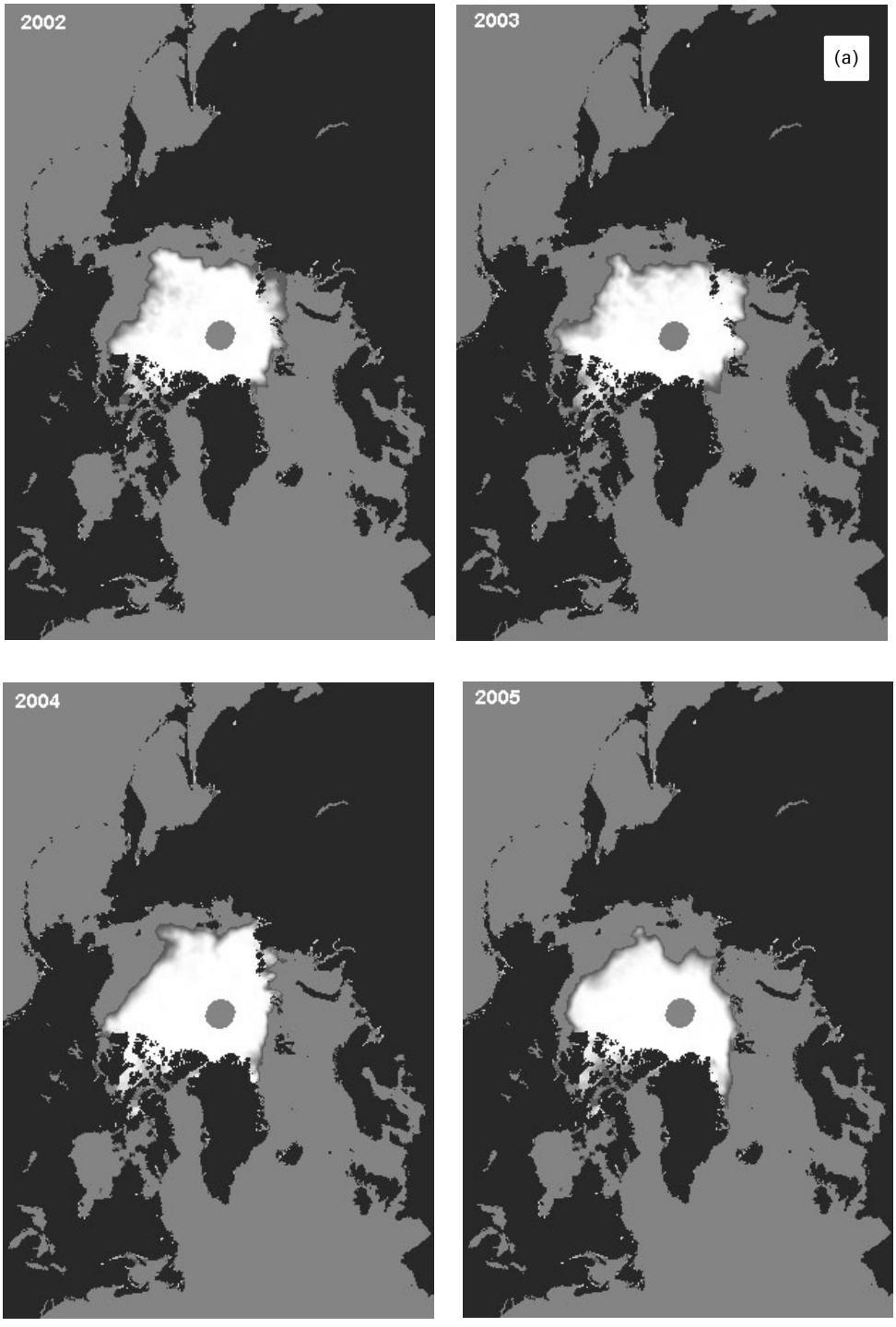
2002
2003
(a)
2004
2005

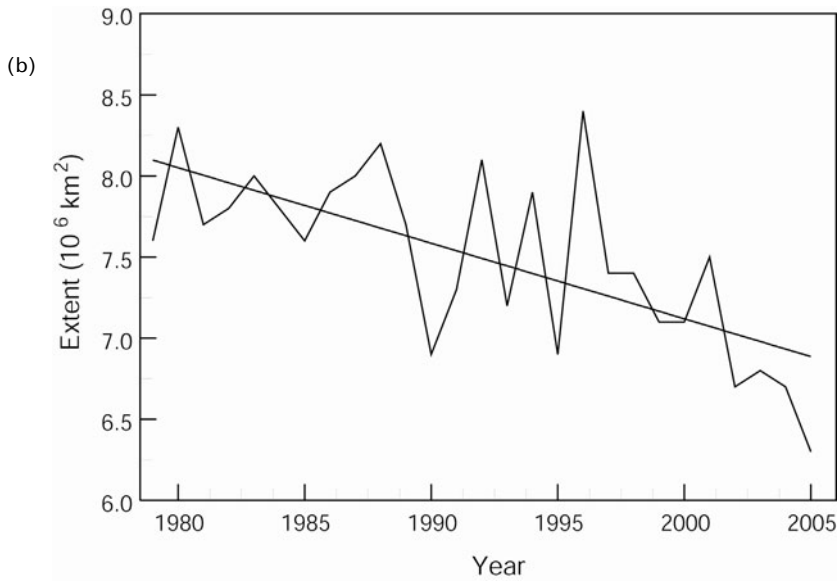

Figure 7.11. (a) (see opposite page) Arctic summer minimum sea ice extent (mean for September month) for 2002 to 2005 (see also color section); and (b) mean for September from 1979 to 2005 (courtesy: NERSC, Bergen, Norway).

pronounced negative ice anomalies in summer in the 1990s and the present decade imply consequential changes in other aspects of ice cover—that is, a reduction in winter multi-year ice (MYI) area that could be due to increased summer melt and/or ice export, which occurs primarily through the Fram Strait via the East Greenland Current. Because MYI is ~3 times thicker than first-year ice (FYI), changes in its areal distribution could both reflect and effect further changes in the Arctic Ocean, underscoring the geophysical rationale for identifying and understanding large-scale MYI variability. Furthermore, the amount of MYI is a key factor in navigability.

MYI and FYI have different radiative properties, which in theory permit discrimination using multi-channel passive microwave T_B data from winter months, when their signatures are relatively stable. In summer, the effects of melt ponds and melting snow on the ice confound the signal. Even in winter, errors associated with MYI estimates can arise from emissivity variations and variations in physical ice temperatures (Gloersen *et al.*, 1992). The possibility of passive microwave monitoring of interannual variations in MYI area was explored more than a decade ago (Comiso, 1990), but its potential had been scarcely realized until recently. Comiso (1990) analyzed SMMR data to derive and compare winter MYI area to the preceding summer ice minimum, which should correspond—aside from ice export and divergence/convergence effects. The problem has been that ice-type algorithms—such as the NASA Team—substantially underestimate the MYI fractions: discrepancies of 25–40% were found between winter MYI area and the preceding summer's ice minimum (Comiso, 1990). Subsequent research (e.g., Thomas and Rothrock, 1993)

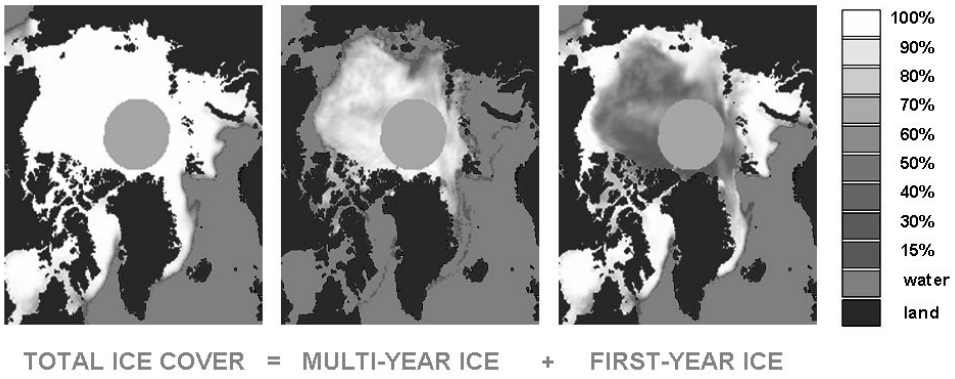

Figure 7.12. Arctic total sea ice concentration (left) and its two components: multi-year (*center*) and first-year (*right*) ice, derived from satellite passive- microwave sensor data. The gray-scale indicates the fraction (%) of each ice type (black = 0%, white = 100%). *Source*: Elena V. Shalina, NIERSC, St. Petersburg, Russia, as featured in Kerr (1999) (see also color section).

has reduced some inconsistencies in the NASA Team algorithm, but there remain some biases and errors. Johannessen *et al.* (1999a) applied the Norwegian Remote Sensing Experiment (NORSEX) algorithm (Svendsen *et al.*, 1983) to SMMR and SSM/I data to produce and analyze time series of MYI and FYI areas in winter (Figure 7.12). The methods were based on the Bjørgo *et al.* (1997) approach used for merging SMMR–SSM/I data, with additional techniques for estimation of MYI and FYI areas (Shalina *et al.*, 1999).

Johannessen *et al.* (1999a) found a relatively large (~7% per decade) reduction in MYI area in 1978–1998, compared with ~2% per decade in total ice area in winter. The negative trend in MYI area from Johannessen *et al.*'s (1999a) analysis has often been cited as evidence of a substantial change in the nature of the Arctic sea ice cover, more than merely a peripheral effect. This analysis has been updated and Figure 7.13 shows that the variability and trend for MY ice from 1979 to 2005 gives the same negative trend as before—that is, 7% per decade.

Subsequently, Comiso (2002) used a simpler, though roundabout, approach to estimate MYI area from SMMR–SSM/I data (1979–2000), taking summer minimum total ice extent as a proxy for MYI area. Comiso (2002) found a negative trend very similar to Johannessen *et al.*'s (1999a) and noted that "the general location of the perennial sea ice cover changes from one year to another and depends on many factors, the most important of which is advection or ice drift, which has been shown to be strongly influenced by atmospheric circulation." The latter can be in cyclonic mode where ice is normally advected to the west causing large open water areas in the east (e.g., Laptev and Kara Seas) and relatively small open areas in the west (e.g., Beaufort Sea and Chukchi Seas) or in anti-cyclonic mode in which the opposite occurs. During 1978 and 1998, the largest decrease occurred in the western area (Beaufort and Chukchi Seas) while considerable decreases were also apparent in the eastern region (Siberian, Laptev and Kara Seas).

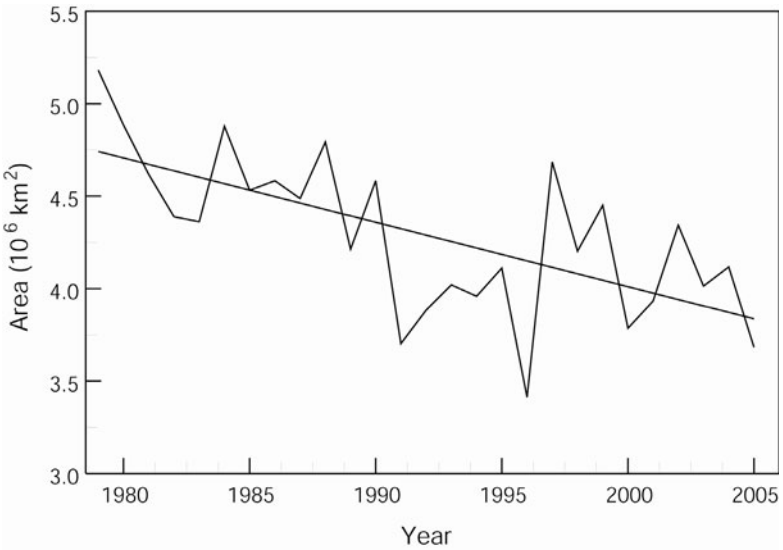

Figure 7.13. Variability and trends in winter multi-year ice (MYI) area, mean of February and March from 1978 to 1998 (courtesy: NERSC, Bergen, Norway).

Johannessen *et al.*'s (1999a) and Comiso's (2003) analyses include data only up to 1998. Since then a 26-year (1979–2004) observational record of mid-winter multi-year sea ice distributions, derived from neural network analysis of SMMR–SSM/I data (Belchansky *et al.*, 2004, 2005). Belchansky *et al.* (2005) confirmed dense and persistent cover in the central Arctic Basin surrounded by expansive regions of highly fluctuating interannual cover. Following a decade of quasi-equilibrium, pronounced declines in MYI commenced in 1989 when the NAO/AO shifted to a pronounced positive phase. Although extensive survival of first-year ice during autumn 1996 (after the record positive-to-negative NAO reversal in 1995/1996) replenished the area of MYI, a subsequent and accelerated decline returned the depletion to record lows (Belchansky *et al.*, 2005). The most dramatic MYI declines occurred in the East Siberian, Chukchi and Beaufort Seas.

Despite a more neutral state of the NAO/AO in recent years, there is no indication that the MYI decline is reversing (see Figure 7.13). Indeed, the post-1997 MYI decline rivals that of the early 1990s, despite comparatively neutral AO conditions. Rigor and Wallace (2004) propose that residual effects of the strong positive AO phase during the early 1990s still persist. They found that much of the Arctic's oldest MYI was expelled through the Fram Strait during the high-index AO phase, leaving a younger and thinner ice pack more vulnerable to summer melt. Serreze *et al.* (2003) point out that increased heat advection into the Arctic during spring, and persistent low pressure and high temperatures during summer, have exacerbated sea ice retreat in the most recent years. These conditions also promote production and entrainment of young ice, thus perpetuating anomalous retreats in following years (Rigor and Wallace, 2004).

Whether past sea ice conditions will return or a new equilibrium is established remains an important topic for continued monitoring and research. Passive microwave remote sensing data from U.S. satellites have been of fundamental importance in observing variability in sea ice cover during the last quarter of century and in the study of both natural and anthropogenic variability. It is therefore of utmost importance that this or similar satellite programs continue in the future.

7.3 21ST CENTURY SEA ICE SCENARIOS: STATISTICAL MODELING (*I.Ye. Frolov, Z.M. Gudkovich, V.P. Karklin*)

The variability and trends in sea ice observed through the 20th century (Section 7.1) and through the most recent years (Section 7.2) may provide insight to predict future behavior. The simplest statistical model, aside from climatology, is projection of the linear trend—that is, an extrapolation like that performed by Comiso (2003) for perennial ice cover. The linear trend approach is flawed for at least two statistical reasons: (1) its dependence on and sensitivity to the sampled, often short period, and (2) its oversimplicity, ignoring quasi-periodic fluctuations or other polynomial behavior, thereby failing to consider longer term variability including low-frequency oscillations (as described in Section 7.1 and below).

This section presents statistical models based on observed variability and trends in Russian Arctic seas in the 20th century, developed by the AARI co-authors of this chapter. The rationale is that numerical models have several shortcomings, such as their inability to consistently model either the real observed distribution of sea ice or quasi-periodic variability across a range of time scales. The statistical forecast of possible changes in sea ice extent of Arctic regions in the 21st century is based on three components that have contributed most to long-term variability in ice extent in the 20th century—namely, the "half-secular" cycle, the linear trend in the second half of the century and the "20-year cycle" (for western seas).

To specify the average duration of the amplitude and initial phase of the "half-secular" (50–60 years) cycle, harmonic analysis of the polynomial trend of total ice extent was done separately for western and eastern seas. The duration of the cycle used in the forecast was 60 years for western and 55 years for eastern seas with amplitudes of 210×10^3 km^2 and 70×10^3 km^2, respectively.

The forecast takes into account the "worst case" throughout the 21st century relative to the slightly decreasing linear trend in the second half of the 20th century. It follows from analysis of the plots presented in Figure 7.14 that the oscillatory variation in ice extent changes is expected to be preserved in the 21st century. We forecast an increase in ice extent between the 2020s and 2040s with a maximum around 2030 in eastern seas and around 2020 and 2040 in western seas. The second maximum falls approximately between 2080 and 2090. The amplitude of fluctuations in the western region approaches 0.5×10^6 km^2. Short-period fluctuations will in addition still prevail in the eastern region.

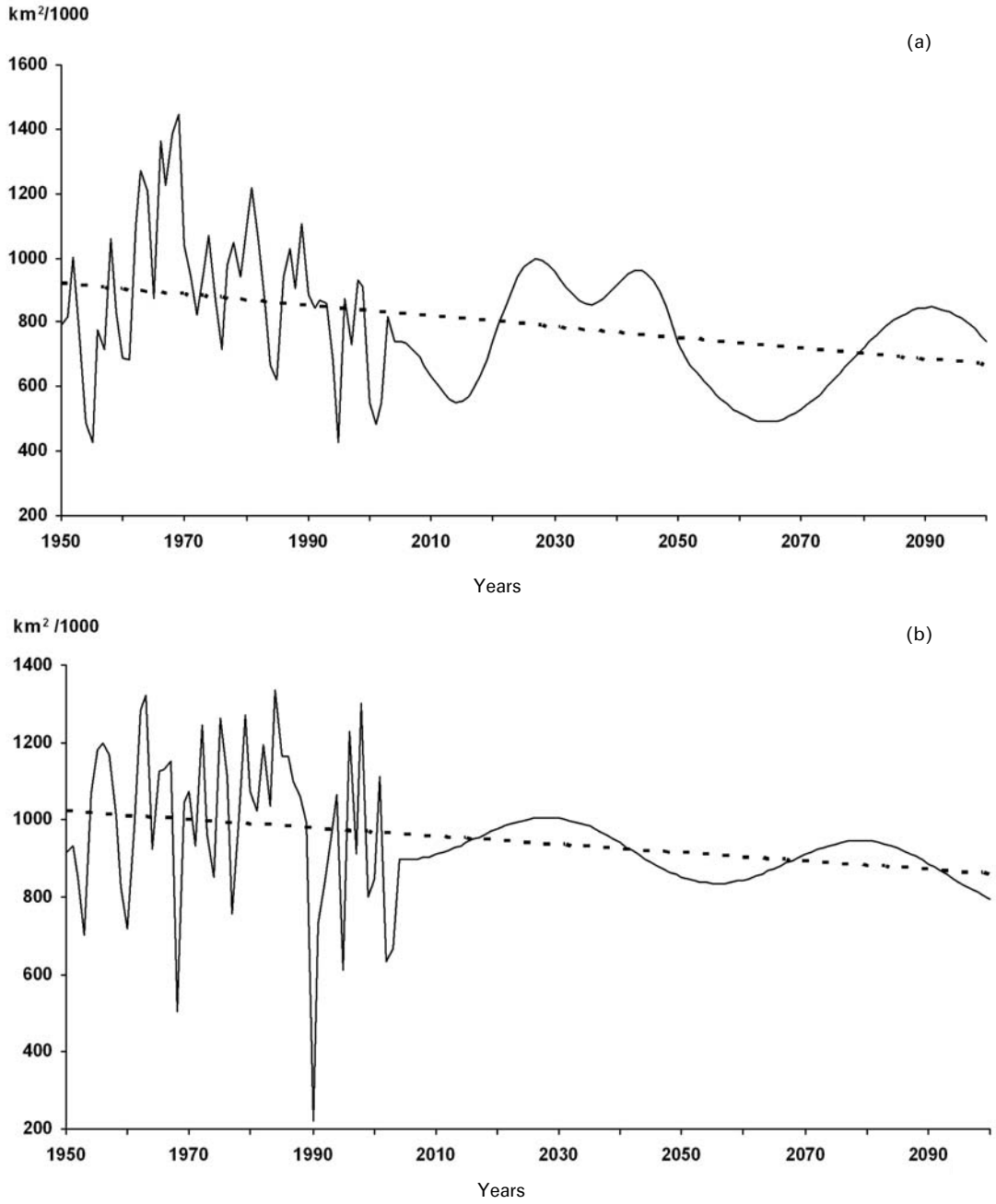

Figure 7.14. Statistical model forecast of climatic components of total ice extent in western (a) and eastern (b) Arctic seas for the 21st century relative to the linear trend: long dashed line = 2005 to 2050; short dashed line = after 2050.

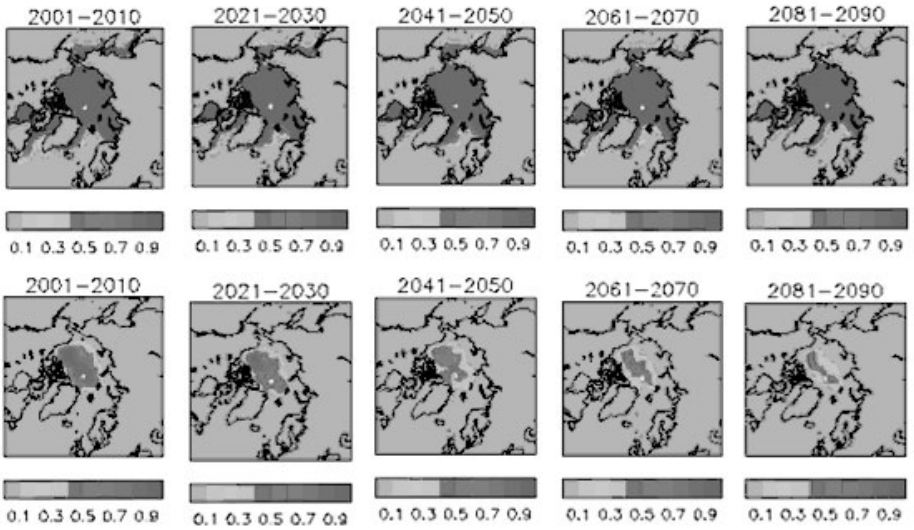

Figure 7.15. HadCM3-modelled northern hemisphere sea ice concentrations in winter (*upper panels*) and summer (*lower panels*). The results shown here are using the IPCC SRES B2 emission scenario. The color code below gives ice concentration (© Crown copyright, published by the Met Office, courtesy Dr. Howard Cattle) (see also color section).

7.4 21ST CENTURY SEA ICE SCENARIOS: NUMERICAL MODELING (*O.M. Johannessen, M.W. Miles, C. Myrmehl*)

7.4.1 Numerical model predictions

The statistical models developed in the previous section represent a simple way of predicting sea ice variability. However, it may be contended that statistical modeling for forecasting sea ice years to decades in advance is stretching the limit to which they can be used, whereas significant advances in numerical modeling both including anthropogenic forcing and natural variability, continue to be made. The following paragraphs summarize results from numerical model predictions of sea ice extent under increasing GHG and aerosol scenarios.

Several years ago, the annual sea ice extent in the northern hemisphere was modeled and compared with observations in independent analyses (Vinnikov *et al.*, 1999; Johannessen *et al.*, 2001), which predicted an annual reduction of ~15% up to the year 2050 under an IPCC greenhouse gas scenario. However, the potentially large and important spatial and seasonal aspects were not considered.

Recently, Johannessen *et al.* (2004) modeled both the spatial and seasonal variability of the ice cover and its response to anthropogenic forcing up to 2100, using two different state-of-the-art models including different IPCC GHG and aerosol emission scenarios. The models employed were the ECHAM-4 and HadCM3, from the Max-Planck Institute for Meteorology in Hamburg, Germany, and the Hadley Centre at the UK Met Office, respectively. HadCM3 results are shown in Figure 7.15 for five decades—2000s, 2020s, 2040s, 2060s and 2080s. The results shown here are those using IPCC SRES emission scenario B2,[2] although results using the higher A2 scenario

have also been produced. The key feature is prediction of moderate changes in winter and drastic changes in summer, with up to 80% reduction expected late in the 21st century.

These results and other results from Johannessen *et al.* (2004) were included in the ACIA report, which further incorporated composite predictions from additional models (see Walsh and Timlin, 2003) and five-model mean predicted spatial fields for the 2010s–2020s, 2040s–2060s and 2070s–2080s. Walsh and Timlin (2003) compared 21st century projections for northern hemisphere sea ice from these five coupled global atmosphere–ocean–ice models, including the Hadley Centre model. The synthesis, as incorporated in the ACIA reports, included enhancement of informational content for projections. Each of the five models shows a substantial decrease in sea ice through the 21st century when forced by the B2 scenario, in particular during summer.

However, Walsh and Timlin (2003) noted that differences in the present-day ice coverage simulated by these models are sufficiently large that they dominate across-model variances in projected ice extents. Adjustments based on present-day biases remove much of the spread between projections. Annual decreases in adjusted ice extent by the year 2100 range from about 12% to about 46%. Percentage decreases are much larger in summer than in winter; much of the Arctic Ocean could well be ice-free at the time of the summer ice minimum by 2100. However, it should be mentioned that recent research (Bengtsson *et al.*, 2006) indicated that the internal variability of the climate system is essentially chaotic in nature, as, for example, observed by the huge warming event peaking around 1940, causing a major reduction in sea ice extent (Johannessen *et al.*, 2004), which can offset these predictions.

7.4.2 Climate and its implications for the Northern Sea Route

The numerical model generated sea ice scenarios presented in the above section clearly indicate that predicted reductions in sea ice cover will enhance operational capabilities in the Northern Sea Route and transportation and offshore activities elsewhere in the Arctic. However, caveats are that decadal to multi-deacdal oscillations, such as observed and statistically modeled in Sections 7.1 and 7.3 or the chaotic internal variability of the climate system, may be important, especially if a positive phase of low-frequency oscillation (LFO) is manifested as increases in sea ice extent in the coming decades, as predicted by Russian authors.

The navigation season is commonly used to indicate the number of days per year when there are easily navigable ice conditions, depending on operational definitions. Projected changes in the length of the navigation season for the Northern Sea Route in the 21st century, based on five-model output (ACIA, 2004) are shown in Figure 7.16. The different curves represent various ice concentration thresholds (e.g., 25%, 50% and 75%). The 75% ice concentration threshold is considered feasible for icebreakers. The future distribution of first-year seasonal ice vs. thicker multi-year will also be a factor in navigability.

The length of the navigation season is only one aspect to consider. In any given year or average of years, the same sea ice extent or area will have markedly different

[2] Further information on this and the IPCC model scenarios can be found at *http://www.grida.no/climate/ipcc_tar/wg1/029htm#storya2*

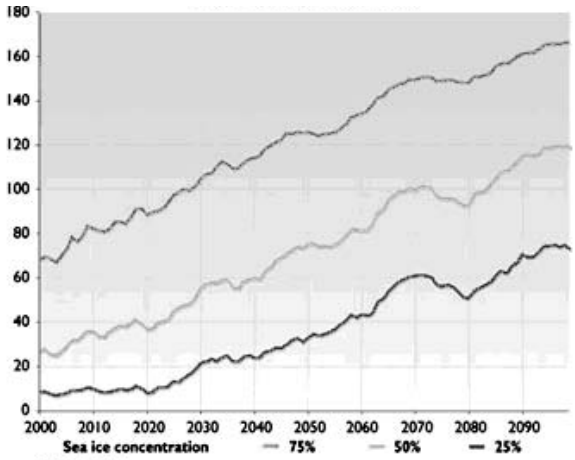

Figure 7.16. Projected changes in the navigation season (in days) for the Northern Sea Route in the 21st century, based on five-model output. The curves represent ice concentration thresholds: 25%, 50% and 75%. *Source*: ACIA (2004) (see also color section).

geographic configurations. This is evident from year-to-year differences in the satellite record where, for instance, each summer ice distribution is different with respect to ice conditions in the Eurasian Arctic (e.g., Figure 7.11). Each of the past four summer minima 2002–2005, while similar in terms of overall extent, has a different geographical pattern. The distribution of negative and positive anomalies varies substantially from year to year. In 2002 the marginal seas of the NSR were essentially ice-free—especially the Laptev Sea and the adjacent Arctic Basin. In 2003 the distribution was similar except for a displacement of the ice pack towards the Barents and Kara Seas, with anomalously high concentrations in the northern Barents and Kara Seas. In 2004 and 2005 the patterns were again different, with 2005 essentially ice-free in Siberian seas.

The implications of expected reductions in sea ice for routes in the NSR, ranging from near-coastal to over-the-pole routes, depend both on the physical conditions that may develop and on the economic conditions that may be in effect. For example, it may be that exploitation of hydrocarbon resources, primarily in western Eurasian Arctic seas, will mean that the western part of the NSR will predominate the agenda. In terms of physical conditions, the spatial distribution of expected changes in sea ice cover is difficult to model consistently, as noted in the previous section. Even when model means are compared, there are large discrepancies—let alone when comparing spatio-temporal variability around the mean, which is even more uncertain, particularly several decades into the 21st century.

Therefore, we strongly recommend that further studies be performed, including proper validation of models on past data, before further prediction is done. An important issue is also proper ''downscaling'' or ''nesting'' of global climate models to the regional scale, along the Northern Sea Route, in order to be useful for increasing activities in this region and for future strategic planning.

8

Afterword

(I.Ye. Frolov, V.Yu. Alexandrov, Ye.U. Mironov, A.G. Gorshkovsky, N.G. Babich, V.G. Smirnov)

The Arctic Ocean has some of the largest deposits of oil and gas in the world, with resources on the Russian Arctic Shelf being estimated at 70 billion tons. About 80% and 75% of Russian reserves of natural gas and oil, respectively, are concentrated in the Arctic, as are many strategically important nonferrous and precious metals. In the western Eurasian Arctic alone approximately 2.2 million km^2 are of potential interest for oil and gas exploration.

The highest priority areas for exploration and development of gas resources are the northeastern Barents Sea shelf, the shallow part of the Pechora shelf, the Yamal shelf of the Kara Sea, as well as Ob' and Taz Bays. Eleven fields of hydrocarbons with total resources of about 4.5 billion tons of oil equivalent, including 360 million tons of oil, are confined within the Barents and Pechora Seas. Three gas and condensate fields with a total 8 billion tons of oil equivalent, including 220 million tons of liquid hydrocarbons, have been discovered within the Kara Sea basin (Bambuliak and Frantsen, 2005). Proven probable and possible reserves of gas of the Yamal and Gydanskiy peninsulas, plus adjacent offshore zones, are some 50 billion tons of oil equivalent, according to Russian geologist estimates (Laiho *et al.*, 2005). Maximum gas production in the fields of the southern Kara region may amount to at least 100 billion m^3/year. It should also be mentioned that the Noril'sk industrial area of Taymyr provides 20% of the world's production of nickel (Velikhov *et al.*, 2001).

At present, the development of western Arctic fields is only just beginning; however, oil and gas production will significantly increase in the near future. Oil production within the Barents Sea shelf has begun with the startup of the Prirazlomnoye oil field deployment in 2006. In accordance with the Russian federal program for development of the Timano–Pechora oil–gas complex, the volume of oil produced here will increase five- to six-fold up to 2010. There are also plans to begin oil production in the northern part of the Timano–Pechora oil producing area in the very near future (Velikhov *et al.*, 2001). In the longer term, the immense Shtokman

field and the fields of the Barents Sea in the Murmansk region will be substantially developed.

According to economic predictions, oil and gas production will increase in the Ob'–Yenisey region (Ob' and Yenisey basins, Gydanskiy region and the upper reaches of the Taz River) in the next decades. Tambeyneftegas estimates that the maximum production in the company's gas fields in Yamal peninsula will be 20 million tons of liquefied natural gas (LNG) and 12.5 million tons of condensate annually. It is also planned to transport its products via the Northern Sea Route (NSR) using tankers that will be able to operate independently in ice (Laiho *et al.*, 2005).

The NSR is important not only as an export corridor, but also as a national transportation route. Technical and economic studies proved that the NSR is the most economically beneficial and ecologically safe system for the delivery of natural resources from the Russian North and Siberia (Peresypkin, 2002). The Murmansk, Arctic, Primorsk, Northern and Far Eastern Shipping companies constantly conduct operations along the NSR. Cargo volumes transported by the NSR, excluding oil transport, totaled 1.7 million tons in 2003. Of this amount, the transport of Noril'sk nickel ore and metal constituted 1 million tons, while the state's Northern Delivery Program and commercial transport to northern population centers, operated by the Murmansk Shipping Company (MSCO), totaled 450,000 tons. The Northern Delivery Program supplies remote parts of northern Russian territories with fuel, provisions and other vital cargoes, providing for the needs of people during winter. Shipping and cargo flows through the NSR are directly connected to the development of mineral resource production and to industrial production increase in areas of the far north. The development of the transport system including the NSR, communications and power production can thus be considered the priority for Arctic development (Chilingarov, 2001). The principal approach of the Russian government to the development of the NSR is determined by the fact that it is down to the state to preserve, maintain and develop the federal transport infrastructure (including icebreakers, hydrometeorological and navigation–hydrographic support) and protect the environment (Yakovlev *et al.*, 2002). Modernization of the Arctic transport system should provide strategic control over the Russian Arctic sector and stable export through northern sea lanes, as well as promoting the development of northern territories.

A draft federal law "On the Northern Sea Route" was laid down in 2005. It emphasizes the achievement of long-term objectives, such as securing the national interests of the Russian Federation concerning the NSR, centralized state direction of the transport system, icebreaker support and guaranteeing equal access rights to interested cargo carriers, including foreign carriers.

In accordance with Article 234 of the UN Convention on Maritime Law, coastal states have the right to pass and secure nondiscrimination laws and regulations on prevention, reduction and control of marine environment pollution by ships in ice-covered regions within the limits of their exclusive economic area (EEA). In these areas in the Russian Arctic, the particularly severe climatic conditions and presence of ice cover during most of the year represent obstacles or increased danger for navigation, and marine environmental pollution may damage the ecological balance. The

intention is to extend the law to Russian- and foreign-owned ships that call at NSR ports opened for international navigation. Enactment of the federal law "On the Northern Sea Route" is expected in the near future.

In compliance with the law, the Northern Sea Route Administration organizes sea ice and hydrometeorological support for navigation in the NSR, which necessitates the availability of a centralized ice information system. An example of such an ice information system is the Russian system "Sever", which was created specially for information support of navigation in the NSR as well as other applications in the Arctic Shelf (Smirnov *et al.*, 2000; Frolov *et al.*, 2003, 2005). In many cases "Sever" operates like a typical distributed system (i.e., with allocated functionality) in which a local user is served by a specific regional Roshydromet department and simultaneously obtains information from the Arctic and Antarctic Research Institute (AARI).

In conclusion, an ice information system for supporting navigation in the NSR should be organized along these lines:

(1) Ice information delivery from a common Russian information center, one that is responsible for the accuracy, orderly maintenance and delivery of this information.
(2) Receipt and preliminary and thematic processing of satellite information in a limited number of different Russian and foreign centers. The selection of such centers must consider the experience and accuracy of sea ice interpretation from satellite images in different spectral bands (e.g., microwave).
(3) Collection of heterogenous information in the Russian Center with joint analysis of its accuracy and preparation of integrated information products for dissemination to the user.

Glossary of sea ice terms

From Johannessen et al. (1997) and WHO (2004)

The typical SAR backscatter (low or high) is indicated.

Brash ice A concentration of ice fragments not more than 2 m across, the wreckage of other ice forms. High backscatter.

Concentration of ice The ratio in tenths of the surface covered by ice of any ice form to the total surface area. Size of area is determined by the observation method and/or by context (average concentration). Special terms are (nearest tenth):

- Compact ice: Concentration 10/10, no water visible.
- Very close ice: Concentration 9/10 to 10/10, water visible.
- Close ice: Concentration 7/10 to 8/10.
- Open ice: Concentration 4/10 to 6/10.
- Very open ice: Concentration 1/10 to 3/10.
- Open water: Concentration less than 1/10 with the possibility of ice.
- Ice-free: No ice present.

Consolidated ice Floes frozen together with no water visible (compact ice concentration). Mainly low backscatter.

Deformed ice General term for ice squeezed together and in places forced upward and downward. Includes rafting, ridging and hummocking. Higher backscatter than **Level ice**.

Fast ice Sea ice remaining stationary attached to the coast or grounded. Mainly low backscatter.

First-year ice (FY) Ice formed since the previous summer from **Young ice**, more than 30 cm thick. May be subdivided into Thin FY 30–70 cm, Medium FY 70–120 cm and Thick FY more than 120 cm thick. Backscatter lower than MY ice.

Flaw The separation zone between pack ice and fast ice, usually a shear zone with ice pieces in chaotic state depending on ice motion. High backscatter.

Flaw lead and Flaw polynya A navigable opening between the **Pack ice** and **Fast ice**. Usually low backscatter.

Floe Relatively flat piece of ice more than 20 m across. Subdivided into Giant (over 10 km), Vast, Big, Medium and Small (less than 100 m) floes. *See also* **Ice cake**.

Fracture Any break or rupture through ice of high concentration or single floes. May be open water (low backscatter) or filled with ice fragments (high backscatter), *See also* **Lead**.

Frazil ice A form of **New ice** with small ice plates suspended in the water. Low backscatter.

Frost owers Needles of salty hoar ice crystals formed by condensation on bare thin ice. Very high backscatter.

Grease ice A form of **New ice** where the ice crystals form a soupy layer on the surface. Low backscatter.

Gray ice and Gray/white ice Ice of thickness 10–15 cm and 15–30 cm, respectively. *See* **Young ice**.

Hummocking Forming of hills of broken ice (hummocks) forced together by pressure. The degree of hummocking is the area in fifths occupied by the deformed ice. *See also* **Ridging**. High backscatter.

Iceberg A large volume of freshwater ice broken (calved) from a glacier. Smaller pieces are called bergy bits and growlers.

Ice cake Relatively flat piece of ice less than 20 m across. *See also* **Floe**.

Ice edge The boundary between the open sea (**Open water** or **Ice-free**) and the main area with sea ice. It may be termed compact or diffuse, usually dependent on the wind direction relative to the edge.

Ice-free Open water without ice of any type. The backscatter depends on the windspeed.

Lead A **Fracture** navigable by surface vessels.

Level ice Ice unaffected by deformation. Lower backscatter then for **Deformed ice**.

Melt pond Accumulation of melt-water on the ice surface in summer. Low backscatter.

Multi-year ice (MY) Ice which has survived at least one summer melting. Note that for remote-sensing applications the WMO term Second-year ice (survived only one summer) is included in this term. Usually thicker than **First-year ice**. Backscatter higher than FY ice.

New ice General term of very recently formed ice with crystals only weakly frozen together. Includes **Frazil ice** and **Grease ice**. Very low backscatter.

Nilas Elastic crust of ice up to 10 cm thick. May be subdivided into dark nilas under 5 cm and light nilas over 5 cm thick. Low backscatter.

Old ice Sea ice which has survived at least one summer's melt. Most topographic features are smoother than for **First-year ice**. May be subdivided into **Second-year** and **Multi-year (MY) ice**.

Open water Freely navigable water where ice is present in concentration under 1/10 but not **Ice-free**. Note that the term in remote sensing may include undeformed thin ice not possible to separate from calm water. Backscatter dependent on windspeed.

Pack ice (or drift ice) All types of sea ice other than **Fast ice**, no matter shape or distribution. Usually in motion.

Pancake ice Circular pieces of ice up to 3 m across and 10 cm thickness with raised rims, formed by swell or waves, common near the **Ice edge** and often mixed with **Grease ice**. Very high backscatter.

Polynya A non-linear opening enclosed in ice. *See* **Flaw polynya** and **Shore polynya**. It may contain **Open water** or thin ice. The backscatter depends on the windspeed and ice type.

Rafting Formation of thicker (rafted) ice by pressure-forced overriding of one piece on another. Common for **Young ice** and thinner ice types. High backscatter.

Recurring polynya (area) A larger area where repeated opening and closing of polynyas create a special pattern of ice every year. Variable (often banded) backscatter.

Ridging Formation of ridges of thick pieces of broken ice forced together by pressure. Common for **First-year ice** and thicker ice. The degree of ridging is counted in fifths—that is, fraction of the area occupied by deformed ice. *See also* **Hummocking**. High backscatter.

Shore lead and Shore polynya An opening between **Pack ice** and the coast navigable by surface vessels. Usually low backscatter.

Stamukhas Russian term for grounded pieces of sea ice floes, often standing edgeways, formed by **Ridging**. Very thick (i.e., more than 15 m).

Summer ice Common term in remote-sensing applications, describing ice at summer melt, when generally no distinction between thickness types can be made.

Young ice Ice 10–30 cm thick. May be subdivided into **Gray ice** under 15 cm and **Gray/white ice** over 15 cm thick. Backscatter increases with thickness.

Water Term in remote sensing used for areas with **Open water** (less than 1/10 ice concentration, or with thin ice not separable from a water surface), or an **Ice-free** area. The backscatter depends on the windspeed.

DEFINITIONS OF BASIC SYMBOLS IN OVAL FORM (according to *WMO Sea Ice Nomenclature*, Suppl. No. 4, WMO No. 259)

Concentration (C)

C	Total concentration of ice in the area, reported in tenths (see symbols in Table G.1). *Note:* Ranges of concentration may be reported.
C_a C_b C_c	Partial concentrations of thickest (C_a), second thickest (C_b) and third thickest (C_c) ice, in tenths. *Note:* Less than 1/10 is not reported. 10/10 of one stage of development is reported by C, S_a and F_a or C S_a F_p F_s.

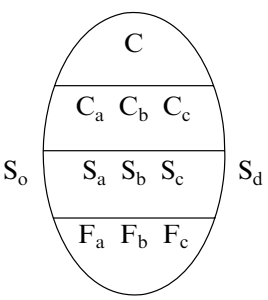

Stage of development (S)

S_a S_b S_c	Stage of development of thickest (S_a), second thickest (S_b) and third thickest (S_c) ice, of which the concentrations are reported by C_a, C_b, C_c, respectively (see symbols in Table G.2).

Notes:

(1) If more than one class of stage of development remains after selection of S_a and S_b, S_c should indicate the class having the greatest concentration of the remaining classes (see also Note (2)).

(2) Reporting of S_a, S_b and S_c should generally be restricted to a maximum of three significant classes. In exceptional cases, further classes can be reported as follows: So – stage of development of ice thicker than Sa but having a concentration of less than 1/10; Sd – stage of development of any other remaining class.

(3) No concentrations are reported for S_o and S_d.

Form of ice (F)

(a) First variant

F_a F_b F_c Form of ice (floe size) corresponding to S_a, S_b and S_c, respectively (see symbols in Table G.3).

Notes:

(1) Absence of information on any one of these forms of ice should be reported with an "×" at the corresponding position.

(2) When icebergs are present in sufficient numbers to have a concentration figure, this situation can be reported with $F_a = 9$, the appropriate symbol for S_a and the corresponding partial concentration C_a.

(3) In situations when only two stages of development are present, a dash (—) should be added in place of F_c to separate these situations from those when F_p and F_s are being reported.

(b) Second variant

F_p F_s Predominant (F_p) and secondary (F_s) floe size, reported independently from S_a, S_b and S_c, respectively (see symbols in Table G.3).

Note: If only the predominant floe size (form of ice) is reported, only the symbol for F_p should be reported.

Table G.1. Total concentration of ice (C).

Concentration	*Symbol*
Ice-free	—
Less than one tenth	0
1/10	1
2/10	2
3/10	3
4/10	4
5/10	5
6/10	6
7/10	7
8/10	8
9/10	9
More than 9/10 less than 10/10	9+
10/10	10
Undetermined or unknown	×

Table G.2. Stage of development and thickness (S_a S_b S_c S_o S_d).

Number from WMO Sea Ice Nomenclature	*Element*	*Thickness*	*Symbol*
	No stage of development	—	0
2.1	New ice	—	1
2.2	Nilas; ice rind	<10 cm	2
2.4	Young ice	10–30 cm	3
2.4.1	Gray ice	10–15 cm	4
2.4.2	Gray–white ice	15–30 cm	5
2.5	First-year ice	30–200 cm	6
2.5.1	Thin first-year ice	30–70 cm	7
2.5.1.1	Thin first-year ice, first stage	30–50 cm	8
2.5.1.2	Thin first-year ice, second stage	50–70 cm	9
2.5.2	Medium first-year ice	70–120 cm	1.
2.5.3	Thick first-year ice	>120 cm	4.
2.6	Old ice		7.
2.6.1	Second-year ice		8.
2.6.2	Multi-year ice		9.
10.4	Ice of land origin		▲.
	Undetermined or unknown		×

Table G.3. Form of ice (F_a F_b F_c F_p F_s).

Element	*Floe size*	*Symbol*
Pancake ice	—	0
Small ice cake; brash ice	<2 m	1
Ice cake	2–20 m	2
Small floe	20–100 m	3
Medium floe	100–500 m	4
Big floe	500 m^{-2} km	5
Vast floe	2–10 km	6
Giant floe	>10 km	7
Fast ice	—	8
Icebergs, growlers or floebergs	—	9
Undetermined or unknown	—	×

References

Abramov, V. (1996) *Atlas of Arctic Icebergs: The Greenland, Barents, Kara, Laptev, East-Siberian and Chukchi Seas and the Arctic Basin* (70 pp.). Backbone Publishing.

ACIA (2004) *Arctic Climate Impact Assessment: Summary Assessment Report*. Cambridge University Press, Cambridge, UK. Online at *http://www.amap.no/acia*

Adamovich, N.M. (1987) Sea ice conditions in the western part of the Soviet Arctic during the cold period of the year and their influence on navigation. Ph.D. thesis, Arctic and Antarctic Research Institute, St. Petersburg [in Russian].

Alekseev, G.V., Myakoshin, O.I. and Smirnov, N.P. (1997) Variability of ice transport through Fram Strait. *Meteorologiya i Gidrologiya* **9**, 52–57 [in Russian].

Alekseev, G.V., Bulatov L.V., Zakharov V.F. and Ivanov B.V. (1998) Heat expansion of Atlantic waters in the Arctic Basin. *Meteorologiya i Gidrologiya* **7**, 69–78 [in Russian].

Alexandrov, V.Yu. and Kolatschek, J. (1997) Sea-ice remote sensing. *Berichte zur Polarforschung* **248**, 28–29.

Alexandrov, V.Yu. and Loshchilov, V.S. (1985) Quantitative interpretation of satellite radar images of sea ice using a-priori data. *Earth Observations and Remote Sensing* **3**, 28–31 [in Russian].

Alexandrov, V.Yu. and Loshchilov, V.S. (1993) Sea ice sensing using aircraft and satellite radars. In: I. Jones, Y. Sugimori and R.W. Stewart (eds), *Satellite Remote Sensing of the Oceanic Environment* (pp. 324–333). Seibutsu Kenkyusha, Tokyo.

Alexandrov, V.Yu., Loshchilov, V.S. and Terentiev, I.V. (1989) Assessment of possible automated determination of the characteristics of discontinuities in the ice cover from satellite radar images. *Earth Observations and Remote Sensing* **3**, 12–17 [in Russian].

Alexandrov, V.Y., Eicken, H. and Martin, T. (1994) Determination of ice drift in the Laptev Sea from satellite images and buoys data. In: L.A. Timokhov (ed.), *Scientific Results of the LAPEX 93 Expedition* (pp. 174–179). Gidrometeoizdat, St. Petersburg [in Russian].

Alexandrov, V.Y., Loshchilov, V.S. and Provorkin, A.V. (1996) Studies of icebergs and sea ice in Antarctic using Almaz-1 SAR data. In: I.K. Popov and V.A. Voevodin (eds), *Icebergs of the World Ocean* (pp. 30–36). Gidrometeoizdat, St. Petersburg [in Russian].

Alexandrov, V.Y., Melentyev, V.V., Bobylev, L.P., Korotkevich, O.E., Bogdanov, A.V., Zaitsev, L.V., Zemeszirks, K.E., Babich, N.G., Gorshkovsky, A.G., Sandven, S. *et al.*

(1998) *Satellite SAR Ice Charting and Routing Validation and Assessment* (NIERSC Technical Report No. 12, 77 pp.). Nansen International Environmental and Remote Sensing Centre, St, Petersburg.

Alexandrov, V.Y., Sandven, S., Lundhaug, M., Dalen, O., Bogdanov, A. and Kloster, K. (1999) Analysis of winter sea ice in the Kara Sea region using SAR data and field observations. *Proceedings of the 15th International Conference on Port and Ocean Engineering under Arctic Conditions, Espoo, Finland, 23–27 August 1999* (Vol. 1, pp. 181–190).

Alexandrov, V.Y., Martin, T., Kolatschek, J., Eicken, H., Kreyscher M. and Makshtas, A.P. (2000a) Sea ice circulation in the Laptev Sea and ice export to the Arctic Ocean: Results from satellite remote sensing and numerical modelling. *Journal of Geophysical Research* **105**(C7), 17143–17159.

Alexandrov, V.Y., Sandven, S., Johannessen, O.M., Pettersson, L.H. and Dalen, Ø. (2000b) Winter navigation in the Northern Sea Route using RADARSAT data. *Polar Record* **36**(199), 333–342.

Alexandrov, V.Y., Bogdanov, A.V., Filatov, N.N., Johannessen, O.M., Bobylev, L.P., Sandven, S. and Alexandrov, M.V. (2002) Radar signature distinctive features of ice in the Gulf of Finland, Ladoga and Onega lakes as retrieved from ERS images. *Earth Observations and Remote Sensing* **3**, 71–80 [in Russian].

Alexandrov, V.Y., Sandven, S. and Kloster, K. (2003) Iceberg identification in the Eurasian Arctic using SAR images. *Proceedings of the International Geoscience and Remote Sensing Symposium, 21–25 July 2003, Toulouse, France* (CD-ROM).

Alexandrov, V.Y., Sandven, S., Kloster, K., Bobylev, L.P. and Zaitsev, L.V. (2004) Comparison of sea ice signatures in OKEAN and RADARSAT radar images for the northeastern Barents Sea. *Canadian Journal of Remote Sensing* **30**(6), 882–892.

Anapolskaya, A.Ye. and Gandin, L.R. (1958) Methodology for determining calculated wind-speeds for the design of wind loads on construction structures. *Meteorologiya i Gidrologiya* **10**, 9–17 [in Russian].

Anderson, V.H. (1966) High altitude side-looking radar images of sea ice in the Arctic. *Proceedings of the Fourth Symposium on Remote Sensing of Environment, University of Michigan, June 1966* (pp. 845–857). U.S. Army Cold Region Research and Engineering Laboratory, Hanover, NH.

Andreeva, E.N. (2000) Methods of study of socio-economic problems of the Russian Arctic Coastal Zone. *Third Workshop on Land Ocean Interactions in the Russian Arctic (LOIRA), Moscow, 5–8 December* (Abstract, pp. 7–9).

Antonov, V.S., Bushuev, A.V. and Nalimov, Yu. V. (1970) Detection of deepwater scours across the bars of Arctic rivers. *Proceedings of the AARI* **390**, 83–91 [in Russian].

Appel, I.L and Gudkovich, Z.M. (1992) *Numerical Modeling and Forecasting of Ice Cover Evolution of Arctic Seas during the Period of Melting* (144 pp.). Gidrometeoizdat, St. Petersburg [in Russian].

Arikainen, A.I. (1984) *Transport Artery of the Soviet Arctic* (192 pp.). Nauka, Moscow [in Russian].

Armstrong, T. (1996) *Historical and Current Uses of the Northern Sea Route* (Part I, INSROP Working Paper 28(IV.1.1), pp. 1–58). INSROP, Oslo.

Askne, J., Carlstrom, A., Dierking, W. and Ulander, L. (1994) ERS-1 SAR backscatter modeling and interpretation of sea ice signatures. *Proceedings of International Geoscience and Remote Sensing Symposium, 8–12 August, Pasadena, CA* (pp. 162–164).

Asmus, V.V. Milekhin, O.Ye., Krovotyntsev, V.A. and Selivanov, A.S. (2002) Use of radar data of Okean satellite for addressing the problems of hydrometeorology and environmental monitoring. *Earth Observations and Remote Sensing* **2**, 1–8 [in Russian].

Avgevich, V.I. (1951) *Application of Aerial Photography for Ice Regime Studies* (119 pp.). Izd. Glavsevmorputi, Moscow [in Russian].

Baidal, M.H. (2001a) *Climate Scenarios in the 21st Century* (36 pp.). VNIIGMI-MTsD, Obninsk, Russia [in Russian].

Baidal, M.H. (2001b) *Main Climate Features of Kaluzhskaya and Adjoining Districts in 2001–2025* (92 pp.). VNIIGMI-MTsD, Obninsk [in Russian].

Bambuliak, A. and Frantsen, B. (2005) *Transportation of Oil and Gas from the Russian Part of the Barents Sea up to January 2005* (91 pp.). Svanhovd Ecological Centre, Svanhovd.

Banfield, J. (1991) Automated tracking of ice floes: A stochastic approach. *IEEE Transactions on Geoscience and Remote Sensing* **29**(6), 905–911.

Barber, D.G., Fung, A.K., Grenfell, T.C., Nghiem, S.V., Onstott, R.G., Lytle, V.I., Perovich, D.K. and Gow, A.J. (1998a) The role of snow on microwave emission and scattering over first-year sea ice. *IEEE Transactions on Geoscience and Remote Sensing* **36**(5), 1750–1,763.

Barber, D.G., Thomas, A. and Papakyriakou, T.N. (1998b) Role of SAR in surface energy flux measurements over sea ice. In: C. Tsatsoulis and R. Kwok (eds), *Analysis of SAR Data of the Polar Oceans: Recent Advances* (pp. 35–67). Springer-Verlag, Berlin.

Barber, D.G., Yackel, J.J. and Hanesiak, J.M. (2001) Sea ice, RADARSAT-1 and Arctic climate processes: A review and update. *Canadian Journal of Remote Sensing* **27**(1), 51–60.

Barr, W. (1991) The Arctic Ocean in Russian history to 1945. In: L.W. Brigham (ed.), *The Soviet Maritime Arctic* (pp. 11–32). Naval Institute Press, Annapolis, MD.

Batskikh, Y.M., Borodachev, V.Y. and Potapov, V.P. (1987) Estimate of the meteorological factor influence on safety of good transportation on fast ice. *Problems of the Arctic and Antarctic* **63**, 102–107 [in Russian].

Beaven, S.G., Gogineni, S.P. and Shanableh, M. (1994) Radar backscatter signatures in the central Arctic. *International Journal of Remote Sensing* **15**(5), 1149–1154.

Belchansky, G.I., Douglas, D.C., Alpatsky, I.V. and Platonov, N.G. (2004) Spatial and temporal multiyear sea ice distributions in the Arctic: A neural network analysis of SSM/I data, 1988–2001. *Journal of Geophysical Research* **109**, C10017, doi:10.1029/2004JC002388.

Belchansky, G.I., Douglas, D. C., Eremeev, V. A. and Platonov, N. G. (2005) Variations in the Arctic's multiyear sea ice cover: A neural network analysis of SMMR–SSM/I data, 1979–2004. *Geophysical Research Letters* **32**, L09605, doi.10.1029/2005GL022395.

Belkin, S. (1983) *Crushing Ice* (192 pp.). Znaniye, Moscow [in Russian].

Belov, M.I. (1956) *Arctic Navigation from the Earliest Times to the Mid-Nineteenth Century: The History of the Discovery and Exploration of the Northern Sea Route* (Vol. 1, 592 pp.). Morskoy Transport, Moscow [in Russian].

Belov, M.I. (1959) *Soviet Arctic Navigation 1917–1932: The History of the Discovery and Exploration of the Northern Sea Route* (Vol. 3, 511 pp.). Morskoy Transport, Leningrad [in Russian].

Belov, M.I. (1969) *Scientific and Economic Exploration of the Soviet North in 1933–1945: The History of the Discovery and Exploration of the Northern Sea Route* (Vol. 4, 616 pp.). Gidrometeoizdat, Leningrad [in Russian].

Belov, M.I. (1970) Geographical study of the Soviet Arctic and the Northern Sea Route. In: I.P. Gerasimov (ed.), *The Soviet Arctic: Seas and Islands of the Arctic Ocean* (pp. 23–46). Nauka, Moscow [in Russian].

Belov, M.I. (1977) *Following in the Tracks of Polar Expeditions* (142 pp.). Gidrometeoizdat, Leningrad [in Russian].

Benediktsson, J.A., Swain, P.H. and Ersoy, O.K. (1990) Neural network approaches versus statistical methods in classification of multisource remote sensing data. *IEEE Transactions on Geoscience and Remote Sensing* **28**(4), 540–552.

Bengtsson, L., Semenov, V. A. and Johannessen, O. M. (2004) The early twentieth-century warming in the Arctic: A possible mechanism. *Journal of Climate* **17**(20), 4045–4057.

Bengtsson, L., Hodges, K.I., Roeckner, E. and Brokopf, R. (2005) On the natural variability of the pre-industrial European climate. *Climate Dynamics* (submitted).

Bertoia, C., Falkingham, J. and Fetterer, F. (1998) Polar SAR data for operational sea ice mapping, In: C. Tsatsoulis and R. Kwok (eds), *Analysis of SAR Data of the Polar Oceans: Recent Advances* (pp. 202–234). Springer-Verlag, Berlin.

Bertoia, C., Manore, M., Steen Andersen, H., O'Connor, C., Hansen, K.Q. and Evangeno, C. (2004) Synthetic aperture radar for operational ice observation and analysis at the US, Canadian and Danish National Ice Centers. In: C.R. Jackson and J. R. Apel (eds), *Synthetic Aperture Radar: Marine User's Manual* (pp. 417–442). National Oceanic and Atmospheric Administration, Camp Springs, MD.

Beveridge, J.R., Griffith, J., Kohler, R.R., Hanson, A.R. and Riesman, E.M. (1989) Segmenting images using localizing histograms and region merging. *International Journal of Computer Vision* **2**(3), 311–347.

Bishop, C.M. (1995) *Neural Networks for Pattern Recognition*. Clarendon Press, Oxford, U.K.

Bjørgo, E., Johannessen, O.M. and Miles, M.W. (1997) Analysis of merged SMMR–SSM/I time series of Arctic and Antarctic sea ice parameters 1978–1995. *Geophysical Research Letters* **24**(4), 413–416.

Blidberg, D.R., Corell, H.W. and Westheart, A.S. (1979) Probable ice thickness of the Arctic Ocean. *Proceedings of the POAC 79, 13–19 August* (Vol. 1, pp. 253–267).

Bogdanov, A.V., Sandven, S., Johannessen, O.M., Alexandrov, V.Yu. and Bobylev L.P. (2005) Multi-sensor approach to automated classification of sea ice image data. *IEEE Transactions on Geoscience and Remote Sensing* **43**(7), 1648–1664.

Bogorodsky, V.V. and Martynova, Ye.A. (1978) *On Thermal Emission of the Snow–Ice Cover of the Arctic Seas* (38 pp.). Gidrometeoizdat, Leningrad [in Russian].

Bogorodsky, V.V. and Paramonov, A.I. (1984) On the possibility of factorization of space of hydrometeorological elements for IR radiometry of sea ice. *Proceedings of the AARI* (Vol. 386, pp. 19–29) [in Russian].

Bogorodsky, V.V. and Paramonov, A.I. (1985) Determination of ice situation of the polar seas from radiation measurements from airplanes and satellites. *Proceedings of the AARI* (Vol. 395, pp. 5–17) [in Russian].

Bogorodsky, V.V., Gusev, A.V., Doronin, Yu. P., Kuznetsova, L.N. and Shifrin, K.S. (1978) *Physics of the Ocean* (294 pp.). Gidrometeoizdat, Leningrad [in Russian].

Borodachev, V.E. (1998) *Sea Ice of the Kara Sea* (182 pp.). Gidrometeoizdat, St. Petersburg [in Russian].

Borodachev, V.Ye. and Shilnikov, V.I. (2002) *History of Airborne Ice Reconnaissance in the Arctic and the Ice-covered Seas of Russia (1914–1993)* (441 pp.). Gidrometeoizdat, St. Petersburg [in Russian].

Bourke, R.H. and Garret, R.P. (1987) Sea ice thickness distribution in the Arctic Ocean. *Cold Regions Science and Technology* **13**(3), 259–280.

Brestkin, S.V., Gorbunov Yu.A. and Losev, S.M. (1995) Results of statistical analysis of satellite data on discontinuities in ice cover in the south-western Kara Sea and their possible use for planning sea operations during the winter–spring period. *Proceedings of POAC 95, 15–18 August 1995, Murmansk* (Vol. 3, pp. 60–68).

Brigham, L.W. (1991) *The Soviet Maritime Arctic* (Woods Hole Oceanographic Institution No. 7609). Naval Institute Press, Annapolis, MD. ISBN 1-55750-753-8.

Brigham, L.W. (1995) Icebreaker transit analysis for a voyage across the Arctic Ocean. *Proceedings of International Conference on Northern Sea Program, 1–6 October, Tokyo* (pp. 391–396).

Brigham, L. and Ellis, B. (eds) (2005) *Arctic Marine Transport Workshop Final Report, 28–30 September 2004, Cambridge, U,K.*

Buinitsky, V.Kh. (1951) Formation and drift of the ice cover in the Arctic Basin. *Proceedings of the Drifting Expedition onboard the Icebreaker G. Sedov, 1937–1940* (Vol. 4, pp. 74–151) [in Russian].

Bushuev, A.V. (1961) Circular plan-perspective aerial photo camera (author's certificate No. 134980). *Bulletin of Inventions* **1**, 123–125 [in Russian].

Bushuev, A.V. (1991) Development and improvement of the system and method of ice observations. *Problems of the Arctic and Antarctic* **66**, 170–183 [in Russian].

Bushuev, A.V. (1997) Collection, processing and analysis of ice data. In: I.Ye. Frolov and V.P. Gavrilo (eds), *Sea Ice: Collection and Analysis of Observation Data, Physical Properties and Forecasting of Ice Conditions* (pp. 317–386). Gidrometeoizdat, St. Petersburg [in Russian].

Bushuev, A.V. and Bychenkov, Yu.D. (1978) *Study of Sea Ice Distribution and Dynamics from TV Images of Meteor Satellite: Temporary Instruction* (132 pp.). Gidrometeoizdat, Leningrad [in Russian].

Bushuev, A.V. and Loshchilov, V.S. (1967) Accuracy of airborne observations and mapping of sea ice. *Proceedings of the AARI* **257**, 84–92 [in Russian].

Bushuev, A.V. and Volkov, N.A. (1974) *Sea Ice Nomenclature: Symbols for Ice Charts* (87 pp.). Gidrometeoizdat, Leningrad [in Russian].

Bushuev, A.V., Volkov, N.A., Gudkovich, Z.M., and Loshchilov, V.S. (1967) Results of the expedition studies of the ice cover drift and dynamics in the Arctic Basin in spring of 1961. *Proceedings of the AARI* **257**, 25–44 [in Russian].

Bushuev, A.V., Lazarev, E.I. and Finkelshtein, M.I. (1977a) Some results of using a radar video-impulse meter of sea ice thickness for ice reconnaissance. *Proceedings of the AARI* **343**, 114–121 [in Russian].

Bushuev, A.V., Volkov, N.A., Gudkovich, Z.M., Novikov, Yu.R. and Prokofiev, V.A. (1977b) Automated ice-information system for the Arctic (ALISA). *Proceedings of the AARI* **343**, 6–16 [in Russian].

Bushuev, A.V., Bychenkov, Yu.D., Loshchilov, V.S. and Masanov, A.D. (1983) Ice cover study by means of side-looking airborne radar (SLAR) stations. *Methodological Manual* (120 pp.). Gidrometeoizdat, Leningrad [in Russian].

Bushuev, A.V., Volkov, N.A. and Grishchenko, V.D. (1995) Observations of sea ice and its study, creation of the automated ice-information system. *Problems of the Arctic and Antarctic* **70**, 104–119 [in Russian].

Bushuev, A.V., Loshchilov, V.S., Smirnov, V.G. and Shcherbakov, Yu.A. (2004) Satellite monitoring of the ice cover. *Proceedings of the Second All-Russia Scientific Conference: "Remote Sounding of the Earth's Surfaces and Atmosphere by Aero-space Means", 16–18 June 2004* (pp. 42–47). RSHMU, St. Petersburg [in Russian].

Buzuyev, A.Ya., Romanov, I.P. and Fedyakov, V.Ye. (1979) Variability of snow distribution on sea ice of the Arctic Ocean. *Meteorologiya i Gidrologiya* **9**, 76–86 [in Russian].

Buzuyev, A.Y., Dubovtsev, V.F., Zakharov, V.F. and Smirnov, V.I. (1988) *Conditions of Navigation in Sea Ice of the Northern Hemisphere* (280 pp.). Main Department of Navigation and Oceanography of the Ministry of Defense, Leningrad [in Russian].

Buzuyev, A.Ya., Gorbunov, Yu.A., Gudkovich, Z.M., Losev, S.M. and Mironov, Ye.U. (1999) Study of the ice cover dynamics and morphometry of the Arctic Basin. *Problems of the Arctic and the Antarctic* **71**, 106–128 [in Russian].

Carsey, F. D. (ed.) (1992) *Microwave Remote Sensing of Sea Ice* (Geophysical Monograph 68). American Geophysical Union, Washington, D.C.

Carsey, F., Harfing, R. and Wales, C. (1998) Alaska SAR Facility: The US Center for Sea Ice SAR Data. In: C. Tsatsoulis and R. Kwok (eds), *Analysis of SAR Data of the Polar Oceans: Recent Advances* (pp. 189–200). Springer-Verlag, Berlin.

Cavalieri, D.J. and Häkkinen, S. (2001) Arctic climate and atmospheric planetary waves. *Geophysical Research Letters* **28**, 791–794.

Cavalieri, D.J., Gloersen, P. and Campbell, W.J. (1984) Determination of sea ice parameters with the NIMBUS-7 SMMR. *Journal of Geophysical Research* **89**(D4), 5355–5369.

Cavalieri, D.J., Gloersen, P., Parkinson, C.L., Zwally, H.J. and Comiso, J.C. (1997) Observed hemispheric asymmetry in global sea ice changes. *Science* **278**, 1104–1106.

Chapman, W. L. and Walsh, J. E. (1993) Recent variations of sea ice and air temperature in high latitudes. *Bulletin of the American Meteorological Society* **74**, 33–47.

Chilingarov, A.N. (2001) Arctic at the threshold of the III millennium. *Symposium of European Community Countries, Russia, Canada and USA: Common Approach to Collaborative Technological Research for Arctic Development", Brussels, 25–27 October 2001* (pp. 5–12).

Chizhov, O.P. (1976) *Glaciation of the Northern Polar Area* (240 pp.) Nauka, Moscow [in Russian].

Classification and Terminology of Ice Encountered at Sea (1954) (21 pp.). Gidrometeoizdat, Leningrad [in Russian].

CMIP2 (2003) Climate Model Intercomparison Project—2 (*http://www-pcmdi.llnl.gov/cmip/*), J. Raisanen, Rossby Centre, Swedish Meteorological and Hydrological Institute, Norrkjöping, Sweden.

Collins, M.J. (1992) Information fusion in sea ice remote sensing. In: F.D. Carsey (ed.), *Microwave Remote Sensing of Sea Ice* (Geophysical Monograph No. 68, pp. 431–441). American Geophysical Union, Washington, D.C.

Collins, M.J. and Emery, W.J. (1988) A computational method for estimating sea ice motion in sequential Seasat synthetic aperture radar imagery by matched filtering. *Journal of Geophysical Research* **93**(C8), 9241–9251.

Collins, M.J., Livingstone, C.E. and Raney, R.K. (1997) Discrimination of sea ice in the Labrador marginal ice zone from synthetic aperture radar image texture. *International Journal of Remote Sensing* **18**(3), 535–571.

Comiso, J.C. (1990) Arctic multiyear ice classification and summer ice cover using passive-microwave satellite data. *Journal of Geophysical Research* **95**, 13411–13422.

Comiso, J.C. (2002) A rapidly declining perennial sea ice cover in the Arctic. *Geophysical Research Letters* **29**(20), 1956, doi:10.1029/2002GL015650.

Comiso, J.C. (2003) Warming trends in the Arctic from clear sky satellite observations. *Journal of Climate* **16**, 3498–3510.

Comiso J. C., Cavalieri, D. J., Parkinson, C. L. and Gloersen, P. (1997) Passive microwave algorithms for sea ice concentration: A comparison of two techniques. *Remote Sensing of the Environment* **60**, 357–384.

Comiso, J.C., Yang, J., Honjo, S. and Krishfield, R.A. (2003) Detection of change in the Arctic using satellite and in situ data. *Journal of Geophysical Research* **108**(C12), 3384, doi:10.1029/2002JC001347.

Crane, R.G. and Anderson, M.R. (1994) Springtime microwave emissivity changes in the southern Kara Sea. *Journal of Geophysical Research* **99**, 14303–14309.

Daida, J. and Samadani, R. (1990) Object-oriented feature-tracking algorithms for SAR images of the marginal ice zone. *IEEE Transactions on Geoscience and Remote Sensing* **28**(4), 573–589.

De Abreu, R., Flett, D., Scheuchl, B. and Ramsay, B. (2003) Operational sea ice monitoring with RADARSAT-2: A glimpse into the future. *Proceedings of the International Geoscience and Remote Sensing Symposium, 21–25 July 2003, Toulouse, France* (CD-ROM).

Delworth, T. L. and Mann, M. E. (2000) Observed and simulated multidecadal variability in the Northern Hemisphere. *Climate Dynamics* **16**, 661–676.

Demin, I.D., Akkuratov, V.I. and Gorbachev, A.A. (1958) *Manual on Application of Aircraft Radar Stations in Airborne Ice Reconnaissance* (65 pp.). GUSMP Polar Aviation, Moscow [in Russian].

Deser, C., Walsh, J. E. and Timlin, M. S. (2000) Arctic sea ice variability in the context of recent atmospheric trends. *Journal of Climate* **13**, 617–633.

Dickson, R. R., Osborn, T. J., Hurrell, J. W., Meincke, J., Blindheim, J., Adlandsvik, B., Vinje, T., Alekseev, G. and Maslowski, W. (2000) The Arctic Ocean response to the North Atlantic Oscillation. *Journal of Climate* **13**, 2671–2696.

Divine, D., and Dick, C. (2006) Historical variability of sea ice edge position in the Nordic Seas. *Journal of Geophysical Research* **111**, C01001, doi.:10.1029/2004JC002851.

Dokken, S.T. (2000) Sea ice and ocean environmental applications of spaceborn SAR. Ph.D thesis, Chalmers University of Technology, Goteborg, Sweden.

Dokken, S.T., Häkansson B., and Askne, J. (2000) Inter-comparison of Arctic sea ice concentration using RADARSAT, ERS, SSM/I and in-situ data. *Canadian Journal of Remote Sensing* **26**(6), 521–536.

Dokken, S.T., Winsor, P., Markus, T., Askne, J. and Björk, G. (2002) ERS SAR characterization of coastal polynyas in the Arctic and comparison with SSM/I and numerical model investigations. *Remote Sensing of Environment* **80**(2), 321–335.

Doronin, Yu.P. (1964) Methodology of calculation of ice thickness and temperature. *Proceedings of the AARI* **267**, 127–142 [in Russian].

Drinkwater, M.R. (1998) Satellite microwave radar observations of Antarctic sea ice. In: C. Tsatsoulis and R. Kwok (eds), *Analysis of SAR Data of the Polar Oceans: Recent Advances* (pp. 35–68). Springer-Verlag, Berlin.

Drinkwater, M.R., Kwok, R., Rignot, E., Israelsson, H., Onstott, R.G. and Winebrenner, D.P. (1992) Potential applications of polarimetry to the classification of sea ice. In: F.D. Carsey (ed.), *Microwave Remote Sensing of Sea Ice* (Geophysical Monograph No. 68, pp. 419–430). American Geophysical Union, Washington, D.C.

Drinkwater, M.R., Early, D.S. and Long, D.G. (1994) ERS-1 investigations of Southern Ocean sea ice geophysics using combined scatterometer and SAR images. *Proceedings of International Geoscience and Remote Sensing Symposium, 8–12 August, Pasadena, CA* (pp. 165–167).

Drivenes, E.-A. and Jølle, H.D. (2004) *Norsk Polarhistorie, Vol. 1: Ekspedisjonene* (475 pp.). Gylhendal Norsk Forlag AS, Oslo [in Norwegian].

Eckes, C. and Fritzke, B. (2001) *Classification of Sea-ice with Neural Networks: Results of the EU Research Project ICE ROUTES* (Interim Report 2001-02). Institut für Neuroinformatik, Ruhr-Universität, Bochum, Germany.

Edel, H., Shaw, E., Falkingham, J. and Borstad, G. (2004) The Canadian RADARSAT Program. *Backscatter* **15**(1), 11–15.

Eicken, H., Alexandrov, V., Bogdanov, V., Martin, T., Reimnitz, E. and Syrtsov, S. (1994) Iceberg observations. *Berichte zur Polarforschung* **149**, 76–78.

Emery, W.J., Fowler, C.W. and Maslanik, J.A. (1997) Satellite derived maps of Arctic and Antarctic sea ice motion 1988–1994. *Geophysical Research Letters* **24**(8), 897–900.

EOS Science Steering Committee (1988) *From Pattern to Process: The Strategy of the Earth Observing System* (NASA Report Vol. 2, 233 pp.). NASA, Washington, D.C.

Fetterer, F.M., Gineris, D.J. and Kwok, R. (1994) Sea ice type maps from Alaska synthetic aperture radar facility imagery: An assessment. *Journal of Geophysical Research* **99**(C11), 22443–22458.

Fily, M. and Rothrock D.A. (1987) Sea ice tracking by nested correlations. *IEEE Transactions on Geoscience and Remote Sensing* **25**(5), 570–580.

Finkelshtein, M.I. and Glushnev, V.G. (1972) Device for sea ice thickness measurement (author's certificate No. 353204). *Bulletin of Inventions* **29**, 111–112 [in Russian].

Finkelshtein, M.I. and Lazarev, E.I. (1977) Radar video-impulse meter of sea ice thickness as a perspective means ice reconnaissance. *Proceedings of the AARI* **343**, 104–113 [in Russian].

Fisher, R.A. (1936) The use of multiple measurement in taxonomic problems. *Annals Eugenics* **7**, 179–188.

Fleshe, H. (1988) Estimation of ice motion from satellite images. MSc thesis, Division of Electronics and Computer Technique, Norwegian Institute of Technology (NTH), Trondheim, Norway [in Norwegian].

Flett, D. G. (2003) Operational use of SAR at the Canadian Ice Service: Present operations and a look to the future. *ESA Proceedings of the Second Workshop on Coastal and Marine Applications of SAR, 12–15 September 2003, Svalbard, Norway*.

Flett, D. and Vachon, P.W. (2004) Marine applications of SAR in Canada. *Backscatter* **15**(1), 16–21.

Flett, D., De Abreu, R. and Falkingham, J. (2004) Operational experience with ENVISAT ASAR wide swath data at the CIS. *ENVISAT Symposium, Salzburg, 6–10 September 2004* (Abstract No. 363).

Frank, S.O. (2000) Opening speech: International shipping on the Northern Sea Route—Russia's perspective. In: C.L. Ragner (ed.), *Proceedings of the Northern Sea Route User Conference: The 21st Century—Turning Point for the Northern Sea Route?", Oslo, 18–20 November 1999* (pp. 7–14). Kluwer Academic Publishers, Dordrecht, The Netherlands.

Frolov, I.Ye. (1995) Current state and perspectives of scientific studies in the Arctic. *Problems of the Arctic and Antarctic* **70**, 45–49 [in Russian].

Frolov, I.Ye. (2002) Hydrometeorological support of the Northern Sea Route: History and perspectives. *Proceedings of the Scientific–Practical Conference: "Hydrometeorological Support for Economic Activity in the Arctic and Ice-covered Seas", St. Petersburg, 27–29 March 2002* (pp. 45–50) [in Russian].

Frolov, I.Ye., Danilov, A.I., Brestkin, S.V. and Mironov, Ye.U. (2003). Automated ice-information system for the Arctic and its use for the exploration of hydrocarbons on the shelf. *Proceedings of the 6th International Conference RAO-03, St. Petersburg, 16–19 September 2003* (pp. 304–307).

Frolov, I.Ye., Gudkovich, Z.M., Radionov, V.F., Shirochkov, A.V. and Timokhov, L.A. (2005) *The Arctic Basin: Results from the Russian Drifting Stations*. Springer-Praxis, Chinchester, UK. ISBN 3-540-24142-6.

Frolov, I.Ye., Brestkin, S.V. and Mironov, Ye.U. (2005). Hydrometeorological support of cargo transportation in the Arctic and freezing seas. *Abstracts of the 8th International Conference "Russian Shipbuilding and Navigation, Ports Activity, Exploration of the Ocean and Shelf", St. Petersburg, 26–27 September 2005* (pp. 75–78).

Frolov, S.V. (1997a) Ice conditions of navigation in the central Arctic Ocean. *Proceedings of the 16th International Conference on OMAE, ASME 4, New York* (pp. 401–406) .

Frolov, S.V. (1997b) The main regularities in distribution of the ice cover characteristics and their influence on icebreaker sailing in the Arctic Basin during the summer period (from the data of high-latitude sailings). *Proceedings of the AARI* **437**, 83–98 [in Russian].

Frolov, S.V. and Klyachkin, S.V. (2001) Consideration of the influence of fracture orientation in sea ice cover on velocity of ship sailing in ice. *Proceedings of the AARI* **443**, 103–111 [in Russian].

Frolov, I.Ye., Gudkovich, Z.M., Radionov, V.F., Shirochkov, A.V. and Timokhov, L.A. (2005) *The Arctic Basin: Results from the Russian Drifting Stations* (272 pp.). Springer-Praxis, Chichester, UK (*www.praxis-publishing.co.uk*). ISBN: 3-540-24142-6.

Furevik, B.R., Johannessen, O.M. and Sandvik, A.D. (2002) SAR-retrieved wind in polar regions: Comparison with *in situ* data and atmospheric model output. *IEEE Transactions on Geoscience and Remote Sensing* **40**(8), 1720–1732.

Gill, R.S. and Valeur, H.H. (1999) Ice cover discrimination in the Greenland waters using first-order texture parameters of ERS SAR images. *International Journal of Remote Sensing* **20**(2), 373–385.

Gill, R.S., Valeur, H.H. and Nielsen, P. (1997) Evaluation of the RADARSAT imagery for the operational mapping of sea ice around Greenland. *Proceedings of GER 97 Symposium "Geomatics in the Era of RADARSAT", Ottawa, 25–30 May*.

Gineris, D.J. and Fetterer, F.M. (1994) An examination of the radar backscatter of sea ice in the East-Siberian and Chukchi Seas. *Proceedings of International Geoscience and Remote Sensing Symposium, 8–12 August 1994, Pasadena, CA* (pp. 499–502).

Gloersen, P. (1995) Modulation of hemispheric ice cover by ENSO events. *Nature* **373**, 503–505.

Gloersen, P. and Campbell, W. J. (1991) Recent variations in Arctic and Antarctic sea-ice covers. *Nature* **352**, 33–36.

Gloersen, P. and Yu, J. (1997) Oscillatory behavior in Arctic sea ice concentrations. *Journal of Geophysical Research* **101**, 6641–6650.

Gloersen, P., Ramseier, R.O., Campbell, W.J., Kuhn, P.M. and Webster, W.J., Jr. (1975) Ice thickness distribution as inferred from infrared and microwave remote sensing during the Bering Sea experiment. In: K.Ya. Kondratyev, Yu.I. Rabinovich and W. Nordberg (eds), *Proceedings of the Final Symposium on the Results of the Joint USSR/USA Bering Sea Experiment* (pp. 282–293). Gidrometeoizdat, Leningrad.

Gloersen, P., Campbell, W.J., Cavalieri, D.J., Comiso, J.C., Parkinson, C.L. and Zwally, H.J. (1992) *Arctic and Antarctic Sea Ice 1978–1987: Satellite Passive-Microwave Observations and Analysis* (NASA SP-511, 290 pp.). NASA, Washington, D.C.

Gloersen, P., Parkinson, C.L., Cavalieri, D.J., Comiso, J.C. and Zwally, H.J. (1999) Spatial distribution of trends and seasonality in the hemispheric sea ice covers: 1978–1996. *Journal of Geophysical Research* **104**(C9), 20827–20835.

Glushkov, V.M., Kontorov, S.Ye., Loshchilov, V.S., Nikolsky, S.S., Chubakov, K.N. and Shevelev, M.I. (1970) New tool for acquisition of ice information. *Marine Fleet* **9**, 37–38 [in Russian].

Gogineni, S.P., Moore, R.K., Grenfell, T.C., Barber, D.G., Digby, S. and Drinkwater, M. (1992) The effects of freeze-up and melt processes on microwave signatures. In: F.D. Carsey (ed.), *Microwave Remote Sensing of Sea Ice* (Geophysical Monograph 68, pp. 330–341). American Geophysical Union, Washington, D.C.

Gonzalez, R.C. and Wintz, P. (1987) *Digital Image Processing*. Addison-Wesley, Reading, MA.

Gorbunov, Y.A. (1967) About the possibility of studying ice drift peculiar features using aerial photosurvey. *Problems of the Arctic and Antarctic* **26**, 57–61 [in Russian].

Gorbunov, Y.A. (1979) Ice exchange through the Novosibirskiye Straits. In: A.F. Treshnikov (ed.), *POLEX-SEVER-76* (Vol. 2, pp. 66–72). Gidrometeoizdat, Leningrad [in Russian].

Gorbunov, Y.A. (1981) Drift of compact ice in the East-Siberian Sea. *Study of Ice Conditions of the Arctic Seas* (pp. 40–79). Gidrometeoizdat, Leningrad [in Russian].

Gorbunov, Y.A. and Losev, S.M. (1974) Use of side-looking airborne radar Toros for ice drift studies. *Proceedings of the AARI* **316**, 153–162 [in Russian].

Gorbunov, Y.A. and Losev, S.M. (1977) Ice motion in the straits. *Proceedings of the AARI* **341**, 18–23 [in Russian].

Gorbunov, Y.A. and Losev, S.M. (1978a) Influence of islands on ice motion. *Proceedings of the AARI* **354**, 38–43 [in Russian].

Gorbunov, Y.A. and Losev, S.M. (1978b) Vortical perturbations in the ice drift field. *Proceedings of the AARI* **354**, 52–57 [in Russian].

Gorbunov, Y.A. and Losev, S.M. (1979) About the estimate of spatial variability of ice drift in Arctic seas during summer. *Proceedings of the AARI* **364**, 5–13 [in Russian].

Gorbunov, Y.A. and Losev, S.M. (1994) Ice drift features in the northern regions of the Laptev and the East-Siberian Seas and the adjacent Arctic basin in July–September 1993. In: L.A. Timokhov (ed.), *Scientific Results of the LAPEX 93 Expedition* (pp. 180–192). Gidrometeoizdat, St. Petersburg [in Russian].

Gorbunov, Y.A. and Losev, S.M. (1998) Structure of the ice drift velocity field and sea ice conditions near to natural obstacles. *Proceedings of the III International Conference Exploration of the Russian Arctic Seas Shelf RAO-97", St. Petersburg, 22–26 September 1997* (Vol. 1, pp. 566–569).

Gorbunov, Y.A. and Moroz, V.G. (1972) Major results of studies of the ice drift in the Arctic Ocean obtained by using radio beacons and drifting automatic weather stations (DARMS). *Problems of the Arctic and Antarctic* **39**, 33–39 [in Russian].

Gorbunov, Y.A., Losev, S.M. and Timokhov, L.A. (1977) Ice drift in the presence of grounded hummocks. *Proceedings of the AARI* **338**, 79–94 [in Russian].

Gorbunov, Y.A., Gudkovich, Z.M. and Appel, I.L. (1979a) Peculiarities of ice drift in the southeastern Laptev Sea. In: A.F. Treshnikov (ed.), *POLEX-SEVER-76* (Vol. 2, pp. 45–65). Gidrometeoizdat, Leningrad [in Russian].

Gorbunov, Y.A., Karelin, I.D., Kuznetsov, I.M. and Nikolaeva, A.Y. (1979b) *Atlas of Ice Drift in the Arctic Seas* (28 pp.). Gidrometeoizdat, Leningrad [in Russian].

Gorbunov, Yu.A., Losev, S.M. and Kulakov, I.Yu. (1982) Peculiarities of the ice drift field structure in the Arctic Basin. *Materials of Glaciological Studies* **45**, 51–56 [in Russian].

Gorbunov, Yu.A., Losev, S.M. and Kulakov, I.Yu. (1985) Large-scale eddy motions in the ice cover of the Arctic Basin. *Proceedings of the AARI* **400**, 7–32 [in Russian].

Gorbunov, Y.A., Karelin, I.D. and Losev, S.M. (1986a) About the causal factors of discontinuities in sea ice cover during the winter period. *Problems of the Arctic and Antarctic* **62**, 110–116 [in Russian].

Gorbunov, Y.A., Karelin, I.D. and Losev, S.M. (1986b) Causes of discontinuities in sea ice cover during the winter time. *Materials of Glaciological Studies* **55**, 131–134 [in Russian].

Gorbunov, Y.A., Losev, S.M. and Dyment L.N. (2001) Techniques of diagnostics and medium-term forecast of fractures in ice cover of the Kara Sea. *Proceedings of the AARI* **443**, 96–105 [in Russian].

Gordienko, P.A. (1941) Some characteristics of ice drift in real conditions. *Problems of the Arctic* **6**, 5–12 [in Russian].

Gordienko, P.A. (1971) *Fast Ice in the Arctic Seas* (Part 1, pp. 1–176). Gidrometeoizdat, Leningrad [in Russian].

Gordienko, P.A. and Karelin, D.B. (1945) Problems of ice distribution and movement in the Arctic Basin. *Problems of the Arctic* **3**, 5–35 [in Russian].

Gorshkov, S.G. (ed.) (1980) *Atlas of the World Ocean: Arctic Ocean* (189 pp.). USSR Ministry of Defence, VMF, Moscow [in Russian].

Gramberg, I.S. and Ushakov, V.I., (eds) (2000) *Severnaya Zemlya: Geological Structure and Minerageny* (188 pp.). Vniiokeangeologiya, St. Petersburg [in Russian].

Grayevsky, A.P., Nalimov, Yu.V., and Timerev, A.A. (1980) Reflectivity of young ice at the mouths of Arctic rivers. *Proceedings of the AARI* **358**, 35–39 [in Russian].

Green, W.B. (1989) *Digital Image Processing: A Systems Approach*. Van Nostrand Reinhold, New York.

Grenfell, T.G. and Maykut, G.A. (1977) Optical properties of ice and snow in the Arctic Basin. *Journal of Glaciology* **18**(80), 445–463.

Grenfell, T.C., Cavalieri, D.J., Comiso, J.C., Drinkwater, M.R., Onstott, R.G., Rubinstein, I., Steffen, K. and Winebrenner, D.P. (1992) Considerations for microwave remote sensing of thin sea ice. In: F.D. Carsey (ed.), *Microwave Remote Sensing of Sea Ice* (Geophysical Monograph 68, pp. 291–301). American Geophysical Union, Washington, D.C.

Grenfell, T.C., Barber, D.G., Fung, A.K., Gow, A.J., Jezek, K.C., Knapp, E.J., Nghiem, S.V., Onstott, R.G., Perovich, D.K., Roesler, C.S. *et al.* (1998) Evolution of electromagnetic signatures of sea ice from initial formation to the establishment of thick first-year ice. *IEEE Transactions on Geoscience and Remote Sensing* **36**(5), 1642–1654.

Groverman, B. S. and Landsberg, H. E. (1979) Simulated northern hemisphere temperature: 1579–1880. *Geophysical Research Letters* **6**, 767–769.

Gudkovich, Z.M. and Doronin, Yu.P. (2001) *Sea Ice Drift* (112 pp.). Gidrometeoizdat, St. Petersburg [in Russian].

Gudkovich Z.M. and Kovalev, Ye. G. (2002) On some mechanisms of cyclic climate changes in the Arctic and the Antarctic. *Oceanography* **42**(6), 1–7 [in Russian].

Gudkovich, Z.M. and Nikolayeva, A.Y. (1961) Some results of ice drift studies using drifting radio beacons. *Problems of the Arctic and Antarctic* **8**, 11–18 [in Russian].

Gudkovich, Z.M. and Nikolayeva, A.Ya. (1963) Ice drift in the Arctic Basin and its connection with the ice extent in Soviet Arctic seas. *Proceedings of the AARI* **104**, 1–186 [in Russian].

Gudkovich, Z.M. and Pozdnyshev, S.P. (1995) Seasonal and spatial changes in the average ice drift velocities and gradient currents in the East-Greenland ice flow. *Problems of the Arctic and Antarctic* **69**, 116–123 [in Russian].

Gudkovich, Z.M., Kirillov, A.A., Kovalev, Y.G., Smetannikova, A.V. and Spichkin, V.A. (1972) *The Basis of Techniques for Long-term Ice Forecasts in the Arctic Seas* (348 pp.). Gidrometeoizdat, Leningrad [in Russian].

Gudkovich, Z.M., Voinov, G.N. and Losev, S.M. (1989) *On the Methodology of Calculation of Maximum Ice Drift Velocities: Regime-forming Factors, Information Base and Methods for Its Analysis* (pp. 232–237). Gidrometeoizdat, Leningrad [in Russian].

Gudmansen, P., Thomsen, B.B., Pedersen, L.T., Skriver, H. and Minnett, P.J. (1995) North-East Water Polynya: Satellite observations summer 1992 and 1993. *International Journal of Remote Sensing* **16**(17), 3307–3324.

Haarpaintner, J., Gascard, J.-C. and Haugan, P.M. (2001) Ice production and brine formation in Storfjorden, Svalbard. *Journal of Geophysical Research* **106**(C7), 14001–14013.

Haas, C. (2004) Late summer sea ice thickness variability in the Arctic Transpolar Drift 1991–2001 derived from ground-based electromagnetic sounding. *Geophysical Research Letters* **31**(L09402), doi:10.1029/2003GL019394.

Haas, C., and Eicken, H. (2001) Interannual variability of summer sea ice thickness in the Siberian and Central Arctic under different atmospheric circulation regimes. *Journal of Geophysical Research* **106**(C3), 4449–4462.

Haas, C., Dierking, W., Busche, T., Hoelemann, J. and Wegener, C. (2004) Monitoring polynya processes and sea ice production in the Laptev Sea. *Envisat Symposium, Salzburg, 6–10 September 2004* (Abstract No. 137).

Hall, D.L. (1992) *Mathematical Techniques in Multisensor Data Fusion*. Artech House, Norwood, MA.

Hallikainen, M. and Winebrenner, D.P. (1992) The physical basis for sea ice remote sensing. In: F.D. Carsey (ed.), *Microwave Remote Sensing of Sea Ice* (Geophysical Monograph 68, pp. 29–46). American Geophysical Union, Washington, D.C.

Handbook on Airborne Ice Reconnaissance (1981) (240 pp.) Gidrometeoizdat, Leningrad [in Russian].

Hara, Y., Atkins, R.G., Shin, R.T., Kong, J.A., Yueh, S.H. and Kwok, R. (1995) Application of neural networks for sea ice classification in polarimetric SAR images. *IEEE Transactions on Geoscience and Remote Sensing* **33**(3), 740–748.

Haralic, R.M., Shanmugan, K. and Dinstein, I. (1973) Textural features for image classification. *IEEE Transactions on Systems, Man and Cybernetics* **3**(6), 610–621.

Henning, R. (1961) *Terra Incognitae* (Vol. 2, 518 pp.). Foreign Literature, Moscow [in Russian].

Hibler, W.D. (1980) Modeling a variable thickness sea ice cover. *Monthly Weather Review* **108**(12), 1949–1973.

Hilmer, M. and Lemke, P. (2000) On the decrease of Arctic sea ice volume. *Geophysical Research Letters* **27**(22), 3751–3754.

Holloway, G. and Sau, T. (2002) Has Arctic sea ice rapidly thinned? *Journal of Climate* **15**, 1691–1698.

Holmes, Q.A., Nüesch, D.R. and Shuchman, R.A. (1984) Textural analysis and real-time classification of sea ice types using digital SAR data. *IEEE Transactions on Geoscience and Remote Sensing* **22**(2), 113–120.

Houssais, M.-N. and Herbaut, C. (2003) Variability of the ice export through Fram Strait in 1993–98: The winter 1994/95 anomaly. *Polar Research* **22**(1), 99–106.

Hu, A., Rooth, C., Bleck, R. and Deser, C. (2002) NAO influence on sea ice extent in the Eurasian coastal region. *Geophysical Research Letters* **29**, 2053–2056.

Hvidegaard, S.M. and Forsberg, R. (2002) Sea ice thickness from airborne laser altimetry over the Arctic Ocean north of Greenland. *Geophysical Research Letters* **29**(20).

IICWG (2004) *Intergovernmental Panel on Climate Change (IPCC) Climate Change 2000* (Third Assessment Report). Cambridge University Press, Cambridge, U.K.

International Symbols for Sea Ice Charts and Sea Ice Nomenclature (1984) (56p.). Gidrometeoizdat, Leningrad [in Russian].

Ivanov, A. (1979) Absorption of solar energy in the ocean. In: E.V. Krauss (ed.), *Modeling and Prediction of Upper Ocean Layers* (pp. 64–77). Gidrometeoizdat, Leningrad [in Russian].

Jeffries, M.O., Schwartz, K. and Li, S. (1997) Arctic summer sea-ice SAR signatures, melt-season characteristics, and melt-pond fractions. *Polar Record* **33**(185), 101–112.

Jevrejeva, S., Moore, J. C. and Grinsted, A. (2004) Atmospheric and oceanic linkages between ENSO and ice in the European Arctic. *Geophysical Research Letters* **31**, 24, L24210, doi: 10.1029/2004GL020871.

Johannessen, O.M. and Sandven, S. (1992) ERS-1 SAR ice routing of L'Astrolabe through the Northeast Passage. *Arctic News-Record, Polar Bulletin* **8**(2), 26–31.

Johannessen, O.M. and Sandven, S. (2002) Monitoring of the Arctic Ocean. In: *Operational Oceanography, Implementation at the European and Regional Scales: Proceedings of the*

Second International Conference on EuroGOOS, 11–13 March 1999, Rome, Italy (pp. 165–177, Elsevier Oceanography Series 66).

Johannessen, O.M., Johannessen, J.A., Svendsen, E., Shuchman, R.A., Campbell, W.J. and Josberger, E. (1987) Ice-edge eddies in the Fram Strait marginal ice zone. *Science* **236**, 427–429.

Johannessen, O.M., Sandven, S., Skagseth, O., Kloster, K., Kovacs, Z., Sauvadet, P., Geli, L., Weeks, W.F. and Louet, J. (1992a) *ERS-1 SAR Ice Routing of L'Astrolabe through the Northeast Passage* (NERSC Technical Report No. 56, 31 pp.). Nansen Environmental and Remote Sensing Centre, Bergen, Norway.

Johannessen, O.M., Sandven, S., Skagseth, Ø., Kloster, K., Kovacs, Z., Sauvadet, P., Geli, L., Weeks, W.F. and Louet, J. (1992b) ERS-1 SAR ice routing of L'Astrolabe through the Northeast Passage. *ESA Proceedings of the European International Space Year Conference in Munich, Germany, April* (pp. 997–1002).

Johannessen, O.M., Campbell, W.J., Shuchman, R., Sandven, S., Gloersen, P., Johannessen, J.A., Josberger, E.G. and Haugan, P.M. (1992c) Microwave study programs of air–ice–ocean interactive processes in the seasonal ice zone of the Greenland and Barents Seas. In: F.D. Carsey (ed.), *Microwave Remote Sensing of Sea Ice* (Geophysical Monograph 68, pp. 261–289). American Geophysical Union, Washington, D.C.

Johannessen, O.M., Sandven, S., Budgell, W.P., Johannessen, J.A. and Shuchman, R.A. (1994a) Observation and simulation of ice tongues and vortex pairs in the marginal ice zone. In: O.M. Johannessen, R.D. Muench and J.E. Overland (eds), *The Polar Oceans and Their Role in Shaping the Global Environment: The Nansen Centennial Volume* (Geophysical Monograph 85, pp. 109–136). American Geophysical Union, Washington, D.C.

Johannessen, O.M., Pettersson, L.H., Sandven, S., Melentyev, V.V., Miles, M., Kloster, K., Bobylev, L.P., Stette, M., Drottning, A. and Kondratyev, K.Ya. (1994b) *Real-time Sea Ice Monitoring of the Northern Sea Route Using ERS-1 Satellite Radar Images* (ESA ERS-1 Pilot Demonstration Project, Terra Orbit Technical Report No. 1/94, 33 pp.). NERSC, Bergen, Norway.

Johannessen, O.M., Muench, R.D. and Overland, J.E. (eds.) (1994c) *The Polar Oceans and Their Role in Shaping the Global Environment: The Nansen Centennial Volume* (Geophysical Monograph 85, 525 pp.). American Geophysical Union, Washington, D.C.

Johannessen, O.M., Miles, M.W. and Bjørgo, E. (1995a) The Arctic's shrinking sea ice. *Nature* **376**, 126–127.

Johannessen, O.M, Sandven, S., Kloster, K., Miles, M., Melentyev, V.V. and Bobylev, L. (1995b) *A Sea Ice Monitoring System for the Northern Sea Route using ERS-1 SAR data* (NERSC Technical Report No. 103, 50 pp.). Nansen Environmental and Remote Sensing Centre, Bergen, Norway.

Johannessen, O. M., Sandven, S., Pettersson, L.H., Miles, M., Kloster, K., Melentyev, V.V., Bobylev, L.P. and Kondratyev, K.Ya. (1996) Near-real time sea ice monitoring in the Northern Sea Route using ERS-1 SAR and DMSP SSM/I microwave data. *Acta Astronautica* **38**(4–8), 457–465.

Johannessen, O.M., Volkov, A.M., Grischenko, V.D., Bobylev, L.P., Sandven, S., Kloster, K., Hamre, T., Asmus, V., Smirnov, V.G., Melentyev, V. *et al.* (1997a) ICEWATCH: Ice SAR monitoring of the Northern Sea Route. In: J.H. Stel, H.W.A. Behrens, J.C. Borst and L.J. Droppert (eds), *Operational Oceanography: The Challenge for European Co-operation—Proceedings of the First International Conference on EuroGOOS, 7–11 October 1996* (Elsevier Oceanography Series No. 62, pp. 224–233). Elsevier, The Hague, The Netherlands.

Johannessen, O.M., Volkov, A.M., Grishchenko, V.D., Bobylev, L.P., Asmus, V.V., Hamre, T., Jensen, V., Kloster, K., Melentyev, V.V., Pettersson, L.H. *et al.* (1997b) ICEWATCH: *Real-time Sea Ice Monitoring of the Northern Sea Route Using Satellite Radar Technology* (NERSC Technical Report No. 113, 126 pp.). Nansen Environmental and Remote Sensing Centre, Bergen, Norway.

Johannessen, O.M., Sandven, S., Drottning, A., Kloster, K., Hamre, T. and Miles, M. (1997c) *ERS-1 SAR Sea Ice Catalogue* (89 pp.). ESA/ESTEC, Noordwijk, The Netherlands.

Johannessen, O.M., Sandven, S., Kloster, K., Pettersson, L.H., Melentyev, V.V., Bobylev, L.P. and Kondratyev, K.Ya. (1997) ERS-1/2 SAR monitoring of dangerous ice phenomena along the western part of the Northern Sea Route. *Int. J. Remote Sensing* **18**(12), 2477–2481.

Johannessen, O.M., Shalina, E.V. and Miles, M.W. (1999a) Satellite evidence for an Arctic sea ice cover in transformation. *Science* **286**, 1937–1939.

Johannessen, O.M., Alexandrov, V.Y., Sandven, S., Pettersson, L.H., Bobylev, L.P., Khizhnichenko, V.M., Volkov, A.M., Lundhaug, M., Dalen, O., Kloster, K. *et al.* (1999b) Synergestic use of RADARSAT, ERS and Okean'' radar images for sea ice studies in the Northern Sea Route. *Proceedings of the International Geoscience and Remote Sensing Symposium, 28 June–2 July 1999, Hamburg, Germany* (pp. 1570–1572).

Johannessen, O.M., Sandven, S., Pettersson, L.H., Volkov, A.M., Asmus, V.V., Milekhin, O.E., Krovotyntsev, V.A., Grishchenko, V.D., Smirnov, V.G., Bobylev, L.P. *et al.* (1999c) ICEWATCH: Demonstration of satellite SAR ice data in the Northern Sea Route. *Proceedings of the 15th International Conference on Port and Ocean Engineering under Arctic Conditions, Espoo, Finland, 23–27 August 1999* (Vol. 2, pp. 498–507).

Johannessen, O. M., Volkov, A. M., Bobylev, L. P., Grischenko, V. D., Sandven, S., Pettersson, L. H., Melentyev, V. V., Asmus, V., Milekhin, O. E., Krovotyntsev, V. A. *et al.* (2000) ICEWATCH: Real-time sea ice monitoring of the Northern Sea Route using satellite radar (a cooperative earth observation project between the Russian and European Space Agencies). *Earth Observation and Remote Sensing* **16**(2), 257–268.

Johannessen, O.M., Shalina, E.V., Kuzmina, S., Miles, M.W. and Nagurnyi, A. (2001) Shrinking of the Arctic ice cover over the last decades. In: W. L. Smith and Y. M. Timofeyev (eds), *Proceedings of International Radiation Symposium, St. Petersburg, Russia, 24–29 July 2000* (pp. 1007–1011). A. Deepak, Hampton, VA.

Johannessen, O.M., Sandven, S., Dalen, Ø., Kloster, K., Lundhaug, M., Hamre, T., Melentyev, V., Alexandrov, V., Bogdanov, A. and Babich, N.G. (2003) *SAR Sea Ice Interpretation Guide* (NERSC Technical Report No. 227, 105 pp.). Nansen Environmental and Remote Sensing Centre, Bergen, Norway.

Johannessen, O.M., Bengtsson, L., Miles, M.W., Kuzmina, S.I., Semenov, V.A., Alekseev, G.V., Nagurnyi, A.P., Zakharov, V.F., Bobylev, L.P., Pettersson, L.H. *et al.* (2004) Arctic climate change: Observed and modeled temperature and sea ice variability. *Tellus* **56A**, 328–341.

Karelin, D.B. (1945) Influence of hydrometeorological conditions on ice conditions in the Laptev Sea. *Proceedings of the ARI* **188**, 1–259 [in Russian].

Karelin, D.B. (1949) *Sea Ice conditions of the East-Siberian Sea and Techniques of Their Forecasting* (182 pp.). Izd. Glavsevmorputi, Moscow [in Russian].

Karelin, D.B., Volkov, N.A., Zhadrinsky, V.V. and Gordienko, P.A. (1946) *Airborne Ice Reconnaissance* (135 pp.). Water Transport, Moscow [in Russian].

Karelin, I.D. (1985) Study of the large-scale sea ice flows from TV satellite images. *Problems of the Arctic and Antarctic* **60**, 86–93 [in Russian].

Karelin, I.D. (1997) Flaw polynyas of the Kara Sea from satellite data. *Proceedings of the AARI* **437**, 99–107 [in Russian].

Karelin, I.D. (1998) Systems of large fractures in drifting ice of the Kara Sea during the winter period. *Proceedings of the AARI* **438**, 51–62 [in Russian].

Karelin, I.D. (2001) Fast ice formation in the eastern Arctic region from satellite data. *Proceedings of the AARI* **443**, 76–88 [in Russian].

Karklin, V. P. (1978) Changes in the atmospheric pressure field at high and temperate latitudes of the Northern Hemisphere in 11-year cycles of solar activity. *Problems of the Arctic and Antarctic* **54**, 62–68 [in Russian].

Karklin, V.P. (1987) Frequency of occurrence of large anomalies of the stable ice formation dates in the Arctic Seas. *Proceedings of the AARI* **402**, 93–102 [in Russian].

Karklin, V. P., Yulin, A.V., Karelin, I. D. and Ivanov, V.V. (2001) Climatic oscillations of ice cover extent of the Arctic Seas of the Siberian Shelf. *Proceedings of the AARI* **443**, 5–12 [in Russian].

Karvonen, J.A. (2004) Baltic Sea ice SAR segmentation and classification using modified pulse-coupled neural networks. *IEEE Transactions on Geoscience and Remote Sensing* **42**(7), 1566–1574.

Katsov, V.M. (2003) Scenarios of Arctic climate changes in the 21st century. *Meteorologiya i Gidrologiya* **10**, 5–19 [in Russian].

Key, J., Maslanik, J.A. and Schweiger, A.J. (1989) Classification of merged AVHRR and SMMR Arctic data with neural networks. *Photogrammetric Engineering and Remote Sensing* **55**(9), 1331–1338.

Kerr, R. (1999) Will the Arctic Ocean lose all its ice? *Science* **286**, 1828.

Khmyznikov, P.K. (1937) *Description of Ship Voyages in the Laptev Sea and in the Western Area of the East-Siberian Sea from 1878 to 1935* (61 pp.). Izd. Glavsevmorputi, Leningrad [in Russian].

Kim, Y.S., Moore, R.K., Onstott, R.G. and Gogineni, S. (1985) Towards the identification of optimum radar parameters for sea-ice monitoring. *Journal of Glaciology* **31**(109), 214–219.

Kloster, K., Fleshe, H. and Johannessen, O.M. (1992) Ice motion from airborne SAR and satellite imagery. *Advanced Space Research* **12**(7), 149–153.

Klyashtorin, L.B. and Lyubushin, A.A. (2003) On the coherence between dynamics of the world fuel consumption and global temperature anomaly. *Energy and Environment* **14**, 773–782.

Koberle, C. and Gerdes, R. (2003) Mechanisms determining the variability of Arctic sea ice conditions and export. *Journal of Climate* **16**, 2843–2858.

Koesner, R.M. (1973) The mass balance of sea ice in the Arctic Ocean. *Journal of Glaciology* **12**, 173–186.

Kolchak, A.V. (1909) Ice of the Kara and Siberian Seas. *Proceedings of the Imperial Academy of Science, St. Petersburg* (170 pp.). Imperial Academy of Science, St. Petersburg [in Russian].

Komarov, A.V. and Shchukin, G.G. (1985) Determination of some characteristics of fast ice and drifting ice using MRL-2. *Proceedings of the MGO 490* (pp. 66–70) [in Russian].

Kondratyev, K.Ya. (2004) Global climate changes: Unsolved problems. *Meteorologiya i Gidrologiya* **6**, 118–128 [in Russian].

Kondratyev, K.Ya., Melentyev, V.V., Bobylev, L.P., Johannessen, O.M., Sandven, S. and Pettersson, L.H. (1995) Experience of applying ERS-1 SAR images for monitoring and improving hydrometeorological servicing of ice navigation in the Northern Sea Route. *Earth Observations and Remote Sensing* **13**, 94–112.

Konstantinov, Yu.B. and Grachev, K.I. (2000) *The High-latitudinal Airborne Sever Expeditions* (176 pp.). Gidrometeoizdat, St. Petersburg [in Russian].

Korsnes, R. (1993) Quantitative analysis of sea ice remote sensing imagery. *International Journal of Remote Sensing* **14**(2), 295–311.

Kovalev, Ye.G. and Yulin, A.V. (1998) Automated forecasting system for the purpose of scientific–operational support of the navigation in the Arctic. *Proceedings of the AARI* **438**, 73–82.

Kramer, H.J. (1996) *Observation of the Earth and Its Environment: Survey of Missions and Sensors* (960 pp.). Springer-Verlag, Berlin.

Krutskikh, B.A. (1970) Ice formation peculiarities in Arctic seas. *Proceedings of the AARI* **292**, 106–117 [in Russian].

Kupetsky, V.N. (1973) About cryotectonic lineaments. *Proceedings of the AARI* **318**, 160–166 [in Russian].

Kuzmichev, A.P. (2002) System of collection and distribution of information over the Arctic. *Proceedings of the Scientific–Practical Conference "Hydrometeorological Support of Economic Activity in Arctic and Ice-covered Seas", St. Petersburg, 27–29 March 2002* (pp. 186–189) [in Russian].

Kuznetsov, I.M. and Timerev, A.A. (1972) Change of ice albedo depending on the state of its surface from aircraft measurements. *Problems of the Arctic and Antarctic* **40**, 71–77 [in Russian].

Kwok, R. (1998) The RADARSAT Geophysical Processor System. In: C. Tsatsoulis and R. Kwok (eds), *Analysis of SAR Data of the Polar Oceans: Recent Advances* (pp. 235–257). Springer-Verlag, Berlin.

Kwok, R. and Cunningham, G.F. (1994) Backscatter characteristics of the winter ice cover in the Beaufort Sea. *Journal of Geophysical Research* **99**(C4), 7787–7802.

Kwok, R. and Cunningham, G.F. (2002) Seasonal ice area and volume production of the Arctic Ocean: November 1996 through April 1997. *Journal of Geophysical Research* **107**(C10), 8038, doi:10.1029/2000JC000469.

Kwok, R., Curlander, J.C., McConnell, R. and Pang, S.S. (1990) An ice-motion tracking system at the Alaska SAR Facility. *IEEE Journal of Oceanic Engineering* **15**(1), 44–54.

Kwok, R., Cunningham, G. and Holt, B. (1992a) An approach to identification of sea ice types from spaceborne SAR data. In: F. Carsey (ed.), *Microwave Remote Sensing of Sea Ice* (Geophysical Monograph 68, pp. 355–360(. American Geophysical Union, Washington, D.C.

Kwok, R., Rignot, E., Holt, B. and Onstott, R.G. (1992b) Identification of sea ice types in spaceborne synthetic aperture radar data. *Journal of Geophysical Research* **97**(C2), 2391–2402.

Kwok, R., Nghiem, S.V., Martin, S., Winebrenner, D.P., Gow, A.J., Perovich, D.K., Swift, C.T., Barber, D.G., Golden, K.M. and Knapp, E.J. (1998) Laboratory measurements of sea ice: Connections to microwave remote sensing. *IEEE Transactions on Geoscience and Remote Sensing* **36**(5), 1716–1730.

Kwok, R., Cunningham, G.F. and Nghiem, S.V. (2003) A study of the onset of melt over the Arctic Ocean in RADARSAT synthetic aperture radar data. *Journal of Geophysical Research* **108**(C11), 3363, doi:10.1029/2002JC001363.

Kwok, R., Cunningham, G.F. and Pang, S.S. (2004a) Fram Strait sea ice outflow. *Journal of Geophysical Research* **109**(C01009), doi:10.1029/2003JC001785.

Kwok, R., Zwally, H. J. and Yi, D. (2004b) ICESat observations of the Arctic sea ice: A first look. *Geophysical Research Letters* **31**, L16401, doi:10.1029/2004GL020309.

Lachenbruch, P.A. (1975). *Discriminant Analysis*. Hafner Press, New York.

Laiho, L., Rahikainen, P., Jourio, B. and Sala, S. (2005) *Industry Interests in the Northern Sea Route* (ARCOP Report, WPC: Workshop Activity, 148 pp.). Ministry of Trade and Industry, Helsinki.

Lassen, K. and Thejll (2005) *Multidecadal Variation of the East Greenland Sea Ice Extent: AD 1500–2000* (Scientific Report 05-02). Danish Meteorological Office, Copenhagen.

Laur, H.P., Bally, P., Meadows, P., Sanches, J., Schertler, B. and Lopino, E. (1997) *ERS SAR Calibration* (Document No. ES-TN-RS-PM-HL09, issue 2, rev. 4). ESA European Space Research Institute (ESRIN), Frascati, Italy.

Lavrov, S.A. and Golubtsov, I.N. (2002) Transmission of meteorological information via the television broadcast nets using message lines. *Proceedings of the Scientific–Practical Conference "Hydrometeorological Support of Economic Activity in Arctic and Ice-covered Seas", St. Petersburg, 27–29 March 2002* (pp. 190–194) [in Russian].

Laxon S., Peacock N. and Smith D. (2003) High interannual variability of sea ice thickness in the Arctic region. *Nature* **425**, 947–950.

Lebedev, A.A. and Mironov, Ye. U. (2001) Reconstruction of ice conditions in the North Atlantic and the adjoining seas during World War II. *Proceedings of the AARI* **443**, 30–37 [in Russian].

Lebedev, A.A. and Paramonov, A.I. (1999) Automated determination of sea ice types and heat conductivity in polar regions based on satellite IR sounding data. *Proceedings of the 15th International Conference on Port and Ocean Engineering under Arctic Conditions, 23–27 August 1999* (Vol. 1, pp. 239–248).

Lebedev, A.A. and Uralov, N.S. (1981) Assessment of the balance of sea ice volume in the Northern Hemisphere. *Proceedings of the AARI* **384**, 61–77 [in Russian].

LeSchack, L.A. (1974) *Potential Use of Satellite IR Data for Ice Thickness Mapping: The Coast and Shelf of the Beaufort Sea* (pp. 243–267). Arctic Institute of N.A., Arlington, VA.

LeSchack, L.A. (1983) Arctic Ocean ice deformation chart using sonar data recorder from nuclear submarine. *Proceedings of the International Conference on Port and Ocean Engineering under Arctic conditions, Helsinki, Finland, 5–9 April 1983* (Vol. 1, pp. 148–153).

Lestgaft, E.F. (1913) *Ice of the Arctic Ocean and a Sea Route from Europe to Siberia* (28 pp.). Imperial Academy of Science, St. Petersburg [in Russian].

Lomonosov, M.V. (1952) *Complete Works* (Vol. VI). USSS Academy of Science, Moscow [in Russian].

Lopés, A., Fjørtoft, R, Ducrot, D., Marthon, P. and Lemaréchal, C. (1999) Edge detection and segmentation of SAR images. In: C.H. Chen (ed.), *Homogeneous Regions: Information Processing for Remote Sensing* (p. 139). World Scientific, Singapore.

Losev, S.M., Gorbunov, Yu.A. and Kulakov, I.Yu. (1986) Some peculiarities of ice movement in the Arctic Basin from data of automatic FGGE buoys. *Problems of the Arctic and Antarctic* **62**, 77–88 [in Russian].

Losev, S.M., Gorbunov, Yu.A. and Sergeyeva, I.A. (2002) Technology for simulating ice drift velocity fields in the Arctic Basin from data of automatic buoys. *Proceedings of the AARI* **445**, 101–112 [in Russian].

Loshchilov, V.S. (1970) *Airborne Observations of the Ice Cover by Means of a Side-looking Airborne Radar Station* (methodological manual, 60 pp., Rotaprint). Arctic and Antarctic Research Institute, St. Petersburg [in Russian].

Loshchilov, V.S. and Paramonov, A.I. (1997) Determination and mapping of sea ice thickness in the Arctic from satellite images in the IR-range. *Earth Observations and Remote Sensing* **5**, 63–72 [in Russian].

Lubin, D. and Massom, R. (2006) *Polar Remote Sensing* (Vol. 1, 756 pp.). Springer–Praxis, Chinchester, UK.

Lundhaug, M. (2002a) ERS SAR studies of sea ice signatures in the Pechora Sea and Kara Sea region. *Canadian Journal of Remote Sensing* **28**(2), 1–14.

Lundhaug, M. (2002b) Sea ice studies in the Northern Sea Route by use of synthetic aperture radar. Ph.D. thesis, The Norwegian University of Science and Technology, Bergen, Norway.

Makynen, M. and Hallikainen, M. (1998) C-band backscattering signatures of Baltic sea ice. *Proceedings of the International Geoscience and Remote Sensing Symposium, 6–10 July 1998, Seattle, WA*.

Malmgren, F. (1933) On the properties of sea-ice. In: H.U. Sverdrup (ed.), *The Norwegian North Polar Expedition with the Maud'' 1918–1925: Scientific Results*. Geofysisk Institutt, Bergen in co-operation with other institutions (Vol. Ia: *Special Reports*, pp. 1–67. A.S. John Griegs Boktrykkeri, Bergen, Norway).

Manabe, S. and Wetherald, R.T. (1967) Thermal equilibrium of atmosphere with a given distribution of relative humidity. *Journal of Atmospheric Science* **24**, 241–259.

Markus, T. and Dokken, S.T. (2002) Evaluation of late summer passive microwave Arctic sea ice retrievals. *IEEE Transactions on Geoscience and Remote Sensing* **40**(2), 348–356.

Martin, S., Steffen, K., Comiso, J., Cavalieri, D., Drinkwater, M. and Holt, B. (1992) Microwave remote sensing of polynyas. In: F.D. Carsey (ed.), *Microwave Remote Sensing of Sea Ice* (Geophysical Monograph 68, pp. 303–311). American Geophysical Union, Washington, D.C.

Martin, S., Wakatsuchi, M. and Ono, N (1995) Ice and ocean processes in the Tatarskiy Strait, Japan Sea, as revealed by ERS-1 SAR. *International Journal of Remote Sensing* **16**(17), 3227–3243.

Martin, T. and Augstein, E. (2000) Large-scale drift of Arctic sea ice retrieved from passive satellite microwave data. *Journal of Geophysical Research* **105**(C4), 8775–8788.

Martyn, P., Williams, J., Nicoll, J., Guritz R. and Bicknell T. (1999) Calibration of the RADARSAT SWB processor at the Alaska SAR facility. *Proceedings of the International Geoscience and Remote Sensing Symposium, Hamburg, 28 June–2 July 1999* (pp. 2355–2359).

Maslanik, J., Serreze, M.C. and Barry, R.G. (1996) Recent decreases in Arctic summer ice cover and linkages to atmospheric circulation anomalies. *Geophysical Research Letters* **23**, 1677–1680.

Maslanik, J.A., Serreze, M.C. and Agnew, T. (1999) On the record reduction in western Arctic sea-ice cover in 1998. *Geophysical Research Letters* **26**, 1905–1908.

Massom, R. (1991) Satellite Remote Sensing of Polar Regions (307 pp.). Belhaven Press, London.

Matushenko, N.I. (2000) What can we offer? Russia is optimistic about the future of the Northern Sea Route. In: C.L. Ragner (ed.), *Proceedings of the Northern Sea Route User Conference: ''The 21st Century—Turning Point for the Northern Sea Route?'', Oslo, 18–20 November 1999* (pp. 23–32). Kluwer Academic Publishers, Dordrecht, The Netherlands.

Maykut, G.A. and Untersteiner, N. (1971) Some results from time-dependent thermodynamic model of sea ice. *Journal of Geophysical Research* **76**(6), 1440–1475.

McConnell, R., Kwok, R., Curlander, J.C., Kober, W. and Pang, S.S. (1991) Psi-S correlation and dynamic time warping: Two methods for tracking ice floes in SAR images. *IEEE Transactions on Geoscience and Remote Sensing* **29**(11), 1004–1012.

McLaren, A.S., Wadhams, P. and Weintraub, R. (1984) The sea ice topography of McClure Strait in winter and summer of 1960 from submarine profiles. *Arctic* **37**(2), 110–120.

McPhee, M.G., Stanton, T.P., Morison, J.H. and Martinson, D.G. (1998) Freshening of the upper ocean in the Arctic: Is perennial sea ice disappearing? *Geophysical Research Letters* **25**, 1729–1732.

Melentyev, V.V., Kondratyev, K.Ya., Bobylev, L.P., Glushko, Yu.F., Johannessen, O.M., Sandven, S., Pettersson, L.H. and Kloster, K. (1997) The use of ERS-1/2 radar images for improving hydrometeorological support of navigation in the western part of the Northern Sea Route in 1993–1996. *Russian Meteorology and Hydrology* **5**, 61–67.

Melling, H. (1998) Detection of features in first-year pack ice by synthetic aperture radar (SAR). *International Journal of Remote Sensing* **19**(6), 1223–1249.

Methodological Instructions on the Problems of Receiving, Processing and Use of Satellite Ice Information: Determination of Ice Cover Characteristics from Radar Images of Kosmos-1500'' Satellite (1985) (Issue 1, 75 pp., Rotaprint). Arctic and Antarctic Research Institute, St. Petersburg [in Russian].

Miles, M. W. and Barry, R. G. (1998) A 5-year climatology of winter sea ice leads in the western Arctic. *Journal of Geophysical Research* **103**, 21723–21734.

Mironov, Ye.U. (1986a) Assessment of sea ice volume in the Arctic Basin taking into account ridged ice features. *Materials of Glaciological Studies* **56**, 69–72 [in Russian].

Mironov, Ye.U. (1986b) Some regularities of ice thickness distribution in the Arctic Basin. *News of the All-Union Geographical Society* **118**(3), 202–207 [in Russian].

Mironov, Ye.U. (1987) Estimation of the volume of sea ice in the Arctic Ocean taking pressure ridges into account. *Polar Geography and Geology* **11**(1), 69–75.

Mironov, Ye.U. (1996) Uniform ice regions of the Barents Sea. *Proceedings of IAHR 96, 27–31 August 1996, Beijing, China* (Vol. 1, pp. 361–369).

Mironov, Ye.U. (2004) *Ice Conditions of the Greenland and Barents Seas and Their Long-range Forecasting* (320 pp.). Gidrometeoizdat, St. Petersburg [in Russian].

Mironov, Ye.U. and Uralov, N.S. (1991) Year-to-year variations of ice transport from Arctic Basin through straits of Canadian Arctic Archipelago and Fram Strait. *IAHS* **208**, 128–141.

Mironov, Ye.U. and Uralov, N.S. (1994) Variability of the multiyear ice thickness in the Arctic Basin. *Problems of the Arctic and Antarctic* **67–68**, 129–143 [in Russian].

Mironov, Ye.U., Spichkin, V.A. and Egorov, A. (1994) Seasonal changes of sea ice conditions and their interannual variability in the shelf exploration regions of the Barents and Kara Seas. *Proceedings of the First International Conference on Development of the Russian Arctic Offshore (RAO-93), St. Petersburg, 21–24 September 1993* (pp. 110–121).

Mironov, Ye.U., Spichkin, V.A. and Sergeeva, I.A. (2000) Thermal, dynamic and morphographic conditions of fast ice development in the shelf of the Barents and Kara Seas. *Proceedings of the 6th International Conference on Ships and Marine Constructions in the Cold Regions, ICETECH 2000, St. Petersburg, 12–14 September 2000* (pp. 500–507).

Mironov, Ye.U., Brestkin, S.V. and Smirnov, V.G. (2002) The ice-information system for the Arctic and development of hydrometeorological support technologies. *Proceedings of the Scientific–Practical Conference: ''Hydrometeorological Support of Economic Activity in Arctic and Ice-covered Seas'', St. Petersburg, 27–29 March 2002* (pp. 130–136, Rotaprint). Arctic and Antarctic Research Institute, St. Petersburg [in Russian].

Moctezuma Flores, M., Maitre, Y. and Parmiiggiani, F. (1994) Sea-ice velocity fields estimation on Ross Sea AVHRR images. *Proceedings of the International Geoscience and Remote Sensing Symposium, Pasadena, CA, 8–12 August* (pp. 1300–1302).

Moore, R.K., Soofi, K.A. and Purduski, S.M. (1980) A radar clutter model: Average scattering coefficients of land, snow, and ice. *IEEE Transactions on Aerospace and Electronic Systems* **16**(6), 783–799.

Mountfield, D. (1974) *A History of the Polar Exploration* (208 pp.). Hamlyn, London.

Mulherin, N.D. (1996) *The Northern Sea Route: Its Development and Evolving State of Operations in the 1990s* (CRREL Report No.96-3, 77 pp.). U.S. Army Cold Regions Research and Engineering Laboratory, Hanover, NH.

Mulherin, N.D., Sodhi, D.S. and Smallidge, E. (1994) *Northern Sea Route and Ice-breaking Technology: An Overview of Current Conditions* (CRREL Report MP 3520, 162 pp.). U.S. Army Cold Regions Research and Engineering Laboratory, Hanover, NH.

Mysak, L. A. and Venegas, S. A. (1998) Decadal climate oscillations in the Arctic: A new feedback loop for atmosphere–ice–ocean interactions. *Geophysical Research Letters* **24**, 3607–3610.

Nansen, F. (1898) *Farthest North: Being the Record of a Voyage of Exploration of the Ship Fram 1893–96 and of a Fifteen Months' Sleigh Journey by Dr. Nansen and Lieut. Johansen* (679 pp.). Harpers & Brothers, New York.

Nansen, F. (1902) The oceanography of the North Polar Basin. In: F. Nansen (ed.), *The Norwegian North Polar Expedition 1893–1896: Scientific Results* (Vol. 3, pp. 357–386). Longmans, Green & Co., Harlow, U.K.

Nansen, F. (1911) *In Northern Mists: Arctic Exploration in Early Time* (Vol. 1, 384 pp.; Vol. 2, 420 pp.). Frederick A. Stokes, New York.

Nazirov, M., Pichugin, A.P. and Spiridonov, Y.G. (1990) *Radar Observations of the Earth's Surface from Space* (200 pp.). Gidrometeoizdat, St. Petersburg [in Russian].

Nghiem, S. (2004) On the use of ENVISAT ASAR for remote sensing of sea ice. *ENVISAT Symposium, Salzburg, 6–10 September 2004* (Abstract No. 672).

Nghiem, S.V., Martin, S., Perovich, D.K., Kwok R.M., Drucker, R. and Gow, A.J. (1997) A laboratory study of the effect of frost flowers on C-band radar backscatter from sea ice. *Journal of Geophysical Research* **102**(C2), 3357–3370.

Nghiem, S.V., Kwok, R., Yueh, S.H., Gow, A.K., Perovich, D.K., Hsu, C.-C., Ding, K.-H., Kong, J.A. and Grenfell, T.C. (1998) Diurnal thermal cycling effects on microwave sgnatures of thin sea ice. *IEEE Transactions on Geoscience and Remote Sensing* **36**(1), 111–124.

Nikolaeva, A.Y. (1970) On the influence of fast ice on ice drift. *Problems of the Arctic and Antarctic* **33**, 110–114 [in Russian].

Nordenskjöld, A.E. (1936). *Voyage on the Vega* (Vol. II, p. 21). Izd. Glavsevmorputi, Moscow [in Russian].

Nystuen, J.A. and Garcia, Jr., F.W. (1992) Sea ice classification using SAR backscatter statistics. *IEEE Transactions on Geoscience and Remote Sensing* **30**(3), 502–509.

Onstott, R.G. (1992) SAR and scatterometer signatures of sea ice. In: F.D. Carsey (ed.), *Microwave Remote Sensing of Sea Ice* (Geophysical Monograph 68, pp. 73–104). American Geophysical Union, Washington, D.C.

Onstott, R.G. (1997) Results of satellite and in situ remote sensing measurement and modelling studies of Arctic sea ice, which supports the monitoring of changes in the global climate. *Proceedings of the International Geoscience and Remote Sensing Symposium, Singapore, 3–8 August* (pp. 1294–1296).

Onstott, R.G., Gogineni, P., Gow, A.K., Grenfell, T.C., Jezek, K.C., Perovich, D.K. and Swift, C.T. (1998) Electromagnetic and physical properties of sea ice formed in the presence of wave action. *IEEE Transactions on Geoscience and Remote Sensing* **36**(5), 1764–1783.

Onstott, R.G. and Shuchman, R.A. (2004) SAR measurements of sea ice. In: C.R. Jackson and J.R. Apel (eds), *Synthetic Aperture Radar Marine User's Manual* (pp. 81–115). U.S. Department of Commerce, Washington, D.C.

Paola, J.D. and Schowengerdt, R.A. (1995) A detailed comparison of backpropagation neural network and maximum-likelihood classifiers for urban land use classification. *IEEE Transactions on Geoscience and Remote Sensing* **33**(4), 981–996.

Paramonov, A.I. and Chebotareva, V.A. (1982) Use of IR aerospace observations of the Arctic Seas for navigation and for solution of other economic problems. In: *Study of the Arctic, the Antarctic and the World Ocean* (pp. 159–169). Gidrometeoizdat, Leningrad [in Russian].

Paramonov, A.I. and Lebedev, G.A. (2004) Algorithm of a non-linear similarity between radiation field relief and relief of sea ice true thickness relief for investigation of the dynamics of age gradations of the sea ice cover from satellite observation data in the thermal IR-range channel. *Proceedings of the Second All-Russia Scientific Conference: ''Remote Sounding of the Earth's Surfaces and the Atmosphere by Aerospace Means* (Vol. 2, pp. 71–75) [in Russian].

Parkinson, C.L., Comiso, J.C., Zwally, H.J., Cavalieri, D.J., Gloersen, P. and Campbell, W.J. (1987) *Arctic Sea Ice 1973–1976: Satellite Passive-Microwave Observations* (NASA publication SP-489, 296 pp.). NASA, Washington, D.C.

Parkinson, C.L., Cavalieri, D.J., Gloersen, P., Zwally, H.J. and Comiso, J.C. (1999) Arctic sea ice extents, areas, and trends, 1978–1996. *Journal of Geophysical Research* **104**(C9), 20837–20856.

Parmiggiani, F. (2004) A first experiment of near real time (NRT) processing of Envisat/ASAR images to assist ship routing in Antarctica. *ENVISAT Symposium, Salzburg, 6–10 September 2004* (Abstract No. 12).

Pasetsky, V. (1983) Gavriil Andreyevich Sarychev. In: L. Demin (ed.), *Explorers* (pp. 76–129). Molodaya Gvardiya, Moscow [in Russian].

Peresypkin, V.I. (2000) Introduction to the Northern Sea Route History and INSROP's background. In: C.L. Ragner (ed.), *Proceedings of the Northern Sea Route User Conference: ''The 21st Century—Turning Point for the Northern Sea Route?'', Oslo, 18–20 November 1999* (pp. 23–32). Kluwer Academic Publishers, Dordrecht, The Netherlands.

Peresypkin, V.I. (2002) The Northern Sea Route: Its state and prospects of development. *Proceedings of the scientific–practical conference ''Hydrometeorological Support of Economic Activity in Arctic and Ice-covered Seas'', St. Petersburg, 27–29 March 2002* (pp. 71–77) [in Russian].

Perovich, D.K., Longacre, J., Barber, D.G., Maffione, R.A., Cota, G.F., Mobley, C.D., Gow, A.K., Onstott, R.G., Grenfell, T.C., Pegau, W.S. and Roesler, C.S. (1998) Field observations of the electromagnetic properties of first-year sea ice. *IEEE Transactions on Geoscience and Remote Sensing* **36**(5), 1705–1715.

Pettersson, L.H., Sandven, S., Dalen, Ø., Melentyev, V.V., Bogdanov, A.V., Kloster, K. and Lundhaug, M. (1999a) *Arctic Demonstration and Exploratory Voyage (ARCDEV): The Nansen Center Contribution* (WP3: ice conditions; WP10: remote services and maintenance; NERSC Technical Report No. 167, 49 pp.). Nansen Environmental and Remote Sensing Centre, Bergen, Norway.

Pettersson, L.H., Sandven, S., Dalen, Ø., Melentyev, V.V. and Babich, N.G. (1999b) Satellite radar ice monitoring for ice navigation of the ARCDEV tanker convoy in the Kara Sea. *Proceedings of the 15th International Conference on Port and Ocean Engineering under Arctic Conditions, Espoo, Finland, 23–27 August* (Vol. 1, pp. 181–190).

Pettersson, L.H., Johannessen, O.M., Olaussen, T.I., Guerre, L.-F., Hirschfel, A., Bobylev, L.P., Melentyev, V.V., Korotkevich, O.E., Kouraev, A.V., Kotova, L.A. *et al.* (1999c) *Synergetic Use of ERS and ENVISAT Synthetic Aperture Radar (SAR) with Other EO*

Data: A Market Survey for the Russian Territories (NERSC Technical Report No. 165, 73 pp.). Nansen Environmental and Remote Sensing Centre, Bergen, Norway

Pfirman, S., Haxby, W.F., Colony, R.L. and Rigor, I.G. (2004) Variability of Arctic sea ice drift. *Geophysical Research Letters* **31**(L16402), doi:10.1029/2004GL020063.

Polyakov, I.V. and Johnson, M.A. (2000) Arctic decadal and interdecadal variability. *Geophysical Research Letters* **27**, 4097–4100.

Polyakov, I.V., Proshutinsky, A.Y. and Johnson, M.A. (1999) Seasonal cycles in two regimes of Arctic climate. *Journal of Geophysical Research* **104**, 25761–25788.

Polyakov, I., Alekseev, G.V., Bekryaev, R.V., Colony, R.L., Bhatt, U.S., Johnson, M.A., Karklin, V.P., Makshtas, A.P., Walsh, D. and Yulin, A.V. (2002) Observationally based assessment of polar amplification of global warming. *Geophysical Research Letters* **1878**, doi:1029/2001GL011111.

Polyakov, I., Alekseev, G.V., Bekryaev, R.V., Bhatt, U.S., Colony, R.L., Johnson, M.A., Karklin, V.P., Walsh, D. and Yulin, A.V. (2003) Long-term ice variability in Arctic marginal seas. *Journal of Climate* **16**, 2078–2085.

Poulin, A.O. (1975) Significance of surface temperature in the thermal infrared sensing of sea and lake ice. *Journal of Glaciology* **15**(73), 277–281.

Proshutinsky, A.Y. and Johnson, M.A. (1997) Two circulation regimes of the wind-driven Arctic Ocean. *Journal of Geophysical Research* **102**, 12493–12514.

Provorkin, A.V. (1972) Sea ice studies from the images of Soviet meteorological satellites. *Proceedings of the All-Union Conference of Young Scientists of the USSR Hydrometeorological Service, Leningrad* (pp. 66–72) [in Russian].

Provorkin, A.V. (1975) The ice cover structure during the spring period from images of meteorological satellites. *Proceedings of the AARI* **126**, 23–35 [in Russian].

RADARSAT Data Products Specifications (Document RSI-GS-026, ver. 3.0). RADARSAT International, May 2000 (133 pp.). Technical document available online at *www.rsi.ca*

Ragner, C.L. (ed.) (2000) *The 21st Century: Turning Point for the Northern Sea Route?* Kluwer Academic, Dordrecht, The Netherlands. ISBN 0-7923-6365-5.

Ramsay, B.R., Weir, L., Wilson, K. and Arkett, M. (1996) Early results of the use of RADARSAT ScanSAR data in the Canadian Ice Service. *Proceedings of the Fourth Symposium on Remote Sensing of the Polar Environments, Lyngby, Denmark, 29 April–1 May 1996* (pp. 95–117).

Ramseier, R.O., Gray, L. and Campbell, W.J. (1977) Scatterometer and image radar results obtained over Big Bear, AIDJEX 1975. *Proceedings of Symposium on Sea Ice Processes and Models* (Vol. 1, pp. 30–40).

Remund, Q.P., Long, D.G. and Drinkwater, M.R. (2000) An iterative approach to multisensor sea ice classification. *IEEE Transactions on Geoscience and Remote Sensing* **38**(4), 1843–1856.

Rigor, I.G. and Wallace, J. M. (2004) Variations in the age of sea ice and summer sea ice extent, *Geophysical Research Letters* **31**, doi:10.1029/2004GL019492.

Rigor, I.G., Wallace, J.M. and Colony, R.L. (2002) Response of sea ice to the Arctic Oscillation. *Journal of Climate* **15**, 2648–2663.

Robinson, I.S. (2004) *Measuring the Oceans from Space: The Principles and Methods of Satellite Oceanography* (669 pp.). Springer-Verlag, Berlin.

Romanov, I.P. (1992) *Ice Cover of the Arctic Basin* (211 pp., Rotaprint). Arctic and Antarctic Research Institute, St. Petersburg [in Russian].

Rosenblatt, F. (1958) The perceptron: A probabilistic model for information storage and organization in the brain. *Psychological Review* **65**, 386–408.

Rothrock, D.A., Yu, Y. and Maykut, G.A. (1999) Thinning of the Arctic sea-ice cover. *Geophysical Research Letters* **26**(23), 3469–3472.

Rothrock, D.A., Zhang, J. and Yu, Y. (2003) The Arctic ice thickness anomaly of the 1990s: A consistent view from observations and models. *Journal of Geophysical Research* **108**(C3), 3083, doi:10.1029/2001JC001208.

Rozhkov, V.A. (2001) *Theory and Methods of Statistical Assessment of Probabilistic Characteristics of Random Values and Functions with Hydrometeorological Examples* (340 pp.). Gidrometeoizdat, St. Petersburg [in Russian].

Rudnev, D. and Kulik, N. (1915) *Materials for the Study of the Northern Sea Route from Europe to the Ob' and the Yenisey* (127 pp.). A.E. Kollins, Petrograd [in Russian].

Ruksha, V.V. (2002) Seventy years for the Northern Sea Route is not an age. *Water Transport* **17–18**, 4–5 [in Russian].

Rumelhart, D.E., Hinton, G.E. and Williams, R.J. (1986) Learning representations by back-propagating errors. *Nature* **323**, 533–536.

Ruthe, (1943) Die Fahrt des hilfskreuzers "Komet" durch die Nordostpassage. *Polar Forschung, Mitteilungen fuer die Vereinigung zur Forderung des Archives fuer Polarforschung* **1**, 5–7 [in German].

Sabaidash, A.V. (2002) The contemporary technology of hydrometeorological information dissemination in the interests of supporting safety navigation. *Proceedings of the Scientific–Practical Conference: "Hydrometeorological Support of Economic Activity in Arctic and Ice-covered Seas", St. Petersburg, 27–29 March 2002* (pp. 167–170) [in Russian].

Sanderson, R.W. (1975) Changes in the area of Arctic sea ice 1966 to 1974. *Meteorological Magazine* **104**(1240), 313–323.

Sandven, S., Kloster K. and Johannessen, O.M. (1991) *SAR Ice Algorithms for Ice Edge, Ice Concentration, and Ice Kinematics* (NERSC Technical Report 38). Nansen Environmental and Remote Sensing Centre, Bergen, Norway.

Sandven, S., Johannessen, O.M. and Kloster, K. (1993) Real time use of satellite data in ice monitoring for Arctic operations. *Proceedings of the 12th International Conference on Port and Oceanic Engineering under Arctic Conditions.*

Sandven, S., Johannessen, O.M., Pettersson, L.H., Miles, M. and Drottning, Å. (1994) A pilot ice monitoring service using ERS-1 SAR images. *Proceedings of First Workshop on ERS-1 Pilot Projects, Toledo, Spain, 22–24 June 1994* (pp. 139–143, ESA SP-365).

Sandven, S., Kloster, K., Hamre, T. and Stette, M. (1995) *Satellite Monitoring of the Northern Sea Route in the Summer of 1995: Project Report for Ice and Snow Engineering Labs. Engineering Center, NKK Corporation, Japan* (NERSC Technical Report No. 105, 54 pp.). Nansen Environmental and Remote Sensing Centre, Bergen, Norway.

Sandven, S., Groenvall, H., Seina, A., Valeur, H.H., Nizrovsky, M., Gill, R., Andersen, H. S., Haugen, V.J. andKloster, K. (1997) *Operational Sea Ice Monitoring by Satellites in Europe* (NERSC Technical Report No. 129). Nansen Environmental and Remote Sensing Centre, Bergen, Norway.

Sandven, S., Alexandrov, V.Yu., Melentyev, V.V. and Smirnov, V.G. (1998a) Demonstration of RADARSAT ScanSAR data for summer ice navigation in the Northern Sea Route. *INSROP Newsletter* **1**(6), 11–13.

Sandven, S., Maekynen, M., Hallikainen, M., Similae, M., Gronvall, H., Cavanie, A., Ezraty, R., Maroni, C., Gill, R., Valeur, H.H. *et al.* (1998b) *Integrated Use of New Microwave Satellite Data for Improved Sea Ice Observation (IMSI): Development of New Satellite Ice Data Products* (NERSC Technical Report No. 145, 76 pp.). Nansen Environmental and Remote Sensing Centre, Bergen, Norway.

Sandven, S., Johannessen, O.M., Miles, M.W., Pettersson, L.H. and Kloster, K. (1999a) Barents Sea seasonal ice zone features and processes from ERS-1 synthetic aperture radar: Seasonal Ice Zone Experiment 1992. *Journal of Geophysical Research* **104**(C7), 15843–15857.

Sandven, S., Alexandrov, V., Dalen, O., Lundhaug, M., Melentyev, V., Smirnov, V., Babich, N. and Kloster, K. (1999b) *Practical Demonstration of Real-time RADARSAT SAR Data for Ice Navigation on the Northern Sea Route* (INSROP Working Paper 134, pp. 1–32). INSROP, Oslo.

Sandven, S., Lundhaug, M., Dalen, Ø., Kloster, K. and Alexandrov, V. (1999c) Satellite observations, In: K. Riska and J. Tuhkuri (eds), *Local Ice Cover Deformation and Mesoscale Ice Dynamics* (Vol. 1, pp. 317–331, Final Scientific Report). Helsinki University of Technology, Espoo, Finland.

Sandven, S., Dalen, O., Lundhaug, M., Kloster, K., Alexandrov, V.Y. and Zaitsev, L.V. (2001) Sea ice investigations in the Laptev Sea area in late summer using SAR data. *Canadian Journal of Remote Sensing* **27**(5), 502–516.

Sandven, S., Kloster, K., Tangen, H., Andreassen, T. S., Goodwin, H. and Partington, K. (2004) Sea ice mapping using ENVISAT ASAR Wideswth images. *ESA Proceedings of the Second Workshop on Coastal and Marine Applications of SAR, 12 – 15 September 2003 (SP-565, 2004), Svalbard, Norway*.

Sandven, S., Johannessen, O.M., Fahrbach, E., Buch, E., Cattle, H., Toudal Pedersen, L. and Vihma, T. (2005) The Arctic Ocean and the need for an Arctic GOOS. *EuroGOOS* **22**, 1–50.

Sandven, S. and Johannessen, O.M. (2006) Sea ice monitoring by remote sensing. In: J. Gower (ed.), *Remote Sensing of the Marine Environment* (Manual of Remote Sensing, 3rd edn, Vol. 6, pp. 241–283). American Society for Photogrammetry and Remote Sensing, Bethesda, MD.

Scheuchl, B., Caves, R., Flett, D., De Abreu, R., Arkett, M. and Cumming, I. (2004) The potential of cross-polarization information for operational sea ice monitoring. *Proceedings of the ENVISAT Symposium, Salzburg, 6–10 September 2004* (Abstract No. 493).

Schmith, T. and Hansen, C. (2003) Fram Strait ice export during the nineteenth and twentieth centuries reconstructed from a multiyear sea ice index from southwestern Greenland. *Journal of Climate* **16**, 2782–2791.

Schwartz, K., Jeffries, M.O. and Li, S. (1994) Using ERS-1 SAR data to monitor the state of the Arctic Ocean sea ice surface between spring and autumn, 1992. *Proceedings of International Geoscience and Remote Sensing Symposium, IGARSS 94, 8–12 August, Pasadena, CA* (pp. 1759–1762).

Schlesinger, M.E. and Ramankutty, N. (1994) An oscillation in the global climate system of period 65–70 years. *Nature* **367**, 723–726.

Sea Ice Information Services in the World (2000) (WMO Publication No. 574). World Meteorological Organization, Geneva, Switzerland.

Sephton, A.J. and Partington, K.C. (1998) Towards operational monitoring of Arctic sea ice by SAR. In: C. Tsatsoulis and R. Kwok (eds), *Analysis of SAR Data of the Polar Oceans: Recent Advances* (pp. 259–279). Springer-Verlag, Berlin.

Serreze, M.C., Maslanik, J.A., Scambos, T.A., Fetterer, F., Stroeve, J., Knowles, K., Fowler, C., Drobot, S., Barry, R.G. and Haran, T.M. (2003) Record minimum sea ice cover in the Arctic Ocean for summer 2002. *Geophysical Research Letters* **30**, 1110–1113.

Shalina, E.V., Johannessen, O.M. and Miles, M.W. (1999) Arctic ice transformations: Multiyear ice changes in comparison with summer minima. *Proceedings of the Inter-*

national Geosciences and Remote Sensing Symposium, IGARSS99, 28 June–2 July 1999, Hamburg, Germany (pp. 2023–2026).

Shapiro, I., Colony, R.L. and Vinje, T. (2003) April sea ice extent in the Barents Sea, 1850–2001. *Polar Research* **22**(1), 5–10.

Sharov, A.I. (2002) *Satellite Hydrographic Monitoring and Assessment of Environmental Trends along the Russian Arctic Coast (AMETHYST)* (Final Scientific Report, 148 pp.). Institute of Digital Image Processing Forschungsgesellschaft Joanneum Research mbH, Graz, Austria.

Shcherbakov, Yu.A., Loshchilov, V.S., Smirnov, V.G. and Grishin, Ye.A. (2002) Operational ice-information support for navigation in an ice-covered sea. *Navigation and Hydrography* **15**, 67–77 [in Russian].

Shesterikov, N.P. (1963) On some regularities of the ice albedo change in summer in the Arctic. *Problems of the Arctic and Antarctic* **14**, 27–31 [in Russian].

Shokr, M.E. (1991) Evaluation of second-order texture parameters for sea ice classification from radar images. *Journal of Geophysical Research* **96**(C6), 10625–10640.

Shokr, M.E. (1998) Field observations and model calculations of dielectric properties of Arctic sea ice in the microwave C-Band. *IEEE Transactions on Geoscience and Remote Sensing* **36**(2), 463–478.

Shuchman, R.A., Onstott, R.G., Fett, R.W. and Wackerman, C.C. (1994) Satellite remote sensing of the Beaufort Sea during LEADEX 92. *Proceedings of International Geoscience and Remote Sensing Symposium, 8–12 August 1994, Pasadena, CA* (pp. 1015–1017).

Shuchman, R.A, Onstott, R.G., Johannessen, O.M., Sandven, S. and Johannessen, J.A. (2004) Processes at the ice edge: The Arctic. In: C.R. Jackson and J.R. Apel (eds), *Synthetic Aperture Radar Marine User's Manual* (pp. 373–395). U.S. Department of Commerce, Washington, D.C.

Skokov, R.M. (1985) About forecasting fast ice break-up. *Proceedings of the Hydrometeorological Scientific Centre of USSR* (Vol. 270, pp. 52–57) [in Russian].

Smirnov, V.I. (1974) *Sea Ice Conditions of Navigation in the Canadian–Alaska Arctic* (180 pp.). Gidrometeoizdat, Moscow [in Russian].

Smirnov, V.G. (2000) Use of SAR data for ice navigation support in Russia. *Proceedings of a Workshop on Mapping and Archiving of Sea Ice Data: "The Expanding Role of Radar", Ottawa, 2–4 May 2000* (pp. 159–165).

Smirnov, V.G., Bushuev, A.V. and Deviataev, O.S. (1997) Satellite monitoring of the ice cover in the region of Prirazlomnoye oil field. *Navigation and Hydrography* **4**, 100–107 [in Russian].

Smirnov, V. G., Bychenkov, Yu. D., Priamikov, S.M. and Shcherbakov, Yu.A. (1999) The use of satellite information for ice navigation support. *Proceedings of 15th International Conference on Port and Ocean Engineering under Arctic Conditions, Espoo, Finland, 23–27 August 1999* (Vol. 2, pp. 154–165).

Smirnov, V., Frolov, I., Grishchenko, V. and Mironov, Ye. (2000). Russian ice information services in the future. *Proceedings of the Northern Sea Route User Conference, Oslo, 18–20 November 1999* (pp. 169–176). Kluwer Academic Publishers, Dordrecht, The Netherlands.

Smith, D.M. (1998) Recent increase in the length of the melt season of perennial Arctic sea ice. *Geophysical Research Letters* **25**, 655–658.

Soether, R. (2000) What do we need? The shipping industry's views on the Northern Sea Route's potential and problems. In: C.L. Ragner (ed.), *Proceedings of the Northern Sea Route User Conference: "The 21st Century—Turning Point for the Northern Sea Route?", Oslo, 18–20 November 1999* (pp. 35–38). Kluwer Academic, Dordrecht, The Netherlands.

Soh, L.K. and Tsatsoulis, C. (1999) Texture analysis of SAR sea ice imagery using gray level co-occurrence matrices. *IEEE Transactions on Geoscience and Remote Sensing* **37**(2), 780–795.

Soh, L.-K., Tsatsoulis, C. and Holt, B. (1998) Identifying ice floes and computing ice floe distributions in SAR images. In: C. Tsatsoulis and R. Kwok (eds), *Analysis of SAR Data of the Polar Oceans: Recent Advances* (pp. 9–34). Springer-Verlag, Berlin.

Soh, L.K., Tsatsoulis, C., Gineris, D. and Bertoia, C. (2004) ARKTOS: An intelligent system for SAR sea ice image classification. *IEEE Transactions on Geoscience and Remote Sensing* **42**(1), 229–248.

Soon, W. (2005) Variable solar irradiance as a plausible agent for multidecadal variations in the Arctic: Wide surface air temperature record of the past 130 years. *Geophysical Research Letters* **32**, doi:10.1029/2005GL023429.

Soviet Arctic (1938) (No. 5, p. 21). Izd. Glavsevmorputi, Moscow [in Russian].

Steffen, K. and Heinrichs, J. (1994) Feasibility of sea ice typing with synthetic aperture radar (SAR): Merging of Landsat thematic mapper and ERS-1 SAR satellite imagery. *Journal of Geophysical Research* **99**(C11), 22413–22424.

Steffen, K., Key, J., Cavalieri, D.J., Comiso, J., Gloersen, P., Germain, K.S. and Rubinstein, I. (1992) The estimation of geophysical parameters using passive microwave algorithms. In: F. Carsey (ed.), *Microwave Remote Sensing of Sea Ice* (Geophysical Monograph 68, pp. 205–209). American Geophysical Union, Washington, D.C.

Stroeve, J. C., Serreze, M. C., Fetterer, F., Arbetter, T., Meier, W., Maslanik, J. and Knowles, K. (2005) Tracking the Arctic's shrinking ice cover: Another extreme September minimum in 2004. *Geophysical Research Letters* **32**, L04501, doi:10.1029/2004GL02810.

Sun, Y. (1992) Ice motion retrieval from SAR imagery in terms of intensive derivative. *Proceedings of the International Geoscience and Remote Sensing Symposium, May 1992, Houston, TX* (Vol. 1, pp. 585–587).

Sun, Y. (1994) A new correlation technique for ice motion analysis. *EARSeL Advances in Remote Sensing* **3**(2), 57–63.

Sun, Y., Calrlström, A. and Askne, J. (1992) SAR image classification of ice in the Gulf of Bothnia. *International Journal of Remote Sensing* **13**(13), 2489–2514.

Svendsen, E., Kloster, K., Farrelly, B., Johannessen, O.M., Johannessen, J.A., Campbell, W.J., Gloersen, P., Cavalieri, D. and Matzler, C. (1983) Norwegian Remote Sensing Experiment: Evaluation of NIMBUS-7 SMMR for sea ice research. *Journal of Geophysical Research* **88**(C5), 2781–2791.

Svendsen, E., Maetzler, C. and Grenfell, T.C. (1987) A model for retrieving total sea ice concentration from spaceborne dual-polarized passive microwave instrument operating near 90 GHz. *Int. Journal of Rem. Sens.* **8**(10), 1479–1487.

Sverdrup, H.U. (1928) *Tre Aar i Isen Med Maud.* Gylendal Norsk Forlag, Oslo.

Sverdrup, H.U. (1933) Results of astronomical observations. In: H.U. Sverdrup (ed.), *The Norwegian North Polar Expedition with the "Maud" 1918–1925* (scientific results). Geofysisk Institutt, Bergen, Norway, in co-operation with other institutions (Vol. Ia, Special Reports, pp. 1–24. A.S. John Griegs Boktrykkeri, Bergen, Norway).

Sverdrup, H.U. (1936a) The waters on the North-Siberian Shelf. In: H.U. Sverdrup (ed.), *The Norwegian North Polar Expedition with the "Maud" 1918–1925* (scientific results). Geofysisk Institutt, Bergen, Norway, in co-operation with other institutions (Vol. IV, Oceanography, pp. 1–131. A.S. John Griegs Boktrykkeri, Bergen, Norway).

Sverdrup, H.U. (1936b) The wind-drift of the ice on the North-Siberian Shelf. In: H.U. Sverdrup (ed.), *The Norwegian North Polar Expedition with the "Maud" 1918–1925* (scientific results). Geofysisk Institutt, Bergen, Norway, in co-operation with other

institutions (Vol. IV, Oceanography, pp. 1–46. A.S. John Griegs Boktrykkeri, Bergen, Norway).

Tammiksaar, E. (1998) Wrangell or Wrangel: Which is it? *Polar Record* **34**(188), 55–56.

Tamvakis, M. (2000) The NSR's commercial potential and restraints. In: C.L. Ragner (ed.), *Proceedings of the Northern Sea Route User Conference: ''The 21st Century—Turning Point for the Northern Sea Route?'', Oslo, 18–20 November 1999* (pp. 23–32). Kluwer Academic, Dordrecht, The Netherlands.

Thomas, D.R. and Rothrock, D.R. (1993) The Arctic Ocean ice balance: A Kalman smoother estimate. *Journal of Geophysical Research* **98**(C6) 10053–10067.

Thompson, D. W. J. and Wallace, J. M. (1998) The Arctic Oscillation signature in wintertime geopotential height and temperature fields. *Geophysical Research Letters* **25**, 1297–1300.

Timokhov, L.A. (1994) Regional characteristics of the Laptev and the East-Siberian Seas: Climate, topography, ice phases, thermohaline regime, circulation. *Berichte zur Polarforschung* **144**, 15–31.

Treshnikov, A.F. (ed.) (1985) *Atlas of the Arctic* (204 pp.). GUGiK, Moscow [in Russian].

Tucker III, W.B., Perovich, D.K., Gow, A.J., Weeks, W.F. and Drinkwater, M.R. (1992) Physical properties of sea ice relevant to remote sensing. In: F.D. Carsey (ed.), *Microwave Remote Sensing of Sea Ice* (Geophysical Monograph 68, pp. 9–28). American Geophysical Union, Washington, D.C.

Tucker III, W.B., Weatherly, J.W., Eppler, D.T., Farmer, L.D. and Bentley, D.L. (2001) Evidence for rapid thinning of sea ice in the western Arctic Ocean at the end of the 1980s. *Geophysical Research Letters* **28**(14), 2851–2854.

Ulaby, F.T., Moore, R.K. and Fung, A.K. (1981) *Microwave Remote Sensing—Active and Passive, Vol. 1: Microwave Remote Sensing Fundamentals and Radiometry, 1981; Vol. 2: Radar Remote Sensing and Surface Scattering and Emission Theory; Vol. 3: Volume Scattering and Emission Theory, Advanced Systems and Applications* (Vol. 1, p. 456). Addison-Wesley, Reading, MA.

Ulander, L.M.H., Carlstrøm, A. and Askne, J. (1997) Effect of frost flowers, rough saline snow and slush on the ERS-1 SAR backscatter of thin Arctic sea-ice. *International Journal of Remote Sensing* **16**(17), 3287–3305.

Vainio, J. (2004) Near real time use of the Envisat ASAR images as an aid of winter navigation in the Baltic Sea. *ENVISAT Symposium, Salzburg, 6–10 September 2004* (Abstract No. 509).

Veidenbakh, V.A. (1958) The process of diffusive transfer of the photographic picture. *Journal of Scientific and Applied Photography and Cinematography of the USSR Academy of Science* **3**(4), 306–310 [in Russian].

Velikhov, E., Pashaev, D. and Kuznetsov, V. (2001) Russia in the process of Arctic Shelf hydrocarbons fields development: State, perspectives, problems. *Symposium of European Community Countries, Russia, Canada and USA: ''Common Approach to Collaborative Technological Research for Arctic Development'', Brussels, 25–27 October 2001* (pp. 32–50).

Venegas, S. A. and Mysak, L. A. (2000) Is there a dominant timescale of natural climate variability in the Arctic? *Journal of Climate* **13**, 3412–3433.

Vesecky, J.F., Samadani, R., Smith, M.P., Daica, J.M. and Bracewell, R.N. (1988) Observations of sea-ice dynamics using synthetic aperture radar Images: Automated analysis. *IEEE Transactions on Geoscience and Remote Sensing* **26**(1), 38–48.

Vinje, T. (1985) *Physical Environment Western Barents Sea: Drift, Composition, Morphology and Distribution of the Sea Ice fields in the Barents Sea* (Norsk Polarinstitutt Skrifter No. 179C, 26 pp.). Norsk Polarinstitutt, Oslo.

Vinje, T. (2001) Fram Strait ice fluxes and atmospheric circulation: 1950–2000. *Journal of Climate* **14**, 3508–3517.

Vinje, T.E. and Finnekasa, F. (1986) *The Ice Transport through the Fram Strait* (Norsk Polarinstitutt Skrifter 186, 39 pp.). Norsk Polarinstitutt, Oslo.

Vinje, T., Nordlund, N. and Kvambekk, A (1998) Monitoring ice thickness in the Fram Strait. *Journal of Geophysical Research* **103**(C5), 10437–10449.

Vinnikov, K.Ya., Robock, A., Stouffer, R.J., Walsh, J.E., Parkinson, C.L., Cavalieri, D.J., Mitchell, J.F.B., Garrett, D. and Zakharov, V.F. (1999) Global warming and the northern hemisphere sea ice extent. *Science* **286**, 1934–1937.

Vize, V.Yu. (1939) *Seas of the Soviet Arctic* (567 pp.). Izd. Glavsevmorputi, Leningrad [in Russian].

Vize, V.Yu. (1940) *Climate of the Soviet Arctic Seas* (124 pp.). Izd. Glavsevmorputi, Moscow [in Russian].

Vnukov, N. (2000) *Great Travelers: Biographical Dictionary* (734 pp.). Azbuka, St. Petersburg [in Russian].

Voevodin, V.A. and Popov, I.K. (1996) Contemporary techniques and technical means for iceberg observations and studies. In: V.A. Voevodin and I.K. Popov (eds.), *Icebergs of the World Ocean* (pp. 18–29). Hydrometeoizdat, St. Petersburg [in Russian].

Volkov, N.A. and Gudkovich, Z.M. (1967) Main results of the ice drift studies in the Arctic Basin. *Problems of the Arctic and Antarctic* **27**, 55–64 [in Russian].

Volkov, V.A., Johannessen, O.M., Borodachev, V.E., Voinov, G.N., Pettersson, L.H., Bobylev, L.P. and Kouraev, A.V. (2002) *Polar Seas Oceanography: An Integrated Case Study of the Kara Sea* (450 pp.). Springer-Verlag, Berlin.

Vorobiev, V.N. and Gudkovich, Z.M. (1976) On the intra-annual variability of the ice drift and currents of the Arctic Basin. *Proceedings of the AARI* **319**, 23–32 [in Russian].

Vovinkel, E. and Orvig, S. (1970) The climate of the North Polar Basin. In: S. Orvig (ed.), *Climates of Polar Regions: World Survey of Climatology* (Vol. 14, pp. 129–252). Elsevier, NewYork.

Wackerman, C.C. (1992) Digital SAR image formation. In: F.D. Carsey (ed.), *Microwave Remote Sensing of Sea Ice* (Geophysical Monograph 68, pp. 105–110). American Geophysical Union, Washington, D.C.

Wackerman, C.C. and Miller, D.L. (1996) *An Automated Algorithm for Sea Ice Classification in the Marginal Ice Zone Using ERS-1 Synthetic Aperture Radar Imagery* (ERIM Technical Report). ERIM, Ann Arbor, MI.

Wadhams, P. (1994) Sea ice thickness changes and their relation to climate. In: O.M. Johannessen, R.D. Muench and J.E. Overland (eds), *The Polar Oceans and Their Role in Shaping the Global Environment* (Geophysical Monograph 85, pp. 337–361). American Geophysical Union, Washington, D.C.

Wadhams, P. and Davis, N.R. (2000) Further evidence of ice thinning in the Arctic Ocean. *Geophysical Research Letters* **27**(24), 3973–3975.

Walker, E.R. and Wadhams, P. (1979) Thick sea ice floes. *Arctic* **32**(2), 140–147.

Walsh, J. E. (1995) Long-term observations for monitoring of the cryosphere. *Climate Change* **31**, 369–394.

Walsh, J.E. and Johnson, C.M. (1979) An analysis of Arctic sea ice fluctuations, 1953–1977. *Journal of Physical Oceanography* **9**(3), 580–591.

Walsh, J.E. and Timlin, M. S. (2003) Northern Hemisphere sea ice simulations by global climate models. *Polar Research* **22**(1), 75–82.

Wang, J. and Ikeda, M. (2000) Arctic Oscillation and Arctic sea-ice oscillation. *Geophysical Research Letters* **27**(9), 1287–1290.

Weeks, W. and Ackley, S.F. (1986) The growth, structure, and properties of sea ice. In: N. Untersteiner (ed.), *The Geophysics of Sea Ice* (NATO ASI Series, Series B: Physics, Vol. 146, pp. 9–164). Plenum Press, New York.

Wendler, G., Gilmore, D. and Curtis, J. (1997) On the formation of coastal polynyas in the area of Commonwealth Bay, Eastern Antarctica. *Atmospheric Research* **45**, 55–75.

Werbos, P.J. (1974) Beyond regression: New tools for prediction and analysis in the behavioural sciences. Ph.D. thesis, Harvard University, Cambridge, MA.

Willis, C.J., Macklin, J.T., Partington, K.C., Teleki, K.A., Rees, W.G. and Williams, R.G. (1996) Iceberg detection using ERS-1 Synthetic Aperture Radar. *International Journal of Remote Sensing* **17**(9), 1777–1795.

Winebrenner, D.P., Bredow J., Fung, A.K., Drinkwater M.R., Nghiem, S., Gow, A.J., Perovich, D.K., Grenfell, T.C., Han, H.C., Kong, J.A. *et al.* (1992) Microwave sea ice signature modelling. In: F.D. Carsey (ed.), *Microwave Remote Sensing of Sea Ice* (Geophysical Monograph 68, pp. 137–175). American Geophysical Union, Washington, D.C.

Winebrenner, D.P., Holt, B. and Nelson, E.D. (1996) Observation of autumn freeze-up in the Beaufort and Chukchi Seas using the ERS-1 synthetic aperture radar. *Journal of Geo-Physical Research* **101**(C7), 16401–16419.

Winebrenner, D.P., Long, D.G. and Holt, B. (1998) Mapping the progression of melt onset and freeze-up on Arctic sea ice using SAR and scatterometry. In: C. Tsatsoulis and R. Kwok (eds), *Analysis of SAR Data of the Polar Oceans: Recent Advances* (pp. 129–144). Springer-Verlag, Berlin.

Winsor, P. (2001) Arctic sea ice thickness remained constant during the 1990s. *Geophysical Research Letters* **28**(6), 1039–1041.

WMO Sea Ice Nomenclature (1989) (WMO Report No. 259, 147 pp.). World Meteorological Organization, Geneva.

WMO (2004) *Ice Chart Colour Code Standard* (WMO/TD No. 1215, JCOMM Technical Report No. 24, 11 pp.). World Meteorological Organization, Geneva.

Yakovlev, A.N., Romantsov, V.A. and Brestkin, S.V. (2002) Economical and normative–legal aspects of the commercial use of hydrometeorological information for supporting navigation in the Northern Sea Route. *Proceedings of the Scientific–Practical Conference: ''Hydrometeorological Support of Economic Activity in Arctic and Ice-covered Seas'', St. Petersburg, 27–29 March 2002* (pp. 110–118) [in Russian].

Yanes, A.V. (1962) Snow and ice melting in the Central Arctic. *Problems of the Arctic and Antarctic* **11**, 59–65 [in Russian].

Yegorov, A.G. and Spichkin, V.A. (1994) Techniques of local–genetic typification of sea ice conditions. *Proceedings of the AARI* **432**, 146–163 [in Russian].

Yu, Y. and Rothrock, D.A. (1996). Thin ice thickness from satellite thermal imagery. *Journal of Geophysical Research* **101**(C10), 25753–25766.

Yulin, A.V. (1997) Conjugacy of extreme fast ice development and summer sea ice conditions in the East-Siberian Sea. *Proceedings of the AARI* **437**, 115–123 [in Russian].

Zakharov, V.F. (1966) Some features of estimated ice drift in the Laptev Sea. *Problems of the Arctic and Antarctic* **23**, 45–46 [in Russian].

Zakharov, V.F. (1976) Cooling in the Arctic and ice cover of the Arctic Seas. *Proceedings of the AARI* **337**, 1–95 [in Russian].

Zakharov, V.F. (1981) *Ice of the Arctic and Modern Natural Processes* (136 pp.). Gidrometeoizdat, Leningrad [in Russian].

Zakharov, V.F. (1996) *Sea ice in the Climate System* (213 pp.). Gidrometeoizdat, St. Petersburg [in Russian].

Zhang, J., Rothrock, D.A. and Steele, M. (2000) Recent changes in Arctic sea ice: The interplay between ice dynamics and thermodynamics. *Journal of Climate* **13**, 3099–3114.

Zhu, S.C. and Yuille, A. (1996) Region competition: Unifying states, region growing, and Bayes/MDL for multi-band image segmentation. *IEEE Transactions on Pattern Analysis and Machine Intelligence* **18**(9), 884–900.

Zubakin, G.K. (1987) *Large-scale Variability in Ice Cover State of North-European Basin Seas* (160 pp.). Gidrometeoizdat, Leningrad [in Russian].

Zubakin, G.K., Naumov, A.K. and Buzin, I.V. (2004) Estimates of ice and iceberg spreading in the Barents Sea. *Proceedings of the Fourteenth International Offshore and Polar Engineering Conference, Toulon, France, May 23–28, 2004* (pp. 863–870).

Index

Colour plates

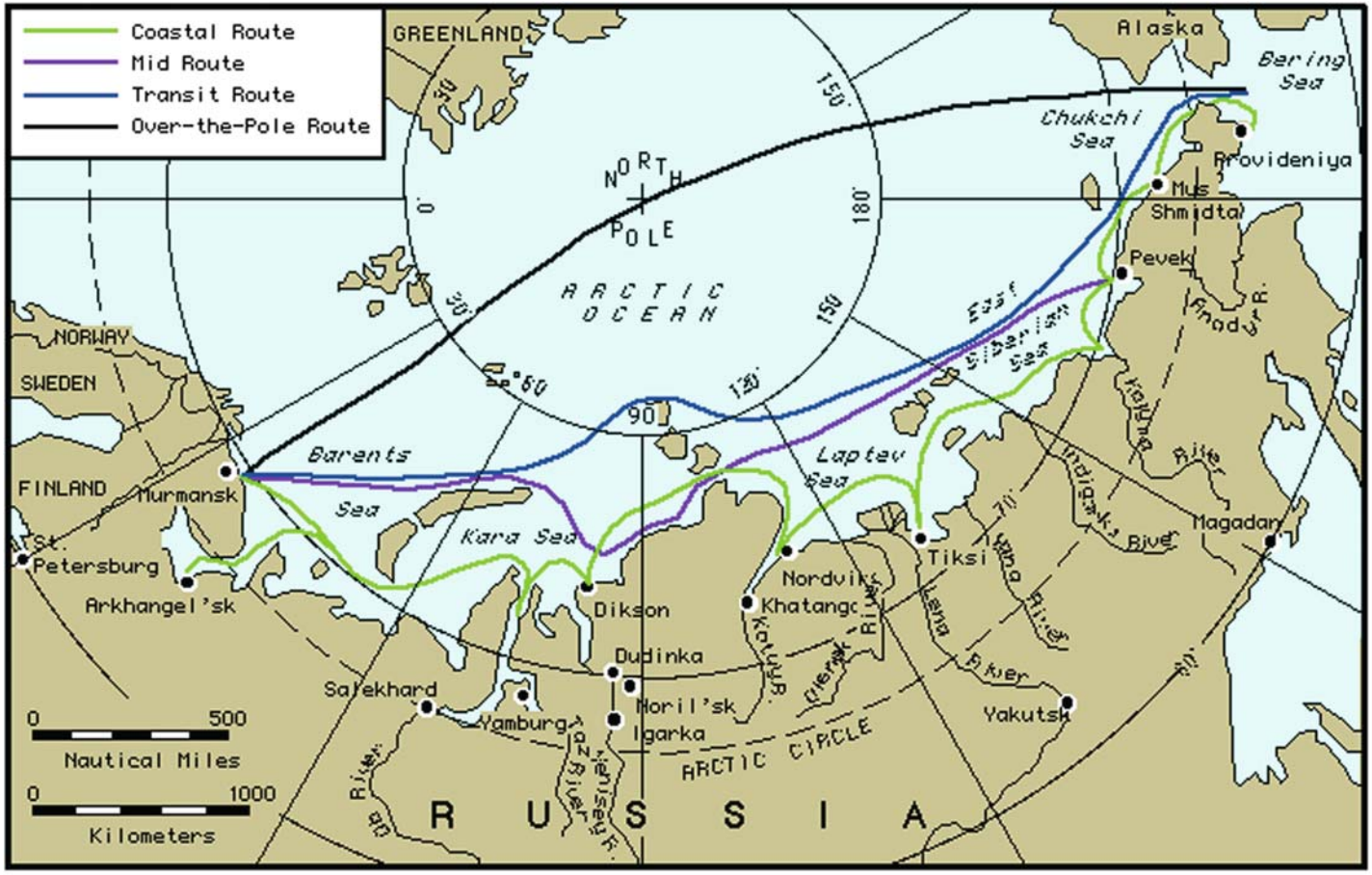

Figure 1.7. Map of the Northern Sea Route with the main transit routes. From Mulherin (1996).

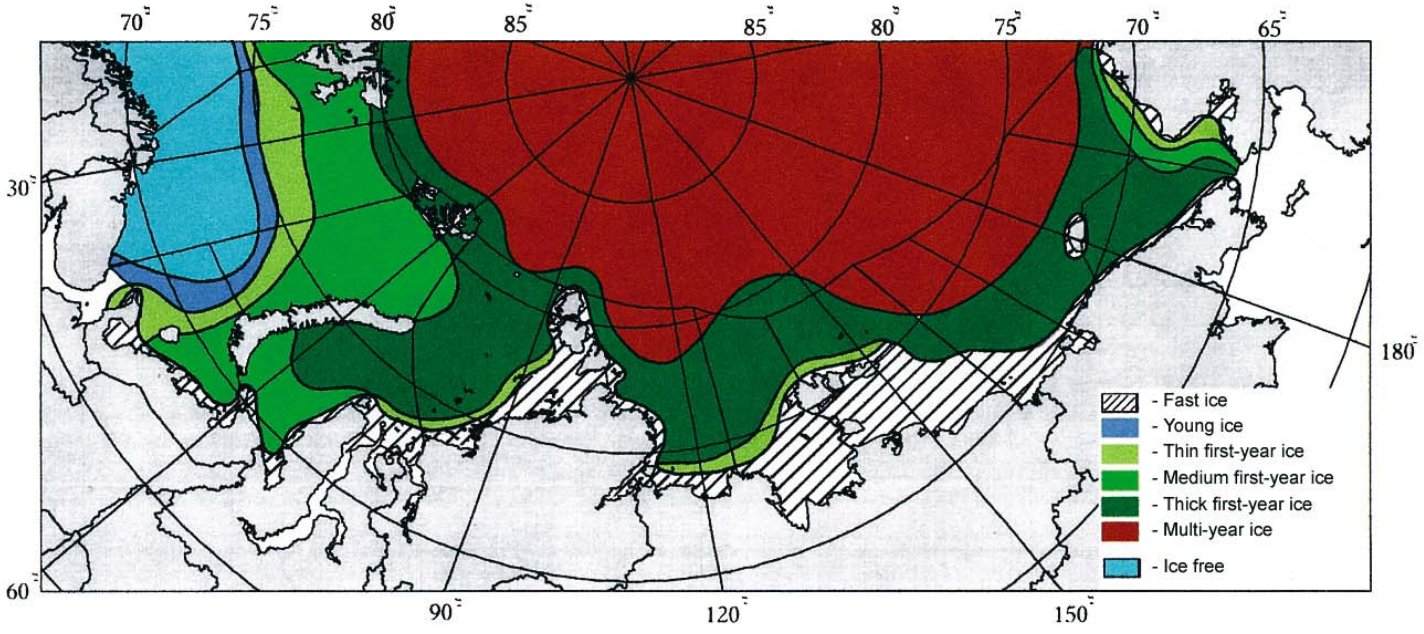

Figure 2.12. Average distribution of ice of different age in the Arctic seas at the end of the ice cover freezing period.

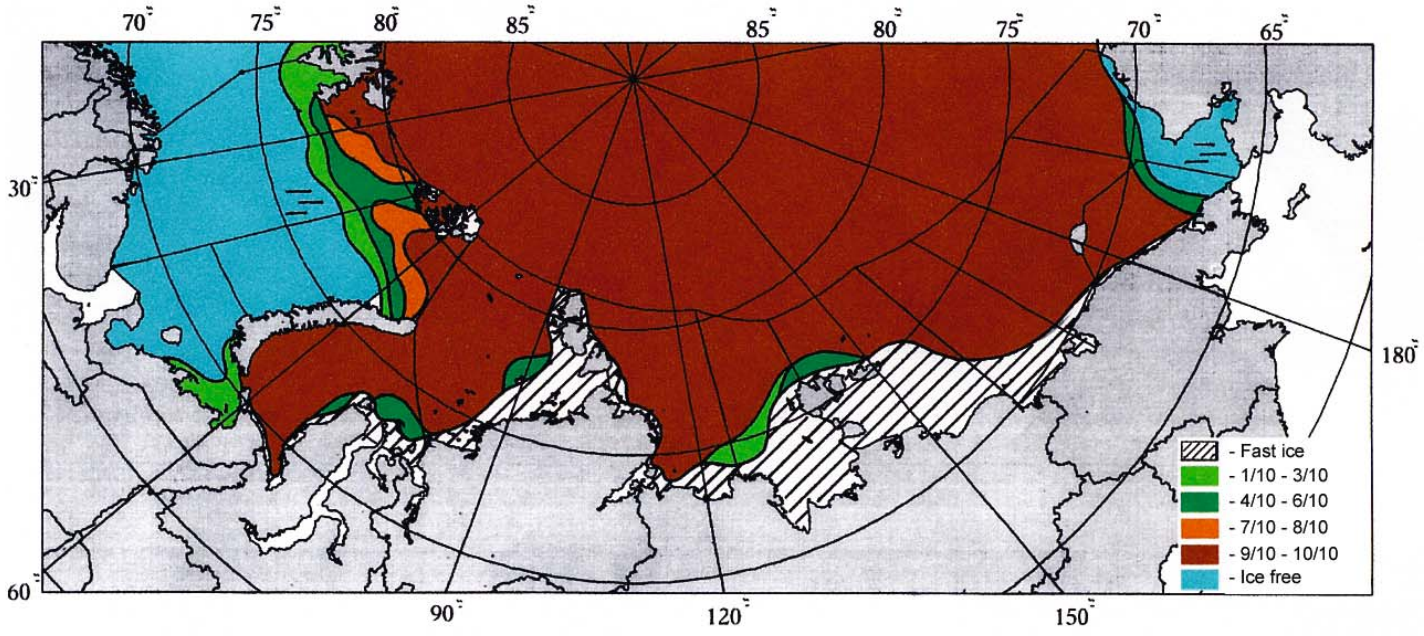

Figure 2.15. Distribution of ice of different concentration in June (with a probability of 50%).

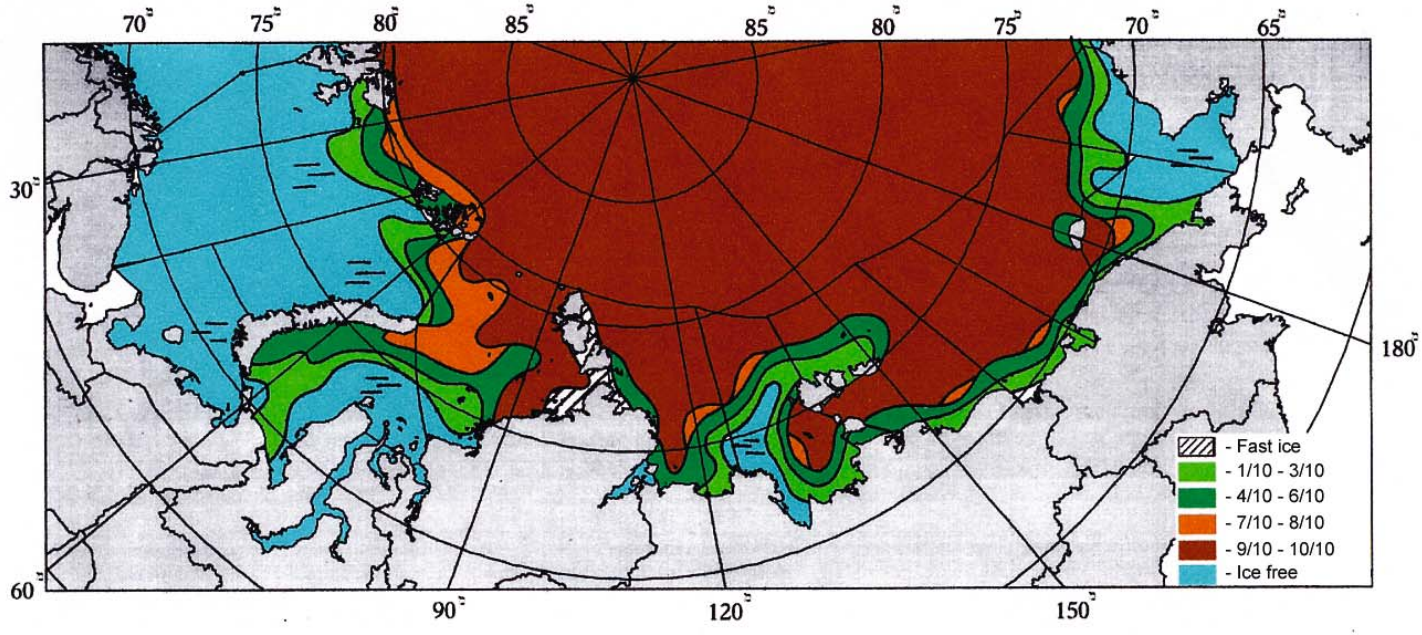

Figure 2.16. Distribution of ice of different concentration in July (with a probability of 50%).

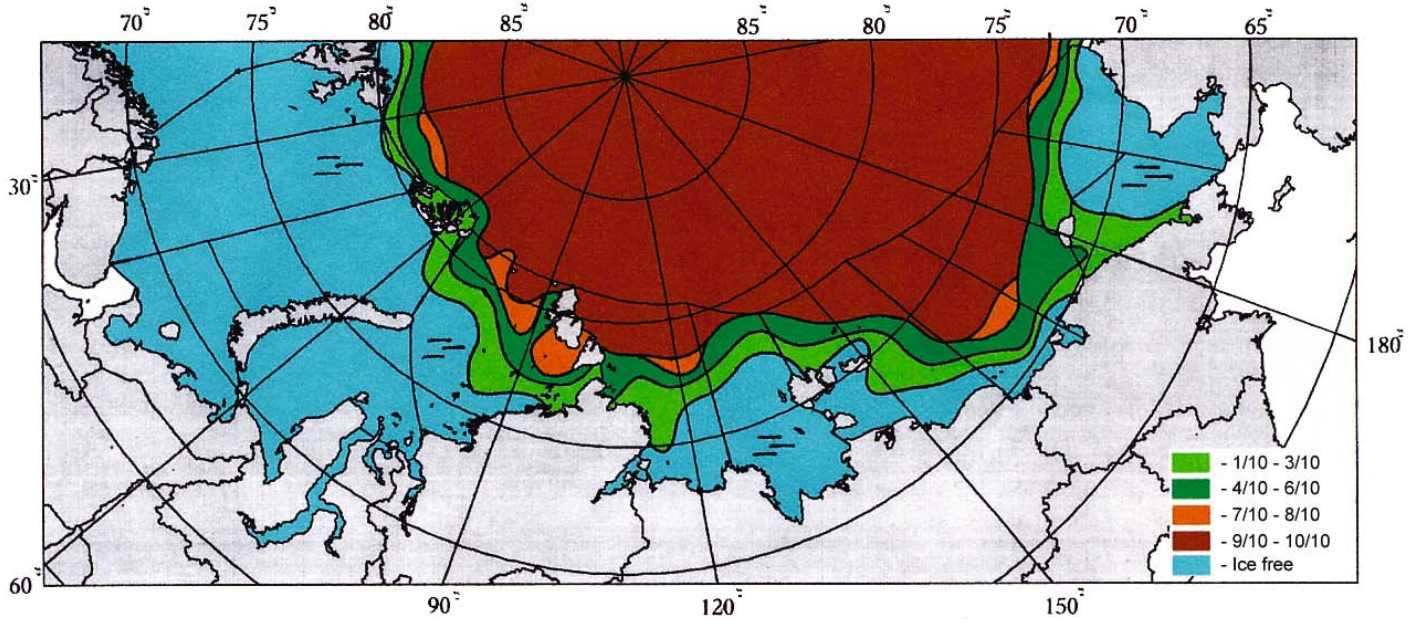

Figure 2.17. Distribution of ice of different concentration in August (with a probability of 50%).

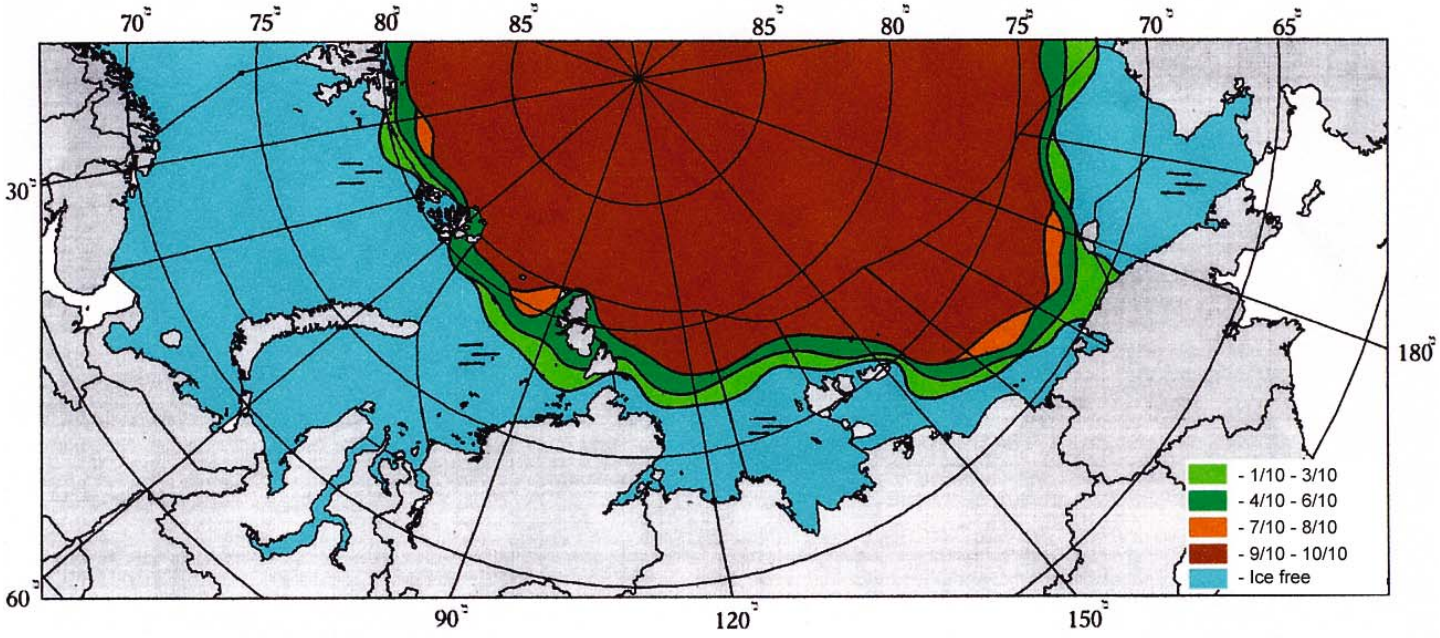

Figure 2.18. Distribution of residual ice of different concentration in September (with a probability of 50%).

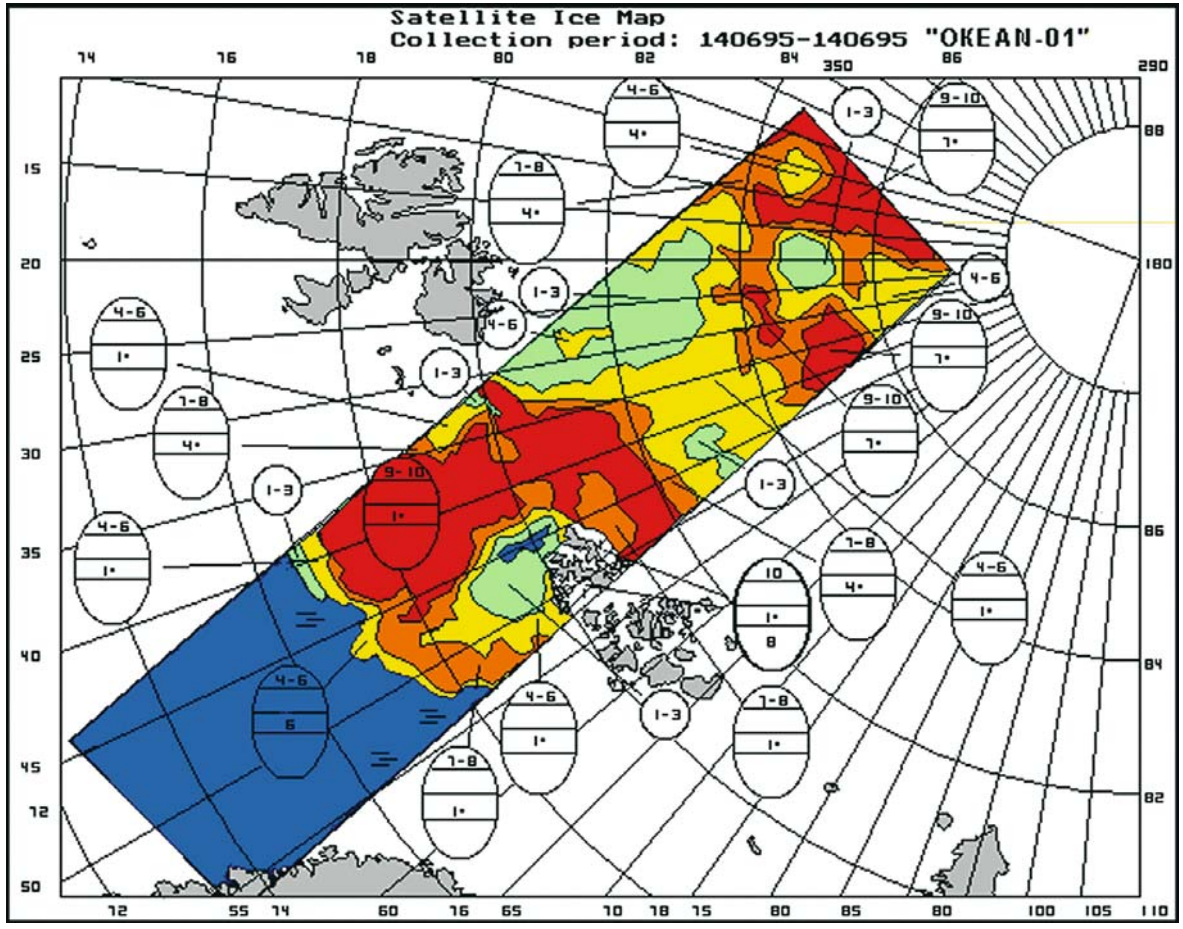

Figure 3.14(a). Example of an operational ice chart based on one SLR image.

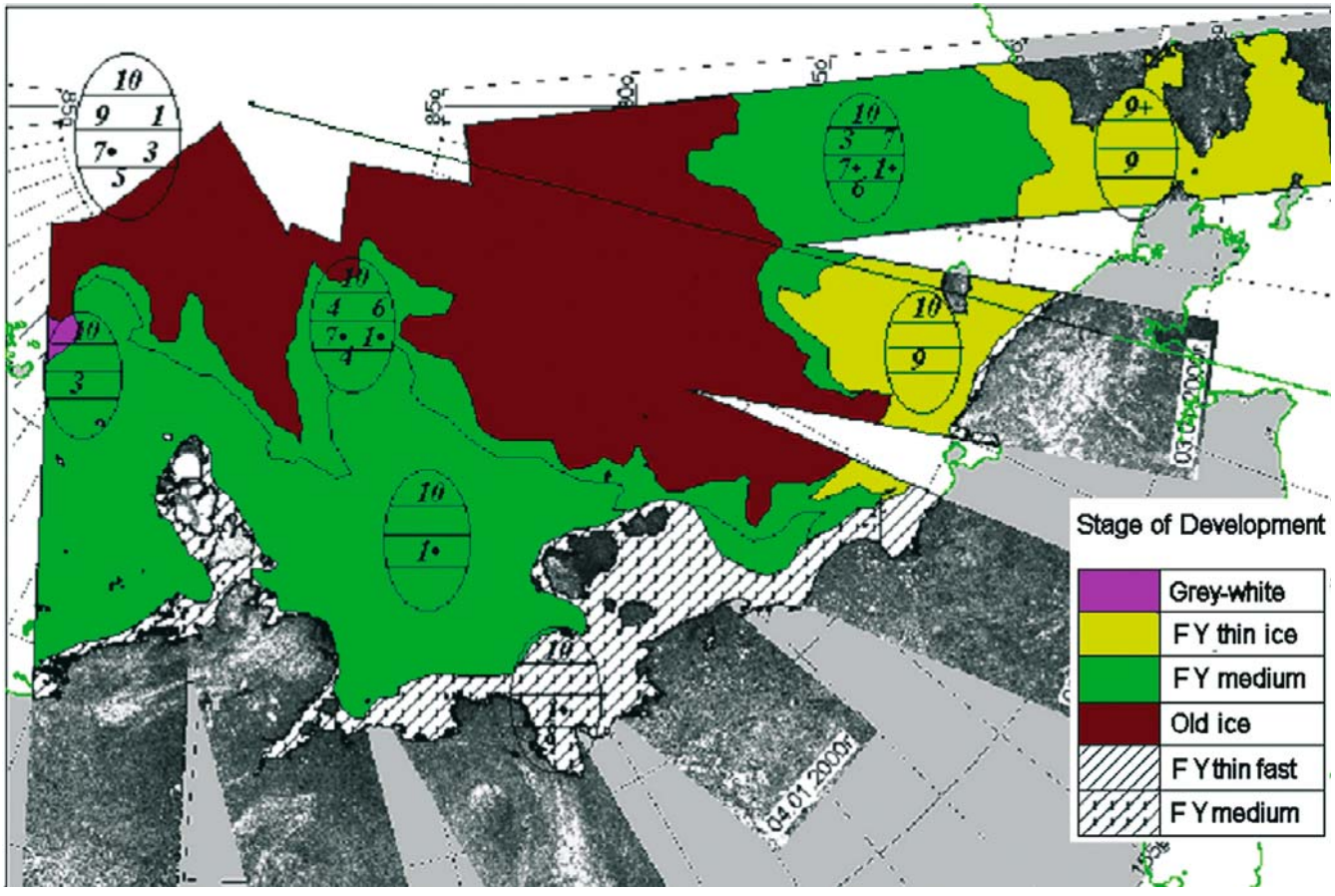

Figure 3.14(b). Example of an operational ice chart based on weekly composite ice chart from a mosaic of *Okean* radar images from seven successive orbits on 1–7 January 2000.

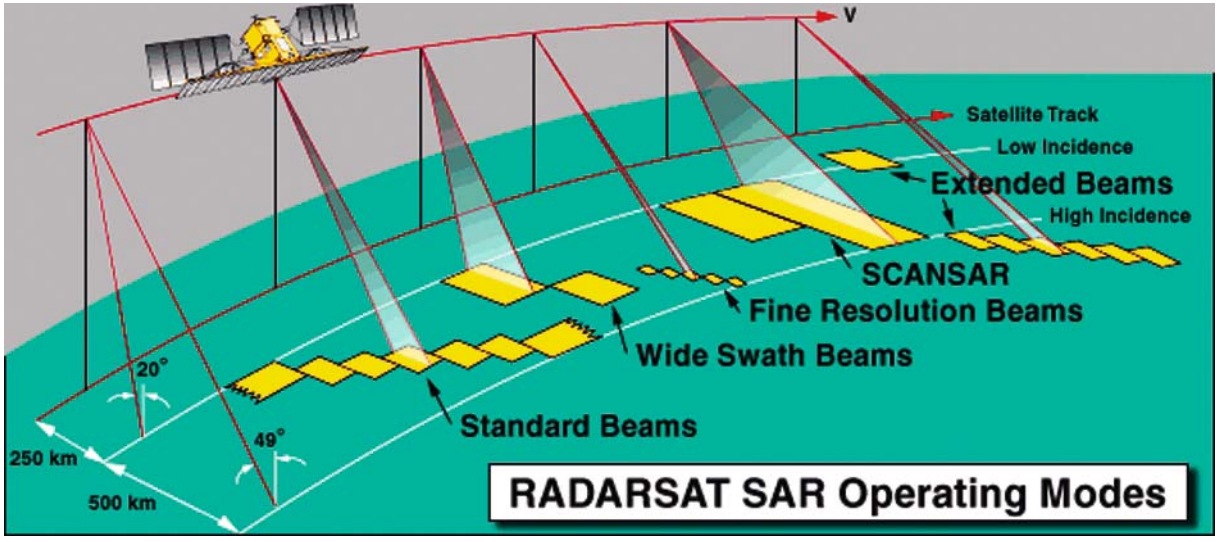

Figure 3.16(a). Modes of operation of contemporary SAR systems: *Radarsat* SAR, courtesy of CSA.

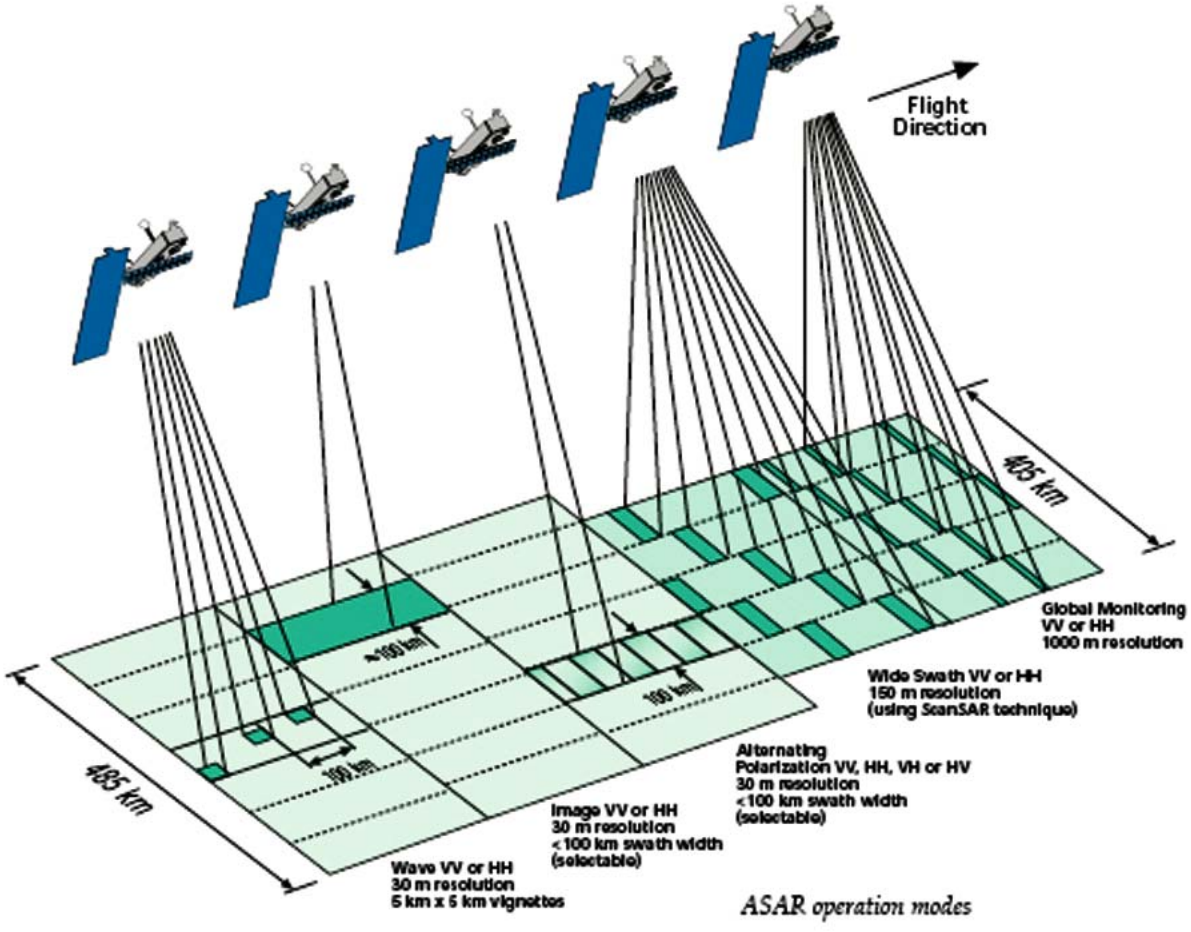

Figure 3.16(b). Modes of operation of contemporary SAR systems: *Envisat* SAR, courtesy of ESA.

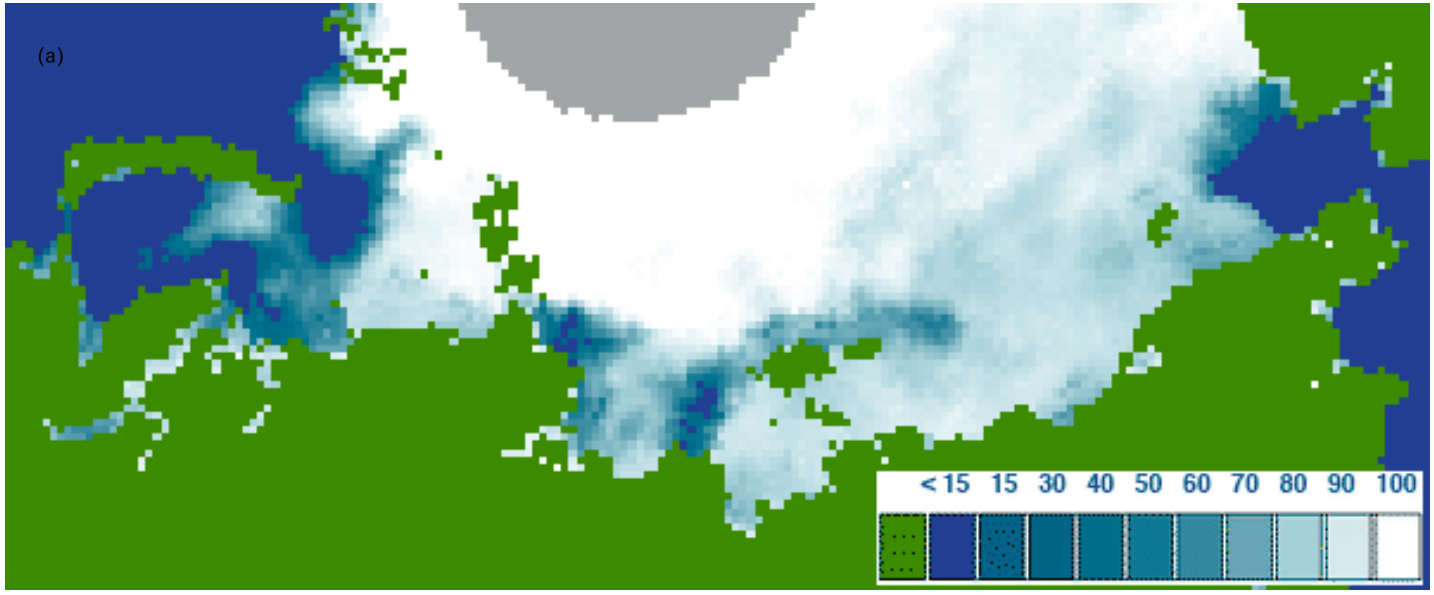

Figure 3.19. Examples of ice concentration maps in the Northern Sea Route for 3 July 2006, using (a) SSM/I data with 30-km resolution, (b) AMSR-E data with about 10-km resolution. The SSM/I product is procued by NERSC and is used for estimation of long-term statistics (1978 to present) and for assimilation in the TOPAZ ice–ocean forecasting system. The AMSR-E product is produced by the Institute of Environmental Physics at the University of Bremen, and is used for daily monitoring of sea ice in different parts of the Arctic (courtesy: G. Heygster). Note that spatial resolution, scale and color coding of the ice concentration (displayed in %) is different for the two examples.

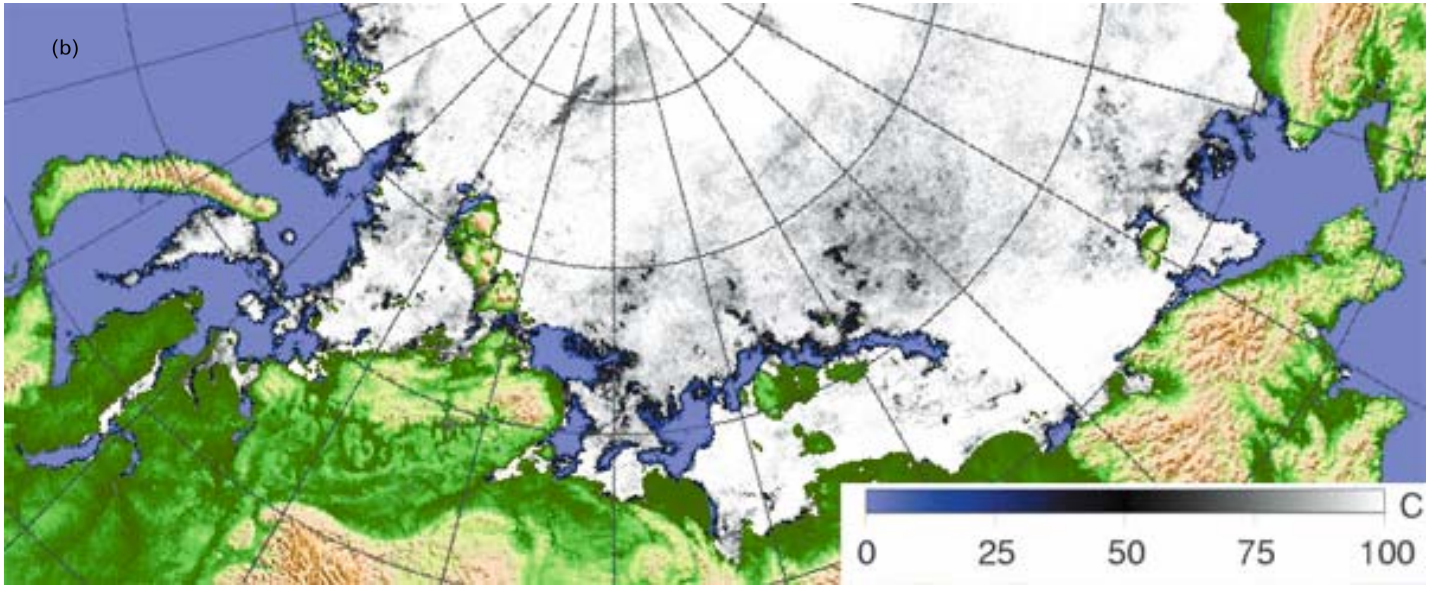

Figure 3.19 (*cont.*). See previous page for caption.

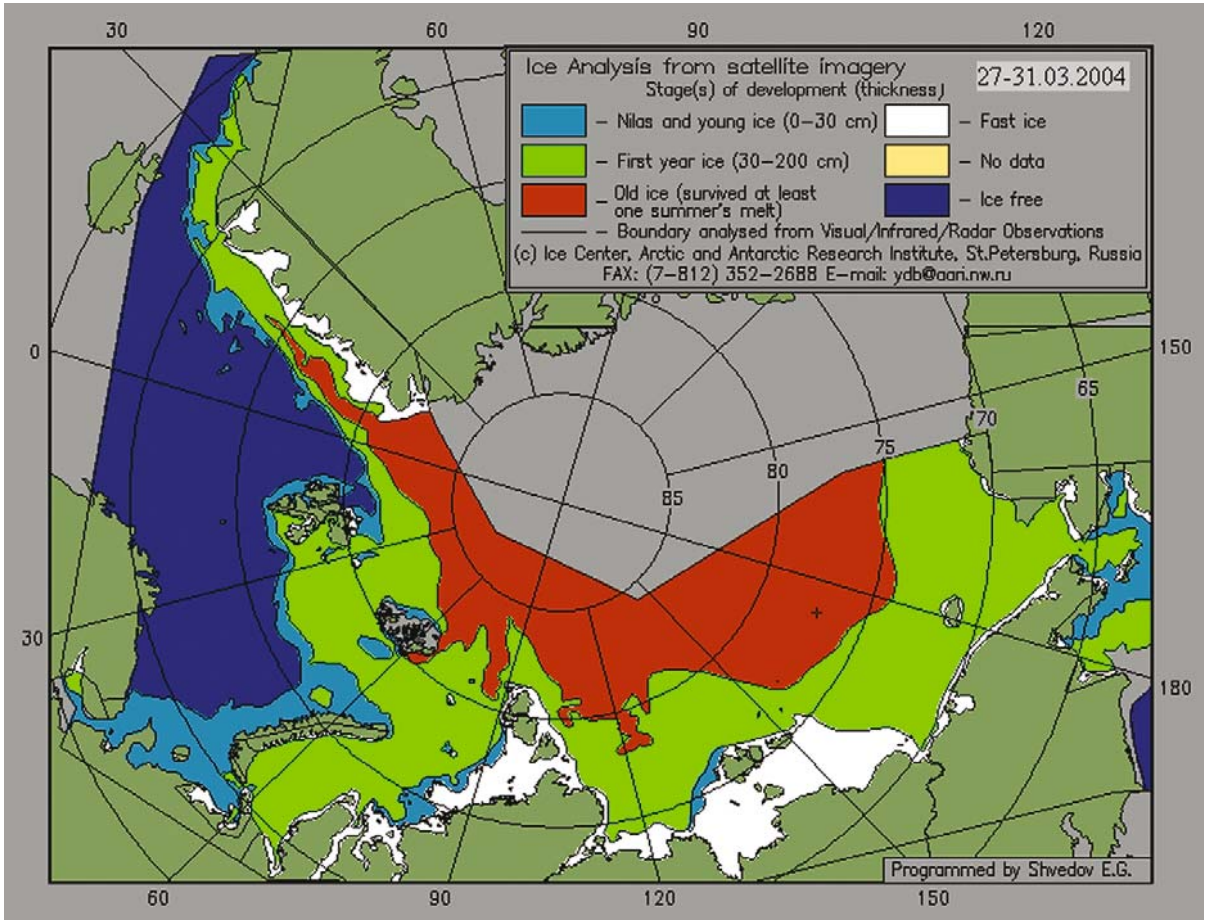

Figure 3.23. Example of a weekly ice chart posted at the AARI Internet site.

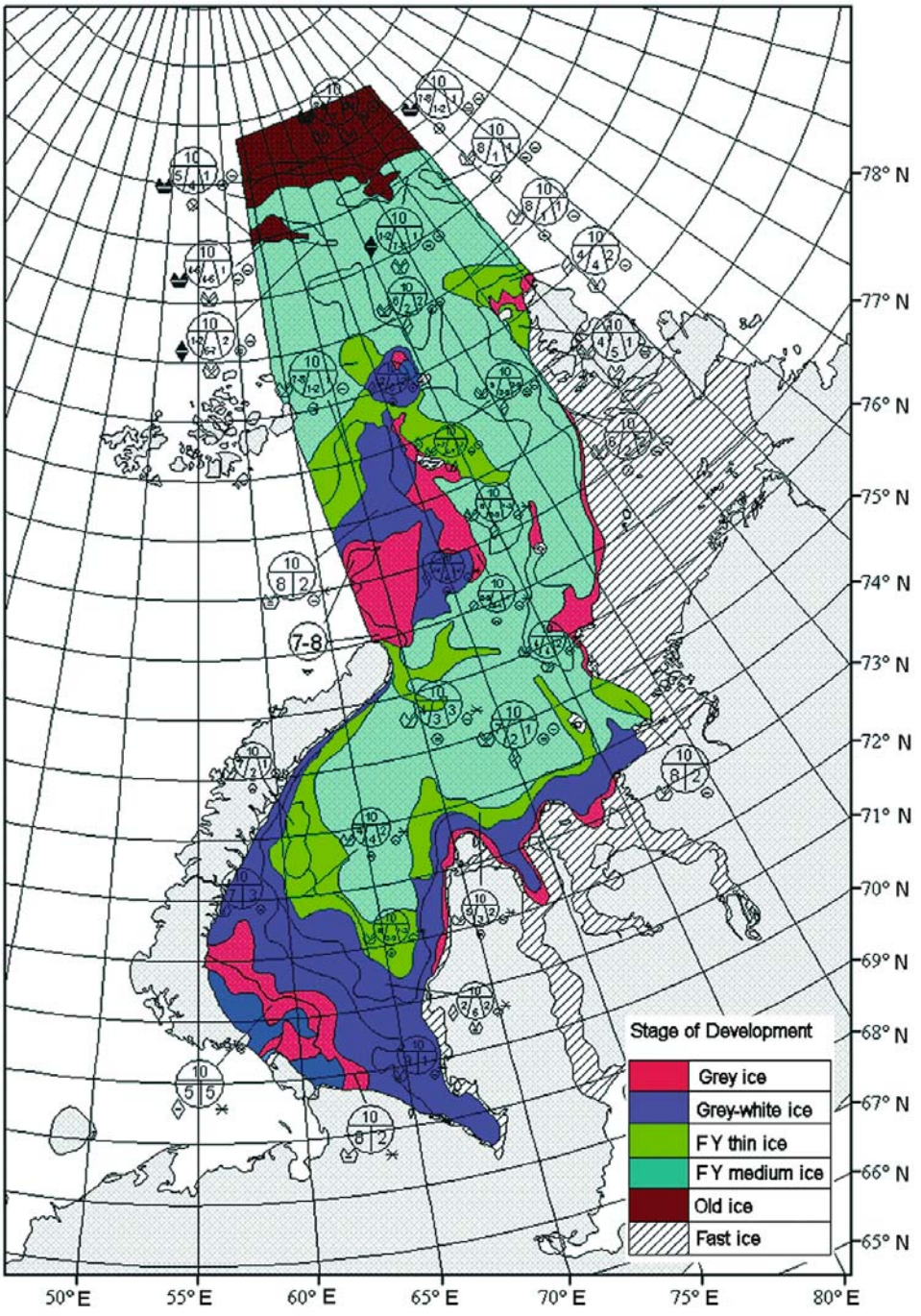

Figure 3.24(a). A weekly ice chart of the Kara Sea for the winter season (03–05.01.2005).

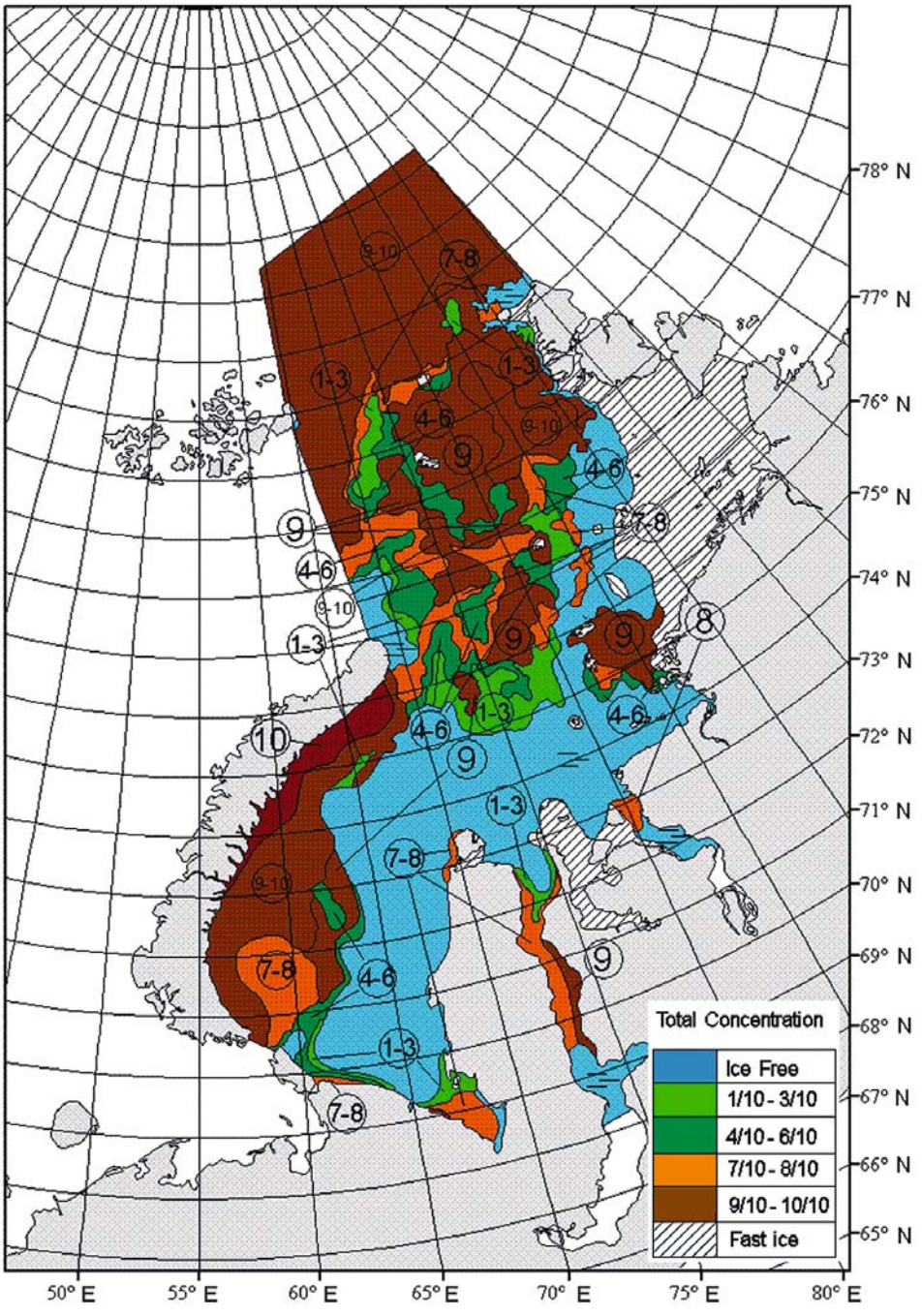

Figure 3.24(b). A weekly ice chart of the Kara Sea for the summer season (24–28.07.2005).

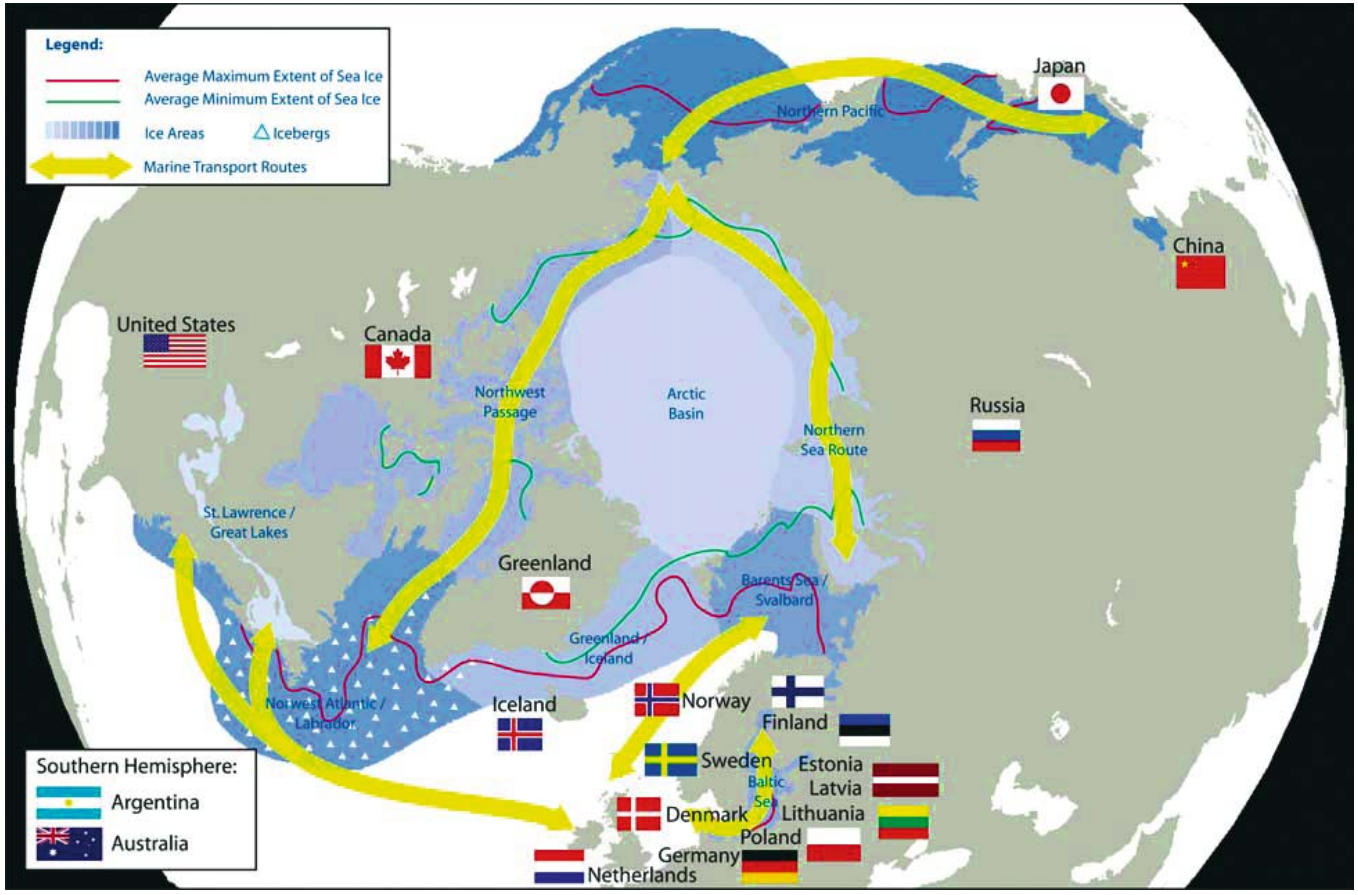

Figure 3.27. Countries with national ice services in the Northern Hemisphere, including ice-affected areas and the main Arctic shipping routes (IICWG, 2004).

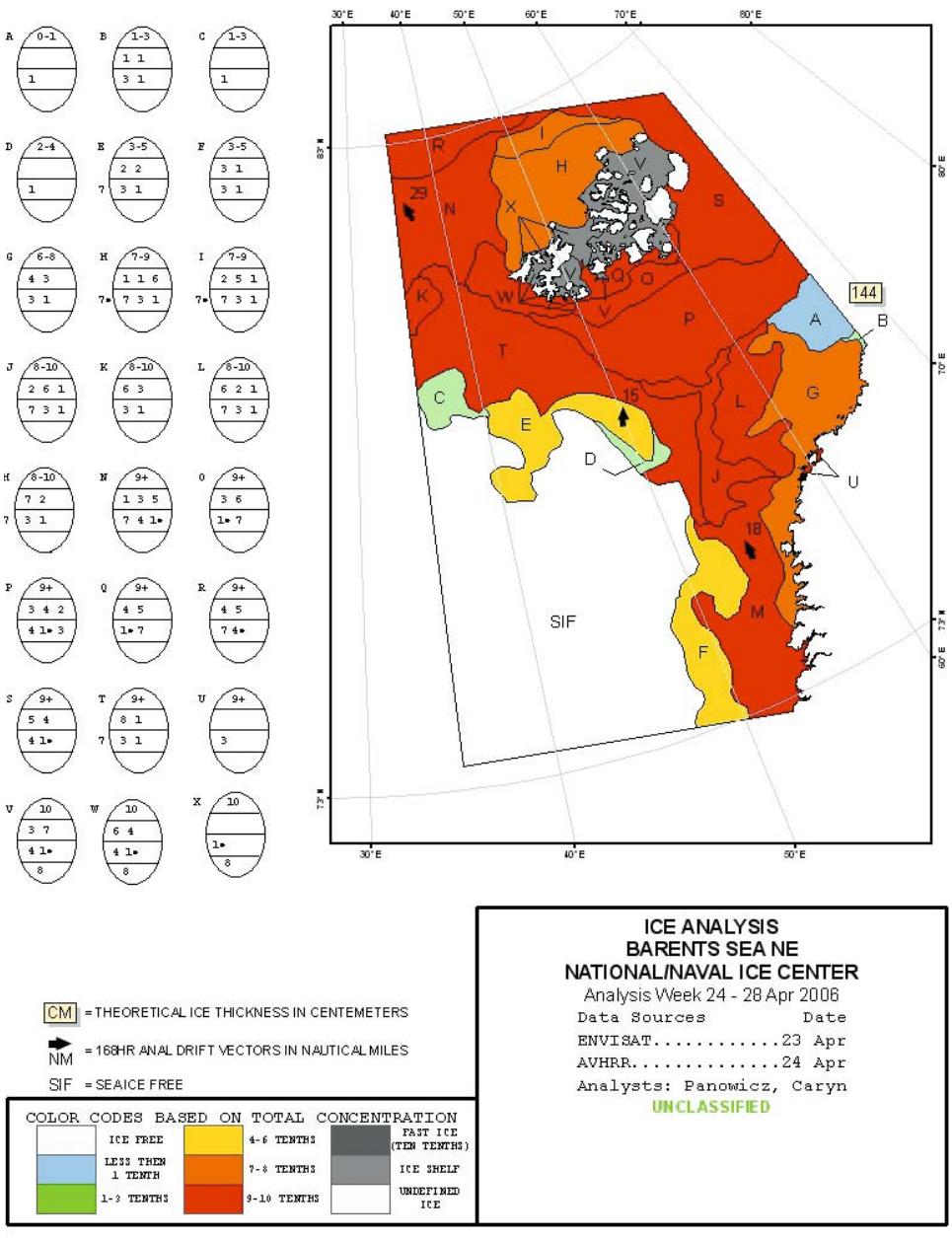

Figure 3.28. Example of regional ice chart for the southwestern Barents Sea produced by NIC for 24–28 April 2006.

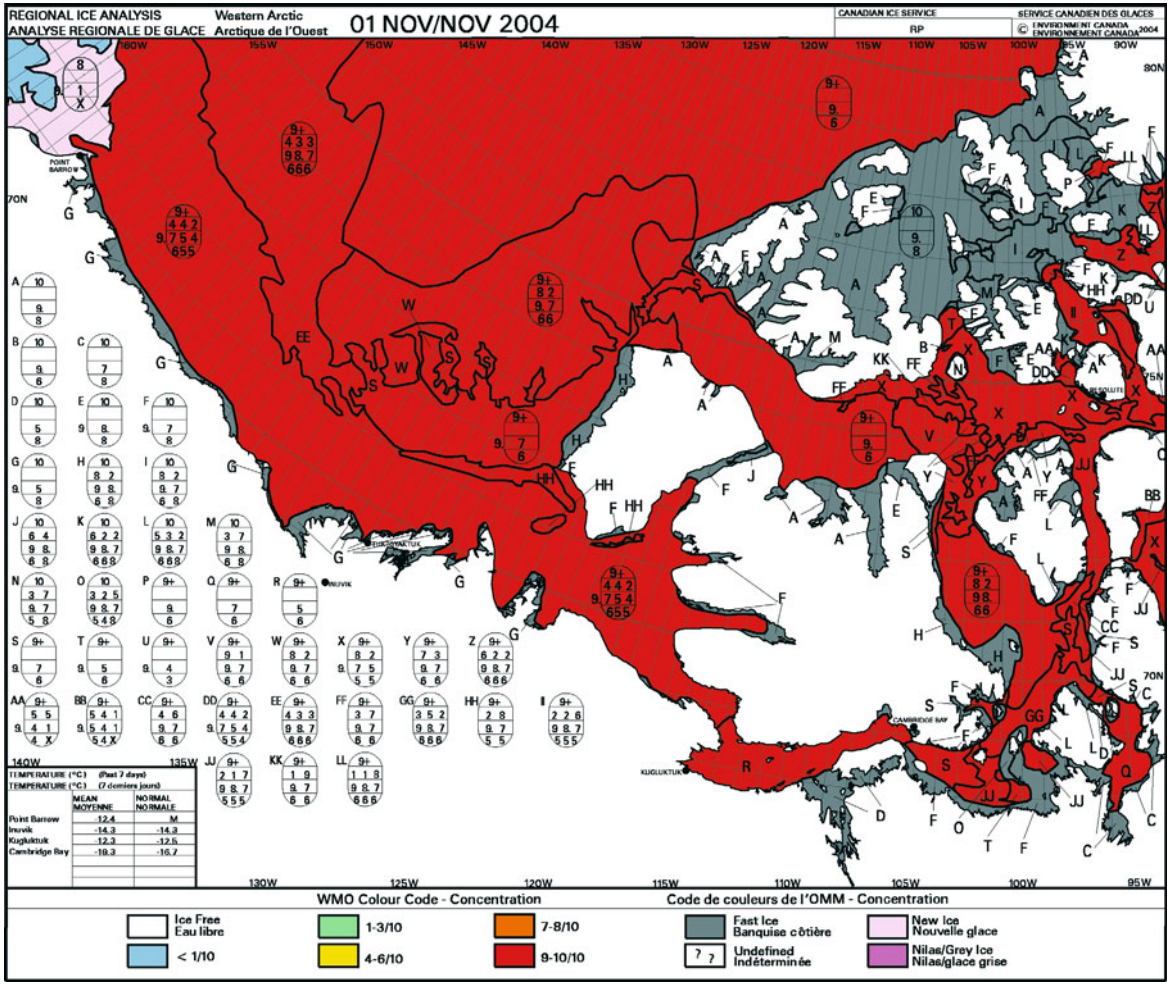

Figure 3.29. Ice chart of the western Canadian Arctic for 1 November 2004 produced by CIS.

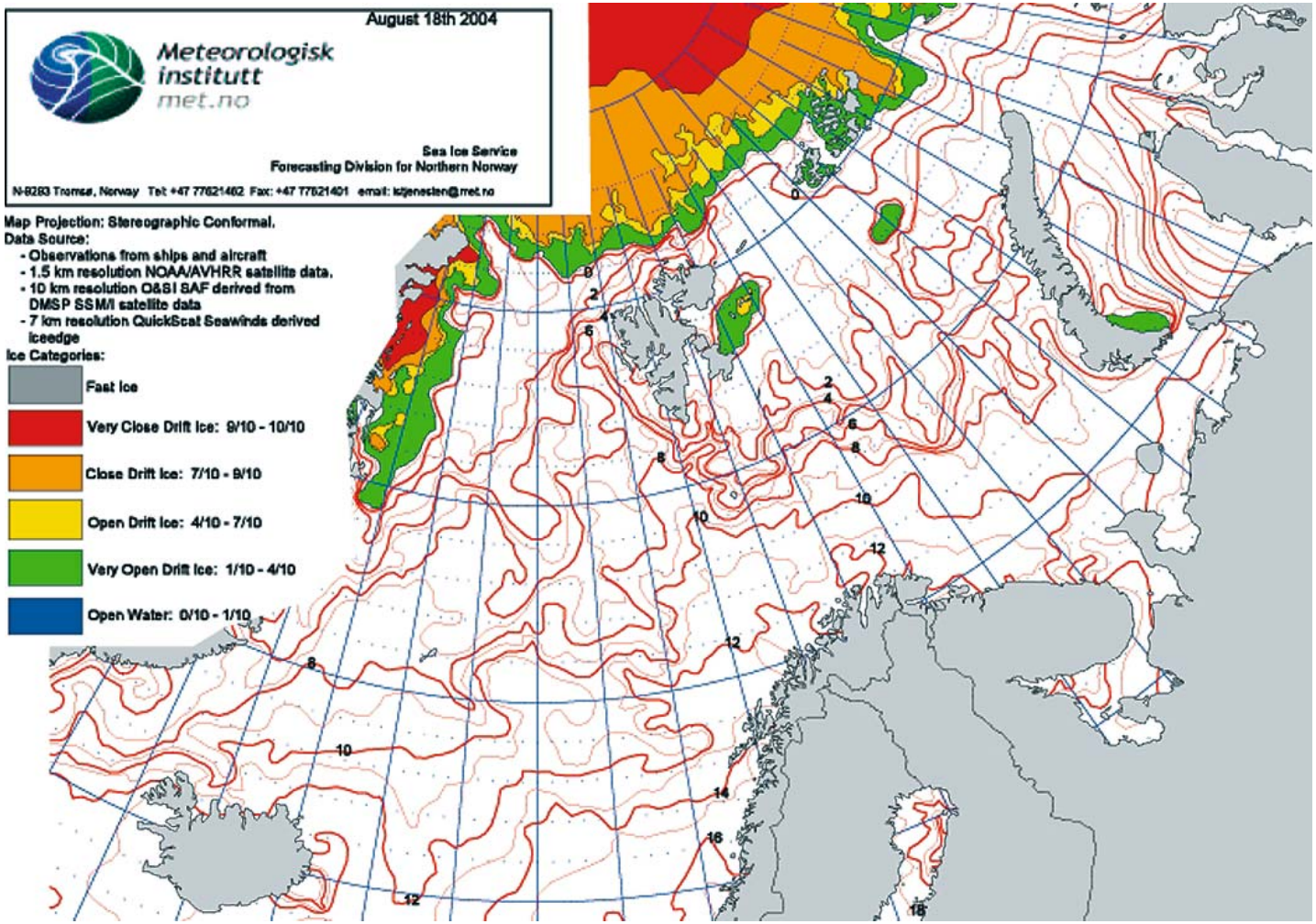

Figure 3.32. Example of ice and sea surface temperature (SST) map produced by met.no.

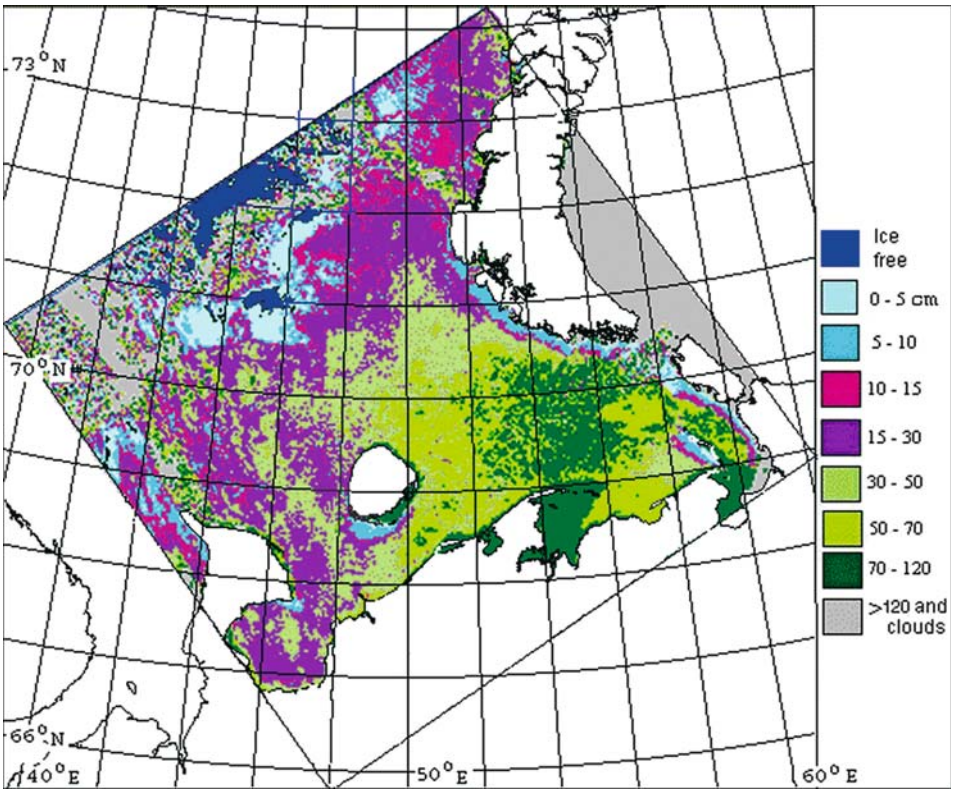

Figure 4.7. Example of ice thickness in the Barents Sea derived from *NOAA* AVHRR IR image (channel 4) taken on 4 May 2001 at 08:20 GMT.

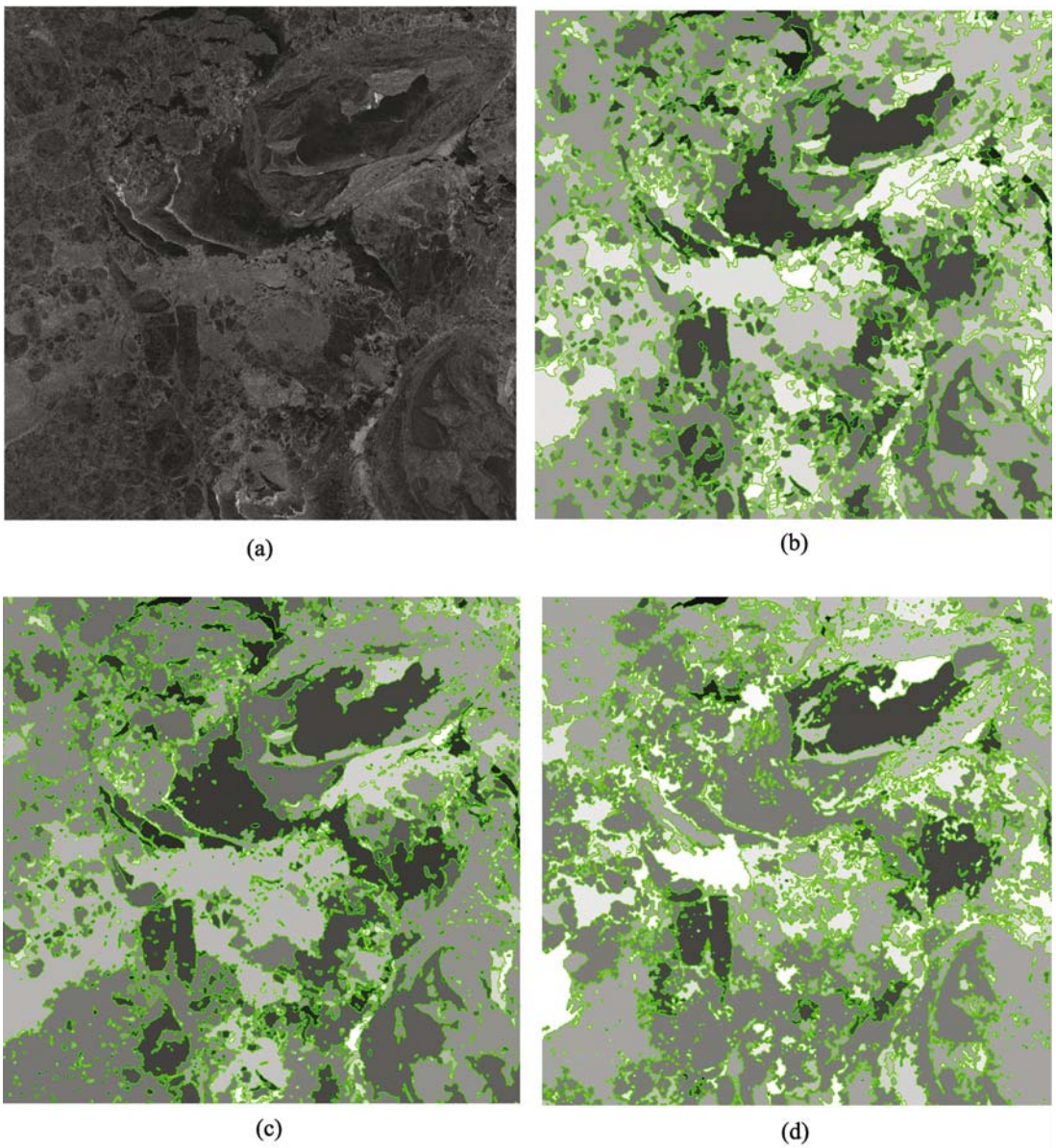

Figure 4.37. Examples of sea ice segmentation of an *ERS* SAR image (a) taken on 30 April 1998 of the Kara Sea using (b) simple histogram-based thresholding followed by application of morphological operators of erosion and dilation and iterative region merging; (c) watershed segmentation algorithm followed by iterative region merging (Soh *et al.*, 1998); and (d) image brightness-based region-growing algorithm followed by iterative region merging. The brightness of segments is proportional to the mean image brightness (image data © European Space Agency).

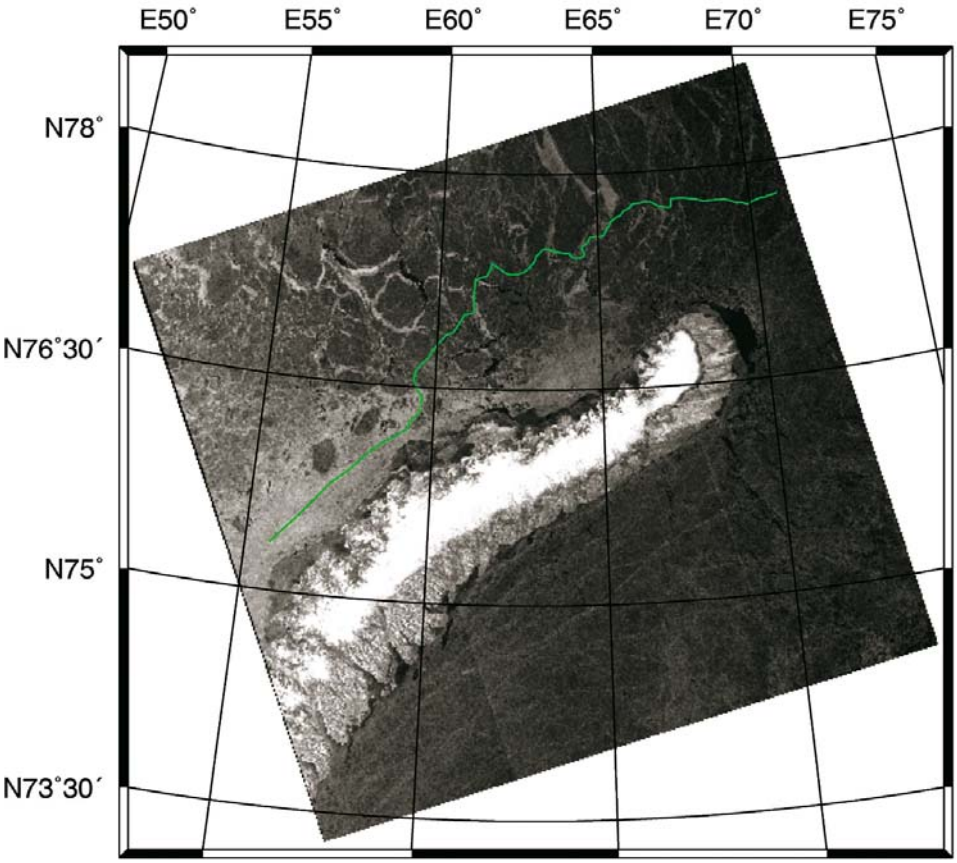

Figure 4.38(a). Example of MLP-based sea ice classification of a *Radarsat* ScanSAR image (© Canadian Space Agency) acquired 25 April 1998 over the Kara Sea. Separation of drifting and fast ice is done manually.

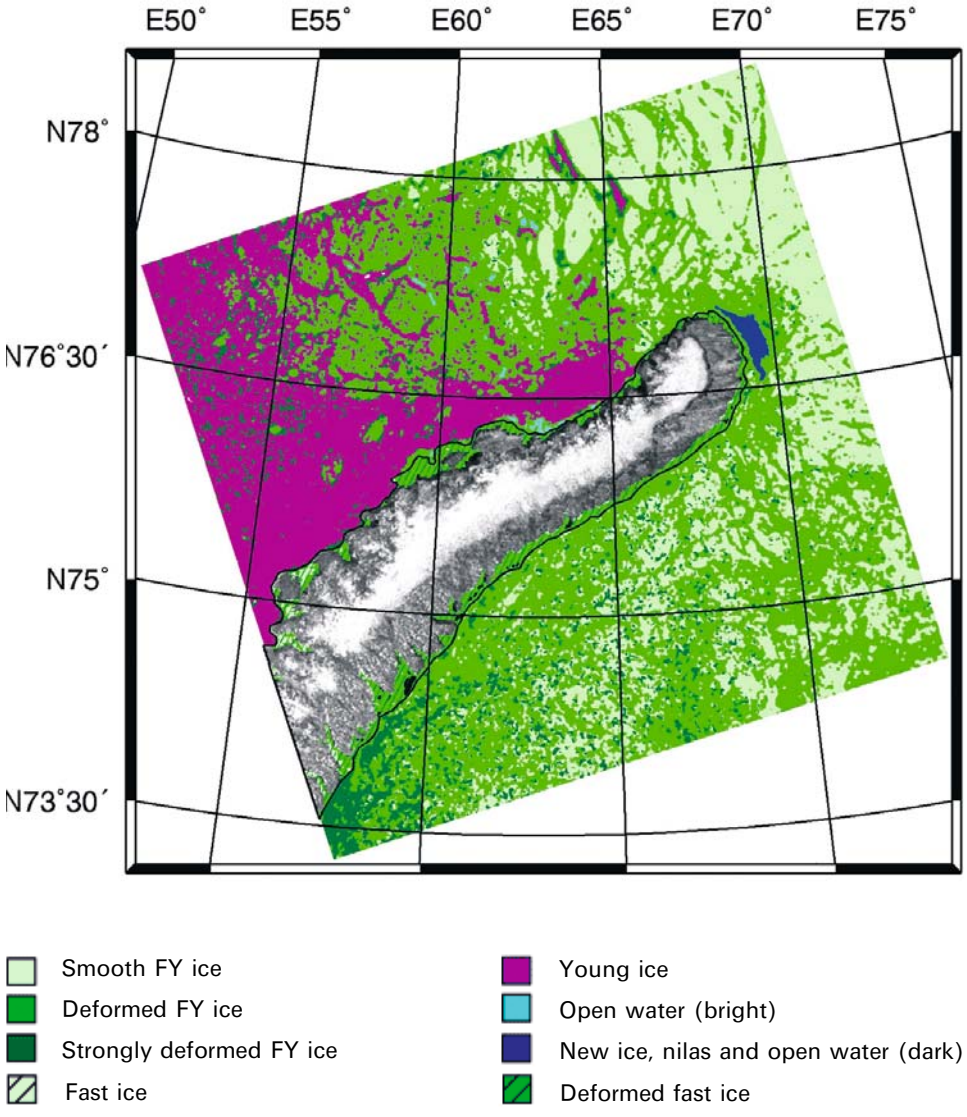

Figure 4.38(b). Example of MLP-based sea ice classification of a *Radarsat* ScanSAR image (© Canadian Space Agency) acquired 8 May 1998 over the Kara Sea. Separation of drifting and fast ice is done manually.

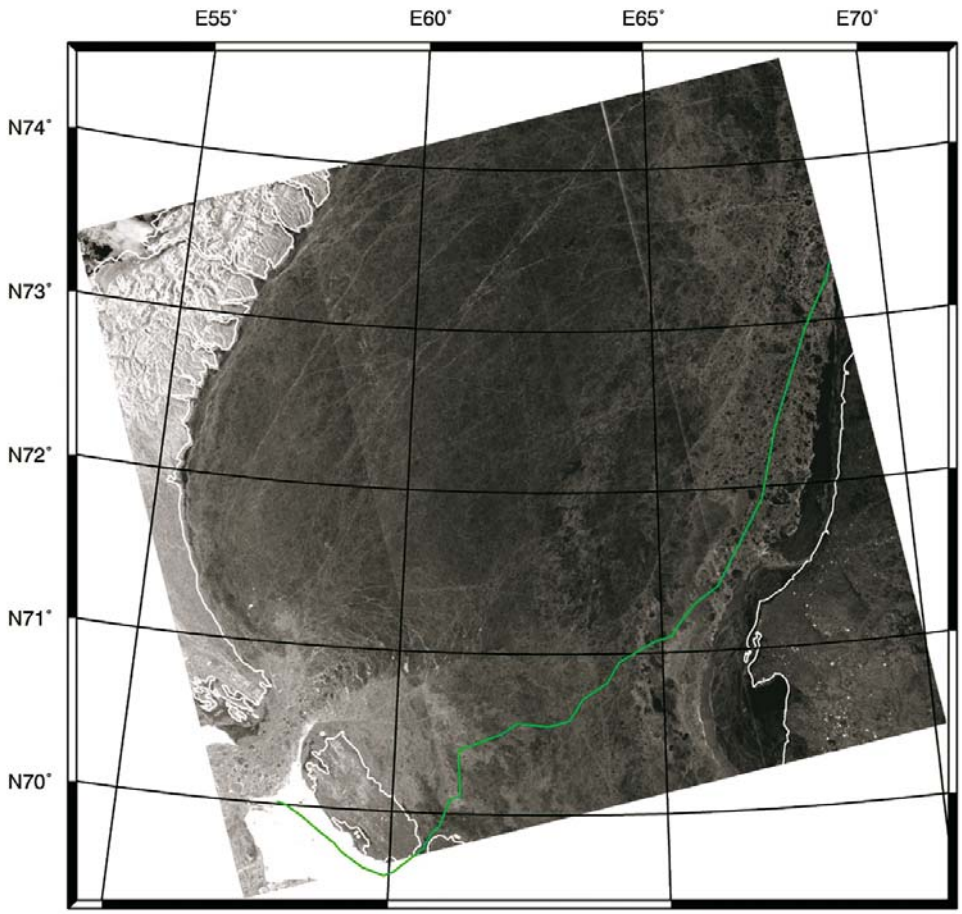

Figure 4.38(c). Example of MLP-based sea ice classification of a *Radarsat* ScanSAR image (© Canadian Space Agency) acquired 25 April 1998 over the Barents Sea. Separation of drifting and fast ice is done manually.

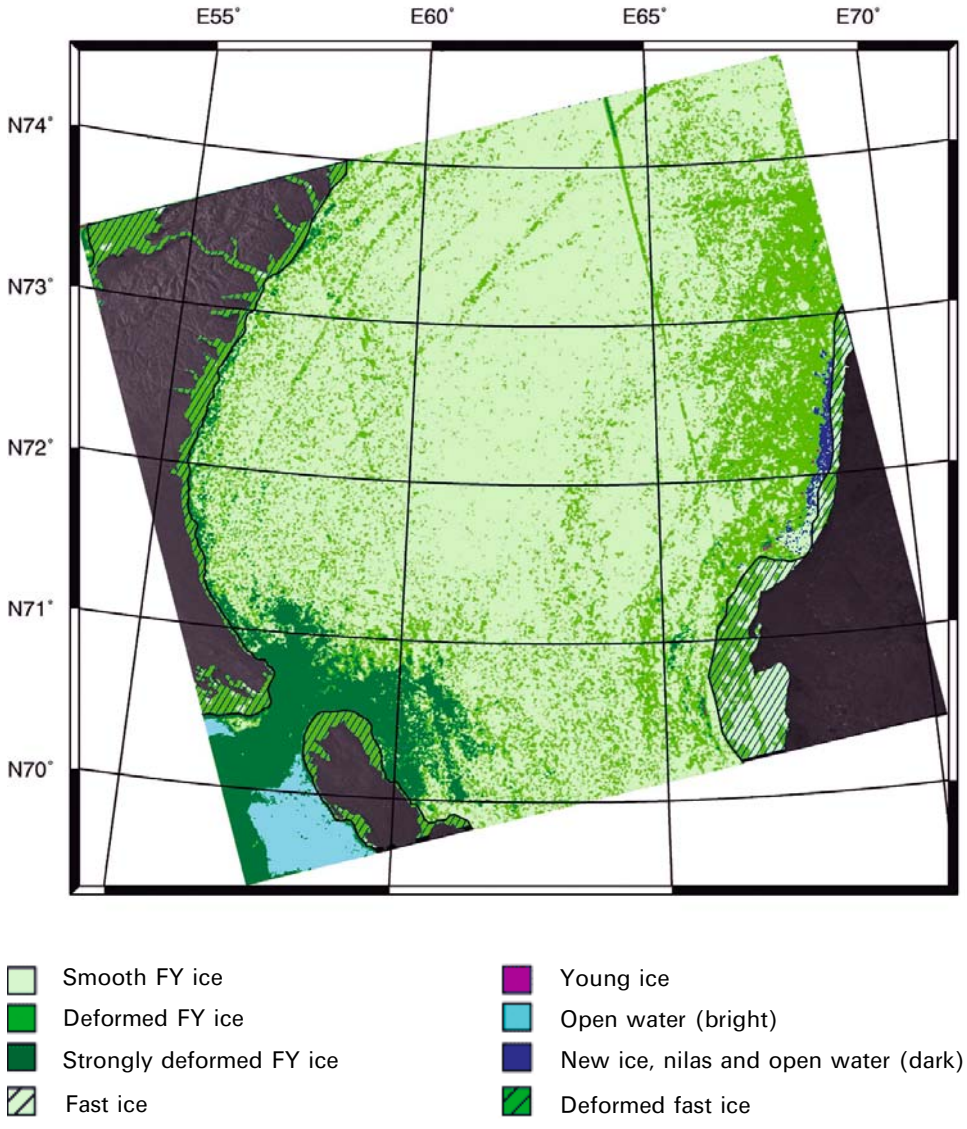

Figure 4.38(d). Example of MLP-based sea ice classification of a *Radarsat* ScanSAR image (© Canadian Space Agency) acquired 8 May 1998 over the Barents Sea. Separation of drifting and fast ice is done manually.

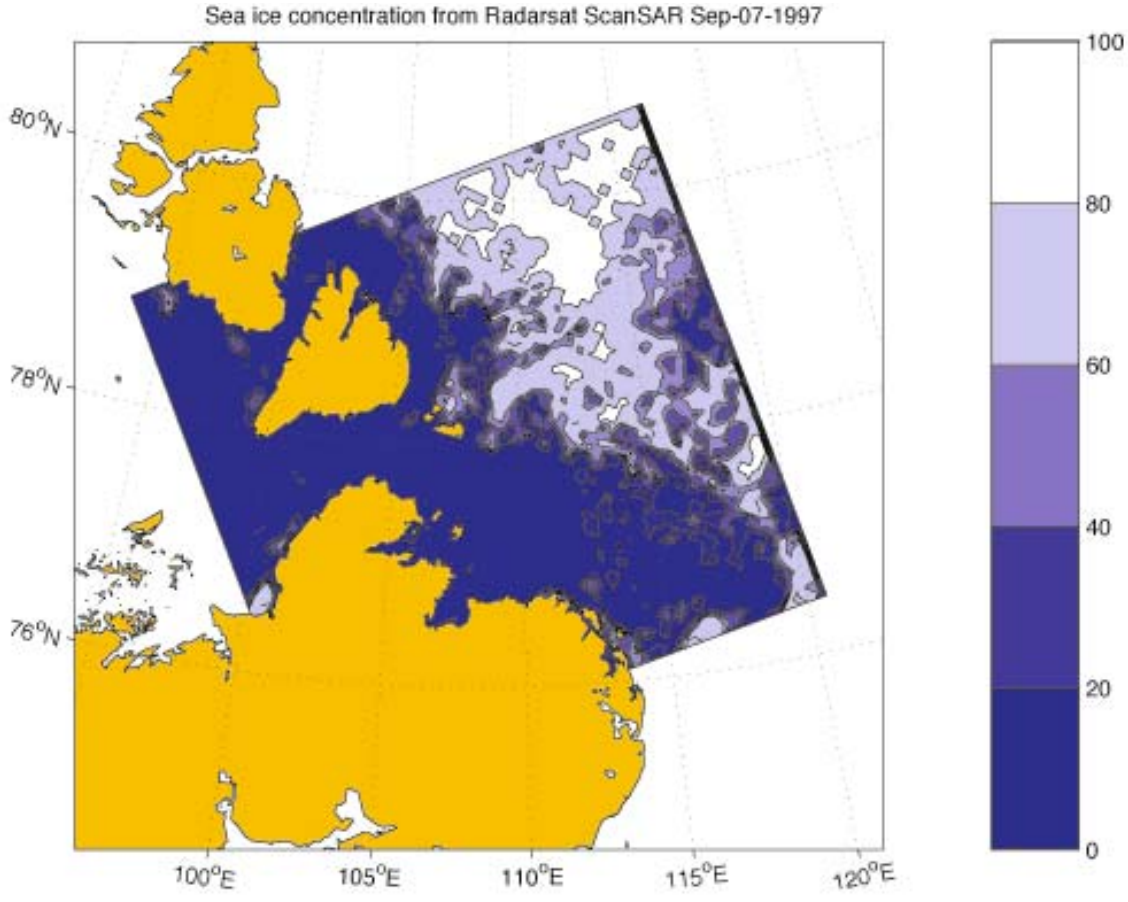

Figure 4.39(a). Ice concentration analysis from ScanSAR image data (© Canadian Space Agency) of 7 September 1997, presented with a spatial resolution of about 6 km.

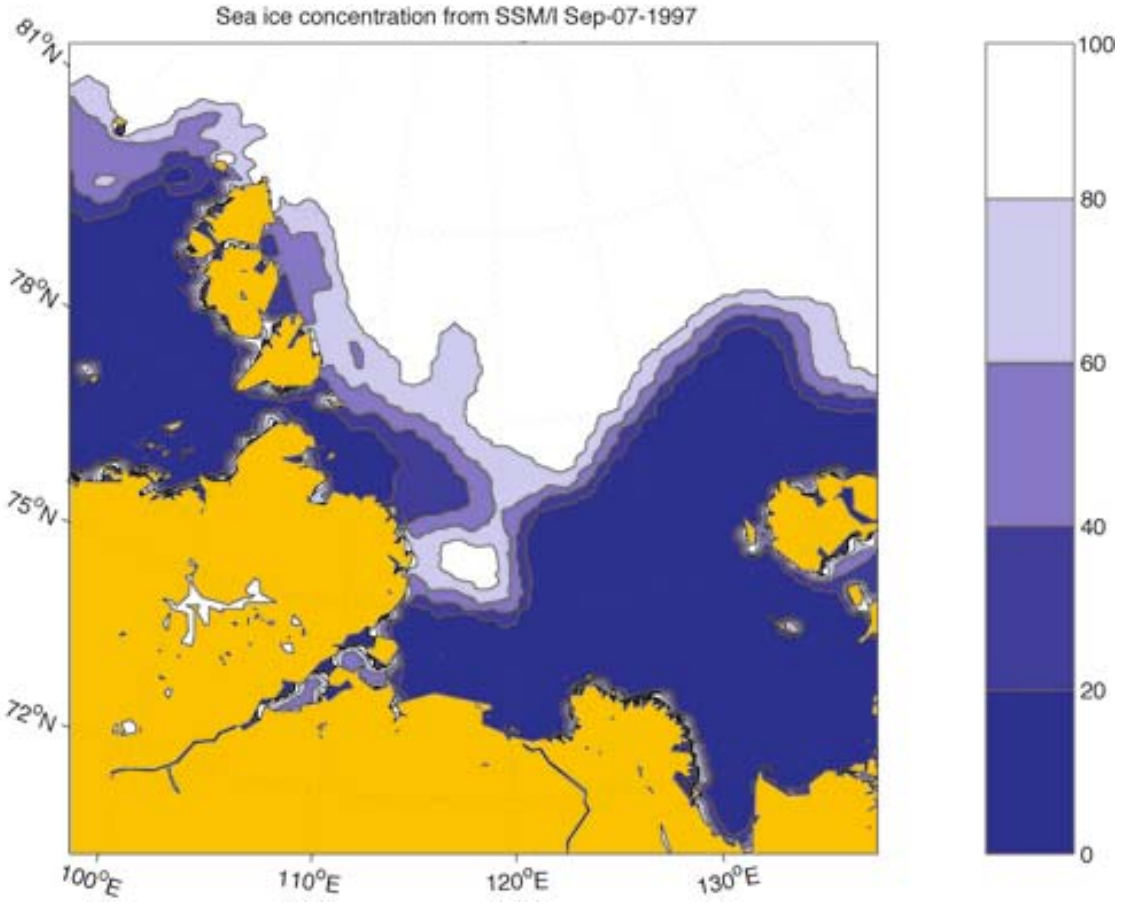

Figure 4.39(b). Ice concentration analysis from SSM/I data on the same day using the NORSEX algorithm (Svendsen *et al*., 1983) using the 85-GHz channel.

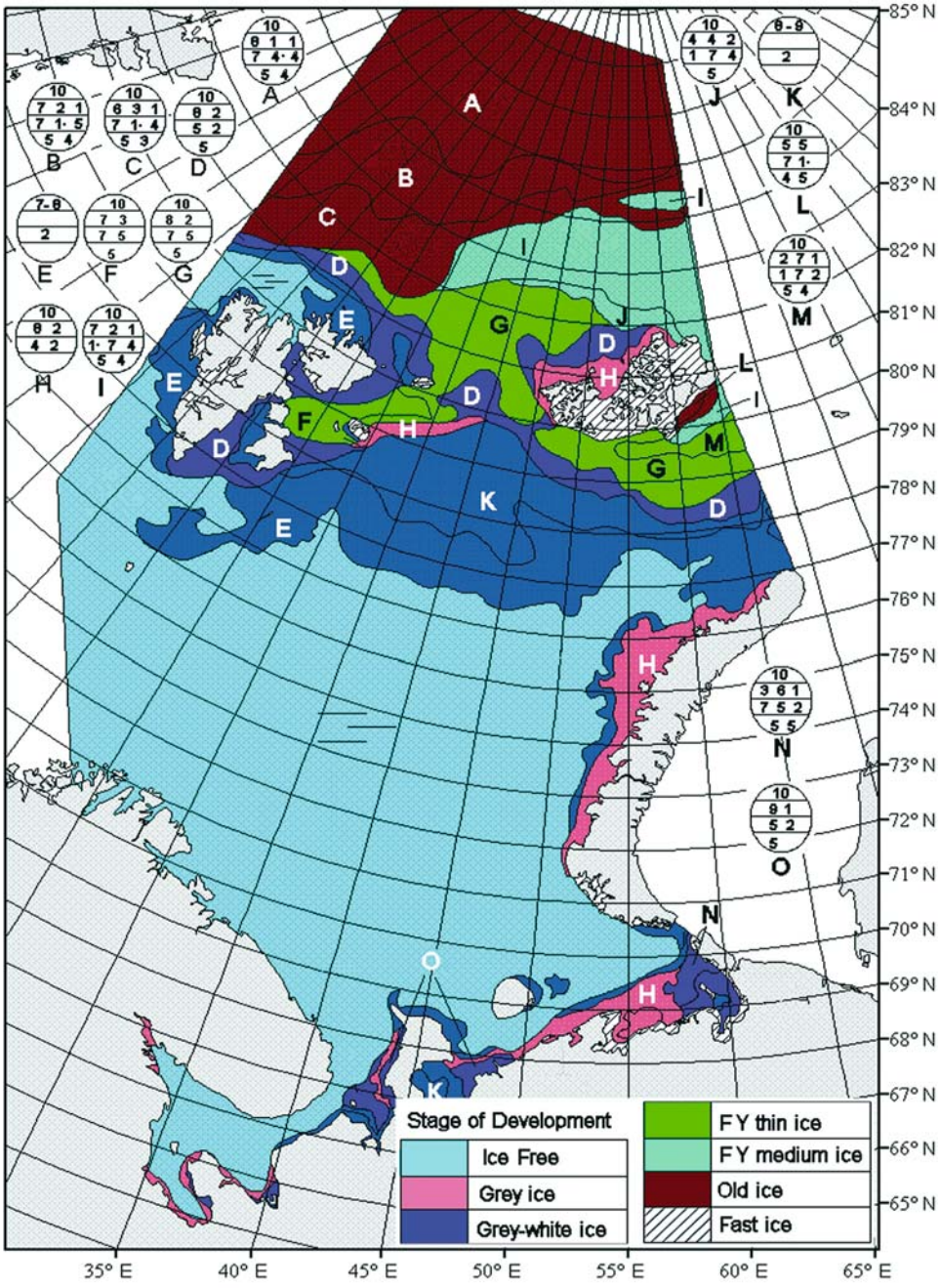

Figure 4.43(a). Example of an ice chart compiled from visible satellite images: an individual ice chart of the Barents Sea made from analysis of the *NOAA* AVHRR image for 3 January 2005.

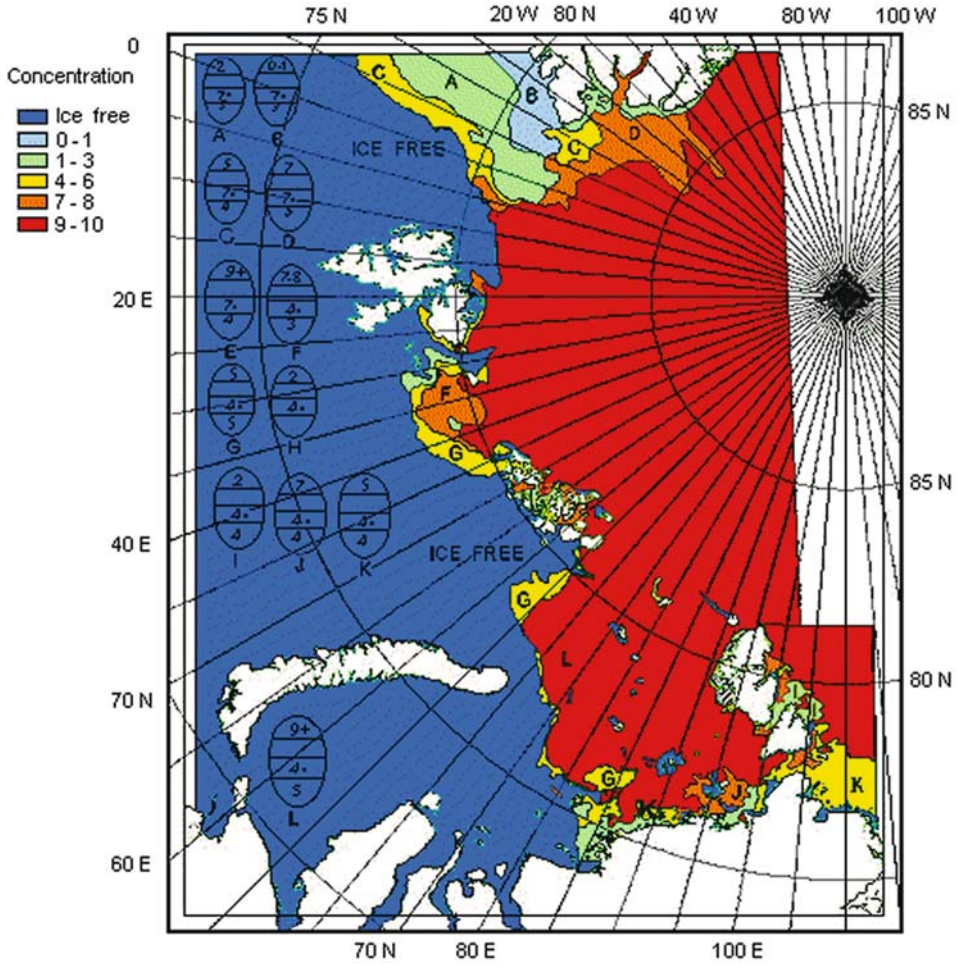

Figure 4.43(b). Example of an ice chart compiled from visible satellite images: composite ice chart of the Barents and Kara Seas made from a composite image (mosaic) of four AVHRR images for 26–28 July 2003.

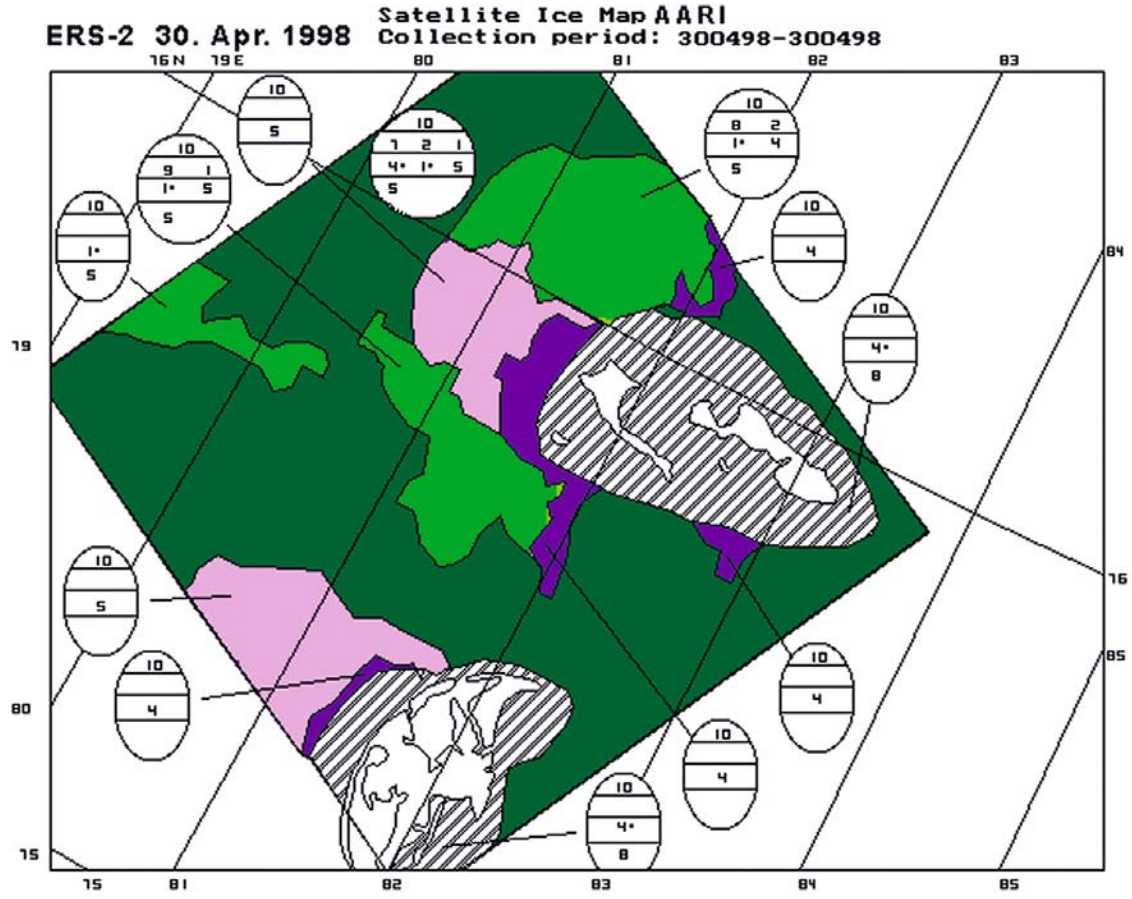

Figure 4.44(a). Example of an ice chart compiled from satellite SAR images: ice chart compiled from an *ERS* SAR image of sea ice in the Kara Sea, 30 April 1998.

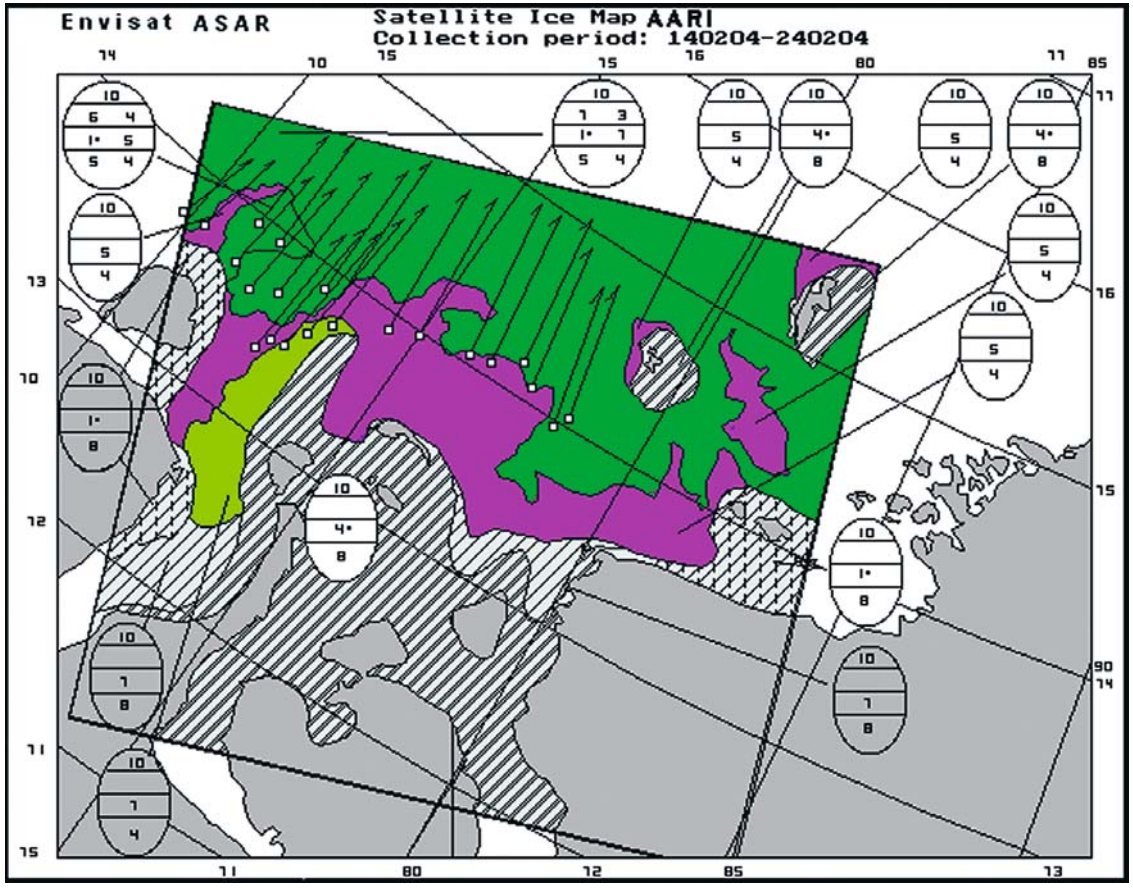

Figure 4.44(b). Example of an ice chart compiled from satellite SAR images: ice chart compiled from an *Envisat* ASAR image of sea ice in the Kara Sea, 24 February 2004).

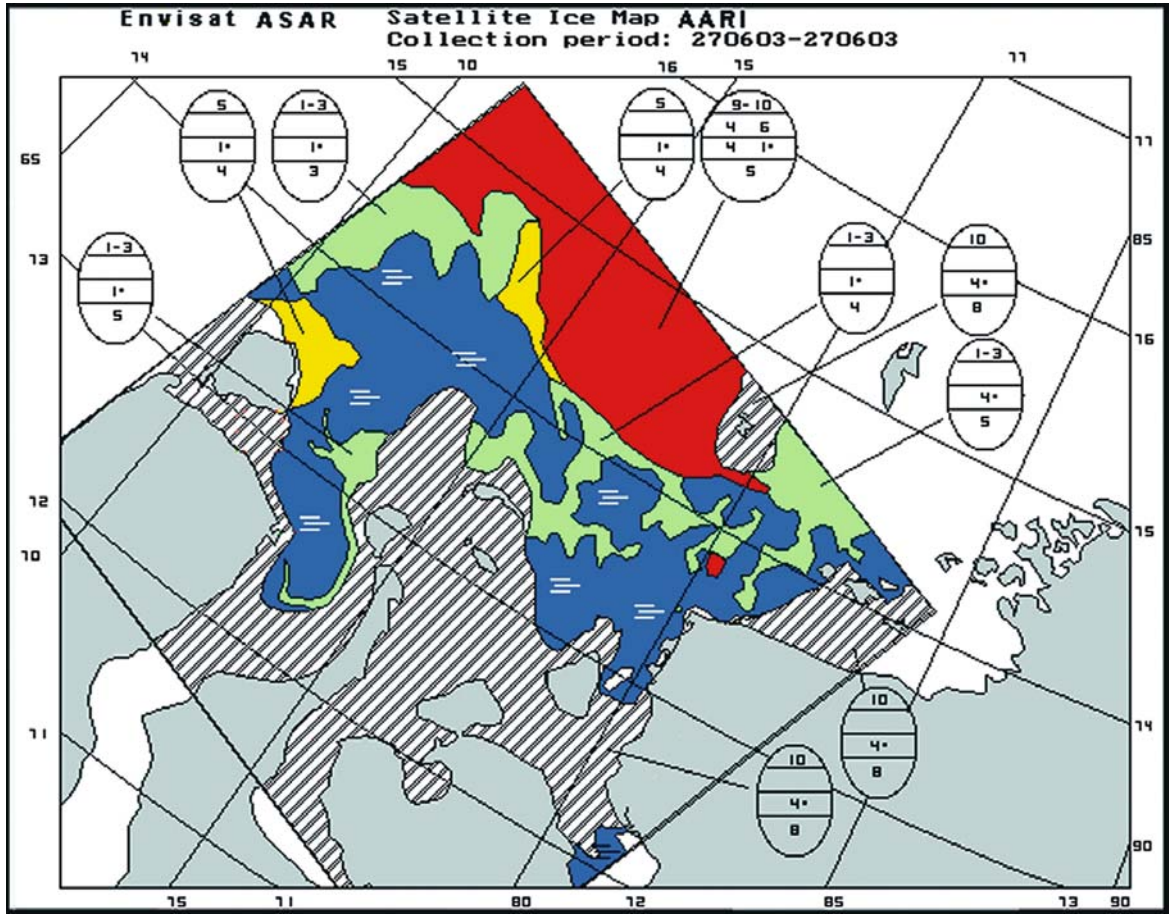

Figure 4.44(c). Ice chart compiled from the *Envisat* ASAR image of sea ice in the Kara Sea, 27 June 2003).

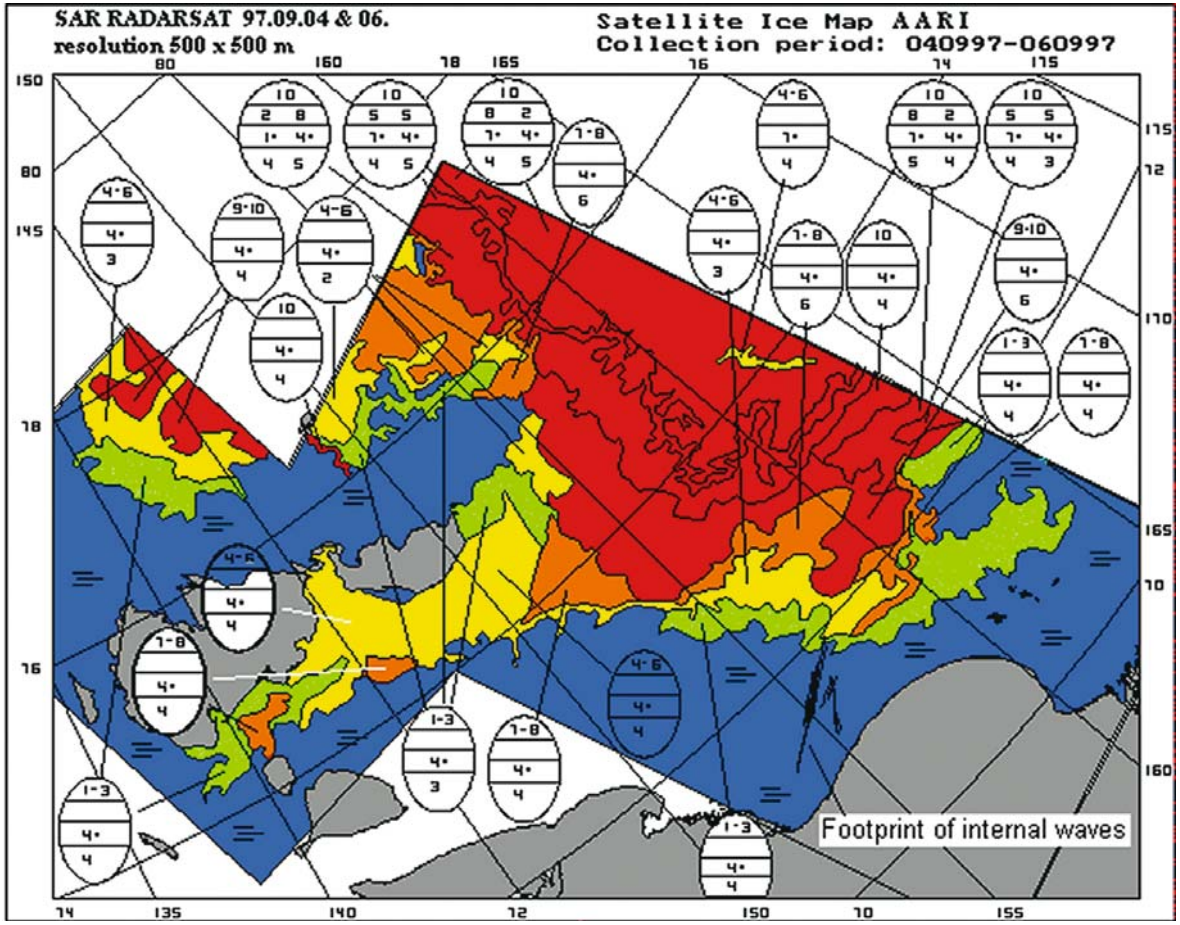

Figure 4.44(d). Composite ice chart (mosaic) compiled from two *Radarsat* SAR images in the East Siberian Sea, 4 and 6 September 1997.

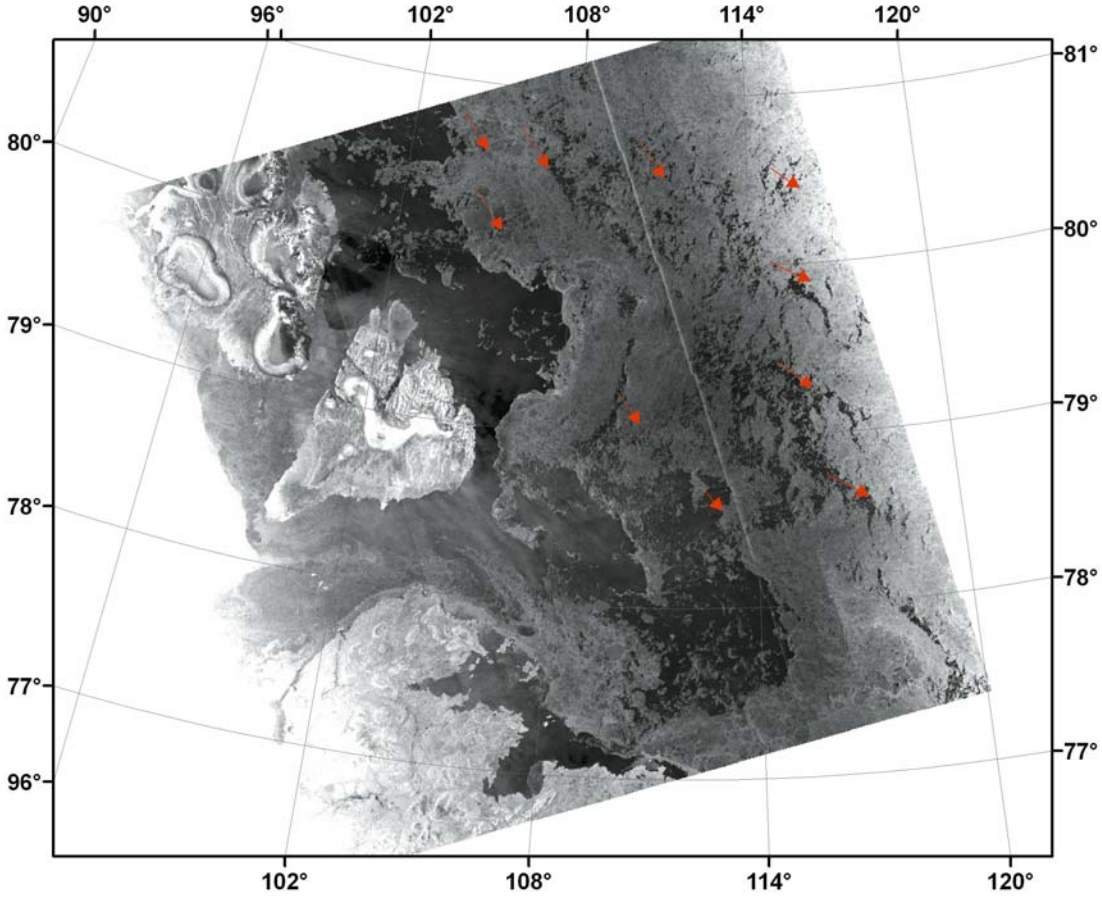

Figure 5.35(a). Ice drift in the Laptev Sea in August–September 1997: *Radarsat* ScanSAR image of 14 August 1997, with ice drift vectors until 15 August superimposed (© Canadian Space Agency).

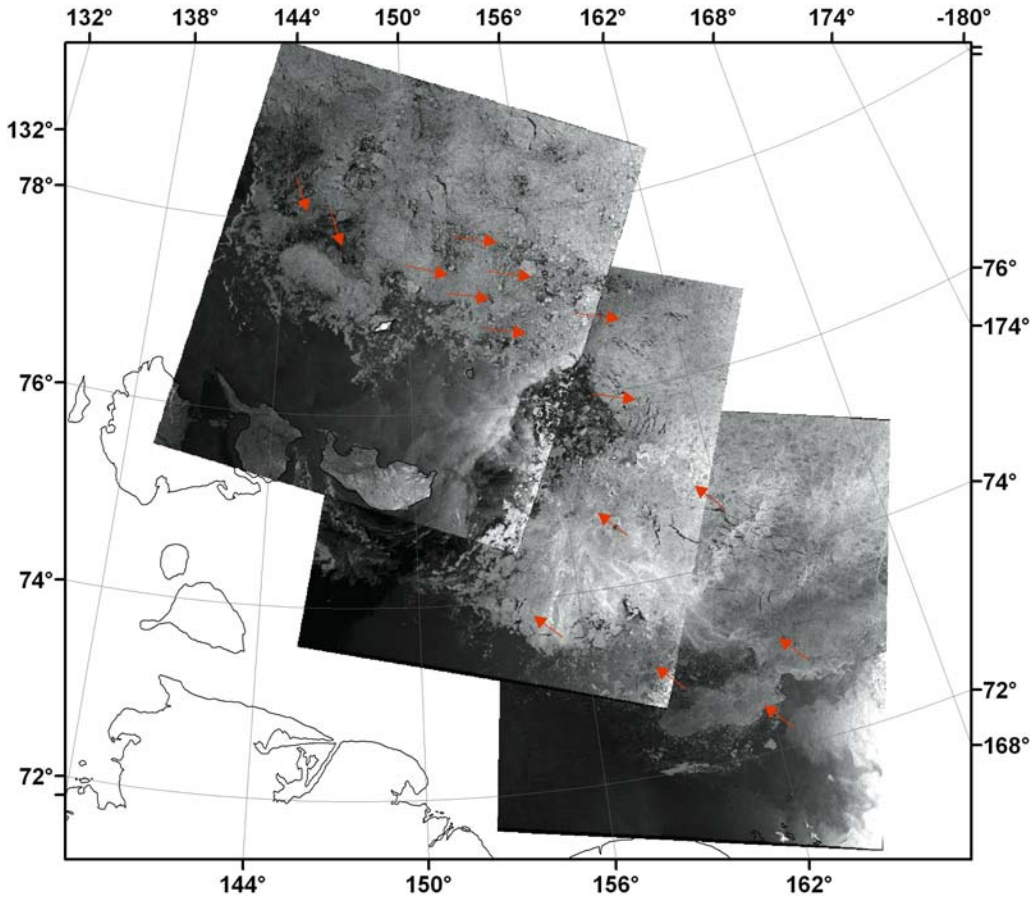

Figure 5.35(b). Ice drift in the Laptev Sea in August–September 1997. Mosaic of *Radarsat* ScanSAR images taken in the area of New Siberian Islands from 4 to 6 September 1997, with 1-day ice drift vectors superimposed (© Canadian Space Agency).

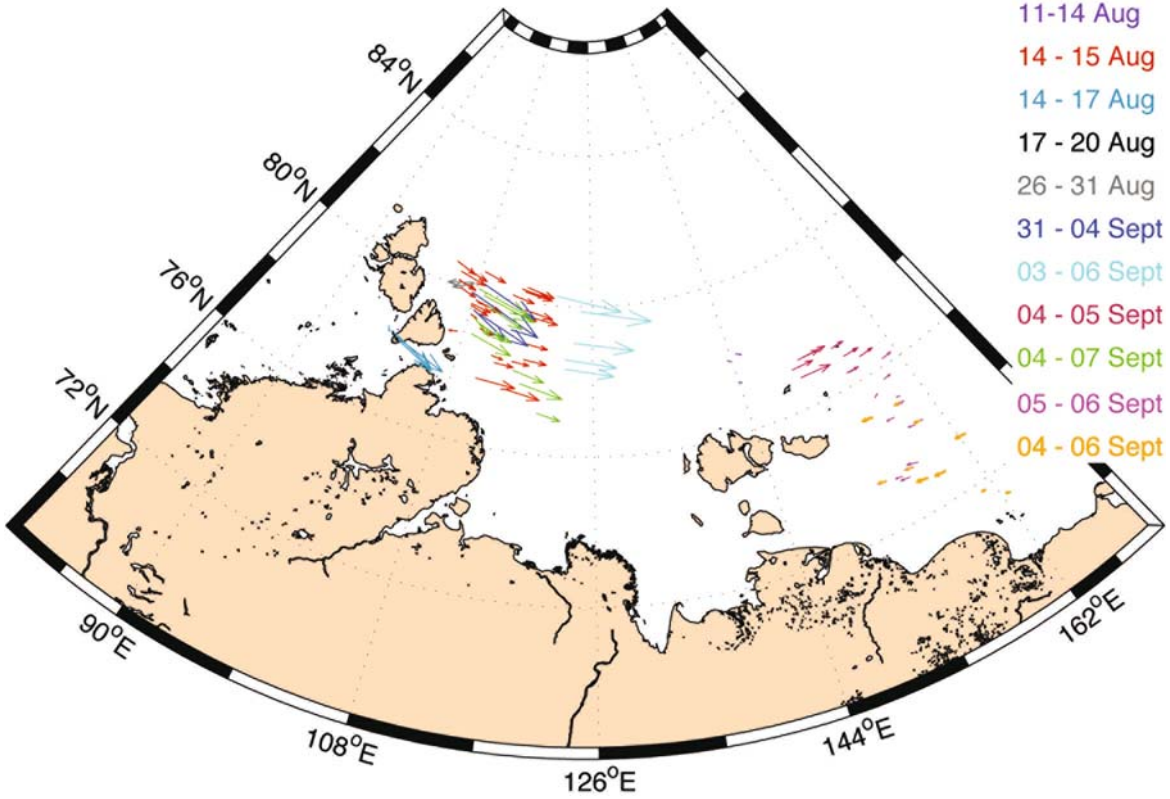

Figure 5.35(c). Mosaic of *Radarsat* ScanSAR images taken in the area of New Siberian Islands from 3 to 6 September 1997, with ice drift vectors superimposed (© Canadian Space Agency).

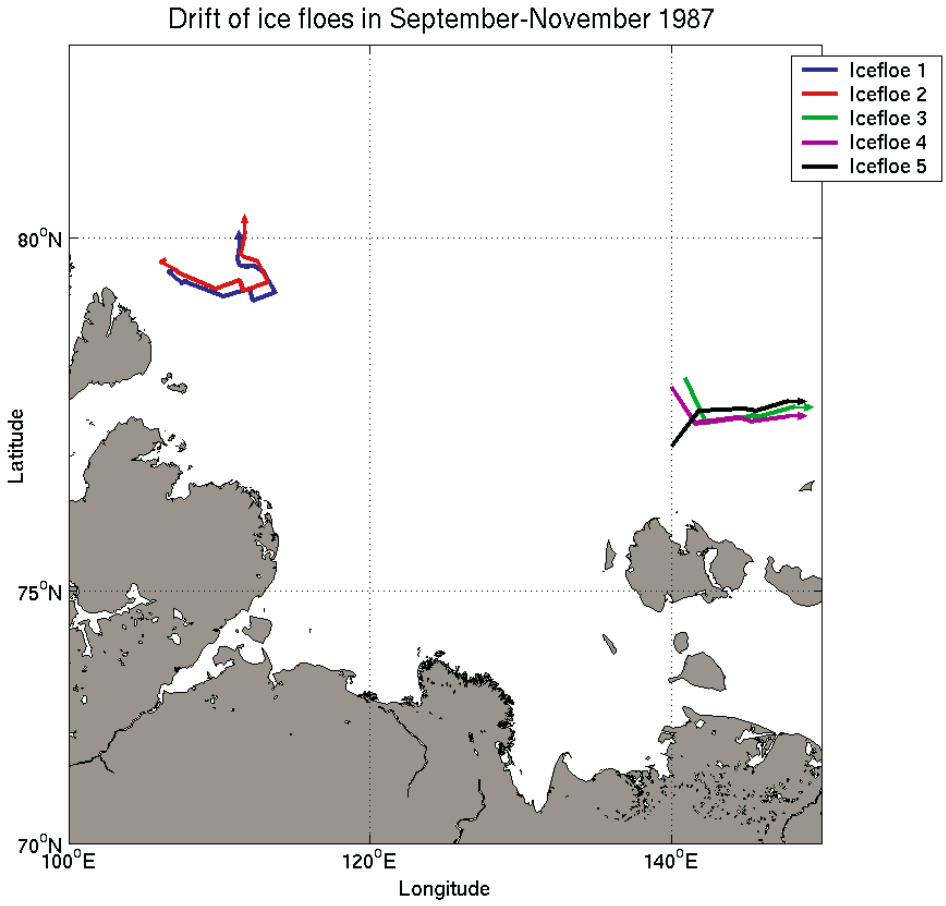

Figure 5.37. Detailed ice drift trajectories of selected ice floes in the Laptev Sea measured from successive *Okean* images.

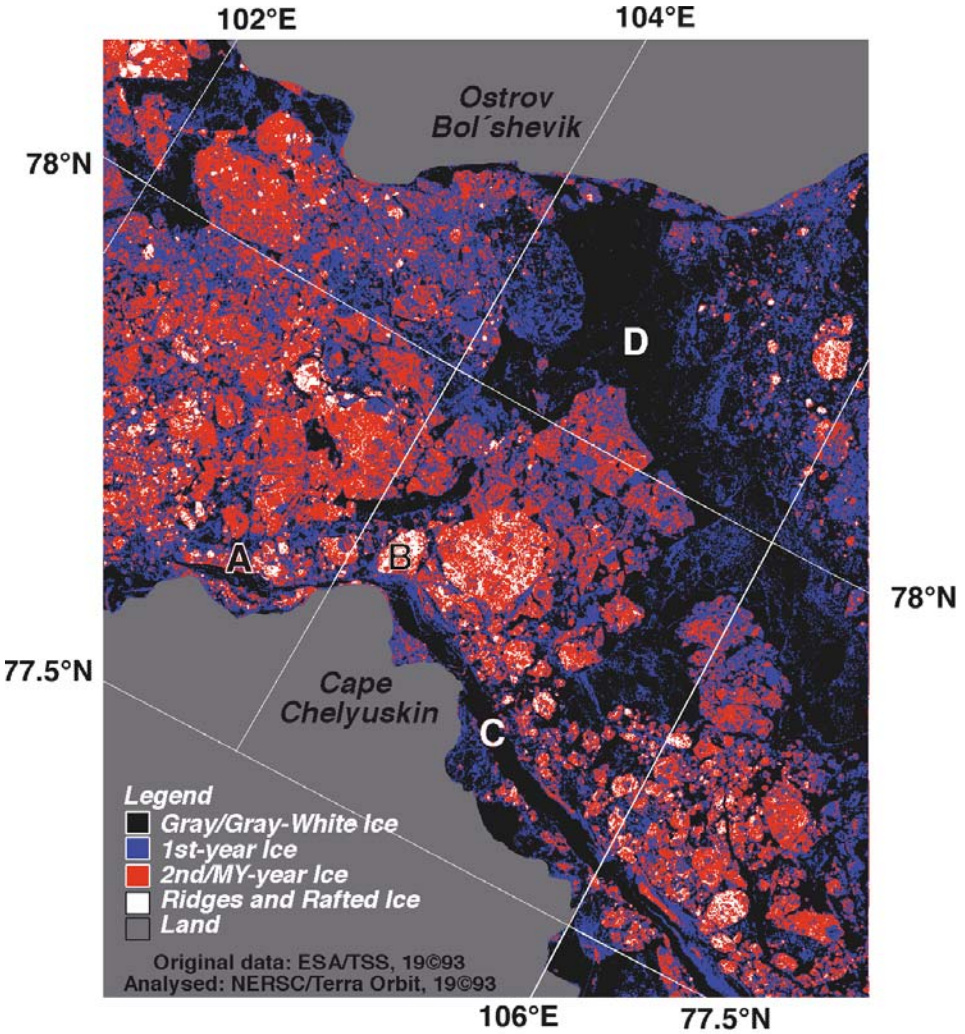

Figure 6.5(e). An example of a simple threshold classification of radar backscatter intensity in order to determine the various sea ice types. The SAR data are from 4 November 2003 shown in Figure 6.5(b) (© TerraOrbit AS/European Space Agency).

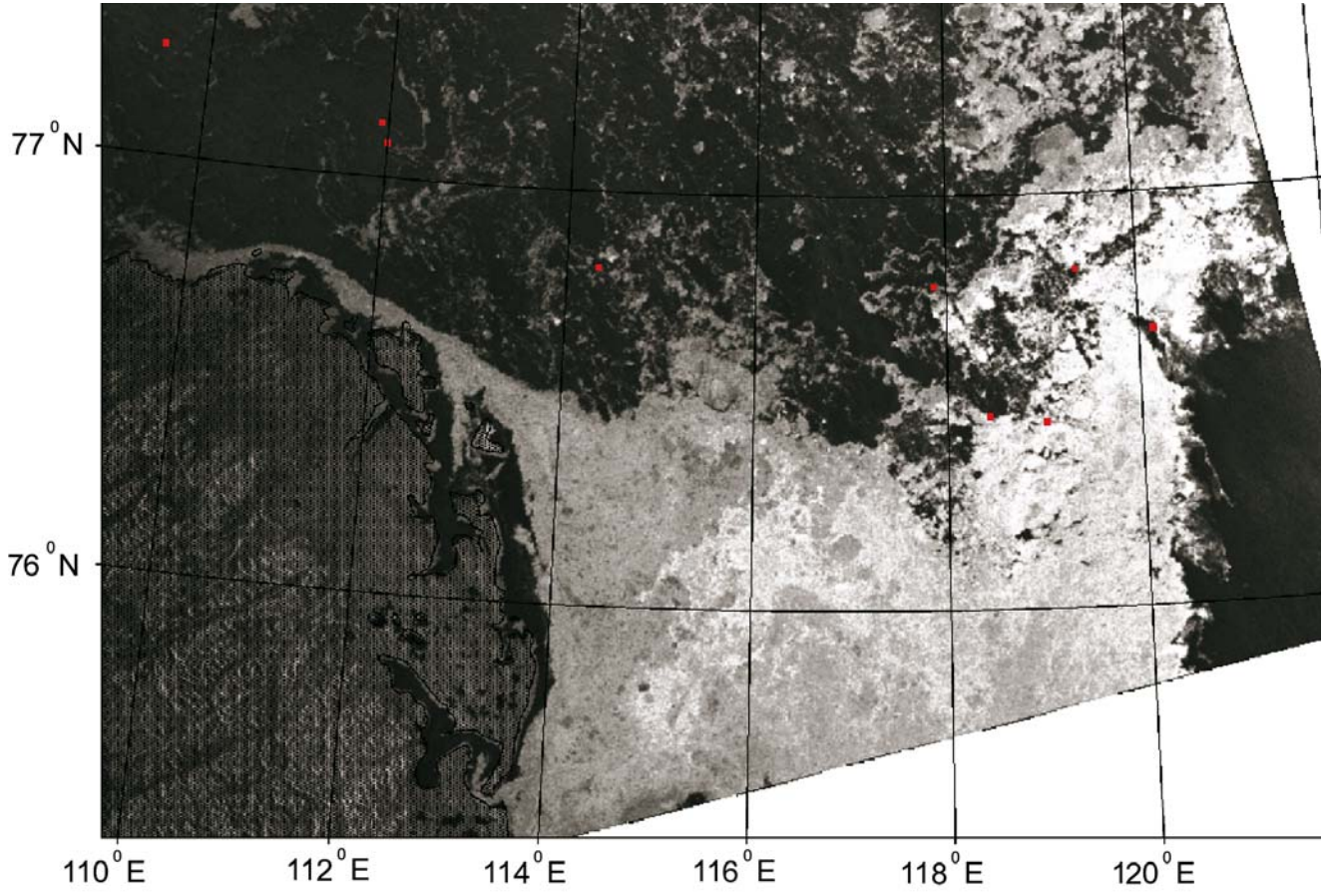

Figure 6.11(b). Subset of *Radarsat* ScanSAR image on 4 September, showing the area east of Vilkitsky Strait where the Taymyr ice massif reaches the mainland coast (© Canadian Space Agency).

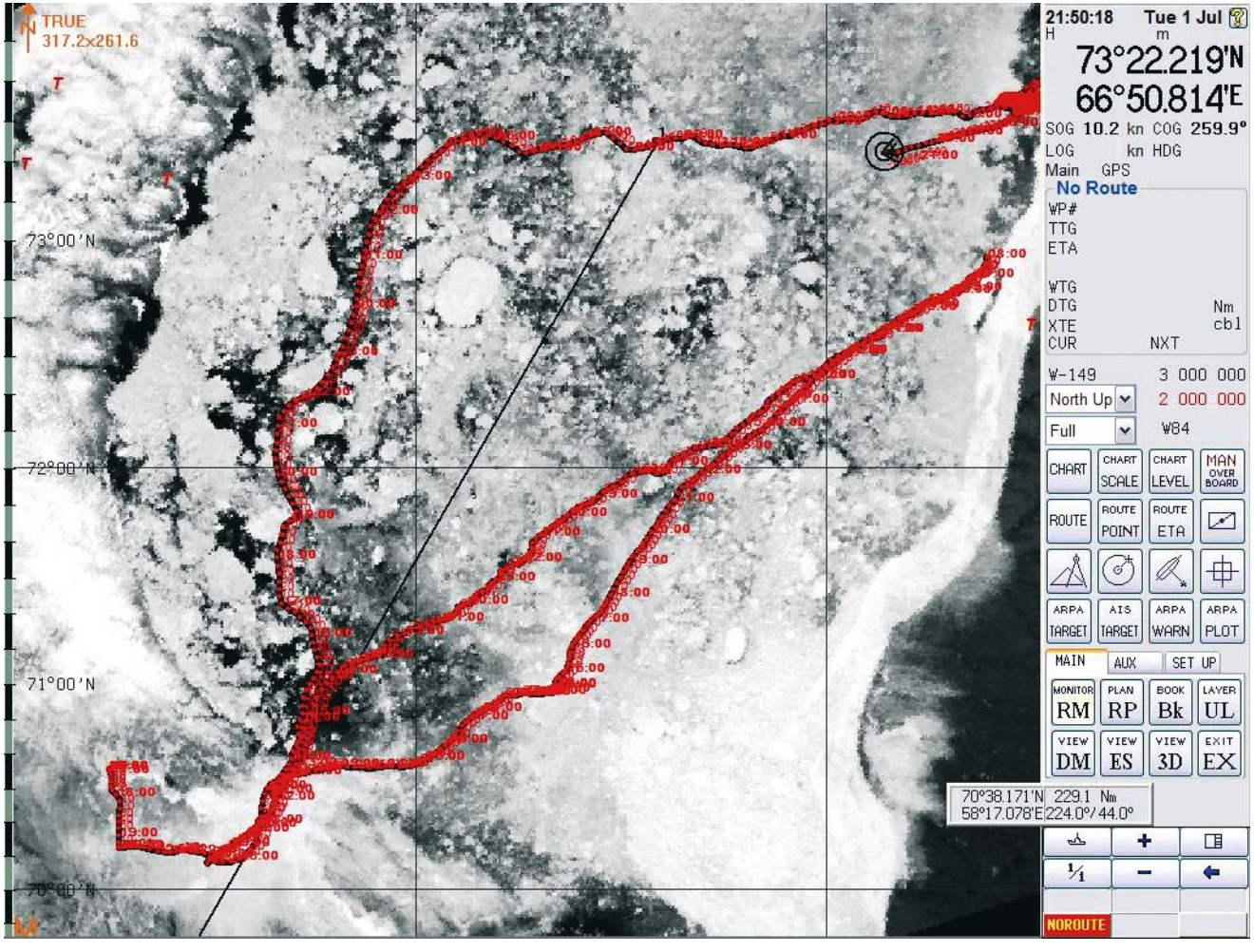

Figure 6.21(a). Example of a combined depiction of the *NOAA* raster image and the navigation chart in ECDIS (the nuclear icebreaker *Sovetsky Soyuz*, the Kara Sea, June–July 2003).

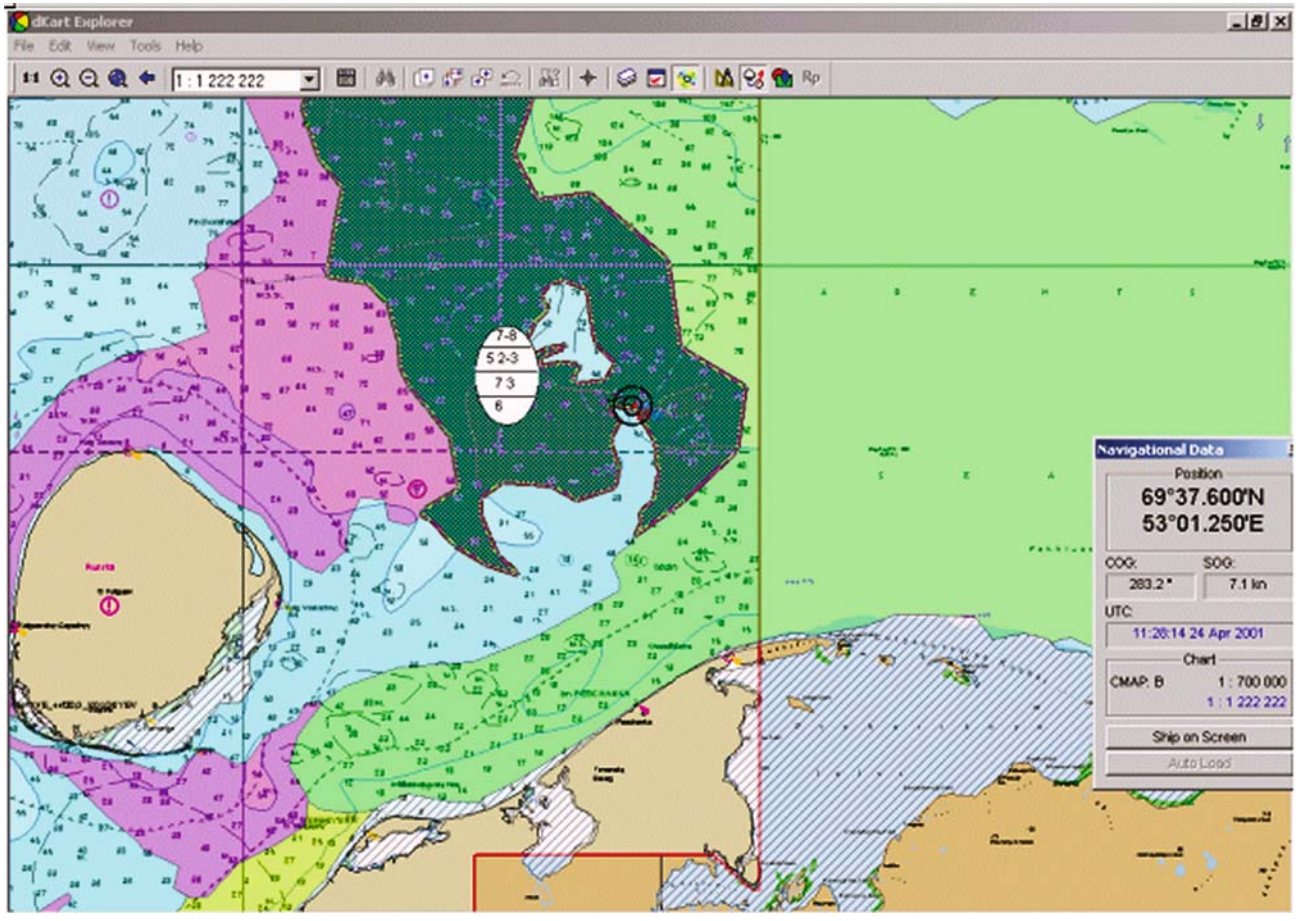

Figure 6.21(b). Example of a combined depiction of the ice chart and the navigation chart in ECDIS.

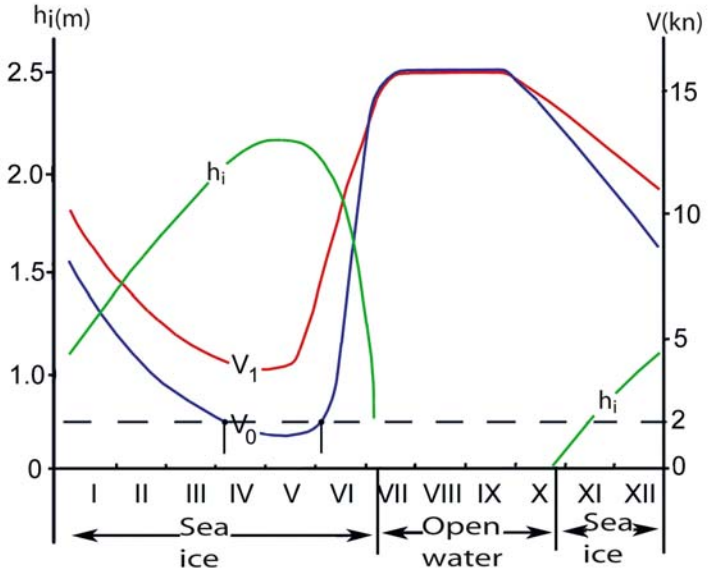

Figure 6.25. Seasonal change in monthly mean speed of convoys when tactical ice reconnaissance data are used (V_1) and when such data are not used (V_0) for year-round navigation in the Kara Sea; the mean monthly ice thickness in the region is also indicated.

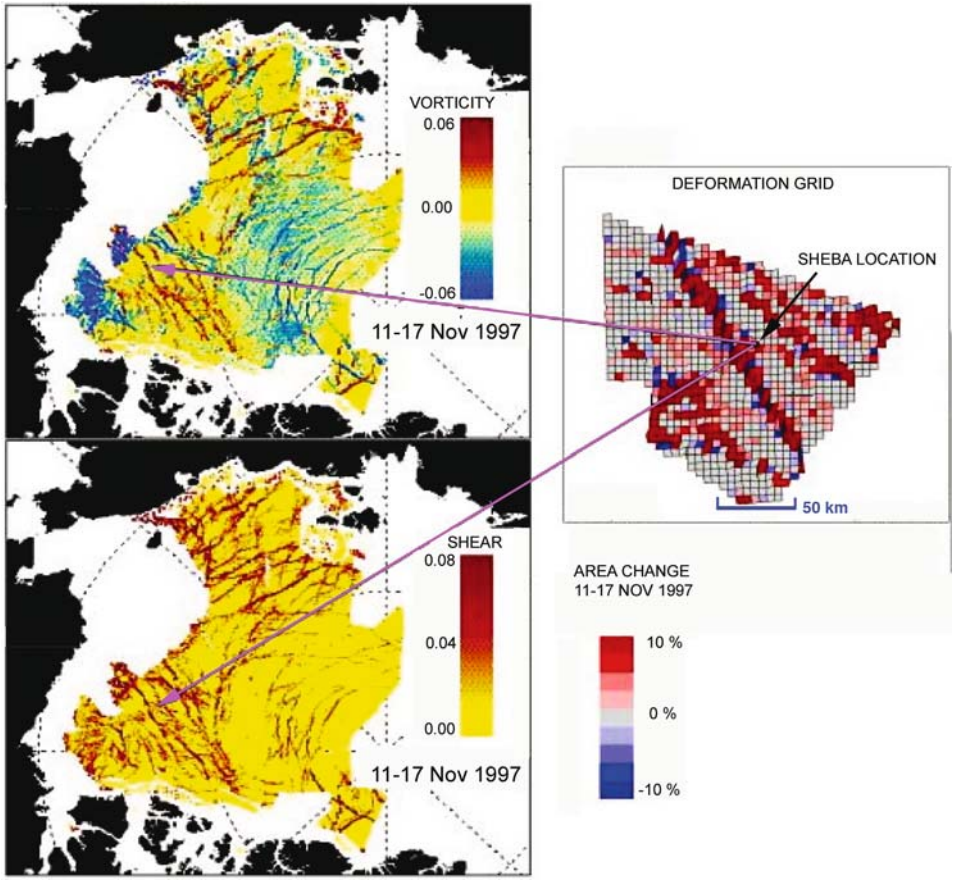

Figure 6.27. Sea ice vorticity and shear fields are examples of a linear kinematic field calculated from 6-day interval mosaics of the Arctic ice cover using the deformation grids explained in Figure 6.26 (courtesy: R. Kwok) (Kwok and Cunningham, 2002).

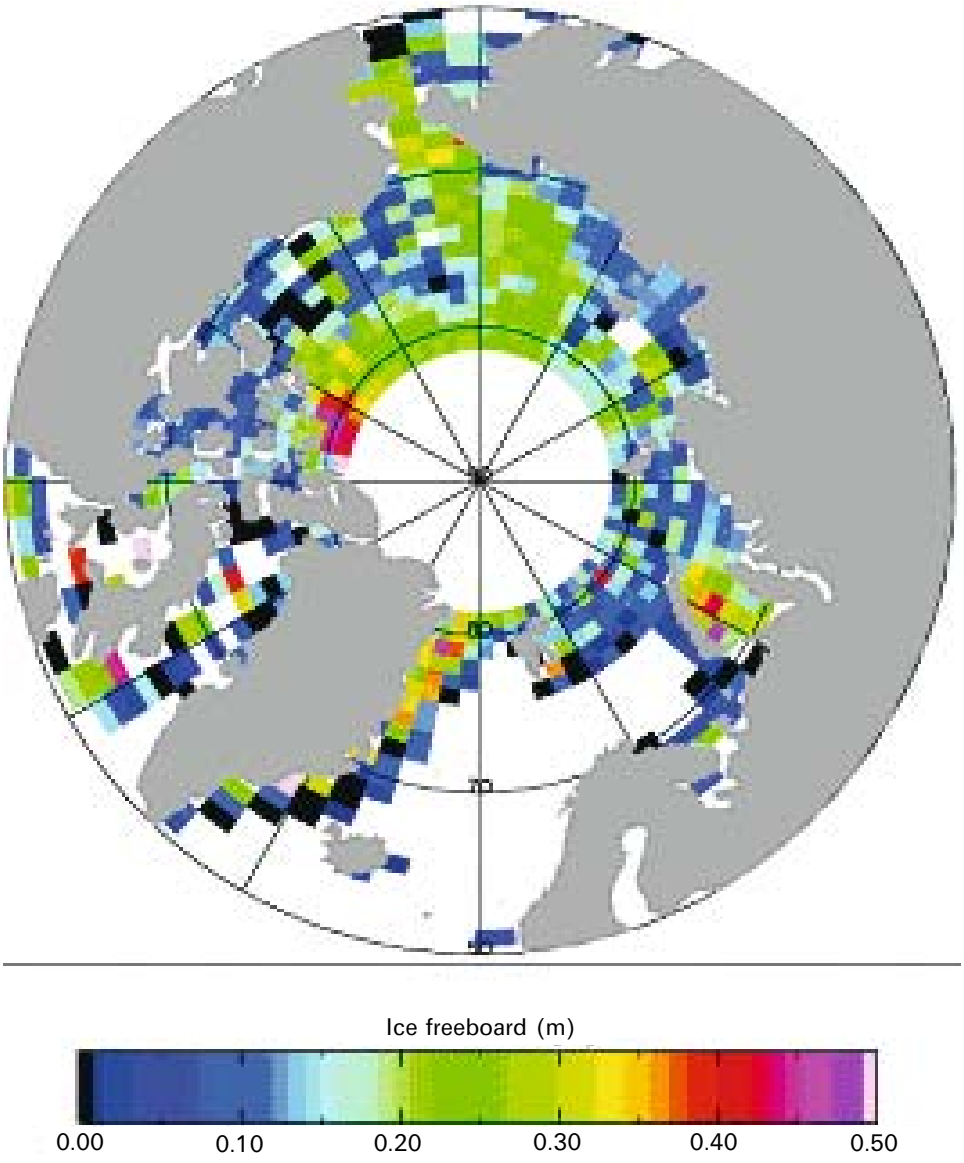

Figure 6.29(a). Sea ice freeboard from one 35-day cycle of *ERS* radar altimeter data (cycle 97). The products have been developed by University College London (UCL).

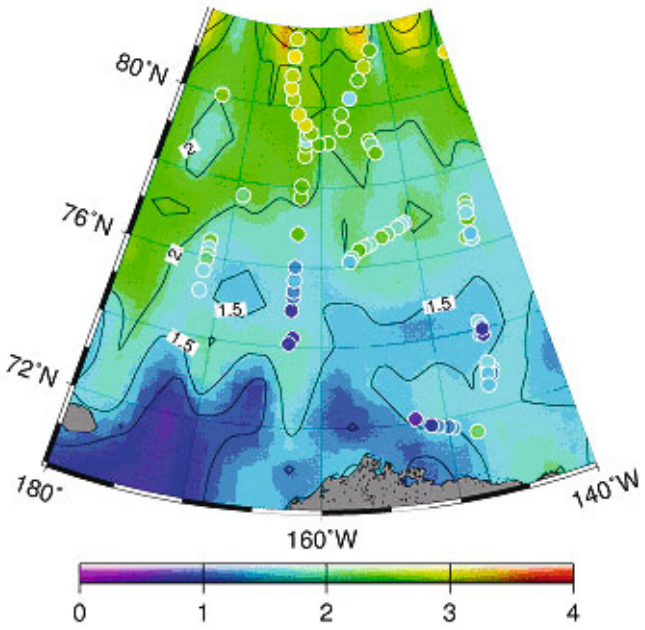

Figure 6.29(b). Ice thickness map of the Beaufort Sea-area where dots represent validation data from submarine sonar profiles. The products have been developed by University College London (UCL).

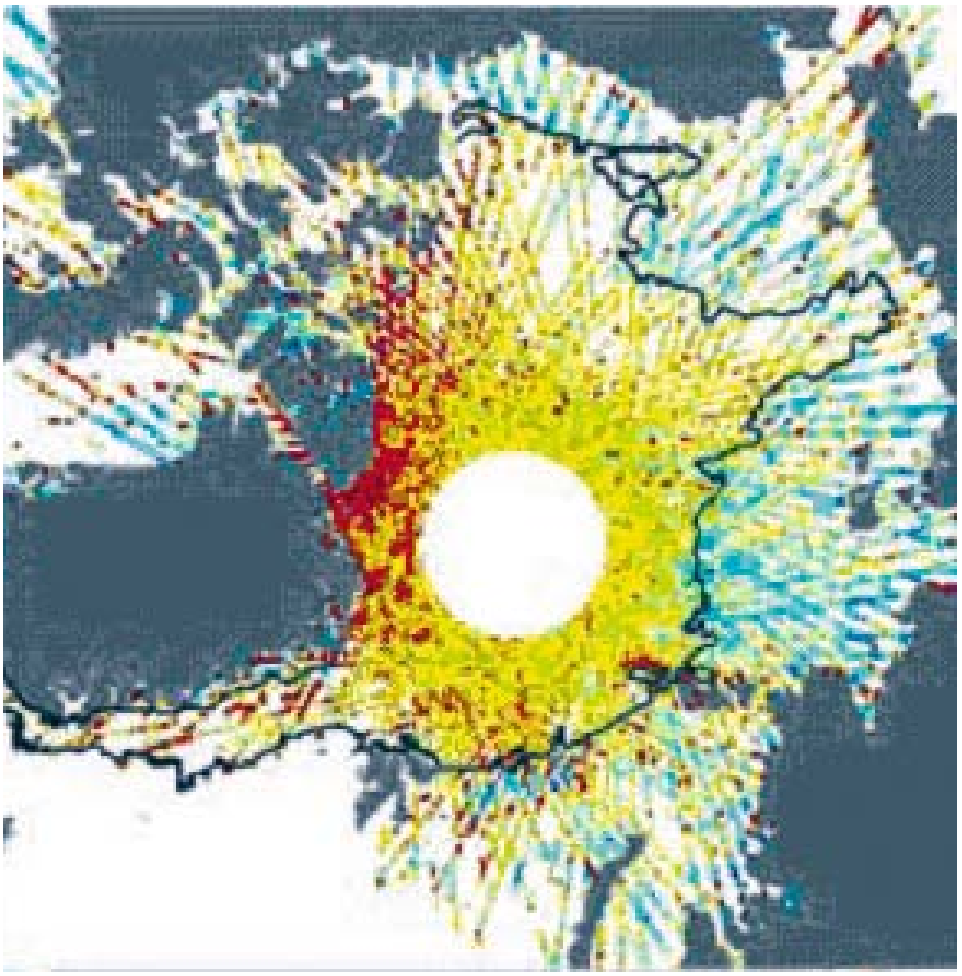

Figure 6.30. Ice surface height from *IceSat* for the period 10–18 March 2003. Red shows high values of surface height, while blue shows low values. The gray line is the extent of multi-year ice retrieved from scatterometer data (Kwok *et al.*, 2004).

(a)

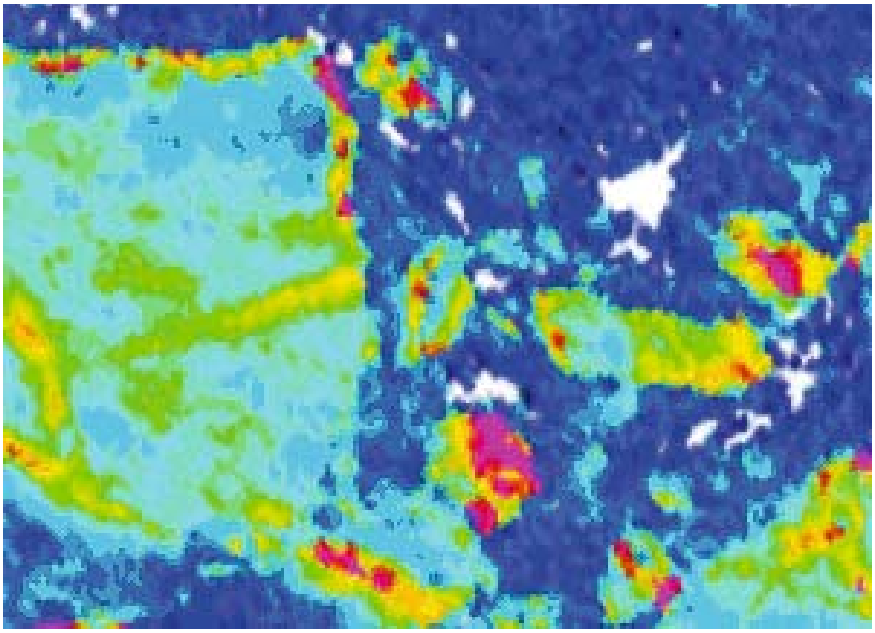

(b)

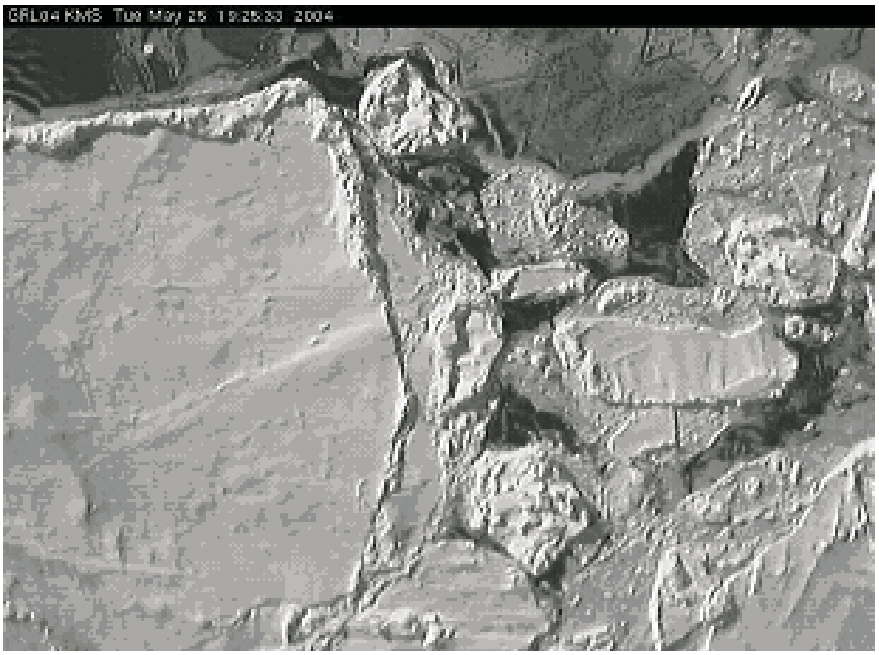

Figure 6.32. (a) Ice freeboard image from scanning laser in which dark blue is thin or open water and ridges having up to 2-m freeboard are yellow–red; (b) same area as in (a) observed by a vertical video-camera. The size of the area is about 100×100 m.

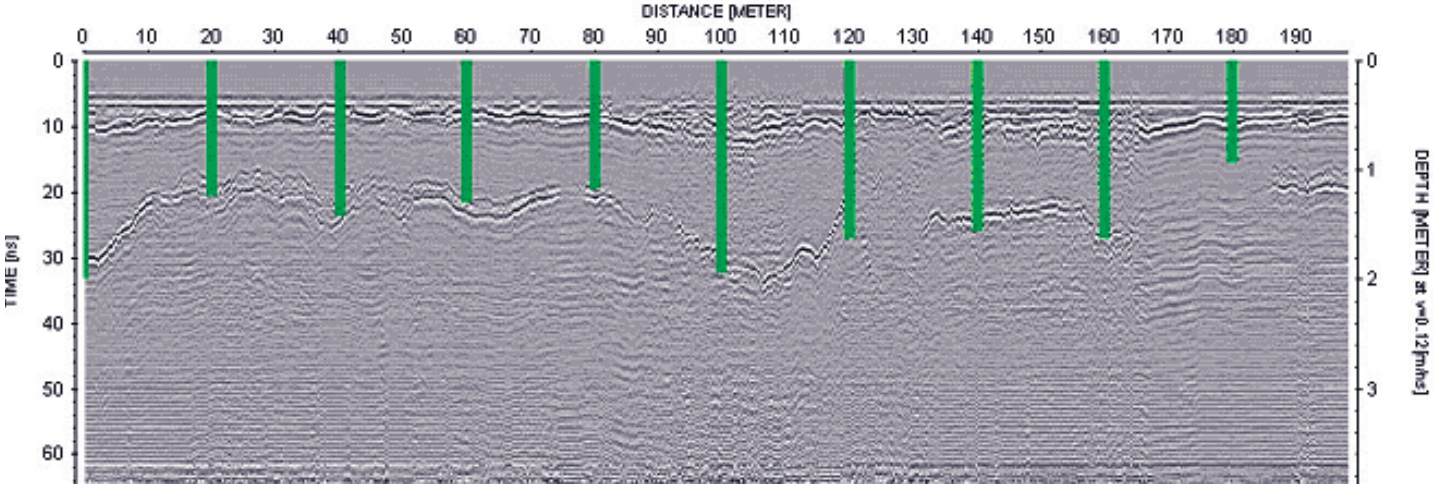

Figure 6.35. GPR section (radargram) obtained from a sled covering a distance of 200 m on a multi-year floe north of Svalbard. Data from drilling holes are plotted as green bars (courtesy: Alfred Wegener Institute (AWI)).

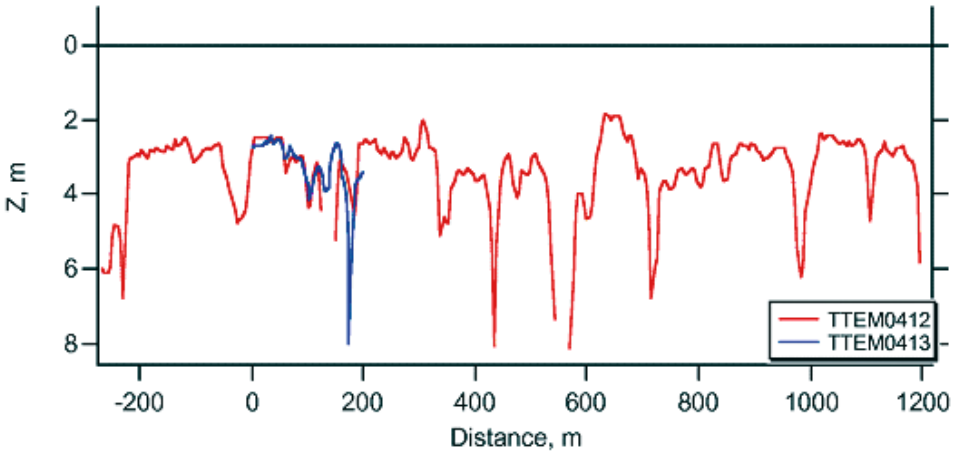

Figure 6.36. Example of a comparison of EM draft data from a helicopter (red curve) with ground penetrating draft data from a sled (blue curve). The data were obtained during the *Polarstern* expedition north of Svalbard in April 2003 (courtesy: C. Haas, AWI).

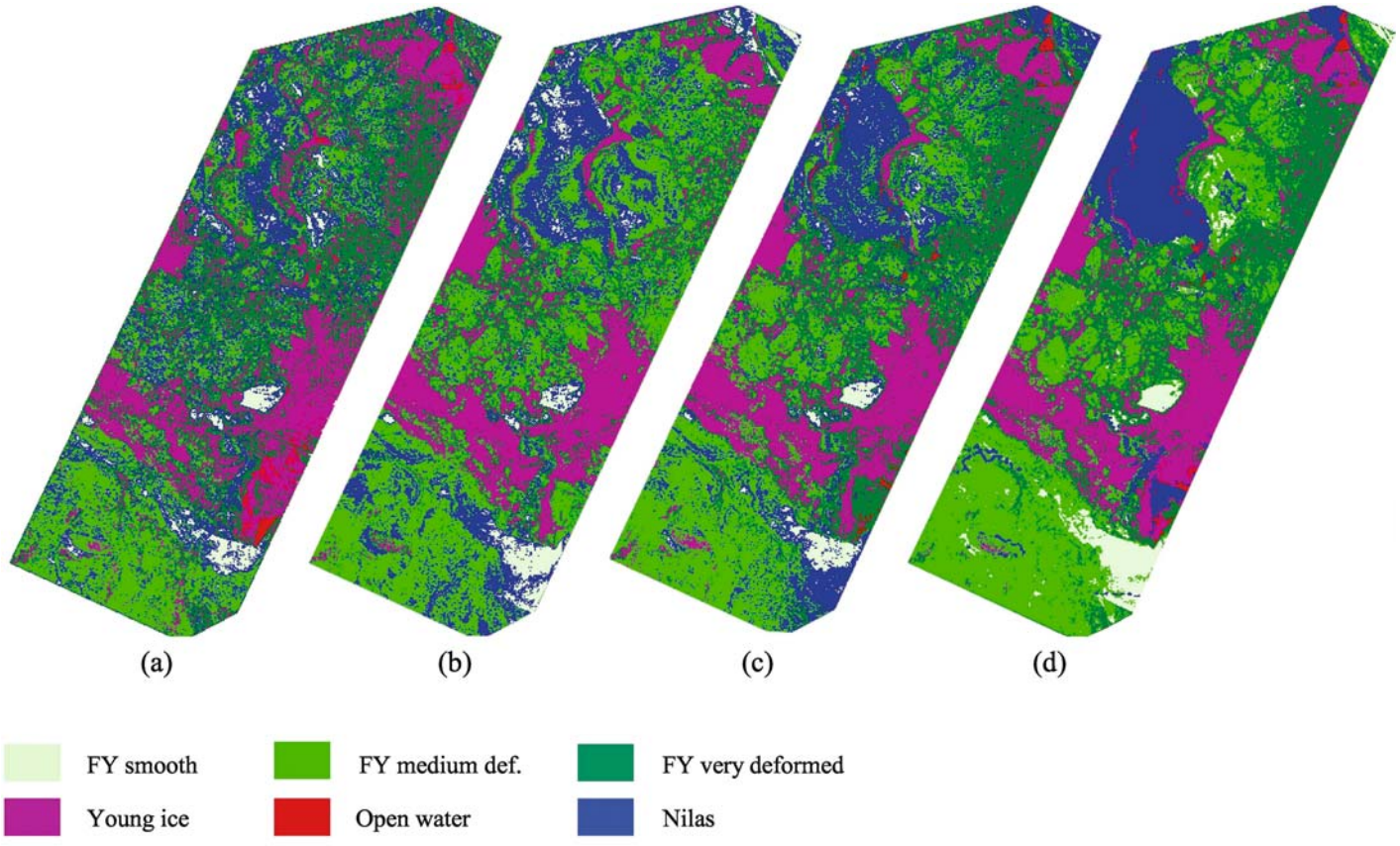

Figure 6.38. MLP sea ice classification maps obtained using (a) *ERS*, (b) *Radarsat*, (c) *ERS* and *Radarsat* and (d) *ERS*, *Radarsat* and *Meteor* images.

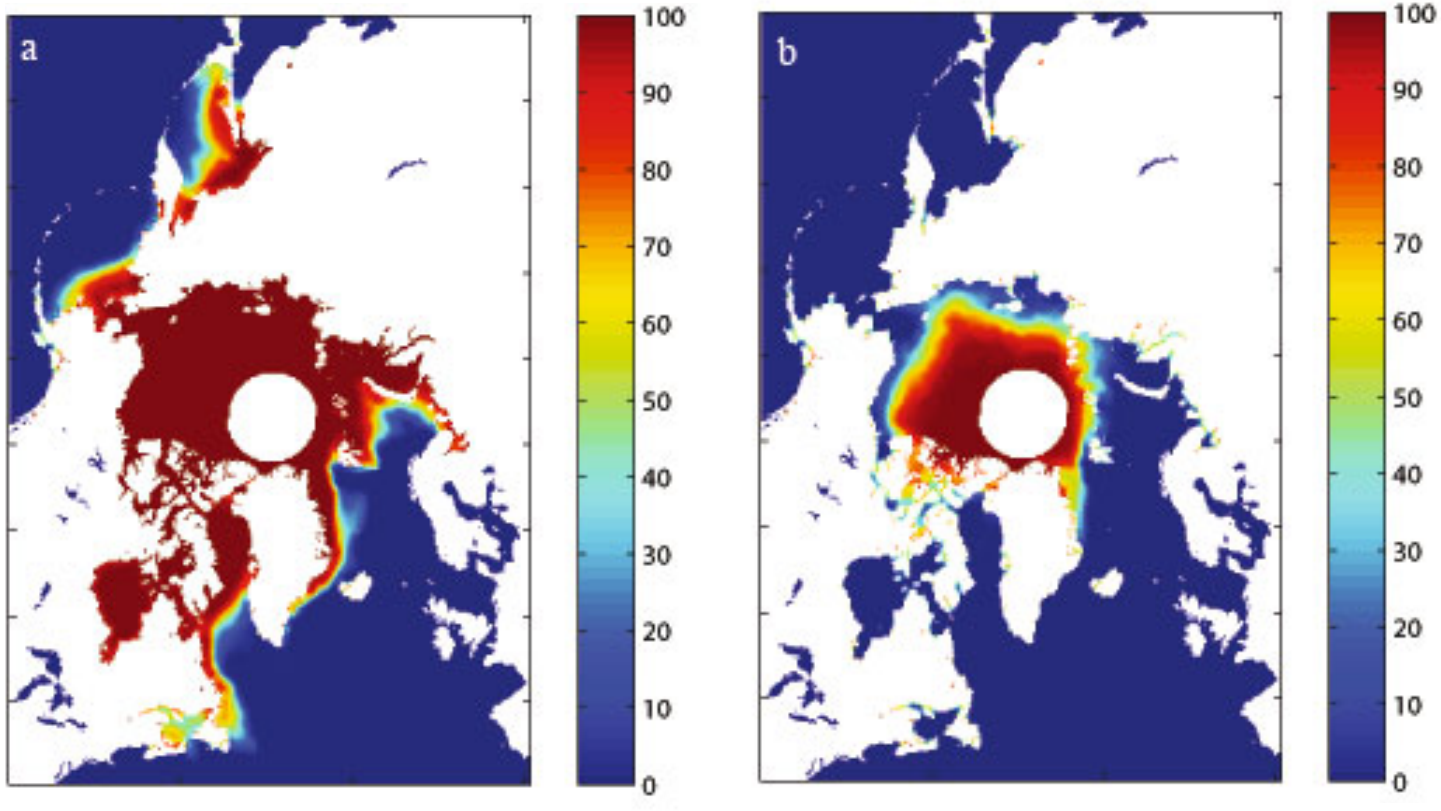

Figure 7.8. Mean sea ice concentration in the Arctic, derived from satellite passive microwave sensor data, 1978–2005: (a) in winter; (b) in summer. *Source*: NERSC, Bergen, Norway, updated from Johannessen *et al.* (2004).

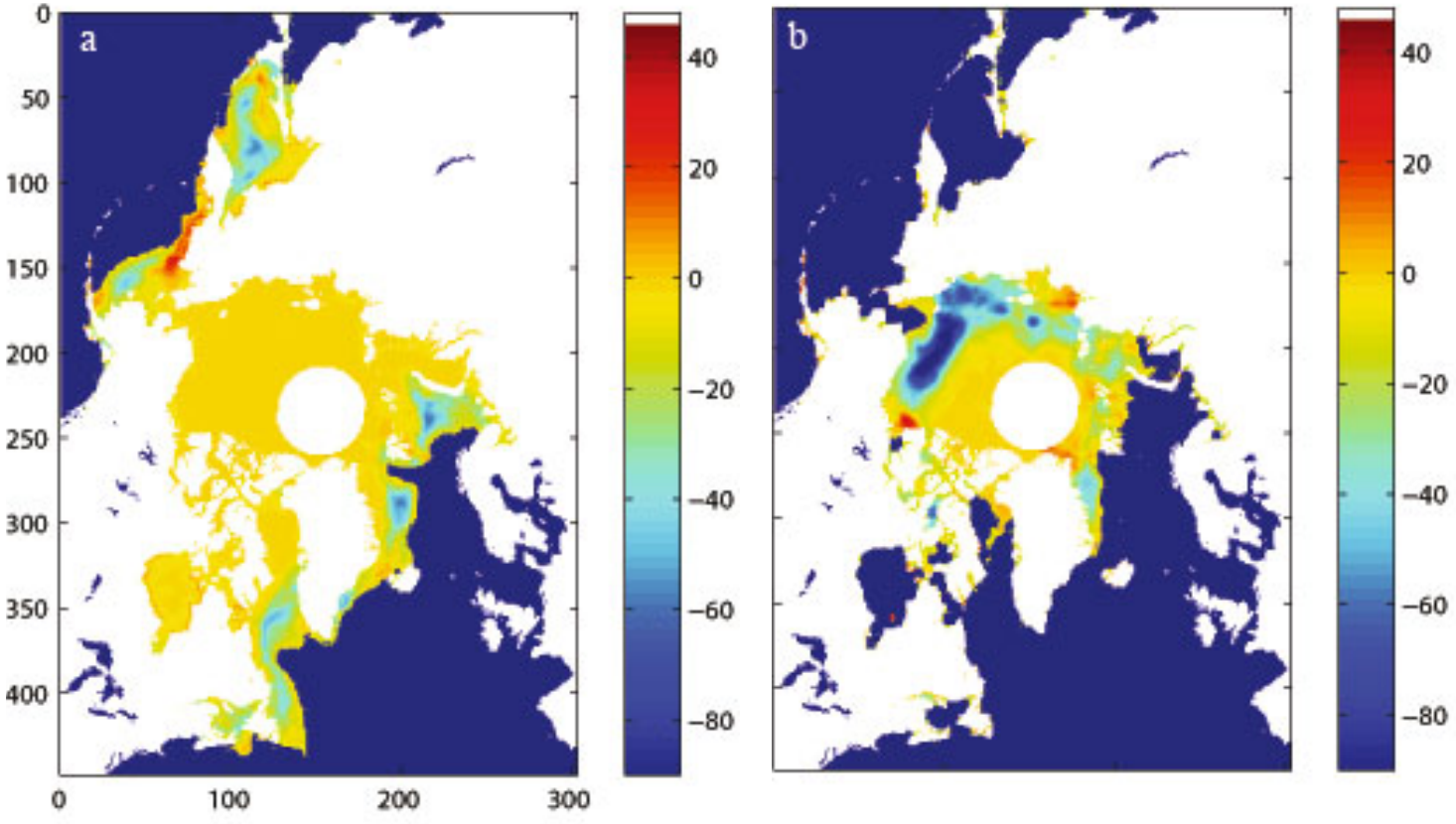

Figure 7.10. Linear trends in Arctic sea ice concentration, derived from satellite passive microwave sensor data, 1978–2005: (a) in winter; (b) in summer. *Source*: NERSC, Bergen, Norway, updated from Johannessen *et al.* (2004).

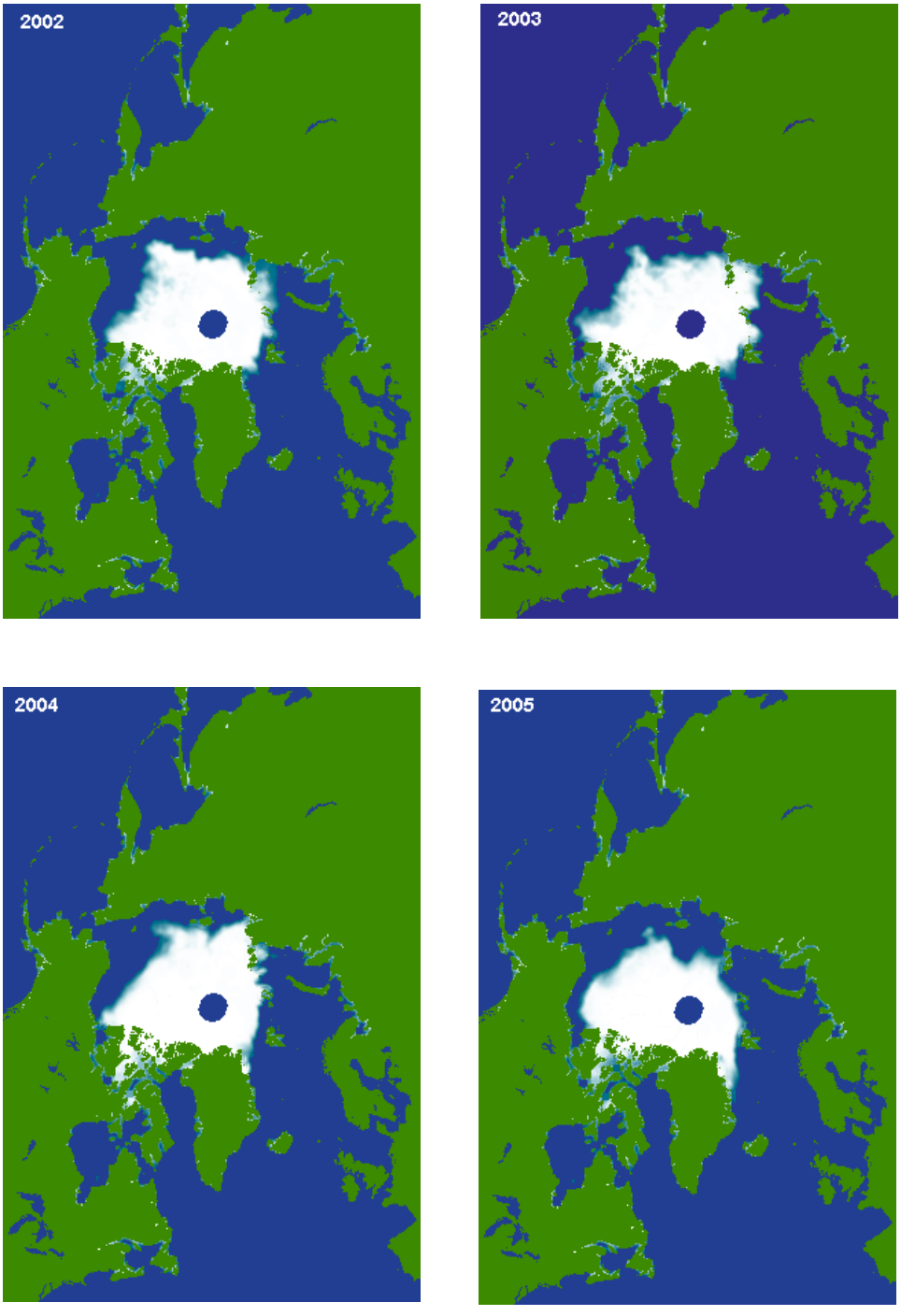

Figure 7.11. Arctic summer minimum sea ice extent (mean for September) for 2002 to 2005.

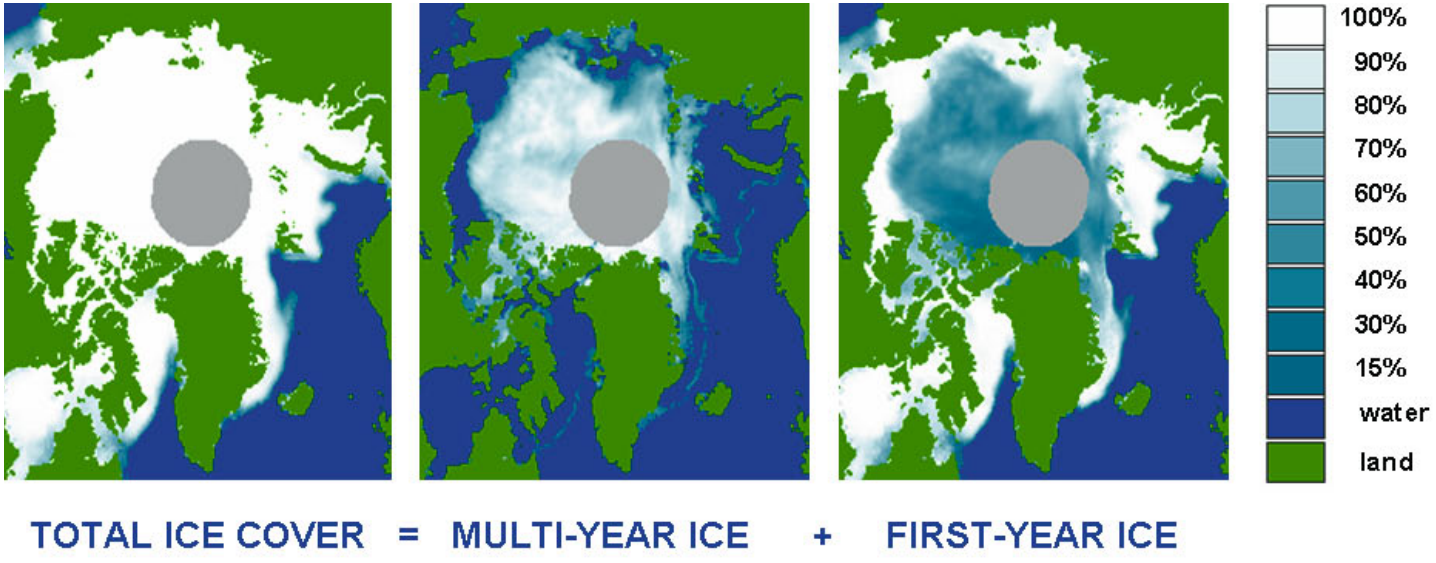

Figure 7.12. Arctic total sea ice concentration (left) and its two components: multi-year (*center*) and first-year (*right*) ice, derived from satellite passive- microwave sensor data. The gray-scale indicates the fraction (%) of each ice type (black = 0%, white = 100%). *Source*: Elena V. Shalina, NIERSC, St. Petersburg, Russia, as featured in Kerr (1999).

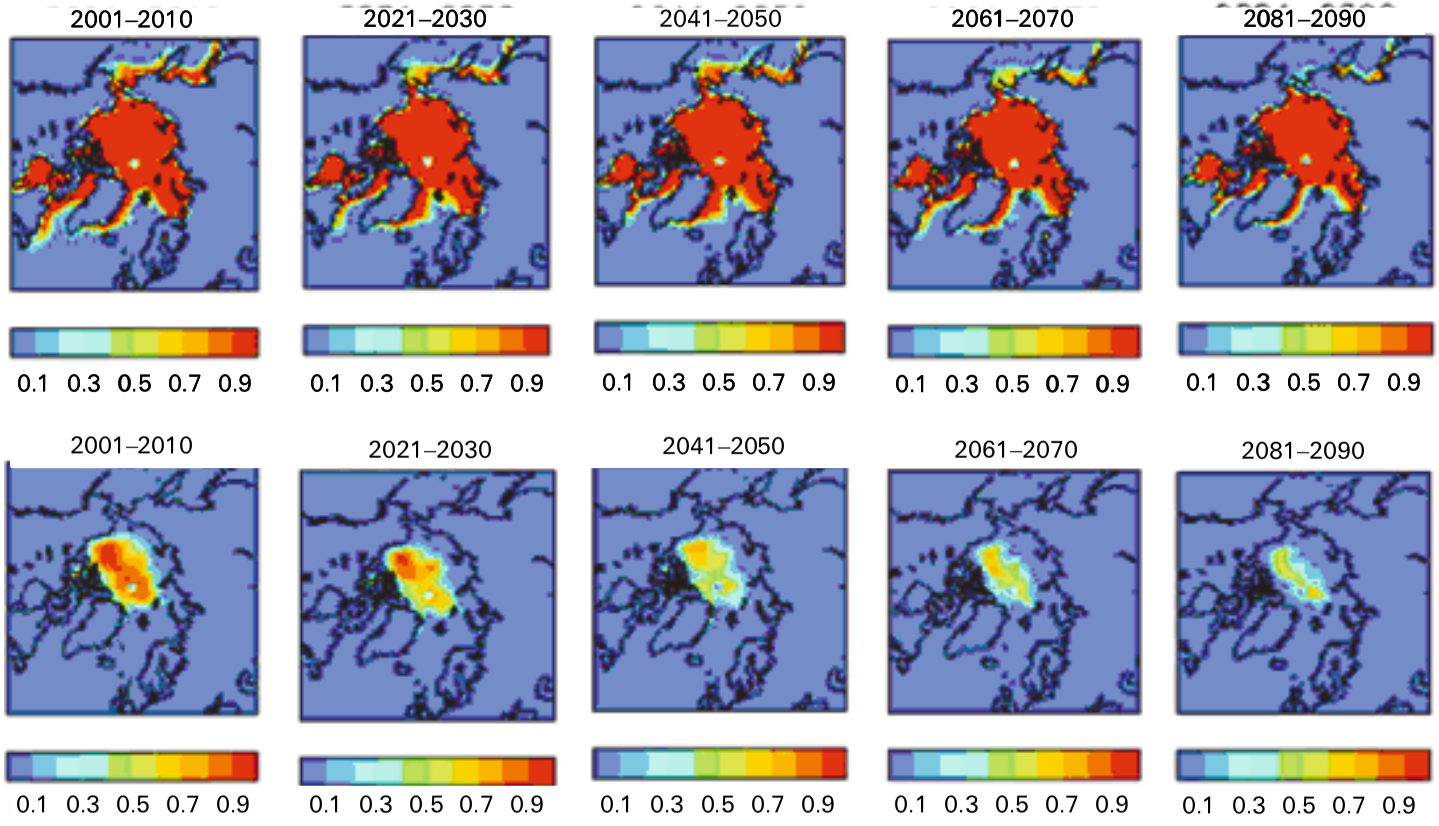

Figure 7.15. HadCM3-modelled northern hemisphere sea ice concentrations in winter (*upper panels*) and summer (*lower panels*). The results shown here are using the IPCC SRES B2 emission scenario. The color code below gives ice concentration (© Crown copyright, published by the Met Office, courtesy Dr. Howard Cattle).

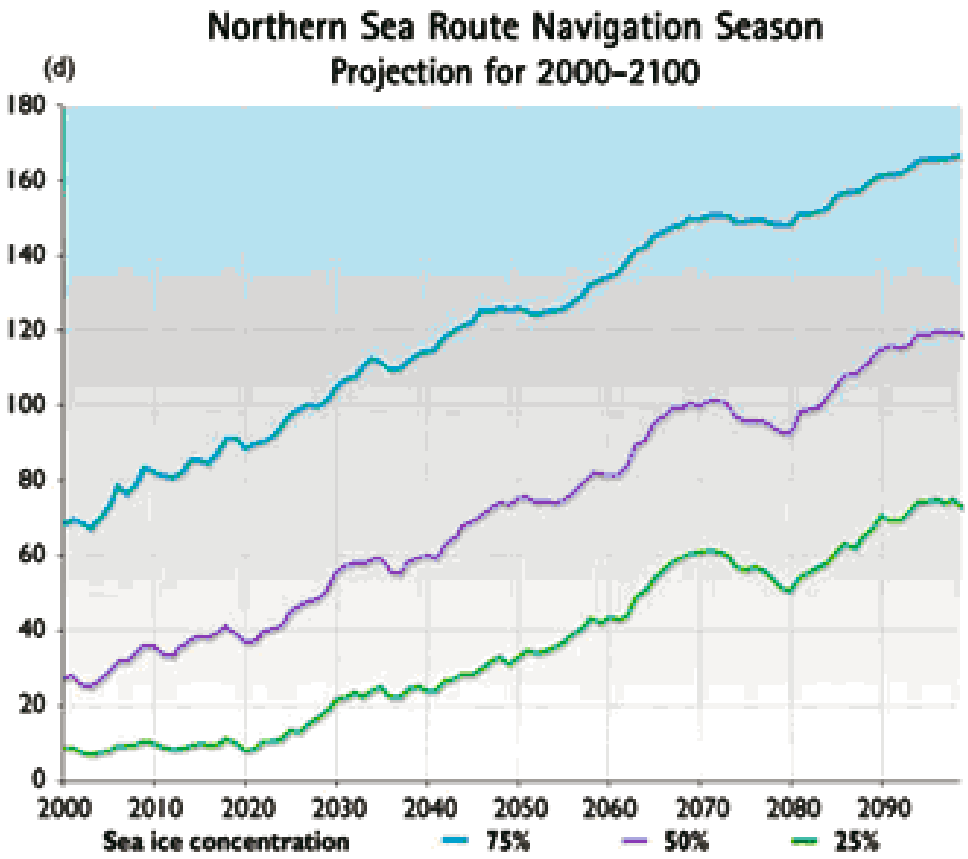

Figure 7.16. Projected changes in the navigation season for the Northern Sea Route in the 21st century, based on five-model output. The curves represent ice concentration thresholds: 25%, 50% and 75%. *Source*: ACIA (2004).